Numerical Modelling of Reinforced Concrete Bridge Pier under Artificially Generated Earthquake Time-Histories

by

Van Bac Nguyen

A thesis submitted to
The University of Birmingham
for the degree of
DOCTOR OF PHILOSOPHY

Department of Civil Engineering
The University of Birmingham
June 2006

ABSTRACT

Numerical Modelling of Reinforced Concrete Bridge Pier under Artificially Generated Earthquake Time-Histories

This thesis focuses on the numerical generation of artificially generated earthquake time-histories (AGETH) fitting to a design response spectrum as well as the numerical modelling of reinforced concrete piers under monotonic, cyclic and earthquake loadings. In particular, attentions are mainly focused upon the validation of finite element (FE) smeared crack models and the minimum representative number of AGETH required for non-linear dynamic analysis.

A number of AGETH compatible with a Eurocode 8 (EC8 ENV and prEN versions) response spectrum are randomly generated using SIMQKE software and the average generated spectrum compares well with the EC8 response spectrum. A parametric study is then carried out on effects from both the program parameters and properties of AGETH to establish issues on choosing suitable sets of AGETH to be used in dynamic analysis and design.

Two FE smeared crack models, named Multi-crack and Craft, are used to analyse RC bridge piers under the AGETH. They are first verified against various cases of concrete and RC structures under monotonic and cyclic loadings. Comparisons with experimental results are performed to examine the applicability and advantage of the two models. The results obtained are in good agreement with experimental data available. Comparisons with the experimental results for cyclic loading show that, though the Multi-crack model is able to capture some key responses, the damping and unloading stiffness have been overestimated. In contrast, Craft model is capable of capturing the hysteretic behaviour of RC bridge piers under cyclic loading.

In an attempt to gain further analytical understandings about the localised problem that may cause convergence difficulties and mesh-dependency to FE static nonlinear analysis, an analytical

solution for concrete and RC beams is developed and validated against the FE results of the smeared crack models and an analytical model published in literature.

The FE smeared crack models are then used in the analysis of RC bridge piers under different sets of twenty AGETH. Several techniques including Fourier analysis, normalised cumulative spectrum, energy dissipation and damage index as well as probability theory are applied to quantify the structural response of the RC bridge piers for various sets of AGETH. Based on these assessments and the convergence of the representative response for different sets of different numbers of AGETH, a minimum representative number of AGETH are proposed for a non-linear dynamic analysis. In particular, it is found that the number of AGETH from 6 to 11 may be sufficient depending on the confidence band width from the mean of all damage responses. Effects of several parameters of the earthquake and structure such as earthquake amplitude, earthquake duration, soil condition, viscous damping, seeds of random number for earthquake generation, pier height, the presence of axial load and the amount of steel reinforcement to the response and damage of the bridge pier are investigated in the parametric study part. Throughout this study, with similar results have been obtained when using the same set of AGETH in different orders and, in some cases, with completely different sets of AGETH, the proposed number of artificial earthquake time-histories required for non-linear dynamic analysis is thus validated.

DEDICATION

This thesis is dedicated to:

my beloved Mum Phú, Dad Sang
my beloved brothers Tỉnh, Nam and sister Hà
my beloved wife Thảo and newborn son Nam Anh

ACKNOWLEDGEMENTS

I would like to express my deepest thanks foremost to Professor Andrew Chan for the invaluable support, inspiration, guidance, discussions and comments made throughout this research. Andrew, I am very grateful for the precious moments you shared with me to discuss research problems whenever and wherever it is possible, especially during our trips to the conferences in Glasgow, Cardiff, and Bristol. It is an unforgettable time in my memory of your discipline and kindness.

I should like to express my thanks to Dr Anthony Jefferson (University of Cardiff, UK) for supporting me to use his recent and new concrete models and for fruitful discussions in using them. Thanks also go to Prof Les Clark and Dr David Chapman for reviewing, helpful comments and guidance in construction of the thesis during my yearly reviews (2002, 2003, and 2004).

I should like to thank the examiners, Prof Aleksandar Pavic (University of Sheffield, UK) and Dr Gordon Little (University of Birmingham, UK), for their useful comments on the thesis and valuable feedback from the PhD viva examination.

I am indebted to all those who have assisted me in many ways towards my research:
Dr Edmund Booth (Edmund Booth Consulting Engineer, UK), Dr Julian Bommer (Imperial College, UK) and Dr Varpasuo Pentti (Fortum Coporation, Finland) for helpful discussions in the generation of artificial earthquakes,
Dr Jens Ulfkjaer (ETH Zurich, Switzerland) for sending me his PhD thesis and explaining things related to his analytical model for concrete beams,
Dr Giang Nguyen (New Mexico University, USA) for many stimulating discussions in fracture mechanics during his PhD time at University of Oxford,
Prof Riyadh Hindi (Bradley University, USA) for helping me in using the damage index for earthquake loading,
Dr Gaetano Elia (Polytechnic University of Bari, Italy) for sharing experiences in dynamic analysis during his time in Birmingham, and

Dr Aung Shein (University of Birmingham, UK) for many interesting discussions in the analytical solution for concrete beams and the probability theory used for the number of artificially generated earthquake time-histories.

My gratitude is also due to my sponsors: the Vietnamese government for financial supports in my MPhil study and a part in my PhD study, the UK Universities for ORS scholarship and the Department of Civil Engineering for PGTA scholarship during my PhD study. This thesis cannot be completed without their supports.

I would like to thank Doreen Hammond, my "English Mum", for always being love and care to me since I met her in my very first days in the UK. Thanks also are due to Rachael and Alex Royal for the good friendship and accompanying enjoyable activities during the four years in Birmingham.

I would like to express special thanks to my parents, brothers and sister, and my parents-in-law for their love, encouragement and support during my away years from home. Last but most importantly, I am deeply indebted to my wife Thanh Thảo and my newborn son Nam Anh for their endless patience, love, understanding and tremendous encouragement. Apologies from the bottom of my heart should go to them for the time I could not be along with them since my wife went home with pregnancy and then gave birth to Nam Anh in Vietnam.

CONTENTS

Chapter 6 Analytical solution for non-linear flexural concrete beams

Chapter 7 Response of bridge pier and number of artificial time-histories required for non-linear dynamic analysis

LIST OF SYMBOLS AND ABBREVIATIONS

List of common symbols

E	Young's modulus
f_c	maximum compressive strength
f_t	maximum tensile strength
f_y	yield strength of steel reinforcement
G	shear modulus
G_f	fracture energy per unit area
H	hardening parameter
l_c	characteristic length
ε_c	strain at maximum compressive strength
ε_t	strain at maximum tensile strength
ε_0	strain at end of softening curve
ρ	steel reinforcement ratio
ξ	viscous damping ratio
ν	Poisson's ratio
ω	natural circular frequency

List of symbols used in Chapter 2

C_{lsf}	local compliance matrix
D	standard stiffness matrix of elastic constants
D_L	local elastic constitutive matrix
e	local strain $e = [e_r, e_s, e_t]^T$
f_s	equivalent fracture stress
$F(\ )$	yield function
g_i	strain relative to a contact surface
$H_f(\ )$	contact function
I	identity matrix

I_1	first invariant of stress tensor
J_2	second invariant of deviatoric stress tensor
J_3	third invariant of deviatoric stress tensor
m_g	slope of the contact surface
N_i	stress transformation
r	"roughness-cohesion" factor
r_ζ	shear intercept to tensile strength ratio for local damage surface
s	local stress $s = [s_r, s_s, s_t]^T$
β	shear retention factor
ε_c	strain at maximum compressive strength
ε_t	strain at maximum tensile strength
ε_0	strain at end of softening curve
ε	global strain $\varepsilon = [\varepsilon_{xx}, \varepsilon_{yy}, \varepsilon_{zz}, \varepsilon_{xy}, \varepsilon_{yz}, \varepsilon_{xz}]^T$
ε^e	elastic strain
ε^p	plastic strain
λ	plastic multiplier
μ	friction factor
μ_ε	asymptotic friction factor
σ_1, σ_2, σ_3	first, second, third principal stresses
σ	global stress $\sigma = [\sigma_{xx}, \sigma_{yy}, \sigma_{zz}, \sigma_{xy}, \sigma_{yz}, \sigma_{xz}]^T$
$\bar{\sigma}$, $\bar{\varepsilon}$	equivalent uniaxial stress and strain
$\bar{\varepsilon}^p$	equivalent uniaxial plastic strain
ζ, ρ, θ	Haigh-Westergaad coordinates
$\phi_{int}(\,)$	interlock function
$\phi(\,)$	damage function
$\Phi(\,)$	plastic potential function
ψ	dilatancy coefficient

† The superscript *T* represents matrix transpose

† The subscript *i* represents the crack plane number

† The subscript *j* represents a number of active cracks in the crack plane number *i*

† The subscript *x*, *y*, *z* represent the axes of the global coordinate

† The subscript *r*, *s*, *t* represent the axes of the local coordinate

List of symbols used in Chapter 3

A_i	amplitude of sinusoidal waves at *i*th frequency
$\lvert F(\omega)\rvert$	Fourier amplitude
$G(\omega)$	power spectral density function
G_0	ground intensity
$I(t)$	Intensity function
$r_{s,p}$	peak factor
S_v	velocity response spectrum
$x(t)$	sinusoidal waves or artificial earthquake ground motion
δ_Ω	dispersion of the central frequency
ξ_g	viscous damping for the ground
ω_g	natural circular frequency of the ground
Ω	central circular frequency

† The subscript *s* represents the duration

† The subscript *p* represents the probability factor

List of symbols used in Chapter 4

A_{gauss}	Elemental area
b_e	element thickness
$detJ_i$	Jacobian of the transformation between the local, isotropic coordinates and the global coordinates
V_{gauss}	Elemental volume
w_i	weight factor
α	model modification factor
ε_n	normal uniaxial strain
σ_n	normal uniaxial stress

List of symbols used in Chapter 6

b	beam width
h	beam depth
F_{ci}	compressive force in concrete
F_{ti}	tensile force in concrete
F_{si}	tensile force in steel reinforcement
I	moment of inertia
$M_{1,i}$	moment at cross-section 1
$M_{2,i}$	moment at cross-section 2
P_i	applied load
$y_{1,i}$	deflection at cross-section 1
$y_{2,i}$	deflection at cross-section 2
w_c	softening zone width or crack band width
δ_{cr}	critical crack opening
ε_{ci}	compressive strain at the extreme surface fibre
ε_{ti}	tensile strain at the extreme surface fibre
ε_t	tensile strain at an internal fibre
ε_{tp}	tensile strain at the maximum tensile strength
κ_i	curvature
$\kappa_{1,i}$	curvature at cross-section 1
$\kappa_{2,i}$	curvature at cross-section 2
σ_t	tensile stress at an internal fibre
σ_{ti}	tensile stress at the extreme surface fibre

† The subscript *i* represents the stage *i* of strain increment

† The subscript *c* represents compression

† The subscript *t* represents tension

List of symbols in Chapters 7 and 8

C	damping matrix
D	damage index
E	energy dissipation
$f'_{\max}$	maximum frequency of an earthquake
K	stiffness matrix
M	mass matrix
n	number of artificial earthquake time-histories
N	number of different orders of n artificial earthquake time-histories
P	applied load
Q_y	yield strength of the structure
T_n	structural period of nth vibration mode
α, β	mass, stiffness Rayleigh damping factors
β	structural parameter dependent on several structural parameters (used in damage index formula only)
Δ	standard error of estimation
Δt	time step
δ	dispersion
δ_m	the maximum displacement reached in the current cyclic loading
δ_u	the ultimate displacement under monotonic load
κ	mean number of damage responses
μ	mean
ξ_n	viscous damping ratio of nth vibration mode
σ	sigma ($\sigma = \delta / \sqrt{n}$)
ω_n	natural circular frequency of nth vibration mode
$\int dE$	cumulative dissipated energy

List of abbreviations

CBM	crack band model
CDF	Cumulative Distribution Function
EC8	Eurocode 8
DIH	damage index histories
FCM	fictitious crack model
FE	finite element
FEM	finite element method
LEFM	linear elastic fracture mechanics
MC82	LUSAS Multi-crack model (model 82)
MDOF	multiple-degree-of-freedoms
EDH	energy dissipation histories
NDCS	normalised displacement cumulative spectra
PMF	Probability Mass Function
POD	plane of degradation
RC	reinforced concrete
RS	response spectrum/spectra
SDOF	single-degree-of-freedom
2-D	two-dimensional
3-D	three-dimensional

LIST OF PUBLICATIONS

Nguyen, V.B., and Chan, A.H.C., (2005). Comparisons of smeared crack models for reinforced concrete bridge piers under cyclic loading. Proceedings of the 13th Annual ACME Conference, University of Sheffield, England, UK, 123-126.

Nguyen, V.B., and Chan, A.H.C., (2005). Smeared crack models for reinforced concrete bridge piers under cyclic loading. Proceedings of the Society for Earthquake and Civil Engineering Dynamics SECED Young Engineers Conference, University of Bath, Bath, UK. (CD-ROM)

Nguyen, V.B., and Chan, A.H.C., (2004). Comparisons of crack models for concrete beams under monotonic loading. Proceedings of the 12th Annual ACME Conference, University of Cardiff, Wales, UK.

Nguyen, V.B., Chan, A.H.C., (2004). Non-linear analysis for reinforced concrete structural members under randomly generated artificial earthquake-like ground motion. Proceedings of the 5th International PhD Symposium in Civil Engineering, 16-19 June, 2004, Delft, the Netherlands. Vol. 2, 961-969. A. A. Balkema Publisher, London.

Nguyen, V.B., and Chan, A.H.C., (2003). Some observations from linear time stepping dynamic analysis and non-linear analyses for RC structures. Proceedings of LUSAS Annual Conference for Industrial Applications, the Institution of Structural Engineers, London, UK.

Nguyen, V.B., and Chan, A.H.C., (2003). Preliminary numerical analysis of bridge piers under randomly generated artificial earthquake-like ground motions. Proceedings of the 11th Annual Association of Computational Mechanics in Engineering (ACME) Conference, University of Strathclyde, Glasgow, UK, 141-144.

Publications in preparation

Smeared crack models for reinforced concrete bridge piers under artificially generated time-histories. (Journal Paper)

The influence of artificial earthquake and structural characteristics on the seismic response of RC bridge piers. (Journal Paper)

The number of earthquake records required for non-linear dynamic analysis of RC bridge piers. (Journal Paper)

A new analytical solution for cracked reinforced concrete beams. (Conference Paper)

Generation of artificial time-histories fitting to an EC8 response spectrum by using SIMQKE program. (Conference Paper)

Non-linear dynamic responses of RC bridge piers under artificially generated earthquake time-histories. (Conference Paper)

CHAPTER 1

INTRODUCTION

1.1 BACKGROUND AND AIMS OF THE RESEARCH

Strong earthquakes can immediately cause very dangerous effects such as ground shaking, surface faulting, ground failure and tsunamis which can cause the collapse of buildings, bridges, highways, fires, spills of hazardous chemicals from nuclear plants and severe floods. In recent years, more strong earthquakes have often occurred resulting in heavy death tolls with many injured and homeless. For example, the death toll is about 87,000 people in the Kashmir earthquake (Pakistan, India, 2005); 286,000 people in the Indian Ocean earthquake and tsunamis (outside Indonesia, 2004); 31,000 to 41,000 people in the Bam Earthquake (Iran 2003); and 20,000 people in the Gujarat earthquake (India 2001). Intense earthquakes not only cause death and injury to people, damage to buildings, and then destroying the socio-economic substructure, but also be able to create psychological effects and diseases lasting for years on societies. Therefore, it is not surprising that a lot of research is recently carried out to model and improve the scientific understanding of earthquake engineering and structural responses.

Apparently, earthquake engineering is one of the most visible aspects which can be easily illustrated due to the extent and variety of structural damage in earthquakes. Also it is always necessary to understand the structural behaviour and structural performance during earthquakes, as well as to validate theoretical and experimental research on structural components and structural systems in the field of earthquake-resistant design. In practice, this knowledge is translated into some well established code provisions in the world such as USA codes, Japan Society of Civil Engineering code, and EU code. Therefore, there is a large number of the recent research focusing on the field of earthquake engineering, and a large portion of them are about earthquake resistance of reinforced concrete (RC) structures.

In the analysis of earthquake resistance of structures, several methods are applicable for the structural analysis of RC structures under seismic excitations such as time integration dynamic methods (Clough and Penzien 1975) or response spectrum method (Newmark and Hall 1982). The differences between the methods lie in the way they incorporate the seismic input and in the idealisation of the structure. In most of seismic codes, for simplicity, the conventional procedure for seismic design is based on the elastic response spectrum, which represents the earthquake-like ground motion, and structures are modelled as single-degree-of-freedom systems. This procedure is quite simple but it is only applicable for elastic quasi-static analysis and cannot provide insight to the dynamic response of structures, especially structures with irregular configuration or important structures such as bridges or nuclear power station. For that reason, most seismic codes would allow the use of time domain dynamic analysis, i.e. time integration dynamic analysis, by numerical integration of the differential equations of motion. However, in order to use the time domain dynamic analysis, an input earthquake motion is always required. Therefore, many models for generation of earthquake-like ground motion have been put forward by various researchers in an effort to provide a means to extrapolate earthquake time-histories from available seismic data or indirectly from an elastic spectrum (e.g. Housner 1964, Gasparini and Vanmarcke 1976, Papageorgiou 2000).

Strong earthquake-like ground motions are generated based on the main seismic-ground motion characteristics such as total energy and frequency ranges which can be provided from real earthquake records or from response spectra in practical codes. Because of the paucity of real recorded earthquakes for many particular regions, the most straightforward procedure is to generate earthquake time-histories compatible with a target spectrum. However, there has been relatively little published guidance in the literature and in seismic design codes on the subject of generating and selecting artificial earthquake time-histories compatible with the design spectrum. Therefore, one of the objectives of this research is to generate a set of time-histories records compatible with a target response spectrum to be used in numerical time stepping analysis for non-linear dynamic analysis of reinforced concrete structures. Through this, the study attempts to present the issues involved and offer some insights as well as some guidance for generating and selecting artificial time-histories for either research or practical design. In addition, as the

Eurocode 8 (EC8) is going to be adopted as the definitive seismic code of the European Union, this should be an important event for either research or practical design. Thus, both the ENV (ENV 1998-1: 1996) and the EN (prEN 1998-1:2004) EC8 response spectra are employed as target response spectra for generation of artificial earthquake time-histories in this thesis.

Under general loading, or earthquake loading in particular, the response of a structure depends not only on the characteristics of the loading, but also on the material behaviour of the structural material itself. In reinforced concrete structures, the behaviour of concrete material is very complex and there has been a vast number of research studies carried out to develop models to simulate it. Amongst different models, stress-strain constitutive models are the most popular as they provide more realistic representation of concrete behaviour such as stress-strain relationship, and non-linear behaviour in cracking and crushing; and they have been used in modelling of the structure based on the computationally powerful method, the Finite Element Method. In constitutive modelling of concrete materials, it is known that either plasticity-fracture or plasticity-fracture-damage models are required in order to simulate concrete behaviour well (Jefferson 1999, 2002a, 2003a). In literature, however, no one constitutive model is yet able to properly describe all aspects of non-linear concrete behaviour because of the complexity of multi-axial behaviour of concrete. In addition, not many constitutive models have been successfully implemented into engineering practice to deal with both complex RC structures and earthquake loadings. Therefore, another important objective of the research is to employ two of the most recently developed constitutive models, one based on the plasticity-fracture approach, namely Multi-crack model (Jefferson 1999) and the other based on plasticity-fracture-damage approach, namely Craft model (Jefferson 2003a, 2003b), for modelling concrete and RC structures under different types of loading. In this thesis, these models are validated against experimental data for concrete, RC beams and bridge piers under monotonic and cyclic loadings before applying them to artificially generated earthquake loadings.

In concrete material, strain-softening problem is a common phenomenon (Hillerborg *et al.* 1976, Bazant and Oh 1983). This is also considered in the constitutive models used in this study, based on continuum mechanics. Strain-softening can induce localised instabilities in the numerical

procedure and consequently, non-unique solutions or mesh-dependency problems for numerical analysis (Crisfield 1982, Zienkiewicz and Taylor 1991, Crisfield 1996), and thus use of classical continuum mechanics in this case has been proved to be inadequate (Comi 2001, Jrasek and Bazant 2002). In an attempt to avoid mesh dependency problem, the fracture energy provisions of crack is used (Hillerborg *et al.* 1976). In the smeared cracking approach, cracking is assumed to be spread over a 'numerical' fracture process zone which is numerically or mathematically equated the characteristic length of an element. As this characteristic length is related to the adopted finite element size, the spurious mesh dependency can be eliminated (Bazant and Oh 1983, Oliver 1989). Due to these softening-related problems, the identification of model parameters and non-linear procedures play a crucial part in the validation and application of the models. Thus, in this study, special interests on strain-softening problems are investigated based on the models used, especially when using the models for 2-D plane stress problems because the way the constitutive models are implemented in the LUSAS software used. In addition, in order to gain more understandings about the effect of localised problem to the structural behaviour (e.g. the post-peak moment-curvature and load-deflection responses, softening zone width, and stress and strain distributions in this softening zone width), an analytical model proposed by the Author is presented and validated against the numerical and experimental results for concrete and RC beams.

Today's seismic design of buildings is an international challenge that demands consideration of accuracy, speed and cost of the analysis. Computational tools have been developed to accurately obtain seismic responses and speed up the seismic design process. However, attentions should be paid to RC bridges or RC bridge piers in particular, as they are important civil structures. Seismic design of RC bridge piers is increasingly performed using dynamic analysis in the time domain, where the responses of the structure to appropriately selected time-histories is strongly dependent on the characteristics of the earthquake ground motions. Besides, the dynamic effects that arise from the random ground motions should be taken into account for the characterisation and the modelling of the non-linear and damage behaviour of RC bridge piers through its material models. However, seismic applications of finite element material models have not been widely used for such investigations due to technical challenges in implementing them into non-linear

dynamic analysis. As a result, very little work has been done into the non-linear dynamic response and damage behaviour as well as their quantitative measures for RC bridge piers under earthquake time-histories (Kwan and Billing 2003, Hindi and Sexsmith 2004). Therefore, the non-linear dynamic response and damage are also pursued in this study, with the use of non-linear material models for the analyses of RC bridge piers under artificially generated time-histories.

In non-linear dynamic analysis, there is always been questions on the number of time-histories, which are representative of all possible expected earthquake sources with roughly the same magnitude, to be used in the analysis. This number is controlled by the degree of the scatter of structural responses which are dependent on the characteristics of the selected time-histories. The number of time-histories required for use in the analysis of a structure is subject to much contention, but there has been a very little research into it perhaps due to great challenges in selecting suitable time-histories and material models to provide realistic representation of non-linear responses. A previous research in literature (Shome *et al.* 1998) proposed an example number of records used in practice based on an acceptable confidence used in Statistics. However, as their research is based on a simplified structure (e.g. a MDOF system) and analytically phenomenological material models, it did not hold particular well for the response in terms of dissipated hysteretic energy, and thus the number of records. This does, however, essentially mean that if an accurate presentation of time-histories for an earthquake event and an accurate material model are used for the structure it would possibly be able to give a better representative number of time-histories required for the dynamic analysis. The author therefore decided to use the artificially generated earthquake time-histories and the modern constitutive material models chosen (Multi-crack and Craft models) for the non-linear dynamic analysis. Several techniques including Fourier analysis (Bathe 1982), cumulative spectrum of responses (Barenberg 1989), dissipated energy (Gosain *et al*. 1977, Banon *et al*. 1981), and damage index (Park and Ang 1985, Park *et al*. 1987) are employed to deal with the numerical results obtained in order to find a minimum representative number of time-histories required. In addition, a great number of parametric studies from both the earthquake and structural characteristics to

sufficiently confirm the breadth of the conclusions made are always required. These are the principal aims of the current research.

In this study, the non-linear dynamic analysis is limited to RC bridge piers and based on plasticity-fracture model as the other model which based on plasticity-fracture-damage theory has difficulty in implementation procedures. The actual results using different concrete material model could be different. However, as the aims of this research is not to carry out exactly quantitative measures, but rather qualitative ones of the same structure under different time-histories, therefore, it is believed that the minimum number of earthquakes required for a particular confidence requirement should remain relatively similar for other models.

In summary, the main objectives of the research are:

(i) to generate and select suitable sets of artificial time-histories for non-linear dynamic analysis,

(ii) to examine the models for concrete materials in finite element modelling of concrete and reinforced concrete structures under monotonic and cyclic loadings,

(iii) to propose an analytical solution for non-linear flexural behaviour of concrete and RC beams,

(iv) to evaluate the response and damage of RC bridge piers under artificial time-histories and in particular, represent a minimum necessary number of time-histories required for a non-linear dynamic analysis, and

(v) to study the influence of several parameters of the material model, earthquake and structural characteristics to the structural response and damage.

1.2 OUTLINE OF THE THESIS

The thesis consists of 9 chapters beginning with this introductory chapter, stating the background and research aims as mentioned above. In this thesis, for the reader's convenience, the literature reviews is not presented in a separate chapter like many others, but included in each chapter regarding their specific problems. The literature reviews are focused on

(i) the mechanical behaviour and constitutive models for concrete material,

(ii) the generation of earthquake time-histories,

(iii) the application of constitutive models for analysing reinforced concrete bridge piers under earthquake time-histories,

(iv) the analytical approach for predicting non-linear flexural behaviour of concrete structures, and

(v) the recommended minimum number of earthquake time-histories required for non-linear dynamic analysis

The starting point of Chapter 2 is a brief review of the mechanical behaviour of concrete and the constitutive modelling of the material. Emphasis here is placed on simulating faithfully important mechanical features of concrete material in the constitutive modelling, especially using two major approaches: plasticity-fracture and plasticity-fracture-damage models. Alongside with this review are critical discussions on the choice of concrete models for the research, which leads to the presentation of the theoretical background of the models.

Chapter 3 also begins with a brief literature review on the generation of earthquake time-histories, especially on main theoretical aspects of the generation of artificial time-histories compatible with a seismic response spectrum using the program SIMQKE (Gasparini and Vanmarcke 1976). Next, a number of artificial time-histories fitting to the Eurocode 8 design spectrum (from the ENV (ENV 1998-1: 1996) and the EN (prEN 1998-1:2004) versions) are randomly generated and compared with EC8 requirements. A comprehensive study on the effects of program parameters and earthquake characteristics to the generated earthquake time-histories are carried out in order to select suitable sets of artificial time-histories for the subsequent research.

The validation of the two proposed concrete models, namely Multi-crack model (Jefferson 1999) and Craft (Jefferson 2003a, 2003b), against experimental data (Carpinteri 1989, Ozbolt and Bazant 1991) for un-notched concrete beams under monotonic loading is shown in Chapter 4. Also in this chapter, the modification of the fracture energy used in the Multi-crack model for 2-

D plane stress problems is implemented as, in this model the fracture energy is only implemented for 3-D problems.

In Chapter 5, the two concrete models are examined against the experimental results for RC beams which were tested under monotonic loading (Bresler and Scordelis 1963, Carpinteri 1989). The detailed behaviour on the capability of the two models in predicting the flexural and shear failure of RC beams is discussed. In order to provide a better understanding of the use of these models in practical applications, some main features of non-linear solution strategy, effects of numerical approximation, and FE mesh configuration are also investigated. Following this study, the two models are applied to a RC bridge pier under cyclic loading and their results are compared with experimental results (Pinto 1996). Subsequently, some critical comments are made concerning the use of the models for cyclic loading, or earthquake-like dynamic loading in general.

In Chapter 6, a new analytical solution for non-linear flexural behaviour of concrete and reinforced concrete beams is presented to provide some more understandings about strain-softening problems in concrete beams, of which the finite element models sometimes faces mesh-dependency problems. The review briefly shows the development of an analytical model for predicting the non-linear behaviour of concrete beams, particularly in strain-softening problems in tensile concrete and effects of structural size. In order to capture the moment-curvature and load-deflection responses of concrete beams, the proposed analytical model employs the beam theory and the assumption of softening zone at mid-section area of the beam from the crack band width model (Bazant and Oh 1983), in which the stress-strain relationships are given in either linear or bilinear forms. The analytical results are verified against another analytical model published in literature (Ulfkjaer *et al.* 1995), numerical and experimental results for various cases of concrete and RC beams.

Chapter 7 is devoted to the non-linear dynamic response of a RC bridge pier and, in particular, the minimum representative number of artificial time-histories required for the analysis. It begins with a review on the recommended number of earthquake time-histories and application of FE

material models for seismic response analysis to show why the research in this area is greatly necessary. Main procedures of a non-linear dynamic analysis and subsequently the numerical results of the RC bridge pier using the Multi-crack model under a set of 20 artificially generated earthquake time-histories (Chapter 3) are presented. Based on these numerical results, several techniques including Fourier analysis, normalised cumulative spectrum, dissipated energies and damage indices, and some basis of statistics and probability theory are employed to partially understand the responses and to find a minimum representative number required for the analysis.

Chapter 8 is mainly devoted to the parametric study and validation of the minimum representative number of artificial time-histories required for non-linear dynamic analysis. In order to assess the accuracy of the finite element integration, the influence of some principal parameters such as time step, element mesh, numerical damping and viscous damping are studied first. In the parametric study, the influence of a number of parameters concerning earthquake and structural characteristics on the structural responses, especially on the degree of damage, are investigated. In each parametric study, a set of twenty artificial time-histories, which were generated fitting to the EC8 response spectrum (prEN 1998-1:2004), are employed. As different number of non-linear dynamic analyses (from the same set of time histories) are used throughout this parametric study, the minimum representative number of time-histories required for the analysis which was suggested in Chapter 7, are validated.

In the last chapter, conclusions are drawn and further studies are proposed.

CHAPTER 2

CONCRETE MATERIAL MODEL

2.1 INTRODUCTION

Work on developing non-linear finite element models for concrete structures has been on-going for over thirty years and major developments have been carried out in the constitutive models used for simulating concrete. However, no one constitutive model is yet able to properly describe all aspects of non-linear concrete behaviour and, also, no one model type has been generally accepted. One reason for this is, undoubtedly, the complexity of multiaxial concrete behaviour. In addition, although there have been a lot of models published, not many constitutive models have been successfully implemented into engineering practice to deal with either complex structures, i.e. reinforced concrete ones, or complex loadings, i.e. earthquake ones. Further validation and application of the concrete material models is therefore needed.

A brief review on the concrete material behaviour and then an overview on the constitutive modelling of concrete along with a critical discussion on the choice of models for the current research are first presented in this chapter. The following section presents the theoretical background of the models considered in this research.

2.2 A BRIEF REVIEW OF CONSTITUTIVE MODELLING OF CONCRETE

In this section, some important mechanical features of concrete material are first summarised in order to provide a basic background for the review and further understandings on the constitutive modelling of concrete in the following sections. It is followed by a brief review on the constitutive modelling of concrete material. Discussions on the choice of models for this research are presented next.

2.2.1 Mechanical behaviour of concrete

Concrete material parameters such as compressive strength, elastic modulus, tensile strength, and fracture energy may be defined from standardised tests. Available experimental data describe the response of concrete subjected to uniaxial compressive and tensile loadings as well as multiaxial loadings. Experimental testing of plain and reinforced concrete elements may be used to characterise the response of plain concrete subjected to loading in shear.

2.2.1.1 Uniaxial behaviour

In uniaxial direct compression, five different deformational zones had been outlined by Mehta and Monteiro (1993) as shown in Figure 2.1. The uniaxial compressive behaviour of concrete under increasing strain is essentially linear elastic, with microcrack in the transition zone (the zone in the immediate vicinity of the coarse aggregate particles, known to be the weakest link in this composite material with cracks usually occurring at this zone) remaining nearly unchanged, until the load reaches approximately 30% of the maximum compressive strength f_c (Zone A). In the second zone, loading which leads to compressive stress between $0.3 f_c$ and $0.5 f_c$, results in some reduced material stiffness (Zone B) due to a significant increase in crack initiation and growth in the transition zone. The third zone is between $0.5 f_c$ and $0.75 f_c$, results in further reduction in material stiffness (Zone C). Here the reduced stiffness is a result of crack initiation and growth in the cement paste and of the development of unstable crack propagation that continues to grow. Beyond this stress level, between $0.75 f_c$ and f_c, is the fourth zone (Zone D) in which the compressive strain increases under constant loading. This results from spontaneous crack growth in the transition zone and cement paste as well as from the consolidation of microcracks into continuous crack systems. Further loading results in reduced compressive strength (Zone E) and may cause localisation (the phenomenon that under increasing strain, the stress developed follows the softening stress-strain curve). This response is a result of the development of multiple continuous cracks, normally parallel to the direction of applied load. Figure 2.1 also illustrates the behaviour of concrete under uniaxial

cyclic compressive loading. The stiffness of unloading and reloading cycles is approximately equal to the elastic stiffness at small and moderate strain levels, but it is decreasing in high compressive strain.

However, in uniaxial direct tension, the behaviour of concrete observed from experiments is different from that in compression. Figures 2.2, 2.3 and 2.4 show the typical stress-deformation response of concrete subjected to uniaxial tensile deformation under uniaxial monotonic, reserved cyclic and uniaxial cyclic loading. In uniaxial monotonic loading (Figure 2.2), the tensile behaviour is essentially linear elastic until the tensile strength is achieved, and this response corresponds to the initiation of a small number of microcracks remaining nearly unchanged in the transition zone. With further loading on the concrete, stress level reaches the maximum tensile strength, f_t, in concrete and results in reduced stiffness and a significant development of crack propagation in the transition zone and partly in cement paste. Since the existing microcracks remain nearly unchanged under a stress less than $0.6f_t$ to $0.8f_t$, this stress level can be regarded as the limit of elasticity in tension. Loading beyond this stress level results in loss of load capacity. This response corresponds to the development of continuous crack systems in the transition zone and the cement paste. In uniaxial and reserved cyclic loading, unloading and reloading cycles that initiate at tensile strains in excess of that corresponding to the maximum tensile strength occur at a material stiffness that is significantly less than the original material modulus. This reduction in material stiffness within post-peak stage is a result of cracks that remains opening as long as the concrete is carrying tensile stress. Unlike in a compressive test, where splitting cracks are usually parallel to the direction of the compressive stress (Sfer *et al*. 2002, Jansen and Shah 1997) or in the form of a zig-zag band depending on the specimen height (van Mier 1986), the direction of crack propagation in a tensile test is transverse to the stress direction. This results in a reduction of the load carrying area, and therefore after the maximum stress level, unstable crack propagation in tension starts very quick, resulting in the brittle nature of concrete.

The available experimental data for cyclic loading test is usually obtained from test performed that resulted either in tensile failure (Reinhardt *et al*. 1986, Sinha *et al*. 1964) or in

compressive failure (Bahn and Hsu 1998, Sinha *et al*. 1964). Alternatively, Figure 2.5 shows the uniaxial behaviour of concrete under both tensile and compressive cyclic loadings. It can be observed that the unloading and reloading stiffness is approximately equal to the elastic stiffness at small and moderate strain levels, but it is highly inelastic at large strains. There is some degradation of the stiffness in compression at the end of loading but not much, therefore the behaviour is still similar to linear elastic.

As observed from experiments, when concrete reaches its compressive limit there is a general degradation in all directions, whereas in tension the degradation of strength is largely confined to one direction, i.e. the direction normal to the resulting crack. Nonetheless, failure under compression, e.g. crushing or microcracks in concrete, is believed to have extreme effects on the tensile behaviour of concrete through the compression-induced stiffness degradation in tension. However, the stiffness degradation does not happen in tension-compression load reversal. This is because the microcracks, which open under tension loading, will close upon load reversal, resulting in the stiffness recovery in transferring from tension to compression (Figures 2.3 and 2.5).

It is also experimentally observed in concrete under loading that the inelastic strains are permanent both in compression and in tension with small strains (Figures 2.1, 2.3, and 2.4). Therefore the unloading behaviour is substantially elastic and the behaviour is thereby in agreement with the assumptions of plasticity theory, somehow at macroscopic level (Jirasek and Bazant 2002).

Experimental data demonstrates that concrete material exhibits a significant strain-softening behaviour beyond the maximum stress, in both uniaxial tension and compression. The softening behaviour of stress-deformation or stress-strain has been suggested by many investigators to model microcracking and its propagation (Petersson 1981, Hillerborg *et al*. 1976, Bazant and Oh 1983). Furthermore, these models have been employed for evaluation of fracture properties, i.e. fracture energy. However, there is no unique post-peak stress-deformation or stress-strain behaviour (Gopalaratnam and Sah 1985, Ansari 1987). This is

demonstrated in the experiments by Ansari (1987) that in post-peak softening region, stress-strain and stress-deformation responses are not unique. This observation and lack of data on the experimentally observed zone of microcracking and inconsistency of available information on the complete load-deformation response of concrete subjected to uniaxial tension has led to controversial results for fracture properties. Therefore, in finite element modelling, accurate and adequate experimental data are vital to have numerical results close to the real behaviour.

2.2.1.2 Shear behaviour

Concrete exhibits shear deformation in the response and volume changes during shear. In plain concrete, shear forces transfer across the crack plane is achieved primarily through aggregate interlock, the development of bearing forces between pieces of aggregates. This mechanism of shear force transfer implies that the capacity of concrete in shear is determined by the width of the crack opening. Considering shear transfer in concrete specimens with precracked, unreinforced, constant width crack zones, it is experimentally observed that the shear stress-shear displacement relation is essentially dependent on the crack width (Figure 2.6). It also shows that for small crack widths the shear stress versus slip relationship is linear to peak strength of approximately $0.20 f_c$. For increased crack width, the shear stress versus slip exhibits some loss of stiffness at low load levels, but maintains a peak capacity of approximately $0.20 f_c$. Low shear transfer capacity is found between $0.06 f_c$ to $0.09 f_c$ for large crack widths, i.e. greater than 0.8 mm (Laible *et al.* 1977). In reinforced concrete, it was observed from experiment that shear strength and stiffness increase with increasing volume of reinforcement crossing the crack plane with the peak strength of the system limited to $0.30 f_c$ (Figure 2.7). The experimental studies also show that for systems in which crack width is controlled by the tensile response of steel reinforcement crossing the crack plane, the shear stress versus slip relationship exhibits deteriorating stiffness up to the peak load and then softening. It may be explained as due to the fact that the slip is always accompanied by an increase of crack opening and if the opening is restrained (by the steel reinforcement) then a large compressive stress is induced on the crack surface. In addition, the compressive stress

must be balanced by tensile forces in the reinforcement, which are in addition to those needed to balance the applied tensile forces. It is important to note that for these systems in which reinforcement crosses the crack plane, the direct contribution of steel reinforcement to shear capacity and stiffness (dowel action) is minimal at moderate slip levels. Similar results for systems in which steel reinforcement crosses the crack plane are presented by Walraven and Reinhardt (1981). Here peak shear strength, achieved with high volumes of reinforcement crossing the crack plane, varies between $0.26\,f_c$ and $0.32\,f_c$.

2.2.1.3 Multiaxial behaviour

The failure surface (or yield surface, which predicts whether the material responds elastically or plastically) and the evolution of this surface under increased loading are used to characterise the material behaviour in multiaxial loading. Results of experimental investigations have been confirmed that concrete has a fairly consistent failure surface in two- and three-dimensional principal stress space (e.g. Figures 2.8 and 2.10). In two-dimensional loading, the result of the investigation conducted by Yin *et al*. (1989) show a failure surface that is slightly stronger than that developed by Kupfer *et al*. (1969). The difference in these failure surfaces may be due to a number of factors including load rate, conditions of the specimens during testing, preparation of the specimens, properties of the mixes or size effects. Under confined compression, i.e. applying low levels of confining pressure in the third dimension of 5% to 10% of one of in-plane stresses, it shows that a relatively small confining pressure in the out-of-plane reaction can significantly increase the strength of concrete in the plane of the primary loading (data from van Mier (1986), as shown in Figure 2.8). The typical experimental results for concrete indicate that the failure surface in the principal stress space is a deformed cone with three planes of symmetry that all intersect at the hydrostatic axis (Figure 2.9).

Analytical models can be used to characterise the failure surface and the evolution of the failure surface. Two separate kinds of strength envelope should be distinguished: the elastic-limit surface defining the elastic region, and the failure surface characterising the maximum-

strength envelope of concrete (Figure 2.10). The elastic-limit surface is believed to exhibit "cap behaviour" while the failure surface is of open shape (Figure 2.11). Under high compression, the elastic-limit surface expands and gradually opens towards the negative compression axis and finally coincides with the failure surface.

The shape of the failure surface in meridian plane (e.g. the intersections of the failure surface with half-planes that start from the hydrostatic axis) and the deviatoric planes (e.g. planes perpendicular to the hydrostatic axis) are shown in Figure 2.12.

With the assumption of isotropic behaviour, the equations for both surfaces, elastic-limit and failure surfaces, can be expressed in terms of the stress invariants I_1, J_2, and J_3, or in terms of the three principal stresses σ_1, σ_2, and σ_3. The stress invariants are usually expressed in terms of the Haigh-Westergaard coordinates ζ, ρ, and θ, such as $\zeta = I_1/\sqrt{3}$ and $\rho = \sqrt{2J_2}$. For the definitions and expressions of I_1, J_2, and J_3 and ζ, ρ, and θ, one can refer to Appendix 2A or several plasticity books, such as Chen and Han (1988).

The experimental data (Kupfer *et al.* 1969, Yin *et al.* 1989, van Mier 1986, Imran and Pantazopoulou 1996, Salami and Desai 1990) also show that the failure surface is a non-linear function of $\sqrt{J_2}$ and I_1 and that the relationship between them is a function of the ratio of the principal stresses. Similar to these observations, experiments (Kupfer *et al.* 1969, Palaniswamy and Shah 1974) have also shown that the strength and deformation of a concrete specimen is significantly affected by the confining compression. The data from Figure 2.13 illustrate that the axial and lateral strains at failure increase with increasing confining compressive stress. In addition, the axial and lateral strains under confining compression at failure are much larger than those in uniaxial compression. Also, it was experimentally found that the concrete dilatancy is revealed in the volumetric strain versus compression load for concrete tested in biaxial compression (Figure 2.14). Here the dilatancy contributes to the volumetric expansion of concrete (Figure 2.14 or Chen and Han 1988).

2.2.2 Constitutive modelling of concrete materials

The above-mentioned experimental features of concrete behaviour are all of macroscopic nature and cannot always represent what truly happens at the microscopic nature. It is desirable for the above-mentioned macroscopic features of the material behaviour to be reflected in constitutive models for concrete materials. This is because the internal mechanisms that govern the mechanical behaviour of concrete have not been observed directly. For example, the controlling mechanisms such as fracture, slip, friction, crushing, crack bridging, void growth and dilatancy in cracked concrete are not observed directly but indirectly derived from experimental measurements and surface observations (Karihaloo 1995, Etse and Willam 1994). These mechanisms are then developed into mathematical models using the theories of elasticity, plasticity, and damage with certain extrapolations and assumptions. Consequently, all current models have limitations and are able to simulate only certain aspects of behaviour (Jefferson 1999, 2003a). In the constitutive modelling approach, therefore, it will only simulate the macroscopic features of microscopic nature, i.e. micro-cracking, in an approximate manner. However, it is it quite difficult to incorporate all those material behaviours in the constitutive modelling as it needs a good theoretical framework from which to build up all identifiable mechanisms of behaviour. Nevertheless, despite the underlying theories of the constitutive models, the implementation of the models and the practical capabilities of finite element codes for concrete analysis need to be considered.

This section, therefore, will present a brief review on the constitutive models proposed by various researchers and point out their main features and limitations. This focuses on the behaviour features of the constitutive models based on continuum mechanics which are able to capture some of the macrosopic behaviour observed in experiments. Constitutive models such as isotropic and orthotropic total stress-strain, and implicit incremental models (Kupfer and Gerstle 1973, Kotsovos and Newman 1980, Cedolin *et al.* 1977, Buyukozturk and Shareef 1985, Ottosen 1979, Bazant and Tsubaki 1980, Gerstle 1981a, 1981b) are appealing because of their conceptual simplicity and potential ease of implementation. Since the relationships are obtained by direct curve fitting of experimental data, the expressions can become very

complex if accurate models are required (Bazant and Tsubaki 1980). Nevertheless, the models do not provide a natural framework for modelling loading/unloading behaviour in which the plasticity-based model provides a far more nature framework (details on the other constitutive models is well presented in literature through the above references). Therefore, the following review will be devoted on plasticity-based constitutive models.

The plasticity-based constitutive modelling includes two main classes of constitutive models: plasticity-fracture models and plasticity-damage models. The first models use plasticity theory to represent the compressive behaviour of concrete as well as various total and incremental fracture theories to simulate directional cracking on predefined failure plane, or plane of degradation, POD (POD is terminology from Weihe *et al.* 1998) from which a constitutive law is postulated (Owen *et al.* 1983, de Borst and Nauta 1985, Cervera *et al.* 1987, Rots 1988). The complex constitutive behaviour of the material is then obtained by transforming the constitutive relations in the reduced space (2-D plane of degradation) to the 3-D continuum level. This transformation can be of geometric nature (fixed crack models) or based on the principle of virtual work (microplane models). These models use the smeared crack approach to model cracking which includes single fixed crack models, multidirectional fixed crack models, rotating crack models and the closely related micro-plane models. However, none of the above plasticity-fracture models were explicitly developed with a consistent thermomechanical and micromechanical frameworks; and therefore certain aspects of the model formulations were rather ill-defined such as cracking closure behaviour and inelastic unloading/reloading.

The second family of models, which is based on continuum damage mechanics and the thermomechanical theoretical frameworks as well as all aspects of smeared crack models, can provide more formal treatment to the problems relating to plasticity-fracture approach, as illustrated by de Borst (2002). During the past twenty years, there have been major developments in constitutive theories. The following is a small sample of the developments: new damage based models and theories (Krajcinovic 1996, di Prisco and Mazars 1996, Comi and Perego 2001), formulations for combining plasticity and damage (Ortiz 1985, Simo and Ju

1987, Hansen and Schreyer 1994, Ekh and Ruesson 2000), plastic damage models (Klisinski and Mroz 1988, Lubiner *et al.* 1989, Lee and Fenves 1998a, 1998b, Meschke *et al.* 1998, Carol *et al.* 2001a, 2001b, 2001c), thermodynamically damage model (Armero and Oller 2000). In addition, there are many other models based on plasticity and damage, in which there is particular reference to non-local model. In local continuum mechanism, the physical state at a given point in the body is assumed to be completely determined by the material state at the mathematical point, where the quantities of the continuum theory are defined. In smeared crack model, the continuum quantities are assumed to be averaged over a certain volume called a "representative volume element" whose size depends on every material and is proportional to the characteristic length of the material (Bazant and Oh 1983). However, in the non-local model, the effects of the whole body on a material point in the local zone, i.e. strain-softening zone, are taken into account. Details about the non-local models are not included here but can be referred as to a comprehensive review document by Jirasek and Bazant (2002).

Though there have been a lot of models developed based on the two above-mentioned approaches, no one constitutive model is yet able to properly describe all aspects of non-linear concrete behaviour and, also, no one model type has been generally accepted. One reason for this is, undoubtedly, the complexity of multi-axial concrete behaviour, which includes several characteristic features of concrete behaviour (see Section 2.2). It is believed that for a model to be generally acceptable, it will need to be mechanistic, with each identifiable mechanism of behaviour, such as debonding, post-crack friction, surface separation and crushing, being represented by a separate component of a model. These components would build to form a model that simulates the correct characteristic behaviour. Towards this idea, Jefferson (1999) proposed a plasticity-fracture model, namely Multi-crack model, which provides a theoretical framework from which to build a material model for concrete which has the possibility to form complex features of concrete. At this stage, the model, however, does not simulate crushing in compression, the loss of unloading stiffness with increasing fracture strain or hysteresis behaviour with cyclic loading. Nevertheless, the manner in which the model simulates the mechanism of non-orthogonal crack plane formation, i.e. employed PODs, and subsequent frictional behaviour, make it an ideal platform from which to develop a more

comprehensive material model, which does incorporate the above aspects of behaviour. Jefferson (2002a) developed further this plasticity-fracture model to include the effect of compressive crushing to the tensile strength of concrete by using simple local yield functions to represent both compressive and tensile behaviour. The local responses from all active plastic surfaces are coupled in a multi-surface plasticity formulation, which provides the interaction between compressive and tensile behaviour in a natural way. However, this model is still not able to capture some complex behaviour such as cracking closure, stiffness degradation and inelastic unloading/reloading in concrete due to it is based on the plasticity-based framework. It is realised that to accurately simulate all the important characteristics of the mechanical behaviour of concrete, a combination of plasticity and damage theories is required. Thus, Jefferson (2003a, 2003b) has proposed a new model, namely Craft, which employs plasticity, damage and contact theories in a consistent thermodynamic framework in order to simulate all the important characteristics of the mechanical behaviour of concrete including cracking closure and stiffness degradation in concrete. As the above-mentioned multi-crack models (Jefferson 1999, 2002a) and Craft model (Jefferson 2003a, 2003b) are typically representative for the plasticity-fracture approach and plasticity-damage approach, respectively, in a high level of the model development, and are available for the Author to use, they are employed in this thesis for numerical modelling of concrete and reinforced concrete structures. Main features of the theoretical background of these models are presented after the literature reviews.

In detail, any one of the above constitutive models also includes the following important basic features for a constitutive model: plastic behaviours, smeared crack concepts with the concepts of strain-softening behaviour, shear behaviour, and numerical solutions for implementation into finite element codes. Therefore, a brief review on theses features is presented in the following sections.

2.2.2.1 Plasticity theory

The inclusion of plasticity theory can be very useful in simulating concrete behaviour. This theory assumes that concrete behaviour is linear elastic until it reaches a limiting surface, after which perfectly plastic yielding is assumed to occur (Figure 2.10), remembering that cracking is treated separately in concrete fracture concepts. The natural development of the plasticity theory was the application of hardening plasticity theories to concrete modelling. This theory is attractive for a number of reasons. Firstly, the behaviour of concrete in compression is accurately simulated with plasticity theory. This is because, the experimental data show that for a wide range of uniaxial, biaxial, and triaxial stress-strain paths, the inelastic strains are almost permanent, and the unloading and reloading are substantially elastic. This behaviour is thereby in agreement with the assumptions of standard plasticity theory. Secondly, plasticity theory can be coupled with fracture and/or damage theory in a computational framework in modelling concrete in tension.

Numerous forms of yield surfaces have been proposed and can be classified based on either the number of model parameters (Chen and Han, 1988) or on the shape of the surface in principal stress space. The Von Mises and Tresca criteria are two typical examples of one-parameter pressure-independent yield surfaces, which were initially designed for metallic materials and would completely misrepresent the tensile parts of the actual failure envelope for concrete (Jirasek and Bazant 2002). However, the use of these criteria to model the concrete behaviour in compression-compression region could be accepted as the first approximation. Among the two-parameter models, the Drucker-Prager and Mohr-Coulomb surfaces are probably the simplest types of pressure-dependent criteria (Chen and Han 1988). However, one of the shortcoming of the Drucker-Prager surface is that they assume a linear relationship between $\sqrt{J_2}$ and I_1 and the large deviation in tensile region due to the lack of dependence of the deviatoric section, on the Lode angle θ; while one of the deficiency of the Mohr-Coulomb surface is that it is also linear in the meridian plane in both tensile and compressive regions. In contrast, experimental data show that the failure surfaces in meridian plane are to be non-linear (Figures 2.9 and 2.12). Other failure criteria with more than two

parameters for which the models can reproduce experimentally closed failure surfaces e.g. non-linear failure surface in meridian plane and the dependence of the deviatoric section on the Lode angle θ, have been proposed by many researchers such as Ottosen (1977), Murray *et al.* (1979), Hsieh *et al.* (1982), Willam and Warnke (1975), Kang and Willam (1999), Imran and Pantazopoulou (2001), Grassl *et al.* (2002).

In addition, some models assume that the shape of the yield surface remains the same with the elastic region expanding and contracting as a function of load history (Kupfer *et al.* 1969, Chen and Chen 1975, Murray *et al.* 1979). However, by using this approach the plastic strains can be overestimated in tension while being underestimated in compression (Chen and Han 1988). Many models account for variation in the shape of the yield surface that occurs as concrete is loaded from the point of initial inelasticity to the point of maximum load and beyond to the point of minimal capacity. Models that propose variable shaped yield surfaces include that proposed by Han and Chen (1985), Ohtani and Chen (1988), Chen and Han (1988), Zaman *et al.* (1993). Amongst them, the model proposed by Chen and Han (1988) incorporates many of the techniques currently used in development of a concrete yield surface that evolves under a variable load history. This model proposes that at the maximum load, the yield surface appropriately may be defined following the recommendations of any of several researchers (Ottosen 1977, Hsieh *et al.* 1982, Willam and Warnke 1975). The evolution of the yield surface is shown in Figure 2.11.

In modelling the response of concrete, the application of the associated flow rule may not be appropriate because experimental data show that concrete displays shear dilatancy characterised by volume change associated with shear distortion of the material (Figure 2.14). In order to improve modelling of concrete material response non-associated flow models in which the yield and plastic potential functions are not identical, should be used instead. Models which employ this feature include that of Chen and Han (1988), Lee and Fenves (1988a, 1988b), Lubliner *et al.* (1989), Kang and Willam (1999), and Grassl *et al.* (2002).

In the model adopted in this thesis, Craft model (Jefferson 2003a, 2003b), the non-associated flow model used by Lubliner *et al.* (1989) and the variable shaped yield surface recommended by Willam and Warnke (1975) are used to develop a smooth triaxial yield surface. As the surface is smooth and convex, there are no corners to require special treatment.

2.2.2.2 Models based on fracture mechanics

a. Plasticity-fracture approach

Experimental data show that the behaviour of concrete remains almost purely elastic up to its maximum tensile/compressive strength and then exhibits strain-softening behaviour with cracks developed (Petersson 1981, Bahn and Hsu 1998). The non-linear behaviour of concrete is mainly caused by the initiation of microcracks due to loading and partially caused by the propagation and coalescence of existing microcracks. Microcracks may always be present in concrete even before loading, which are believed to have some impact on the integrity of the material behaviour at a macroscopic scale. This leads inevitably to a progressive change in the mechanical properties of concrete and it should be included in any model designed to predict the concrete behaviour. Unfortunately, the conventional plasticity theory cannot be used alone to model such behaviour in concrete materials because it does not account for the underlying microscopic failure mechanisms of the material. One of the assumptions made by the conventional theory of plasticity is that unloading behaviour is elastic. This does not, therefore, allow for any change in the elastic properties of the material. This assumption is valid for many metals but is less valid for concrete as experimental observations show that a gradual degradation of elastic properties of concrete are associated with its inelastic behaviour (Bahn and Hsu 1998, Yankelevski and Reinhardt 1987, Reinhardt *et al.* 1986 or see Figures 2.1, 2.3 and 2.4). The idea of using the mechanism of micro-cracking or elastic damage in modelling the unloading behaviour of concrete was first introduced in the “progressively fracturing” model of Dougill (1976) and Dougill and Rida (1980). This model assumes that, upon loading, no permanent plastic strain remains and the material will always return to a condition of zero stress and strain. Therefore, combination of plasticity and “progressively fracturing” model as proposed by Bazant and Kim (1979), Chen and Han (1988), and Klisinski

and Mroz (1988) resolves their corresponding deficiencies in many cases to model the behaviour of concrete. Details on these models can be found in relevant publications (Bazant and Kim 1979, Chen and Han 1988, and Klisinski and Mroz 1988). However, none of these models presented attempt to describe directionally localised fracture, i.e. cracks forming in one direction following the strain-softening behaviour as observed in experimental data (Petersson 1981, Bahn and Hsu 1998). In addition, the complexity of the material functions and more feasible for implementation in a finite element program makes the models unattractive (Jefferson 1989).

b. Smeared crack approach

One of the first finite element codes to model the crack behaviour of concrete as so-called discrete crack approach was that proposed by Ngo and Scordelis (1967) and then Nilson (1968). In this type of models, any cracking that took place in the concrete was simply represented by separating the concrete element on either side of the crack. This was done by assigning a different nodal point and node number on each side of the crack. However, this approach also requires a redefining of the element topology every time a new crack appears. A major disadvantage which is entailed in this approach is the fact that the topology of the finite mesh is changed continuously. Moreover, the redefining of the element topology is extremely complex to program. This seems to limit the scope of the approach to research applications as in practical situations such concepts are rather unwieldy.

A very different approach, the so-called smeared crack approach, was then proposed by Rashid (1968). In this type of model, the cracks occur at a special material level instead of creating gaps between elements, and the formation of cracks is simulated by replacing the isotropic stiffness matrix by an orthotropic stiffness matrix upon crack formation. In the early days of the smeared crack approach, it was assumed that the stress normal to the crack direction was immediately released and dropped to zero when cracking happens. This seems completely inappropriate as the experimental data show that the stress normal to the crack follows a strain-softening behaviour until it reaches a zero value (Petersson 1981, Bahn and Hsu 1998). However, the introduction of a shear retention factor or a dilatancy factor (Suidan

and Schnobrich 1973) to model aggregate interlock in concrete and the replacement of the sudden drop in tensile stress after crack formation by more advanced strain-softening behaviour (Bazant and Oh 1983) have enhanced the capabilities of smeared crack models significantly. In recent days, smeared crack models have developed and evolved so far that even detailed crack propagation analyses of concrete materials can be undertaken successfully (Rots 1988, Jefferson 1989).

c. Strain-softening behaviour

It has been well established that in many brittle materials such as concrete the strain-softening can induce localised instabilities and non-unique solutions for the load-displacement relationship (Bazant and Oh 1983, Zienkiewicz and Taylor 1991, Crisfield 1996). Traditional FE static non-linear analysis techniques have considerable difficulties with such problems. This may account for the convergence difficulties and mesh-dependency that are often encountered with structural concrete members. In an attempt to avoid mesh-dependency caused by localised instabilities, the approach of fracture energy dissipation during crack propagation is commonly used (Hillerborg *et al.* 1976). The fracture energy is assumed to be a material property by many researchers (Petersson 1981, Rots and de Borst 1987, Bazant and Pfeiffer 1986). In the smeared cracking approach, it is well-established that a crack is assumed to be spread over a zone width associated with integration points and thus the 'numerical' fracture process zone is assumed to depend upon the element size. This width of the fracture process zone is numerically or mathematically equated the characteristic length of an element (Bazant and Oh 1983, Oliver 1989). When this characteristic length is related to the adopted finite element size, the spurious mesh dependency on the structural load-deformation response can be eliminated (Bazant and Oh 1983, Leibengood *et al.* 1986, Crisfield 1986, Cervera *et al.* 1987, Han and Chen 1987). The relation between the characteristic length and the element size can be determined by trial-and-error fitting the numerical results with some reliable results, i.e. experimental results or selected discrete crack results (Rots 1988). It is believed that in reality, upon increasing the damage level, cracking tends to localise in a band of decreasing characteristic length. By simply relating this characteristic length to the finite element size (in 2-D problems, the elemental area A_e; in 3-D problems, the elemental volume V_e), one cannot

capture such decrease of this characteristic length upon the decrease of damage. A remedy to such short coming is to adapt the finite element mesh to the present level of cracking. However, this adaptation requires continuous modification of the topology of the finite element mesh and needs a robust transfer operator (Owen *et al.* 1995). Therefore, such tasks in a highly non-linear problem are difficult to execute. More recently, a practical adaptation of the characteristic length, without any change in the topology of the finite element mesh, is developed (Mosalam and Paulino 1997). However, it is beyond the scope of this thesis to look at the change of the characteristic length during the crack propagation, thus the constant characteristic length (Bazant and Oh 1983, Oliver 1989) is employed with the models used in this research.

d. Parameter identification

It would be worth noting again, the approach of strain-softening is not however, without its difficulties, and the most serious of which relates to the use of a strain softening relationship. The problem with strain-softening structures is that equilibrium solutions can become non-unique since the structure stiffness matrix becomes non-positive definite. In particular, for smeared crack models the material data provided by experimental standard tests do not always suffice to identify all model parameters. In the case of concrete in tension, besides some properties for the elastic behaviour of the material, the additional data could include the fracture energy G_f, with the physical meaning of energy dissipated per unit cracked area, a length related to the width of the damage zone, and data on the unloading responses of the material. Difficulties in carrying out experimental tests to measure these properties, especially the material crack band width and the representative fracture energy, make the identification extremely difficult, even impossible (see Section 2.2.1.1). The test method for the determination of G_f and even its precise definition has been a subject of intense debate among researchers because it has been found to vary with the size and shape of the test specimen, i.e. notched or un-notched specimens, and with the test method used, i.e. uniaxial or three-point bending tests (Petersson 1981, Phillips and Zhang 1990, van Mier and Nooru-Mohamed 1990, Bazant and Becq-Giraudon 2002, Karihaloo *et al.* 2003). Therefore, it depends upon the accuracy of the supplied value of the parameter G_f from the experimental data collection, the

numerical result can closely match or diverge from the experimental one (See Chapters 4 and 5). In addition, the shape of the strain-softening curve is also an important parameter which will sensitively affects the numerical results. Various softening stress-strain relationships have been proposed in order to be implemented into the smeared crack approach included: linear relationship (Hillerborg *et al.* 1976), bilinear relationship (Hilsdorf and Brameshuber 1991), and exponential relationship (Gopalaratnam and Shah 1985, Gopularatnam and Ye 1991, Ratanalert and Wecharatma 1989). Amongst these, experimental data show that the exponential relationship seems to be the best approximation, especially for tensile softening (Petersson 1981, Phillips and Zhang 1990, van Mier and Nooru-Mohamed 1990, Gopalaratnam and Shah 1985, Elices *et al.* 2002, and Karihaloo *et al.* 2003). Thus, the exponential stress-strain relationship is employed in the models used in this research.

e. Shear Retention factor

As mentioned earlier, in plain concrete, the main shear transfer mechanism is aggregate interlock and the main variables involved are the aggregate size and grading. In reinforced concrete, dowel action plays a significant role, the main variable being the reinforcement ratio, the size of the bars and the angle between the crack and the bars (Paulay and Loeber 1974). However, in concrete modelling, the above-mentioned mechanisms cannot be directly included in the smeared crack model. A simplified approach is generally employed to take into account of the reduced shear transfer capacity of cracked concrete. The process consists of replacing the shear modulus corresponding to the crack plane by a reduced value, G_c, defined as $G_c = \beta G$ in the cracked stress-strain D-matrix, where G is the shear modulus of uncracked concrete and β is the shear retention factor. Suidan and Schnobrich (1973) proposed a so-called shear retention factor (SRF) β, which is a constant value, to model aggregate interlock. However, some investigators have considered the assumption of a constant SRF too crude (Cedolin and Dei Poli 1977, Kolmar and Mehlhorn 1984, Scotta *et al.* 2001) and proposed variable shear retention factors to model shear transfer during the crack propagation.

It should be noted that variable shear retention factors are usually introduced into two-dimensional models in order to prevent tensile stresses, significantly greater than the

maximum stress, being generated when the principal axes rotated away from the orthogonal crack axes. However, in the adopted models (Multi-crack and Craft), this cannot occur since a new crack forms in a non-orthogonal direction if excessive tensile stresses build up (see the following section). Thus, a constant shear retention factor is reasonably introduced into the models adopted in this thesis. Moreover, in Craft model, contact theory is used to model the contact between the crack surfaces and therefore accurately model the shear transferred between them (Jefferson 2002b, 2003a).

f. Types of cracks

In the earlier smeared crack models, the crack direction is fixed in the direction of the first principal stress that exceeds the cracking stress, although the subsequent principal stress may rotate during the analysis (Suidan and Schnobrich 1973, Cedolin and Dei Poli 1977, Kolmar and Mehlhorn 1984, Bazant and Oh 1983). Physical support for this was possibly found in macro-cracking where the crack, due to the complete loss of material resistance, cannot rotate. However, it is experimentally shown that many important cases such as beams and slabs failed because of shear in forms of diagonal cracks. Therefore, the fixed crack approach produced over-stiff results and relies on a somewhat arbitrary shear retention factor (Crisfield and Wills 1989). In addition, since no integration is involved over the material volume (different orientations), the crack plane causes an immediate and sharp anisotropy in the material, which does not seem to be consistent with the physical experience (Petrangeli and Ozbolt 1996).

In fact, a crack is formed in the maximum principal stress direction and this leads to a change in stiffness, and consequently leading to unbalanced stresses. At this stage, owing to aggregate interlock or dowel action, there may be unbalanced shear stresses acting parallel to the crack. The principal stress direction in concrete is then no longer perpendicular to the crack. If the principal tensile stress in concrete exceeds its tensile capacity either immediately or after more loading is applied, a new crack would be formed. It is assumed that the original crack is "closed" before the new crack is formed. This process continues until the principal tensile stress in concrete is no longer in excess of its tensile capacity and equilibrium is established. This is known as a rotating crack approach (Cope *et al.* 1980, Bazant 1983, Milford and

Schnobrich 1985, Rots 1988, Foster and Gilbert 1996). However, in this approach, the crack will always orientate in a direction normal to the principal tensile stress and therefore the system cannot rebuild the tensile stress coordinate transformation stiffness matrix without the crack plane chasing and releasing it. This will cost a lot of computational effort, especially when non-linear stress-strain relations are used, the coordinate transformation stiffness matrix must be iteratively upgraded inside the load step. Moreover, the rotating crack model cannot simulate post crack shear response on a crack plane and also relies on the questionable device of computing Poisson's ratio from current stress and strain components such that the coaxility of the principal stresses and strains is maintained (Rots 1988, Petrangeli and Ozbolt 1996, Freenstra and de Borst 1995).

The multiple fixed crack model (or called multi-crack model) is based on the same assumptions as the single fixed crack model. It circumvents the over stiff results of the single fixed crack model by allowing for the formation of secondary crack(s). The first crack is initiated analogous to the single fixed crack model when the principal tensile stress in concrete exceeds its tensile capacity. A second crack is allowed to form after the change in principal stress directions has exceeded a certain threshold value, say 30^0 or 45^0. If on subsequent loading a further rotation in principal stress directions would occur, even a third crack is allowed to occur (de Borst and Nauta 1985). The material behaviour is found from coupling multiple planes, each representing a different crack orientation with a linear elastic material. Every single crack plane holds what has been said for the single fixed crack model. The possibility of having a multiple crack plane gives more accurate results when stresses are rotating due to change in the load pattern or shift in principal stress directions. However, the multidirectional fixed crack model does not overcome the problems arising from the inconsistency of the material model already mentioned in the single fixed crack model such as sharp anisotropy in the material. Despite this shortcoming, for the sake of simplicity and the purpose of the Author's research (See Chapter 1), the multiple fixed crack model will be adopted in this thesis.

g. Solution methods

Softening materials are known to induce 'strain-localisation', in which a local region softens (or cracks) while the adjoining material unloads elastically. These localisations may be accompanied by 'snap-throughs' or 'snap-backs'. The former phenomenon involves a jump to a new displacement state at a fixed load level, while the latter involves a dynamic jump to a new load level under a fixed displacement state (Figure 2.15). Traditional static non-linear analysis techniques such as Newton-Raphson based methods (Owen and Hinton 1980), have considerable difficulties in dealing with such phenomena and this may account for the convergence difficulties that are often encountered with concrete problems. With load control, analyses are not able to overcome limit points at all, and with direct displacement control it is not possible to properly analyse snap-back behaviour. Fortunately, a very general and useful technique, so-called "arc-length" technique, has been developed within the realm of geometrically non-linear analysis. In this method, the incremental-iterative process indirectly uses a norm of incremental displacements (Crisfield 1983, 1986) and this norm is used as a constraint equation. Traditionally, load-controlled analyses equated failure of the structures with the failure of the iterative solution technique. As a consequence, in a brittle environment, they can fail to establish the particular cracks or mechanism which initiates the collapse because there is no converged equilibrium to study. Unlike the load control method, in which the load is kept constant during a load step, or in the displacement control method, in which the displacement is kept constant during increment, in the arc-length method, the load-factor at each iteration is modified so that the solution follows some specified path until convergence is archived (Crisfield 1983, 1986). Although the arc-length method has been suggested to be successful in tracing the equilibrium response beyond the maximum load, the Author has found that this method does not always guarantee a convergent result and this will be presented by a problem of a reinforced concrete structure in Chapter 5.

2.2.2.3 Discussions

From the above review (see Section 2.2.2), there is recognition that both plasticity-fracture and plasticity-fracture-damage models are required to simulate concrete behaviour well. It is

desirable for these models to be based on plasticity theory and include an elastic constitutive relationship, the assumption of total strain decomposition, suitable failure criteria (e.g. experimentally closed failure surface), and a non-associated flow rule in order to reproduce experimentally closed failure surfaces in the meridian plane. In addition, if based on fracture and damage mechanics, it is desirable for the models to use the smeared crack approach, in particular the multidirectional fixed models or rotating models, and are able to simulate the key characteristics of concrete material such as increasing deviatoric strength with increasing compressive confinement, non-linear behaviour in compression, softening in tension leading to the formation of fully formed stress-free cracks, aggregate interlock on partially and fully formed cracks, shear behaviour, interaction between compressive and tensile strengths, crack opening and closing with both shear and normal crack surface movements (as mentioned in Section 2.2.1).

In some respects, the plasticity-fracture models still have a measure of greater success at simulating certain of the above characteristics than many of the new models. In engineering application, the plasticity-fracture models have been developed with much attention for more than thirty years, and therefore it has been well established and proven in many practical problems. The plasticity-fracture-damage models have not been as widely used for concrete and reinforced concrete structures because of both the complexity in understanding and difficulty in the implementation into finite element codes, and they are still under improvement. In this manner, it suits the Author's research objectives (see Chapter 1) to adopt either a plasticity-fracture model or a plasticity-fracture-damage model, which has to be considered applicable and available for modelling concrete and reinforced concrete structures under different types of loading.

In this research, the plasticity-fracture model, Multi-crack model (Jefferson 1999), is employed for analysis as the model is based on plasticity theory with many of the required features (e.g. non-linear failure surface and a non-associated flow rule), multidirectional fixed crack approach, and has the possibility of simulating key characteristics of concrete behaviour

such as non-linear behaviour, strain-softening, shear behaviour, unloading and reloading behaviour.

As mentioned above, there is no one constitutive model able to properly describe all aspects of non-linear concrete behaviour and, also, no one model type has been widely accepted. Fortunately, in the middle of the Author's PhD research, a new model, namely Craft, also developed by Jefferson (2003a, 2003b), has been launched which uses plasticity, damage and contact theories and retained certain features of the Multi-crack model, which aims at simulating all these above features of concrete behaviour within the same framework. It is also well assessed against a range of experimental data, which includes data from uniaxial tension tests with and without unloading-reloading cycles, and then loaded in shear, and uniaxial, biaxial, and triaxial tests; and the capability of simulating the stiffness degradation under compressive and tensile loadings (see Jefferson 2003a, 2003b), this new model had interested the Author. Therefore the Author decided to use this model in parallel with the Multi-crack models for most of the modelling work in this PhD Thesis. The detailed reasons will be discussed further at the end of the next section.

The theoretical back ground and applicability of these two models will be presented in next sections.

2.3 THEORETICAL BACKGROUND OF THE MODELS USED IN THE RESEARCH

2.3.1 Introduction

In this thesis, plasticity theory has been used in the modelling of reinforcement and concrete in the reinforced concrete structures. It is used not only in the modelling of steel reinforcement and compressive concrete, but is also used in combination with fracture or damage theory in the modelling of behaviour of the tensile concrete. The basic components of the plasticity theory are yield criterion, flow rule and hardening rule. However, as they are well presented in

many books (e.g. Mendelson 1968, Kachanov 1974, Johnson and Mellor 1983, Jirasek and Bazant 2002), it will not be presented again in the thesis.

In this section, the plasticity models used for steel reinforcement and compressive concrete are presented first. The theoretical background of the plastic-fracture model, Multi-crack model, used in modelling concrete in tension will be presented next. In the last part, the theoretical background of the plastic-fracture-damage-contact model, Craft model, will also be provided.

2.3.2 Plasticity model for steel reinforcement

In this study, Von Mises yield criterion (Figure 2.16) with "isotropic hardening" rule (see e.g. Kachanov 1974, Johnson and Mellor, Owen and Hinton 1980) is used in the modelling of steel reinforcement. The steel reinforcement is modelled as one-dimensional elasto-plastic material with a linear hardening parameter, as shown in Figure 2.17. This model is available in the FE program LUSAS (LUSAS User Manual 2001). The steel reinforcement is represented by bar elements and then connected to concrete elements. In LUSAS, the location of the steel elements needs to lie at the element boundaries by fixing node to node. The overall stiffness matrix of the reinforced concrete would then be made up of two components, the concrete element component and the reinforcement component. It is assumed that there is perfect bond between the steel reinforcement and concrete.

2.3.3 Plasticity model for compressive concrete

In the Multi-crack model (Jefferson 1999), the compressive behaviour is assumed linear elastic. This section presents the plasticity component for modelling compressive concrete used in Craft model. In this model, a smooth triaxial yield surface is developed from the yield function used by Lubliner *et al.* (1989) and from Willam and Warnke's (1975) smoothing function. Figures 2.18 and 2.19 show the model's yield function meridians and yield function on the π-plane. The model includes friction hardening and softening to account for pre- and

post-peak non-linear behaviour, and uses work hardening in which the total work required to reach the peak stress envelope is made a function of the mean stress. The model is developed with a dilatancy parameter that allows plastic flows to be associated or non-associated. Moreover, in the model, the local responses from all active plastic surfaces are coupled in a multi-surface plasticity formulation, which provides the interaction between compressive and tensile behaviour. Thus, the crushing effects to the structural behaviour can be captured. However, as the model does not simulate non-linearity under hydrostatic compression and the yield function has straight meridians, the accuracy of the model reduces for stress states with high triaxial confinement. Details on the model can be found in (Jefferson 2003a, 2003b) and not presented here again.

2.3.4 Fracture and damage models for concrete in tension

2.3.4.1 Multi-crack model theory (Jefferson 1999)

A plastic fracture approach has been used in modelling concrete in tension. A model based on this approach, namely Multi-crack model, was developed by Jefferson (1999) and has been incorporated into the program LUSAS (LUSAS Manual 2001) which is used in this research. The model is a further development of a Multi-crack plasticity approach proposed by Carol and Bazant (1995) and in the model, the procedure developed for modelling cracks is similar to the non-orthogonal fixed smeared crack model presented by de Borst and Nauta (1985) and Rots (1988). It should be noted that in this Multi-crack model, tensile cracking is accounted for but crushing failure in compression is neglected. Also, in this model, linear elastic behaviour is employed for concrete in compression.

2.3.4.1.1 Predefined cracking plane (de Borst and Nauta 1985, Weihe *et al.* 1998)

In this model, it is assumed that, at any one material point, there are a predefined number of permissible cracking directions. The number, and orientation, of these cracks are chosen such that the fracture criterion is not exceeded in any direction. In the present situation, the directions for the three-dimensional case are those of the 21 integration directions of spherical

integration rule, and for the two-dimensional cases, 8 in-plane and 1 out-of-plane directions are used (Bazant and Oh 1983, Hasegawa 1995). Each direction defines a plane of possible cracking, and for each one of these planes there is a separate yield surface and a set of yield state parameters. The local co-ordinate system for a cracking plane is illustrated in Figure 2.20.

2.3.4.1.2 Local and global stress and strain systems

The relationship between the local and global stresses is as follows:

$$s_i = N_i \sigma \tag{2.1}$$

where the subscript *i* represents the crack plane number and

$$s = [s_r, s_s, s_t]^T \tag{2.2a}$$

$$\sigma = [\sigma_{xx}, \sigma_{yy}, \sigma_{zz}, \sigma_{xy}, \sigma_{yz}, \sigma_{xz}]^T \tag{2.2b}$$

$$N_i = \begin{bmatrix} r_1^2 & r_2^2 & r_3^2 & 2r_1r_2 & 2r_2r_3 & 2r_1r_3 \\ r_1s_1 & r_2s_2 & r_3s_3 & r_2s_1 + r_1s_2 & r_3s_2 + r_2s_3 & r_1s_3 + r_3s_1 \\ r_1t_1 & r_2t_2 & r_3s_3 & r_2t_1 + r_1t_2 & r_3t_2 + r_2t_3 & r_1t_3 + r_3t_1 \end{bmatrix} \tag{2.2c}$$

r_1, r_2, r_3 are the *x*, *y*, *z* components, respectively, of the unit vector *r*, normal to the crack surface, and similarly for *s* and *t*, the in-plane vectors forming an orthogonal set.

The local stresses are related to the normal and principal shearing stresses on the cracking plane as follows

$$\sigma_n = s_r \tag{2.3a}$$

$$\tau = \sqrt{s_s^2 + s_t^2} \tag{2.3b}$$

Local strain contributions are transformed to global strains by the relationship

$$\varepsilon = N_i^T e_i \tag{2.4}$$

where

$$e = [e_r, e_s, e_t]^T \tag{2.5a}$$

$$\varepsilon = [\varepsilon_{xx}, \varepsilon_{yy}, \varepsilon_{zz}, \varepsilon_{xy}, \varepsilon_{yz}, \varepsilon_{xz}]^T \tag{2.5b}$$

2.3.4.1.3 Decomposition strain tensor into elastic and plastic parts

The total strain tensor is split into elastic and plastic parts, as:

$$\dot{\varepsilon} = \dot{\varepsilon}^e + \dot{\varepsilon}^p \tag{2.6}$$

in which the superior dot denotes the time derivative

$\dot{\varepsilon}^e$, $\dot{\varepsilon}^p$ are elastic and plastic strains

The plastic strain is summed from the transformed components from the various crack directions

$$\dot{\varepsilon}^p = \sum_{j=1}^{m} N_{i_j}^T \dot{e}_{i_j} \tag{2.7}$$

where *i* represents a crack plane number (*i* = 1, *n*), and *j* represents a number of active cracks in plane *i* (j = 1, *m*).

2.3.4.1.4 Failure envelope and yield function (Kroplin and Weihe 1997)

In this model, the yield function, which is similar to that used by Kroplin and Weihe (1997) and is illustrated in Figure 2.21, is adopted. This function, which is applied to each crack direction, depends upon the local stress *s*, equivalent fracture stress f_s, and the friction factor μ, and the "roughness-cohesion" parameter *r*, as follows:

$$F(s, f_s, \mu) = \frac{s_r}{2}\left[1 + \left(\frac{\mu}{r}\right)^2\right] + \frac{1}{2r}\sqrt{(r^2 - \mu^2)s_r^2 + 4r^2(s_s^2 + s_t^2)} - f_s \leq 0 \tag{2.8}$$

The plastic potential, Φ, required to control the direction of local strain increments, takes a similar form to the yield function except that the dilatancy coefficient, ψ, is used in place of μ, is as follows:

$$\Phi(s, f_s, \psi) = \frac{s_r}{2}\left[1 + \left(\frac{\psi}{r}\right)^2\right] + \frac{1}{2r}\sqrt{(r^2 - \psi^2)s_r^2 + 4r^2(s_s^2 + s_t^2)} - f_s \leq 0 \tag{2.9}$$

2.3.4.1.5 Softening rule

It is assumed that, in the model, the concrete can soften after reaching the tensile strength, and eventually loses all strength if the strain continues to increase in any one of the predefined

cracking directions. An exponential softening curve is assumed and, for direct tension loading in one direction, this gives the normal stress-strain relationship shown in Figure 2.22.
Softening is controlled by an equivalent plastic (or fracture) strain parameter, $\bar{e}$, takes the form of an exponential softening function as follows (Gopalaratnam and Shah 1985):

$$f_s = f_t e^{-5\left(\frac{\bar{e}}{e_0}\right)} \tag{2.10}$$

With respect to the normal stress-strain softening curve in Figure 2.22, $e_0 = \varepsilon_0$.

In both the Multicrack and the Craft model, the strain parameter depends upon a characteristic length and the fracture energy per unit area following the approach of Bazant and Oh (1983). In finite element applications this characteristic length is dependent on the element size (Bazant and Oh 1983, Oliver 1989). For example, in the recent models, the characteristic length l_c is evaluated from the elemental volume V_{gauss} associated with a gauss point as $l_c = \sqrt[3]{V_{gauss}}$ (see Section 2.2.2.2).

2.3.4.1.6 Overall stress-strain relationship

The incremental fracture strains on an individual cracking plane are obtained from the flow rule Φ as:

$$\dot{e}_i = \dot{\lambda}_i \left(\frac{\partial \Phi}{\partial s}\right)_i \tag{2.11}$$

in which

$$\dot{e}_i = [\dot{e}_{rr}, \dot{e}_{rs}, \dot{e}_{rt}]_i^T \tag{2.12}$$

The incremental elastic strains can be obtained from Equations (2.6), (2.7), and (2.11) as

$$\dot{\varepsilon}^e = \dot{\varepsilon} - \sum_{j=1}^{m} N_{i_j}^T \dot{e}_{i_j} = \dot{\varepsilon} - \sum_{j=1}^{m} N_{i_j}^T \dot{\lambda}_{i_j} \left(\frac{\partial \Phi}{\partial s}\right)_{i_j} \tag{2.13}$$

The elastic stress-strain relationship is given by

$$\dot{\sigma} = D\dot{e}^{e} = D\left[\dot{\varepsilon} - \sum_{j=1}^{m} N_{i_j}^{T}\dot{\lambda}_{i_j}\left(\frac{\partial\Phi}{\partial s}\right)_{i_j}\right] \tag{2.14}$$

where i represents a crack plane number (i = 1, n), and j represents a number of active cracks in plane i (j = 1, m). In general, for 3-D problems, D is the standard 6x6 matrix of elastic constants in stiffness.

The yield surface changes shape as cracking progresses and, in the limit of full fracture, it takes the shape of a friction plane. If the friction factor is taken as a constant, then the shape of the yield function is governed by the equivalent fracture stress f_s, which is a function of the accumulated fracture strain as defined by the stress-strain softening function as shown in Figure 2.22.

In order to derive relationships between incremental stresses and strains, the consistency condition is applied to all active yield surfaces. If the stress is on the yield surface i, then the consistency condition is:

$$\left(\frac{\partial F}{\partial s}\right)_i^T \dot{s}_i + \left(\frac{\partial F}{\partial f_s}\right)_i \dot{f}_{s_i} = 0 \tag{2.15}$$

The increment of equivalent stress in Equation (2.15) can be related to the local plastic strain rate as follows:

$$\dot{f}_{s_i} = \left(\frac{df_s}{d\bar{e}}\right)_i \left(\frac{d\bar{e}}{de}\right)_i^T \dot{e}_i = \left(\frac{df_s}{d\bar{e}}\right)_i \left(\frac{d\bar{e}}{de}\right)_i^T \dot{\lambda}_i \left(\frac{\partial\Phi}{\partial s}\right)_i \tag{2.16}$$

Introducing the variable A that

$$A_i = \left(\frac{\partial F}{\partial f_s}\right)_i \left(\frac{df_s}{d\bar{e}}\right)_i \left(\frac{d\bar{e}}{de}\right)_i^T \left(\frac{\partial\Phi}{\partial s}\right)_i \tag{2.17}$$

Substituting (2.14) into (2.1) and the result into (2.15) and then (2.16) and (2.17) into (2.15) gives:

$$\left(\frac{\partial F}{\partial s}\right)_{i_j}^T N_{i_j} D\left[\dot{\varepsilon} - \sum_{j=1}^{m} N_{i_j}^{T}\dot{\lambda}_{i_j}\left(\frac{\partial\Phi}{\partial s}\right)_{i_j}\right] - A_{i_j}\dot{\lambda}_{i_j} = 0 \tag{2.18}$$

This may be arranged into the form of a matrix equation with $\dot{\lambda}_{i_j}$ as the unknown, as follows:

$$\Omega\Lambda = \Gamma\dot{\varepsilon} \tag{2.19}$$

in which the matrix Ω are coupled equations and is shown in the following form:

$$\Omega = \begin{bmatrix} \left(\frac{\partial F}{\partial s}\right)_{i_1}^T N_{i_1} D N_{i_1}^T \left(\frac{\partial \Phi}{\partial s}\right)_{i_1} + A_{i_1} & \left(\frac{\partial F}{\partial s}\right)_{i_1}^T N_{i_1} D N_{i_2}^T \left(\frac{\partial \Phi}{\partial s}\right)_{i_2} & \left(\frac{\partial F}{\partial s}\right)_{i_1}^T N_{i_1} D N_{i_3}^T \left(\frac{\partial \Phi}{\partial s}\right)_{i_3} \\ \left(\frac{\partial F}{\partial s}\right)_{i_2}^T N_{i_2} D N_{i_1}^T \left(\frac{\partial \Phi}{\partial s}\right)_{i_1} & \left(\frac{\partial F}{\partial s}\right)_{i_2}^T N_{i_2} D N_{i_2}^T \left(\frac{\partial \Phi}{\partial s}\right)_{i_2} + A_{i_2} & \left(\frac{\partial F}{\partial s}\right)_{i_2}^T N_{i_2} D N_{i_3}^T \left(\frac{\partial \Phi}{\partial s}\right)_{i_3} \\ \left(\frac{\partial F}{\partial s}\right)_{i_3}^T N_{i_3} D N_{i_1}^T \left(\frac{\partial \Phi}{\partial s}\right)_{i_1} & \left(\frac{\partial F}{\partial s}\right)_{i_3}^T N_{i_3} D N_{i_2}^T \left(\frac{\partial \Phi}{\partial s}\right)_{i_2} & \left(\frac{\partial F}{\partial s}\right)_{i_3}^T N_{i_3} D N_{i_3}^T \left(\frac{\partial \Phi}{\partial s}\right)_{i_3} + A_{i_3} \end{bmatrix} \tag{2.20}$$

and the vectors Λ and Γ are given by:

$$\Lambda = \begin{bmatrix} \dot{\lambda}_{i_1} \\ \dot{\lambda}_{i_2} \\ \dot{\lambda}_{i_3} \end{bmatrix} \qquad \Gamma = \begin{bmatrix} \left(\frac{\partial F}{\partial s}\right)_{i_1} N_{i_1}^T D \\ \left(\frac{\partial F}{\partial s}\right)_{i_2} N_{i_2}^T D \\ \left(\frac{\partial F}{\partial s}\right)_{i_3} N_{i_3}^T D \end{bmatrix} \tag{2.21}$$

Hence, the vectors of plastic parameters can be expressed as

$$\Lambda = \Omega^{-1}\mathrm{T}\dot{\varepsilon} \tag{2.22}$$

From Equation (2.18), defining the matrix Ξ as follows

$$\Xi = \begin{bmatrix} N_{i_1}^T \left(\frac{\partial \Phi}{\partial s}\right)_{i_1} & N_{i_2}^T \left(\frac{\partial \Phi}{\partial s}\right)_{i_2} & N_{i_3}^T \left(\frac{\partial \Phi}{\partial s}\right)_{i_3} \end{bmatrix} \tag{2.23}$$

and substituting (2.22) and (2.23) into (2.14) gives

$$\dot{\sigma} = \left[D - \Xi\Omega^{-1}\Gamma\right]\dot{\varepsilon} = D_T\dot{\varepsilon} \tag{2.24}$$

where D_T is the tangent constitutive matrix for loading. Equation (2.24) defines the incremental stress-strain relationship.

2.3.4.2 Craft model theory (Jefferson 2003a, 2003b)

The Craft model employs plasticity, damage and contact theory in the formulation and yet retains certain of the features of the early plasticity-fracture models (Multi-crack model). The model aims to be able to simulate directional cracking, crack closure and shear contact (or aggregate interlock) behaviour in an integrated manner, which also accounted for the type of damage and triaxial frictional response that characterises the behaviour of concrete in compression. In this model, embedded damage-contact planes were integrated with a plasticity component by using a thermodynamically consistent plastic-damage framework. The essential elements of the model are:

- A local stress - strain relationship, which here is a damage-contact model
- A function from which local strains can be computed such that the local and global constitutive relationships are both satisfied. This is termed the total-local function.
- A triaxial plasticity component for simulating frictional behaviour and strength increase with triaxial confinement

Here only the main governing relationships relevant to the present applications will be provided.

2.3.4.2.1 Predefined damage-contact plane

This plane is similar to the predefined cracking plane of the Multi-crack model as shown in Figure 2.20.

2.3.4.2.2 Local stress-strain relationship

In the crack plane model, the local stress comprises two components, the undamaged component and the damage-contact component, with the former being associated with the proportion of material that is undamaged (1 - ω) and the latter the proportion that is damaged

ω, with ω being a damage variable that lies in the range 0 to 1. The local stress is then as follows

$$s_i = \left[(1-\omega_i)D_L e_i\right] + \left[H_f(e)\omega_i D_L g_i\right] = \begin{bmatrix} undamaged \\ component \end{bmatrix} + \begin{bmatrix} damage-contact \\ component \end{bmatrix} \tag{2.25}$$

in which s_i, e_i, D_L are the local stress, local effective strain and local elastic constitutive matrix, respectively, for damage plane i. s_r and e_r denote normal components and s_s, s_t and e_s, e_t, shear components of the local stress and strain vectors respectively. $H_f(e)$ is a function that varies from 1 to 0 with the increasing crack opening parameter e_g, and this simulates the observed phenomena that the wider a crack is open, the less the shear that can be transferred across it. Details of the function H_f can be seen in Jefferson (2002b).

ω_i is the scalar damage variable, depends upon a local strain parameter ζ_i. When the material has experienced a degree of "crushing" in compression, there is a general loss of tensile strength (Kupfer *et al.* 1969), and in the present model, this is simulated with an increase in damage and a reduction in first fracture stress (details of the determination of ω_i can be seen in Jefferson (2003a)). g_i is the strain relative to a contact surface, which is illustrated in Figure 2.23. It is related by a transformation to the local strains e_i, as follows:

$$g_i = \Phi_g e_i \tag{2.26}$$

where

$$\Phi_g = \frac{1}{1+m_g^{\,2}}\left(\left(\frac{\partial \phi_{\text{int}}}{\partial e}\right)\cdot\left(\frac{\partial \phi_{\text{int}}}{\partial e}\right)^T + \phi_{\text{int}}\frac{\partial^2 \phi_{\text{int}}}{\partial e^2}\right) \tag{2.27}$$

where $\phi_{\text{int}}(e)$ is the interlock function, $\phi_{\text{int}}(e) = m_g e_r - \sqrt{e_s^2 + e_t^2}$, and in which m_g is the slope of the interlock contact surface, as shown in Figure 2.23(b). In the open state, the stress in the damaged contact component is assumed to be zero. In the interlock state the damaged contact component is derived from a contact law in which the stress is assumed to depend upon the distance (in local strain terms) to the contact surface that is denoted by the strain vector g_i. In the closed state (Figure 2.23(a)), g_i is equal to the local strain vector since the contact point coincides with the origin of the local strain space.

Finally, the local stress is expressed as follows

$$s_i = D_L \left[(1-\omega) + H_f(e)\omega_i \Phi_g \right] e_i = D_L M_{x_i} e_i \tag{2.28}$$

2.3.4.2.3 Failure envelope and yield function

It should be noted that in this model, a strain based damage surface is used with a kinematic constraint, then damage will continue to be predicted even if a macro crack has completely opened. It is because the problem with a stress based damage surface (Figure 2.21) is that the surface shrinks to zero size in stress space with complete damage, resulting in undefined gradients. Furthermore, it is not easy to decide upon what local strains the transformed stresses should be linked to.

A plane of degradation (POD) is assumed to form when the principal stress reaches the fracture stress (f_t), with the POD being normal to the major principal axis. Thereafter, it is assumed that damage on the plane can occur with both shear and normal strains. The damage surface, which is similar to that used by Kroplin and Weihe (1997) and is illustrated in Figure 2.24, as follows

$$\phi(e,\zeta) = \frac{e_r}{2}\left[1 + \left(\frac{\mu_\varepsilon}{r_\zeta}\right)^2\right] + \frac{1}{2r_\zeta}\sqrt{(r_\zeta^2 - \mu_\varepsilon^2)e_r^2 + 4r_\zeta^2(e_s^2 + e_t^2)} - \zeta \quad \leq 0 \tag{2.29}$$

in which r_ζ is the shear intercept to tensile strength ratio for local damage surface, μ_ε is the asymptotic friction factor.

2.3.4.2.4 Softening rule

This softening rule is similar to the one used in the Multi-crack model as shown in Figure 2.22.

2.3.4.2.5 Overall stress-strain relationship

The global stress-strain relationship is given by

$$\sigma = M_c D_e (\varepsilon - \varepsilon_p) \tag{2.30}$$

where D_e is the elastic tensor; ε_p is the plastic strain tensor; ε is the total strain; the contact matrix M_c is given by

$$M_c = \left(I + D_e \sum_{i=1}^{n_p} N_i^T C_{lsf_i} N_i \right)^{-1} \tag{2.31}$$

in which I is the identity matrix; n_p is the number of damage planes; N_i is the stress transformation which is similar to the one shown in Equations (2.1) and (2.2c).

C_{lsf_i} is the local compliance matrix which has different forms dependent upon cracking states (open, interlock or closed) of the damage-contact component.

2.3.4.2.6 Total-local function

In this model, a total-local vector function is used to allow the local and global constitutive relationships, as well as the stress transformation (Equation 2.1), to be simultaneously satisfied for multiple damage planes. The model therefore has full coupling between damage surfaces. The function, shown below, gives the error between the transformed global stresses computed from Equation (2.30) and the local stresses computed from Equation (2.28). This equated to zero and solve for the unknown local strains e_i

$$f_{e_i} = N_i \sigma - s_i = N_i \left\lfloor M_c D_e (\varepsilon - \varepsilon_p) \right\rfloor - D_L M_{x_i} e_i = 0 \tag{2.32}$$

2.3.5 Summary and conclusions

The aim of this section is to describe the theoretical backgrounds of the models used in this PhD thesis including the plasticity theory used for modelling the behaviour of steel reinforcement and compressive concrete, as well as the plasticity-fracture model and plasticity-damage model for tensile concrete.

For modelling of the steel reinforcement, the von Mises yield function and a linear isotropic hardening rule are employed. For modelling of compressive concrete, the associated non-linear hardening plasticity theory, which requires the definition of a yield surface and a hardening rule, is employed. The yield surface has been designed to fit the multiaxial strength envelope of concrete and the hardening rule has been based on the uniaxial stress-strain curve of concrete.

For modelling of the tensile concrete, a plasticity-fracture model is presented first. The model assumes that, at any one material point, there are a predefined number of permissible cracking directions. Each direction defines a plane of possible cracking, and for each one of these planes there is a separate yield surface and set of yield state parameters. The hyperbolic yield surface, which is asymptotic to a Coulomb friction surface, which is found reasonably fitted to the triaxial strength envelope of concrete, and an exponential softening rule are employed to describe the yield and fracture progress of concrete. The model does not, however, simulate crushing in compression, the loss of unloading stiffness with increasing fracture strain or hysteretic behaviour with cyclic loading.

The above chief flaws with the Multi-crack model can be overcome by adopting the Craft model which combines plasticity, damage and contact theories on a thermodynamic framework. The relatively simple functions used in the local POD plane allow the accurate simulation of direct tension behaviour. Furthermore, the incorporation of a contact model on damaged PODs enables crack opening and closing, shear contact, aggregate interlock behaviour, and inelastic unloading/reloading behaviour to be simulated with reasonable accuracy. In addition, the use of the frictional hardening plasticity component is adequate for simulating the compressive behaviour of concrete up to a medium level of confining stresses (Jefferson 2003a). However, as the model uses an open yield surface with linear meridians, the compressive behaviour of concrete at high triaxial confining stresses is not captured well. Also, the model is not yet able to simulate the unloading/reloading hysteretic behaviour in concrete because no frictional behaviour is included in the tension behaviour and it is impossible to know the lower stress which will be reached at the beginning of unloading loop (Figures 2.1, 2.3 and 2.4).

As mentioned in Chapter 1, one of main objectives of this research is to validate ones of the most updated smeared crack models for various concrete and reinforced concrete structures under monotonic and cyclic loadings against experimental and analytical data, and to further use them for analysis of reinforced concrete bridge piers under artificial earthquake loadings.

Regarding this objective in connection with the literature review made above, the Author believes that the two models, Multi-crack and Craft, have some certain possibilities to simulate concrete behaviour well for a wide range of applications. It is understandably expected that the Multi-crack model may be, in general, not capable to capture the cyclic behaviour of the structure because, in the model, the unloading behaviour in concrete is assumed to be linear elastic with the initial modulus, and also it does not include the crushing effects of the compressive concrete. However, as the model has plastic strain part, it can still capture the overall non-linear behaviour of the structure under cyclic and earthquake loadings. On the contrary, the Craft model is expected to capture the cyclic behaviour of the structure well because it is capable of capturing the inelastic unloading/reloading behaviour, crushing effects of the compressive concrete and crack opening and closing behaviour (see Jefferson 2003a and 2003b for the well-compared results with physical reality). Therefore, it is worth to adopt both the Multi-crack and Craft models to predict the behaviour of RC structures under cyclic loading and to point out useful comments related to the use of these models subject to cyclic and earthquake loadings.

As perfect bond between concrete and steel reinforcement is assumed in the modelling of RC structures in this thesis, it is expected that the numerical results will overestimate the structural stiffness, especially for the case of cyclic loading. It is because the experimental investigations show that cyclic loading produces a progressive deterioration of bond between concrete and steel reinforcement (Bresler and Bertero 1968, Edwards and Yannopoulos 1978, Rehm and Eligehausen 1979). Though it is out of the scope of this research to include the bond slip between concrete and steel reinforcement in the FE modelling, this effect will be studied through the comparison between numerical and experimental results of RC structures under monotonic and cyclic loadings. However, in the qualitative assessment of damage responses under different earthquake time-histories (see Chapters 7 and 8) using the Multi-crack or Craft models, the assumption of perfect bond would not significantly affect the conclusions.

Besides, the reason of adopting the two models, is not only to validate the models for various applications, but also to compare them with each other in order to show that the Craft model is

capable of capturing some key features of concrete behaviour such as crushing effects, crack opening and closing, inelastic unloading and reloading of which the Multi-crack model is not able to. Through this comparison, extra comprehensive understandings about the advantages and limitations of the two models can be pointed out.

Furthermore, another major reason why both Multi-crack and Craft models are chosen is because of the availability of their source codes for academic research use from the models' author, Dr. Tony Jefferson, so that in some circumstances, they can be referred to understand the underlying theories and solutions of the models used.

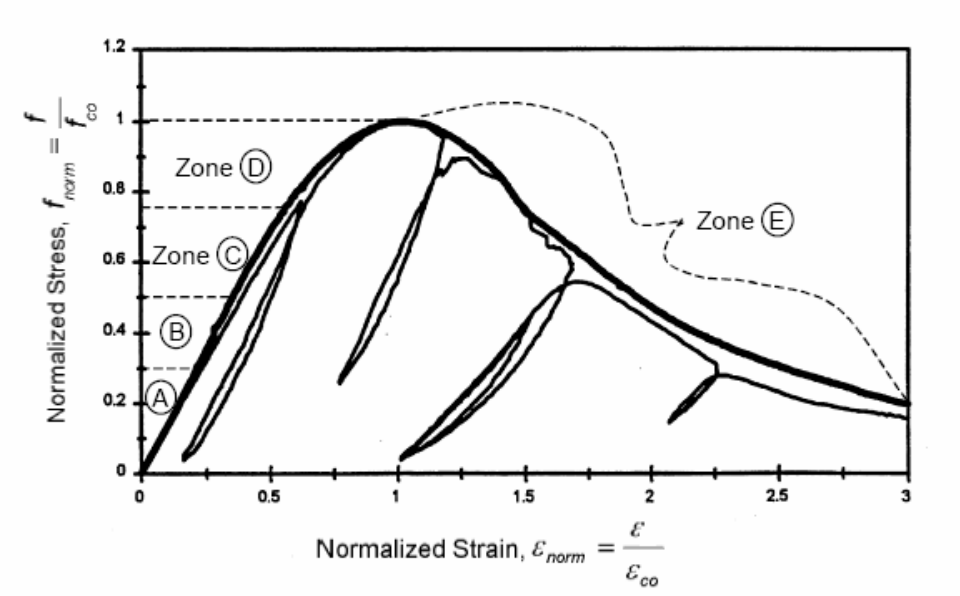

Figure 2.1 Behaviour of concrete under uniaxial monotonic and cyclic compressive loading (after Bahn and Hsu 1998)

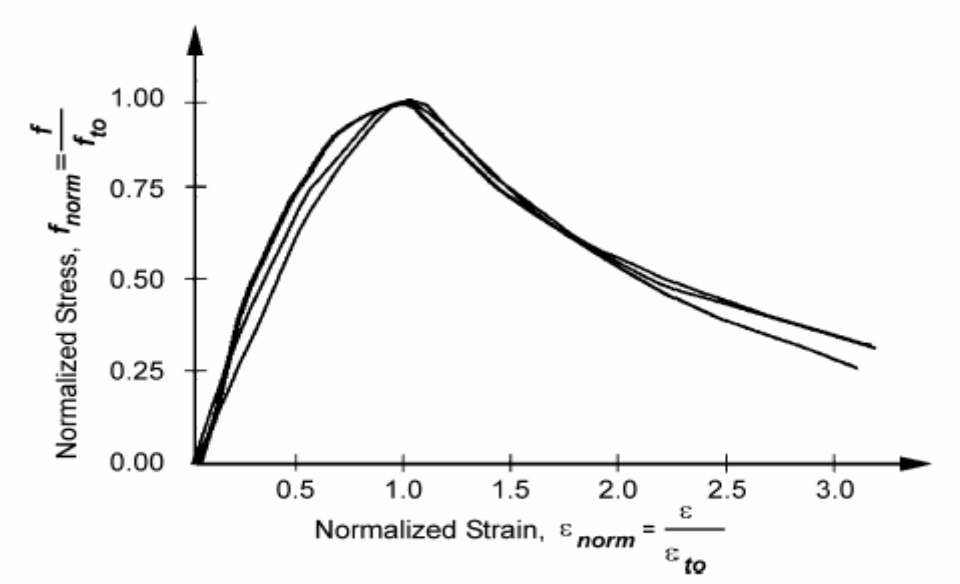

Figure 2.2 Behaviour of concrete under uniaxial monotonic tensile loading (Yankelevski and Reinhardt 1987)

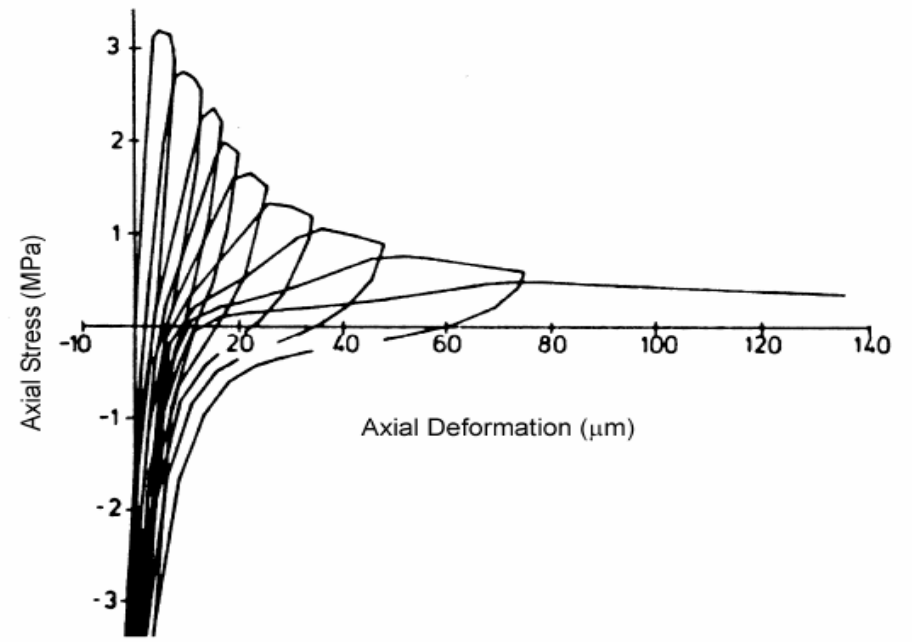

Figure 2.3 Stress-deformation curve of concrete subjected to reserved cyclic tensile loading (Reinhardt *et al.* 1986)

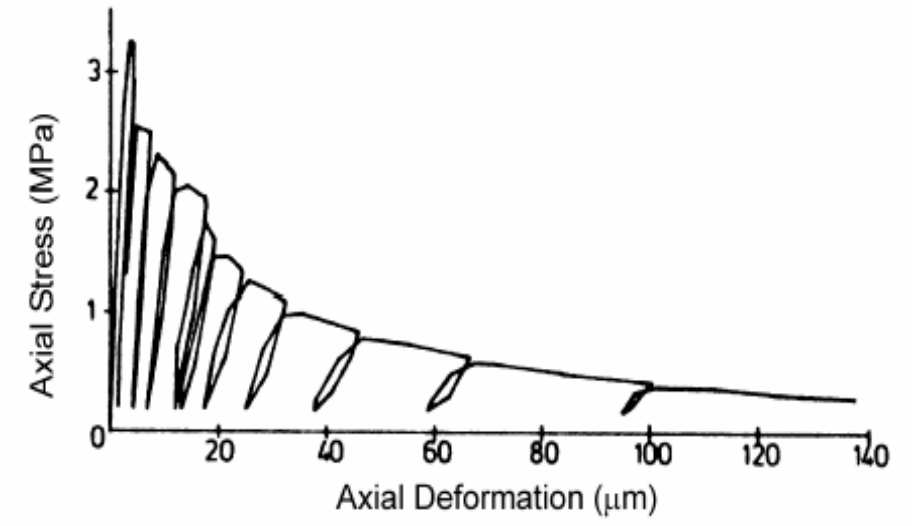

Figure 2.4 Stress-deformation curve of concrete subjected to uniaxial cyclic tensile loading (Reinhardt *et al.* 1986)

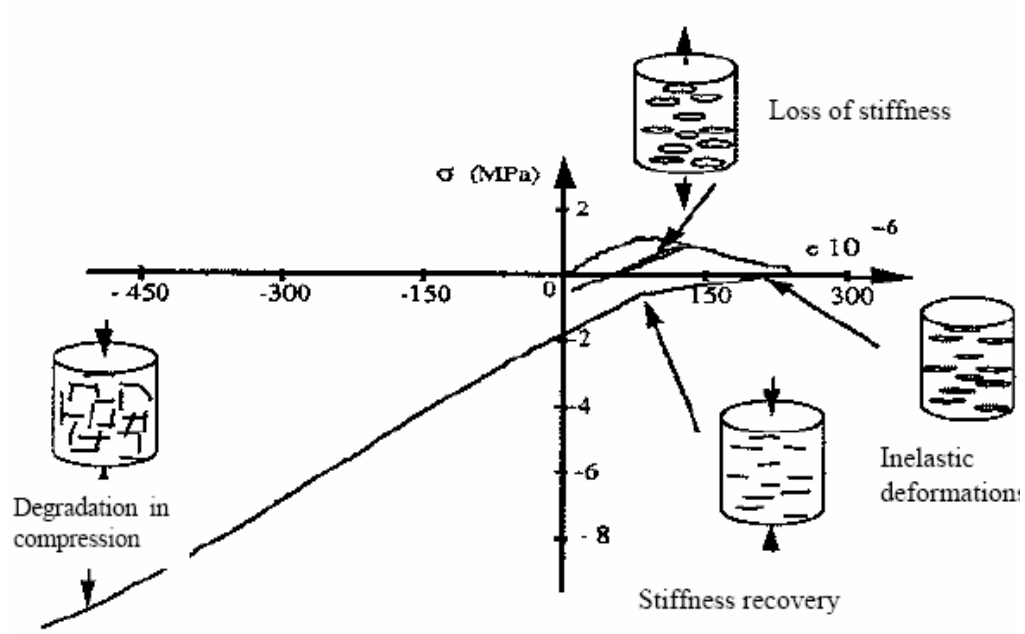

Figure 2.5 Uniaxial Behaviour of concrete under cyclic loading (Ramtani 1990; as presented by Nechnech 2000)

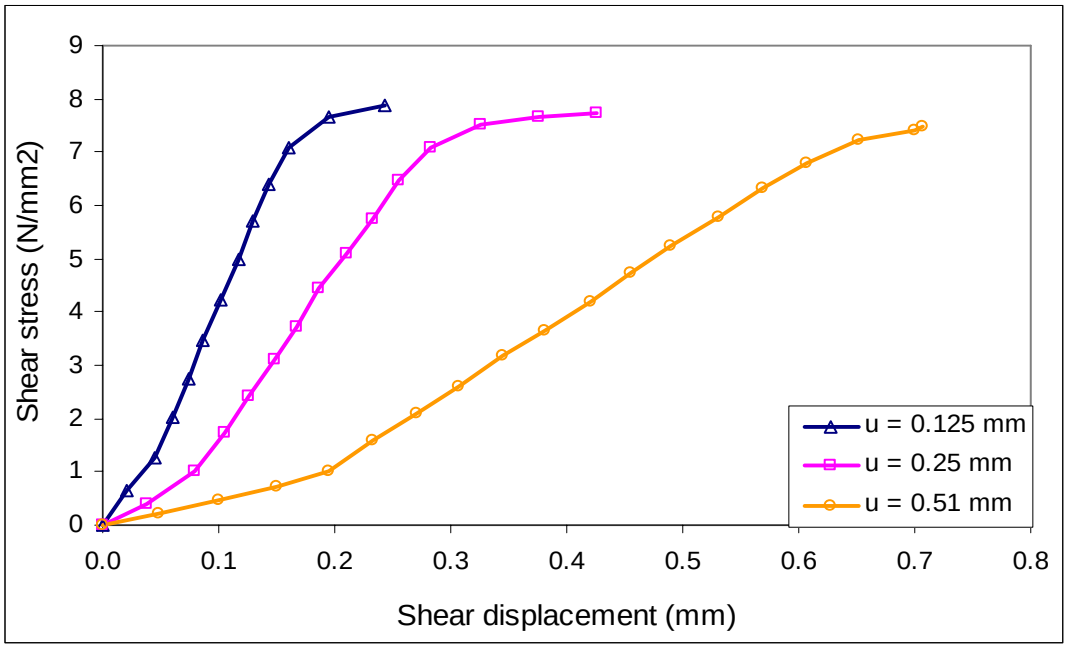

Figure 2.6 Shear test results by Paulay and Loeber (1974)
(u - opening displacement of the crack)

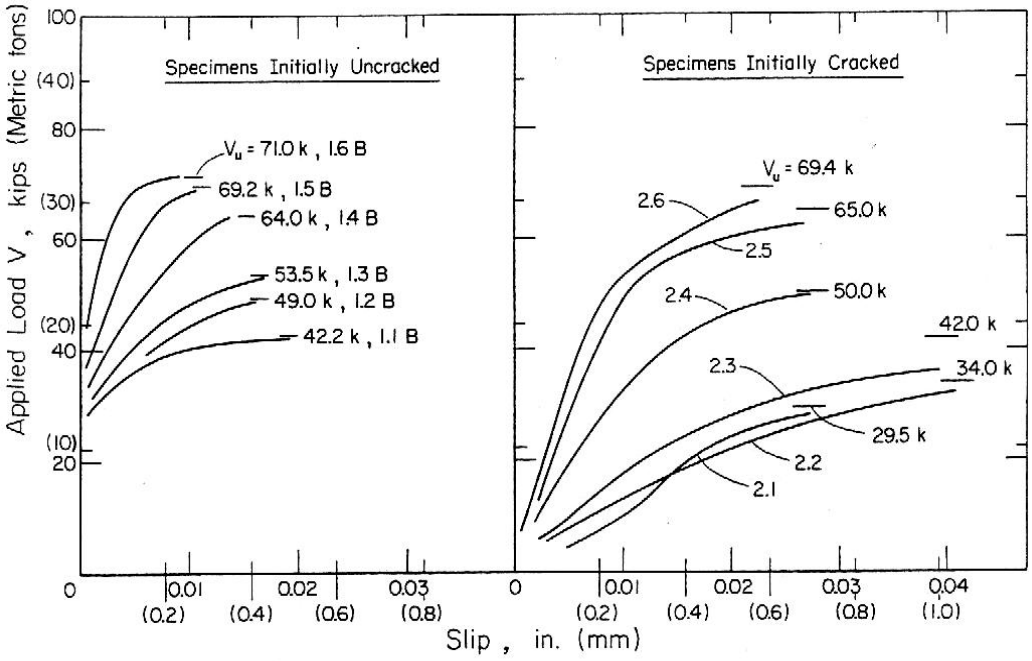

Figure 2.7 Shear test results by Hofbeck *et al.* (1969)

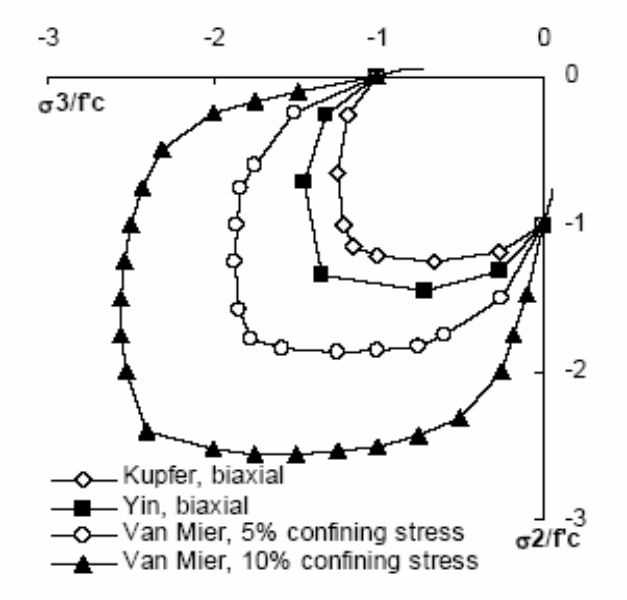

Figure 2.8 Biaxial compressive failure surface for concrete (data from Kupfer *et al.* 1969, Yin *et al.* 1989, and van Mier 1986; as presented by Lowes 1999)

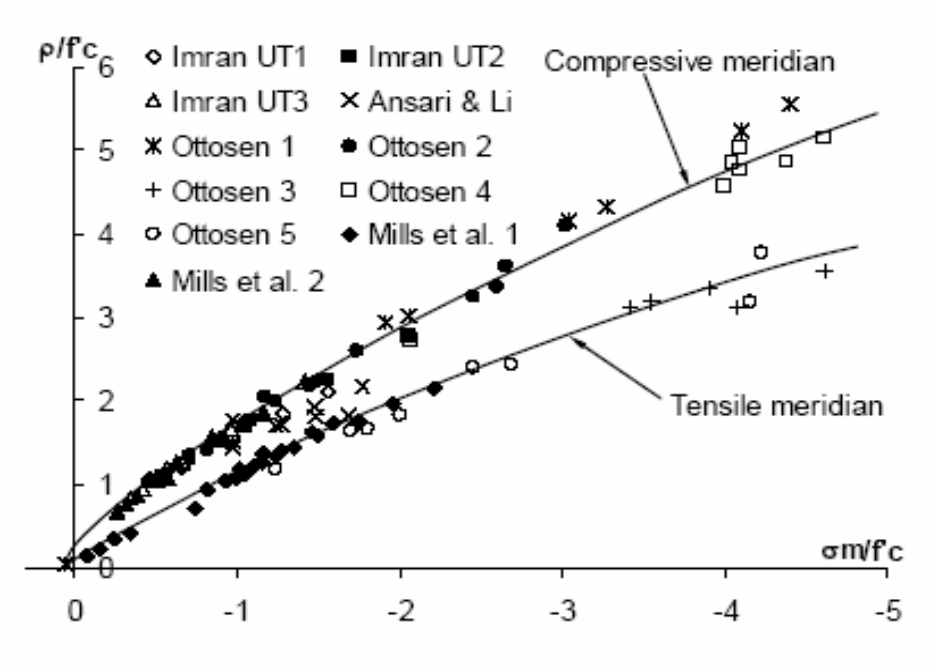

Figure 2.9 Tensile and compressive meridians of the failure envelope (data from Ansari and Li 1998, Imran and Pantazopoulou 1996, Ottosen 1977, and Mills and Zimmerman 1970; as presented by Chen and Han 1988 and Imran and Pantazopoulou 2001)

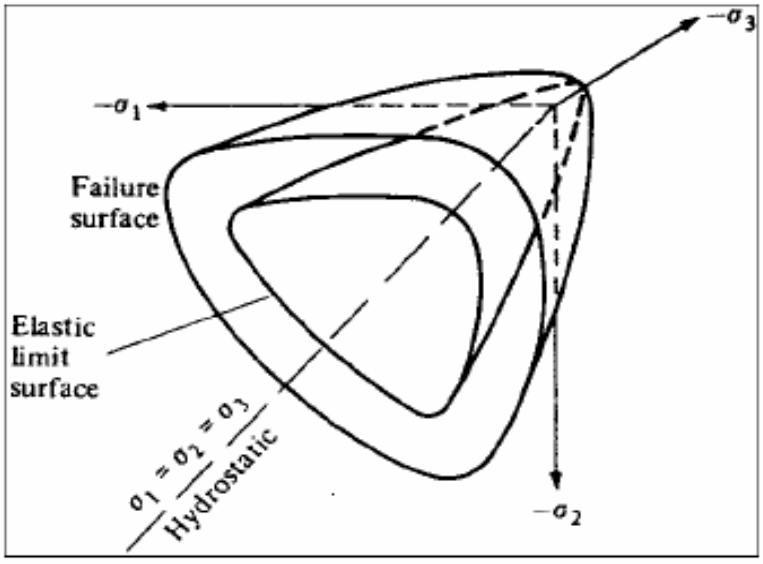

Figure 2.10 Failure surface and elastic-limit surface in principal stress space (Chen 1982)

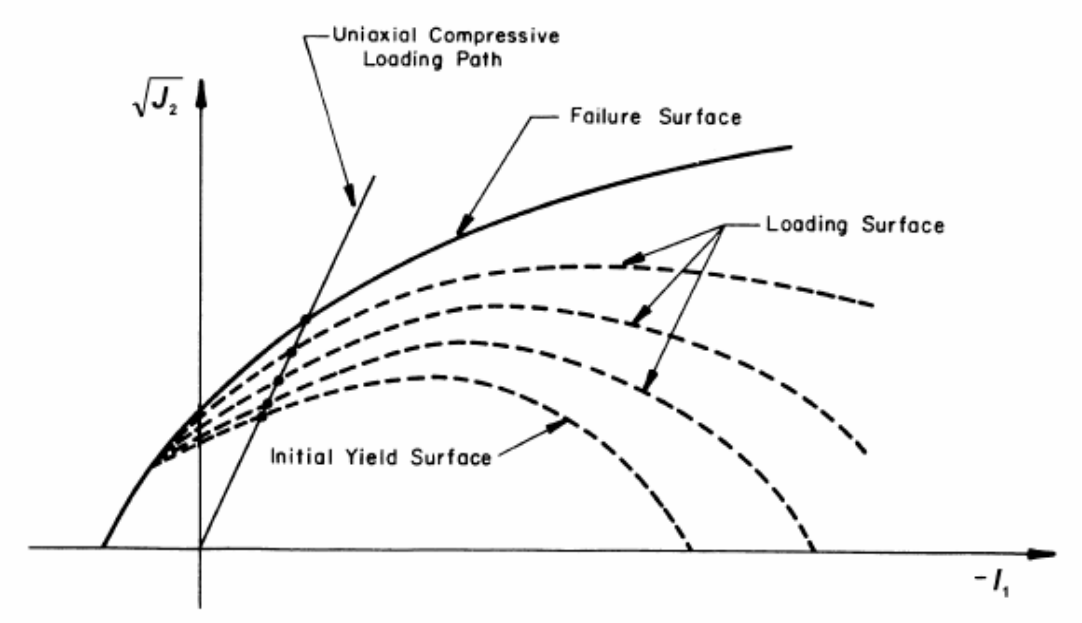

Figure 2.11 Evolution of the yield surface (Chen and Han 1988)

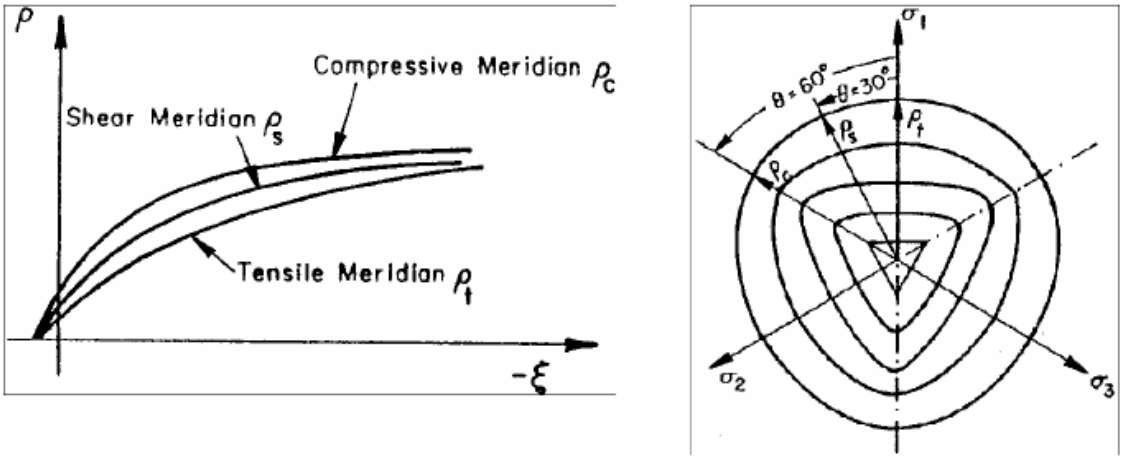

(a) Meridian planes (b) Deviatoric planes

Figure 2.12 Failure surface in meridian and deviatoric planes (Chen and Han 1988)

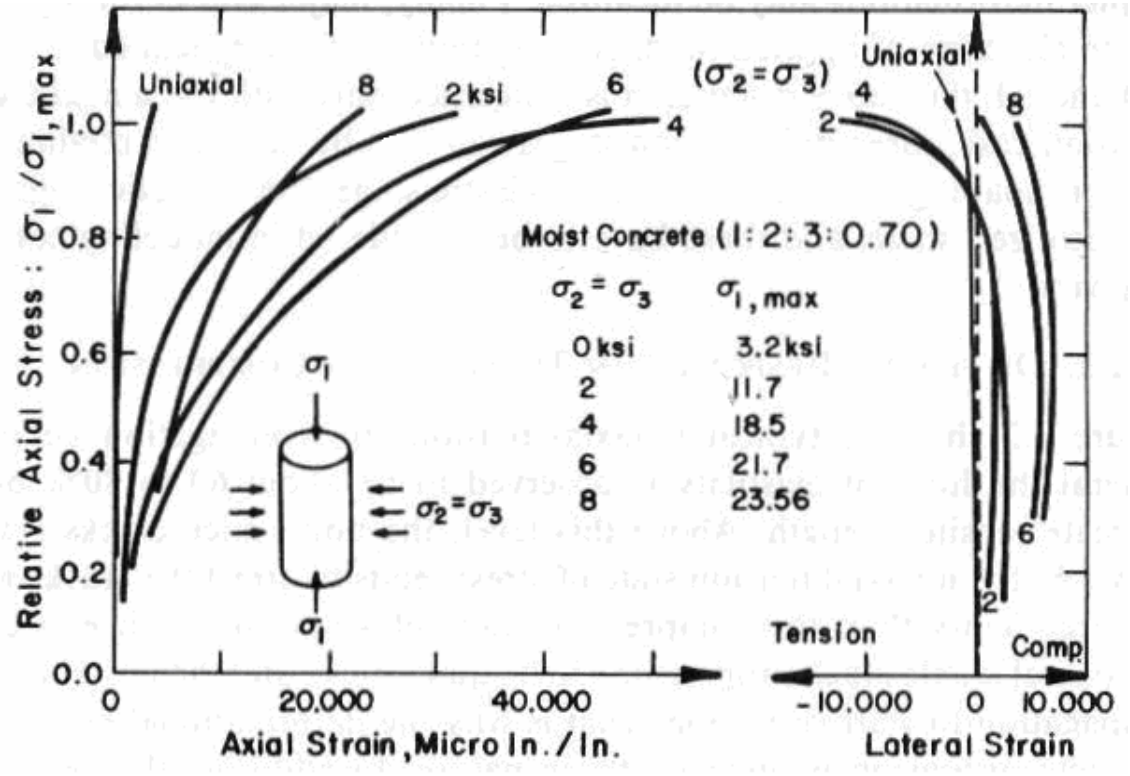

Figure 2.13 Stress versus axial strain and lateral strains curves (Palaniswamy and Shah 1974)

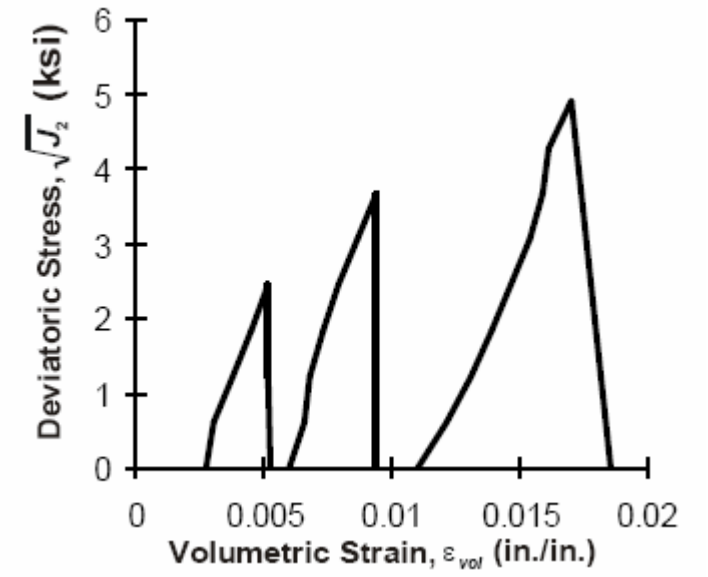

Figure 2.14 Deviatoric stress versus volumetric strain (data from Stankowski and Gerstle 1985; as presented by Lowes 1999)

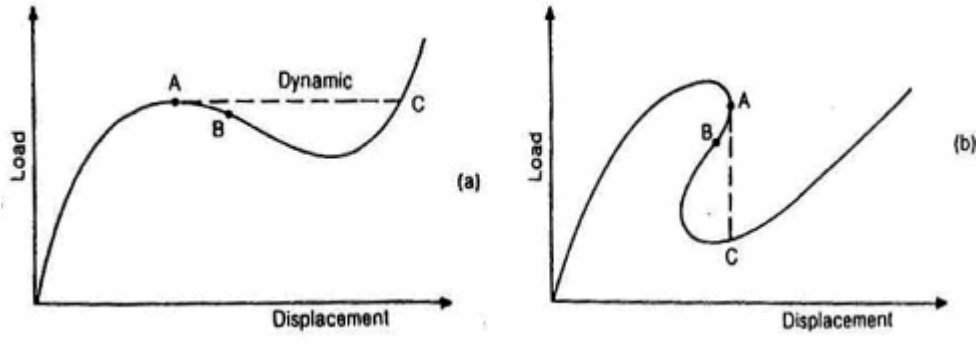

Figure 2.15 Snap-though (left) and snap-back (right)

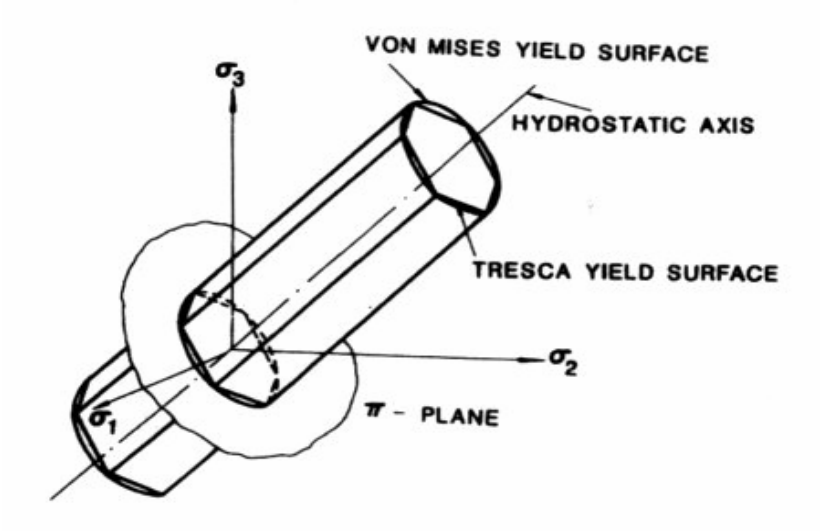

Figure 2.16 Von Mises yield surface in principal stress space

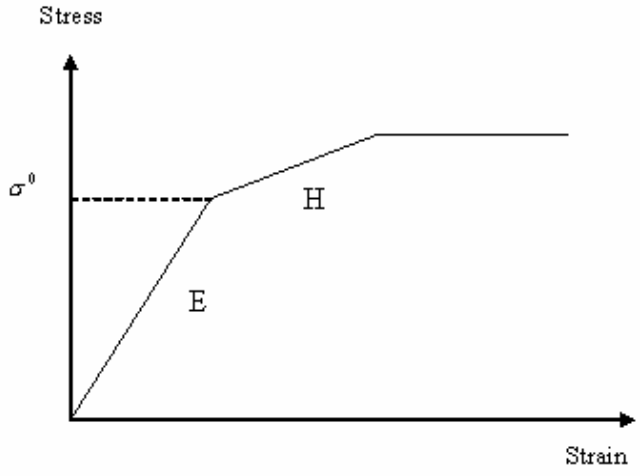

Figure 2.17 One dimensional elasto-plastic material for steel (H is the hardening modulus)

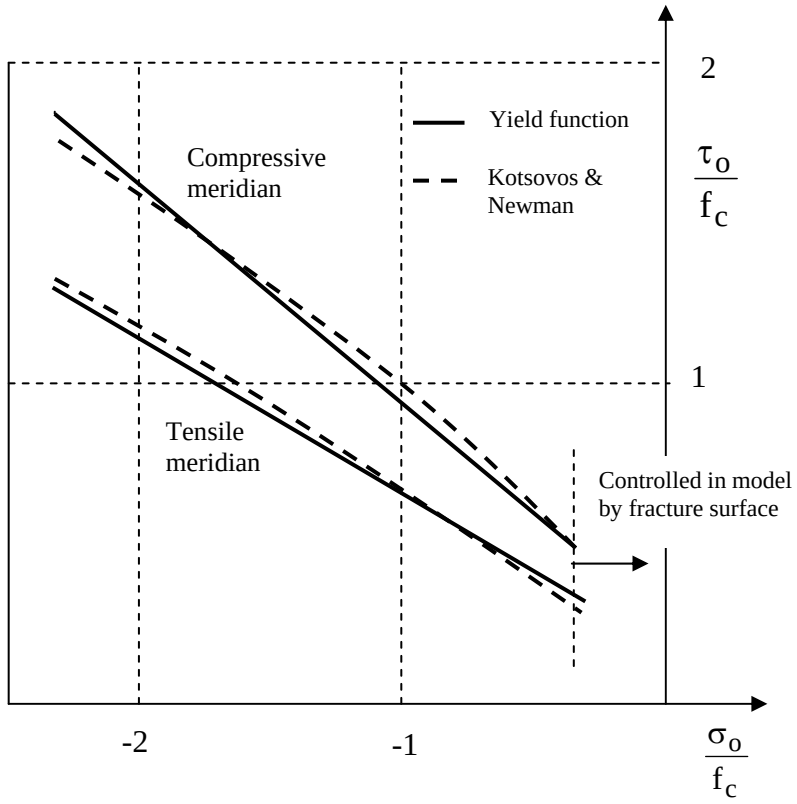

Figure 2.18 Yield function meridians

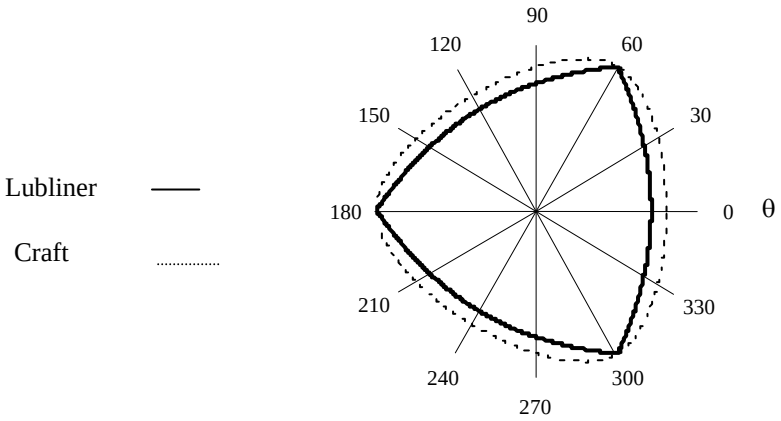

Figure 2.19 Yield function on the π-plane

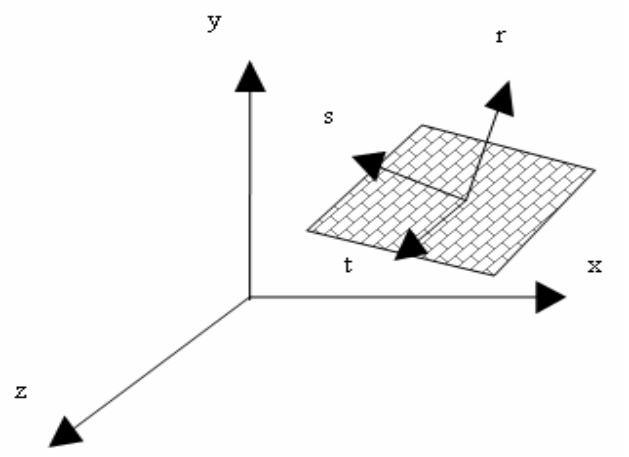

Figure 2.20 Crack plane: local and global co-coordinate systems

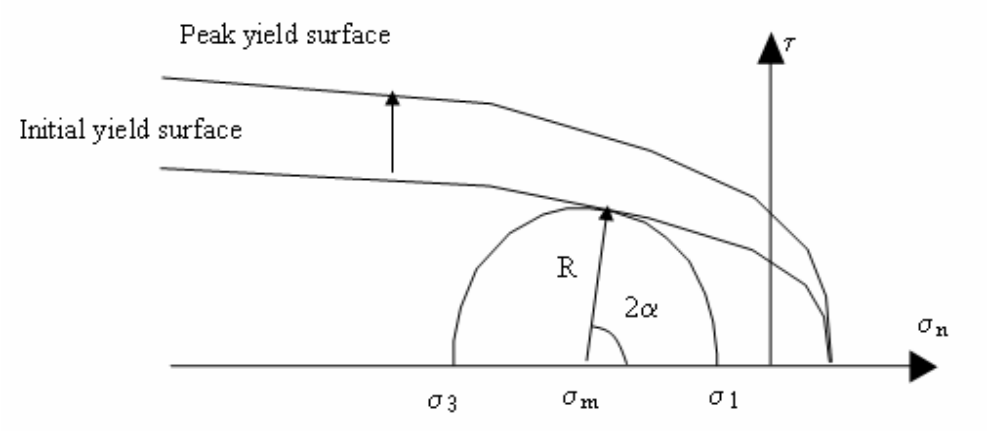

Figure 2.21 Local failure surface

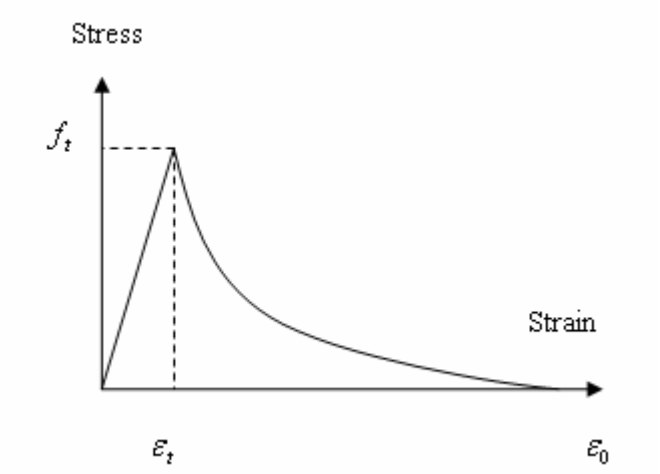

Figure 2.22 Stress-strain softening behaviour normal to a crack plane

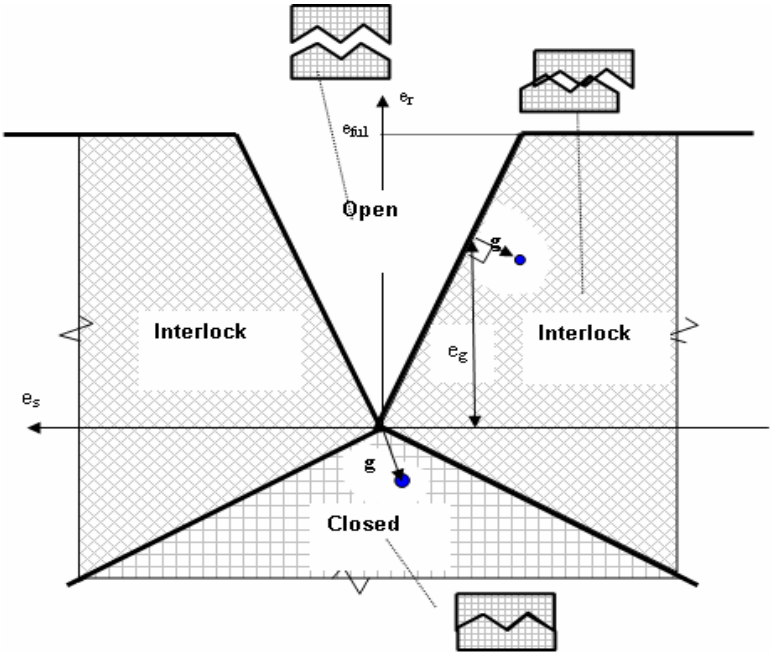

Figure 2.23(a) Local contact states

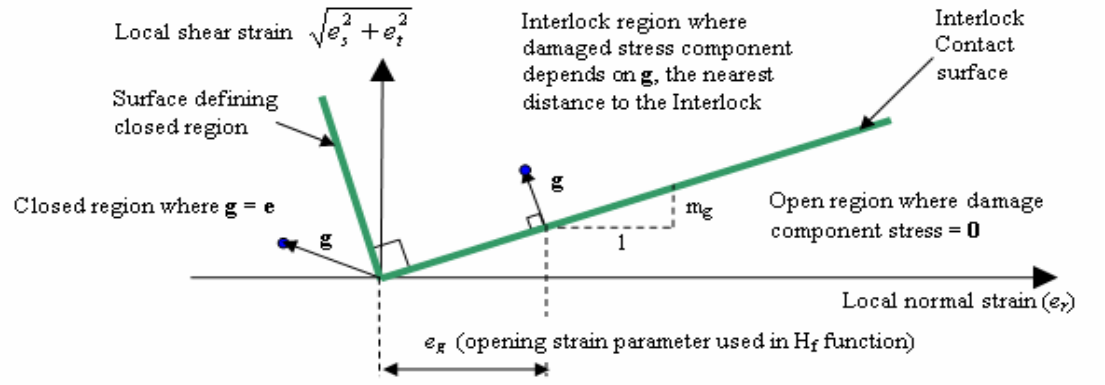

Figure 2.23(b) Contact surface

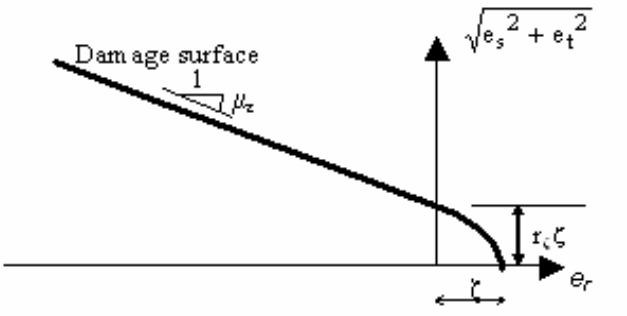

Figure 2.24 Local strain-based damage surface

CHAPTER 3

NUMERICAL GENERATION OF ARTIFICIAL TIME-HISTORIES FITTING TO EUROCODE 8 ELASTIC RESPONSE SPECTRA

3.1 INTRODUCTION

In this chapter, artificial time-histories fitting to a Eurocode 8 (EC8) elastic design spectrum were numerically generated. The primary objective is to use the program SIMQKE (SIMQKE User Manual 1976) to generate appropriate sets of artificial time-histories to be used in the non-linear dynamic analysis in Chapters 7 and 8. The chapter begins with a brief literature review on main theoretical aspects of the generation of artificial earthquake-like ground motions. Following this review, the methodology proposed by Gasparini and Vanmarcke (1976) which is the basis of procedures implemented in the program SIMQKE is briefly presented. In the following sections, a number of artificial earthquake-like ground motion time-histories fitting to the EC8 response spectrum are randomly generated. In order to assess the applicability of the program SIMQKE, a comparison between the average of five and twenty generated velocity spectra and the target spectrum is made in agreement with the requirements of EC8. In the last part of this chapter, investigations on parametric studies and properties of the generated artificial earthquakes are made to fully understand the behaviour of the SIMQKE program, effects of several parameters to the generated artificial earthquake, and to refine its applications for the research in particular cases.

3.2 LITERATURE REVIEW

3.2.1 Overview

Earthquake time-histories (or, alternatively saying, accelerograms in many context presented in this thesis) are the most presentation of earthquake ground motion because they contain a wealth of information about the nature of seismic wave propagation and ground properties. Earthquake

time-histories are usually recommended to be used for dynamic analysis and design of building with irregularities as well as evaluation of the response of earth structures in terms of stability, deformation, and liquefaction potential (Priestley *et al.* 1996, Bommer and Ruggeri 2002). The paucity of strong recorded accelerograms for many seismic zones together with the widespread use of time-history dynamic analysis to assess structural response are still the primary motivations for the generation of time-histories for dynamic analysis and design (Lestuzzi *et al.* 2004). Strong earthquake time-histories are generated from one of three fundamental types of accelerograms (Bommer and Ruggeri 2002):

1. synthetic records obtained from seismological models
2. real accelerograms recorded in earthquakes,
3. and artificial records, compatible with the design response spectrum.

The synthetic accelerograms are usually generated from seismological source models and accounting for path and site effects. These models range from point source deterministic or stochastic simulations through their extension to finite sources, to fully dynamic models of stress release, although the latter are still under development. There has been significant developments on the generation of synthetic ground-motion accelerograms (e.g. Zeng *et al.* 1994, Atkinson and Boore 1997, Beresnev and Atkinson 1998, Boore 2003). However, their applications, in terms of determining the many parameters required to characterise the earthquake source, generally require the engineer to engage the services of specialist consultant in engineering seismology. The determination of the source parameters for previous earthquakes invariably carries a high degree of uncertainty, and the specification of these parameters can also involve a significant degree of expert judgement (Bommer and Acevedo 2004).

The second type of records are real accelerograms recorded during earthquakes, which are now easily accessible in large numbers through global databanks (Lee *et al.* 2001, Row 1996, Ambraseys and Bommer 1990, Ambraseys *et al.* 2000, Abrahamson and Shedlock 1997) and internet sites (Wald 1997) such as the Japanese strong-motion data (the K-Net site) at http://www.k-net.bosai.go.jp/k-net/index_en.shtml, the NGDC site at http://www.ngdc.noaa.gov, the European Strong-motion Data (ISESD) at http://www.isesd.cv.ic.ac.uk, the COSMOS

website at http://db.cosmos-eq.org, and the PEER databank at http://peer.berkeley.edu/smcat. In order to select appropriate records of strong earthquakes for engineering analysis and design, practicing engineer requires both an extensive databank of accelerograms and access to a database of reliably determined parameters (Bommer and Ambraseys 1992). Nonetheless, after the records are selected, there will generally be a requirement to ensure that the records conform to some specified levels of agreement with the ordinates of the design response spectrum in order to use the records as input for dynamic analysis and design purposes. As guidelines on procedures for the selection of acceleration time-series for this purpose are lacking, and seismic design codes are particularly poor in this respect, Bommer and Acevedo (2004) have recently proposed criteria for selecting records in terms of earthquake scenarios and in terms of response spectral ordinates, together with options and criteria for adjusting the selected accelerograms to match the elastic design spectrum.

The third type of records is to use accelerograms generated fitting to a target response spectrum (Gasparini and Vanmarcke 1976). Generally, the approach is to generate a power spectral density function from the smoothed response spectrum, and then to derive sinusoidal signals having random phase angles and amplitudes. The sinusoidal motions are then summed and an iterative procedure can be invoked to improve the match with the target response spectrum, by calculating the ratio between the target and actual response ordinates at selected frequencies. The power spectral density function is then adjusted by the square of this ratio, and a new motion is generated (Section 3.3). The attraction of such an approach is obvious because it is possible to obtain acceleration time-series that are almost completely compatible with the elastic design spectrum, which in many cases will be the only information available to the design engineer regarding the nature of the ground motions. However, there may still be problems in the use of artificial records as they tend to have unrealistically high numbers of cycles of motion; and consequently they possess unreasonably high energy content, especially for inelastic analysis. The reason is the target elastic response spectrum is never intended to present the response of a single-degree-of-freedom structure to any single earthquake ground motion. In contrast, it is intended to envelop multiple earthquake ground motions which correspond to a specified risk level. Therefore, the resulting design spectrum compatible acceleration time-history will contain

energy over the whole range of structural periods that is not seen in actual recorded time-histories. One disadvantage is that this can overestimate the input energy which may result in vastly different estimates of design displacement demand for non-linear structures (Naeim and Lew 1995).

Based on the above reviews, it can be revealed that real accelerograms by definition are free from the problems associated with either synthetic records or artificial spectrum-compatible records. However, even real recorded accelerograms are now widely available as mentioned above, it is noted that a significant gap in the present day collection of accelerograms is that shaking in vicinity of the causative fault in a truly great (Richter Magnitude 8) earthquake has rarely been recorded (Bommer and Acevedo 2004). Individual real earthquake records are limited in the sense that they are conditional on a single realisation of a set of random parameters (magnitude, focal depth, attenuation characteristics, frequency content, earthquake duration, etc), a realisation that will likely never occur again and that may not be satisfactory for analysis and design purposes. In addition, even today with the large number of real accelerograms recorded during the past three decades, it may still be difficult to find groups of strong earthquake time-histories that fulfil the requirements of certain magnitude and distance for design earthquake conditions. Unfortunately, the approach for selecting real accelerograms for dynamic analysis and design is still an on-going research (Bommer and Acevedo 2004, Lestuzzi *et al.* 2004) and therefore it is not yet simple to obtain appropriate accelerograms without the service of an engineering seismologist.

In this thesis, artificial records compatible with the design response spectrum will be adopted because of several advantageous reasons in comparison with synthetic and real accelerograms, and they are listed as follows:

- Several sets of earthquake time-histories compatible with a design response spectrum can be generated for the selection and they are completely suitable for our research purposes as to investigate the dynamic behaviour of the structure under earthquakes coming from the same seismic site.

- Strong-earthquake records can be artificially generated by prescribing frequency content, acceleration amplitude, shaking duration, soil conditions, and time modulating function, which are considered to be appropriate to a particular site. This seems to be impossible to be realised with either synthetic or real earthquake accelerogram approach.
- There is relatively little published guidance in the literature and in seismic design codes on the subject of generating and selecting artificial earthquake time-histories compatible with the design spectrum for dynamic analysis (Bommer and Ruggeri 2002, Lestuzzi *et al.* 2004), and this study therefore attempts to present the issues involved and offer some insights as well as some guidance for either research or practical design.
- Most importantly, the limitation in the use of artificial time-histories, i.e. inducing unrealistically high frequency contents, would not affect the Author's research objectives on the qualitative assessment of damage and the representative number of time-histories required for non-linear dynamic analysis (see Chapters 7 and 8).

In the process of earthquake generation, it is clear that determining the power spectral density function for the ground motion is the most important part. Therefore, reviews were performed on this subject and presented in the following.

3.2.2 Power spectral density function

The power spectral density function has been used as the basis in the most common methods of developing artificial accelerograms because it does describe the energy content of the motion as a function of frequency and is directly compatible with representations of structural models by complex algebra (Crandall and Mark 1963, Liu 1969, Newmark and Rosenblueth 1971, Gasparini and Vanmarcke 1976, and Vanmarcke 1976).

At the beginning, "white noise" theory was used to simulate the earthquake ground motion and the power spectral density function $G(\omega)$ is assumed to be theoretically constant for all frequencies in order to create the earthquake ground motion (Bycroft 1960, Rosenblueth and Bustamante 1962). However, real earthquake ground motion is typically initiated with small

amplitudes that rapidly build up until it reaches an intensity that remains almost stationary for a certain time and then decay, steadily, until the end of the record. Therefore, it is not realistic for $G(\omega)$ to be constant for all frequencies as previously presented. In fact, observations and analyses from many data of real recorded earthquakes showed that a typical spectral density function of real earthquakes usually has only one dominant spectral peak in the frequency range (Liu and Jhaveri 1969, Tajimi 1960 and Kanai 1961). For the sake of simplicity, only this typical spectral density function is investigated in this thesis.

Based on examining, smoothing and/or averaging of the squared Fourier amplitudes $\left|F(\omega)^2\right|$ of actual strong earthquake records, Kanai (1957) and Tajimi (1960) proposed an semi-empirical formula for the power spectral density function:

$$G(\omega) = \frac{G_0\left[1 + 4\xi_g^2(\omega/\omega_g)^2\right]}{\left[1-(\omega/\omega_g)^2\right]^2 + 4\xi_g^2(\omega/\omega_g)^2} \tag{3.1}$$

where ω is the natural circular frequency of the structure, ω_g is the natural ground circular frequency, ξ_g is the viscous damping for the ground, and G_0 is a measure of ground intensity which can be suggested by Kanai (1961), or Der Kiureghian and Neuenhofer (1992). This power spectral density function has been widely used as a filter with "white noise" theory and extended in literature to generate strong-earthquake accelerograms (Housner and Jennings 1964, Liu and Jhaveri 1969, Rosenblueth 1964, Lin and Yong 1987). However, the above Kanai-Tajimi spectrum has the one drawback which is the zero frequency component of the power spectrum not being zero. This fact is physically inconvenient for acceleration and also velocity and displacement spectra as they are not defined at zero frequency. Clough and Penzien (1975) overcame this drawback by passing the Kanai-Tajimi spectrum through additional soil filter parameters to yield finite variances for velocity and displacements.

As the design response spectrum has been widely used in seismic practice, the most attractive and straightforward is to generate the power spectral density function from the design spectrum through a comparable relationship. In this case, the Fourier amplitude spectrum of the response is calculated and set compatible with the target design spectrum. Then the power spectral density

function can be derived from this Fourier amplitude spectrum because the squared Fourier amplitudes $\left|F(\omega)^2\right|$ and the spectral density function are proportional (Jenkins 1961, Rosenblueth 1964). Then artificial earthquakes can be derived from this power spectral density function. It is also known that even using the power spectral density function, the accelerograms cannot be determined uniquely from their response spectrum because the inverse problem does not mathematically have a unique solution subject to phase angles and the number of artificial earthquakes. However, it may be possible to develop accelerograms whose response spectra are close to a given response spectrum. Numerous studies have addressed the problem of generating spectrum compatible accelerograms. The following is a small sample of the works on spectrum compatible accelerograms: Hadjian (1972), Tsai (1972), Priestley (1967), Rizzo *et al.* (1973), Jennings *et al.* (1968), Saragoni and Hart (1974), Scanlan and Sachs (1974), Kaul (1978), Levy and Wilkinson (1976), Iyengar and Rao 1979, Wong and Trifunac 1979. Amongst them, Scanlan and Sachs (1974) was the first to generate an artificial motion by sinusoidal superposition using amplitudes derived from the values of the zero damping response spectrum. Besides, many researchers treat earthquake ground motion as a stationary or non-stationary random process with normal distribution of structural responses, therefore random analysis of the structure can furnish the expected maximum values of the structural response quantities, their variances, and confidence intervals (Ang 1974, Clough and Penzien 1975, Der Kiureghian 1979, Augusti *et al*. 1984). Through the use of random process, they also employed the concept of Kanai-Tajimi spectrum or the squared Fourier amplitude as used in previous research.

However, these above methodologies did not clarify the relationship between the response spectral values for arbitrary damping of the structure and the values of the spectral density function of the ground motion. Gasparini and Vanmarcke (1976) and Vanmarcke (1976) proposed a methodology to clarify this relationship by utilising random vibration theory. In the probabilistic approach, the loads are characterised by their power spectral density function. However, in seismic design, the response spectrum of the loads is known rather than their power density function or time-history. Therefore, the power density function is usually generated from the response spectrum from their relationship established from the probability density function of

the extreme values (e.g. Augusti *et al.* 1984). Since then, there have been numerous studies addressed the generation of spectrum compatible accelerograms such as Pfaffinger (1983), Kimura and Izumi (1989), and Pinto and Pegon (1991), Spanos and Mignolet (1990), Collins *et al.* (1995), Haddon (1996), Sabetta and Pugliese (1996), Ghaboussi and Lin (1998), Lin and Ghaboussi (2001), and Lee and Han (2002). However, they have been based on the same methodology as originally proposed by Gasparini and Vanmarcke (1976). Therefore, this methodology will be adopted in this research. In particular, only power spectral density function, typical of a real earthquake ground motion, is considered. Since this work is the basis of the procedures used in the earthquake simulation program SIMQKE, it will be summarised in the following section. In practice, some researchers have been using SIMQKE in their research and confirmed that SIMQKE works as well as most of the latecomers which use the same theory as SIMQKE (Priestley *et al.* 1996, 2003b, Vaparsuo 2001, 2004).

As Eurocode 8 (EC8) is going to be adopted as the definitive seismic code of the European Union, the significance of the seismic structure design according to Eurocode 8 cannot be over-stated. Therefore, the EC8 design spectrum will be directly adopted in this research as the target spectrum to generate compatible time-histories records. It should be noted that the current version of EC8 (ENV 1998-1:1996) was mainly used in this chapter. However as the pre-norm version of EC8 (prEN 1998-1:2004) was released near the end of this research, it was also included as many additional parts in this chapter.

3.3 THEORETICAL BACKGROUND (SIMQKE User Manual 1976)

3.3.1 SIMQKE Program *(NISEE Software Library, 2nd edition, University of California, Berkeley, USA, 2001)*

SIMQKE is one of softwares supplied by the NISEE Software Library, University of California, Berkeley, USA. The program is written in standard Fortran 77 with Makefiles provided for a variety of operating systems: PC DOS, VAX, UNIX, Sun Solaris, HP-UX, and Linux. It is also available to the Win95/98/NT platforms using the Visual Fortran or the Salford Fortran

Compilers. The basic theoretical background for SIMQKE is the relationship between the response spectrum for arbitrary damping and the expected Fourier amplitudes and Fourier series of ground motion (Gasparini and Vanmarcke 1976) which will be discussed in the following Section.

3.3.2 Theoretical background

In seismic engineering, the recorded earthquake-like ground motions are displayed as a function of time and such records could reveal the nature of earthquake motion. The earthquake-like ground motion can be described as a periodic function, in that it involves cyclical patterns of motion. This is due to the fact that earthquake was the result of propagation of seismic waves. The method used for numerical simulation in this study is based on the fact that any periodic function can be expanded into a series of sinusoidal waves (Housner 1955)

$$x(t) = \sum_{i=1}^{n} A_i \sin(\omega_i t + \varphi_i) \tag{3.2}$$

Characteristics of the sinusoidal waves such as amplitudes A_i, frequencies ω_i can be determined from the power spectral density function $G(\omega)$ and the target response spectrum (RS), respectively. The power spectral density function expressed the relative importance (i.e., the relative contribution to the total power) of sinusoidal waves with frequencies within some specified band of frequency, and it can be calculated from a target RS by using the theory of random vibration and the response of structures. By generating different arrays of phase angles φ_i by seeds of random number, different motions which are similar in general appearance (i.e., in frequency content) but different in details can be generated.

3.3.2.1 Calculating power spectral density function from the target response spectrum

The power spectral density function of the ith contributing sinusoid $G(\omega_i)$ can be expressed in term of the velocity spectrum S_v of a SDOF system at the same frequency, as shown below (Gasparini and Vanmarcke, 1976)

$$G(\omega_i) \approx \frac{1}{\omega_i\left(\frac{\pi}{4\xi_s}-1\right)}\left\{\frac{\omega_i^2 (S_V)_{s,p}^2}{r_{s,p}^2} - \int_0^{\omega_i} G(\omega)d\omega\right\} \tag{3.3}$$

Where $r_{s,p}$ is the peak factor; S_v is the target velocity RS; ω_i is the circular frequency of the i th contributing sinusoid; ξ_s is the fictitious time-dependent damping factor for a duration s, ($\xi_s = \frac{\xi}{1-e^{-2\xi\omega_n s}}$), in which ω_n is the natural circular frequency of the structure and ξ is the viscous damping factor of the structure; p is the probability factor. The definitions of these parameters can be found in Gasparini and Vanmarcke (1976).

3.3.2.2 Calculating amplitude of the motion

Assuming that the circular frequencies ω_i in Equation (3.2) are chosen to lie at equal intervals $\Delta\omega$, the relationship between the amplitude A_i and the power spectral density function can be expressed as

$$G(\omega_i)\Delta\omega = \frac{A_i^2}{2} \tag{3.4}$$

Figure 3.1 shows the value $\frac{A_i^2}{2}$ as the total power of the steady-state motion *x(t)*. Allowing the number of sinusoids in the motion to become very large, the total power will become equal to the area under the continuous curve $G(\omega)$.

3.3.2.3 The procedure of artificial motion generation

The method used for artificial motion generation is the superposition of the sinusoids (Equation 3.2) which have random amplitudes derived from a power spectral density function. The computer uses a "random number generator" subroutine to produce strings of phase angles (or seeds of random number) with a uniform distribution in the range between 0 and 2π. To simulate the transient character of real earthquakes, *x(t)* are usually multiplied by an intensity function *I(t)*.

$$x(t) = I(t)\sum_{i=1}^{n} A_i \sin(\omega_i t + \varphi_i) \tag{3.5}$$

Where A_i is the amplitude and φ_i is the phase angle of the ith contributing sinusoid; *I(t)* is the intensity function used to simulate the transient character of real earthquakes. The intensity function *I(t)* can be a trapezoidal, or exponential, or compound intensity envelope. In this research, the compound intensity envelope functions as proposed by Jennings *et al*. (1968) is utilised for a specific duration (Figure 3.2).

3.3.2.4 Generation of response spectra

Response spectrum *y(t)* is calculated from the following equations for a SDOF system

$$\ddot{y}(t) + 2\xi_t \omega_i \dot{y}(t) + \omega_i^2 y(t) = x(t) \tag{3.6}$$

Where *x(t)* is the artificial earthquake ground motion as shown in Equation (3.5).

3.3.2.5 Improving response spectral matches

Modify power spectral density functions in each smoothing cycle by the ratio of

$$\frac{G(\omega)}{G^c(\omega)} = \left[\frac{S_V}{S_V^c}\right]^2 \tag{3.7}$$

Where S_V and S_V^c are the target spectral value and the computed spectral value, respectively. $G(\omega)$ and $G^c(\omega)$ are target power spectral value and the computed power spectral value, respectively.

3.4 PROGRAM VALIDATION

3.4.1 Introduction

In EC8 including both the current ENV version (ENV 1998-1:1996) and the latest pre-norm version (prEN 1998-1:2004), which is not officially released to the public yet, elastic response

spectrum (RS) is presented in terms of acceleration RS. However, in the program SIMQKE, there is no option for generating of artificial earthquakes directly from an acceleration RS, but a velocity RS. Therefore, in this research, the velocity RS (and also the displacement RS) will be first derived from the acceleration RS by a calculation as shown in Appendix 3A. All the EC8 response spectra for different damping ratios and subsoil classes were calculated and shown in Appendix 3B. Here only the response spectra for subsoil class B of the current ENV version (ENV 1998-1:1996) and the latest pre-norm version (prEN 1998-1:2004) are presented as shown in Figures 3.4 and 3.5, respectively.

In this program validation, elastic design RS for the subsoil class B as defined in the current ENV version of EC8 (ENV 1998-1:1996) is taken as a target response spectrum (Figure 3.4). Also in this test, elastic design RS for the recommended Type 1 for subsoil class B as defined in the latest version of EC8 (prEN 1998-1:2004), is taken as a target response spectrum (Figure 3.5).

Several sets of artificial time-histories will be generated from an EC8 velocity RS, or EC8RS in brief. In order to select the artificial earthquakes from the EC8RS, the corresponding velocity RS are computed for different damping ratios and their average RS are compared with EC8RS and assessed by requirements from EC8.

3.4.2 Generation of artificial earthquakes fitting to a velocity RS in the current ENV version of EC8 (ENV 1998-1:1996)

The velocity spectrum with coefficient of viscous damping ratios ξ = 0.00, 0.02, and 0.05 (Figure 3.4), is taken as an input response spectrum. A 20-second duration of the ground motion is specified. More details on the choice of duration for generation of artificial earthquakes can be found in the parametric study part in this chapter. The peak ground acceleration is assumed to be of 0.35g (m/s^2), as consistent as the motion expected near the epicentre of a Magnitude 6 shock (Jennings *et al.* 1968). Spectral accelerations at 200 different periods in between the period range of 0.02 and 5 seconds, are used. No iteration technique is used. Iteration technique is used to improve the match of the artificial time-histories to the EC8RS of different damping. They will

be mentioned in the parametric study part. A compound intensity envelope function suited with this type of earthquake (Jennings *et al.* 1968) is used to simulate the transient character of a real earthquake, as shown in Figure 3.2. Table 3.1 summarises the parameters used for earthquake generation in this test.

In order to assess of the applicability of SIMQKE program, five statistically independent time-histories are generated (EC8 requires a minimum of 3 acclelerograms should be used (ENV 1998-1:1996 and prEN 1998-1:2004)), and a comparison between the average of five generated velocity spectra and the EC8 spectra for the coefficient of viscous damping ξ = 0.00, 0.02, and 0.05, respectively, was made (Figures 3.6(a), 3.6(b), and 3.6(c), respectively).

It can be seen from Figure 3.6 that, in general, the response spectra corresponding to the generated artificial earthquakes are the smooth curves but with a lot of oscillations, which follow relatively well the EC8RS for ξ = 0.00, 0.02, and 0.05, especially in "high" and "low" frequencies ("very high frequency", "high frequency", "medium frequency" and "low frequency" are the terminologies used by Newmark and Hall (1982), as shown in Figure 3.3). For the case of ξ = 0.00, the velocity RS is somehow different from the EC8RS in high and partially moderate frequency ranges (> 0.86 Hz), but they are, lower than the EC8RS in the low frequency range, from 0.40 Hz to 0.80 Hz but not major discrepancies. For the cases of ξ = 0.02 and 0.05, there is a very good agreement between the average velocity spectra and the EC8RS, especially in the high frequency range, from > 5 Hz. It may be due to no iteration technique was used in this example that causes the difference between the computed RS and the EC8RS for the case of ξ = 0.00.

3.4.3 Generation of artificial earthquakes fitting to a velocity RS in the latest pr-EN version of EC8 (prEN 1998-1:2004)

Further to the validation of the program, a velocity RS (as shown in Figure 3.5), which was derived from the new EC8 recommended Type 1 elastic design RS for the subsoil class B, is also

taken as an input response spectrum to generate artificial time-histories. The characteristics for earthquake generation used in this test are shown in Table 3.2.

Twenty statistically independent time-histories are generated, and a comparison between the average of twenty generated velocity spectra ξ = 0.00, 0.02 and 0.05 and the EC8 spectra, respectively, was made (Figures 3.7(a), 3.7(b), and 3.7(c), respectively).

It can be seen from Figure 3.7 that, in general, the response spectra corresponding to the generated artificial earthquakes are the oscillating smooth curves, which follow relatively well the EC8RS for ξ = 0.00, 0.02 and 0.05, especially in high and low frequencies. For the case of ξ = 0.00, the velocity RS is somehow different from the EC8RS in high and partially moderate frequency ranges (> 0.86 Hz), but they are, in general higher than the EC8RS. For the cases of ξ = 0.02 and 0.05, there is a very good agreement between the average velocity spectra and the EC8RS in the high frequency range, from > 5 Hz or < 0.40 Hz. In the moderate frequency range, from 0.40 Hz to 2 Hz, the generated RS is lower than the EC8RS but not major discrepancies. The reason of the difference between the computed RS and the EC8RS in moderate frequency range could be due to no iteration technique was used in this example. More details about the effects of these parameters will be found in the parametric study part in this chapter.

3.4.4 Validation by the EC8 requirements

We use the requirements made in EC8 to check the suite of artificial time-histories. The current ENV version of EC8 (ENV 1998-2: 1994) states that "*Ensemble of accelerograms shall be validated by computing the average response spectra S for a damping value of ξ = 0.05 and for 100 oscilators with natural periods T_i in a geometric progression with common ratio 1.064786, i.e. with periods 0.04 s, 0.0426 s, 0.0454 s,…, 20.0 s. The ensemble is acceptable if, at least for 50 different periods, the average response spectrum is greater or equal than the site dependent response spectrum $S_e(T_i)$. Further more the geometric average of the ratios $S_e(T_i)/ S_e(T_i)$ for the 13 periods nearest to the fundamental natural period of the structure should be greater than 1*".

In the prEN version of EC8 (prEN 1998-1:2004) it states that "*in the range of periods between $0.2T_1$ and $2T_1$, where T_1 is the fundamental period of the structure in the direction where the acceleration will be applied; no value of the mean 5% damping elastic spectrum, calculated from all time-histories (a minimum of three accelerograms should be used), should be less than 90% of the corresponding value of the 5% damping elastic response spectrum*".

Figure 3.8(a) shows the comparison between the average of 5 computed 5% damping RS (as shown in Figure 3.6(c)) and EC8RS in the requirement of the current ENV version of EC8, in which all the spectral values of 78 oscilators with periods required as 0.04 s, 0.0426 s, 0.0454 s, etc, are plotted. It can be seen that the average RS is almost greater than the elastic response spectrum, i.e. at least for the first 72 different periods, the average response spectrum is greater or equal than the elastic RS. If, for example, the fundamental period of the structure is T_1 = 0.2 s, the ratio between the average RS and the EC8RS for the 16 periods nearest to the fundamental natural period of the structure are found to be greater than 1 (Figure 3.8(a)). Therefore, it is clear that the average of 5 computed RS has satisfied the requirement from the current ENV version of EC8.

Furthermore, herein also check whether or not the artificial time-histories comply with the requirements of the prEN version of EC8, that no value of the average spectrum, calculated from five time-histories is less than 90% of the corresponding value of the target RS. For example, if the fundamental period of the structure is T_1 = 0.2 s, the comparison between the average of 5 RS and the target RS in between $0.2T_1$ and $2T_1$ is shown in Figure 3.8(b). It can be seen from the figure that the average of five generated RS is also satisfactory the requirements of the prEN version of EC8. Although we demonstrate here only for the assessment of the average of 5 computed RS for an example in this section, the procedure of this assessment is general and can be applied for any example in this chapter. Therefore it will not be mentioned again, and also the case of 5% viscous damping will be used in most of examples in the following sections.

Five acceleration time-histories generated for example in 3.4.2 are shown in Figure 3.9. It can be seen that these artificial earthquakes look generally realistic as they show some common features

of a typically real earthquake: the motions are generally extremely irregular, resembling random time functions, highly oscillatory; it is initiated with small amplitudes and rapidly built up until they reach an intensity that remains almost stationary for a certain time and then decay, steadily, until the end of the record. However, the number of strong pulses in the artificial accelerograms seems to be much higher than in real ones, i.e. there are more pulses at the peak acceleration of 0.35g as shown in all five acceleration time-histories (Figure 3.9). It is because of the tendency of saturating the strong-motion duration at the maximum spectral acceleration level in the target RS (see Naeim and Lew 1995, or Section 3.2.1).

3.5 PARMETRIC STUDIES AND PROPERTIES OF GENERATED MOTIONS

Suitable earthquake time-histories can only be generated if the program parameters and properties of an earthquake that affect the generated earthquakes are clearly understood. Therefore, this section investigates the influences from the characteristics of artificial earthquakes such as the power spectral density function $G(\omega)$, earthquake duration, maximum frequency ranges, local soil conditions, and time intervals; and from the program parameters such as the iteration technique and frequency content to the generated earthquakes.

3.5.1 Variation of $G(\omega)$ derived from a typical set of EC8 response spectra

In this study, the current ENV version of EC8 response spectrum for the subsoil class B for coefficient of viscous damping ξ = 0.02, 0.05, and 0.10 is used as a target spectrum. Five artificial earthquakes are generated from the EC8RS with 2%, 5% and 10% of damping for the subsoil class B. Table 3.3 shows the characteristics for earthquake generation used in this study.

As the spectral density function of ground motion at a site $G(\omega)$ is derived from Equation (3.3), its behaviour also depends on the chosen earthquake duration, *s*, and on the viscous damping coefficient, ξ, involved. Effects of earthquake duration on the artificial earthquakes will be discussed in the next section.

Figure 3.10 shows the averaged power spectral density functions for generated earthquakes at various damping ratios. It indicates that for $\xi \geq 0.05$ the power spectra show one dominant spectral peak at around 1.7 Hz in the moderate frequency range, and it means that the generated $G(\omega)$ reasonably presents a typical spectral density function of real earthquakes (Liu and Jhaveri 1969, Tajimi 1960 and Kanai 1961). Moreover, according to the shape of the EC8RS which has increased spectral velocities at in the high frequency range and then equal spectral velocities in moderate frequency range, it means that the spectral density function has a dominant spectral peak in these ranges. For $\xi \leq 0.02$, the resultant $G(\omega)$ has another spectral peak at a frequency at the intersection of the velocity and displacement ranges of the target response spectrum, i.e. 0.34 Hz. This is, in fact, not a typical form of real strong earthquakes (Liu and Jhaveri 1969, Tajimi 1960 and Kanai 1961). Therefore, viscous damping factor $\xi \geq 0.05$ will be adopted for the RC structures modelled in this research.

3.5.2 Effects of duration on $G(\omega)$ and the computed response spectrum

An ENV EC8 velocity RS for the subsoil class B with 5% of viscous damping is taken as an input response spectrum in this study. It is expected to be satisfactory the requirements of EC8 that artificial time-histories shall be generated so as to match the target EC8RS for $\xi = 0.05$. Table 3.4 shows the characteristics for earthquake generation used in this study. In order to investigate the effect of duration (s) to the artificial earthquakes directly through $G(\omega)$ and computed RS seven different values are used for the strong-motion duration: 10, 12, 15, 20, 30, 40 and 60 seconds.

Figure 3.11 shows the power spectral density functions for various values of the duration. It can be seen from the figure that as the duration increases, $G(\omega)$ decreases and this effect is more remarkable in the low frequency range. This is because the area under the $G(\omega)$ function decreases when the duration increases according to mathematical expressions in Gasparini and Vanmarcke (1976). It can also be seen that the change of duration, which affects $G(\omega)$, becomes

more marked in the high period domain. This agrees with the observations by other researchers (Priestley 1996, 2003a) that long duration earthquakes have more effects to structures which have long periods. It can be explained that the response of long period structures is very dependent on the duration of the artificial earthquakes. The response of long period structures remains transient during short duration earthquakes, and steady-state in long duration earthquakes. But the steady-state response depends much on the earthquake ground motion, or its power spectral density function.

Figure 3.11 also indicates that when the duration s is long, i.e. $s > 15$ seconds, $G(\omega)$ shows only one dominant spectral peak at where the EC8RS changes from ascending part to leveling part (at the frequency around 1.7 Hz) and as mentioned above, that is a typical form of most of real strong earthquakes. With short duration motions, $s \leq 15$ seconds, $G(\omega)$ appears to show another dominant spectral peak at where the target RS changes from leveling part to descending part (at the frequency around 0.34 Hz). In other words, the power spectral density function becomes increasingly sensitive to duration as the duration decreases and its shape at low frequencies for short duration artificial earthquakes does not appear to be typical of real earthquakes.

By examining the average of 5 computed RS as shown in Figure 3.12, it is evident that in low frequency range, the spectral match becomes much less oscillatory as the duration increases. Figure 3.12 also shows that the best agreements can be found with s of 20 to 40 seconds. Therefore, artificial earthquake-like ground motion time-histories with duration $s \geq 20$ seconds, particularly $s = 20$ seconds will be adopted in this research.

3.5.3 Effects of the number of smoothing cycles

Since the procedures employed in the program SIMQKE are stochastic in nature, the number of smoothing cycles plays important roles in the resulting response spectra. Starting with different smoothing cycles will result in distinct differences in the shape and values of the computed RS. In another word, these parameters could have significant effects in achieving a better matching between the target response spectrum and calculated RS.

For this study, the ENV EC8 response spectra for the subsoil class B for coefficients of viscous damping ξ = 0.00, 0.02, and 0.05 are used as target spectra. The characteristics for earthquake generation used in this test are shown in Table 3.5.

Number of cycles (n_c) to smooth the computed response spectrum (RS) is chosen increasingly from 1 to 50 cycles. As when a number of cycles (n_c) are more than 10, the process used in the program SIMQKE for smoothing seems to repeat a similar way with n_c = 9 to 1, therefore only 9 cycles will be studied here. Investigations are performed in order to understand the effect of the number of smoothing cycles to the computed response spectra. Five artificial earthquakes are generated from the EC8RS (ENV 1998-1:1996) for the subsoil class B. The average of five velocity RS computed from the corresponding artificial time-histories is compared with target EC8RS for ξ = 0.00, 0.02, and 0.05, but only the case of ξ = 0.00 is presented (shown in Figure 3.13) as it is representative enough.

When the number of cycle is 1, the computed RS matches the target RS very well in high frequency range but varies excessively below the target EC8RS for ξ = 0.00 in moderate and low frequency ranges (Figure 3.13). When n_c increases to 3, 4 or 5 cycles, the program raises the computed RS to match the target RS in moderate and low frequency ranges, but it lowers the computed RS a little bit to below the target RS in high frequency range. The computed RS is well matched with the target RS for ξ = 0.00 can be obtained with n_c = 3 to 5. When n_c increases from 6 to 7 cycles, the program lowers the computed RS to fit the target RS in moderate and low frequency ranges respectively, but it also lowers the computed RS in high frequency range. With n_c = 8 to 9 cycles, the computed RS is lowered a lot below the target RS in moderate and high frequencies. The gap between them increases rapidly in moderate and low frequencies as the number of cycles increases. If n_c > 9 cycles, the program raises the computed RS to gradually match the target RS again, and this procedure will repeat a similar way with n_c = 1 to 9 cycles again.

Table 3.6 shows an example of matching some spectral values of the average of five computed zero damping RS to the EC8RS using different number of smoothing cycles at some periods. The shadowed area describes the increasing spectral values of computed RS to match the EC8RS by using smoothing cycles. It is clear that when the number of cycle is 1, the computed RS matches the target RS very well in high frequency range; when the number of cycle is increasing to 3, the program raises the computed RS to well match the target RS in high frequency and half of moderate frequency ranges; when the number of cycle is increasing to 4 and 5, the program raises the computed RS to well match the target RS in moderate frequency range; when the number of cycle is increasing to 7, it seems that the computed RS intends to match the target RS in low frequency range. However, when the number of cycle is larger than 8, 9, the computed RS is decreasing below the EC8RS in moderate and low frequency ranges.

Matching the spectral values of computed RS to the EC8RS at some frequencies by using smoothing cycles can be explained as: with different cycles chosen, a new set of frequencies ω_i in Equation (3.2) will be chosen to be adjusted to match with the target spectral RS as shown in Equation (3.7). In each cycle, the process is carried out to compute the response spectra and compared with the target RS at a set of control frequencies, not for all frequencies. The ratio of the desired response to the computed response is obtained at each control frequency, and the corresponding value of the power spectral density is modified in proportion to the square of this ratio as shown in Equation (3.7) for any *i*th cycle. With the modified spectral density function, new amplitudes of the sinusoidal components are generated and then a new response spectrum is calculated. This iterative process tries to match the computed RS with the target RS with a given tolerance for a set of control frequencies. Therefore, it is not reasonable to expect to be convergent at all frequencies as can be seen from the results for different cycles mentioned above. Nevertheless, in each cycle, the response at a control frequency is dependent not only on the spectral density value at that frequency but also on other values at frequencies close to frequency of interest. This is the reason that no convergence criteria is implemented in the program SIMQKE and that the user simply specifies a desired number of iterations (Vanmarcke and Gasprini 1976).

Therefore, it can be concluded that there is not a particular number of cycles that can be used to obtain a set of computed RS which match the target RS with all frequencies. It is the most difficult to find the agreement between computed and target response spectra in (1) low frequency domain, and (2) very high frequency domain. The reason for both is because SIMQKE is interested in matching the computed RS and the target RS in a particular range of frequency in between 0.02 Hz and 50 Hz (SIMQKE User Manual 1976). It is probably because this frequency range is mostly recorded in earthquake engineering and seismology. In addition, in low frequency domain, the program generates less determining points from the target RS and the computed RS seems to be ill-defined in the low frequency range. Therefore, it is hard to match the computed RS to the target RS in low frequency range. The reason why there is difficult to find a good agreement in the very high frequency range can be explained as: owing to recording and processing limitations, strong earthquake accelerations provide little information about motion frequency content beyond a circular frequency $\omega_0 = 2\pi/\Delta T$, where ΔT is the minimum period and approximately 0.02 seconds (or a maximum frequency of 50 Hz); consequently, it is difficult to evaluate contributions to, say, the second spectral moment, due to frequencies beyond ω_0 (Gasparini and Vanmarcke 1976).

Approximately, the computed RS can be found to match the target RS in high and moderate frequencies with a small number of cycles, such as from 1 to 3 or 4 cycles depending on the coefficient of viscous damping.

The effect of the number of smoothing cycles can also be seen clearly for the comparison of the average of 20 computed RS with the target RS in the lasted version prEN of EC8 (prEN 1998-1:2004). In this study, the example in 3.4.3 is used with no iteration technique. The result in Figure 3.7(c) shows that, in general, the computed RS follow relatively well the EC8RS, especially in high and low frequency domains, from > 5 Hz or < 0.4 Hz. In the moderate frequency range, from 0.4 Hz to 2 Hz, the generated RS is lower than the EC8RS. Therefore, a number of 3 smoothing cycles are adopted in the generation in order to match the computed RS with the EC8RS in moderate frequencies. The comparison between the average of 20 computed

RS and the EC8RS is shown in Figure 3.14. Compared with Figure 3.7(c), Figure 3.14 clearly shows that there is a better agreement between the computed RS and EC8RS in high and moderate frequency ranges.

3.5.4 Local soil conditions

In this study, the EC8RS for the subsoil classes A, B, and C, respectively, with 5% viscous damping, are taken as target RS. All the characteristics for earthquake generation are shown in Table 3.7.

Figure 3.15 shows the comparison between the average velocity RS of twenty artificial time-histories and the target ones for subsoil classes A, B, and C. It confirms that there is a very good agreement between the computed RS and the EC8RS for each type of subsoil class. Because the computed response values are equal or a little bit higher than those of EC8RS for all frequencies, they are considered well fitted with the target RS according to the EC8 requirements (see Section 3.4.4). From these figures, it is generally observed that, for the same coefficient of viscous damping, the computed RS for subsoil class C is closer to the target EC8RS than those for subsoil classes B and A, respectively.

It can be concluded that when the target RS change according to different subsoil classes, the computed RS also change but still well fitted with the target one. This conclusion is similar to different subsoil classes in the prEN version of EC8 though the result has not been presented here. Therefore, sets of 20 artificial time-histories generated for different subsoil classes can be adopted in this research to investigate the effect of ground conditions to the RC structures.

3.5.5 Effects of frequency content of artificial earthquakes

Recently, no strong-motion seismographs can record earthquakes with frequencies up to 100 Hz - 200 Hz. For example, the strong-motion seismographs (K-NET95) used in Japan can record waveforms with a frequency of 100 Hz (Hiroyuki Fujiwara *et al.* 2004). But in earthquake

engineering, there has been no strong earthquake with frequency higher than 50 Hz recorded so far. In most of literature for different seismic zones, the frequency range of 0.5 Hz to 25 Hz has been quoted (Paul *et al.* 2003, Atkinson 1994, Hiroyuki Fujiwara *et al.* 2004). However, earthquake with frequency of 30 Hz has been recorded by K-NET95 in Japan (Hiroyuki Fujiwara *et al.* 2004). In the field of generation of artificial earthquakes, Varpasuo and van Gelder (2001) chose the frequency range 0.5 Hz to 33.33 Hz; Lee *et al.* (2001) generated artificial time history acceleration with the maximum frequency of 35 Hz; and Dinesh Kumar *et al.* (1998) used the highest frequency of 10 Hz to model synthetic accelerograms for Himalayan earthquakes.

In this investigation, different frequency ranges including 0.2 Hz to 50 Hz, 0.2 Hz to 33.33 Hz, 0.2 Hz to 25Hz, and 0.2 Hz to 12.5 Hz are used as inputs for generation of artificial earthquakes. The EC8RS for the subsoil class B for coefficient of viscous damping ξ = 0.05 is used as a target spectrum. Other input parameters are the same with those in the section 3.4.2. Table 3.8 shows the characteristics used for earthquake generation in this study.

The comparison between the average of five computed RS and the EC8RS is shown in Figure 3.16. It can be seen from the figure that when the maximum frequency range changes, it affects the artificial earthquakes and, consequently, the corresponding response spectra. It is because when the maximum frequency changes, it changes the frequency distribution and values (ω_i), and consequently, changes the distribution of artificial earthquakes as calculated in Equation (3.2). Figure 3.16 also shows that there is not much difference in the distribution of artificial earthquakes for frequency ranges of 0.2 Hz to 50 Hz, 0.2 Hz to 33.33 Hz, and 0.2 Hz to 25 Hz, but there is a significant change for the frequency range of 0.2 Hz to 12.5 Hz. However, it is expected that the gap between the target RS and the computed RS for the frequency range of 0.2 Hz to 12.5 Hz can significantly be reduced if smoothing technique is used.

Table 3.9 shows the values for spectral parameters of the central frequency (Ω) and its dispersion (δ_Ω) which are calculated from artificial earthquakes generated for different frequency ranges (detail calculations can be referred to Gasparini and Vanmarcke 1976). Table 3.10 presents the values of spectral parameters computed from some of real recorded earthquakes (Sixsmith and

Roesset 1970). It can be seen from Tables 3.9 and 3.10 that the spectral parameters for artificial earthquakes generated with the maximum frequency of 20 Hz are close to those of some real earthquakes, i.e. Taft and Olympia ones. The spectral parameters for artificial earthquakes generated with the maximum frequency > 25 Hz exceed those of real earthquakes. It may be because most of the recorded earthquakes have lower frequency ranges (Paul *et al.* 2003, Atkinson 1994, Hiroyuki Fujiwara *et al.* 2004). This observation reinforces the capability of the program SIMQKE in generating artificial earthquakes close to real ones.

Based on the above investigation and literature, it is advised that the maximum frequency of 50 Hz may be too high for the generation of artificial earthquakes. Therefore, the maximum frequency of 33.33 Hz or smaller will be adopted in this research.

3.5.6 Effects of discretisation time interval (Δt)

In order to express an artificial earthquake in time domain, the earthquake duration is usually discretised into equal time intervals. As known, an artificial earthquake can be expanded into a series of sinusoidal components in during the duration of time-histories. It depends on the value of the discretisation interval, or the number of equal intervals, the artificial earthquake may be described in different wave forms, and consequently different frequency contents.

The choice of discretisation interval must only be compatible with the shape of the target response spectrum regarding the maximum frequency of the generated time-history. It should be small enough so that the target RS frequencies can be described accurately enough, and consequently, the frequency content of the motion. For example, if the frequency range is chosen between 0.5 Hz and 33.33 Hz, the maximum ordinate of the EC8RS can be chosen at 33.33 Hz. There is a significant motion at frequency of 33.33 Hz meaning that the minimum period is 0.03 seconds. To describe the sinusoidal wave form of the length of 0.03 seconds, one needs at least 5 points for a crude description, and 9 points for a very good description. Therefore, the largest acceptable interval is 0.0075 seconds, and the good interval is 0.00375 seconds.

To investigate how the time interval affects the artificial time-histories, two different values of Δt, say 0.00375 and 0.0075 seconds, are used. The test using the EC8RS for subsoil class B is carried out for this investigation. Except the time interval, all other parameters are the same with those in the test used in 3.4.2. The results and comparison of typical generated time-histories are shown in Figure 3.17. It is clear from the figure that when the value of time interval is small, the sinusoidal components of the motion are closed together, and vice versa. In other words, when Δt is smaller, the motion has more pulses than that of larger Δt. The difference can be seen more clearly in Figure 3.18 which is extracted from Figure 3.35 for a short duration, i.e. from 6 to 7 seconds.

It can be concluded that smaller time intervals can describe the sinusoidal components of the motion more accurately than large time intervals. Within other earthquake parameters such as duration and frequency range, this parameter may be particularly important for structural analysis because of its influence on a large number of cycles when its value is large. However, as the different small time intervals may not cause much difference in the artificial earthquake forms, it is not necessary to choose a very small time interval in order to suit the practical purposes in non-linear dynamic analysis (see Section 7.3.4.3 in Chapter 7).

3.6 SUMMARY AND CONCLUSIONS

In this chapter, a brief literature reviews on generation of artificial earthquakes fitting to a design response spectrum has been presented first. In particular, the review has focused on the generation of the power spectral density function compatible with the design spectrum.

Then the theoretical background of generation of artificial earthquake-like ground motions compatible with an elastic response spectrum using the program SIMQKE has been briefly presented with its key properties. The program accuracy has been tested by generating several sets of five and twenty artificial time-histories and by comparing the average of these five and twenty generated RS with the target ones including EC8RS in both ENV and prEN versions of EC8. The results show that there is a very good agreement between them, especially at the high

and moderate frequency domain. Different coefficients of viscous damping have been used, but the research has been mainly focus on the structural response with 5% critical damping. This is enough to be satisfactory the requirement of EC8 that artificial time-histories shall be generated so as to match the target EC8RS for 5% viscous damping.

It was followed by parametric study using the program to give insight into the variations of ground motion spectral density function such as different target spectra and durations, and to quantify the effects of iterative techniques through parameters such as the number of smoothing cycles. The properties of generated acceleration time-histories have also been investigated in details through some parameters such as the duration of the earthquake, local soil conditions, maximum frequency range of the earthquake, and time interval. The aim of these studies is to understand all the related parameters and to find the most suitable sets of artificial earthquake-like ground motion time-histories to be used for FE analyses of RC structures. It can be summarised as follows

Literature reviews

1. There are three fundamental methods to obtain earthquake-like ground motion time-histories for dynamic analysis: synthetic records obtained from seismological models, real accelerograms recorded in earthquakes, and artificial records, compatible with the design response spectrum. The artificial earthquake time-histories generated compatible with the design response spectrum is adopted in this thesis because of its convenience and the suit to the Author's research objectives. The limitation of this approach does not affect the conclusion of the research about the representative number required for non-linear dynamic analysis (see Chapters 7 and 8).

2. The most importance of generation of artificial time-histories fitting to the design response spectrum is to find the power spectral density function for the earthquake motion. There has been a vast of research about this matter but Gasparini and Vanmarcke (1976) was the first who clarify the relationship between the response spectral values for arbitrary damping and the values of the

spectral density function of the ground motion by utilizing random vibration theory. Therefore, this methodology will be adopted in this research.

Program validation

1. The computed velocity RS corresponding to the artificial time-histories shown in non-smooth curve, which follow relatively well the target ENV and prEN EC8RS, especially in high frequencies. Using iteration techniques, i.e. the number of smoothing cycles, it can reduce the difference between the computed RS and the EC8RS in moderate or low frequencies and perform a good match.

2. The more numbers of artificial time-histories are generated, the closer the averaged value to the target response spectrum. When twenty artificial time-histories are generated, the averaged RS is smoother and better matched with the target EC8RS than that of five artificial time-histories.

Parametric study using the program

1. With respect to the power spectral density function $G(\omega)$ derived from the EC8 elastic response spectrum, the generated $G(\omega)$ reasonably presents a typical spectral density function of a real earthquake in the case of damping $\xi \geq 0.05$ (Section 3.5.1)

2. The power spectral density function $G(\omega)$ decreases with increasing duration of an earthquake. Artificial earthquake-like ground motions with duration larger than 20 seconds should be considered to ensure the generated $G(\omega)$ on a typical form of real earthquakes and to leave the long-period structures enough time to perform steady-state response (Section 3.5.2)

3. The match between the computed response spectrum and the target one should not be expected to be convergent at all frequencies. The convergence at high frequency range is easiest to obtain

even with no cycling technique used, as the central frequency is located in this range. It will be enough to consider the artificial time-histories if the structure to be analysed having its fundamental periods in this area. However, iteration techniques, i.e. the number of smoothing cycles, could be used to match the computed RS with the target EC8RS in moderate and low frequency ranges. A number of smoothing cycles from 1 to 4 can be adopted in the generation (Section 3.5.3)

4. It is difficult to find the agreement between computed and target response spectra in low frequency domain and very high frequency domain. It is mainly because the program SIMQKE is interested in matching the computed RS and the target RS in a particularly popular range of frequency, i.e. from 0.04 Hz to 25 Hz.

Properties of generated earthquake-like ground motions

1. Local soil properties have effects on the earthquake amplitude through the relative frequency and the duration of the earthquake (Section 3.5.4)

2. The maximum frequency range of 0.2 Hz to a maximum frequency $\leq$ 33.33 Hz can be chosen for the generation of artificial earthquake. Choosing this parameter is based almost on literature of earthquake engineering on the maximum frequency of real recorded earthquakes (Section 3.5.5)

3. The discretisation interval in duration of an artificial earthquake cannot be chosen freely but small enough in order to accurately describe the wave form and frequency content of the earthquake motion (Section 3.5.6)

It can be said again that suitable sets of artificial time-histories are obtained in the manner that their corresponding response spectra are well matched with the target EC8RS, are in typical forms of real-strong earthquakes, and are satisfactory all the requirements from EC8.

Based on the above investigations, suitably refined parameters such as $\xi \geq 0.05$, $s \geq 20$ seconds, maximum frequency range of 0.2 Hz to a maximum frequency ≤ 33.33 Hz, and iteration techniques, such as n_c = 1 to 4 cycles (seeds of random number as defaulted in the program), are used together to match the computed RS with the EC8RS in an allowable tolerance. Other parameters related to a specific seismic site such as soil conditions, peak ground acceleration, or the discretisation time interval used for generation of artificial time-histories will be studied in more details in particular cases in Chapters 7 and 8.

Therefore, several sets of twenty artificial acceleration time-histories compatible with the 5% damping EC8 elastic response spectra for different local soil conditions can now be generated for use in the FE analyses.

Table 3.1 Characteristics for earthquake generation according to example 3.4.2

Characteristics	**Input values**
Target response spectrum	EC8 velocity RS for ξ = 0.00, 0.02 and 0.05 (ENV1998-1:1996)*
Subsoil class	B
Duration	20 (s)
Peak Ground Acceleration (PGA)	0.35g (m/s^2)
Frequency range	0.2 - 50 (Hz)
Intensity envelope function	A compound intensity envelope function (Jennings *et al*. 1968)
Generated response spectrum for damping	ξ = 0.00, 0.02 and 0.05
Iteration number	1

* EC8 velocity RS is obtained from the original acceleration RS in EC8

Table 3.2 Characteristics for earthquake generation according to example 3.4.3

Characteristics	**Input values**
Target response spectrum	EC8 velocity RS for ξ = 0.00, 0.02 and 0.05 (prEN1998-1:2004)
Subsoil class	B
Duration	20 (s)
Peak Ground Acceleration (PGA)	0.35g (m/s^2)
Frequency range	0.25 - 33.33 (Hz)
Intensity envelope function	A compound intensity envelope function (Jennings *et al*. 1968)
Generated response spectrum for damping	ξ = 0.00, 0.02 and 0.05
Iteration number	1

Table 3.3 Characteristics for earthquake generation according to example 3.5.1

Characteristics	**Input values**
Target response spectrum	EC8 velocity RS for ξ = 0.02, 0.05 and 0.10 (ENV1998-1:1996)
Subsoil class	B
Duration	12 (s)
Peak Ground Acceleration (PGA)	0.35g (m/s^2)
Frequency range	0.2 - 50 (Hz)
Intensity envelope function	A compound intensity envelope function (Jennings *et al*. 1968)
Generated response spectrum for damping	ξ = 0.02, 0.05 and 0.10
Iteration number	1

Table 3.4 Characteristics for earthquake generation according to example 3.5.2

Characteristics	**Input values**
Target response spectrum	EC8 velocity RS for ξ = 0.05 (ENV1998-1:1996)
Subsoil class	B
Duration	10, 12, 15, 20, 30, 40, 60 (s)
Peak Ground Acceleration (PGA)	0.35g (m/s^2)
Frequency range	0.2 - 50 (Hz)
Intensity envelope function	A compound intensity envelope function (Jennings *et al*. 1968)
Generated response spectrum for damping	ξ = 0.05
Iteration number	1

Table 3.5 Characteristics for earthquake generation according to the first example in 3.5.3

Characteristics	**Input values**
Target response spectrum	EC8 velocity RS for ξ = 0.00, 0.02 and 0.05 (ENV1998-1:1996)
Subsoil class	B
Duration	20 (s)
Peak Ground Acceleration (PGA)	0.35g (m/s^2)
Frequency range	0.2 - 50 (Hz)
Intensity envelope function	A compound intensity envelope function (Jennings *et al*. 1968)
Generated response spectrum for damping	ξ = 0.00, 0.02 and 0.05
Iteration number	1, 2, 3, 4, 5, 6, 7, 8, 9

Table 3.6 Spectral values of EC8RS and average of five computed RS using different number of smoothing technique at some periods (the shadow area describes the increasing spectral values of computed RS to match the EC8RS)

Period (s)	SPECTRAL VALUES (in/s)						
	EC8RS	Computed RS					
		Number of smoothing cycles					
		1	3	4	5	7	9
0.04	7.43	21.62	26.38	27.57	26.24	27.09	14.80
0.4	40.25	63.60	95.48	80.20	58.17	64.92	40.98
0.6	60.37	62.27	76.78	73.16	65.28	60.83	49.28
1	60.37	45.00	63.09	55.93	49.78	49.90	34.01
1.5	60.37	39.39	68.59	71.15	65.63	40.72	30.73
2	60.37	50.68	51.00	70.90	69.43	53.74	32.28
2.5	60.37	47.25	48.31	50.31	57.01	48.38	28.57
3	60.37	48.24	51.93	52.70	56.71	43.22	22.45
3.5	51.75	39.82	49.30	37.38	52.61	39.84	18.16
4	45.28	35.67	39.22	35.84	36.57	38.24	18.90
4.5	40.24	32.38	37.50	41.85	34.58	38.25	23.08
5	36.22	31.14	31.47	38.32	40.08	46.08	22.32

Table 3.7 Characteristics for earthquake generation according to the first example in 3.5.4

Characteristics	**Input values**
Target response spectrum	EC8 velocity RS for $\xi = 0.05$ (ENV1998-1:1996)
Subsoil class	A, B, C
Duration	20 (s)
Peak Ground Acceleration (PGA)	0.35g (m/s^2)
Frequency range	0.2 - 50 (Hz)
Intensity envelope function	A compound intensity envelope function (Jennings *et al*. 1968)
Generated response spectrum for damping	$\xi = 0.05$
Iteration number	3

Table 3.8 Characteristics for earthquake generation according to example 3.5.5

Characteristics	**Input values**
Target response spectrum	EC8 velocity RS for $\xi = 0.05$ (ENV1998-1:1996)
Subsoil class	B
Duration	20 (s)
Peak Ground Acceleration (PGA)	0.35g (m/s^2)
Frequency range	0.2 - 50 (Hz), 0.2 - 33.33 (Hz), 0.2 - 25 (Hz), and 0.2 - 12.5 (Hz)
Intensity envelope function	A compound intensity envelope function (Jennings *et al*. 1968)
Generated response spectrum for damping	$\xi = 0.05$
Iteration number	1

Table 3.9 Spectral parameters computed from artificial earthquakes with different frequency ranges

Frequency range	Ω (rad/s)	δ_Ω
0.2 Hz - 50 Hz	49.86	0.77
0.2 Hz – 33.33 Hz	44.27	0.74
0.2 Hz - 25 Hz	39.31	0.71
0.2 Hz - 20 Hz	35.43	0.68
0.2 Hz - 12.5 Hz	27.74	0.63

Table 3.10 Spectral parameters computed from some of real recorded earthquakes (Sixsmith and Roesset 1970)

Recorded earthquakes	Ω (rad/s)	δ_Ω
El Centro 1940 NS	31.35	0.73
El Centro 1940 NS	25.51	0.64
Olympia N 10 W	36.07	0.65
Olympia N 10 E	30.85	0.62
Taft N 69 W	27.71	0.66
Taft S 69 W	27.46	0.64

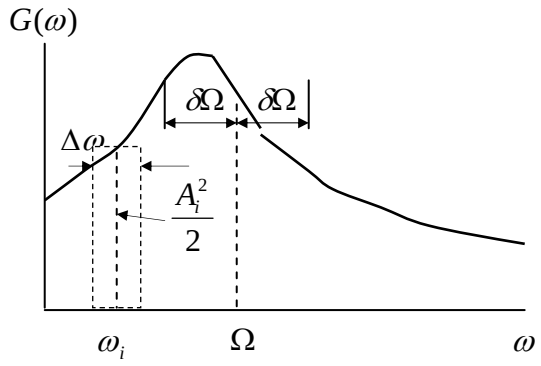

Figure 3.1 Spectral density function $G(\omega)$ and spectral parameters Ω and δ

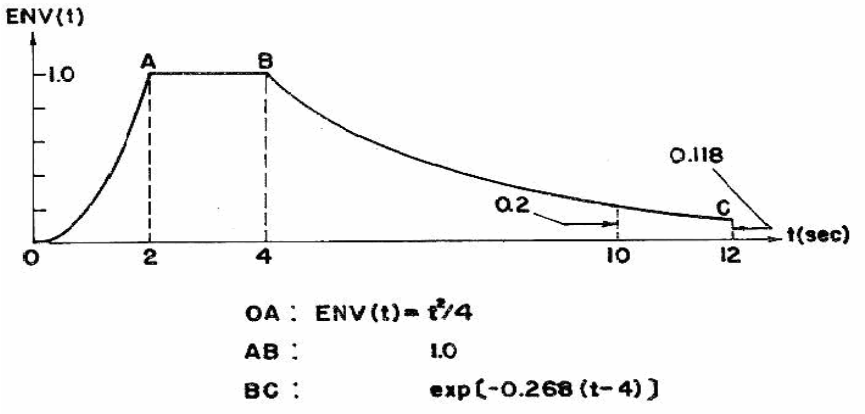

Figure 3.2 Compound intensity function used in the second test (Jennings *et al.* 1968)

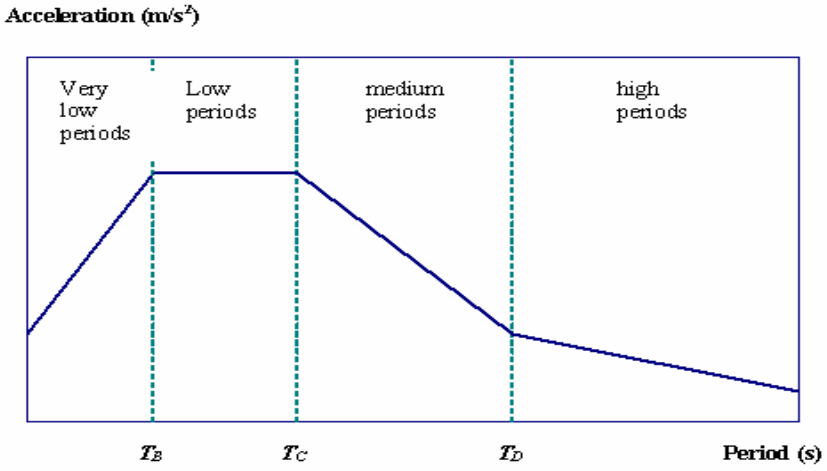

Figure 3.3 Descriptions of very high, high, medium and low frequencies in the acceleration response spectrum (Newmark and Hall 1982). In which T_B, T_C are limits of the constant spectral acceleration branch; T_D is the value defining the beginning of the constant displacement response range of the spectrum.

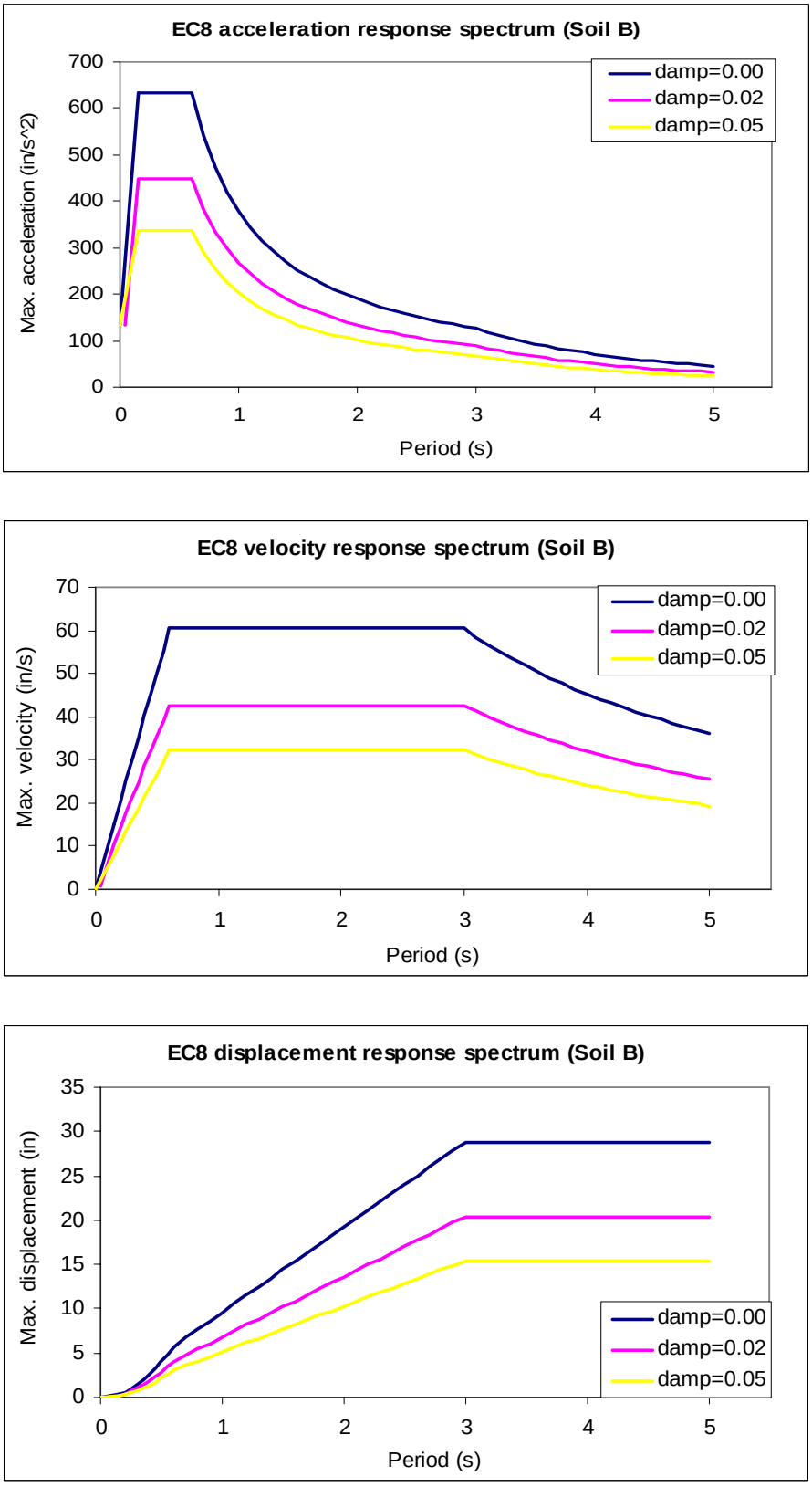

Figure 3.4 Response spectra for the subsoil class B (Eurocode 8, ENV 1998-1:1996)

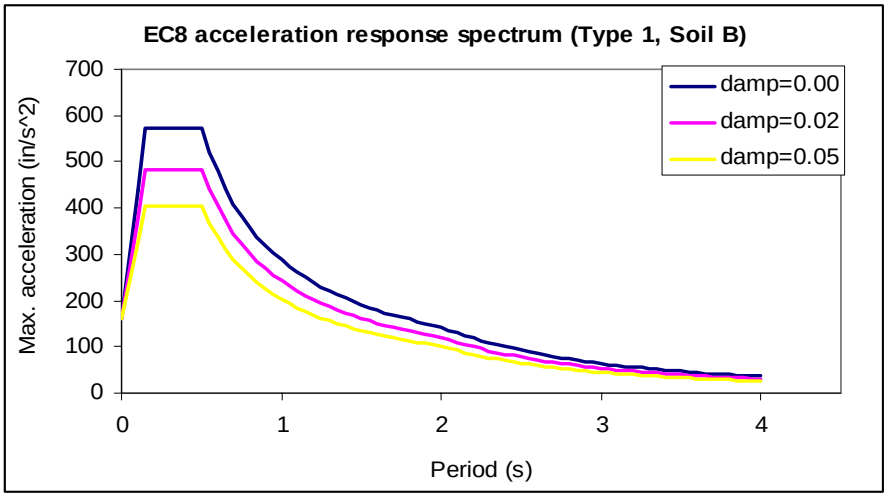

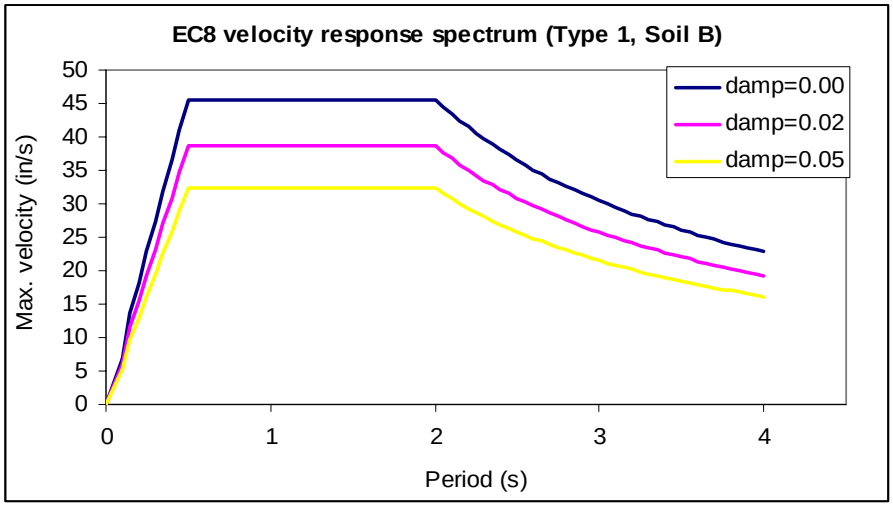

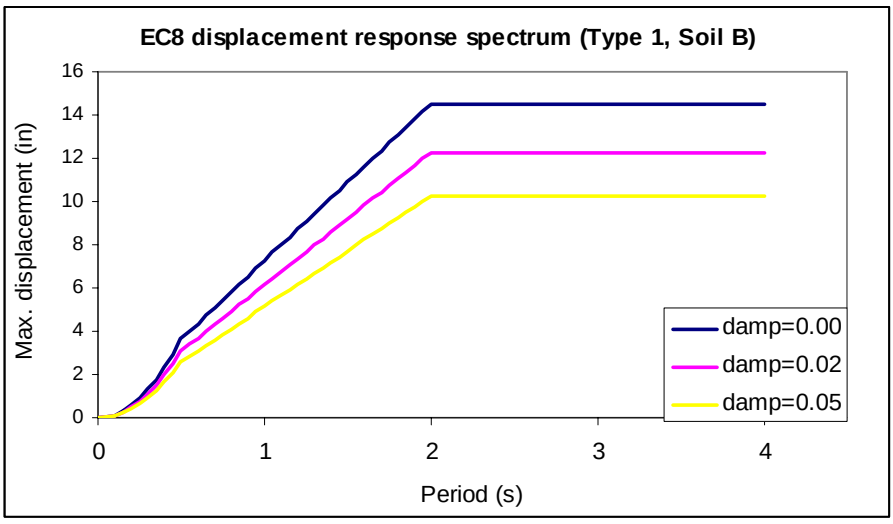

Figure 3.5 Response spectra for the subsoil class B (prEN1998-1: 2004)

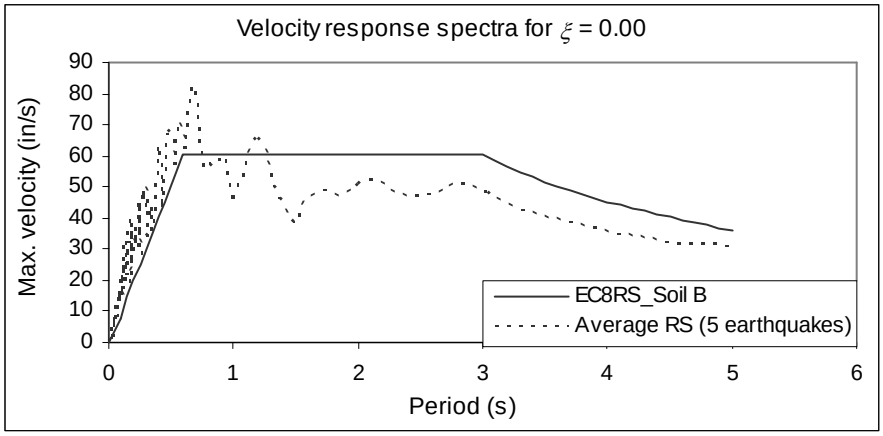

(a)

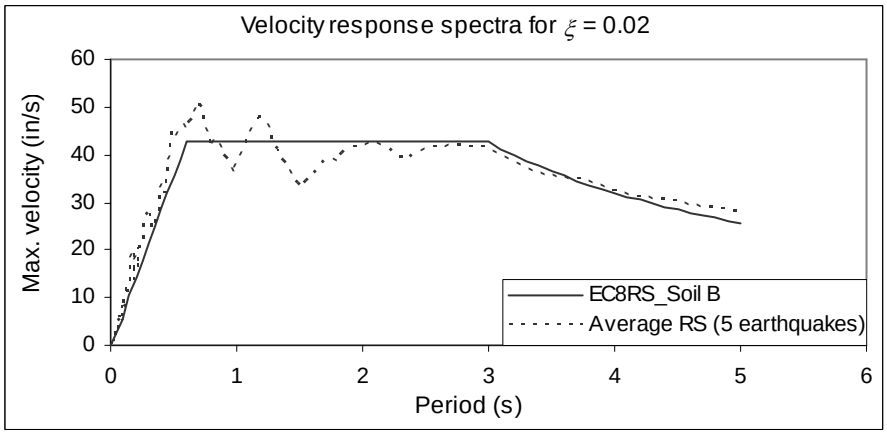

(b)

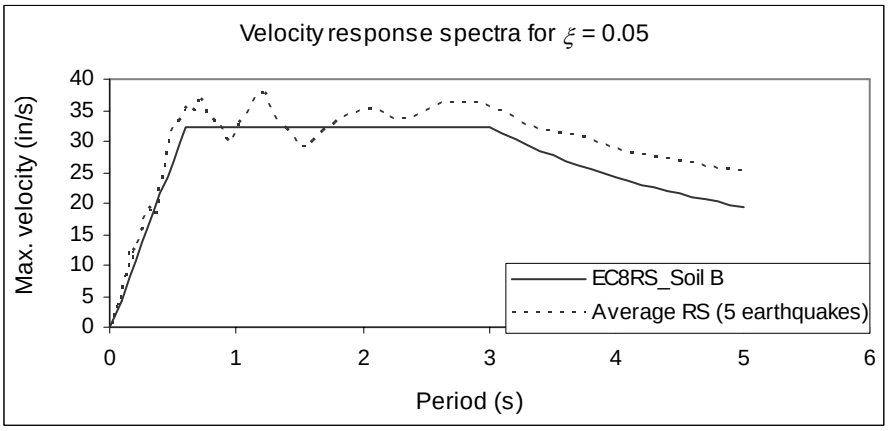

(c)

Figure 3.6 Comparison between the average velocity spectra and the target RS (EC8 ENV1998-1:1996)

(a) Damping coefficient $\xi = 0.00$
(b) Damping coefficient $\xi = 0.02$
(c) Damping coefficient $\xi = 0.05$

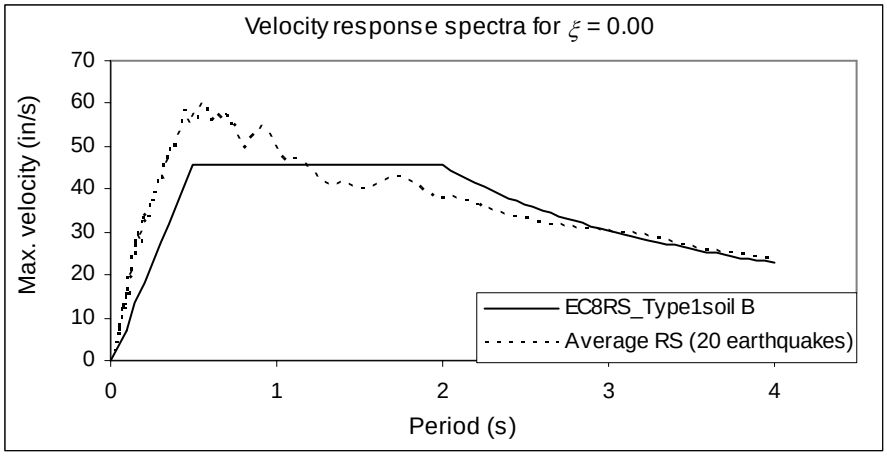

(a)

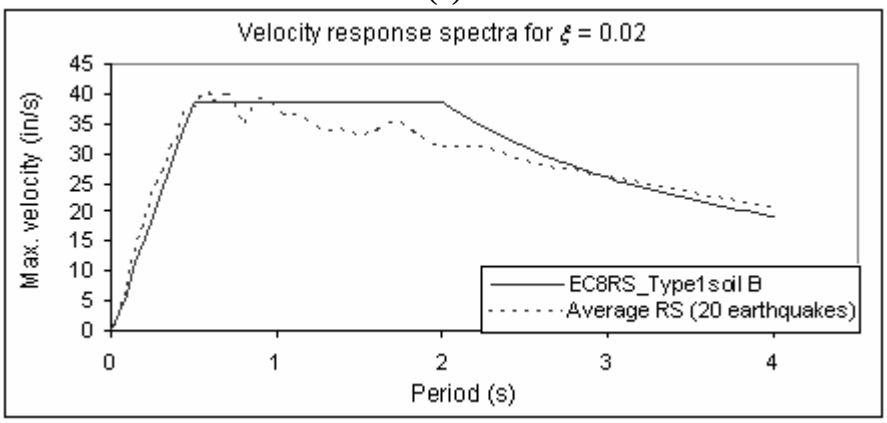

(b)

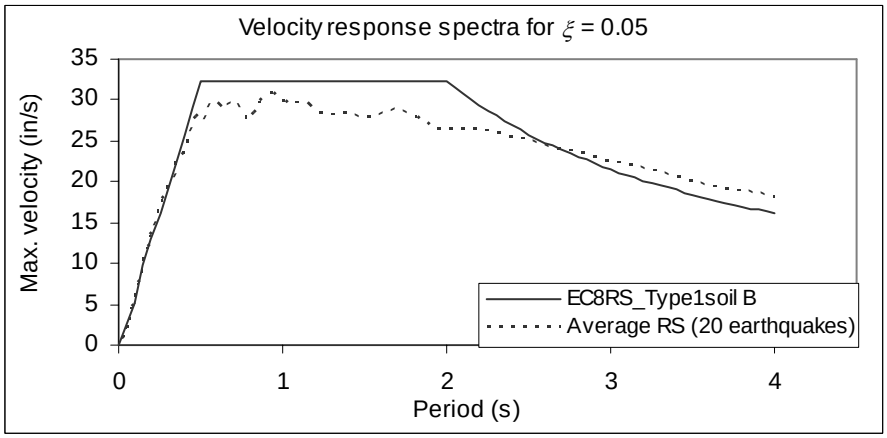

(c)

Figure 3.7 Comparison between the average velocity spectra and the target RS (EC8 prEN1998-1:2004)

(a) Damping coefficient $\xi = 0.00$
(b) Damping coefficient $\xi = 0.02$
(c) Damping coefficient $\xi = 0.05$

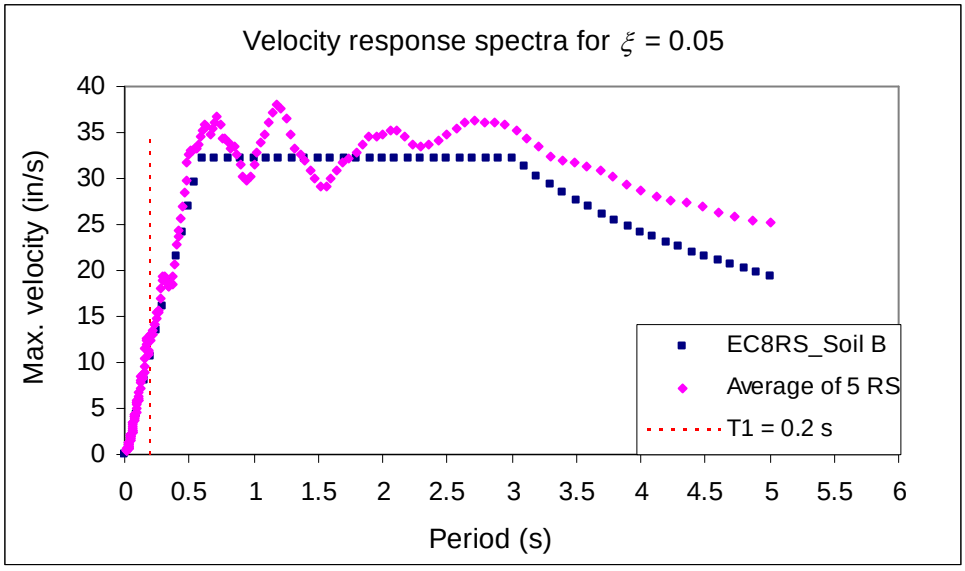

Figure 3.8(a) Comparison between the average of five RS and the EC8RS according to the requirements of the current ENV version of EC8 (ENV 1998-2: 1996). Assuming the fundamental period T_1 is of 0.2 seconds

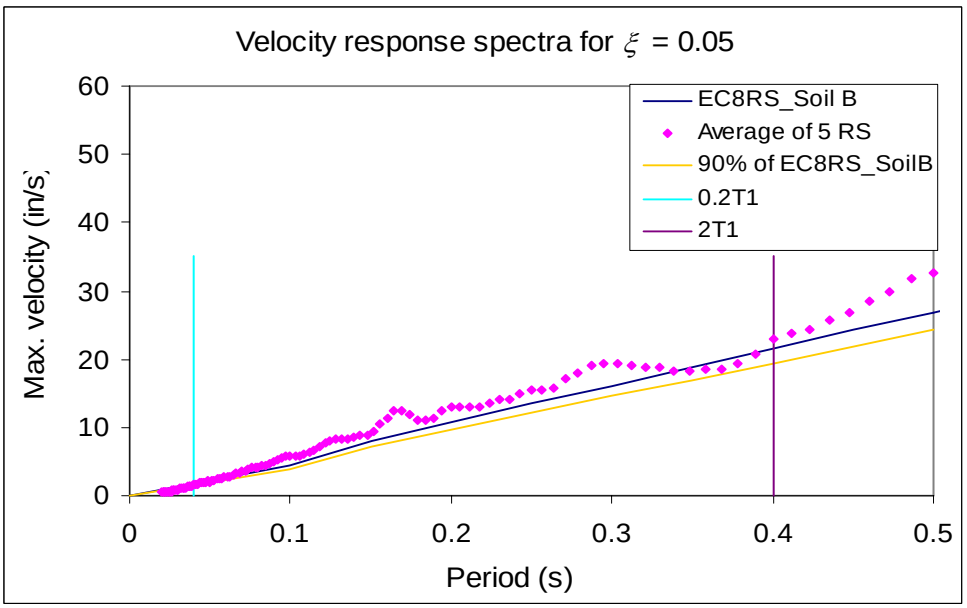

Figure 3.8(b) Comparison between the average of five RS and the EC8RS according to the requirements of EC8 (prEN 1998-1:2004). Assuming the fundamental period T_1 is of 0.2 seconds

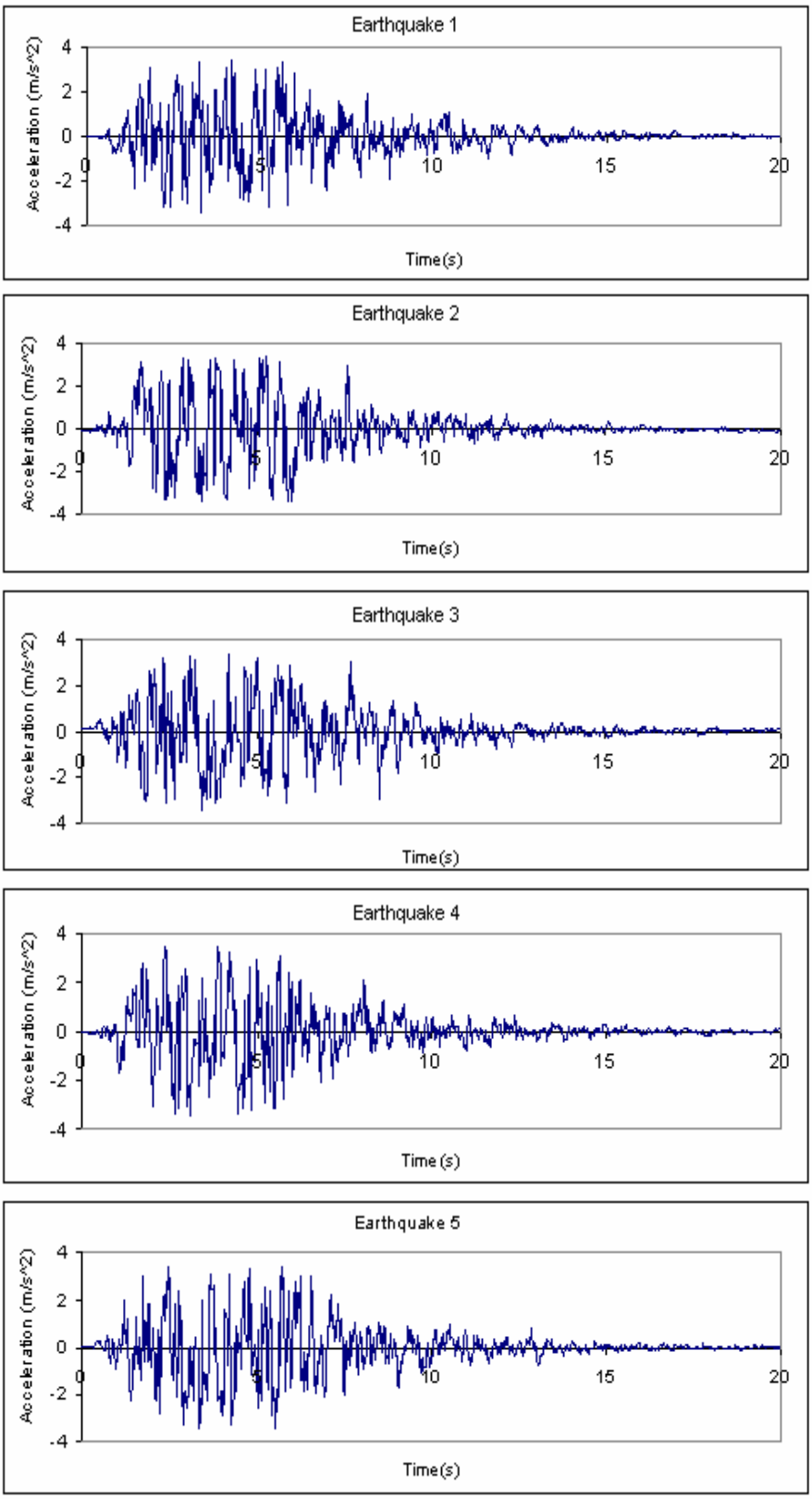

Figure 3.9 Five typical acceleration time-histories generated for example 3.4.2

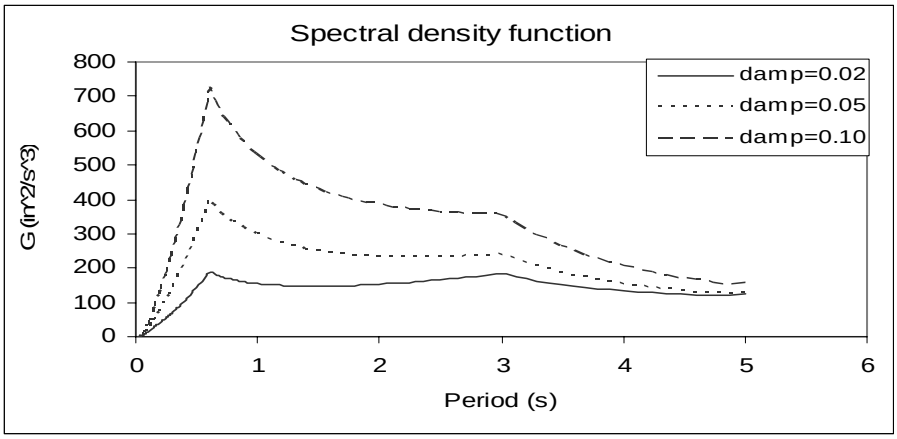

Figure 3.10 Power spectral density function $G(\omega)$ for different coefficients of viscous damping

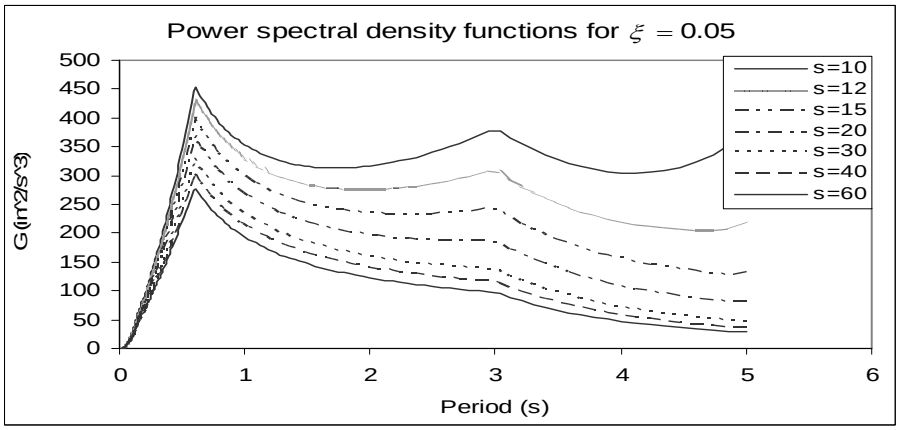

Figure 3.11 Power spectral density function for different durations

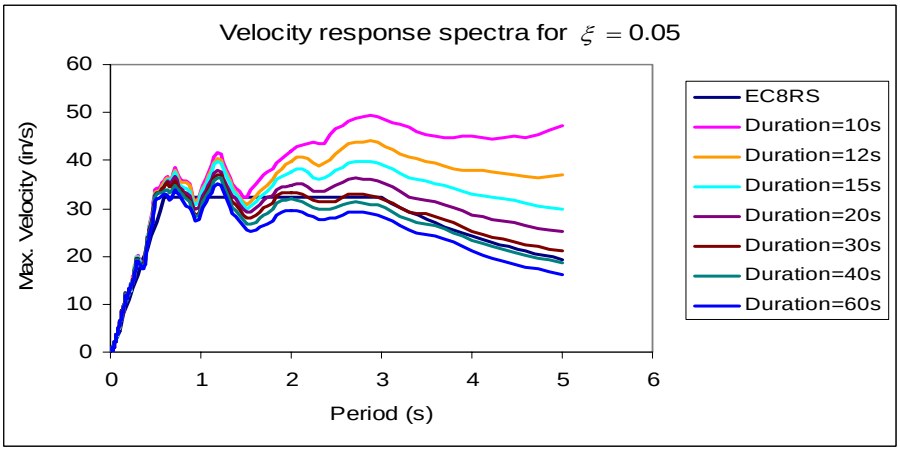

Figure 3.12 Comparison between the averaged RS and the EC8RS for different durations

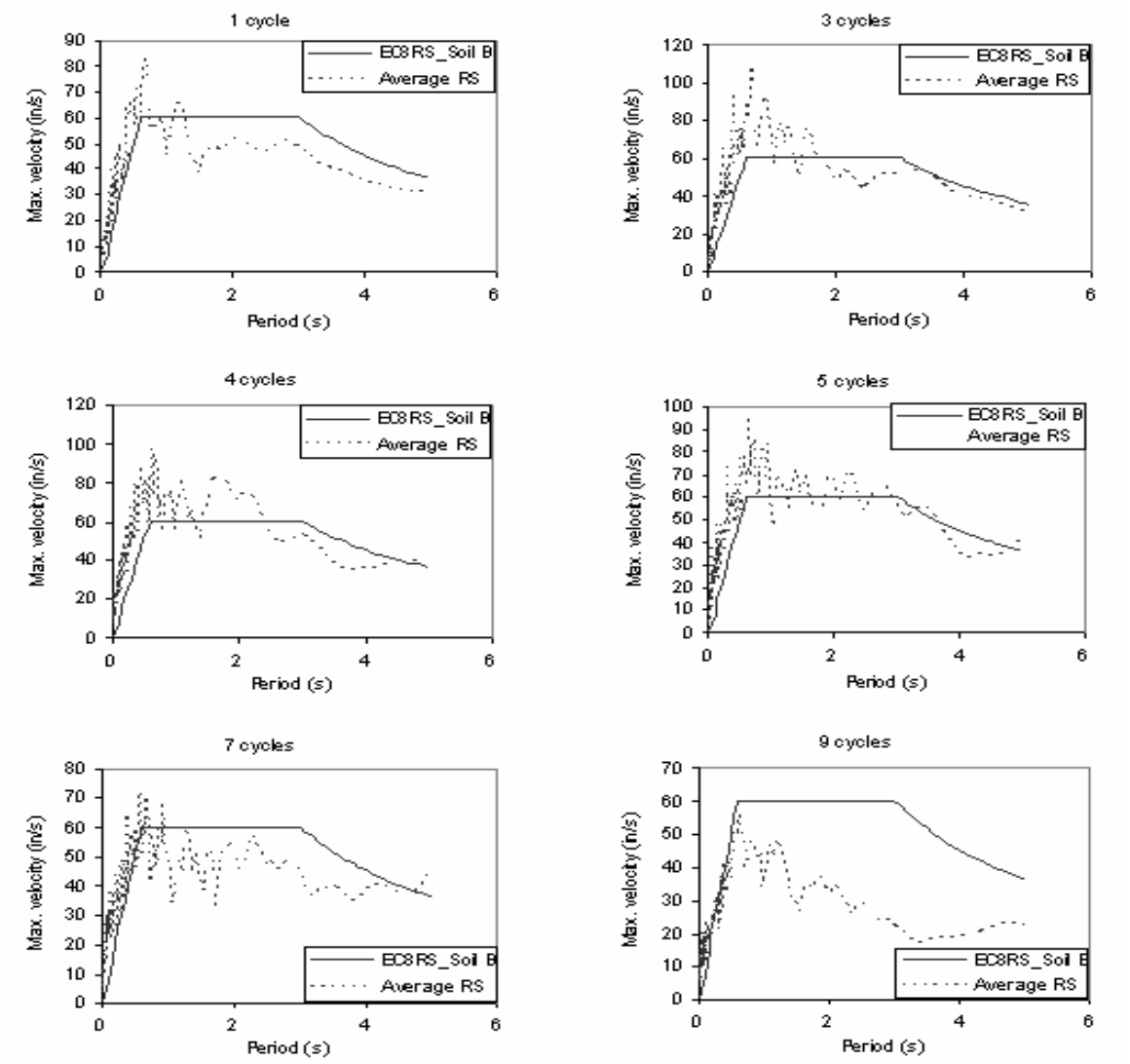

Figure 3.13 Velocity response spectra for 1 for 9 cycles, $\xi = 0.00$

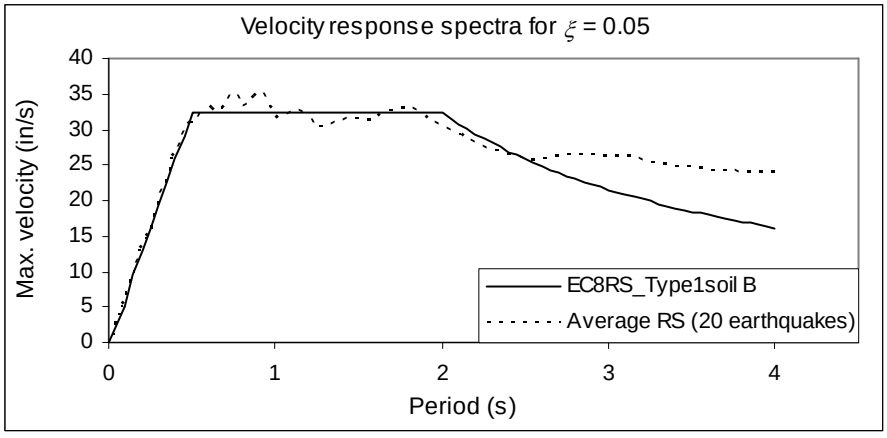

Figure 3.14 Velocity response spectra for 3 cycles, $\xi = 0.05$

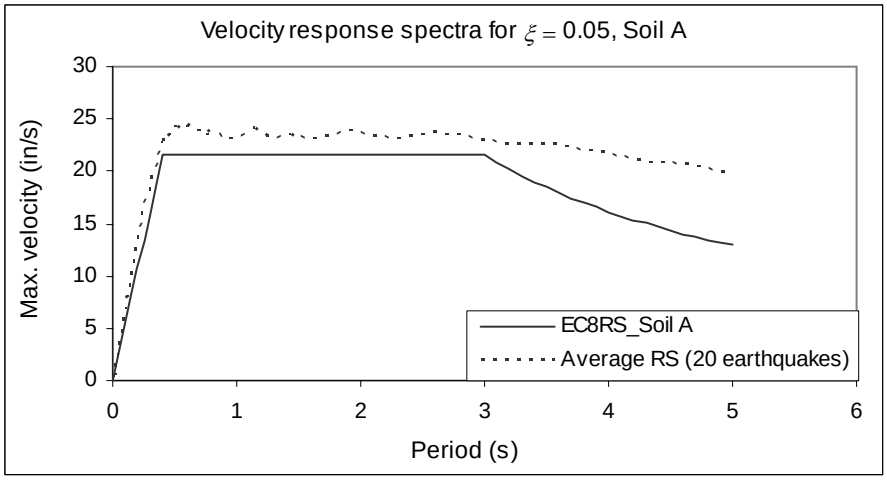

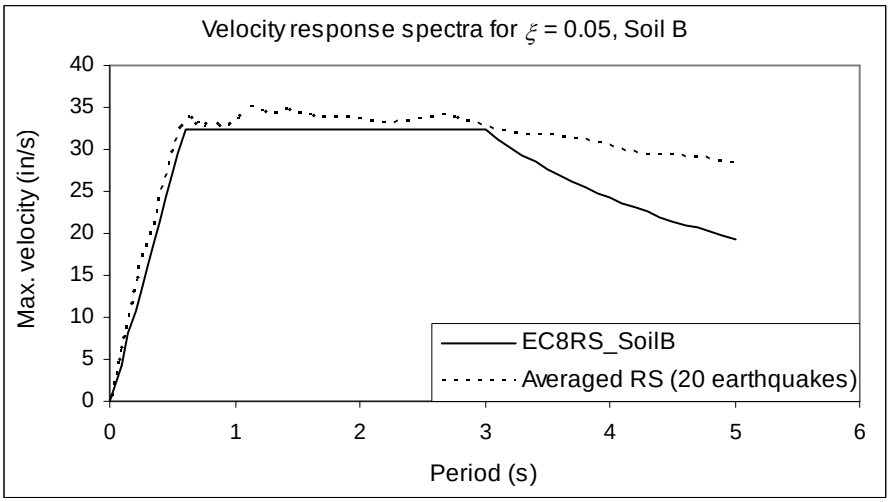

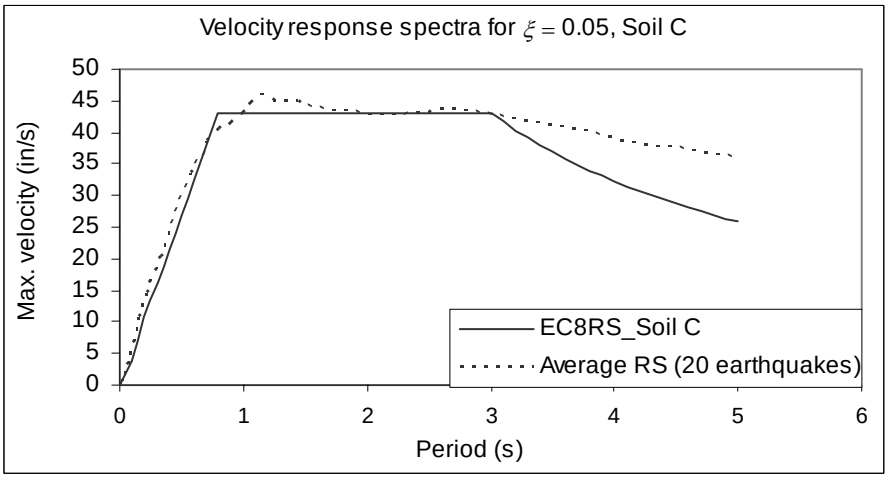

Figure 3.15 Velocity response spectra for 3 cycles, $\xi = 0.05$

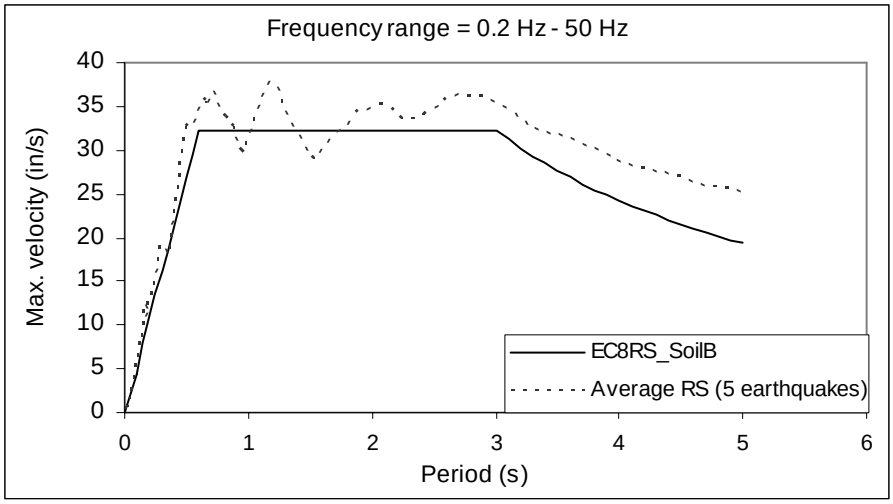
Frequency range = 0.2 Hz - 50 Hz
Max. velocity (in/s)
Period (s)
EC8RS_SoilB
Average RS (5 earthquakes)

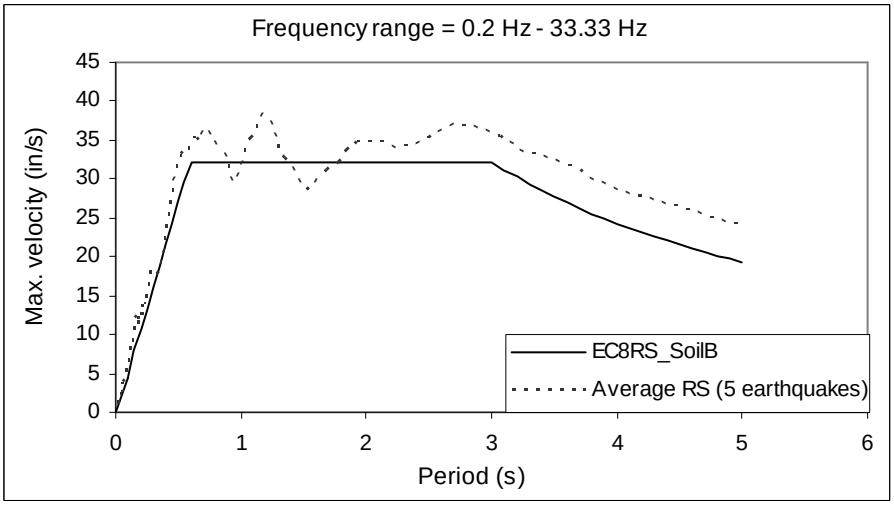
Frequency range = 0.2 Hz - 33.33 Hz
Max. velocity (in/s)
Period (s)
EC8RS_SoilB
Average RS (5 earthquakes)

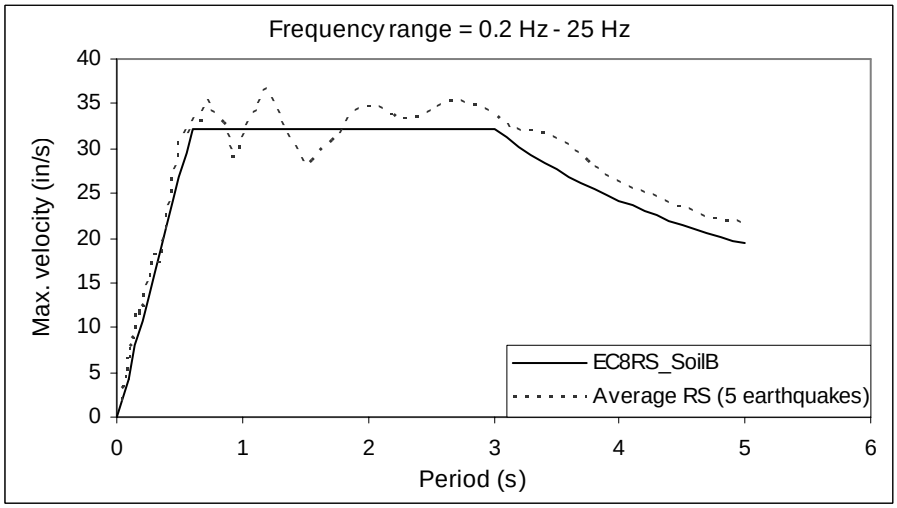
Frequency range = 0.2 Hz - 25 Hz
Max. velocity (in/s)
Period (s)
EC8RS_SoilB
Average RS (5 earthquakes)

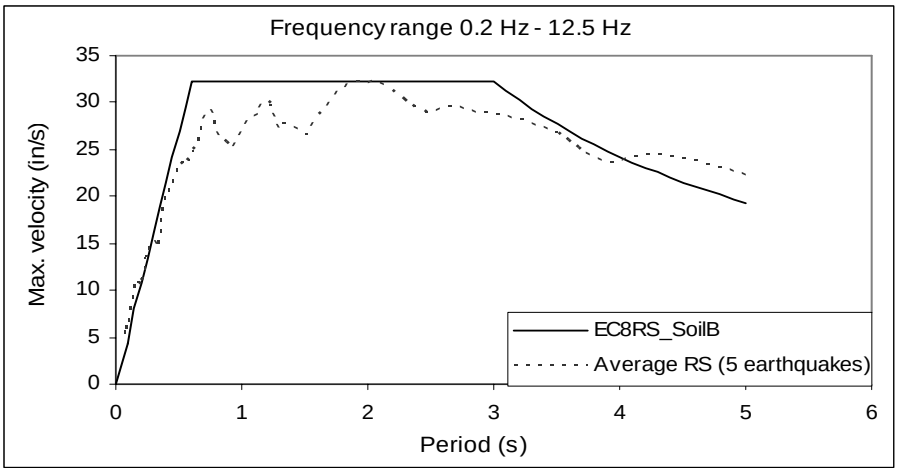

Figure 3.16 Response spectra for $\xi = 0.05$ with different input frequency ranges

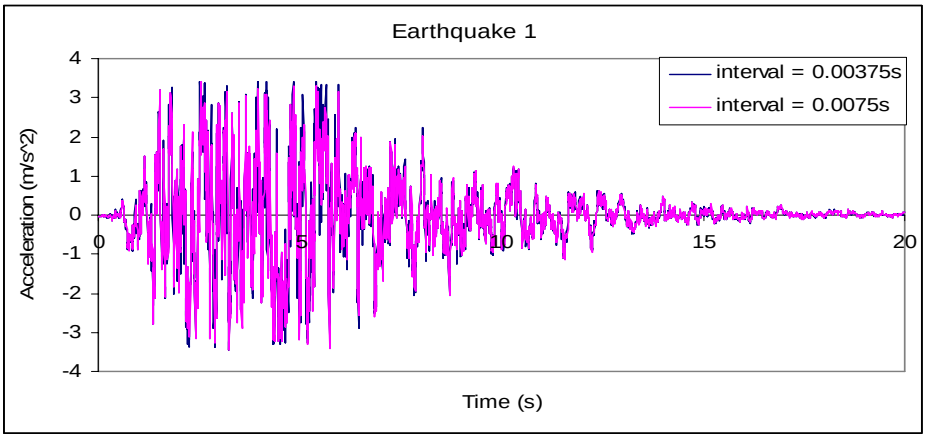

Figure 3.17 Typical acceleration time-histories for time interval Δt = 0.0075 s and 0.00375 s.

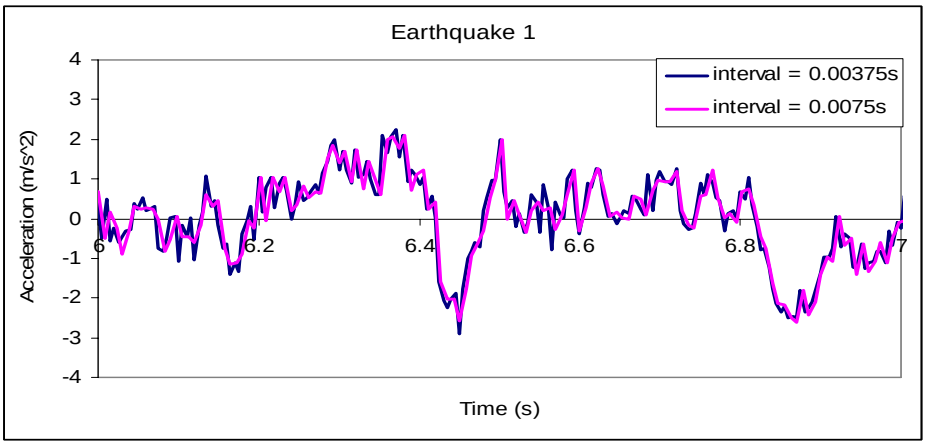

Figure 3.18 Typical acceleration time-histories for time interval Δt = 0.0075 s and 0.00375 s in the duration of 6 s to 7 s.

CHAPTER 4

VALIDATION OF FE SMEARED CRACK MODELS FOR CONCRETE STRUCTURES UNDER MONOTONIC LOADING

4.1 INTRODUCTION

In Chapter 2, various theoretical and practical aspects of the numerical modelling of cracking concrete were described and discussed. The two smeared crack models, namely Multi-crack model or Model 82 (Jefferson 1999, LUSAS Manual 2001) and Craft model (Jefferson 2003a, 2003b) were proposed to be used for the numerical analysis in this thesis. In this chapter, the performance of these models is assessed by analysing various cases of concrete beams under monotonic (or ramp) loading and comparing them with experimental and analytical results (see Chapter 6). A special interest on the application of the fracture energy to capture the localised fracture will be presented and its refinement will be included within the Multi-crack model when used for 2-D problems.

4.2 FINITE ELEMENT ANALYSIS EXAMPLES

The smeared crack models are validated by comparing with various experiments of three-point bending tests for concrete beams. Many experiments and FE analyses have been performed for notched concrete beams (Hillerborg *et al.* 1976, Petersson 1981, Rots and de Borst 1987, Arrea and Ingraffea 1982, Bazant and Pfeiffer 1986, Jefferson 1989). In finite element modelling, it seems many FE analyses have been performed dealing with notched specimens while little work has been done with un-notched specimens. It is because there is lack of good experimental data for un-notched specimen tests, especially in aspects related to the determination of some of the material properties such as fracture energy. Experimentally, due to the relatively mild and distributed stress and the heterogeneity of the material, in un-notched specimen, the failure zone can spread out in a wider area at the beginning of the analysis, i.e. pre-peak part in the load-deflection curve (Phillips and Zhang 1995). This could make the results for un-notched

specimens more scattered and therefore making the determination of representative fracture energy difficult.

In this chapter, in order to understand more about the numerical behaviour of un-notched concrete structures, the Multi-crack and Craft models with the FE program LUSAS are used to verify against the experimental data from two un-notched three-point bending tests (Carpinteri 1989 and Ozbolt and Bazant 1991). The Multi-crack model has been verified against experimental data for some well-known notched beams (Petersson 1981) and shown that the numerical results are well reasonable (Jefferson 1989, Chuang 2001).

4.2.1 CARPINTERI'S (1989) CONCRETE BEAM

4.2.1.1 Experiment-set up

Carpinteri conducted three-point bending tests on initially un-notched and un-cracked reinforced and plain concrete rectangular beams varying in depth from 100 mm to 800 mm (Carpinteri 1989). In this example, the concrete beam with the rectangular cross-section having 100 mm in height and 150 mm in width is studied here. The experimental testing arrangement is shown in Figure 4.1 which also shows a half beam model used in numerical analysis. The simply supported beam is loaded with a monotonic increasing load at the mid-span until the beam fails. The material properties reported is given in Table 4.1.

4.2.1.2 Finite element modelling

This beam is analysed using the two smeared crack models, Multi-crack (or LUSAS model 82), which is called MC82 model from now on, and Craft model. Two-dimensional plane stress meshes and prescribed displacement control are used to analyse the testing beam. The boundary condition of this beam is simply supported (with one pinned support at one end and one roller at the other end) under monotonic loading applied at the centre. The loading is applied via

prescribed displacement at the point of application. Concrete is modelled with 2-D 8-noded quadrilateral elements, and each element has 9 Gauss points.

4.2.1.3 Mesh dependency study

Two different meshes 56- and 224-element meshes (it will be called MESH 56 and MESH 224, respectively) are investigated and they are shown in Figures 4.2 and 4.3. These meshes are designed in such a way that the elements in the crack zone are nearly squares. Square elements are chosen so that it is easier to accurately estimate the value of the characteristic length l_c (Scotta *et al.* 2001, de Borst 2002).

The load-central deflection curves obtained with the two meshes are shown in Figures 4.4 and 4.5 for Craft model and MC82 model, respectively. The material properties given as shown in Table 4.1 are used, in which the fracture energy per unit area used is G_f = 0.09 N/mm as reported in the paper (Carpinteri 1989). The value of ε_o is calculated from this fracture energy and the softening stress-strain relationship (Figure 2.22). In addition, the experimental result is also shown in the Figures 4.4 and 4.5 to assess the capability of each model.

It can be seen from Figure 4.4 that, for Craft model, the two finite element meshes give very similar results. It means the results are not dependent upon the mesh size. By comparing the results obtained from the Craft model and the experimental result, it can be seen that the numerical results show reasonable agreement. The figure also shows that the numerical result is a little stiffer than that of experiment in the ascending branch. In fact, the numerical results also show that the ultimate load is about 12.60 kN and that is higher than the experimental one (11.60 kN). However, the areas under the deflection curves of the numerical and experimental results are similar. It confirms that the Craft model is capable of capturing the fracture behaviour of the concrete beam. On the contrary, the result of MC82 model underestimates the post-peak response of the beam in comparison with the experimental one though the pre-peak response though the peak load are well captured (Figure 4.5). Moreover, it shows the two finite meshes give different

results. It means they are dependent upon the mesh size and the numerical results of MC82 model are not objective and therefore unacceptable.

The reason for not having objective results of the MC82 model is because in the in the LUSAS implementation (LUSAS Manual 2001), the characteristic length l_c is evaluated using the elemental volume V_{gauss} associated with a Gauss point, and so the fracture energy G_f related to this characteristic length is accordingly changed with the volume instead of the 2-D plane stress area. Therefore, if a 2-D analysis is performed with this model in LUSAS, the characteristic length is not changed in the correct ratio when the length and the width are changed with the same ratio because the thickness remains the same. This leads to an incorrect change in the fracture energy. It means that the fracture energy value used for the input of 2-D problems has to be modified to compensate for this effect. If the value of G_f suggested from experiment is used straightaway for the MC82 model in LUSAS without modification, it will result in a wrong and non-objective result as demonstrated in Figure 4.4. The modification of input value of G_f for the MC82 model as suggested by Jefferson (2004) will be presented in the next section.

On the contrary, in the new model, Craft, the characteristic length l_c and fracture energy G_f are calculated correctly not only for 3-D problems but also for 2-D problems. Therefore its load-deflection curve can be used to assess the MC82 model.

4.2.1.4 Modification of fracture energy for 2-D problems in LUSAS for the Multi-crack model

4.2.1.4.1 Introduction

For both the MC82 and Craft models used in this study, an exponential softening curve is assumed and, for direct tension loading in one direction, the normal stress-strain relationship is shown in Figure 2.22. In the case of concrete cracking problems, strains tend to localise into a narrow band, this can lead to strong mesh size dependency in the FE calculations. Therefore, special provisions are necessary to introduce some of fracture energy concepts in fracture

mechanics (Hillerborg *et al.* 1976). In the smeared models, this fracture energy dissipation can be accomplished using the crack band model originally proposed by Bazant and Oh (1983). The energy per unit area G_f required to completely open a crack is defined as

$$G_f = l_c \int_0^{\varepsilon_0} \sigma_n d\varepsilon_n \tag{4.1}$$

in which l_c = element Gauss point characteristic length; σ_n = stress normal to the crack plane; ε_n = strain normal to the crack plane; ε_0 = strain at end of softening curve; G_f = fracture energy per unit area determined from experimental data.

In 3-D problems, l_c is related to the volume associated with a Gauss point within the elemental volume concerned V_{gauss}

$$l_c = \sqrt[3]{V_{gauss}} = \sqrt[3]{w_i \det J_i} \tag{4.2}$$

where w_i = the weighting factors of the integration rule, and $\det J_i$ = the Jacobian of the transformation between the local, isoparametric coordinates and the global coordinate system for the integration point *i*.

Similarly, in 2-D problems, l_c is related to the area associated with a Gauss point within the elemental area concerned A_{gauss}

$$l_c = \sqrt{A_{gauss}} = \sqrt{w_i \det J_i} \tag{4.3}$$

4.2.1.4.2 Modification of input G_f for LUSAS Multi-crack model for 2-D problems (Jefferson 2004)

In the MC82 model, the characteristic length l_c is evaluated from the elemental volume V_{gauss} associated with a Gauss point:

$$l_c = \sqrt[3]{V_{gauss}} = \sqrt[3]{A_{gauss} \times b_e} \tag{4.4}$$

where b_e = the element thickness for 2-D elements used in 3-D.

Therefore, if a 2-D problem is applied for the MC82 model, in order to obtain mesh independent results, the input experimental fracture energy G_f the fracture energy for the same 3-D problem must be adjusted to a modified value G_{f_adj}

From Equations (4.1) and (4.4) we have

$$\int_0^{\varepsilon_0} \sigma_n d\varepsilon_n = \frac{G_{i\_adj}}{\sqrt[3]{A_{gauss} \times b_e}} \tag{4.5}$$

From Equations (4.1) and (4.3) we have

$$\int_0^{\varepsilon_0} \sigma_n d\varepsilon_n = \frac{G_f}{\sqrt{A_{gauss}}} \tag{4.6}$$

Then the adjusted fracture energy G_{f_adj} can be obtained from Equations (4.5) and (4.6) as follows

$$G_{f\_adj} = \frac{G_f \sqrt[3]{b_e}}{\sqrt[6]{A_{gauss}}} \tag{4.7}$$

Where G_{f_adj}, A_{gauss} = the adjusted fracture energy and elemental area, respectively; b_e = the thickness of the element of the 2-D element.

It can be seen from (4.7) that the value of fracture energy input G_{f_adj} for 2-D problems is related to both the mesh size, A_{gauss}, and the thickness of the element, b_e.

4.2.1.5 Load-deflection curves with modified input fracture energy

Using Equation (4.7), the adjusted fracture energy per unit area for MESH 56 and MESH 224 can be calculated to be 0.164 N/mm and 0.206 N/mm, respectively. Then the numerical load-deflection responses for two different meshes of the MC82 model are shown in Figure 4.6, in which the result of Craft model and the experimental result are also presented for comparison. It can be seen that the two meshes of MC82 model give very similar results. As they are no longer

dependent upon the mesh size, it is clear that using the adjusted fracture energy as shown in Equation (4.7), the problem of mesh dependency can be avoided. However, the results of MC82 model have overestimated the experimental results when comparing with those of Craft model and experimental data.

4.2.1.6 The model modification factor α

As mentioned above, the results of Craft model matched the experimental well and their results can be used as a reference for finding the input fracture energy for MC82 model. The difference is when the mesh changed for MC82 model but not the element thickness the input fracture energy should be adjusted accordingly. Furthermore, in order to obtain the same result for MC82 model and Craft model, it needs to convert the input value of fracture energy for Craft to the input value of fracture energy for MC82 model. Therefore, in the following section, we will introduce a single factor α, called *the model modification factor*, which relates input value of fracture energy for Craft model to the input value of fracture energy for MC82 model.

We need to find a single factor α, namely the model modification factor, to adjust the fracture energy calculated from (4.7) to match the MC82 results with the Craft results. Therefore, the new adjusted fracture energy for mesh *i* will be derived from Equation (4.7) as:

$$G_{fi}^{MC82} = \frac{\alpha G_f \sqrt[3]{b_i}}{\sqrt[6]{A_{igauss}}} \tag{4.8}$$

In order to find a suitable value of α, we use trial-and-error fitting of the MC82 results for many different values for α to the Craft results. Though many values for α have been tried, only some values are presented here. The central deflections of the concrete beam obtained with the two meshes for $\alpha = 1$, 0.935, 0.693, and 0.794, in which the fracture energy for an arbitrary mesh can be calculated. The fracture energy for these values of α are obtained by Equation (4.8) and shown in Table 4.2.

The load-deflection curves for different α are shown in Figures 4.7(a), 4.7(b), 4.7(c) and 4.7(d), respectively. The results of Craft model are also plotted in theses figures for comparison. It can be seen from these figures that the best agreement between the results of Multi-crack model MC82 and Craft model can be found in the case of $\alpha = 0.794$. In which, the ultimate load and the area under the load-deflection curves of the two models are very similar (Figure 4.7(d)). In this case, the input fracture energies are 0.130 N/mm and 0.164 N/mm for MESH 56 and MESH 224, respectively.

According to the above observation, we found that using $\alpha = 0.794$ for the MC82 model gives the best agreement with the results of Craft model for the two meshes MESH 56 and MESH 224.

Conclusions

As demonstrated above, if we assume the thickness of the two different meshes (14x4 and 28x8) are the same, the adjusted fracture energy for mesh *i* for 2-D problems using MC82 model can be calculated as $G_{fi}^{MC82} = \frac{\alpha G_f \sqrt[3]{b_i}}{\sqrt[6]{A_{igauss}}} = \frac{0.794 G_f \sqrt[3]{b_i}}{\sqrt[6]{A_{igauss}}}$ (4-9)

So that a very good agreement between the MC82 model and Craft model can be found. In which, the ultimate load and the area under the load-deflection curves of the two models are also very similar (Figure 4.7(d)).

4.2.1.7 Numerical crack pattern and stress distributions

The crack patterns obtained from the numerical analysis are shown in Figures 4.8. Wherein, the numerical crack pattern is represented in terms of crack location and crack angle at each Gauss point where crack happens. As the results of MESH 56 and MESH 224 are similar, only the results of MESH 56 are presented for this study.

The crack pattern through the first crack (at the deflection of 0.110 mm) is shown in Figures 4.8. It can be seen that the cracks initially appeared at the bottom of the beam centre and then gradually developed towards the inside elements and then top elements (increments = 57 to 77). This is because when an un-notched specimen of concrete becomes subjected to load, cracks and stress distribution are spread out in a wider zone at the beginning of the analysis (pre-peak part in the load-deflection curve). In other words, the pre-peak behaviour of an un-notched beam is much more affected by the heterogeneity of the material than that of notched beam as widely seen, i.e. Petersson (1981), where the artificial flaw dominates the material imperfection. This widely spreading zone predicted by numerical analysis can explain the reason why the numerical results are stiffer than those of experiment after cracking in concrete (as can be seen in Figures 4.5, and 4.6). This is because the heterogeneity of the material may have much more effects on the experimentally un-notched beam results and this is an aspect of the behaviour which the numerical model cannot always capture.

The failure of the beam happens when the cracks are continually developed in elements at the central beam area (from increment of 80, as shown in Figure 4.8). In addition, the stress distributions, as shown in Figure 4.9, indicate that the damage zone are highly caused by normal stresses and it supported the view as the concrete beam is localised at the central beam without any shear effects.

It should be mentioned here that all the results presented above were obtained with the displacement control method. Alternatively, in order to assess the non-linear behaviour obtained by this method, the load control method when using the arc-length method or not is also adopted for the analysis. Both the MC82 and Craft models are investigated but only the results achieved from MC82 model are given here because their results and conclusions are roughly similar. Figure 4.10 shows the results of the analyses with load control when using and not using and not using arc-length technique. It shows that without using arc-length technique, the analysis stops at the peak load and failed to converge there (at deflection of 0.161 mm). However, with the use of the arc-length technique it can trace the post-peak behaviour to gain the full load-deflection curve which is very similar to those obtained by using the displacement control method (Figure 4.7(d)

for MC82 results). For that reason, the displacement control method is carried on for all analyses in this chapter.

4.2.1.8 Parametric study

A brief parametric study is made in order to extract further information from this analysis. The parameters selected for the parametric study include: fracture energy, Young's modulus, tensile strength, and compressive strength. The load-deflection curves obtained from the parametric study are shown in Figures 4.11 to 4.14. It is noted that in this investigation, it is no loss of generality to use only one model, either MC82 or Craft models for this study, and so only Craft model is used.

4.2.1.8.1 Fracture energy

The influence of the fracture energy (G_f = 0.06 N/mm, 0.08 N/mm and 0.10 N/mm) on the load-deflection curve is shown in Figure 4.11.

Figure 4.11 shows that the area under the load-deflection curve increases with increasing fracture energy. The reason for this is that a higher value of G_f leads to a higher area under the stress-strain softening curve, and leads to a slower loss of strength in the softening regime, and therefore makes the stress-strain softening curve shifted to the right (it is assumed that the other parameters are unchanged). These results in the load-deflection curve indeed shifted to the right.

4.2.1.8.2 Young's modulus

The influence of the Young's modulus (E = 20000, 25000, and 30000 N/mm^2) on the load-deflection curve is shown in Figure 4.12.

Figure 4.12 shows that, in the pre-peak regime, the slope of the load-deflection curve increases with increasing Young's modulus. This can be explained as a higher value of Young's modulus

leads to a higher value of stress and, therefore, leads to a higher reaction force and it results in a higher value of slope. By contrast, the reaction force in the post-peak regime for the same deformation decreases when the Young's modulus increases. The reason for this is that a higher value of Young's modulus leads to a lower value of the elastic ultimate strain ε_t if the uniaxial tensile strength f_t is assumed unchanged, and therefore, makes the stress-strain softening curve shifted to the left. This leads to a lower value of stress and also lower value of reaction force for the same strain in the post-peak regime as the softening happened faster.

4.2.1.8.3 Tensile strength

The influence of the tensile strength (f_t = 3.3, 4.3 and 5.3 N/mm^2) on the load-deflection curve is shown in Figure 4.13.

Figure 4.13 shows that when the tensile strength increases, the reaction force increases as well. It can be explained as when a higher value of tensile strength is used, the structure can resist a higher applied maximum load and, therefore, leads to a higher maximum reaction force (the maximum applied loads for the cases of f_t = 3.3, 4.3 and 5.3 N/mm^2 are P_{max}= 18.65, 10.60, and 12.60 kN, respectively).

4.2.1.8.4 Compressive strength

The compressive strength (f_c = 45, 55, and 65 N/mm^2) has no effect on the load-deflection curve as shown in Figure 4.14. The reason for this is due to that the tensile behaviour dominates the overall characteristic of this structure under the current flexural loading and there is no crushing in compressive concrete.

4.2.2 OZBOLT AND BAZANT'S (1991) CONCRETE BEAM

4.2.2.1 Experiment-set up

The second example is the test of a simply supported beam subjected to a concentrated load at the centre. This example has been analysed by Ozbolt and Bazant (1991).

The experiment testing arrangement of this test is illustrated in Figure 4.15 showing the rectangular beam subjected to a concentrated load at the centre. The support conditions are one pinned support at one end and one roller at the other. This bending specimen does not contain any reinforcement. Actually, in the test, the load is applied increasingly step-by-step until it almost reaches the maximum load, and then it is unloaded and loaded again for the next loading cycles to perform a cyclic test. However, as the loading speed is very slowly ($\dot{u}$ = 0.0625 mm/s), the beam can be considered under statically monotonic loading, and only the behaviour in the first pre-peak regime is investigated here. The material properties given by the experimental data are listed in Table 4.3.

4.2.2.2 Finite element modelling

Both Craft and MC82 models are used to analyse the testing beam. Two-dimensional plane stress models and the prescribed displacement control are used. The boundary condition of this beam is simply supported under monotonic loading applied at the centre. Concrete material is modelled with 2-D 8-noded quadrilateral elements with 9 Gauss points for each element. As the testing beam is symmetric about its vertically central axis, only a half-mesh is modelled.

4.2.2.3 Mesh dependency study

Two different meshes: 45- and 180-element meshes, which are called MESH 45 and MESH 180, respectively, are investigated (Figures 4.16 and 4.17). All elements are square, in which each side of the latter mesh size is halved that of the first mesh size.

Figure 4.18 shows the central deflections of the concrete beam obtained with the two meshes for Craft model. The central deflections of the concrete beam obtained with the two meshes for the MC82 model without the modification of fracture energy (α = 1), is shown in Figure 4.19. The input fracture energy for the two meshes used with MC82 model are calculated from Equation (4.8) and presented in Table 4.4. In addition, the experimental result is also included in the above figures for assessment. It can be seen that, the two finite element meshes give similar results for the same model.

4.2.2.4 Load-deflection curves

It can be seen from Figures 4.18 and 4.19 that the results obtained from Craft and MC82 models show very good agreement with one of the results of the experiment. The numerical results are very similar and well fitted with the experimental result in the pre-peak regime. It is very similar to the previous test (in the case of Carpinteri's (1989) beam) that the numerical result is a little bit stiffer than experimental one just before the maximum load. The numerical result shows the maximum load at about 30.10 kN and that is quite closed to the experimental value of 30 kN. As there is no experimental data for the load-deflection curve in the softening branch (Ozbolt and Bazant 1991), no comparison between the numerical and experimental results can be done for the post-peak regime.

It can also be seen in Figure 4.19, the result of the MC82 model is well fitted with those of Craft and experiment in pre-peak regime and at the peak load. However, the load-deflection curves obtained from using MC82 model show that their results are overestimated in comparison with those of Craft model in the softening regime. It is because in this case there is no modification for the fracture energy used for the Multi-crack model in this study (α = 1).

4.2.2.5 Using the model modification factor α

As investigated in 4.2.1.6, in 2-D problems, in order to match the result of the Multi-crack model with that of Craft model, the fracture energy G_f for Multi-crack model needs to be modified according to the model modification factor. Therefore, if the element thickness remains constant, the adjusted value for the fracture energy, can be obtained based on the model modification factor α. In this analysis, 45- and 180-element meshes are used, in which each side of the latter mesh size is double that of the first mesh size. Therefore, it is similar to the previous analysis that the model modification factor α is obtained by trial-and-error fitting of the MC82 results for many different values of α to the Craft results. Amongst them, once again, $\alpha = 0.794$ is also used. In this study, the experimental fracture energy is G_f = 0.10 N/mm. The values of input fracture energy for the two meshes (MESH 45 and MESH 180) are calculated from Equation (4.9) and shown in Table 4.5.

In brief, only the result of MC82 model with α = 0.794 is given here though the results of other values of α are also calculated. The comparison between the results of MC82 model and Craft model is shown in Figure 4.20. The figure shows the results of MC82 model are in good agreement with that of Craft model, in which the ultimate load and the area under the load-deflection curves of the two models are all very similar.

This comparison confirms the reasonable result obtained for MC82 model by using the model modification factor α = 0.794 when the second mesh size is halved that of the first mesh.

4.3 SUMMARY AND CONCLUSIONS

In this chapter, the performance of the two smeared crack models, namely Craft and MC82 model for cracking concrete has been assessed by analysing a number of three-point bending tests on concrete beams and by comparing the finite element results with experimental data. In particular for the MC82 model, because in the program coding, the fracture energy is only referred to the

characteristic length of 3-D problems, the modification of the fracture energy in order to use it for 2-D problems is presented and estimated through reliable numerical result of Craft model and the experimental result.

The numerical results have confirmed that mesh-dependency can be avoided by the use of the fracture energy approach. The result of Craft model shows a very good agreement with the experimental result in both pre- and post-peak behaviour. Similarly, the result of the MC82 model is also well fitted with those of experiment and Craft model if the modification of the fracture energy is used for 2-D problems until the coding is corrected. In particular, the numerical results are stiffer than those of experiment after cracking in concrete in pre-peak behaviour. It is reasonable because in un-notched beams, the heterogeneity of the concrete material may have some significant effects on the experimental response and this is an aspect of the complex behaviour that the numerical model cannot always capture.

Modification of fracture energy for MC82 model in 2-D problems

Through the comparison between the results of the MC82 model, experiment and Craft model, it can be concluded that:
(1) Using the modification for fracture energy, it, in general, guarantees that the results of numerical models converge to the same the result and not dependent on the mesh size, and
(2) Using the model modification factor for converting the input value of fracture energy of Craft model to the input value of fracture energy of MC82 model, the result of the MC82 model can be well matched with those of experiment and Craft model.

This issue about the model modification factor (α) can be written and submitted to LUSAS users conference.

Parametric study

A brief parametric study which includes: fracture energy, Young's modulus, tensile strength, and compressive strength to investigate the influence of these parameters on the load-deflection curves has been carried out using Craft model. The results are presented as follows:

1. The area under the load-deflection curve increases with increasing fracture energy.
2. The slope of the load-deflection curve in the pre-peak regime increases with increasing Young's modulus. In addition, the reaction force in the post-peak regime for a given deformation decreases with increasing Young's modulus.
3. The reaction force increases with increasing tensile strength.
4. The reaction force is largely independent of compressive strength.

Table 4.1 Concrete properties of Carpinteri's Beam (1989)

Initial Young's modulus	E = 34300 N/mm^2
Poisson's ratio	ν = 0.2
Uniaxial compressive strength	f_c = 75.7 N/mm^2
Uniaxial tensile strength	f_t = 5.3 N/mm^2
Uniaxial strain at peak compressive strength	ε_c = 0.0023
Fracture energy	G_f = 0.09 N/mm

The value of strain at the end of softening curve ε_o is obtained from G_f and the stress-strain softening curve

Table 4.2 Fracture energy and model modification factor α

α	Mesh	Model	G_f (N/mm)
α = 1	MESH 56 (14x4)	MC82	0.164
		Craft	0.09
	MESH 224 (28x8)	MC82	0.206
		Craft	0.09

α	Mesh	Model	G_f (N/mm)
α = 0.935	MESH 56 (14x4)	MC82	0.143
		Craft	0.09
	MESH 224 (28x8)	MC82	0.18
		Craft	0.09

α	Mesh	Model	G_f (N/mm)
α = 0.693	MESH 56 (14x4)	MC82	0.113
		Craft	0.09
	MESH 224 (28x8)	MC82	0.144
		Craft	0.09

α	Mesh	Model	G_f (N/mm)
α = 0.794	MESH 56 (14x4)	MC82	0.130
		Craft	0.09
	MESH 224 (28x8)	MC82	0.164
		Craft	0.09

Table 4.3 Concrete properties of Ozbolt and Bazant's beam (1991)

Initial Young's modulus	E = 20000 N/mm^2
Poisson's ratio	ν = 0.18
Uniaxial compressive strength	f_c = 30.0 N/mm^2
Uniaxial tensile strength	f_t = 2.25 N/mm^2
Uniaxial strain at peak compressive strength	ε_c = 0.0022
Fracture energy	G_f = 0.1 N/mm

The value of strain at the end of softening curve ε_o is obtained from G_f and the stress-strain softening curve

Table 4.4 Fracture energy and model modification factor α = 1

α	Mesh	Model	G_f (N/mm)
α = 1	MESH 45 (9x5)	MC82	0.10
		Craft	0.10
	MESH 180 (18x10)	MC82	0.126
		Craft	0.10

Table 4.5 Fracture energy and model modification factor α = 0.794

α	Mesh	Model	G_f (N/mm)
α = 0.794	MESH 45 (9x5)	MC82	0.08
		Craft	0.10
	MESH 180 (18x10)	MC82	0.10
		Craft	0.10

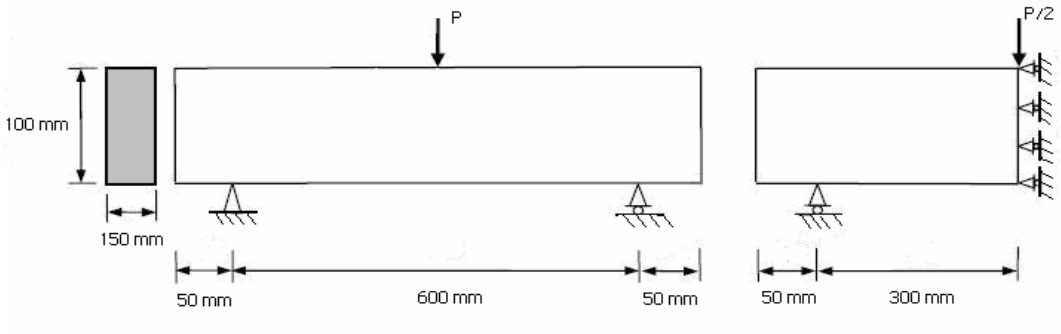

Figure 4.1 Geometrical data (Carpinteri 1989) and half beam model used in numerical analysis (Dimensions are not in a right scale)

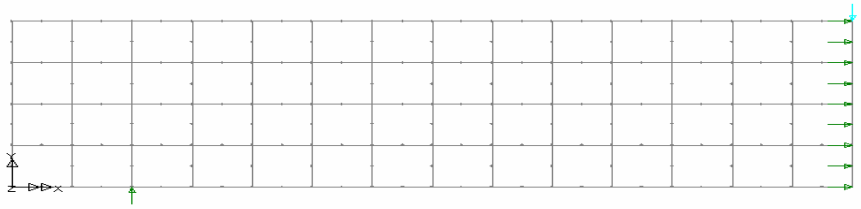

Figure 4.2 Carpinteri's (1989) beam. A half mesh of MESH 56

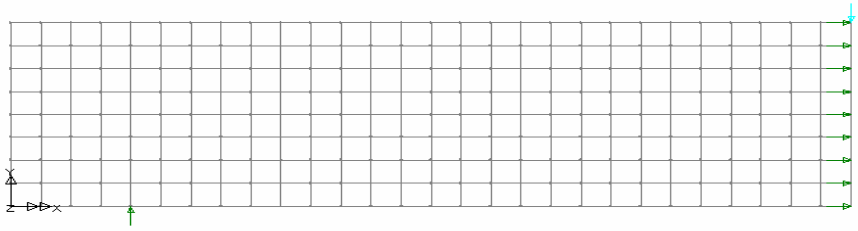

Figure 4.3 Carpinteri's (1989) beam. A half mesh of MESH 224

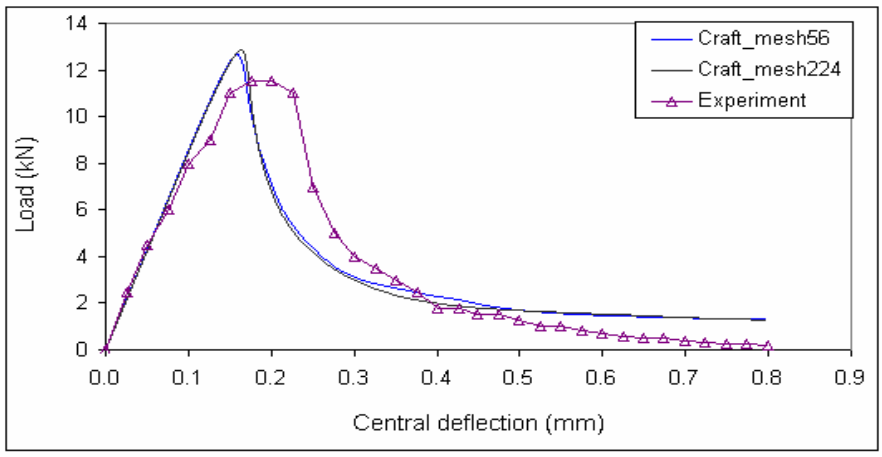

Figure 4.4 Mesh dependency test - Craft model

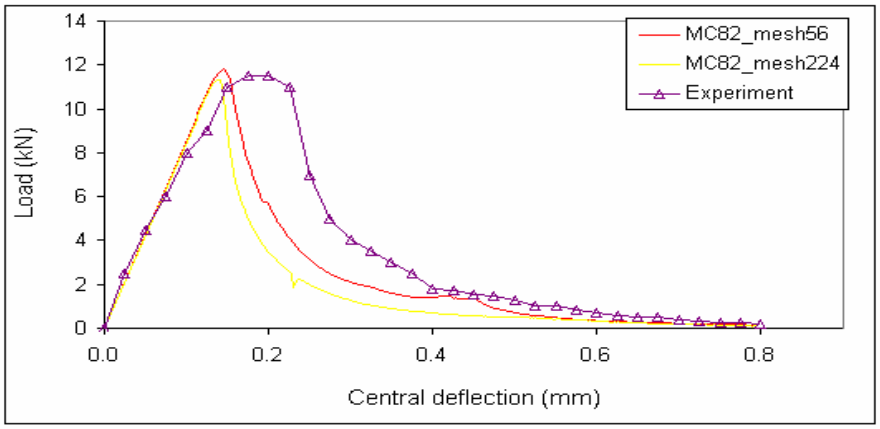

Figure 4.5 Mesh dependency test - Multi-crack (MC82) model

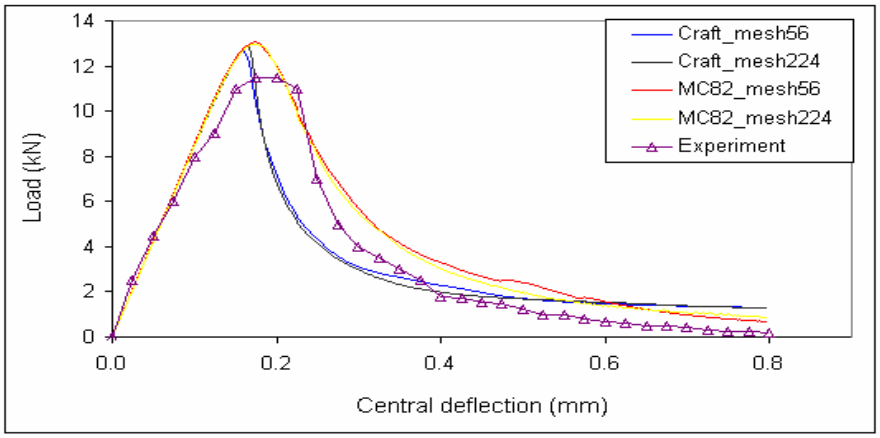

Figure 4.6 Load-deflection responses of Carpinteri's (1989) beam (MC82 model with the fracture energy G_f = 0.164 for MESH 56 and G_f = 0.206 for MESH 224)

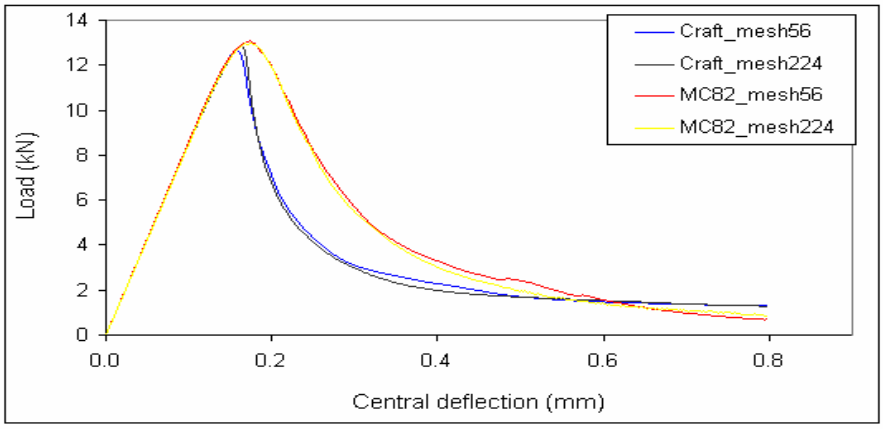

Figure 4.7(a) Load-deflection curves of Carpinteri's (1989) beam (MC82 model with α = 1)

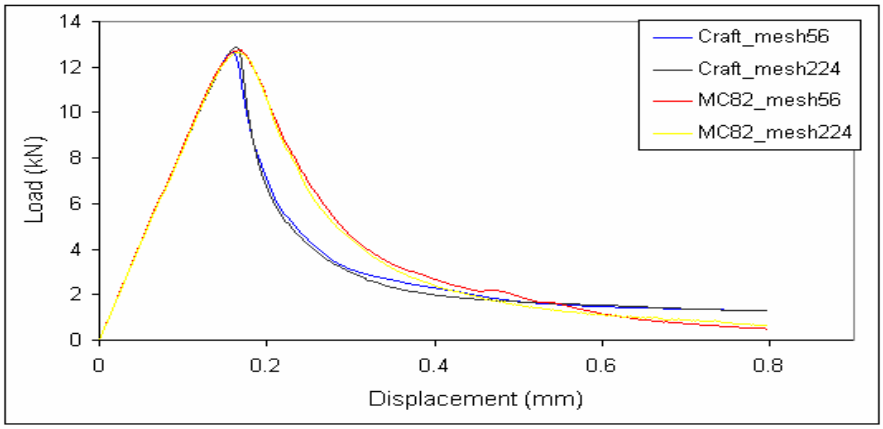

Figure 4.7(b) Load-deflection curves of Carpinteri's (1989) beam (MC82 model with $\alpha = 0.935$)

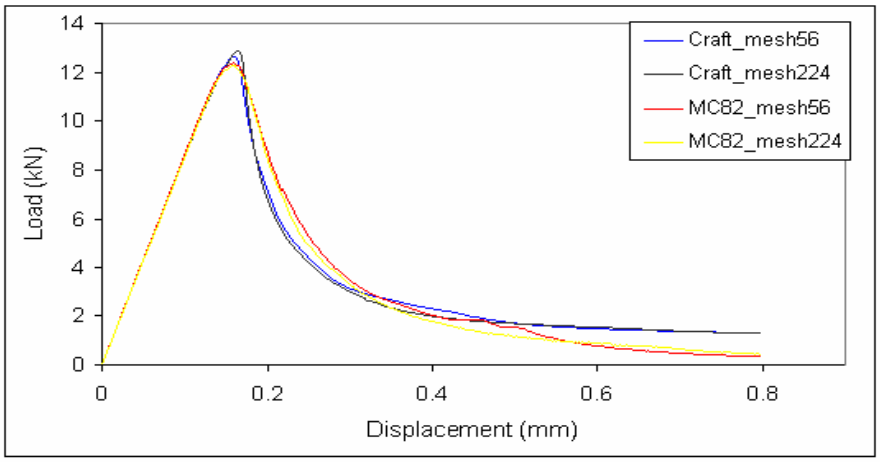

Figure 4.7(c) Load-deflection curves of Carpinteri's (1989) beam (MC82 model with $\alpha = 0.693$)

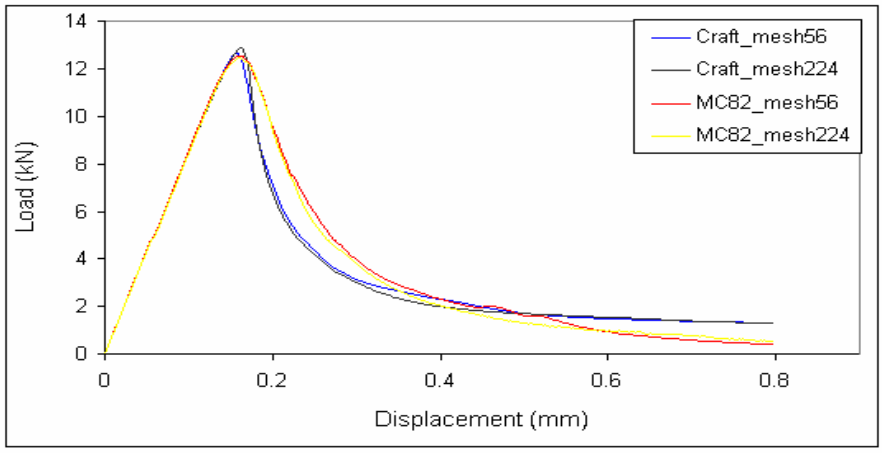

Figure 4.7(d) Load-deflection curves of Carpinteri's (1989) beam (MC82 model with $\alpha = 0.794$)

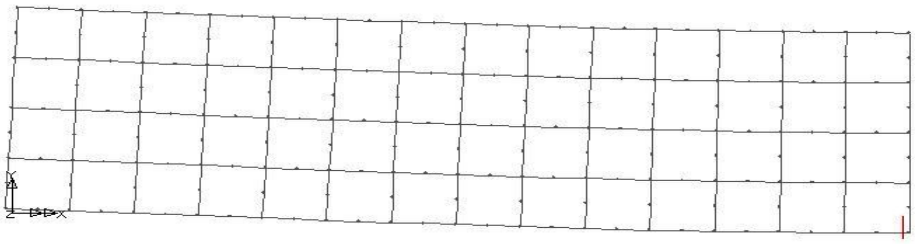

Load increment = 57 (central deflection = 0.110 mm)

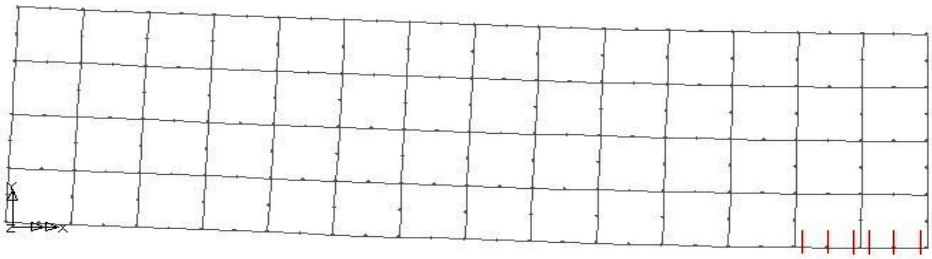

Load increment = 67 (central deflection = 0.130 mm)

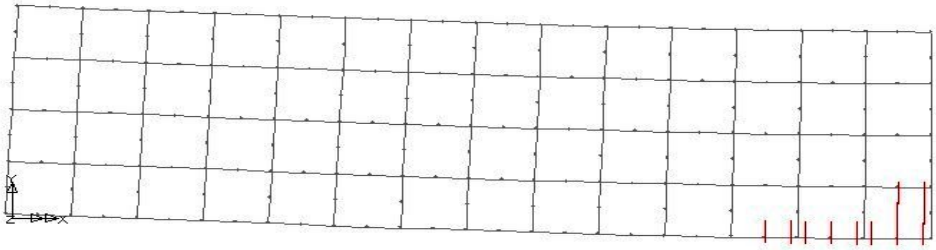

Load increment = 77 (central deflection = 0.150 mm)

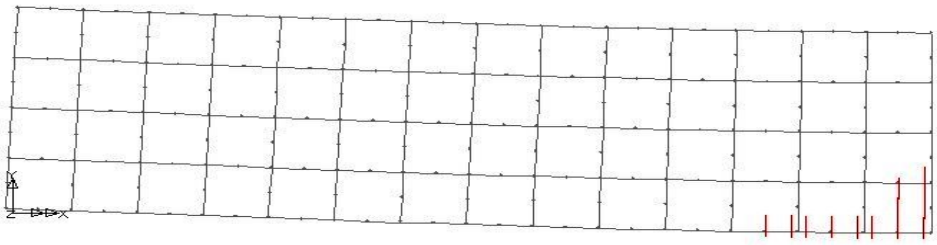

Load increment = 80 (central deflection = 0.160 mm)

Figure 4.8 Crack pattern for different load increments

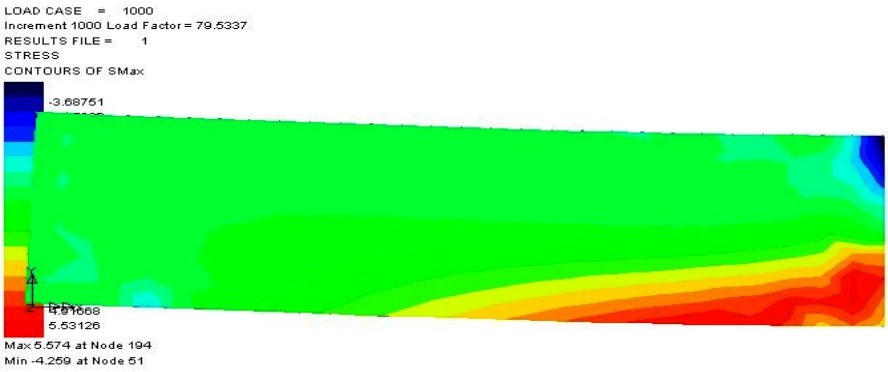

Figure 4.9 Contour of maximum stresses at peak load (deflection = 0.160 mm). The legend colour changes from low to high stresses in the ascending order from top to bottom.

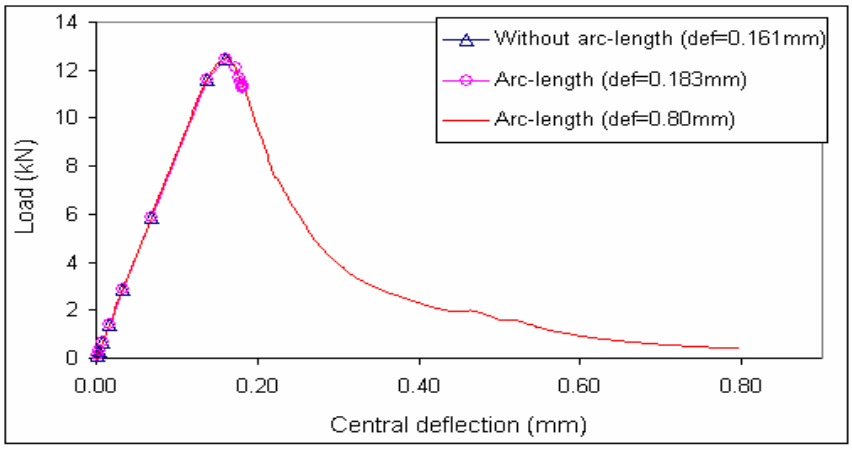

Figure 4.10 Load-deflection curves for the cases with and without using arc-length method in the case of load controlled analysis. (In the figure, def=0.161mm means the deflection at 0.161 mm. Similar for def=0.183mm and def=0.80mm)

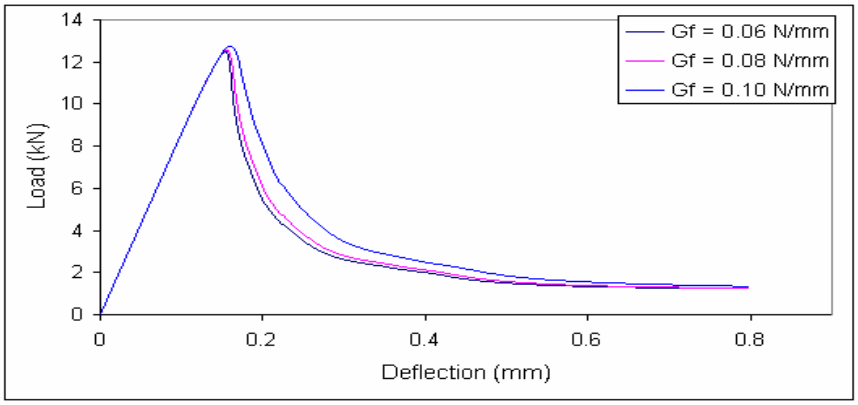

Figure 4.11 Load-deflection curves (G_f = 0.06, 0.08, and 0.10 N/mm)

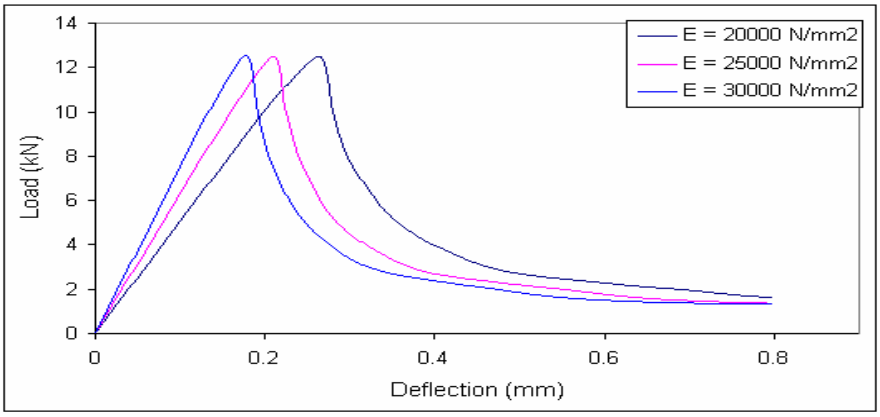

Figure 4.12 Load-deflection curves (E = 20000, 25000, and 30000 N/mm^2)

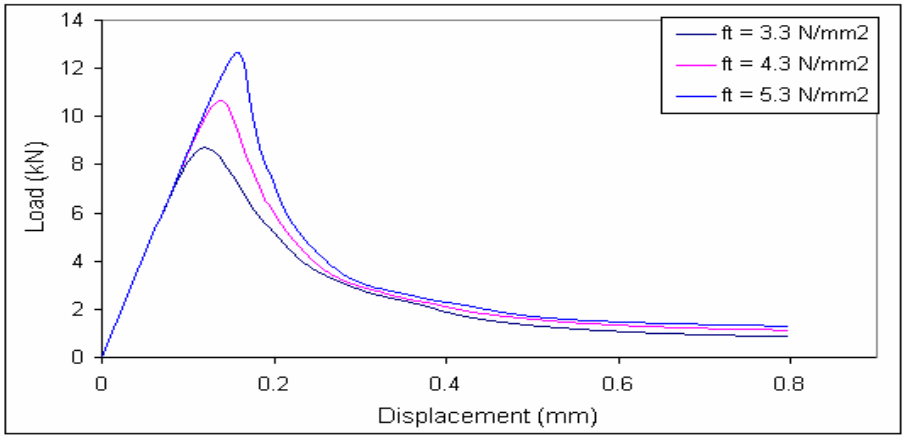

Figure 4.13 Load-deflection curves (f_t = 3.3, 4.3, and 5.3 N/mm^2)

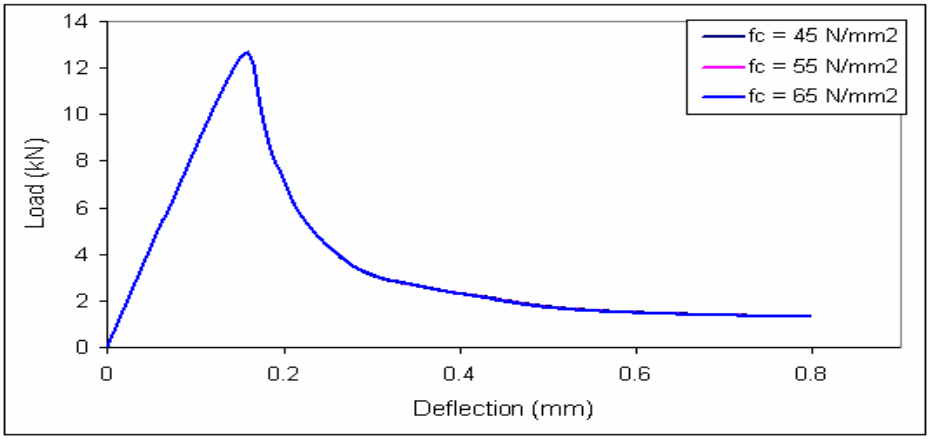

Figure 4.14 Load-deflection curves (f_c = 45, 55, and 65 N/mm^2)

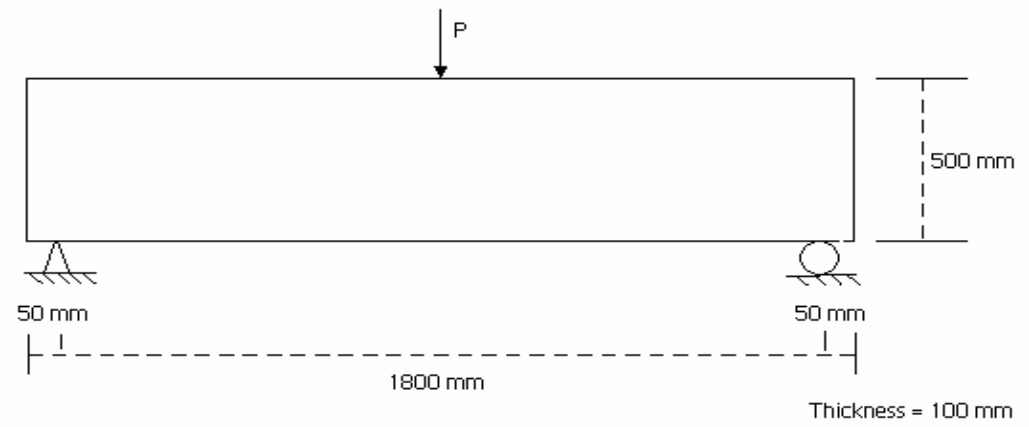

Figure 4.15 Three-point bending beam of Ozbolt and Bazant's test (1991)

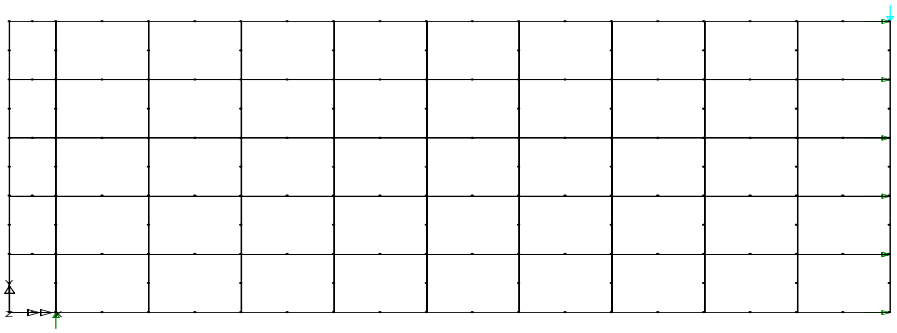

Figure 4.16 Ozbolt and Bazant's (1991) beam. A half mesh of MESH 45

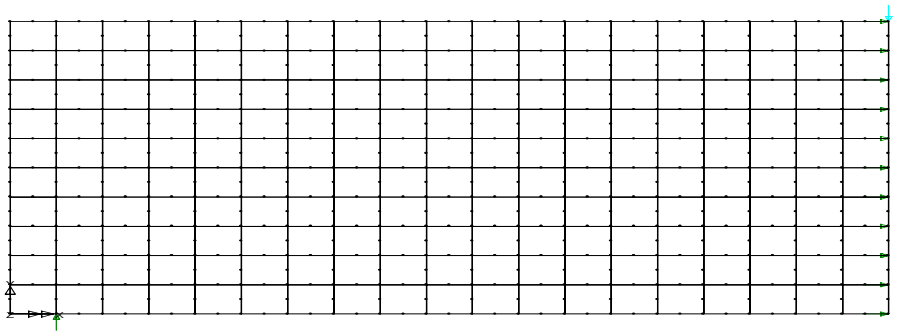

Figure 4.17 Ozbolt and Bazant's (1991) beam. A half mesh of MESH 180

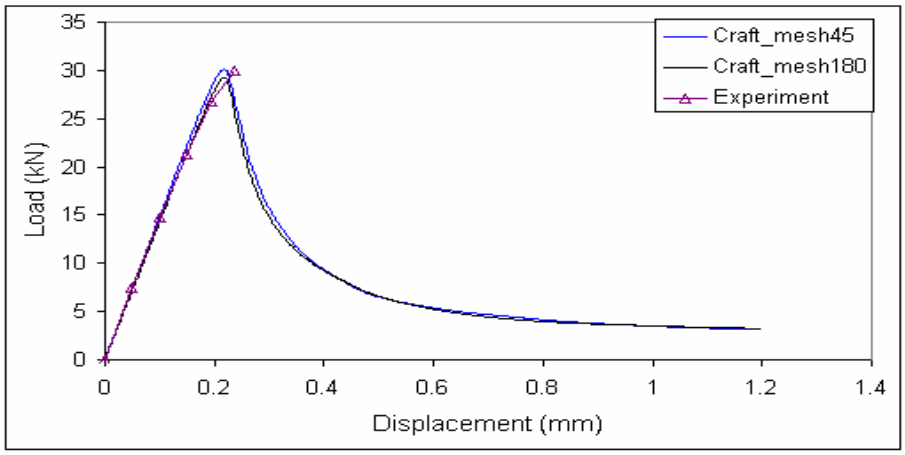

Figure 4.18 Mesh dependency test - Craft model

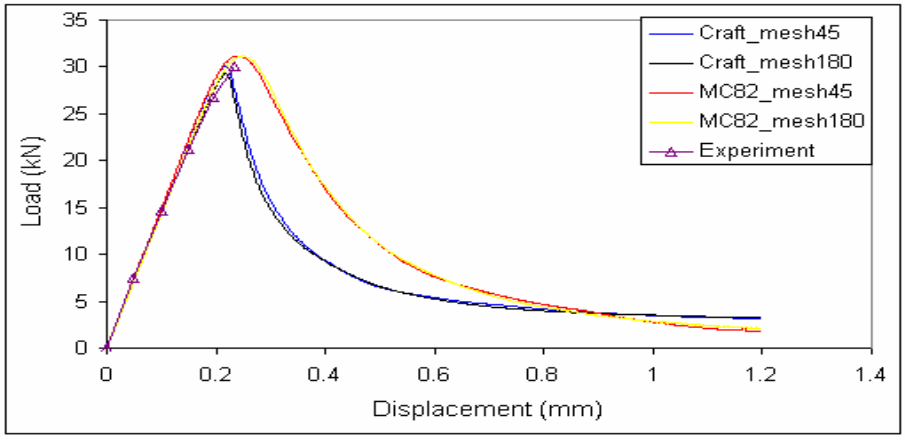

Figure 4.19 Mesh dependency test - MC82 model with $\alpha = 1$

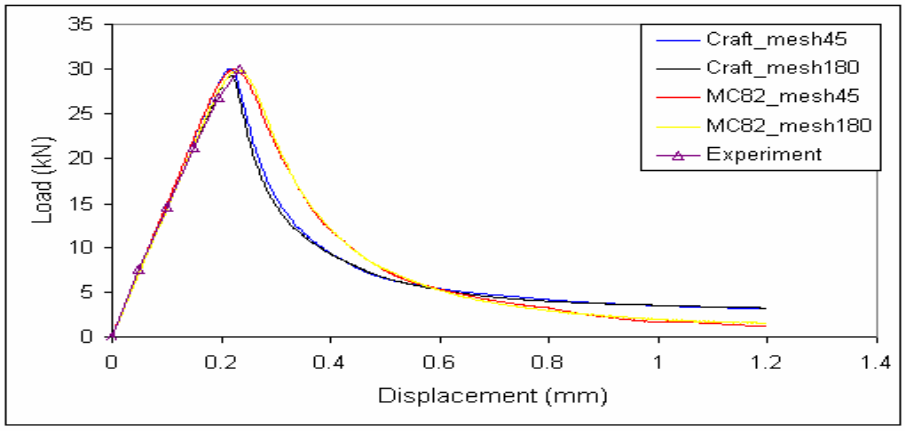

Figure 4.20 Mesh dependency test - MC82 model with $\alpha = 0.794$

CHAPTER 5

VALIDATION OF FE SMEARED CRACK MODELS FOR RC STRUCTURES UNDER MONOTONIC AND CYCLIC LOADINGS

5.1 INTRODUCTION

In this chapter, the Multi-crack (MC82) and Craft models are used to analyse several examples of reinforced concrete (RC) structures. The models are validated against experimental data and analytical results from monotonic tests for RC beams and cyclic tests for RC columns. Monotonic analyses are performed to characterise the stiffness, strength, ductility, and limit-state behaviour of these structures while cyclic analyses are carried out to estimate energy dissipation capacity, residual displacements, and general hysteretic behaviour.

First of all, the two models are evaluated through two series of reinforced concrete beams well known in literature, which were tested under monotonically increasing load. This work is to investigate the performance of the two models in predicting the flexural and shear strength of RC beams. The study is also focused upon some features of non-linear solution strategy, effect of numerical approximations, FE mesh configuration, and load-step size in order to promote a better understanding of using the models in practical applications.

Following the investigation of RC beams under monotonic loading, the two cracking models are applied for a RC bridge pier under cyclic loading. The models are validated through experimental data. Special interest is focused on the characteristics of each model in the modelling of the non-linear response of the RC bridge piers. After the investigation of the performance of the two models, some comments are also made to the use of the models for cyclic loading and, more general, for earthquake-like loading.

5.2 RC BEAMS UNDER STATICALLY MONOTONIC LOADING

5.2.1 INTRODUCTION

Since the pioneering studies of Ngo and Scordelis (1967), Nilson (1968) and Rashid (1968), the non-linear finite element method has been extensively used in the field of reinforced concrete as a powerful tool (Cedolin and Dei Poli 1977, Bedard and Kotsovos 1986, de Borst 2001, Scotta *et al.* 2001). Amongst finite element models, smeared crack models (Rashid 1968, Suidan and Schnobrich 1973) are considered advantageous and have been applied by many researchers. During the last 35 years, researchers have made several attempts to predict flexural and shear strength of reinforced concrete structures using mixed fracture models in smeared crack approach for the simulation of the mechanical behaviour of concrete (Zhu *et al.* 2002). In literature, well-known beams tested by Bresler and Scordelis (1963) have been preferred to as a benchmark test for numerical models for concrete by most of researchers (Bedard and Kotsovos 1986, Jefferson 1989, Bhatt and Kader 1998, Koksal and Arslan 2004). Although the behaviour is described well in terms of the ultimate strength, relatively less emphasis in numerical simulation is paid on the general description of mode of failure of RC beams subjected to flexural and shear loading (Bhatt and Kader 1998, Kosal and Arslan 2004).

In fact, there has been a very little previous research and testing reported on the behaviour of RC beams using MC82 model and Craft model (Jefferson 1989, 2002, and 2003b, Chuang 2001). Therefore, the main attention of this chapter is the validation of the models against several experimental RC beams and columns without web reinforcements which are available in the literature (Bresler and Scodelis 1963 and Carpinteri 1989). For further validation of the smeared crack models, the result of an analytical cracked model using the concept of strain-softening developed by the Author can be seen later in Chapter 6. In order to gain a better understanding of using the models for practical applications, some features concerning to non-linear strategy, numerical solution, FE mesh configuration, and load-step size are also investigated.

5.2.2 BRESLER AND SCORDELIS' (1963) RC BEAM

5.2.2.1 Experimental set-up

Bresler and Scordelis (1963) carried out a series of tests on reinforced concrete beams to investigate their shear and flexural strength. These tests have been used over many years and generally regarded as a benchmark for the numerical models for concrete. One of these beams, namely 0A1, is chosen for this study. The beam is simply supported with rollers at two ends and is monotonically loaded with a central point load. It has two layers of longitudinal reinforcement but does not contain any shear reinforcement. The testing arrangement is shown in Figure 5.1. The geometrical dimensions and the longitudinal reinforcement of the beam are illustrated in Figure 5.2. The observed crack patterns for diagonal tension failure, which are taken from the experimental data, are given in Figure 5.3. The material properties for the test are given in Tables 5.1 and 5.2. The failure, as described by Bresler and Scordelis (1963), occurred suddenly as a result of the longitudinal splitting in the compression zone near the load point, and also by horizontal splitting along tensile reinforcement near the end of the beam (Figure 5.3).

5.2.2.2 Finite element modelling

As the beam is symmetrical about its centre line, only a half-beam is analysed in finite element modelling. The beam is simply supported at the left-hand end with a symmetry support at the right-hand axis of symmetry. A concentrated vertical load is applied at the top of the central beam. Both Craft and MC82 models are used to analyse the testing beam and the results are presented. The concrete is simulated with 2-D eight-noded quadrilateral elements with nine Gauss points, and the reinforcement with three-noded bar elements. The prescribed displacement control is used to simulate the monotonic loading.

The steel reinforcement is replaced by an equivalent smeared area and modelled as a one dimensional elasto-plastic material with a linear hardening parameter. Tensile and compressive stress-strain curves are assumed to be bilinear and identical. In 2-D finite element analysis for RC

structures, the steel bars in the same level could be modelling by a lump element rather than by modelling individual bars (LUSAS Manual 2001). In LUSAS, the location of the steel elements needs to lie between two concrete elements by fixing node to node. In order to allow the steel element to lie between two pieces of concrete element, the total cross-sectional area of steel is divided by the number of steel elements in the cross-section to give the steel area per steel element. This issue is employed for modelling of all RC structures to be analysed in this thesis and therefore it will not be touched again. In addition, it is assumed that there is full bond between the concrete and steel.

Cracking fracture, in general, may be either distributed or localised, depending upon how much reinforcement is present. The terms "localised" and "distributed" relate to the resulting strain patterns. In plain concrete structures, it may be expected, as well known from most experiments, that large discrete cracks will form and the strains will localise at these discrete locations in a crack band with the same degree and therefore the average strains can be numerically calculated from the fracture energy (Bazant and Oh 1983, Oliver 1989, or as shown in Equation (4.1) in Chapter 4). However, in reinforced concrete structures, many cracks will form and the strains do not localise to the same degree, but in well spaced cracks or "distributed". Therefore, the strain at the end of softening curve, which is experimentally measured, would be used rather than being calculated from the fracture energy (Jefferson 1989, LUSAS Manual 2001). Therefore, for un-reinforced concrete structures the "localised" model is used, whereas for structures with at least the minimum quantity of reinforcement, i.e. approximately 0.15% by cross-sectional area (LUSAS Manual 2001), the "distributed" model is appropriate.

The steel ratio ρ ($=A_s/bh$) for this beam can be simply calculated to be 0.015, while the balanced steel ratio can be calculated to be 0.011 by using CP110 (Kong and Evans, 1975), and this beam can be described as an over-reinforced beam. Thus, in this numerical study, the strain at the end of softening curve is used in the models instead of the fracture energy of concrete.

5.2.2.3 Mesh dependency study

Two finite element meshes are employed to study the influence of mesh refinement on the numerical results, i.e. the load-deflection curves of the beam. They are called MESH I and MESH II as shown in Figures 5.4(a) and 5.4(b). The location of the steel element is illustrated in Figure 5.4(c). The load-deflection curves of the RC beam obtained with the two meshes for MC82 model and Craft model are shown in Figures 5.5, and 5.6, respectively. The figures show that the two models and their finite element meshes give similar results. Based on this observation, all subsequently detailed studies are performed using only MESH I.

5.2.2.4 Load-deflection curves

The load-deflection curves obtained from both the experiment and numerical analysis with MC82 model (for MESH I) are shown in Figure 5.7. It should be noted that the load-deflection curve in the experiment (Bresler and Scordelis 1963) is only available for the pre-peak regime and the value of failure load. Therefore in this figure only the numerical response up to the maximum deflection measured from experiment, i.e. 6.60 mm, is plotted for easy comparison. However, the full response of numerical load-deflection will be presented later (Figure 5.10). Figure 5.7 shows that the load-deflection curve obtained from numerical analysis using MC82 model is in very good agreement with the one from experiment and the predicted peak load is within 6% of the failure load of experiment. According to the experiment, the failure load of the beam 0A1 was about 334 kN with a central deflection of 6.60 mm. At a central deflection of 6.60 mm, the numerical analysis predicts a load of 356 kN. Though the numerical result is little stiffer behaviour for beam 0A1, it shows a good correlation between the experimental and numerical in terms of the load and the central deflection of the testing beam. In addition, the load-central deflection curve obtained by the analytical solution (detailed in Chapter 6) is plotted to compare with the numerical and experimental results as given in Figure 5.8. It confirms that the results of the three methods are reasonably close to each other.

The load-deflection curves obtained from the numerical analysis with Craft model is compared with the experimental one as shown in Figure 5.9. It can be seen that, in this case, the numerical result is well agreed with the experimental very in the first stage, i.e. up to the deflection of 4 mm. However, at the final stage, the numerical result underestimated the physical values as the value of load at a deflection of 6.60 mm is about 310 kN. The reason may be due to the model overestimates the crushing effects in compressive concrete or due to overestimated values of parameters used in the contact equations in the model. Also the experimental results are subjected to experimental errors. However, the result is reasonable as the difference with the experimental result in the load-deflection curves is not large.

Recently, a normally identical set of Bresler and Scordelis's beams was tested at the University of Toronto, Canada (Vecchio and Shim 2004) aiming at reproducing the Bresler and Scordelis's results. It was found that most of aspects of behaviour of the duplicate beams such as load-displacement response, load capacity and failure mode were well replicated in comparison with those from the original beams. Unlike the original tests, in the duplicate tests, loading was switched to displacement control near peak load, allowing the continuation of the tests into the post-peak load regimes. Figure 5.10 shows the load-deflection curve of the duplicate beam 0A1 in which the data of originally experimental beam 0A1 and numerical results are also plotted for comparison. In this figure the numerical load-displacements obtained from MC82 and Craft models are presented in full with peak load and post-peak behaviour (see Section 5.2.2.7 for the detail about the selection of non-linear procedures to obtain the post-peak behaviour). The numerical response obtained by using MC82 experiences a peak load of 389 kN while that of Craft model is 321 kN (Figure 5.10). Regarding the duplicate tests (Vecchio and Shim 2004), although best attempts were made to match the Bresler and Scordelis's beam as much as possible in terms of dimensions, and material properties such as steel reinforcement details, and material strengths, the response of the duplicate beam is still different from the original one. For example, the reproduced response has less stiffness and lower maximum load, i.e. 331 kN compared with 334 kN as shown in Figure 5.10. It is due to some unavoidable differences in construction, i.e. concrete age, and testing procedures (Vecchio and Shim 2004). However, this reproduced response can be combined with the original one to provide an image about the experimental range

for the response. Clearly, the numerical results, especially with respect to Craft model, are in this range. Therefore, it can be said that the numerical results are very close to the experimental results (Bresler and Scordelis 1963) within the limit of experimental error.

The comparison between the stress-strain curves at a Gauss point obtained by MC82 and Craft is shown in Figure 5.11(a) for tensile concrete and Figure 5.11(b) for compressive concrete, respectively. In compressive concrete, the Gauss point is taken at the extreme compressive element and closest to the loading point (Gauss point 7 in the top element in Figure 5.12(a)). In tensile concrete, the Gauss point is taken at the extreme tensile element and closest to the centrally vertical line of the beam (Gauss point 1 in the bottom element in Figure 5.12(a)). As the compressive behaviour of concrete is non-linear in Craft (Figure 5.11(b)), the beam sustains more damage in tensile section of the concrete, i.e. cracking, and in compressive concrete, i.e. crushing. This demonstrates why the load-deflection curve obtained by MC82 model predicts higher response at the end, in comparison with that of Craft (Figures 5.7 and 5.9). As the experiment shows that the failure is partly caused by the longitudinal splitting in the compression zone near the load point, or crushing, the numerical result predicted by Craft model is more accurate than that of MC82 model.

5.2.2.5 Numerical crack patterns and stress distributions

In this section, only the numerical result of MC82 model is presented to study the crack pattern and stress distribution as the result of Craft model in terms of crack patterns and stress distribution is very similar. In the non-linear analysis, the necessary information to form the numerical crack pattern is also calculated by the MC82 model. These calculations are conducted for every load increments and the information have then stored on the output file. In this analysis, an automatic controlled displacement is performed with an increment of 0.05 mm. Here, the crack patterns through the first cracks (increment = 11) to the final steps which correspond with the failure case in experiment (increment = 132) are shown in Figure 5.12. With increasing loading, the cracks propagate towards the support point (increment = 60 to 90), and gradually developing inclined cracks. The deformed mesh plot and crack patterns at the failure load

(increment = 132), which shows widespread diffuse cracking, are shown in Figures 5.12(a) to 5.12(e). The stress contour at these final steps is shown in Figure 5.13. A diagonal crack is predicted as major inclined cracks widespread from an area close to the support towards the application point of the load. It can be seen that the numerical crack pattern (Figure 5.12) and the contour of maximum principal stresses (Figure 5.13) are in good agreement with the experimental crack pattern (Figure 5.3).

However, in experiment it is very difficult to determine the value of the diagonal tension stress and cracking load in RC beam because the distribution of shear and flexural stress is not known with certainty (Bazant and Kazemi 1991, Koksal and Arslan 2004). But in this study, the numerical model can predict that first flexural cracks occurred at approximately 18% (62.34 kN) and first diagonal cracks occurred at approximately 52% (187 kN) of the failure load as shown in Figure 5.7. This observation is similar to the result of another numerical study (Koksal and Arslan 2004).

5.2.2.6 Reinforcement yielding and failure mechanics

It is known that the failure of an over-reinforced beam is initiated by the crushing of the concrete, while the strain in the steel is still relatively lower than its yield strain. The failure is therefore characterised by a small deflection and by the absence of extensive cracking in the tensile zone. The failure, often explosive, occurs with little warning.

The numerical result shows that the maximum stress of the steel is about 417 N/mm^2, while the strength of steel is 553 N/mm^2. This implies that this beam has failed before the steel reached its strength. This numerical result supported the view that the beam is over-reinforced.

5.2.2.7 Features of the non-linear FE analyses

The reason for this section appears to lie in the fact that, there is a need for a better understanding on the use of the smeared crack models for practical applications especially concerning the

details of non-linear features such as non-linear procedures including manual and automatic displacement control, iterative procedure, arc-length method, and the adoption of a given mesh size, load-step size, and the convergence tolerance. These are needed in order to obtain an easier and better convergence as well as reasonably accurate results with the use of the models. A brief study on features of non-linear analysis is made to investigate these items. Though both MC82 model and Craft model are used in the analyses, only the results obtained by the MC82 model is presented for the features of non-linear analysis in this study as the conclusions are similar.

5.2.2.7.1 Manual and automatic displacement control

As mentioned at the beginning of the chapter that the displacement increment control is used for the study. Displacement incrementation for non-linear analysis of the beam can be specified in two ways: manual and automatic controls. In this analysis, a uniform increment of 0.05 mm is applied for the displacement increment at the centre of the beam in the manual control scheme while an initial increment of 0.05 mm is applied for the automatic control scheme. The load-deflection curves obtained by manual and automatic controls are shown in Figures 5.14(a) and 5.14(b), respectively, which also shows the iteration number at each increment. The results show that, in the case of manual control, the analysis failed to converge at a deflection of 5.50 mm (increment = 110). This non-convergent point is also confirmed by looking at the iteration number that at this increment, the iteration number suddenly jumps up to 25 iterations from 3 iterations (Figure 5.14(a)). It should be noted that the iteration number is plotted using the scale on the right hand side of the graph. On the contrary, the analysis runs successfully without any non-convergent problem for the case of automatic control. It can be seen from Figure 5.14(b) that the iteration number is stable and no sudden change happens with this number. It is because automatic displacement control adjusts the displacement step size as needed, i.e. reducing if facing any difficulty in iteration, gaining a better balance of the equilibrium equations so as to achieve better convergence.

It can be concluded that automatic displacement control seems to be better as it seems to be able to guarantee a better convergence for non-linear analysis. However, for this research work,

automatic displacement control shall be adopted in subsequent analyses for concrete and RC structures under monotonic loading when facing the difficulty in convergence.

5.2.2.7.2 Load-step size

The concept of load-step size used in this section has the meaning of the displacement increment at each step. The load-step size may have some influence on the prediction of structural behaviour (Bedard and Kotsovos 1986). While a large load-step size may induce cracking at a lower load level thus lead to premature failure, a smaller load-step size would increase the number of load stages to reach failure which may increase considerably the cost of the analysis. In this study, different load-step sizes are employed to study their effects to the numerical results. For the RC beam investigated, keeping the FE mesh (MESH I) and all other parameters the same, four runs are carried out to check the influence of using different values of uniform manual controlled load-step size steps, i.e. 0.05, 0.1, 0.5 and 1 mm, on the numerical results. The predicted load-deflection curves for the RC beam with 4 different load-step sizes are shown in Figure 5.15, which also shows the experimental result. Table 5.3 illustrates the values of ultimate loads and central deflections of numerical results and also shows the experimental values for comparison. The results also show that there is better convergent for load-step sizes of 0.05 and 0.1 mm than those of 0.5 and 1 mm.

For load levels below initiation of cracking, i.e. around a load of 130 kN, the numerical results are essentially independent of the load-step size. Table 5.3 and Figure 5.15 indicate that the influence of the load-size step is slightly different with the adopted FE mesh. When the load-step size is a little bit larger than other load-step sizes, i.e. 1 mm, the numerical ultimate load is lower than those of the others. It may be due to this large load-step size lead to a slightly premature damage in the beam.

Based on the investigation on the different load-step sizes, it can be concluded that all the numerical results converge to the essentially same result when using load-step sizes that are ≤ 0.5 mm, or a ratio of 0.1% to the beam depth. The load-step size of 1 mm is a little bit too large.

Moreover, it confirms that the numerical results are in good agreement with the experimental one, though, in general, the numerical model predicts a slightly higher ultimate load in comparison with experiment (Table 5.3). This may be due to two main reasons: (1) the numerical model does not include non-linear behaviour and crushing failure in compressive zone of concrete, and (2) the numerical model assumed that there is perfect bond between concrete and steel reinforcement. By contrast, experiment shows that there was crushing damage in concrete and also horizontal splitting along tensile reinforcement near the end of the beam (Bresler and Scordelis 1963).

5.2.2.7.3 Iterative procedure

The standard Newton-Raphson iteration method is adopted in this study. With the help of the LUSAS package, the arc-length method (Crisfield 1983) can be easily adopted without expensive programming and testing. In the present analysis, the results did not exhibit snap-back behaviour (Figures 5.10 and 5.15) but may exhibit snap-through behaviour after the peak load. Therefore, a prescribed displacement loading procedure is firstly used. The arc-length method is also adopted for further study as presented in 5.2.2.7.4.

The convergence tolerance used for the residual force norm (r.f.n) and displacement norm (d.n) has significant effects on both the accuracy and convergence of the result. If the chosen tolerance is too tight, the analysis may fail to converge at earlier increments so as to waste computer time performing unnecessary iterations, especially for concrete and reinforced concrete materials. In contrast, if the chosen tolerance is too loose, the result may be incorrect though convergence is easily obtained. Therefore, a suitable convergence tolerance for the materials should be chosen in the manner that the achieved numerical result will be stable and in good agreement with the experimental ones (LUSAS Manual 2001). Figure 5.16 shows the results of two analyses with the residual force norm r.f.n = 0.001 and 2.5, respectively, while the residual displacement norm = 0.1. It can be seen that the analysis with r.f.n = 0.001 failed to converge at a deflection of 0.8mm and a number of 20 iterations. With r.f.n = 2.5, the analysis runs successfully to failure of the structure with a lower number of iterations, i.e., 14. It also shows that in this case the numerical

result is well matched with the experimental result. In addition, LUSAS (LUSAS Manual 2001) suggested that r.f.n = 2.5 can be used for this reinforced concrete beam. Therefore, this value of the residual force norm will be adopted in this study.

5.2.2.7.4 Arc-length method

As presented in Chapter 4, the arc-length method can be regarded as a powerful tool in tracing of the equilibrium path beyond the maximum load of concrete beams. The numerical results obtained from the above studies (Figures 5.5 to 5.15) show that using the displacement controlled scheme and standard non-linear solution (Newton-Raphson method) the numerical behaviour can be accurately traced up to an ultimate load of about 389 kN at the deflection of 7.40 mm. After this peak behaviour, the analysis failed to converge and a stable post-peak behaviour for the beam seems not to be obtained unless a small load-size step and/or a slacken tolerance are used as shown in Section 5.2.2.7.3 or Figure 5.15. However, using a slacken tolerance in residual force and displacement norms may sometimes lead to inaccurate results in the post-peak behaviour (de Borst and Nauta 1985). Therefore, the arc-length method (Crisfield 1983) was adopted to see if it can improve the convergent progress and perform a stable post-peak behaviour for the beam.

The results of the two analyses, with and without using arc-length method, are shown in Figure 5.17(a). It is clear that the two results are very similar and that using the arc-length does not make any improvement in tracing the behaviour after the peak load. Nevertheless, the result of using the arc-length method does show the evidence that the load level is significantly reduced at around the peak load in order to well treat the limit point (Figure 5.17(a)). Figure 5.17(b) shows the comparison of the number of iterations in the cases of with and without the arc-length method. It can be seen that in the first stage of non-linear behaviour in which the beam proceeds until a deflection of about 3.65 mm, the arc-length method performs its effectiveness, i.e. faster convergence, to the numerical solution in comparison with the standard method. At this stage, the total number of iterations for the arc-length method is about 152 while it is 278 for the standard method. However, in the next stage, the arc-length method does not show the effectiveness as the number of iterations for this case is larger than that of the standard method, i.e. 5734 in

comparison with 5211. Therefore, it can be concluded that the use of arc-length method does not help to capture the post-peak behaviour for this case.

5.2.2.7.5 FE mesh configuration

As mentioned above (Section 5.2.2.2), the steel ratio ρ for this beam is 1.5% and this amount of steel is much larger than the minimum quantity of steel reinforcement in an un-reinforced beam (approximately 0.15% by cross-sectional area). Therefore, the distributed cracking, not the localised cracking, predominated when the beam is cracked (Jefferson 1989, Jefferson 2004). It can be said that relatively less attention has been given to the modelling of tension-zone cracks in well-reinforced concrete, mainly because reinforcement stabilises the structural response during cracking. Post-peak load and deformation tend to be less sensitive to the tensile softening response of concrete (Bolander and Le 1999, Ile and Reynouard 2000, Bazant and Cedolin 1980, Oliver 1989). Therefore, not much care is required in the choice of the mesh configuration in order to deal with localised fracture for concrete specimens as shown in Chapter 4.

5.2.3 CARPINTERI'S (1989) RC BEAMS

5.2.3.1 Experiment set-up

The experimental tests were carried out on un-notched reinforced concrete beams by Carpinteri at the Department of Structural Engineering of Politecnico di Torino (Carpinteri 1989). Several reinforced concrete beams of rectangular cross-section varying in depth from 100 mm to 800 mm were tested in order to closely observe the minimum reinforcement requirement and its dependency to the beam depth. Only his four 100-mm depth beams with steel reinforcement ratio ρ = 0.085%, 0.256%, 0.653%, and 1.003%, namely B1, B2, B3, and B4, respectively, are studied here. The beams have one layer of longitudinal reinforcement and there is no shear reinforcement. The beam geometry and the reinforcement arrangement are shown in Figure 5.18, respectively. The material properties are specified in Tables 5.4 and 5.5 for concrete and steel,

respectively. The experimental load-deflection curves for the four beams are illustrated in Figure 5.19.

5.2.3.2 Finite element modelling

For each beam, only a half-beam is modelled because the beam is symmetrical about its centre line. The concrete is simulated with 2-D eight-noded quadrilateral elements with nine Gauss points, and the reinforcement with three-noded bar elements. The steel reinforcement is modelled as a one dimensional elasto-plastic material with a linear hardening parameter. It is assumed that there is perfect bond between steel and surrounding concrete. The boundary condition of the beam is simply supported with rollers at two ends under monotonically increasing load applied, i.e. displacement controlled, at the central beam.

5.2.3.3 Mesh dependency study

Two different meshes, MESH I and MESH II, as shown in Figures 5.20(a) and 5.20(b) are studied here, in which the location of the steel element is also illustrated. If the results of the two different meshes are closed together, it will be again confirmed that the results are mesh independency as investigated in details for plain concrete beams in Chapter 4. In this study, only the mesh dependency study of beam B1 is presented as the conclusion for other three beams would be similar.

As the beams have small amounts of reinforcement, i.e. ρ < 1.5%, (see Section 5.2.3.1), they can be classified into a group of under-reinforced beams. Further, due to the lack of experimental information about the fracture strain in the tests, it is further assumed that the beams can also be classified into a group of un-reinforced beams. Thus, the mesh configuration is assumed to be chosen as a regular mesh (de Borst 2002), and the input fracture energy G_f for the two meshes using MC82 model is calculated according to Equation (4.8) presented in Chapter 4. Thus, the input fracture energies used for MESH I and MESH II are obtained as 0.176 N/mm and 0.222 N/mm, respectively.

The central deflection history of the reinforced concrete beam (B1) obtained with the two finite element meshes are shown in Figure 5.21. It can be seen that the two meshes almost give the same results. Based on this observation, all subsequent studies for the four beams will be performed using only MESH I.

5.2.3.4 Load-deflection curves

The load-deflection curves obtained from both numerical analysis including both MC82 and Craft models as well as the experimental results for beams B1, B2, B3 and B4 are shown, respectively, in Figures 5.22(a), 5.22(b), 5.22(c), and 5.22(d).

For beam B1, the numerical result of Craft model reasonably follows the experimental one in both pre- and at peak behaviour very well while the result of MC82 model overestimates the response at peak load and in post-peak behaviour as illustrated in Figure 5.22(a). The localised fracture is clearly shown for this case. According to the experiment, the peak load of beam B1 was about 12.10 kN with a central deflection of 0.175 mm. The numerical analysis of Craft model predicts a peak load of 12.80 kN at a central deflection of 0.170 mm (a peak load of 14.10 kN at a central deflection of 0.192 mm for MC82 model). This shows a good correlation between the experimental and numerical result of Craft for beam B1 in terms of the load and the central deflection of the testing beam.

For beam B2, the experimental result demonstrates a little transition between brittle and ductile collapse as the post-peak behaviour shows a little snap-through and then a hardening behaviour (Figure 5.22(b)). The numerical result of Craft model shows that the model is capable of capturing this key behaviour. The result of MC82 model overestimates the response and does not show evidence of the transition. Though the numerical result of Craft model is little stiffer than the experiment, it shows a good agreement in pre-peak behaviour and also the predicted peak load value.

The experimental result for beam B3 shows a snap-through behaviour in the load-deflection curve this situation also specifies a transition from brittle to ductile behaviour. As can be seen from Figure 5.22(c), the numerical yield load is higher than that of experiment, i.e. 15.20 kN compared with 13.20 kN, respectively, for Craft model. Also, the numerical result is stiffer for the post-yield behaviour. It may be due to the assumption of perfect bond between steel reinforcement and concrete in the numerical models, and that is not realistic because the bond-slip behaviour was evident in the tests (Carpinteri 1989).

For beam B4, both experimental and numerical results (Figure 5.22(d)) show that the beam behaves in a totally ductile manner. In this case, a distributed model for fracture should be used for numerical analysis. Due to the assumption of perfect bond between steel reinforcement and concrete, the numerical results of both Craft and MC82 models are obviously stiffer than experimental ones in hardening behaviour. Furthermore, the response predicted by MC82 model is stiffer than that of Craft model is due to the assumption of linear compressive behaviour and no crushing in compressive concrete in its model.

The difference between the numerical and experimental results for the behaviour after cracking (Figure 5.22) possibly comes from the use of experimental data for the softening stress-strain curve defined in the models. Herein are the fracture energy, G_f, and strain at the end of softening curve, ε_0. It can be explained in numerical terms as follows:

For un-reinforced concrete structures (e.g. the minimum quantity of reinforcement is less than a reference value, i.e. approximately 0.15%), the localised form can be expected for cracking fracture and the average strains can be obtained from the fracture energy although it may lead to some difference in the response depending on the amount of steel reinforcement. As mentioned above, the beams had small amounts of reinforcement, i.e. $\rho < 1.5\%$, so as they were experimentally tested in order to determine a minimum reinforcement requirement (Carpinteri 1989). Thus they can be classified into a group of under-reinforced beams in this study. For the sake of simplicity, it was further assumed that the beams can be considered un-reinforced beams and localised form was assumed for concrete. As there is lack of experimental information about

the strain at end of softening curve (Carpinteri 1989), in this numerical study, it was assumed that the fracture energy is used for the analysis of the four beams and the strains can be approximately calculated from this fracture energy. The results (Figure 5.22) show the localised behaviour is appropriate for the behaviour of these beams, especially beams B1, and B2; and as the amount of steel reinforcement increases for beams B3 and B4, the difference between the numerical and experiment becomes wider. This could be due to the fact that the localised fracture may not be suitable and the distributed fracture may be increasingly dominant. Also, the difference between the numerical and experimental results could be due to some limit of experimental errors as demonstrated in the previous section (Section 5.2.2). Because of the complicated behaviour of the RC beams with a minimum reinforcement requirement such as transition between brittle and ductile behaviour, it is desirable to have a wide range of experimental data for the same beams so that the comparison made between numerical and experimental results would be more accurate.

5.3 RC BRIDGE PIER UNDER SLOW CYCLIC LOADING

5.3.1 Introduction

Under earthquake loading, the performance of most of RC piers is highly non-linear with changes in both strength and stiffness of the structures. This has to be carefully investigated by taking into consideration the non-linear effects of concrete and reinforced concrete, such as tensile cracking, strain softening, stiffness degradation in concrete, inelastic unloading and reloading, and hysteretic behaviour under cyclic loading.

In order to model the seismic response of RC bridge piers, a large number of experimental work has been done with RC bridge piers using statically cyclic loading (Kraetzig *et al*. 1989, Sritharan *et al.* 1996, Pinto 1996, Wan *et al.* 2001, Pinto *et al*. 2003, and Sinha and Roy 2004). It is because under cyclic loading, the RC bridge piers perform most of important features as under earthquake loading, i.e. as mentioned above, of non-linear behaviour which should be taken into account.

Following the successful application under the monotonic loading, the MC82 and Craft models are used in an investigation into the cyclic behaviour of a reinforced concrete bridge pier. The aim of this numerical analysis is to verify the two models against the experimental result of statically cyclic test in order to apply the model to investigate the performance of RC bridge piers under artificially generated earthquake time histories as will be studied in Chapters 7 and 8. The ability of the concrete model to reproduce the most important characteristics of the non-linear behaviour of the structures is evaluated by comparison with available experimental data.

5.3.2 Experiment set-up

A series of experiment were performed during the PREC8 project (Pinto 1996) to investigate an RC bridge pier under cyclic horizontal loading. The pier chosen is the shortest pier of a 1:8 bridge model specimen supported by three piers which was performed by shaking table tests at the Institute for Experimental Model and Structures (ISMES), Bergamo, Italy (Pires and Da Costa 1995, and Pinto 1996). The pier was first tested under cyclic loading in order to investigate the cyclic behaviour before carrying out the shaking table test for the whole bridge model. Only the cyclic test of this pier is studied here.

The pier has an I cross-section and 0.90 m in height, and was monolithically cast with a heavy reinforced concrete base. The longitudinal reinforcement in the flanges was placed in two layers with 4ϕ6 bars at the exterior face and 2ϕ6 + 2ϕ5 bars at the interior one. At the web, 4ϕ5 bars were used, two bars on each face. The geometric dimensions and the reinforcement arrangement are illustrated in Figure 5.23. The steel reinforcement ratio for the pier cross-section is ρ = 0.583%. The axial load due to the deck was simulated through a 150 kN concrete block located at the top of the pier by means of a swivel. The pier was subjected to displacement controlled cycles of maximum amplitudes of 0.5 mm, 1.5 mm, 3.75 mm, 7.5 mm, and 15 mm as illustrated in Figure 5.24, applied at the top of the pier by means of a servo-controlled actuator across the top. The experiment arrangement is shown in Figure 5.25, which also shows the crack pattern. The cyclic displacement was applied at a rate of about 0.02 mm/sec along the horizontal direction. The load-displacement loops of the pier obtained from the test is shown in Figure 5.26.

5.3.3 Finite element modelling

The pier is modelled with its physical geometry as shown in Figure 5.27(b). The thicknesses of the pier flange and body are 21 cm and 10 cm, respectively. The pier is fixed at its base and is loaded at the top by a statically cyclic incremental control. In experiment, the cyclic displacement was performed with a time history as a pseudo-dynamic test. However, in this test, the speed of applying cyclic displacement is very small (0.02 mm/sec). Therefore, it is assumed that, in this finite element modelling, a statically cyclic displacement is applied at the top of the pier and the effect of inertial force can be neglected. A constant axial load of 150 kN is applied at the top to model the transferred load from the superstructure. The concrete is modelled with 2-D 8-noded quadrilateral elements with 9 Gauss points and the reinforcement with 3-noded bar elements. The concrete and reinforcement material properties used in the analysis are shown in Tables 5.6 and 5.7. The reinforcement properties are E = 210000 N/mm^2, f_y = 636 N/mm^2, and the hardening modulus is assumed to be H = 15000 N/mm^2. For simplicity, longitudinal steel reinforcements in the two flanges are presented in FE modelling and the transverse steel reinforcements are neglected. This assumption would not affect the results much as the amount of the transverse steel reinforcements is small and it does not involve much in the flexural stiffness of the pier. A one dimensional elasto-plastic material with a linear hardening parameter is used to model the steel reinforcement.

5.3.4 Mesh dependency study

Two finite element meshes, named MESH I and MESH II, illustrated in Figure 5.27 (as Figure 5.27(b) in detail) are employed to investigate the influence of mesh refinement on the load-displacement loop of the cyclic test.

The numerical hysteretic response obtained from the Multi-crack model is presented in Figure 5.28. It can be found that the two finite element meshes give similar results. Further analyses for RC pier under monotonic loading (the result not shown), and these also show that the results of

the two FE meshes are very similar. Based on these observations, all subsequent studies are performed using MESH I.

5.3.5 Load-displacement hysteresis

The numerical load-displacement hysteresis of MC82 model obtained for cyclic loading is shown again in Figure 5.29, which also show the experimental one for comparison. It can be clearly observed that the MC82 model can predict the strength envelope (or capacity curve) reasonably. However, the model is, in general, not very capable to simulate the cyclic behaviour though its result is followed well the experimental result for the first cycles where the linear elastic behaviour is dominated. The stiffness at unloading and the stress at zero strain during reloading are too high. It is due to the fact that the model assumes the unloading and reloading behaviour in concrete is to be linear elastic, and also it does not include the non-linear behaviour and crushing effects of concrete in compression. In addition, it can be seen that the model predicts a higher value of peak load at each cycle of loading, in comparison with the experimental result. Therefore, the peak loads in the load-displacement loop for cycles of 6-10 lies above the load-displacement curve for monotonic loading. The reason for it is: because unloading and reloading behaviour in concrete are linear elastic and no stiffness degradation is included in the model, the peak loads then are elevated above the expected ones. It is expected that, if the model can simulate the inelastic unloading and reloading behaviour as well as the stiffness degradation for concrete, the numerical result for cyclic loading should predict the strength envelope more accurately in comparison with the experimental result.

In the contrary, the result of Craft model in Figure 5.30 shows that the numerical hysteresis is generally in good agreement with the experimental one. The best agreement can be found for the first 3 cycles of loading where the elastic behaviour is dominated. Clearly, the model can simulate the stiffness degradation of the pier in unloading and reloading behaviour very well, i.e. the stiffness degradation after 3 cycles of loading. Also, as the model includes the contacting effects of two cracking surfaces in the concrete constitutive formulae (Jefferson 2003a), the pinching effect is well captured as can be seen when transferring from tension to compression in

5th and 6th cycles in Figure 5.30. However, the peak loads at each cycle and stiffness at unloading are still slightly too high. The difference may be due to the slip between concrete and steel reinforcement. Nevertheless, it should be noted that because of the convergent problem, Figure 5.30 presents only the load-displacement hysteresis for 8 and a half cycles of loading.

5.4 SUMMARY AND CONCLUSIONS

In this chapter, the performance of the MC82 and Craft models is assessed by analysing various cases of RC beams from under- to over-reinforced beams under monotonic loading, and a RC bridge pier under cyclic loading. Through the study of the model for RC beams, some important features of non-linear strategy and mesh dependency are investigated in order to gain a better understanding towards the use of the models. Some discussions and conclusions can be drawn regarding the numerical analysis and the experimental results.

Reinforced concrete beams under monotonic loading

1. For the over-reinforced beams, the MC82 and Craft models are able to provide not only a good prediction of the failure load but also on the diagonal crack pattern and deformation behaviour. However, the MC82 model predicts a slightly higher peak load compared with the experiment. It is because this model does not include the non-linear behaviour and crushing failure of concrete in the compressive zone. Also, the bond slip between concrete and steel may have some significant effects. The results predicted by Craft model, in contrast, is lower than that of MC82 model in cracking progress due to the model includes the crushing effects in compressive concrete and this can cause the loss of strength in the beam prematurely.

2. The crack patterns and the contour of maximum stresses obtained from the numerical model are in very good agreement with those of experiments.

3. From the analysis of the Bresler and Scordelis's beam, it can generally be seen that the finite element analysis using MC82 and Craft models offer a complete picture of the response with peak and post-peak behaviour, mode of failure, and the stress distribution in the entire beam, which cannot easily obtained by other analytical or experimental methods.

4. For the under-reinforced beams, localised fracture seems to be more appropriate for modelling the beams with small amount of steel reinforcement, i.e. beams B1 and B2, and therefore, the input fracture energy and the mesh configuration are obtained by the issues given in the previous chapter. The numerical result shows that the peak load and the post-peak responses were captured reasonably by Craft model. The result of MC82 model overestimated the response due to the non-linear behaviour and crushing of concrete in compressive zone is not included.

5. At the transition from brittle to ductile behaviour of RC beams, owing to the small amount of steel reinforcement, the numerical simulations are stiffer than the experimental results (Figure 5.22). It may be due to two reasons: (1) inaccurate softening curve, i.e. strain at end of softening curve, measured from experiments should be used for the model instead of using the fixed fracture energy because in this case a distributed fracture would be more appropriate, and (2) the model assumed that there is a perfect bond between concrete and steel and this is not as realistic as seen from the failure mode observed from the tests (Carpinteri 1989).

6. Regarding the analysis of under-reinforced concrete beams and the problem of transition, the Author would think that there is a need for further research into the identification of parameters used for the model, i.e. the fracture energy or strains for the cracking model approach, in order to simulate the structural behaviour more accurately. However, it is outside the scope of this PhD research.

Features of the non-linear FE analysis

1. It is shown that, in comparing with manual displacement control, the use of automatic displacement control is more likely to give a better convergence characteristic for non-linear analysis. It is because automatic displacement control is able to adjust the displacement step size as needed, i.e. reducing the step size, so as to achieve a better convergence.

2. The load-size step has some influence on the prediction of structural behaviour as well as convergence characteristics. A load-size step of about 0.1%h, in which h is the beam depth, or smaller is advisable to be used in modelling of reinforced concrete structures under monotonic loading.

3. The convergence tolerance used for residual force norm and displacement norm has significant effects on both the accuracy and convergence of the numerical result. Values of 2.5 and 0.1 can be suggested for the residual force norm and residual displacement norm, respectively.

4. Using arc-length method for the analysis of the Bresler and Scordelis's (1963) beam does not seem to be able to capture the post-peak behaviour for the beam.

Reinforced concrete bridge pier under cyclic loading

1. The MC82 model is, in general, not capable of capturing the cyclic behaviour of RC bridge piers. The chief flaw with the model is that unloading behaviour in concrete is linear elastic, which is unrealistic for concrete (Figure 5.29).

2. However, it is still capable of reproducing the correct magnitude of the peak load and displacement at zero load crossings. In this study, although the crushing effect is not

included in the MC82 model it does not affect the numerical results because experimental observations showed that there is no crushing failure in the pier (Pinto 1996).

3. The MC82 model should be used with care if used for analysis of structures under cyclic loading as the damping and unloading stiffness have been overestimated. Refinement of the model would be required for the use of this model if it is to be used for cyclic loading. In physical point of view, the model would be used reasonable in the structures which have high compressive strength and no crushing failure under cyclic loading.

4. The result of the plastic-damage-contact model, Craft, is in good agreement with experimental results of the RC bridge pier under cyclic loading. It is because the model takes into account most of non-linear effects of concrete and reinforced concrete under cyclic loading. However, as the peak load at each cycle and the stiffness are slightly too high compared with experiment, the consideration of bond slip between concrete and steel reinforcement may be necessary in order to obtain response close to reality (Figure 5.30).

5. Based on these investigations, Craft model would be suggested to use for further analyses of RC bridge piers under cyclic and earthquake-like cyclic loading as it would capture the cyclic behaviour more accurately than MC82 model. However, if the response or damage of RC bridge piers under different sets of earthquake time histories is studied in relative comparisons in terms of qualitative measures, the MC82 model can also be used without the loss of accuracy.

Table 5.1 Concrete properties of RC beam (Bresler and Scordelis 1963)

Young's modulus	E = 25000 N/mm^2
Poisson's ratio	ν = 0.2
Uniaxial compressive strength	f_c = 22.6 N/mm^2
Uniaxial tensile strength	f_t = 2.5 N/mm^2
Uniaxial strain at peak compressive strength	ε_c = 0.0022
Uniaxial strain at end of softening curve	ε_0 = 0.0032 *

* This value is taken from Jefferson (2002a, 2003b) and is used for strain at end of softening in FE modelling of concrete

Table 5.2 Steel properties of RC beam (Bresler and Scordelis 1963)

Young's modulus	E = 205000 N/mm^2
Yield stress	f_y = 553 N/mm^2
Hardening parameter	H = 15000 N/mm^2 **

** This value is taken from Jefferson (2002a, 2003b) and is used for hardening modulus in FE modelling of steel reinforcement.

Table 5.3 Numerical results of four different load-step sizes for RC beam

Load-step Size	Numerical Results of MC82				Experimental Results	
	Ultimate Load	Ultimate Deflection	Load at Deflection of 6.60 mm	Deflection at Load of 334 kN	Ultimate Load	Ultimate Deflection
(mm)	(kN)	(mm)	(kN)	(mm)	(kN)	(mm)
(1)	(2)	(3)	(4)	(5)	(6)	(7)
0.05	389.00	7.40	356.00	6.15	334.00	6.60
0.10	390.00	7.40	354.00	6.20	334.00	6.60
0.50	369.00	7.50	350.00	6.35	334.00	6.60
1.00	360.00	8.00	343.00	6.45	334.00	6.60

Table 5.4 Concrete properties of RC beams (Carpinteri 1989)

Young's modulus	E = 34300 N/mm^2
Poisson's ratio	ν = 0.18
Uniaxial compressive strength	f_c = 75.7 N/mm^2
Uniaxial tensile strength	f_t = 5.3 N/mm^2
Uniaxial strain at peak compressive strength	ε_c = 0.0022
Fracture energy per unit area	G_f = 0.09 N/mm

Table 5.5 Steel properties of RC beams (Carpinteri 1989)

Young's modulus	E = 200000 N/mm^2
Yield stress	f_y = 637 N/mm^2 (Beam B1)
	f_y = 569 N/mm^2 (Beam B2)
	f_y = 441 N/mm^2 (Beam B3)
	f_y = 456 N/mm^2 (Beam B4)
Hardening parameter	H = 15000 N/mm^2 (assumed)

Table 5.6 Concrete properties of RC bridge pier (Pinto 1996)

Young's modulus	E = 32000 N/mm^2
Poisson's ratio	ν = 0.2
Uniaxial compressive strength	f_c = 53.6 N/mm^2
Uniaxial tensile strength	f_t = 4.20 N/mm^2
Uniaxial strain at peak compressive strength	ε_c' = 0.0022
Uniaxial strain at end of softening curve	ε_0 = 0.0032

Table 5.7 Steel properties of RC bridge pier (Pinto 1996)

Young's modulus	E = 210000 N/mm^2
Yield stress	f_y = 636 N/mm^2
Hardening parameter	H = 15000 N/mm^2 (assumed)

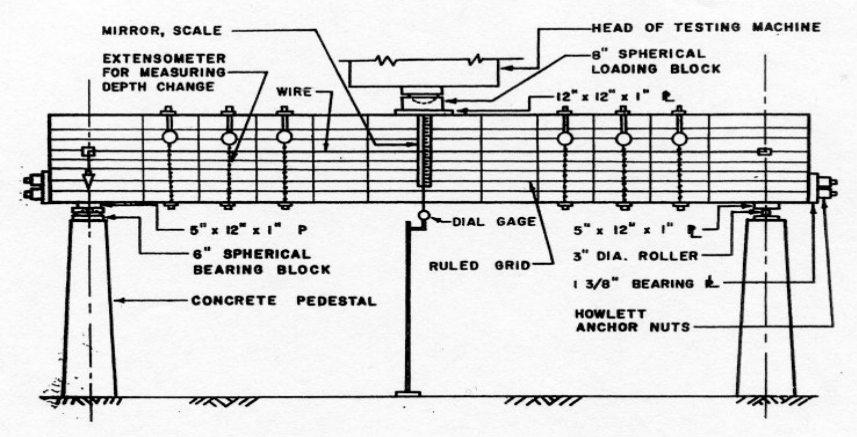

Figure 5.1 Loading arrangement and instrumentation (Bresler and Scordelis 1963)

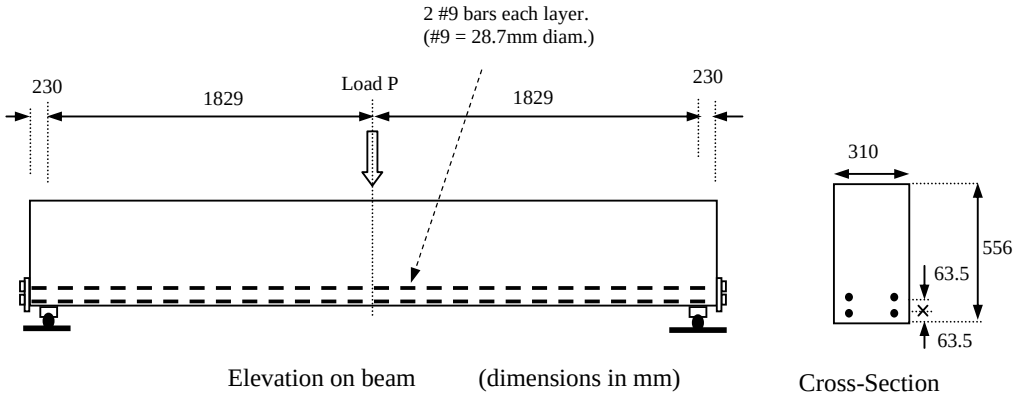

Figure 5.2 Experimental arrangement of Bresler and Scordelis's (1963) beam

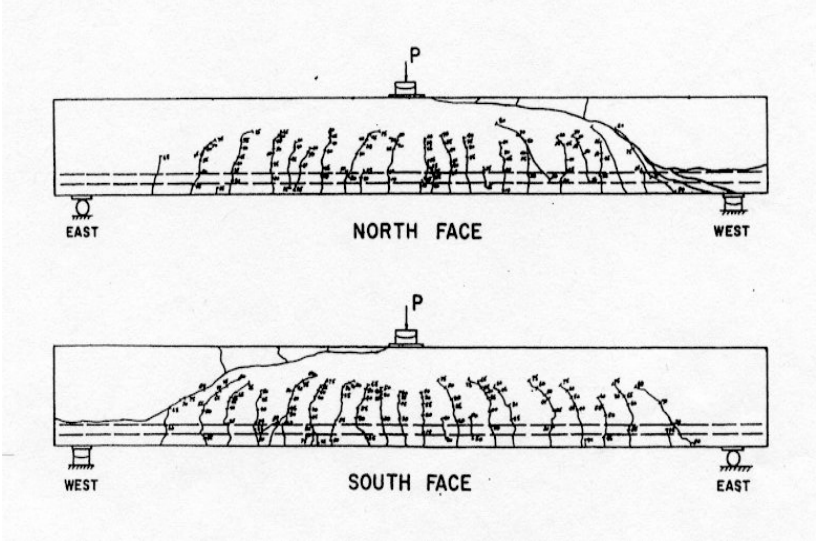

Figure 5.3 Typical crack patterns for diagonal tension failure of the experiment (Bresler and Scordelis 1963)

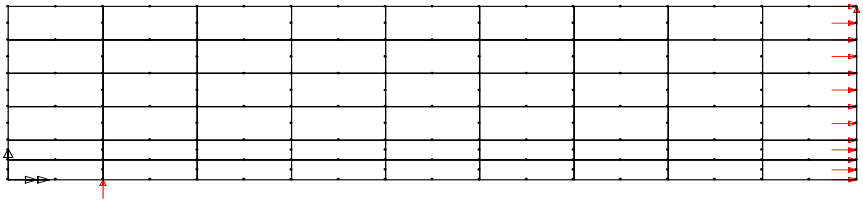

Figure 5.4(a) Reinforced concrete beam. A half of MESH I
(Red arrows are represented the supports for the half-beam)

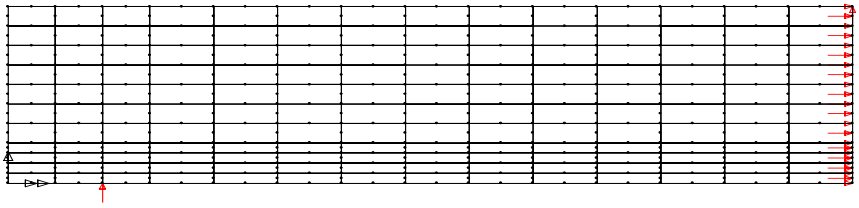

Figure 5.4(b) Reinforced concrete beam. A half of MESH II
(Red arrows are represented the supports for the half-beam)

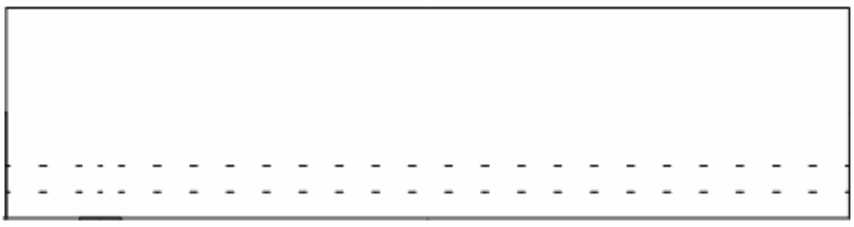

Figure 5.4(c) Line element for steel (dash line)

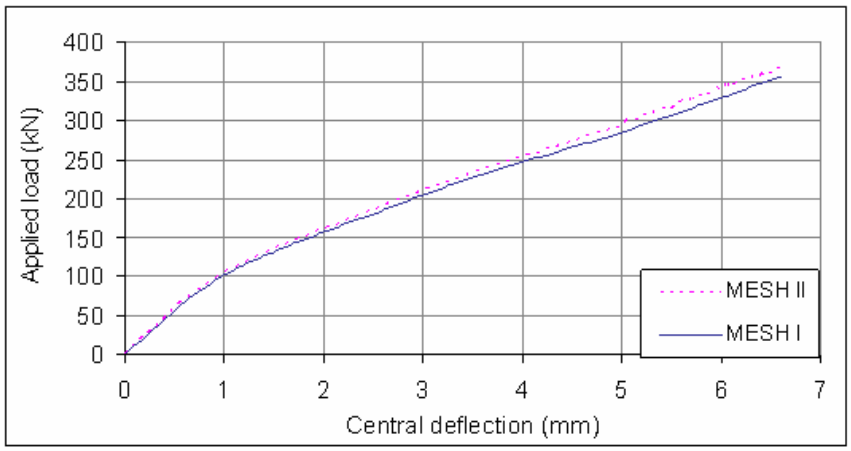

Figure 5.5 Load-central deflection curves of MESH I and MESH II using MC82 model

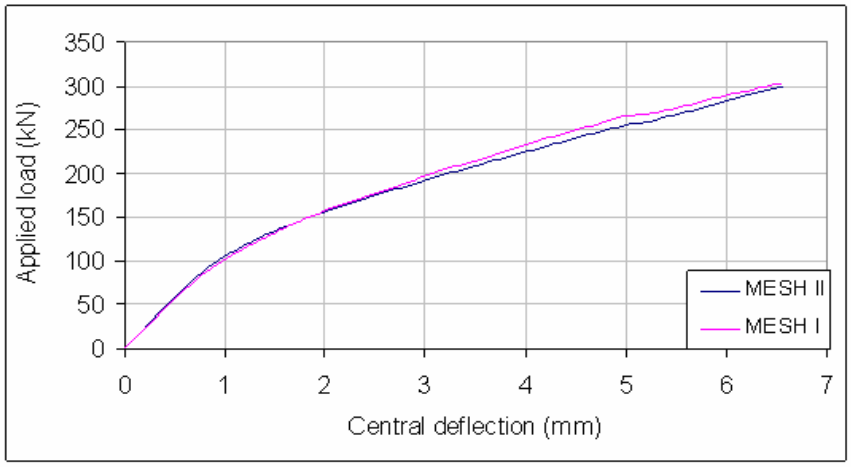

Figure 5.6 Load-central deflection curves of MESH I and MESH II using Craft model

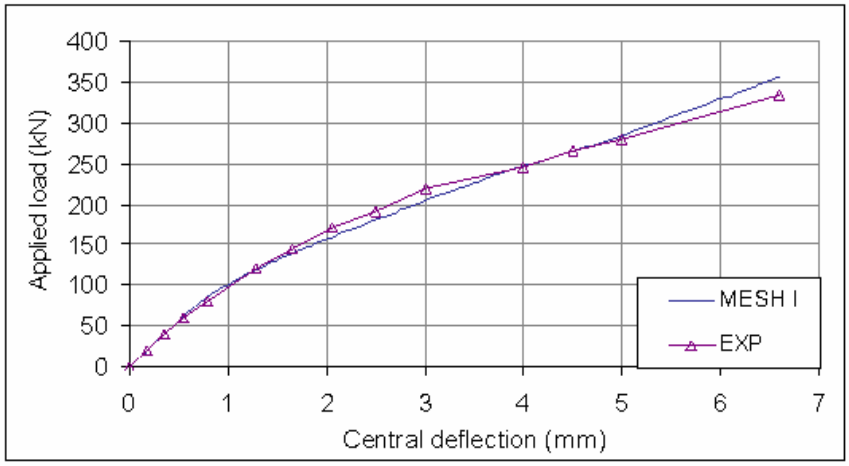

Figure 5.7 Load versus central deflection curves (MC82 model)

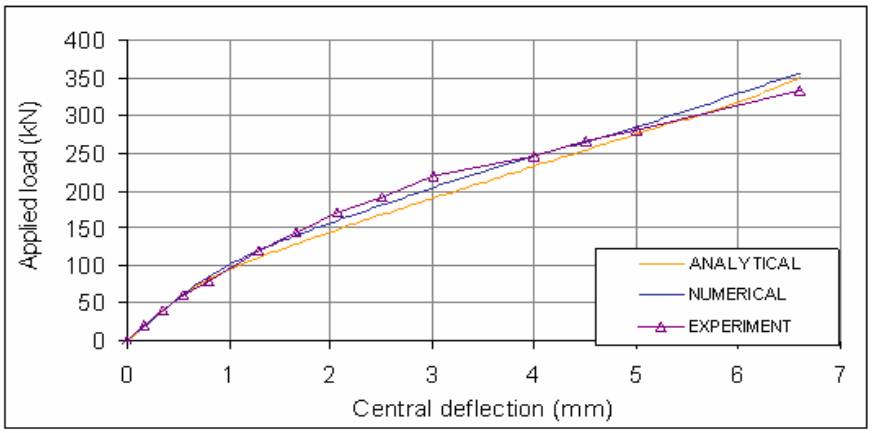

Figure 5.8 Load versus central deflection curves compared with analytical solution

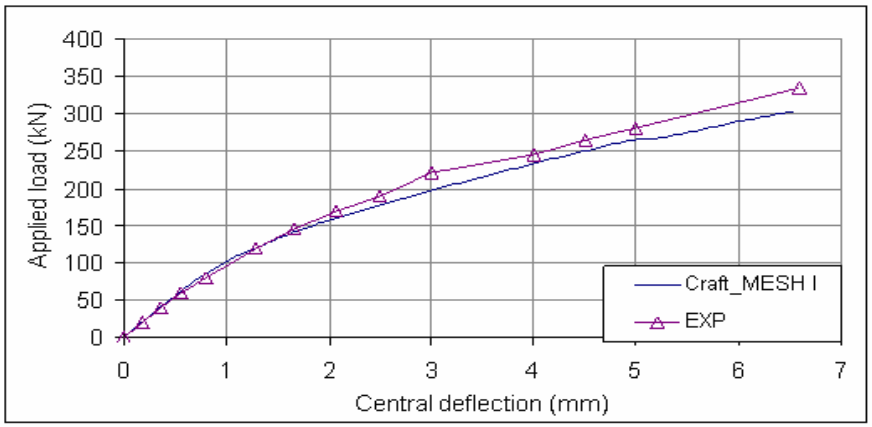

Figure 5.9 Load versus central deflection curve (Craft model)

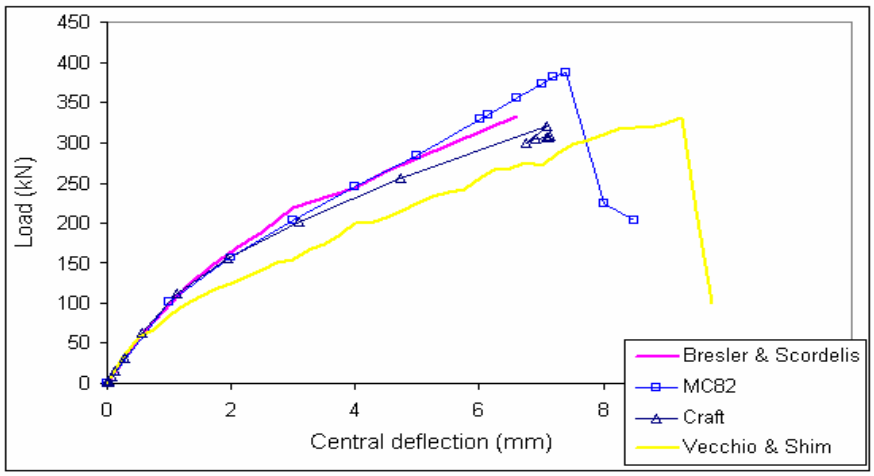

Figure 5.10 Load versus central deflection from MC82 and Craft models and experimental results (Data from Bresler and Scordelis (1963) and Vecchio and Shim (2004))

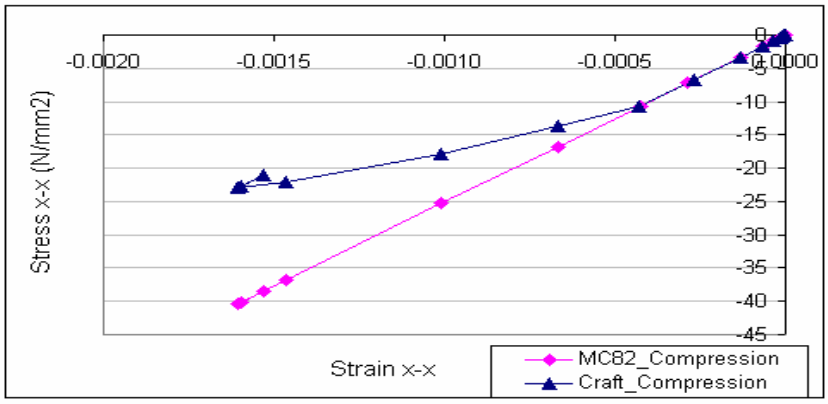

Figure 5.11(a) Stress-strain curve at Gauss point (Gauss point 7 in the top element in Figure 5.12(a))

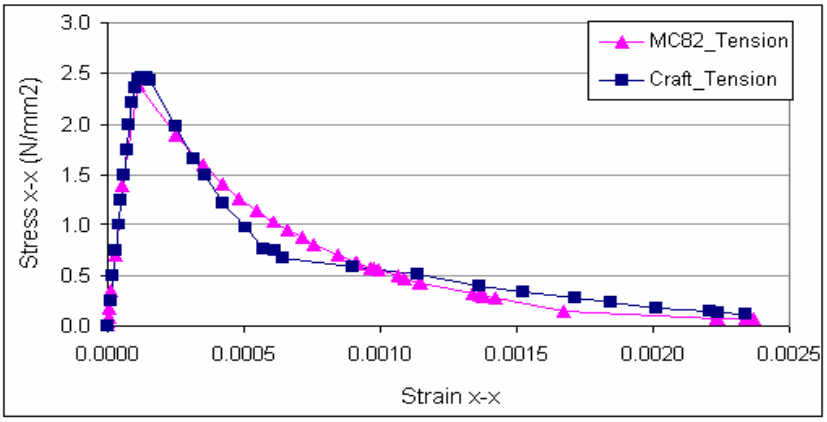

Figure 5.11(b) Stress-strain curve at a Gauss point (Gauss point 1 in the bottom element in Figure 5.12(a))

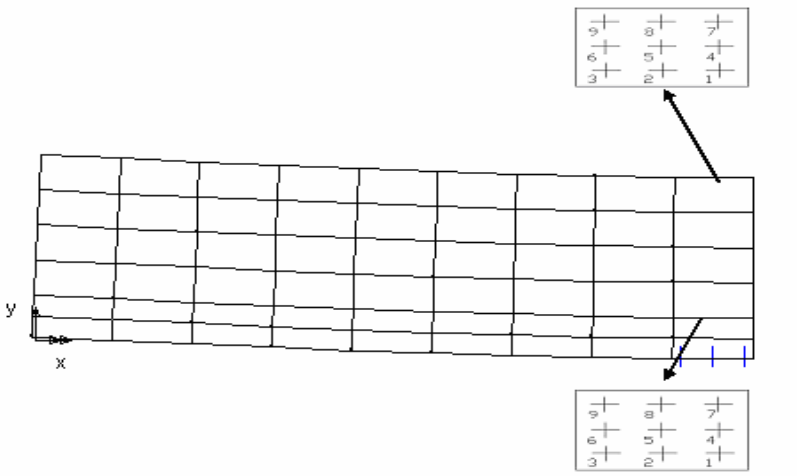

Figure 5.12(a) Load increment = 11, crack pattern (Elements at top and bottom with their Gauss points are shown)

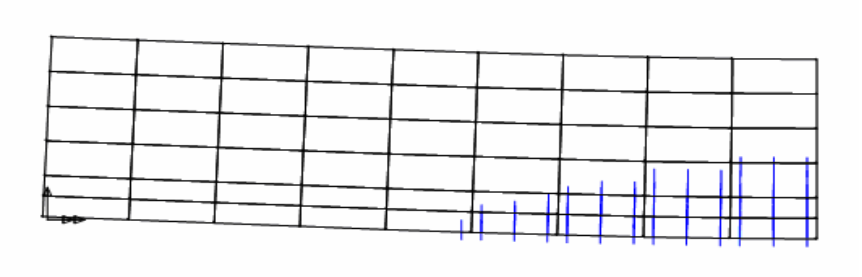

Figure 5.12(b) Load increment = 30， crack pattern

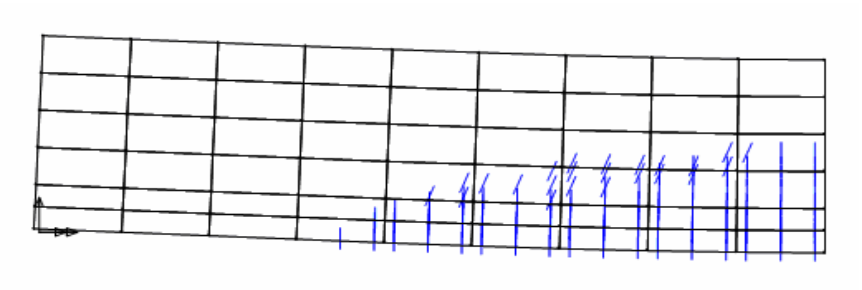

Figure 5.12(c) Load increment = 60, crack pattern

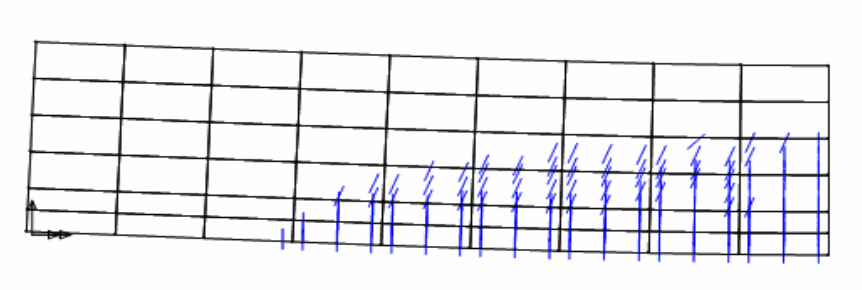

Figure 5.12(d) Load increment = 90, crack pattern

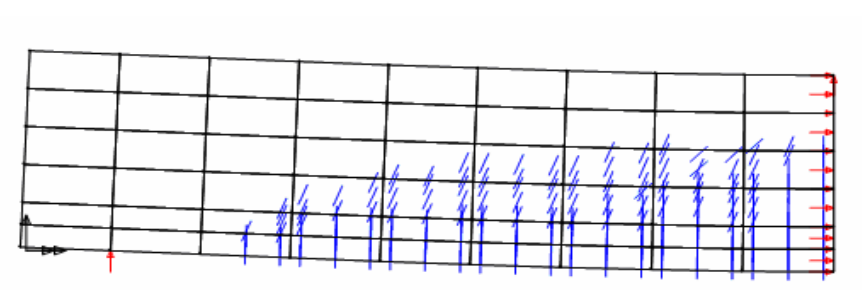

Figure 5.12(e) Load increment = 132, crack pattern
(Red arrows are represented the supports for the half-beam)

Figure 5.12 Deformed mesh and crack patterns

Figure 5.13 Contour of maximum principal stresses at final steps

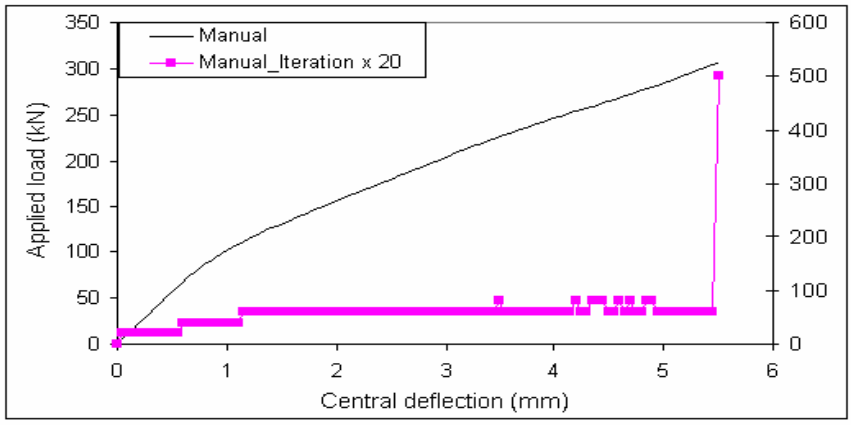

Figure 5.14(a) Manual displacement control

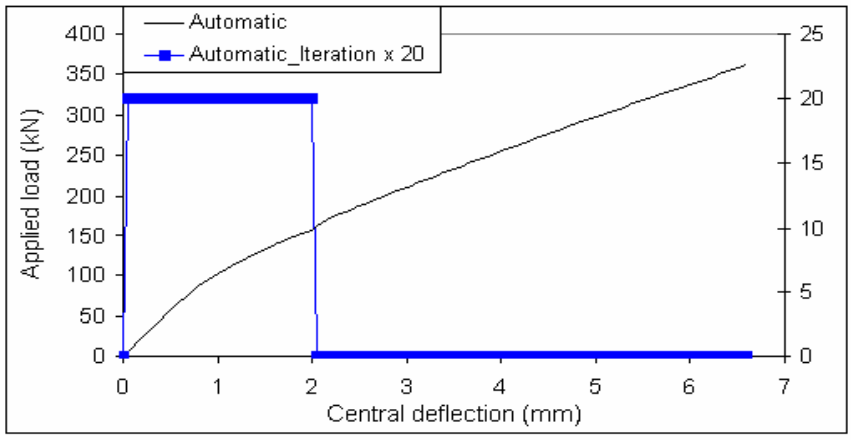

Figure 5.14(b) Automatic displacement control

Figure 5.14 Load-deflection and iteration at failure convergence

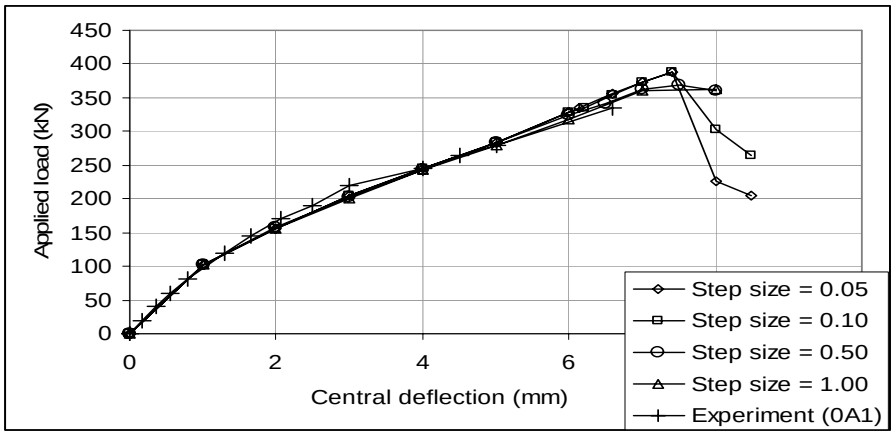

Figure 5.15 Influence of load-step size with the beam behaviour

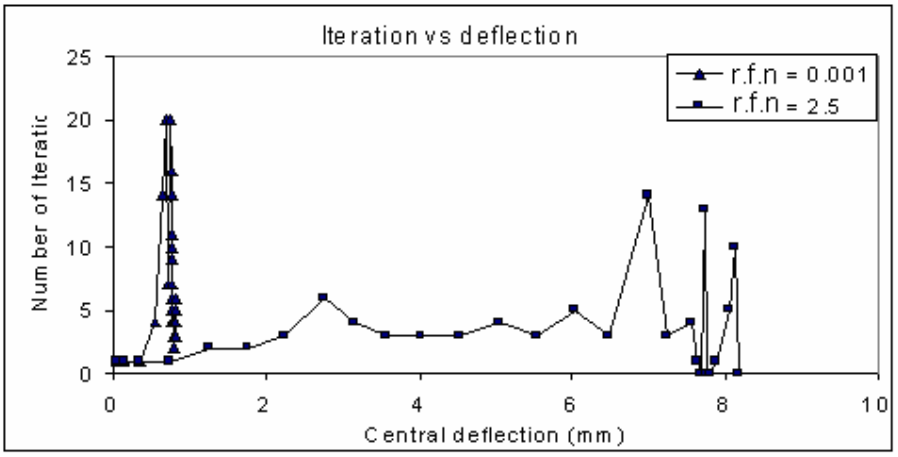

Figure 5.16 Influence of residual force norm (r.f.n) to convergence and iteration

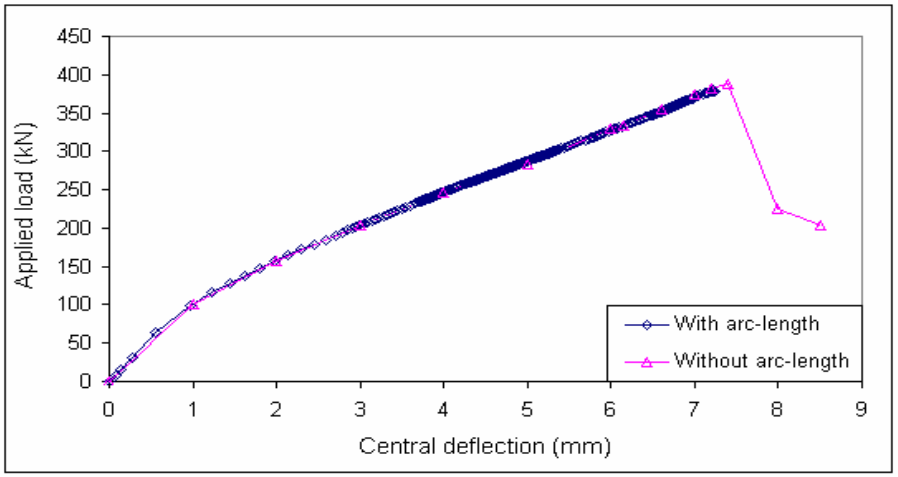

Figure 5.17(a) Load-deflection curves for the cases with and without arc-length method

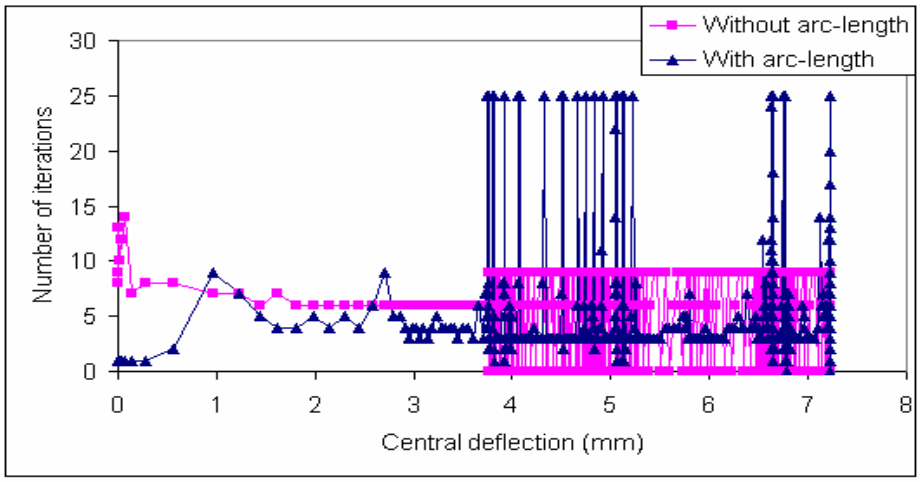

Figure 5.17(b) Number of iterations versus deflection in the cases with and without arc-length method

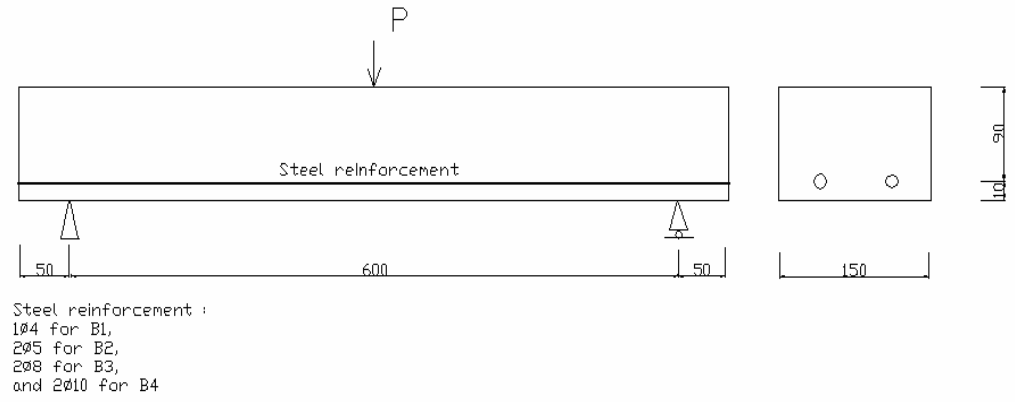

Figure 5.18 Experimental arrangement of Carpinteri's (1989) RC beams

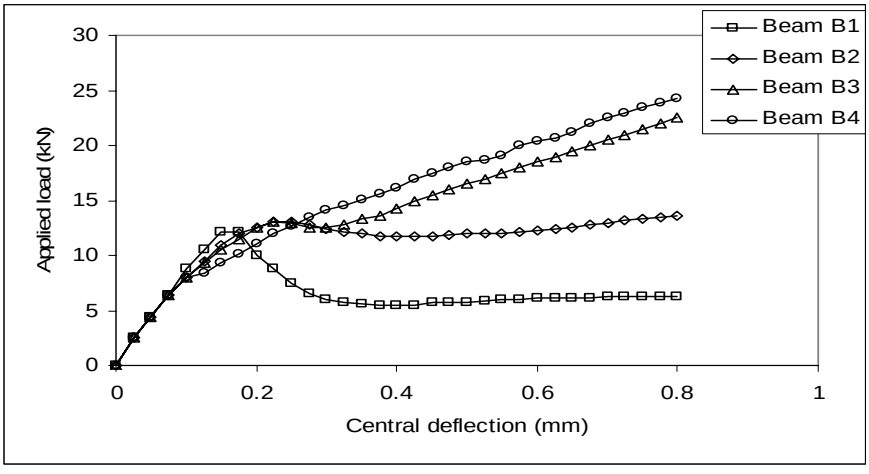

Figure 5.19 Experimental results of the four RC beams (Carpinteri 1989)

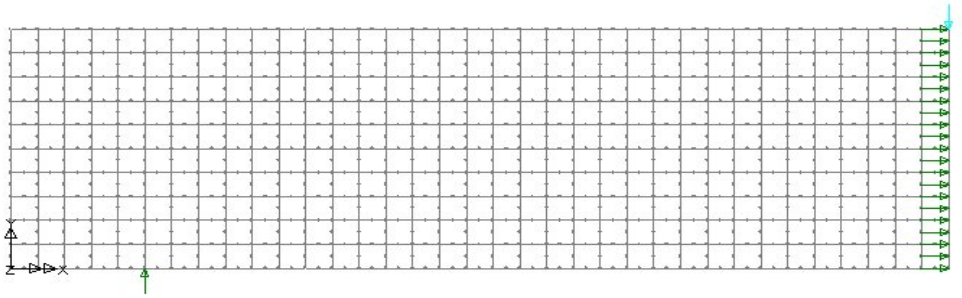

Figure 5.20(a) FE modeling for Carpinteri's beams. A half of MESH I
(Green arrows are represented the supports for the half-beam)

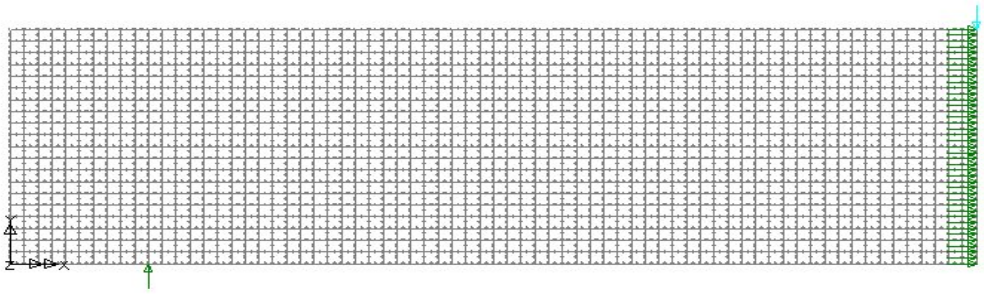

Figure 5.20(b) FE modeling for Carpinteri's beams. A half of MESH II
(Green arrows are represented the supports for the half-beam)

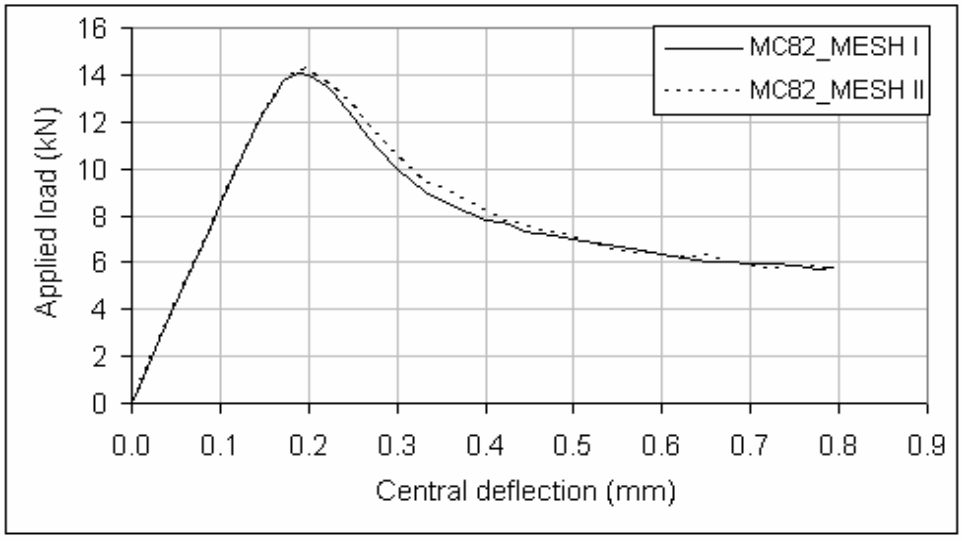

Figure 5.21 Mesh dependency test (G_f = 0.176 N/mm for MESH I, G_f = 0.222 N/mm for MESH II, in which G_f is calculated from Equation (4.8) in Chapter 4)

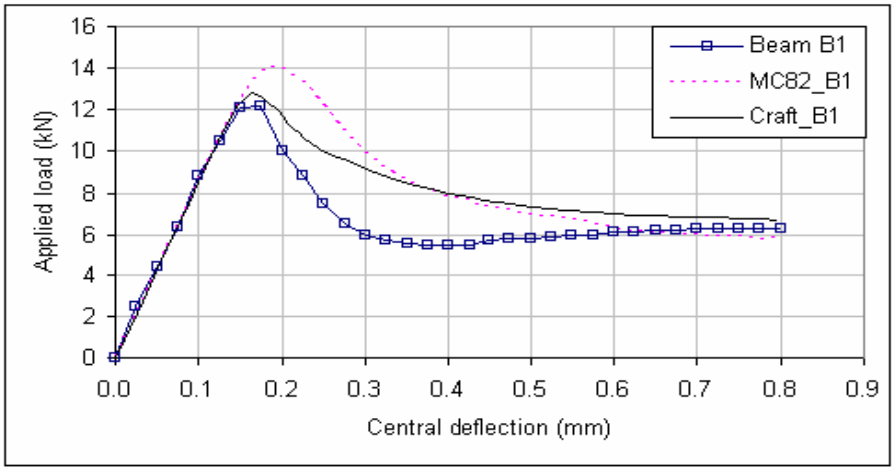

Figure 5.22(a) Load-deflection curve of the beam B1

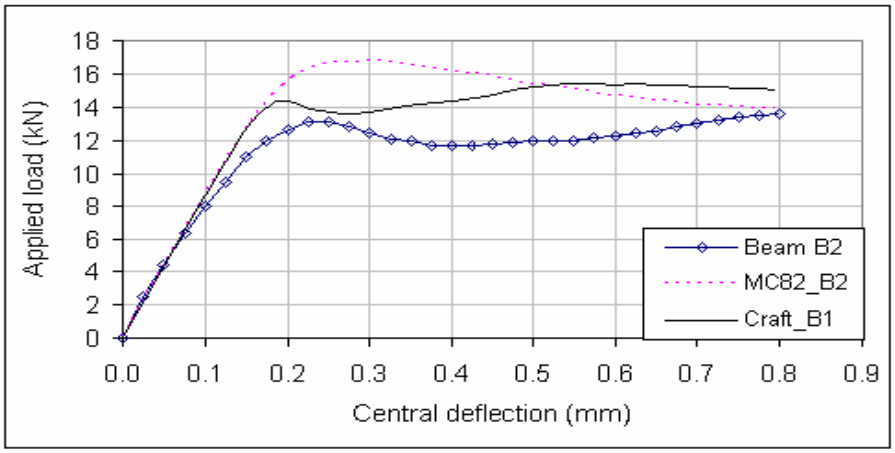

Figure 5.22(b) Load-deflection curve of the beam B2

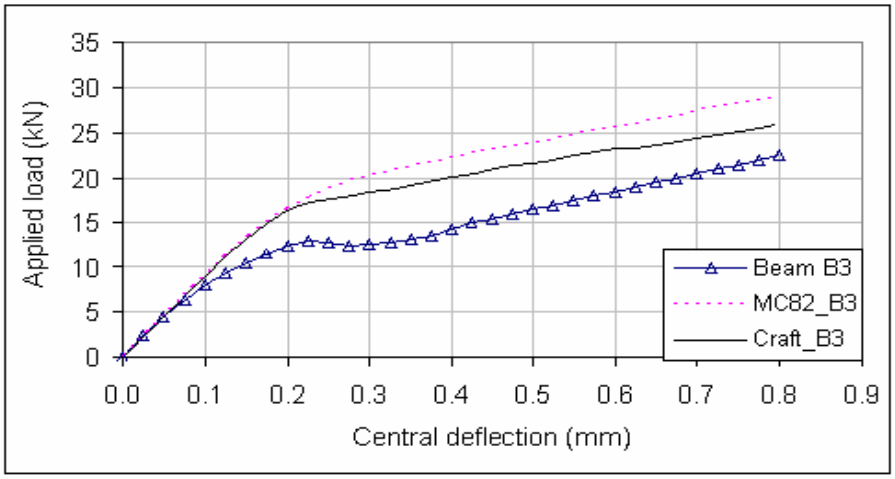

Figure 5.22(c) Load-deflection curve of the beam B3

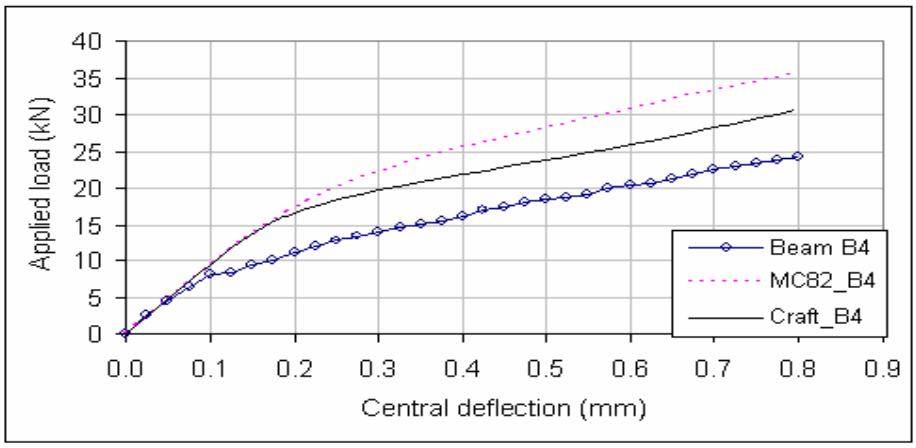

Figure 5.22(d) Load-deflection curve of the beam B4

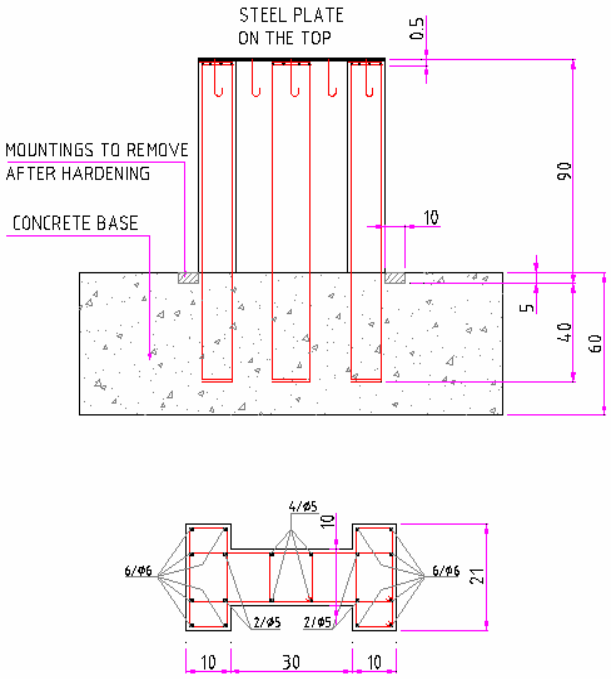

Figure 5.23 Pier geometry and steel arrangement (Geometry dimensions are in cm)

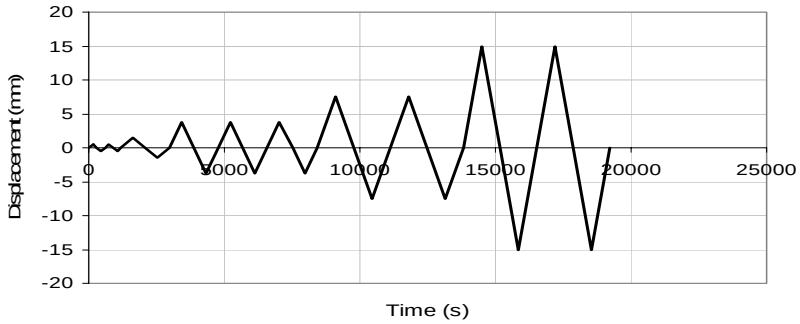

Figure 5.24 Cyclic displacement used in experiment (Pinto 1996)

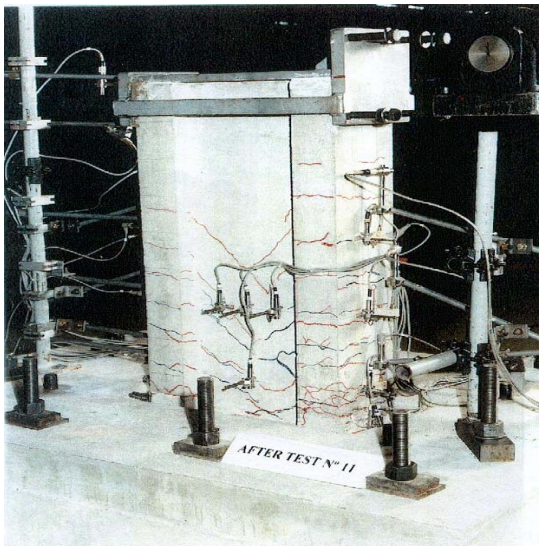

Figure 5.25 Experiment arrangement and the crack pattern

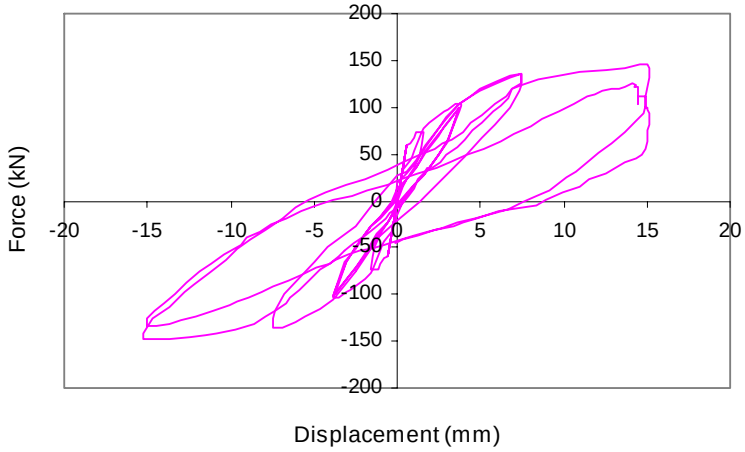

Figure 5.26 Experimental hysteresis behaviour (Pinto 1996)

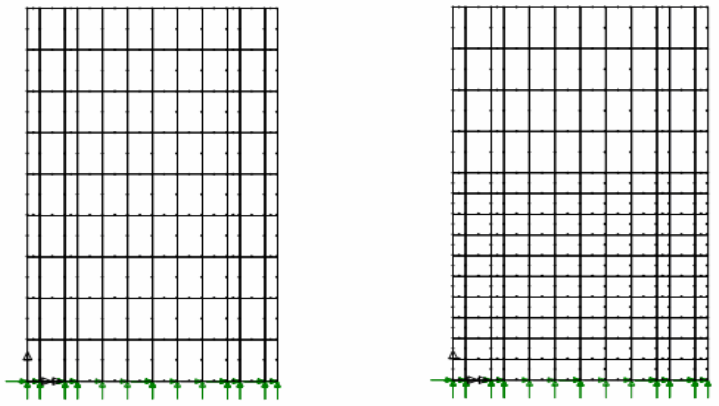

Figure 5.27 Finite element mesh. MESH I (left) and MESH II (right)

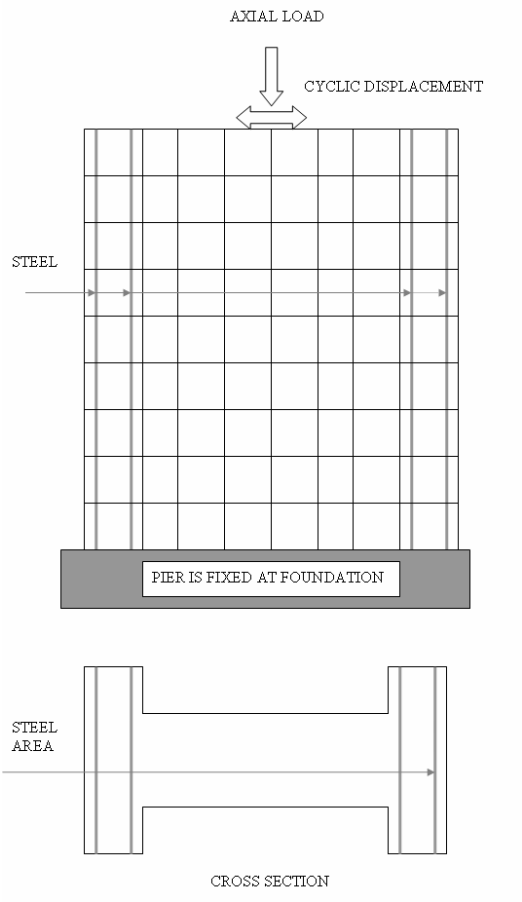

Figure 5.27(b) Finite element modeling for the RC bridge pier. MESH I

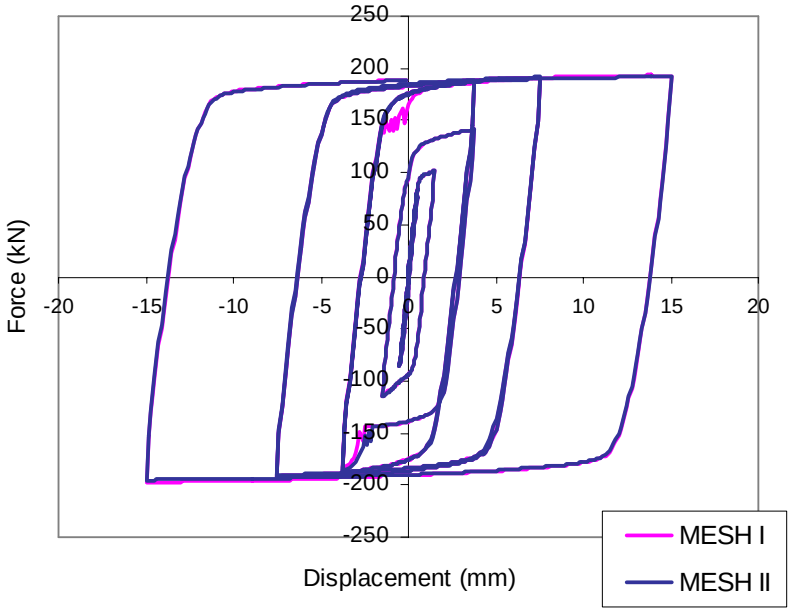

Figure 5.28 Mesh dependency test for cyclic loading, MC82 model (MESH I and MESH II)

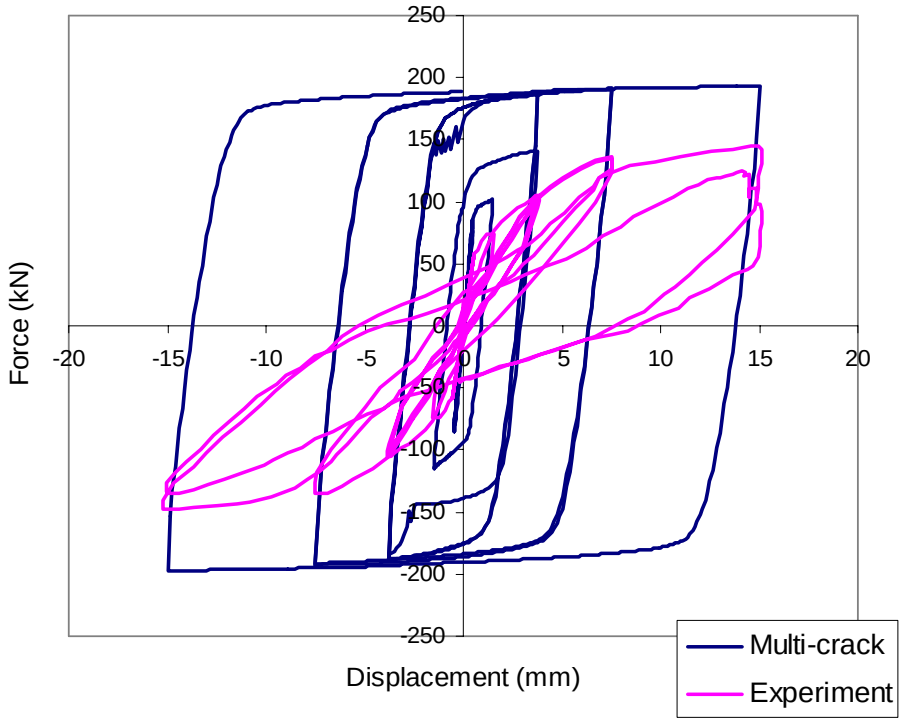

Figure 5.29 Finite element result for cyclic loading, Multi-crack model

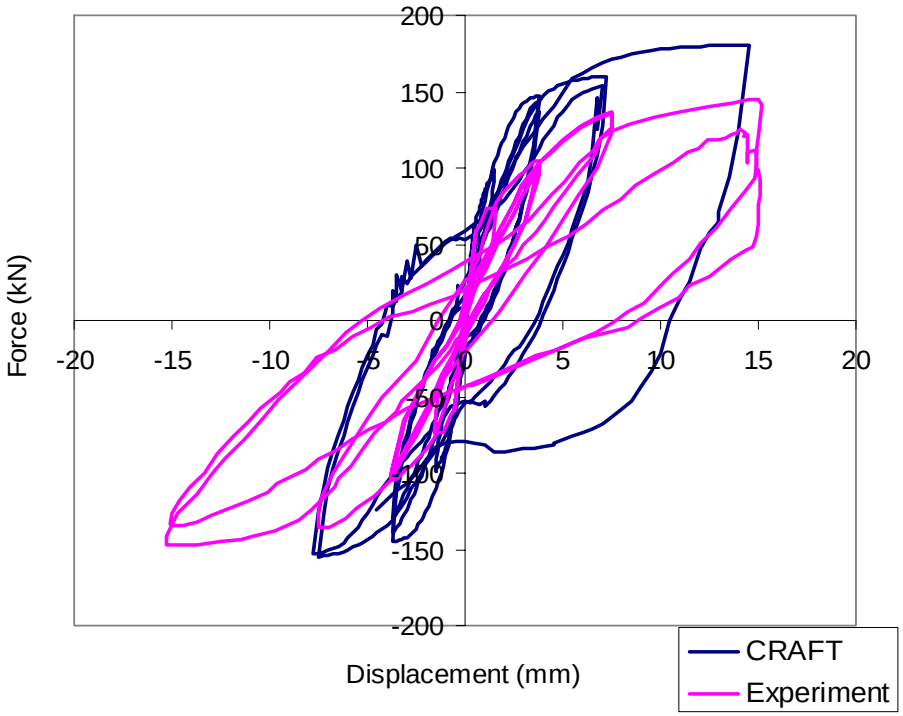

Figure 5.30 Finite element result for cyclic loading, Craft model

CHAPTER 6

ANALYTICAL SOLUTION FOR NON-LINEAR FLEXURAL CONCRETE BEAMS

6.1. INTRODUCTION

It has been well known the finite element approach often suffers from numerical instability, i.e. non-convergent problems, and sensitivity to mesh size (Nayak and Zienkiewicz 1972, Prevost and Hoeg 1975, Criesfield 1982, Zienkiewicz and Taylor 1991) during numerical analysis of progressive deformation of many brittle materials such as concrete exhibiting strain-softening after reaching a peak strength value. In fact, the deformation tends to localise along a crack band whose width is sensitive to the size of selected mesh of finite elements. In an attempt to avoid such mesh-dependency problems, the approach of fracture energy dissipation during crack propagation has been commonly used (Hillerborg *et al.* 1976). In order to validate the FE results of the smeared crack models and to gain further understandings about the localised problem that may cause convergence difficulties and mesh-dependency to FE static non-linear analysis, any analytical solution is always welcome if they are available and comparable to the FE approach used. In the analytical approach, the research tool of fracture mechanics for concrete has been widely developed in the last three decades as it has become clear that the traditionally applied calculation tools (elasticity theory and plasticity theory), are not always applicable of describing certain aspects in concrete. However, there has been not much research about the implementation of strain-softening behaviour and fracture mechanics into an analytical solution in order to establish the flexural behaviour in concrete beams. These reasons are the primary motivations for the development of an analytical solution in this research.

In this chapter, a brief review on analytical models for concrete beams is given first. Then, a new analytical solution for flexural behaviour including moment-curvature and load-displacement curves of cracked concrete beams is presented. This analytical solution is effectively based on the Bernoulli beam bending theory and a constitutive softening stress-strain relationship for concrete

that is consistent with the smeared cracking approach widely used in FEM. The numerically obtained moment-curvature and load-displacement curves are verified through comparison with FE and experimental results for various cases under monotonic loading. In addition, an analytical model published in literature (Ulfkjaer *et al.* 1995) is also employed for the validation. After all, based on the framework for concrete beams, the model is also extended to include reinforced concrete (RC) beams and the results are compared with those from experiments (Bresler and Scoderlis 1963, Carpinteri 1989).

6.2 ANALYTICAL METHOD FOR CRACKED CONCRETE BEAMS - A BRIEF REVIEW

The ideas of using the fracture mechanics approach for concrete first appeared in early 1950's (Bresler and Wollack 1952, Neville 1959). This approach was then comprehensively investigated by Kaplan (1961) to measure properties of linear elastic fracture mechanics (LEFM) model through experiments of notched concrete beam subjected to three- and four-point bending tests. Since this pioneering work, the applicability of LEFM was discussed and continually investigated by many researchers (Blakey and Beresford 1962, Glucklich 1962, Irwin 1962, Bazant and Cedolin 1979, Carpinteri 1989) and is still popular. Today it is widely realised that LEFM is only applicable to large-mass structures with large-scale cracks such as dams (Bazant and Oh 1983, Planas and Elices 1991, Martha *et al.* 1990) and it fails to explain the behaviour of medium and small structures. This is why non-linear fracture mechanics has been developed for description of fracture in normal concrete structures. It has been well established that many brittle materials such as concrete display a phenomenon called strain-softening behaviour (Hillerborg *et al.* 1976, Petersson 1981, Bazant and Oh 1983). Basically, this means that in a uniaxial tensile test for concrete, there is usually a linear stress-strain relationship following Hook's law until the maximum tensile stress is reached. Further applied tensile load causes further strain beyond this point and results in stress reduction which is the strain-softening characteristics of the concrete. This softening behaviour is physically caused by the coalescence of density micro-cracks within a localised softening zone. Outside this localised zone, the rest of the material unloads elastically.

Based on this fracture mechanical point of view, there are originally two main models proposed to describe the strain-softening behaviour of concrete such as
(1) the fictitious crack model (or cohesive crack model) proposed by Hillerborg *et al.* (1976) and
(2) the crack band model by Bazant and Oh (1983).

(1) The fictitious crack model was proposed by Hillerborg *et al.* (1976) and then developed by Planas and Elices (1991) which describes the strain-softening behaviour by using the adoption of a stress (σ)-critical crack opening displacement (δ_{cr}) relationship. In this model, the softening curve has two essential characteristics, the tensile strength (f_t) and the fracture energy (G_f), which are identified, respectively, with the transferred stress at zero opening and with the work supply required to force completely apart the two faces of a unit surface area of crack. Another characteristic property of the softening curve is the critical crack opening (δ_{cr}) for which the stress transferred becomes zero. The model has been widely applied by many researchers to model the fracture of un-reinforced concrete structures and showed good agreements with experimental observations. But this model is most suitable for localised fracture in concrete structures only (Bazant and Oh 1983, Bazant 1986). This is due to the fact that the model is characterised by the softening behaviour based on the adoption of a stress-critical crack opening which is most suitable for a single crack, not many cracks distributed in a crack band. Nonetheless, from the finite element method point of view, this model is only compatible with the discrete method of modelling cracks since the relationship is between normal stress and displacement not between normal strain and stress, as required by the smeared crack approach.

(2) Inspired by Hillerborg's fictitious crack model, Bazant and Oh (1983) developed a crack band model for smeared cracking applications. In this model, they suggested that cracks occurred in a band or zone rather than a line and that over that softening zone the fracture strain may be defined as representative of the openings of the individual micro-cracks $(\sum \delta_{cr})$ within an effective softening zone width (w_c). In the spirit of this approach, an effective stress-strain constitutive relationship can be adopted. The crack band model has the advantage that it can deal with both "localised" and "distributed" cracking, and it is no doubt for this reason that it has been

applied in general FE programs (Bazant 1986). As the FE smeared crack model is also used in the thesis, this crack band model is chosen to describe the strain-softening behaviour for the analytical solution in the present chapter.

So far, there has been limited number of analyses using analytical models which are based on non-linear elastic fracture mechanics, to describe fracture and flexural behaviour in concrete structures. In 1989, Chuang and Mai proposed a model based on the crack band model to establish a correlation between the tensile and bending properties of a composite beam containing a localised strain-softening zone. However, this model predicts no size effect, which is one of the most important consequences of fracture mechanics (Bazant 1984, 1992), and there was lack of experimental work to substantiate the theoretical analysis. The idea of modelling the bending failure of concrete beams that contains an elastic layer around the midsection of the beam and this layer is proportional to the beam depth was introduced in an analytical model by Ulfkjaer *et al.* (1995). Therefore, the model proved that the brittle behaviour of a structure is dependent on the size of the structure. This model, however, is based on the fictitious crack model that is most suitable for situations of localised fracture in concrete structures and not for situations of distributed fracture in RC structures as the crack band model does. Also, this model used a linear stress-strain relationship in the post-peak region. To overcome these shortcomings, Iyengar and Raviraj (2001) has generalised Ulfkjaer *et al.*'s (1995) model to a material exhibiting a power law (with an exponent n) for the post-peak stress-strain relation. However, the close-form solutions proposed by Ulfkjaer *et al.*'s (1995) and used later by Iyengar and Raviraj (2001) are complicated and difficult to apply for practical applications in terms of load-deflection curves. Furthermore, these models did not examine the material behaviour (e.g. stress and strain distribution or curvatures) in the elastic layer apart from the midsection of the beam.

Therefore, in this chapter, an analytical solution for evaluating moment-curvature and load-displacement curves of concrete beams is proposed. The analytical model is based effectively on the smeared crack approach (Bazant and Oh 1983) and the Bernoulli beam bending theory to model the beam behaviour in both linear and non-linear regimes. The model also employs the

assumption from Ulfkjaer *et al.*'s (1995) model that the crack band width is proportional to the depth of the beam in order to account for the size effect.

However, unlike Ulfkjaer *et al.*'s (1995) model and the previous ones which proposed close-form solutions for the structural behaviour, the Author's analytical solution uses the numerical approach to determine moment-curvature and load-displacement curves of concrete beams. This is intended to be used for simply developing a general framework for evaluating flexural behaviour of both concrete beams and reinforced concrete beams. In addition, by expressing the relation of the strains, curvatures between the linear elastic and softening zones, the model has capability of capturing stress and strain distributions on cross-sections inside the softening zone. Being based on the smeared crack approach, the model is very consistent with the FE solution using a smeared crack approach in this thesis and therefore they are compared with the analysis of various cases of concrete and RC beam under monotonic loading.

6.3 ANALYTICAL SOLUTION FOR CONCRETE BEAMS

6.3.1 Basic assumptions

1. The compressive behaviour in concrete is assumed to be linear elastic with identical elastic modulus as in tension. This assumption is justifiable in view of the fact that the compressive strength for many strain-softening solids is at least an order of magnitude higher than the corresponding tensile strength (Gopalarathnam and Shah 1985, Shah and Sankar 1987). Thus, the compression zone of bending beam is most likely in the elastic regime when fracture in the tensile zone intervened.

2. Transverse normal stresses are negligible (plane stress)

3. The tensile behaviour is assumed to follow a strain-softening rule in stress-strain relationship which is normally obtained from the uniaxial experiment as shown in Figure 6.1. When the tensile strain $\varepsilon_t \leq \varepsilon_{tp}$, where ε_{tp} is the strain at which the maximum tensile strength is reached,

the material is assumed linear elastic. After the maximum tensile strength is reached, the material is assumed to exhibit softening stress-strain behaviour within a crack band width w_c in the mid-span of beam. Outside this crack band width, the rest of material unloads elastically. Therefore, the post-peak behaviour of beam includes two constituents: (1) strain-softening behaviour within the zone width w_c, and (2) linear elastic unloading behaviour in the rest of beam.

4. For simplicity, linear and bilinear strain-softening rules are used in this thesis (Figure 6.1). The aim of the model is to demonstrate that even with these simple softening rules, many of the characteristic features associated with cracking of a concrete beam can be well captured.

5. It is assumed that the continuity conditions (e.g. displacements, rotations, and curvatures) at the interface between the strain-softening and linear elastic unloading zones (Bazant and Zubelewics 1988) are preserved; and that curvatures and moments at any cross-section inside the softening zone width are linearly interpolated from those at the interface and mid-span cross-sections. This assumption helps to formulate the load-deflection into a general expression.

6. For a given material, beam geometry and loading configuration, the crack band width w_c is assumed to remain fixed during the crack propagation as observed by Bazant and Zubelewics (1988).

7. It is assumed that the deflection of beams is very small, therefore small deformation theory is applied.

8. The Bernoulli-Navier hypothesis is adopted that assumed planar cross-sections remain plane and normal to the deflection line under bending in both linear elastic zone and softening zone.

6.3.2 The analytical model

All the above assumptions are used to formulate the analytical model. In general, the present model uses three main features: (1) bending equilibrium, (2) piecewise linear or bilinear strain-softening curves for tensile stress-strain relation, and (3) the continuity of curvature between strain-softening and linear elastic zones to obtain moment-curvature and load-displacement curves. Computation of moment-curvature and load-deflection relations is performed incrementally in accordance with incremental strains starting from the extreme surface fibres, and uses the previously computed portions of moment-curvature and load-deflection curves at each strain increment to compute the current increments of the moment-curvature and load-deflection relations. As the tensile strain ε_{ti} of the extreme surface fibre at any stage *i* of loading is incrementally increased, the corresponding moment-curvature and load-deflection characteristics can be numerically computed from equilibrium equations.

Because of the complexity of the constitutive laws (see Figure 6.1), the bending behaviour of the beam can be divided into three distinct phases, each of which is analysed separately depending on the value of the stresses and strains in the tensile side of the beam:

Phase I - Elastic regime: before the tensile strength is reached in the tensile side of the beam, for $0 \le \varepsilon_{ti} \le \varepsilon_{tp}$, $\sigma_t = \varepsilon_t E_c$. So long as strains at the extreme fibre in the mid-section area of the beam are less than ε_{tp}, the beam is fully elastic and the associated deformation is completely reversible.

Phase II - Strain-softening zone growth regime: before the tensile strength is reached in the tensile side of the beam, for $\varepsilon_{tp} \le \varepsilon_{ti} \le \varepsilon_0$, $\sigma_t = f(\varepsilon_t)$. The beam undergoes a transition from the elastic regime to the peak load behaviour and to the first regime of the post-peak behaviour in moment-curvature and load-deflection curves.

Phase III - Crack growth regime: when the tensile strength of the softened portion of extreme tensile fibres of the beam reaches a value of zero, the real crack starts to growth and the crack growth regime ensures, for $\varepsilon_0 \le \varepsilon_{ti}$, $\sigma_{ti} = 0$. The beam continues undergoing the softening behaviour in moment-curvature and load-deflection curves.

in which

ε_{ci} = compressive strain at the extreme surface fibre at stage *i*

ε_{ti} = tensile strain at the extreme surface fibre at stage *i*

ε_t = tensile strain at an internal fibre, $0 \le \varepsilon_t \le \varepsilon_{ti}$

σ_t = tensile stress at an internal fibre

σ_{ti} = tensile stress at the extreme surface fibre at stage *i*

ε_{tp} = tensile strain at the maximum tensile strength

6.3.2.1 Summary of the procedure of the analytical solution

1. Calculate the compressive strain ε_{ci} of the extreme surface fibre using the condition that the resultant force acting on the cross-section is zero as it is assumed that an incremental value of the tensile strain at the extreme fibre of the beam is known and there is no external axial force acting on the cross-section. Detailed calculation is shown in Section 6A.1 (Appendix 6A).

2. The curvature κ_i of the beam at this vertical section for the tensile strain ε_{ti} is calculated using $\kappa_i = \dfrac{\varepsilon_{ti} + \varepsilon_{ci}}{h}$ where *h* is the beam depth.

3. Calculate the total moment in a section M_i for the tensile strain ε_{ti} by taking moment. Detailed calculation is given in Section 6A.2 (Appendix 6A).

4. The deflections y_{2i} at the mid-span cross-section is determined using the following procedures:

4.1. For the linear elastic regime (Phase I), the deflections are determined by using one of well-known methods from beam bending theory, i.e. integration or moment-area or strain energy methods.

4.2. For the non-linear regime (Phase II and III), the deflections are determined by using the fifth assumption and the moment-area method as shown in the following steps:

i. Assign a segment of width w_c of the softening material in the mid-span of beam after the strain of outer fibre in tension side reaches ε_{tp}.

ii. Calculate the curvatures and moments at edge cross-section, Section 1, ($\kappa_{1,i}$, $M_{1,i}$) between the cracked and linear elastic unloading zones and at the mid-span cross-section, Section 2, ($\kappa_{2,i}$, $M_{2,i}$). It is assumed that the material inside the width w_c is strain-softening and the material of the rest of the beam (including the material at two edge cross-sections) is linear elastically unloading. Curvatures and moments at any cross-section in the softening width w_c is assumed to be linearly interpolated from those at the edge cross-section and at mid-span cross-section.

iii. Calculate the deflections of beam (e.g. deflections at the mid-span cross-section y_{2i}) from the diagrams of curvature using moment-area method. Details of this step are given in Section 6A.3 (Appendix 6A).

5. Determine the load at mid-span cross-section using the equation $P_i = \frac{4M_{2i}}{L}$, in which M_{2i} is the bending moment at the mid-span cross-section, and L is the span-length of the beam.

6. The moment-curvature and load-displacement curves can then be plotted.

The main calculation steps of the above procedure for a linear softening rule (Figure 6.1(a)) can be found in Appendix 6A. The analytical model is then extended further to employ this bilinear softening curve, and the process of calculating moment, curvature, load and deflections at the beam section are carried out in a similar manner to that of the linear softening curve. Therefore, the detailed calculations are not presented here and only the analytical results are given.

6.3.2.2 Determination of the crack band width (w_c)

The crack band width or the softening zone width w_c is one of the most important parameters that affect the flexural behaviour of cracked concrete beams. In practice, identification of this parameter is not a straightforward process, especially for localised problems in concrete structures. In FE smeared cracking terminology, this softening zone width is described through an internal length called the characteristic length l_c which is related to the finite element size. By this way, various problems of mesh dependency, strain-softening and determination of the softening zone width w_c can be solved. However, so far there has been very little research in analytical approach to determine w_c for concrete beams. Bazant and Zubelewicz (1988) were the first to propose an analytical solution, which is based on the principle of virtual work, to find the segment w_c using an analysis of strain-localisation instability. Their results showed that w_c is approximately constant during the crack propagation and equal to 0.8 times the beam height. Chuang and Mai in their paper (1989) suggested that the width w_c can be solved from the load-point deflection curve obtained in a bending experiment. However, this experimental information is not always available on load-deflection curve so that this complicated method can be applied. An alternative method to obtain w_c in good agreement with finite element analysis was proposed by Ulfkjaer *et al.* (1995) in their analytical model for fictitious crack model (FCM) in beams. The main idea in their model is that the fictitious crack at the middle of the beam is spread out over an elastic layer of thickness t which is proportional to the depth of the beam $t = kh$, in which k is a constant and h is the beam height. They showed that the best agreement with the results from a finite element analysis (Krenk *et al.* 1994) was obtained for a value of $k = 0.5$; hence, they have assumed k equal to 0.5 for their study using the FCM with a linear softening curve. Iyengar *et al.* (2002) and Iyengar and Raviraj (2001) have extended the analysis for bilinear and exponential softening curves using both crack band model (CBM) and FCM, have shown that the result using $k = 0.5$ agreed very well with those by numerical analysis (Brincker and Dahl 1989). They have also proposed a method to determine k from an experiment and suggested that $k = 0.1$ to 1.0 can be considered. However, there has not been much numerical and experimental work used to substantiate the value of k. Thus, the above suggestions for determining the softening zone width

w_c have not been widely accepted in practical applications. The reason for it is because the softening zone width w_c is not only a size-dependent parameter as mentioned above but also relates to the tensile strength, strain at end of softening curve, fracture energy dissipated and type of softening behaviour. In fact, experimental evidence shows that unique post-peak stress-strain behaviour for concrete in tension is not observed (Ansari 1987, Gopalaratnam and Shah 1985). Such difficulties in experimental tests to measure the material properties, especially the softening zone width and shape of softening curve make the identification extremely difficult, even in some cases, impossible.

Theoretically, if w_c is assumed to be known, then the strain at end of softening behaviour ε_0 can be obtained from the explicit expressions between w_c and ε_0, which are derived from the fracture energy dissipation, i.e. the fracture energy per unit area G_f ($G_f = \int_0^{\delta_0} \sigma d\delta_{cr}$, in which δ_{cr} is the crack opening $\delta_{cr} = \varepsilon w_c$ and δ_0 is the crack opening at end of softening curve) and the strain-softening curve.

For a linear strain-softening curve in stress-strain relation (Figure 6.1(a)):

$$\varepsilon_0 = \frac{2G_f}{w_c f_t} \tag{6.1}$$

For a bilinear strain-softening curve for the stress-strain relation as shown in Figure 6.1(b)

$$\varepsilon_0 = \frac{18G_f}{5w_c f_t} \tag{6.2}$$

However, as there no unique post-peak stress-strain softening behaviour (Petersson 1981, Ansari 1987, Iyengar *et al.* 1996), the above explicit expressions for the relationship between w_c and ε_0 are still not applicable in many cases (see also Section 6.3.3.2). Therefore, in this study, along with using these above expressions, an appropriate set of w_c and ε_0 will be found by trial-and-error fitting of some reliable results (e.g. experimental results or selected numerical results). All these will be presented in the following sections.

6.3.3 Analytical example and parametric study

6.3.3.1 Analytical example

A simple analytical example is proposed in this section to demonstrate the capability of the proposed model (Equations 6A-25, 6A-27, 6A-62, 6A-63, and 6A-64 in Appendix 6A) in capturing the beam behaviour in terms of moment-curvature and load-deflection curves. In particularly, the example of a simply supported beam with a central load used in Ulfkjaer *et al.* (1995) is studied. The beam geometry and material properties are shown in Table 6.1. Results from the analytical model are first compared with results from the Ulfkjaer *et al.*'s (1995) model. This study aims to verify important features of the analytical models in capturing non-linear flexural behaviour of the beam. Furthermore, the validation of the analytical model against experimental data of several concrete beams is furnished in Section 6.4.

Figure 6.2 shows the comparison between the analytical and results obtained using Ulfkjaer *et al.*'s (1995) model in terms of moment-curvature curves. It is clear that the two results are almost identical.

As there is no results of load-deflection curve obtained by Ulfkjaer *et al.* (1995), only the results of the analytical model is presented here. It is assumed that the softening zone width is given a value of a half of the beam depth ($w_c = 0.5h$). The deflection is calculated for 3 different cases:

(1) Case I: The deflection is obtained from Equation (6A-62)
(2) Case II: The deflection is calculated from Equation (6A-63)
(3) Case III: Assuming the beam behaviour is fully linear elastic, the deflection is calculated using the traditional beam theory

The comparison for the results is shown in Figure 6.3. It can be seen that the results are similar when the beam is fully linear elastic (e.g. the tensile stress at the extreme fibres of the beam does not exceed the tensile strength). This confirms the accuracy of the computed load-deflection curves in linear elastic regime. When the tensile strength is reached, the deflection-curves are different for Cases I and II though the peak loads are the same. In fact, the load-deflection curve

for Case II shows that the beam is stiffer than that of Case I. And this is in good agreement with the assumptions made for each method of calculating the deflection. It was assumed for Case II that the strain-softening material is assumed to be "spread out" for the whole beam and the secant rigidity $(EI)_i$, which is calculated from Equation (6A-29), can be applied for the whole beam. Therefore the deflection of the beam can be calculated in the same manner as for a traditional beam theory. In the contrary, Case I assumes that after reaching the maximum tensile stress, only material in a small zone at mid-span continues into strain-softening behaviour while the rest of beam unloads linear elastically. As the result, the analytical load-deflection curve demonstrates such behaviour, especially some snap-back is evident. These qualitative observations are similar to those made by Crisfield (1986) and Zienkiewicz and Taylor (1991) for localisation problems in concrete beams, of which Case II is similar to all elements of the beam being softened while Case I is similar to only one element around the midsection of the beam being softened. Moreover, when w_c = 0, the load-deflection curve of Case I will converge to that of Case III, fully linear elastic beam; and when $w_c = L$, the load-deflection curve of Case I will converge to that of Case II, fully softening beam. Through this study, it is encouraging that the deflection of the beam can be theoretically predicted to reflect the non-linear flexural behaviour of concrete beams very well. Therefore, the governing Equation (6A-62) will be used to calculate the deflection of concrete beam in this chapter.

6.3.3.2 Parametric study

In order to understand the influence of various parameters of strain-softening on the flexural behaviour, the beam mentioned above (see Table 6.1 for the beam geometry and material properties) is considered for this study. The parameters selected for this parametric study include: softening zone width w_c, tensile strength f_t, fracture energy per unit area G_f, and various forms of strain-softening curves.

6.3.3.2.1 Softening zone width

In this research, the values of the softening zone width (w_c) proposed by Bazant and Zubelewicz (1988), Ulfkjaer *et al.* (1995), Iyengar *et al.* (2002) and Iyengar and Raviraj (2001) are used in the proposed analytical solution for concrete beams. In addition, values for w_c that are determined from an empirical formulae based on an uniaxial tensile test for concrete (Wittman 2002, see also Table 6.2) is also employed. Different values of w_c are shown in Table 6.2. The corresponding strains at the end of softening curve ε_0 are calculated from Equations (6.1) and (6.2).

Figure 6.4 shows the load-deflection curves for the beam for different values of softening zone width w_c. As the values of w_c increases, it leads to the reduction of the value of maximum load and the position of the maximum deflection is shifted towards left. Also the slope of the descending branch becomes steeper as w_c decreases from 100 mm to 50 mm. As w_c is assumed to be proportional to the beam depth (Ulfkjaer *et al.* 1995), the flexural behaviour of the beam when increasing the beam depth is the same as increasing the softening zone width w_c as shown in Figure 6.4. This, in turn, means that the analytical model can predict the structural size effect, explaining why large beams are cracking and failure earlier than small beams.

6.3.3.2.2 Tensile strength

The load-deflection curves for the beam for different values of tensile strength (f_t) of concrete are shown in Figure 6.5. It can be seen that when the tensile strength increases, the maximum load also increases and the position of maximum deflection is shifted to the right. This is because when a higher value of tensile strength is used, the structure can resist a higher force and moment (see Equations 6A-11 and 6A-20 in Appendix 6A) and, therefore, leads to a higher maximum reaction force.

6.3.3.2.3 Fracture energy

Figure 6.6 illustrates the load-deflection curves for the beam for different values of fracture energy per unit area G_f. As the value of G_f increases, the value of maximum load increases, and the position of maximum deflection is shifted towards right. The reason for this is that a higher value of G_f leads to a larger area under the stress-strain softening curve (Figure 6.1) and therefore makes the structure have higher capacity under load, i.e. higher area under the load-deflection curve.

6.3.3.2.4 Type of strain-softening curve

In this section, the sensitivity of the analytical model with respect to various forms of strain softening in the stress-strain relationship is studied. For that reason, a bilinear softening in the stress-strain relationship as shown in Figure 6.1(b) is also adopted. As mentioned above, the detailed calculations are similar to that of linear softening case, and therefore only the results are given.

Figure 6.7 shows the linear and bilinear stress-strain softening curves of which the model can predict the same load-deflection behaviour until the peak load as illustrated in Figure 6.8. However, the post-peak behaviour is different for each softening curve. In this case, the softening zone width w_c remains the same but the fracture energy G_f and the strain at end of softening curve ε_0 are not the same because the different shape of stress-strain softening curves.

In Figure 6.9, the linear and bilinear stress-strain softening curves are chosen in the way that the areas under the two curves remain the same. In this case, the load-deflection curves for the two softening curves are similar in the pre- and post-peak regions but are slightly different at the peak load as shown in Figure 6.10. This is because after reaching the tensile strength, the slope of the bilinear softening curve is steeper than that of the linear one (Figure 6.9) and this reduces the magnitude of the peak load in the load-deflection behaviour. Though the value of G_f is the same for the two cases, the values of w_c and ε_0 are not the same.

These above results help to confirm that the predicted results are very sensitive to the shape of the stress-strain softening curve and never be the same, i.e. in terms of the post-peak behaviour or peak load, even the fracture energy is assumed to be constant. This observation agrees well with the ones observed in experiment (Ansari 1987, Gopalaratnam and Shah 1985).

6.4 MODEL VALIDATION FOR CONCRETE BEAMS

In order to check the validity of the analytical model, the results from two analytical and FE analyses are presented. The first is of a plain concrete beam tested by Carpinteri (1989) and the second is also a plain concrete beam but conducted by Ozbolt and Bazant (1991). The details of experimental testing arrangements, experimental and FE analyses for the two beams can be found in Chapter 4. Herein only the experimental and FE results are given to validate the analytical model. In particular, the FE results for MESH 56 of Carpinteri's beam and MESH 45 of Ozbolt and Bazant's beam are presented (see Chapter 4). Both linear and bilinear softening in stress-strain relationships are used in the analytical solution.

6.4.1 Carpinteri's (1989) concrete beam

6.4.1.1 Load-deflection curves

As mentioned above, if w_c is assumed to be known, then the strain at end of softening behaviour ε_0 can be obtained from the explicit expressions for linear and bilinear strain-softening curve in stress-strain relation as shown in Equations (6.1) and (6.2). In this way, the strain at end of softening curve (ε_0) and the softening zone width (w_c) are always dependent on each other and so the fracture energy G_f can always be fixed.

The load-deflection curves obtained by the analytical solution are shown in Figure 6.11, which also shows the experimental and numerical results for comparison. It can be seen that the load-deflection curves obtained by the analytical solution are in good agreement with those of FE

analysis and experimental data for pre-peak behaviour but not so in the post-peak region. In this figure, the analytical results obtained with a softening zone width $w_c = 0.5h$. Many other values of w_c (e.g. from $0.1h$ to $1.5h$) were tried but, unfortunately, a best fit to numerical and experimental results in post-peak behaviour were not able to be found. As mentioned in Section 6.3.3.2, the reason may be because the explicit expressions for the relationship between w_c and ε_0 are not applicable in this case.

Therefore, the process of trial-and-error fitting of the analytical results to numerical and experimental results was carried out in order to find a suitable set of w_c and ε_0. These values should match the analytical results for linear and bilinear softening curves to the numerical results in terms of peak loads and the dissipated fracture energy. Figure 6.12 shows the analytical results for linear and bilinear softening curves, in which $w_c = 1.5h$ and $\varepsilon_0 = 6\varepsilon_{tp}$ for linear softening curve, and $\varepsilon_0 = 11\varepsilon_{tp}$ for bilinear softening curve. It can be seen that the analytical results of both linear and bilinear softening curves are in good agreement with the numerical and experimental results.

6.4.1.2 Stress and strain distributions

In this section, the analytical results which was obtained by an appropriate set of w_c and ε_0 as shown in Figure 6.12 are used. The aim of this comparison is to verify the analytical results against the numerical ones in terms of the softening zone width w_c and stress and strain distributions, and to check the fifth assumption made in Section 6.3.1.

In the FE analysis, the crack pattern at end of loading shows that the band that contains cracks is approximately of 150 mm width (=$1.5h$) as shown in Figure 4.8(d) (see Chapter 4). This firstly confirms that the chosen value of softening zone width ($w_c = 1.5h$) in the analytical solution is well matched with the numerical result. Therefore, the values of stress and strain distributions of FE analysis are calculated at cross-sections inside and at the edge of the softening zone width at the Gauss integration points. Figure 6.13 illustrates all the cross-sections at Gauss integration points within the softening zone width for the finite element mesh, in which cross-section (a) is

closest to the midsection (Section 2 in the analytical solution) and cross-section (k) is closest to the edge cross-section (Section 1 in the analytical solution). In the analytical solution, the values of stress and strain distributions are calculated at cross-sections that are in similar positions of those taken in the FE analysis. The results of all the cross-sections are obtained, but only the values at the mid-span cross-section (Section 2) and the section at the edge of assumed softening zone (Section 1) are presented. It should be noted again that cross-section 1 is the interface between the strain-softening and linear elastic zones. Also, it was assumed that the material in this cross-section is unloading linear elasticity. The analytical results are obtained from two different forms of softening: linear and bilinear strain-softening in the stress-strain relation. The results of the stress and strain distributions on the cross-sections 2 and 1 at some positions of the central deflection in post-peak behaviour are compared in Figures 6.14, and 6.15, respectively.

It can be seen from Figure 6.14 the stress distributions of both cases, linear and bilinear softening curves, are in good agreement with each other and are close to numerical ones. The stress distribution in the case of bilinear strain-softening is better match to the one of numerical analysis. It is because the bilinear strain-softening curve is closer to the exponential strain-softening used in numerical analysis (Figure 2.22). The slight difference in the positions of the tensile strength along the beam depth is due to the different shape of the strain-softening curves. In spite of this, it is clear that the areas under the different stress-strain diagrams are almost the same during loading progress. At the deflection of 0.22 mm, the analytical model using linear softening curve shows that the beam is undergoing Phase III with a crack length of 16 mm while it is still in Phase II for the model with bilinear softening and numerical ones. After the deflection of 0.26 mm, real cracks (or cracks with zero stresses) start developing in the bilinear softening and numerical models. However, the strain distributions are much more different between the analytical and numerical results in the tensile side. The difference increases when more loading is applied (e.g. increasing deflection in the beam). This is not out of our expectation, because in the analytical model, it is assumed that the planar cross-section remain plane and normal to the deflection line under loading (the eighth assumption in Section 6.3.1), therefore the strain distribution is linear. In the contrary, the numerical model includes the effect of shearing force on

the planar cross-section through the width of crack opening (see Chapter 2, Section 2.2). As a result, the strain distribution is not linear but curved as seen in Figure 6.14.

Figure 6.15 illustrates the stress and strain distributions at cross-section 1. The analytical results for both linear and softening curves are similar and close to the numerical ones. The analytical stress and strain distributions are always linear elastic at this cross-section during loading. Under increasing applied load (e.g. deflection of the beam), the magnitude of stresses and strains are decreased, confirming that both compressive and tensile concretes unloads linear elastically. These observations demonstrate that the chosen softening zone width ($w_c = 1.5h$) is acceptable in the manner of the assumption about the continuity conditions for the softening zone.

6.4.2 Ozbolt and Bazant's (1991) concrete beam

Figure 6.16 shows the load-deflection curves obtained by the analytical solution with a softening zone width $w_c = 0.3h$ (chosen amongst other values from $0.1h$ to $1.5h$), and ε_0 is obtained from the explicit expressions for linear and softening curves (Equations 6.1 and 6.2). The experimental and numerical results are also provided in the same figure for comparison. As there is no experimental data for post-peak region, only the experimental pre-peak behaviour is plotted. It can be seen that good agreement between the analytical and numerical and experimental results can be found in the pre-peak behaviour. In the post-peak region, the analytical results are different from those of numerical ones. Again, similar to the previous example, the reason for this may be that the explicit expressions for the relationship between w_c and ε_0 is not well suitable for this case.

Figure 6.17 illustrates the analytical results with $w_c = 1.0h$ and $\varepsilon_0 = 6\varepsilon_{tp}$ for linear softening, and $\varepsilon_0 = 11\varepsilon_{tp}$ for bilinear softening, which also shows the numerical and experimental results. These values of w_c and ε_0 are chosen after the process of trial-and-error fitting of the analytical results to numerical results. It can be seen from the figure that the analytical results of both linear and bilinear softening curves are in good agreement with the numerical results in terms of peak loads and post-peak behaviour. In particular, the result for bilinear softening curve is relatively closer

to the numerical one in post-peak regime. It is because of the bilinear strain-softening curve which is closer to the exponential strain-softening used in numerical model (Figure 2.22).

6.5 ANALYTICAL SOLUTION FOR RC BEAMS

The proposed model for plain concrete beams is extended to RC beams in which the linear softening in stress-strain relationship is used in tensile concrete. Detailed determinations of stresses and strains (Figure 6A.6 in Appendix 6A) and calculations of moments, curvatures, loads and deflections are based on the same procedures as for concrete beams. Therefore, they are not mentioned again. Herein presents the summary of the analytical solution for RC beams: Total compressive force (F_{ci}) and total tensile force (F_{ti}) of the concrete are obtained from as previously explained. The additional tensile force (F_{si}) attributable to tension steel reinforcement is calculated on the stress-strain relationship for tension steel reinforcement and on the basis of the strain in the concrete at the tension steel level. The tensile and compressive stress-strain relationships for steel reinforcement are assumed to be linear elastic-perfectly plastic and identical as shown in Figure 6A.7 (Appendix 6A). It is assumed that there is no slip between concrete and steel reinforcement. For each assumed tensile strain (ε_{ti}) at the extreme fibre of concrete in tension, the total compressive force (F_{ci}) in the concrete equals the total tensile force (F_{ti}) in the concrete plus the tensile force in tension steel reinforcement (F_{si}) corresponding to the strain ε_{ti}. The moment and curvature for this equilibrium condition are calculated. Eventually, the load and deflection of the beam can be achieved. It should be noted that if the amount of steel reinforcement is very small, the localised model with a narrow softening zone width w_c is appropriate and the deflection is calculated from Equation (6A-62). Conversely, if the amount of steel reinforcement is large enough, the distributed model with the softening zone width w_c equal the beam length (e.g. the cracks affect the whole beam stiffness) is appropriate, and thus the deflection can be calculated from Equation (6A-63).

In order to validate the analytical model for reinforced concrete structures, analysis of two sets of RC beams are carried out. The first is of a RC beam tested by Bresler and Scoderlis (1963), and the second is of two RC beams conducted by Carpinteri (1989). The details of Bresler and

Scoderlis's beam 0A1 and the two Carpinteri's beams, namely B3 and B4, are shown in Chapter 5. As the chosen beams have a fair amount of steel reinforcement, it is assumed that the softening zone spreads out in a whole beam, and therefore the analytical deflection is calculated using secant rigidity as shown in (6A-63). The analytical results are compared with experimental results and numerical results (of representative Craft model) to show the potential features and weaknesses of the proposed model.

The analytical load-deflection curve for Bresler and Scoderlis's beam is plotted against the experimental and numerical ones as shown in Figure 6. 18. It demonstrates that the analytical result is in very good agreement with both experimental and numerical results. At the late stage of loading, the analytical result is closer to the experiment and a little bit stiffer than that of numerical results. The reason may be due to the numerical model predicts non-linear behaviour and crushing in compressive concrete.

Figures 6.19 and 6.20 shows the load-deflection plot of analytical model for Carpinter's beams B3 and B4, respectively, in which the experimental and numerical results are also plotted for comparison. It can be seen that although there is some difference in the post-yield regime, the analytical results follow well both the experimental and numerical results. In particular, the analytical result is well matched the numerical one up to the yield point. Figures 6.19 and 6.20 show the analytical model is able to capturing the transitional condition between brittle and ductile behaviours in the beam and results in a very good correlation with the experimental one. However, similar to the numerical result, the analytical behaviour is stiffer than the experiment for the post-yield regime. It may be due to the assumption of perfect bond between steel reinforcement and concrete, which is clearly evident in the tests (Carpinteri 1989). In addition, using the assumption of the distributed model of cracking for the whole beam has affected the analytical results and this cause the difference to the experimental and numerical results. Furthermore, the difference between the analytical and numerical results in the post-yield regime could be due to the issues of choosing "localised" or "distributed" criteria in each model and the relative parameters for softening behaviour (see Chapter 5 for more details on numerical analysis).

6.6 SUMMARY AND CONCLUSIONS

This chapter has presented an analytical model for calculations of moment-curvature and load-deflection curves of concrete and reinforced concrete beams in three-point bending tests. Linear and bilinear softening forms in the stress-strain relationship are used in the analytical solution. A parametric study is performed to understand the influence of various fracture parameters used in the model, and helps to identify model parameters which affect the peak load and post-peak behaviour. The results from the analytical model are compared with the results from numerical analysis and experiments in terms of load-deflection curves and stress and strain distributions within the softening zone. The analytical model also implements the values of the softening zone width w_c in a relation of the beam height h (Ulfkjaer *et al.* 1995) in order to consider the structural size effect on the beam behaviour. The concluding remarks from these studies are that:

1. The accuracy of the analytical solution in evaluating moments and curvatures is confirmed by an excellent agreement between its results and those of an analytical model published in literature (Ulfkjaer *et al.* 1995).

2. By assuming that after the maximum tensile strength is reached, the material exhibits the strain-softening behaviour within a crack band width w_c in the mid-span of beam and unloads elastically in the rest, the moment and curvatures at any cross-section can be evaluated. Therefore, the deflection of the beam can be obtained based on the moment-area method. When the size of the softening zone is changed, the deflection is reasonably changed: if the softening zone width is zero, the deflection is similar to the one calculated by the traditional beam theory; if the softening zone width is equal the beam length, the deflection is converged to the one obtained from the assumption that the whole beam is softened; and if the softening zone width is small enough, only the material in that zone is softened and the material outside is elastically unloading.

3. The parametric study demonstrates that the model parameters including softening zone width w_c, tensile strength f_t, fracture energy per unit area G_f, and various forms of strain-softening

curves have significant effects on the post-peak behaviour of concrete beams. These parameters, especially the softening zone width and the form of the softening curve, are incorporated in various ways in the fracture models for concrete making it difficult, if not impossible, to find a unique post-peak behaviour. Thus, if none of the explicitly existing relationships, i.e. between w_c and ε_0 in particular, is consistently good in predicting the post-peak load-deflection curves, trial-and-error fitting the analytical results to the numerical and/or experimental results should be considered.

4. The analytical model is able to predict the structural size effect behaviour in the load-deflection curve by proportionally relating the softening zone width to the beam depth.

5. Based on the comparison with the experimental and numerical results for two concrete beams under three-point bending tests, it is observed that the analytical model gives good results in pre-peak regime for both linear and bilinear softening stress-strain relationships. However, it is evident that using the explicit expressions to determine the softening zone width w_c and strain at end of softening curve ε_0 is not a suitable method as the post-peak behaviour is not well captured. With an appropriate set of w_c and ε_0 from trial-and-error fitting the analytical results to the numerical and experimental results, good results can be found. For example, in this study, it is found that w_c is approximately equal 1 to 1.5 times the beam depth h; ε_0 is about 6 and 11 times the elastic maximum normal strain in the cases of linear softening and bilinear softening, respectively. In particular, the bilinear strain-softening exhibits a better result.

6. The stress distributions at the mid-section obtained by the analytical model are in good agreement with those of numerical model. In addition, the analytical model also shows a good agreement in the stress, and strain distributions at the interface cross-section between the strain-softening and linear elastic zones. Also, it shows the material in the interface and outside sections unloads elastically during the crack propagation in the softening zone. It confirms the assumption about continuity conditions at the interface between the strain-softening and linear elastic unloading zones (Bazant and Zubelewics 1988). This is an important point, which has rarely discussed in other analytical models in literature. Due to the time limit of this research, the stress

and strain distributions in sections in between the mid-section and edge-section have not been verified.

7. The normal strains at mid-span cross-sections are underestimated in comparison to the FE model as the analytical model assumes that the planar cross-section remain plane and normal to the deflection line under loading (Bernoulli-Navier hypothesis), and the strain distribution is linear. In fact, due to the effects of shearing force, the mid-span cross-section is no longer planar, but warped under loading. As a result, the strain distribution is not linear along the cross-section depth, but much curved (Timoshenko 1955).

8. For reinforced concrete beams, the load-deflection curves predicted by the analytical model compare well with those of numerical model and experiment, especially in pre-yield regime. If the beam is over-reinforced, the analytical result is in very good agreement with experimental and numerical results because the assumption of “distributed” cracks for the whole beam is well appropriate for this case. Also, the analytical model is capable of reproducing the transitional condition between brittle and ductile behaviours in RC beams. Due to the assumption of no loss of bond between steel reinforcement and concrete, the analytical model usually predicts a stiffer behaviour than that of experiment.

Table 6.1 Geometry and material parameters for a concrete beam (Ulfkjaer *et al*. 1995)

Property (1)	Symbol (2)	Unit of measurement (3)	Value (4)
beam depth	h	mm	100
beam width	b	mm	100
beam length	L	mm	800
fracture energy per unit area	G_f	N/mm	0.1
tensile strength	f_t	N/mm^2	3.0
modulus of elasticity	E	N/mm^2	20000

Table 6.2 Values of w_c used in the analytical model for the concrete beam (Ulfkjaer *et al*. 1995)

Method	Value of w_c
Bazant and Zubelewicz (1988)	$w_c = 0.8h = 80$ mm
Ulfkjaer et al. (1995), Iyengar et al. (1998) and Iyengar and Raviraj (2001)	$w_c = 0.5h = 50$ mm
Iyengar et al. (1998) and Iyengar and Raviraj (2001)	$w_c = 1.0h = 100$ mm
Experimental-based formula Wittmann (2002)	$w_c = \frac{EG_f}{f_t^2} = 50$ mm

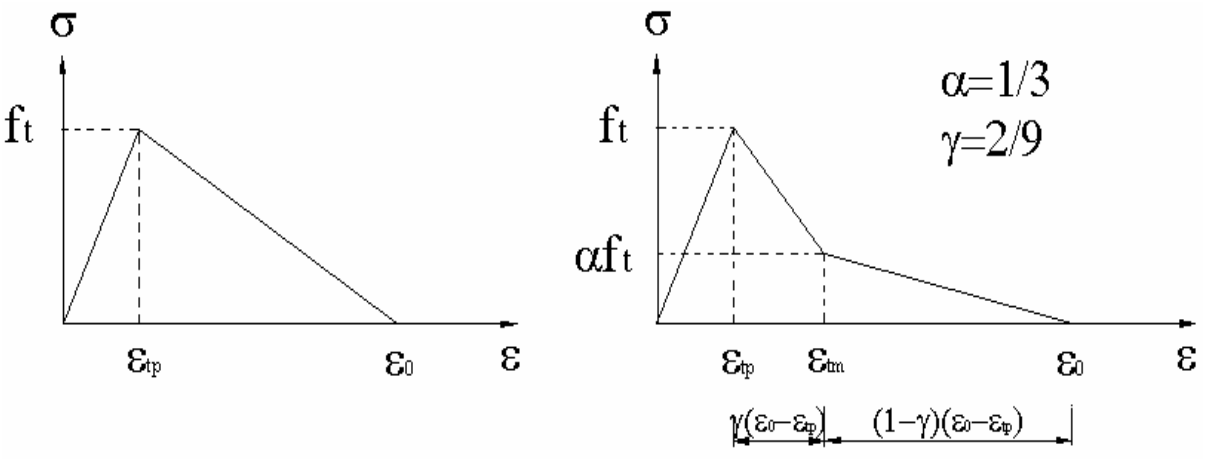

(a) (b)

Figure 6.1 Typical strain softening rule in stress-strain relationship: (a) Linear, (b) Bilinear (Petersson 1981)

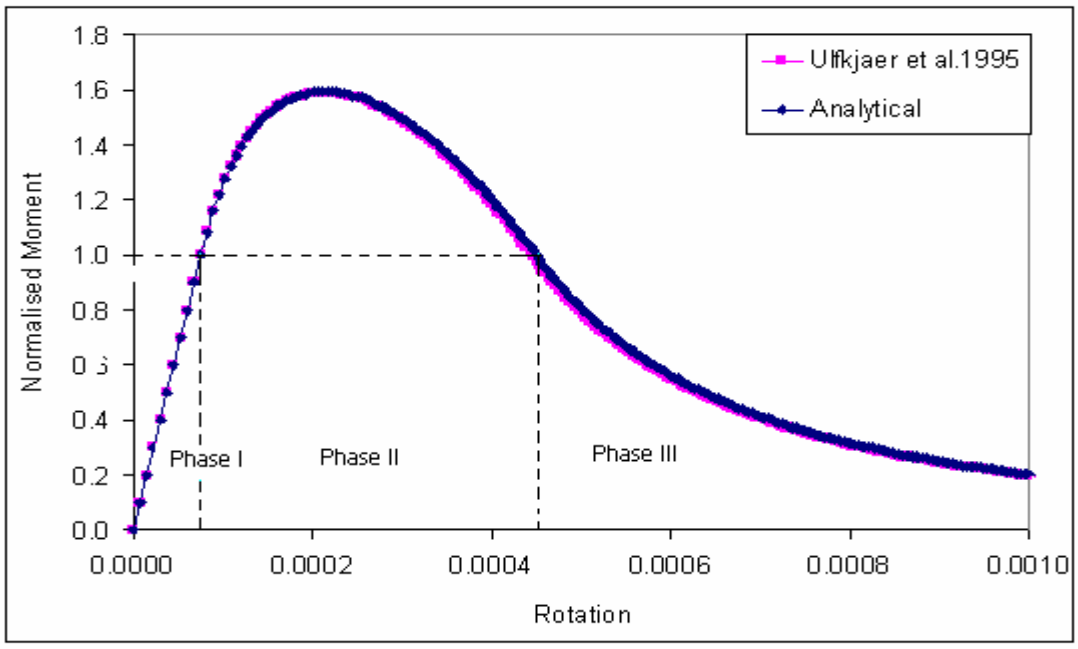

Figure 6.2 Moment-curvature curve of a theoretical beam using analytical model and Ulfkjaer *et al.*'s (1995) model

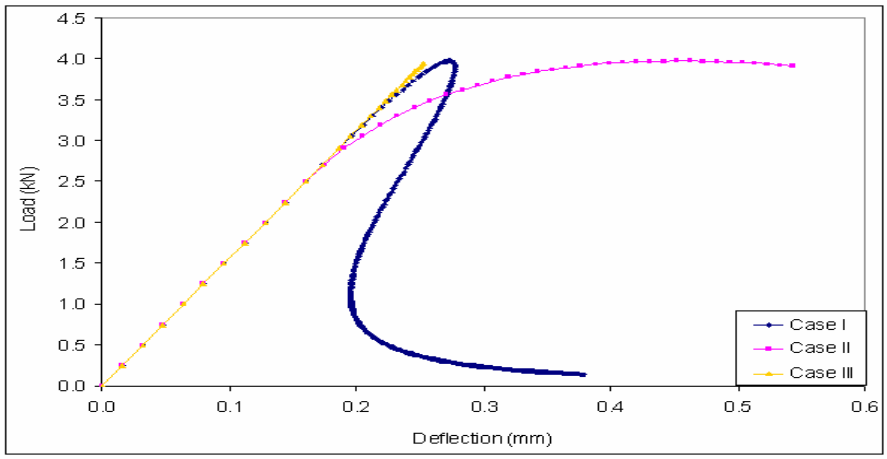

Figure 6.3 Load-deflection curves for 3 different cases of calculating deflection

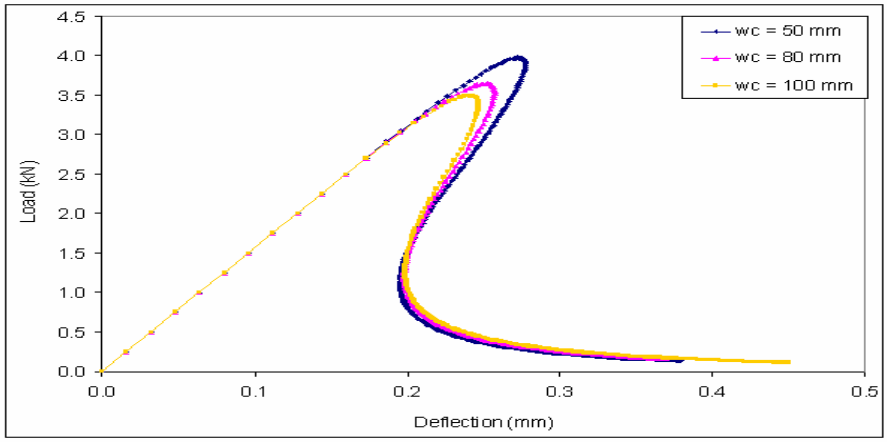

Figure 6.4 Load-deflection curves for different values of softening zone width w_c

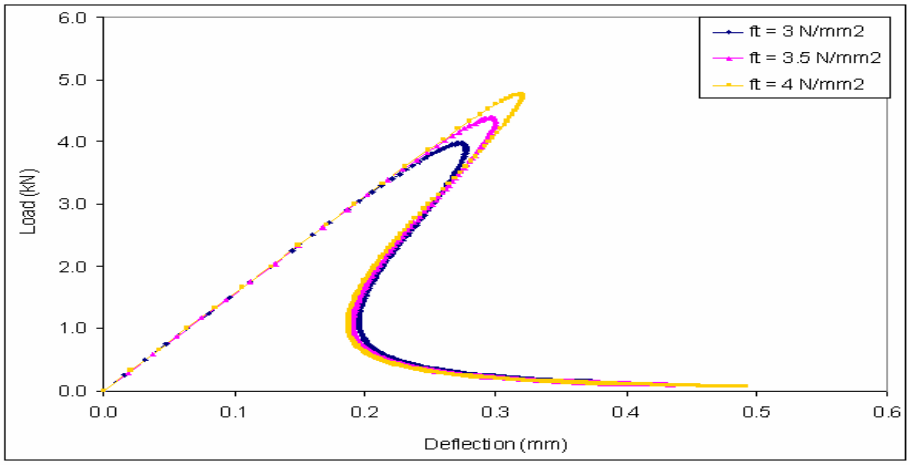

Figure 6.5 Load-deflection curves for different values of tensile strength

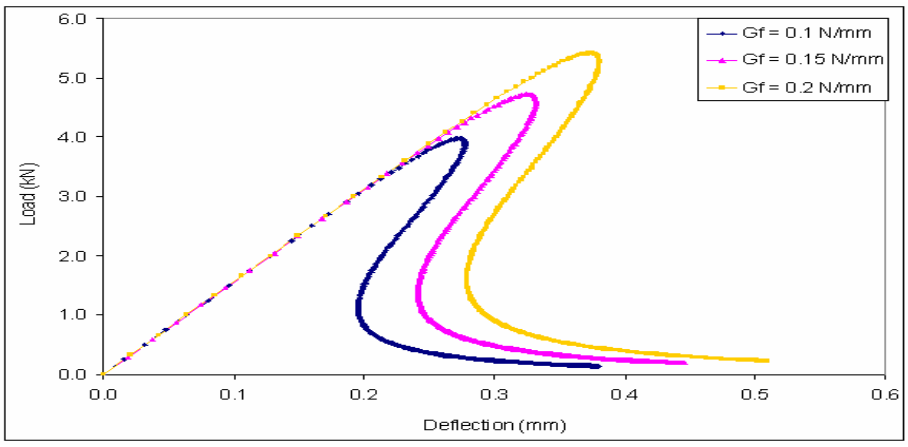

Figure 6.6 Load-deflection curves for different values of fracture energy G_f

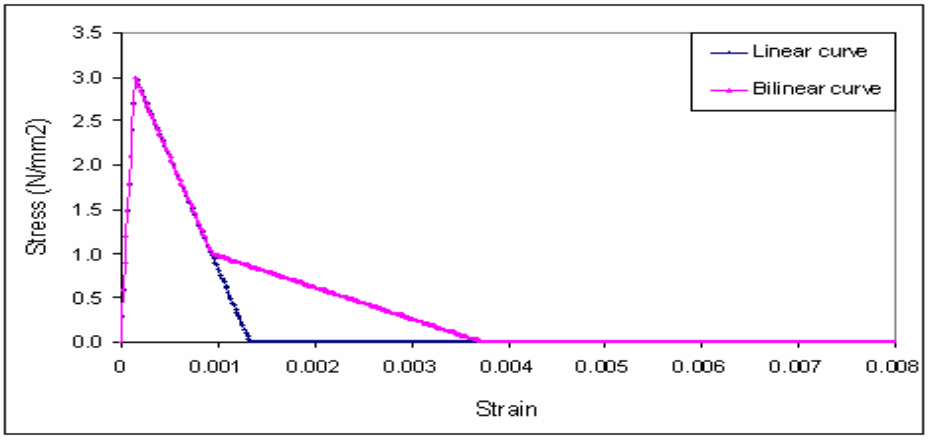

Figure 6.7 Linear and bilinear stress-strain relationship (Petersson 1981)

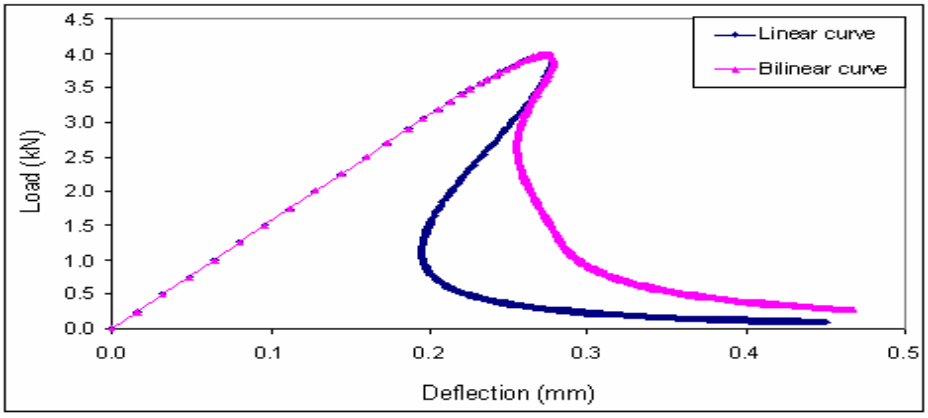

Figure 6.8 Load-deflection curves for linear and bilinear stress-strain relationship (Petersson 1981) shown in Figure 6.7

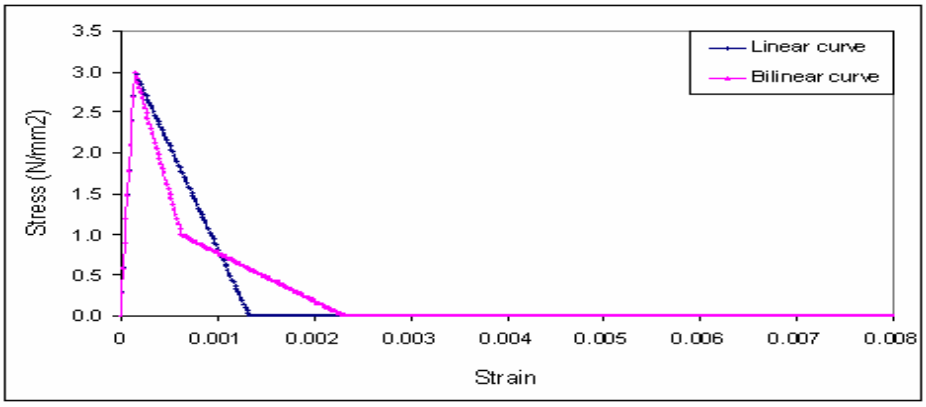

Figure 6.9 Linear and bilinear stress-strain relationship (Petersson 1981)

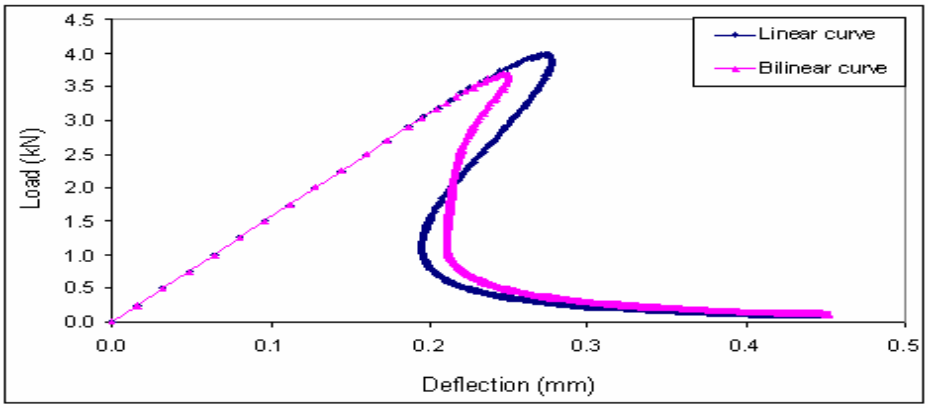

Figure 6.10 Load-deflection curves for linear and bilinear stress-strain relationship (Petersson 1981) shown in Figure 6.9

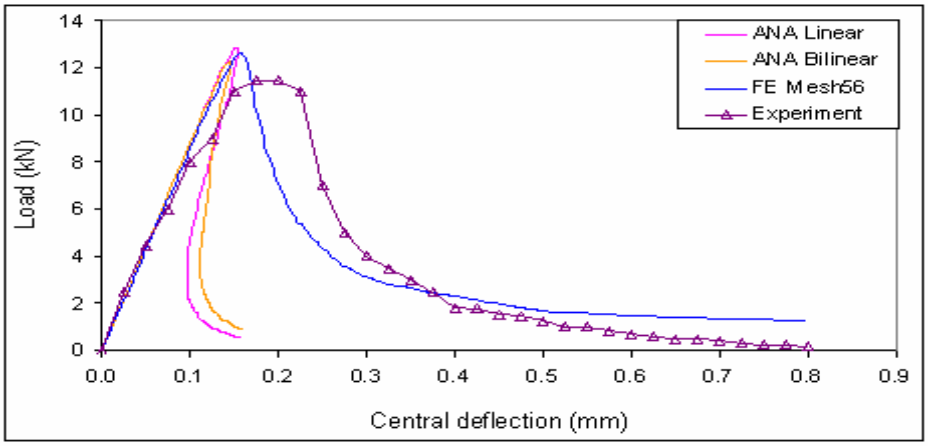

Figure 6.11 Load-deflection curves of Carpinter's (1989) beam for linear and bilinear softening curves (w_c = 0.5h and ε_0 is obtained from explicit expressions for linear and bilinear softening curves)

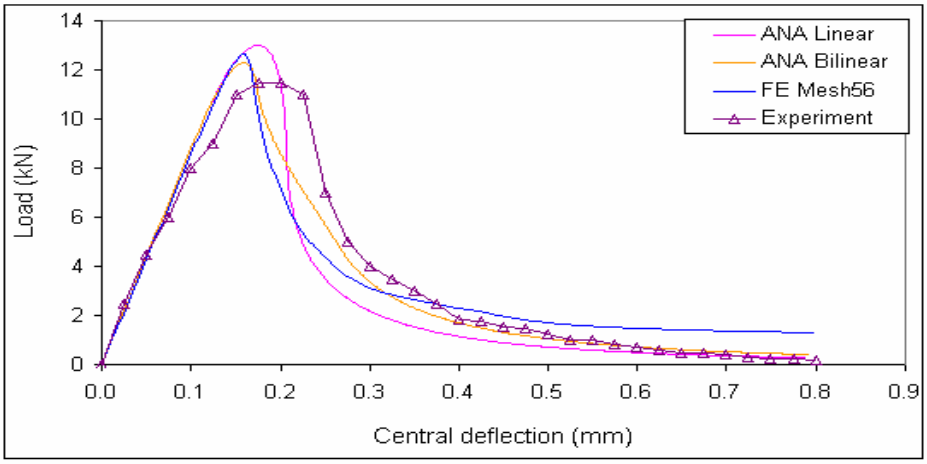

Figure 6.12 Load-deflection curves of Carpinter's (1989) beam for linear and bilinear softening curves ($w_c = 1.5h$ and $\varepsilon_0 = 6\varepsilon_{tp}$ for linear softening, and $\varepsilon_0 = 11\varepsilon_{tp}$ for bilinear softening)

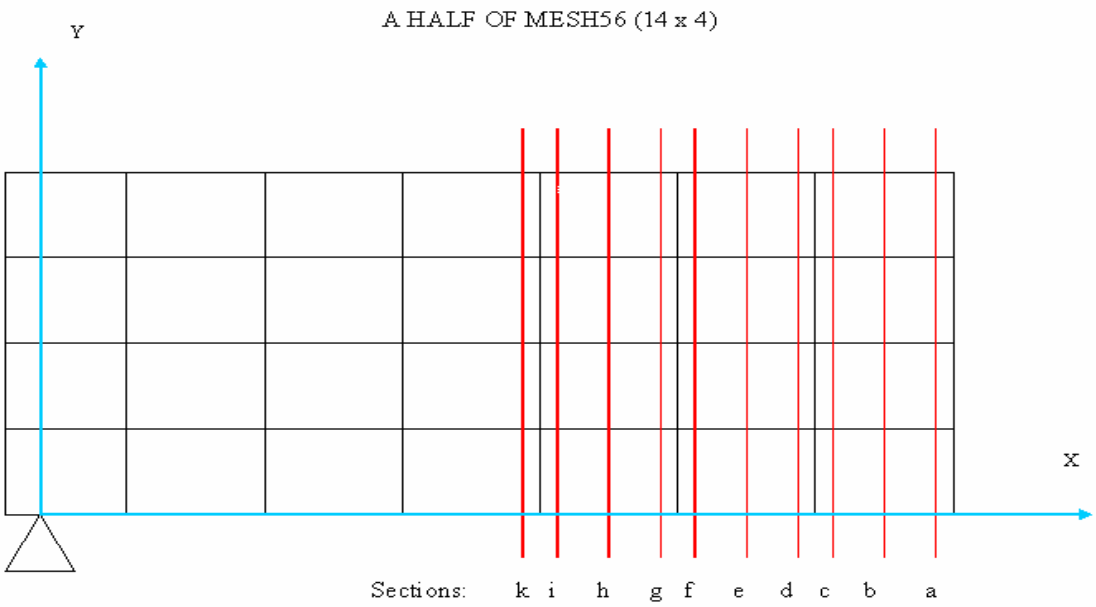

	Section									
	a	b	c	d	e	f	g	h	i	k
Coordinate x (mm)	297.18	287.50	277.82	272.18	262.50	252.82	247.18	237.50	227.82	212.50

Figure 6.13 Cross-sections in FE mesh where stress and strain distributions are extracted. Cross-section (a) is closest to the midsection (Section 2) and cross-section (k) is closest to the edge cross-section (Section 1).

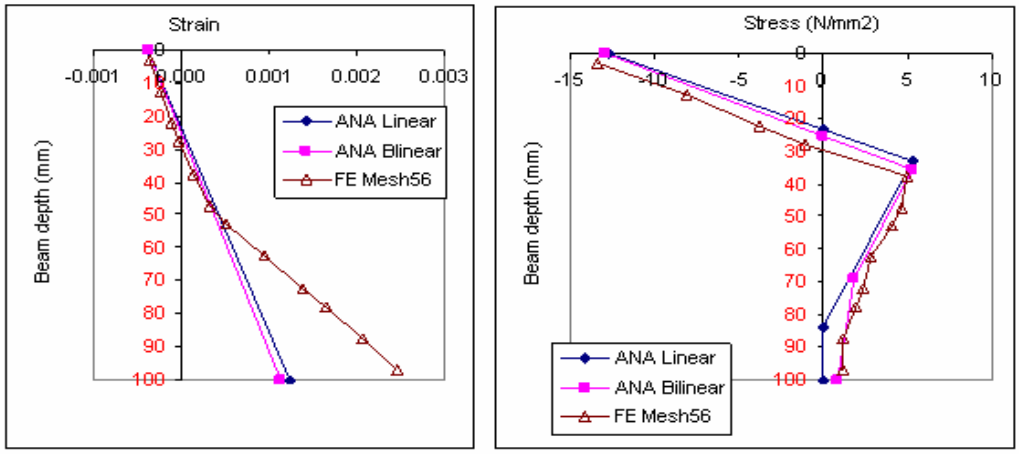

Figure 6.14(a) Stress and strain distributions in the cross-section 2 at a deflection of 0.22 mm

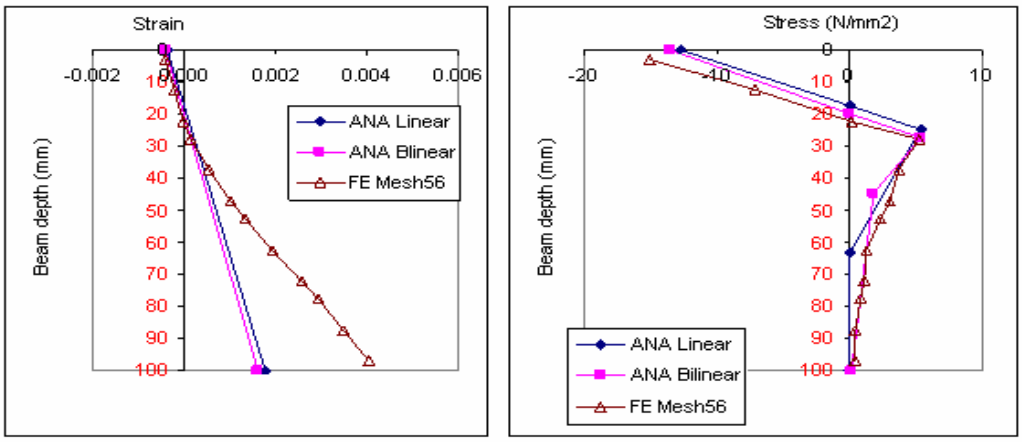

Figure 6.14(b) Stress and strain distributions in the cross-section 2 at a deflection of 0.26 mm

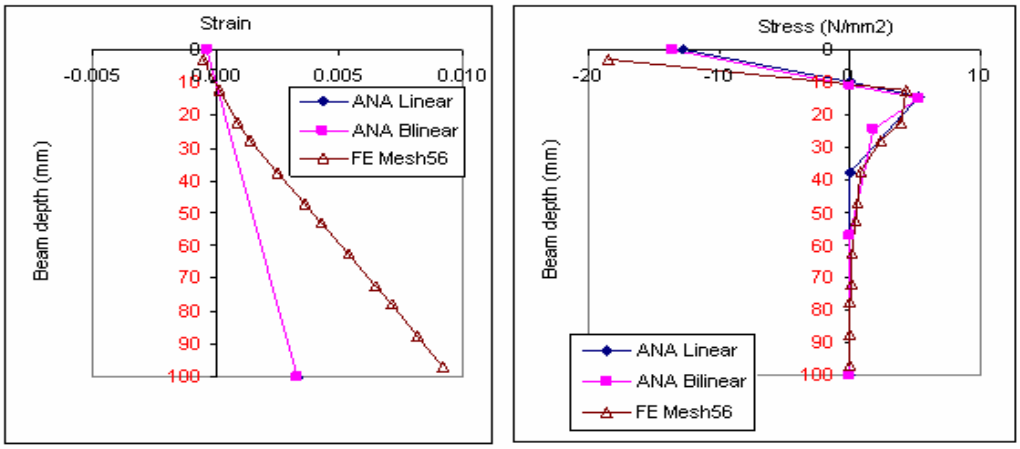

Figure 6.14(c) Stress and strain distributions in the cross-section 2 at a deflection of 0.42 mm

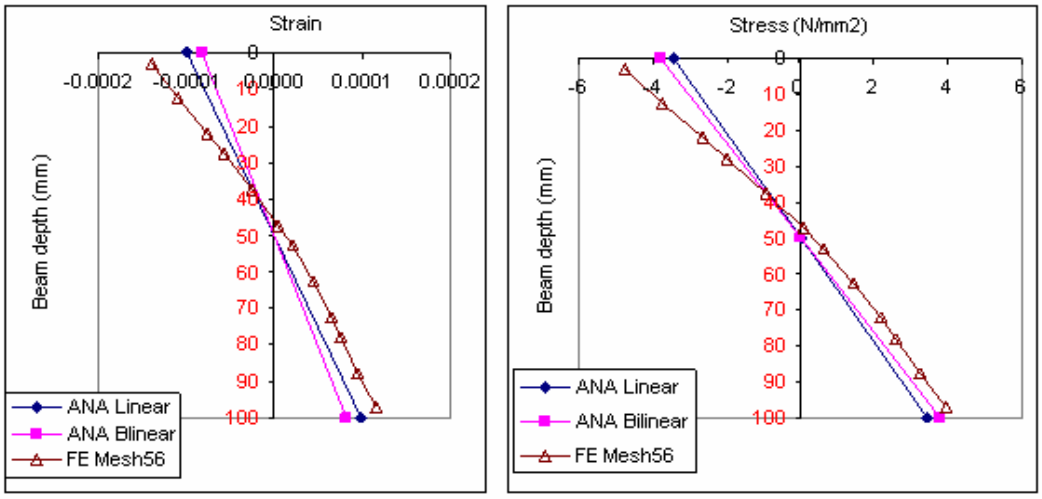

Figure 6.15(a) Stress and strain distributions in the cross-section 1 at a deflection of 0.22 mm

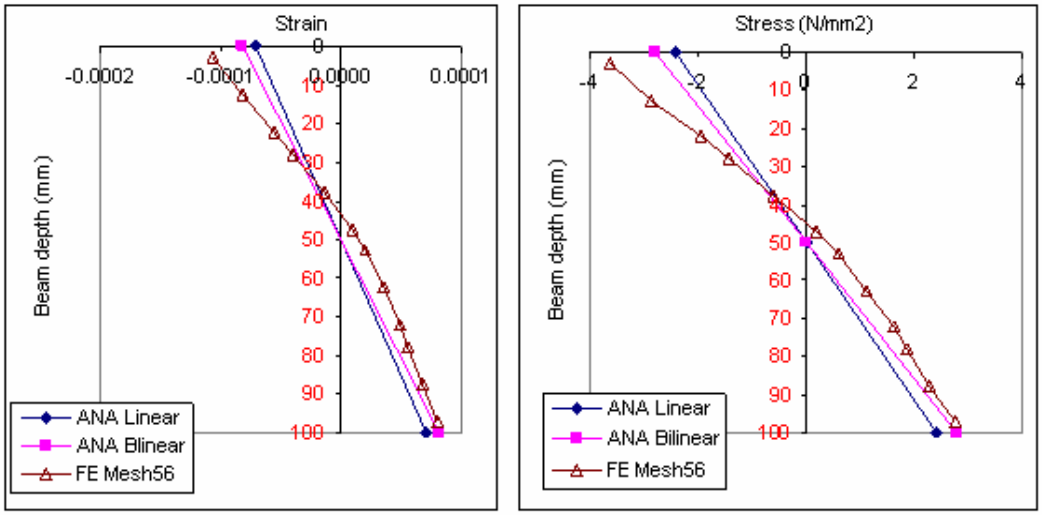

Figure 6.15(b) Stress and strain distributions in the cross-section 1 at a deflection of 0.26 mm

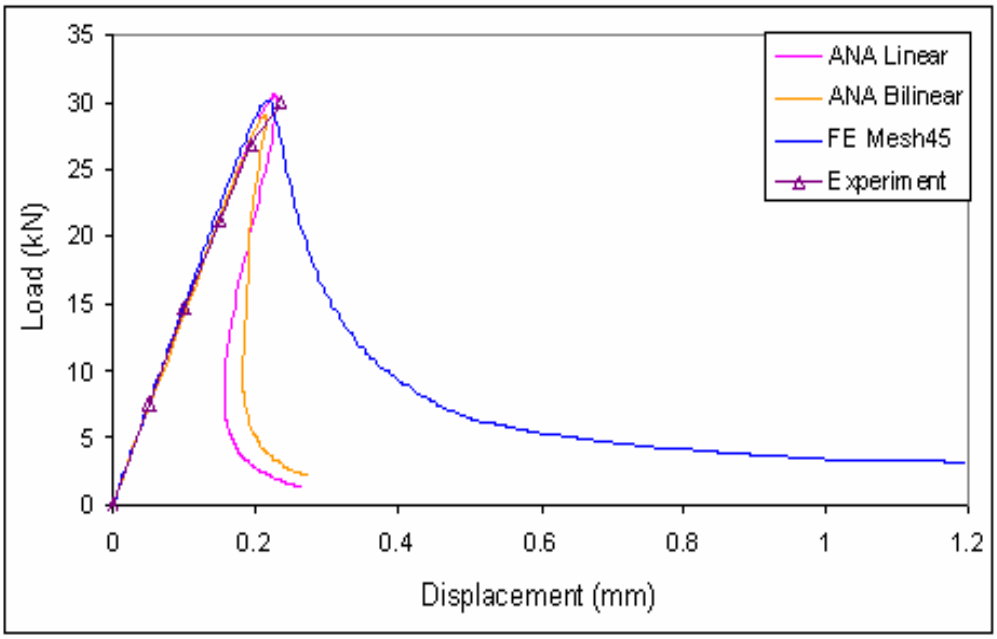

Figure 6.16 Load-deflection curves of Ozbolt and Bazant's (1991) beam for linear and bilinear softening curves ($w_c = 0.3h$ and ε_0 is obtained from explicit expressions for linear and bilinear softening curves)

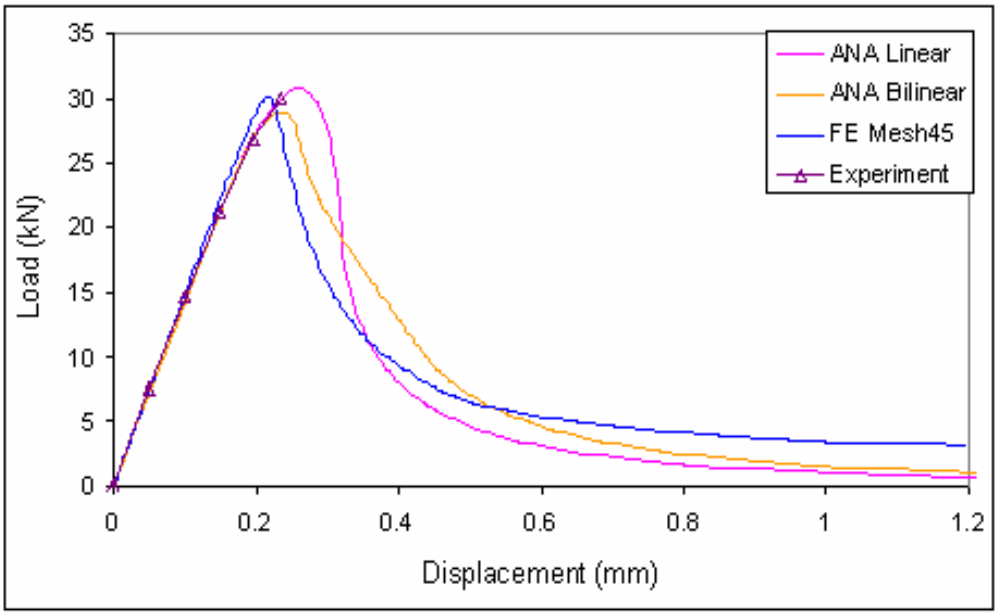

Figure 6.17 Load-deflection curves of Ozbolt and Bazant's (1991) beam for linear and bilinear softening curves ($w_c = 1.0h$ and $\varepsilon_0 = 6\varepsilon_{tp}$ for linear softening, and $\varepsilon_0 = 11\varepsilon_{tp}$ for bilinear softening)

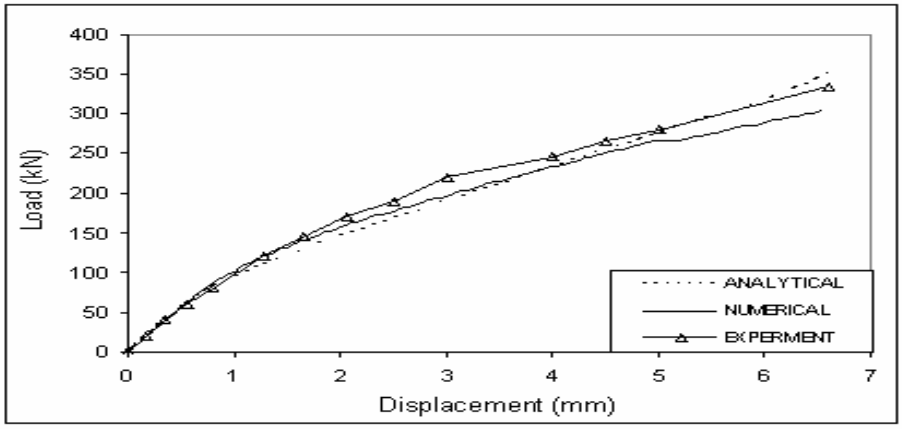

Figure 6.18 Comparison of load-deflection curves of the analytical model and numerical and experimental results for Bresler and Scoderlis's beam (1963)

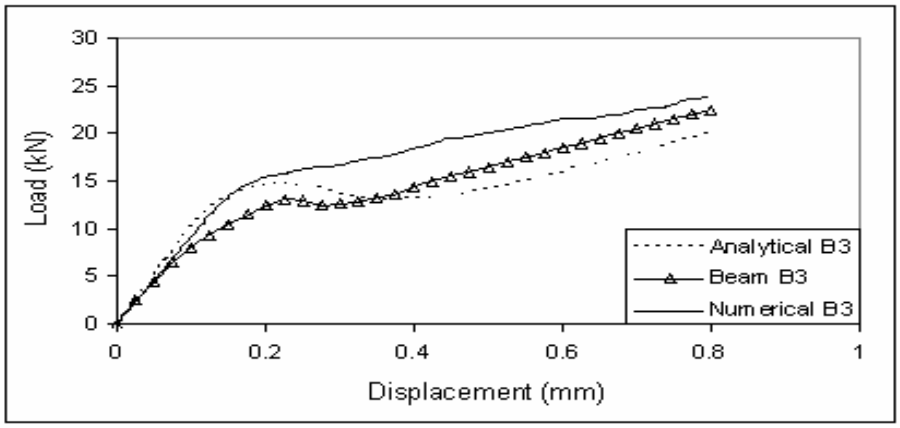

Figure 6.19 Comparison of load-deflection curves of the analytical model and numerical and experimental results for Carpinter's beam B3 (1989)

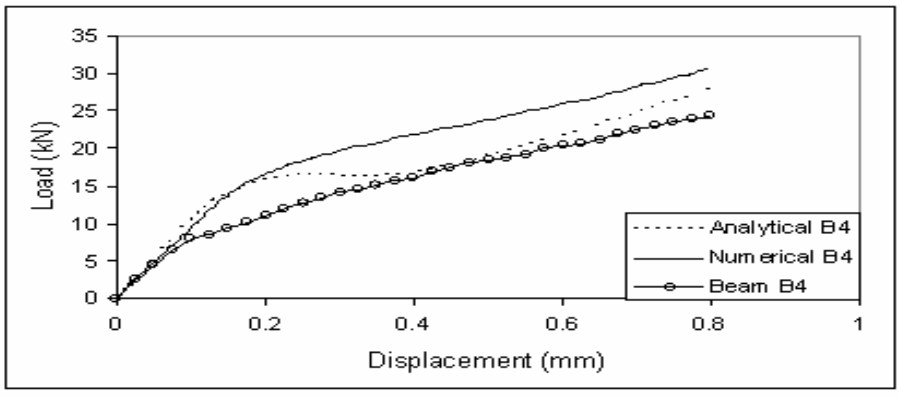

Figure 6.20 Comparison of load-deflection curves of the analytical model and numerical and experimental results for Carpinter's beam B4 (1989)

CHAPTER 7

RESPONSE OF BRIDGE PIER AND NUMBER OF ARTIFICIAL TIME-HISTORIES REQUIRED FOR NON-LINEAR DYNAMIC ANALYSIS

7.1 INTRODUCTION

In this chapter, the non-linear dynamic behaviour and damage of a reinforced concrete bridge pier under different artificial time-histories have been investigated. However, it should be kept in mind that a design response spectrum is never derived from just one single earthquake record, but from an envelope of many records representing all possible expected earthquake sources in the region surrounding a site (Naeim and Lew 1995). Therefore, the earthquake-like ground motion should always be represented by a set of several artificial time-histories which are compatible with the design response spectrum as discussed in Chapter 3. However, there is an important question about how many time-histories are required for the non-linear dynamic analysis so that the results would be representative of the typical behaviour during a real earthquake of the design magnitude.

This chapter aims to explore and attempts to answer the above challenging question with respect to the analysis of RC bridge piers under artificial earthquake time-histories generated according to EC8 response spectra and the use of FE smeared crack models. Therefore, the objective of this chapter is to apply several techniques including vibration analysis, Fourier analysis, normalised cumulative spectrum, dissipated energies and damage indices to quantify the structural response of the RC bridge piers for various sets of artificial time-histories. Based on these assessments and the convergence of the representative response for different sets of different numbers of artificial time-histories to a design confidence band width in probability, an appropriate minimum number of time-histories are proposed for non-linear dynamic analysis under earthquake loading.

The chapter begins with a brief overview on the number of time-histories suggested to be used in the literature and to show why the research on this area is still greatly needed. Following this

review, a brief overview of different methods of quantifying the structural response, i.e. structural damage under different time-histories to provide an appropriate way for the study will be presented. By analysing and evaluating the bridge pier's response in terms of Fourier analysis, normalised cumulative spectrum, dissipated energy and damage index as well as probability applications, the Author aims to understand and find an unbiased and representative quantity to represent the extent of permanent non-linear effects under a different number of artificial time-histories. The suggested appropriate minimum number of time-histories will be validated in Chapter 8 through the parametric study on effects of several parameters of earthquake and structural characteristics.

7.2 LITERATURE REVIEW

7.2.1 Recommended number of earthquake time-histories

The number of earthquake time-histories required for use in the analysis of a structure under seismic loading is subject to much contention, especially for non-linear dynamic analysis. This number is controlled by the degree of the scatter of structural responses amongst the characteristics of the selected time-histories: the greater their dispersion, the more analyses are required. Many seismic codes require or recommend a certain number of real or artificial earthquake records to be used for dynamic analysis. Table 7.1 adopted from Bommer and Ruggeri (2002) summarises the guidelines in current seismic design codes with respect to dynamic analysis in the time domain and the recommended number of records to be used. Most of them recommend the number of 2 to 5 time-history records, but only EC8 states the number of 5 for artificial records. These recommendations have been stated for dynamic analysis and not specifically for linear or non-linear analyses. Without explanatory notes in the code, it is not clear how this number of records comes about, except the explanation that this number of records should be enough to satisfy or to compensate for the lack of randomness if a smaller number of earthquake time-histories are used. In the research field, there have been several analyses using different numbers of real or artificial earthquakes for non-linear dynamic analysis. For example, Booth (1999) generated and used 5 artificial records, Hirao *et al.* (1987) used 12 different

records, and Naeim *et al.* (2004) used 7 records. However, in most of the literature, the number of records is chosen according to the seismic codes and used only as means for the researchers to look at other interests, such as the structural behaviour or the material model behaviour. Nonetheless, there has been very little research about the number of artificially generated earthquake time-histories to be used.

Shome *et al.* (1998) proposed an approach based on an explicitly probabilistic framework to address several issues on earthquake records and non-linear response of a MDOF structure. They found that when scaling earthquake records in a bin to the bin-mean spectral acceleration at the fundamental frequency of the structure before carrying out the non-linear analysis, the mean damage measures of the structure are obtained with significantly reduced dispersion in non-linear response of the structure. This conclusion is attractive for design code applications because suites of records can be scaled to match the elastic acceleration response spectrum already defined in the code (see Chapter 3 for generation of artificial acceleration spectrum fitting to the EC8 elastic acceleration spectrum). Furthermore, Shome *et al.* (1998) suggested that the typical numbers of records used in practice can be found from a set of 20 input earthquakes by giving an acceptable confidence band width. For example, in their study, the use of $\pm 10\%$ of standard error of estimation of the mean value will lead to the conclusion that eight earthquake records sufficient for the non-linear analysis based on the damage measure of displacement ductility; and that unreliable number of records can be found for the non-linear analysis based on the damage measure of dissipated energy.

However, it is important to note that Shome *et al.* (1998) based their conclusions on non-linear analysis of a MDOF structure subject to records from rather large bins of magnitude of 5 and 20 km distance which were recorded in California on stiff soils only. While Kurama and Farrow (2003) showed that scaling methods that work well for ground motions representative of stiff soil and far-field conditions may not provide good results for soft soil and near-field conditions for a wide range of structural characteristics. More importantly, Shome *et al.* (1998) found that the conclusion of their research did not hold particularly well for the response measured in terms of dissipated hysteretic energy (as also mentioned in the above paragraph). The key issue is the

degree of dependence of non-linear structural response on the number of cycles or the duration of earthquake shaking. It is because the seismic response of any structure that accumulates dissipated energy and damage under earthquake loading is dependent not only on the maximum amplitude of the motion but also the number of its cycles, the duration and the frequency characteristics of the input motion (van de Lindt and Goh 2004, Hancock and Bommer 2004, Kunnath and Chai 2004, Ma *et al.* 2003, Malholtra 2002, Chai and Fajfar 2000, Bommer and Martinez-Pereira 1999, Hirao *et al.* 1987).

The seismic response of a structure under the action of an earthquake, however, depends not only on the characteristics of the earthquakes, but also on the material behaviour of the structure itself (Loh and Ho 1990, Kurama and Farrow 2003, van de Lindt 2005). In particular, van de Lindt (2005) compared the results of a seismic analysis, based on the probability of a bilinear hysteretic oscillator, to an analysis using a linear oscillator for the same earthquakes. He showed that the use of a more complex oscillator model in seismic analysis, not only altered the structural response but significantly changed the number of time domain simulations that are thought to be representative of earthquake dangers in the area. In fact, Shome *et al.* (1998) carried out the non-linear dynamic analysis for a MDOF structure using a simple analytical model which seems to unlikely be able to capture the energy dissipation in the structure. This may also explain why their results did not hold well for the non-linear response measured in terms of cumulative dissipated energy and damage. Furthermore, only the first mode of vibration was considered for frequency content analysis in Shome *et al.*'s (1998) study, and this obviously excludes the significant higher-mode effects, or the energy dissipation in turn, to the structural behaviour. So far, in order to investigate the effects of earthquake characteristics including earthquake duration, most of the analyses are based on simple analytical studies (Loh and Ho 1990, Chai and Fajfar 2000, Kunnath and Chai 2004, Malholtra 2002, Jeong and Wan 1988, Hirao *et al.* 1987, and Hancock and Bommer 2005). In the analytical approach, a phenomenological model (Clough 1966, Takeda *et al.* 1970, Saiidi 1982, Stone and Taylor 1992) is set up by defining hysteretic rules to mimic the response. This model is then used to study the response characteristic under different types of ground motions. Although providing valuable information on the parameters affecting the response, these models suffer from lack of accurate modelling of the material stress-

strain relationship and thus may not provide realistic results of non-linear dynamic behaviour. The other approach, namely the experimental one, was used to substantiate the response by providing information on the material and structural behaviour. Conversely, performing experiments under earthquake time-histories with different characteristics were very expensive and sometimes impossible (Usami and Kumar 1996). Seismic applications of finite element material models such as smeared crack models have not yet been widely used for such investigations. It is because they are technically challenging to implement into dynamic analysis so as to perform the analysis successfully. However, using the smeared crack models it is able to provide more detailed understanding of the material behaviour under cyclic loading. With the rapid increase in computer power, improvements of the robustness of FEA packages and advances in the understanding and implementation of material models, it means that the use of such complicated material models are likely to become more widespread in the future. Therefore a study using crack models for earthquake non-linear dynamic analysis is really necessary.

From the above literature review, a significant question emerges that is: how many artificial time-histories are required for non-linear dynamic analysis with the use of FE smeared crack models?

This research attempts to answer this question by using LUSAS Multi-crack and Craft models (see Chapters 2, 4 and 5) with FE approach for non-linear dynamic analysis of RC bridge piers under artificially generated earthquake time-histories. To analyse and quantify the response and damage of the RC piers, some well-known techniques are used. These techniques are briefly introduced in the following section.

7.2.2 Seismic response analysis of RC bridge pier

It is obvious that under different earthquake time history records, the structure experiences different response and damage. In order to analyse and compare the response and damage behaviour of the structure, a method for quantifying the damage has to be devised and used. One class of methods to quantify damage is the use of a “damage index” to create a single measure that adequately represents the complex seismic behaviour. Damage indices aim to provide a mean

of quantifying numerically the damage in reinforced concrete structures sustained under cyclic and earthquake loading (Hindi and Sexsmith 2001, 2004). In earthquake engineering literature, there have been various damage measures proposed and considered in the experimental and theoretical studies to explain damages observed in the structures under artificial ground motions or in actual structures subjected to real earthquake motions such as Park and Ang (1985), Chung *et al*. (1989), Chai *et al.* (1995), Fajfar and Gaspersic (1996), Ghobarah *et al.* (1999), and Hindi and Sexsmith (2001).

Many studies have been performed in the analysis or characterisation of seismically-induced damage to reinforced concrete members and, in particular, RC bridge piers (Banon *et al.* 1981, Park and Ang 1985, Roufaiel and Meyer 1987, Stephens and Yao 1987, Jeong and Iwan 1988, Chung *et al.* 1989, Williams and Sexsmith 1995, William *et al.* 1997, Ghobarah *et al.* 1999, Hindi and Sexsmith 2001, and Erberik and Sucuoglu 2004, Kim *et al.* 2005). However, the majority of these studies are based on data from static cyclic tests in both numerical and experimental areas.

The dynamic effects that arise from random ground motions should be taken into account for the characterization and the modelling of the non-linear response and damage behaviour of RC bridge piers. Unfortunately, very little work has been done into the non-linear response and damage behaviour as well as their quantitative measures for RC bridge piers under seismic excitations either real or artificial ones (Kwan and Billington 2003, Park *et al.* 2003, Hindi and Sexsmith 2004, Kim *et al.* 2005).

In this chapter, results from numerical studies on the full-scaled prototype RC bridge piers subjected to different artificial time-histories are presented and discussed. The study mainly focuses on the structural response and damage behaviour in terms of vibratory responses, Fourier analysis, cumulative spectrum of responses, dissipated energies, and damage indices. Some effects from all aspects of earthquake and structural characteristics such as peak ground accelerations, soil conditions, durations of earthquakes, viscous damping ratios, pier heights, the presence of axial load, tensile strength, Young’s modulus of concrete and the amount of steel

reinforcement will be taken into consideration (see Chapter 8). A minimum representative number of time-histories will be then obtained with respect to the convergence of the responses of different sets of artificial time-histories to a required confidence band from the mean response.

In following subsections, techniques to be used in this research to analyse and quantify the responses of RC bridge piers under different artificial earthquake time-histories are reviewed.

7.2.2.1 Vibratory responses

Under earthquake loading, the RC bridge pier experiences mechanical degradation for which its material consistency and structural properties undergo changes accordingly. These changes are reflected in the evolution of the structural response, i.e. overall structural stiffness, and the damage of the pier. In detail, any change in structural properties, in turn, induces change in the vibratory characteristics and response of the pier. Therefore, vibration analysis of the pier under different sets of artificial time-histories, especially in the frequency domain, provides useful information concerning different changes in structural integrity. DiPasquale and Cakmak (1988) proposed a damage index at the structure level which is based on change of the fundamental period of the structure. It is efficient as damage is evaluated as a quantitative change of the fundamental period of the structure which is due to the change in the structural stiffness during the seismic loading. However, it is not very convenient to use this approach because the fundamental periods must be consecutively calculated during the earthquake loading because of the change of the structural response. For simplicity, this study thus limits the investigation to the vibratory response of the pier in both time and frequency domains. Therefore the damage index at the structure level is not used.

7.2.2.2 Energy dissipation

The dissipated energy, as represented by the cumulative area of the force-displacement hysteretic loops, indicates how much of the input seismic energy is dissipated through various inelastic mechanisms such as plastic behaviour, cracking in concrete as well as yielding in the steel

reinforcement. These inelastic mechanisms induce an overall structural degradation including stiffness and strength degradation. Therefore, the amount of energy dissipated has been frequently used in quantifying the level of structural degradation or damage of the member. Since the absorbed energy and "energy index" for cyclic tests were first proposed by Gosain *et al.* (1977) and Banon *et al.* (1981), respectively, energy dissipation has extensively been used as an important index to quantify the damage in the structure under cyclic and earthquake loadings (Darwin and Nmai 1986, Emls *et al.* 1989, Kratzig *et al.* 1989, Garstka *et al.* 1994, Sucuoglu and Erberk 2004). Dissipated energy will be included in this chapter as one of indices to quantify damage in the RC bridge piers.

7.2.2.3 Combination of ductility and energy dissipation

Park *et al.* (2003) studied the seismic behaviour of a RC bridge column using a shake-table experiment and revealed that the cumulative dissipated energy does not necessarily represent the actual damage level of the column, and rather it tends to overestimate the damage level. Similar findings were reported by Stone and Cheok (1989). From the experimental observations, Park *et al.* (2003) suggested that after cracking and damage, the energy dissipation comes largely from the plastic flow of longitudinal reinforcements without increasing the level of damage in the column. It is because while cracking involves failure of the internal structure of a material, thus constituting physical damage, reversed-cyclic plastic flow simply involves rearrangement of the internal structure of the material via dislocation and therefore does not necessary constitutes physical damage of the material. Therefore, the dissipated energy cannot be used alone to quantify damage induced in the structure. A combination of ductility and dissipated energy has been satisfactorily employed as a seismic damage index by many researchers (Park and Ang 1985, Park *et al*. 1987, Kunnath *et al.* 1991, Cosenza *et al.* 1993, Satish and Usami 1994, Kunnath and Gross 1995, Chai *et al.* 1995). Amongst them, the best-known and most widely used of all cumulative damage indices is that of Park and Ang (1985) damage index model. This is probably because the model is simple and its validity has been checked against results obtained from a large number of physical experiments on both reinforced concrete and steel specimens. Moreover, the model has been calibrated with the damage observed from the real RC buildings

(Park and Ang 1985, Park *et al*. 1987). There has been a lot of studies to the application of the Park-Ang damage model for RC structures under seismic loading and shown that it is a reasonable and useful measure to quantify the damage in the structures in both experimental and numerical areas (Park *et al.* 1987, Stephens *et al.* 1987, Kunnath *et al.* 1991, Cosenza *et al.* 1993, Williams and Sexsmith 1995, Ghobarah *et al.* 1999, Chai *et al.* 1995, Warnitchai and Panyakapo 1999, Hindi and Sexsmith 2001, 2004). As the purpose of this research is not to recommend or assess the suitability of any specific damage method, but to use a damage index to quantify the damage from the results of non-linear FE dynamic analysis under different sets of artificial earthquakes, it was decided to adopt the Park and Ang (1985) damage index in this chapter.

It should be noted that in order to use any damage index in a decision, the relationship between numerical consequences and damage has to be established. It means that the crack sizes and extent, the degree of crushing, and accumulated strain in the reinforcing steel would be important measures of numerical consequences and hence damage. However, these consequences are very complicated and it is beyond of the scope of this research to look at them in detail from the FE results. Therefore the results of crack patterns, crushing effects in concrete and accumulated strain in the reinforcing steel will not be investigated in this chapter.

7.3 NUMERICAL ANALYSIS

In this section, the non-linear dynamic analysis of a RC bridge pier is presented. Initially, before moving into the non-linear dynamic analysis, several linear analyses were made to investigate the performance of a concrete bridge pier through the implicit time stepping FE dynamic analysis. The investigation focuses upon how the responses vary with: (1) the size of time step; (2) the use of different coefficients of viscous damping and (3) the density of the mesh. The results obtained from linear time stepping FE analysis show that the dynamic response of structures depend on the parameters of the integration algorithm, e.g. time step size; the material properties such as different coefficients of viscous damping; and the density of the mesh. The results also show that the model used is capable of predicting the linear dynamic behaviour of bridge piers.

The details are not presented here but they can be found in a paper published by the Author and his supervisor (Nguyen and Chan 2003).

In this chapter, twenty artificial earthquake time-histories which are generated from the EC8RS following the issues of selecting most suitable parameters for earthquake generation as studied in Chapter 3, are used for the non-linear dynamic analysis. Table 7.2 shows the characteristics for the earthquake generation used in this study, and the twenty artificial earthquake time-histories, which are numbered from 1 to 20, are shown in Appendix 7A.

7.3.1 Description of bridge pier model

In Chapter 5, the shortest pier of a 1:8 bridge model specimen supported by three piers used in shaking table tests at ISMES, Bergamo, Italy (Pinto 1996) was chosen to study in finite element modelling as this pier is the only one was tested under pseudo-dynamic cyclic loading. This bridge specimen is pier B in the lower part of Figure 7.1. The prototype bridge, as shown in the upper part in Figure 7.1, consisted of a straight deck supported by three piers, 50 m apart. The pier chosen for study in this chapter is the longest pier of this prototype bridge but it is modelled in the full-scale by a scale from pier C as investigated in the experiment. However, as the model is not exactly a 1:8 model, all the geometric dimensions of the pier are obtained by multiply those of the 1:8 model by a factor of 8 as shown in Figure 7.2. The reason the longest pier is chosen for this study is because this is “the most vulnerable pier” which ensures to have the most non-linear responses that are appropriate to the objectives of the research.

The pier has an I cross section and 21 m in height. The longitudinal reinforcement in the flanges is placed in two layers with 4#16 bars at the exterior face and 2#16 + 2#15 bars at the interior one. At the web, 4#15 bars were used, two bars on each side. The geometry and the reinforcement arrangement of the experimental model are shown in Figure 7.2. The deck is supported on the pier through a supporting device constructed to allow free movement in the longitudinal direction and free rotation. The total weight of the prototype deck applied at the top of the pier is about 730.5 kN. In the finite element modelling, this load is modelled as a constant

axial load distributed at the top of the pier body to model the transferred load from the deck to the pier. In order to reduce the computational effort, this constant load is assumed not to be included in the main study of this chapter, but will be included in the parametric study part to study the influence of axial load. This assumption would not have a significant effect on the objectives of the study on the number of time-histories required for non-linear dynamic analyses though the presence of the axial load would strengthen the pier stiffness when the displacement is small. All the material properties are still the same as those used in the 1:8 scale model bridge pier (Tables 5.6 and 5.7 in Chapter 5).

7.3.2 Finite element modelling

The finite element model of the RC bridge pier is similar to the one illustrated in Figure 5.27(b). The pier is fixed the ground level. The earthquake acceleration is applied to the pier in the form of body force so that the relative displacement responses of the pier can be obtained directly. As mentioned above, for simplicity, axial load is not included in this study. The concrete is modelled with 2D 8-noded quadrilateral elements with 9 Gauss points and the reinforcement with 3-noded bar elements. The concrete and reinforcement material properties used in the analysis are the same as those used in the previous chapter, as shown in Tables 5.6 and 5.7. Steel reinforcements include 8#16 bars which are scaled from the experimental model for each side of the pier (bold lines in Figure 5.27(b)) with a concrete cover of 100mm. A one dimensional elasto-plastic model is used to model the steel reinforcement. For simplicity, only longitudinal steel reinforcements in the two flanges are presented in FE analysis. As there is no transverse steel reinforcement in the body, the pier stiffness will consequently be slightly less than the real one. But this would not affect the results much because the amount of transverse steel reinforcement in the body is very small and it does not contribute much towards the flexural stiffness.

Craft model was implemented into LUSAS program and employed for the analysis of RC bridge piers under the artificial time-histories. However, the analysis using Craft model was not successful, i.e. it was failed to converge at earlier steps. The Author had taken various necessary steps (as given in Chapter 5) in order to resolve this problem such as reducing the time step,

increasing the number of iteration, and adjusting the control parameters. However, none of these steps were able to solve this problem. In addition, the Author has spent a lot of time discussing this problem with the author of the model, Dr. Anthony Jefferson (University of Cardiff, UK), in order to solve this problem. Unfortunately, the problem has not been solved until the time of writing of this Thesis. As investigated in Chapter 5, Craft model is better and more capable of capturing the cyclic behaviour of the RC bridge pier. It, therefore, should also give more accurate results for seismic analyses than the Multi-crack model. However, as the objective of this research mainly focuses on the qualitative assessment of damage due to different sets of artificial time-histories, therefore, in this sense, the Author believes that the Multi-crack model is good enough to obtain the representative results such that the minimum number of time-histories for non-linear dynamic analysis can be evaluated. Therefore, the Multi-crack model is used for the concrete through out all analyses in this chapter.

7.3.3 Time stepping dynamic analysis

In this study, non-linear time stepping dynamic analyses were performed. The general equations of dynamic equilibrium can be presented as

$$M\ddot{U} + C\dot{U} + R(U) = Q \tag{7.1}$$

Where U, $\dot{U}$ and $\ddot{U}$ are vectors of nodal displacements, velocities and accelerations, respectively. *M*, and *C* are the mass and damping matrices, and *R(U)* is the vector of internal resisting forces, *Q(t)* is the vector of external applied forces. The most usual approximation for *C* is the so-called Rayleigh damping (Clough and Penzien 1975), given by a linear combination of mass and stiffness matrices, i.e.

$$C = \alpha M + \beta K \tag{7.2}$$

where α and β are Rayleigh damping factors, so-called numerical damping; *K* is the stiffness matrix.

The viscous damping ratio can be written as (after modal decomposition of the left hand side of Equation 7.1)

$$\xi_n = \frac{\alpha}{2\omega_n} + \frac{\beta\omega_n}{2} \tag{7.3}$$

where ω_n is the *n*th natural circular frequency.

It is apparent that the two Rayleigh damping factors, α and β, can be evaluated by the solution of a pair of simultaneous equations if the damping ratios associated with two specific circular frequencies (modes) are known. In addition, it is generally assumed that the same damping ratio applies to both chosen circular frequencies. If we assume the value of the viscous damping ratio (ξ) is known, then the values of α and β can be calculated using Equation (7.3).

7.3.4 Parameter identifications for FE non-linear dynamic analysis

In order to obtain an effective solution of a dynamic response, or a non-linear dynamic response in particular, it is important to choose an appropriate time integration scheme. This choice mainly depends on the parameters including integration solution, time step, finite element mesh and damping. Therefore, this section presents the selection of these parameters which are carefully followed practical considerations in literature. This aims to choose a set of suitable parameters which will give reasonable results for practical purposes and significantly reduce the computational effort for large number of analyses required in this thesis.

7.3.4.1 Finite element mesh

The selection of an appropriate finite element mesh and the choice of an effective integration scheme for the response solution are closely related and must be considered together. Choosing a finite element mesh in an appropriate way, beside the recommendations given in Chapters 4 and 5, it should be able to capture the highest significant modes upon which the integration scheme is operating. In this study, several pilot runs were done in order to decide the mesh size to be used for the analysis in order to integrate accurately the response up to the second mode of vibration. Consequently, the basic finite element mesh, MESH I, is chosen as shown in Figure 7.3. Two-dimensional plane stress assumption is used to model the bridge pier. The mesh for concrete uses

8-noded quadrilateral elements with 9 Gauss points and that for steel uses 3-noded bar elements with 2 Gauss points.

7.3.4.2 Integration solution

The explicit scheme is not used in this study in order to avoid the use of small time steps which must be always smaller than a critical time step while in the implicit scheme, the time steps can generally be much greater than the explicit critical time step. Moreover, the implicit algorithm is generally used for inertial problems where the response is governed by the low frequency components, i.e. seismic response, as it has been considered the most effective (Bathe 1982, Beshara and Virdi 1991). In addition, it is of our interest to perform an iteration technique for each time step within the implicit scheme. It is due to any non-linear dynamic response, especially under earthquake loading, is highly path-dependent, and therefore the analysis of a non-linear dynamic problem stringently requires iteration at each time step in order to obtain accurate results (Bathe 1982).

In this study, therefore, the implicit Newmark's method (Newmark 1959) is employed. For the solution of the displacements, velocities, and accelerations at time $t + \Delta t$, the equilibrium Equations (7.1) at time $t + \Delta t$ are considered:

$$M \overset{t+\Delta t}{\ddot{U}} + C \overset{t+\Delta t}{\dot{U}} + K \overset{t+\Delta t}{U} = \overset{t+\Delta t}{Q} \tag{7.4}$$

With the following recursive relations are used:

$$\overset{t+\Delta t}{\dot{U}} = \overset{t}{\dot{U}} + [(1-\beta) \overset{t}{\ddot{U}} + \beta \overset{t+\Delta t}{\ddot{U}}]\Delta t \tag{7.5}$$

$$\overset{t+\Delta t}{U} = \overset{t}{U} + \overset{t}{\dot{U}}\Delta t + [(\frac{1}{2}-\alpha) \overset{t}{\ddot{U}} + \alpha \overset{t+\Delta t}{\ddot{U}}]\Delta t^2 \tag{7.6}$$

Where α and β are parameters of the Newmark's method. If α and β are chosen properly and the time step is small enough and representative of current practice for the implicit scheme, it can ensure the result is a good approximation to the actual dynamic response of the bridge pier under consideration.

7.3.4.3 Time step used

The implicit Newmark's method is employed in this study and with a proper choice of parameters, this algorithm is unconditionally stable, i.e. the error for any initial conditions does not grow without bound for any time step size Δt. However, time step size could be limited due to accuracy considerations.

First of all, for dynamic analyses, the response of higher modes may in some cases need to be considered. If the time step is greater than the limiting time step, the higher modes will not be integrated accurately. To accurately integrate all the relevant higher modes, the time step would need to be less than the limiting value for the highest mode considered. However, there is no exact value for the limiting time step but rather a range of values. The size of the ideal time step cannot be identified *a priori* as it would depend on the actual accuracy required. For linear elastic systems, a time step of about $\Delta t = (1/10 - 1/20)T_n$, in which T_n is the period of the highest structural mode required, seems to be a good rule of thumb to ensure reasonably accurate numerical results (Bathe 1982, Chopra 1995). Theoretical limits on the time step required for stability of the solution have not been determined for non-linear systems and there is no guidance on the limiting time step required for non-linear analysis. However, as the issue concerned is about how well the shape of the oscillating motion is represented by the time stepping scheme, one could safely assume that there is no difference in this aspect for linear or non-linear analysis therefore the same limiting time step is assumed in this study.

Furthermore, when postulating how the higher modes may influence the solution, the frequency content of earthquake loading should be considered (Bathe 1982). Assuming the maximum frequency contained in the earthquake loading is f'_{max}, the maximum frequency of the modes that may influence the solution are generally given as $f_{max} \cong 4f'_{max}$, and therefore the time step can be chosen to be $\Delta t < 0.5/f_{max}$ for the SDOF systems (Bathe 1982, LUSAS Manual 2001).

Finally, the time step also depends on the size of the finite element mesh (Bathe 1982, Pal 1998). Simply, the time step can be chosen as $\Delta t < T_n/\pi$ (Bathe 1982).

Therefore, a time step size in the range of $\Delta t = (1/10 - 1/20)T_n$ and $0.5/f_{max}$ and T_n/π will be investigated in this study.

From the eigenvalue analysis (see Section 7.3.6.1), the values of the natural frequency obtained from the first five modes are 5.67 Hz, 29.52 Hz, and 42.23 Hz, 71.10 Hz and 116.102 Hz, respectively. The corresponding periods are T_n = 0.18 s, 0.034 s, 0.024 s, 0.014 s, and 0.009 s, respectively. The maximum frequency of the artificially generated earthquake is f'_{max} = 33.33 Hz (see Table 7.2). Therefore, it depends upon which higher modes are considered in this study, the time step size is assume to be chosen accordingly with reference to $\Delta t = (1/10 - 1/20)T_n$, T_n/π and $0.5/f_{max}$. For the consideration of $0.5/f_{max}$, the limiting time step size is about 0.004 s. The time step size chosen accordingly with reference to $\Delta t = (1/10 - 1/20)T_n$ and T_n/π for the first five modes is shown in Table 7.3. In this study, a time step size of 0.005 s is chosen after many pilot runs with different time step sizes. Although this time step is slightly larger than the time step $\Delta t = (1/10 - 1/20)T_n$ (Table 7.3) for capturing the second mode and $0.5/f_{max}$ for the frequency content of earthquake, it is chosen in order to reduce the computational effort required for the analyses. However, we will show that this time step is able to capture the pier responses with a reasonable accurate solution up to the second mode.

In order to obtain further understandings about how the responses for possible higher modes are being captured, even smaller time steps were considered. Therefore, smaller time step sizes are also applied to calculate the responses of the bridge pier subject to 20 artificial time-histories. In particular, the third and fourth modes are taken to be the highest mode required, respectively, and therefore time step sizes of 0.002 s and 0.001 s are chosen which are assumed to be satisfied the maximum range of 0.0024 s and 0.0014 s, respectively, according to the condition $\Delta t = T_n/10$; or at least the third mode is taken with the time step of 0.001 s which is assumed to have satisfied the maximum range of 0.0012 s according to the condition $\Delta t = T_n/20$ (see also Table 7.3). The

responses of the bridge pier subjected to 20 artificial time-histories using step sizes of 0.005, 0.002, and 0.001s (with 5% Rayleigh damping) were calculated. It was found that though these time steps are small, there is still some different between their responses. The essential reason is because there is an error in the integration time step and that the larger the time step is, the larger the error is. The errors in the numerical integration can be measured in terms of period elongation and amplitude decay (Bathe 1982). For example, there exists the amplitude decay in the relative displacements using time step of 0.005s and this would effectively "filters" the high mode response out of the solution. In fact, the normalised cumulative spectrum (see Section 7.3.5.3) for relative acceleration, velocity and displacement responses showed that there is more higher frequency content for time step of 0.002 s than those of 0.005 s (see Chapter 8, and Figure 8.2). Thus, the results using time step sizes of 0.002 and 0.001 s have more accurate integration, i.e. less numerical damping for the high mode responses.

These observations demonstrate that using different time step sizes have caused some difference in the responses and it can be measured in terms of the high frequency content. The response using time step of 0.005 s have more integration error than those using time steps of 0.002 and 0.001 s because it cannot capture some high frequencies. However, it can be clearly seen that the time step of 0.005 s is small enough to obtain reasonable results for practical purposes up to the second natural mode as demonstrated in Section 7.3.6.3. On the other hand, also with Fourier analysis, it shows that even smaller time steps, i.e. 0.002 and 0.001 s are used, the second natural mode can also be captured but higher mode responses, i.e. third and fourth modes, are not evident although the response using the small time steps contain some higher frequency content. Therefore, if the third mode of vibration is to be accurately obtained, a very small time step should carefully be considered as explained above. This could make the analysis very complicated, time consuming and totally not suitable for practice. For example, in order to perform all non-linear dynamic analyses with time step of 0.002 s including parametric studies for this chapter, there are about 500 analyses (25 cases x 20 earthquakes) needed to be performed. As one analysis takes nearly 8 hours, calculation time for all analyses will be about consecutive 4000 hours (nearly 6 months) on a Pentium IV 1Ghz - PC, so it is not particularly effective (the calculation time for all analyses using time step of 0.005 s is about a half of that). In fact, it is

noted that the considerations of higher modes for the bridge pier may just only be considered to be rather theoretical, because in a practical analysis the higher modes of a bridge pier, i.e. third or four modes, should be negligible for the integration time step to be realistic. In addition, it should also be noted that in order to integrate accurately the response in even higher frequencies, this may require a very small time step (e.g. < 0.001 s). But the accurate integration of high-frequency response predicted by the finite element assemblage is in many cases not justified for practical reasons and therefore not necessary (Bathe 1982).

In addition, the use of constant damping ratio for the two frequencies to calculate Rayleigh damping as shown in Equations (7.2) and (7.3) may also affect the structural response. In this sense, it could also be explained that the difference between the results of time step of 0.005, 0.002 and 0.001 s that may happen could be due to the fact that the resulting damping for the higher frequencies from the Rayleigh damping ratio used is too small. Therefore, the more high frequency content in the responses obtained with time steps of 0.002 and 0.001 s are evident because the higher modes are not damped sufficiently using Rayleigh damping. The energy dissipation due to the concrete model is not effective for small cycles as both the unloading and reloading are mostly elastic. The reason is because in this study we can only use constant damping ratio for the two frequencies to calculate Rayleigh damping as shown in Equations (7.2) and (7.3). This sometimes results in unrealistic results because it does not capture properly the way inelastic and hysteretic response of the bridge pier dissipates energy especially for higher modes. In reality, this dissipation should result in a more rapid increase of damping ratio with frequency. Physical experimental studies often show that damping ratios of various solid materials increase with frequency over a finite bandwidth (Prange 1977, Pritz 2004). This implies that damping is too small and not increasing with frequency fast enough when Rayleigh damping is used. This may cause some difference to the results of time steps of 0.005 s and 0.002 and 0.001 s. Based on the these observations, it could be concluded that the Rayleigh damping used is not a good presentation of real material damping therefore even the converged results for small time steps, i.e. 0.002 and 0.001 s or smaller, is not a good presentation of the real behaviour of the RC pier. In this manner, the use of a larger time step (Δt = 0.005 s) in this study introduces

extra numerical damping to the higher modes and this could in some ways compensate the lack of adequate damping produced by Rayleigh damping for the higher modes.

To summarise, with the Rayleigh damping and the two natural frequencies present, the time step of 0.005 s is small enough to give reasonable results for practical purposes up to the second natural modes and significantly reduce the computational effort for large number of analyses required in this chapter. Therefore, the time step size of 0.005 s will be adopted in all the later studies.

7.3.4.4 Newmark's parameters

The two Newmark's parameters α and β can be varied to obtain optimum stability and accuracy. The integration scheme is unconditionally stable provided that $2\alpha \geq \beta \geq 0.5$ and according to Bathe (1982), the optimal choice is $\alpha = 0.25(\beta + 0.5)^2$, therefore, in this study, α = 0.3025 and β = 0.6 are chosen in order to obtain integration with good accuracy and unconditional stability as well as some numerical damping to damp out spurious numerical oscillations (Wood 1990).

7.3.4.5 Viscous damping ratio

In this study, the value of viscous damping is assumed to be ξ = 0.05 for most of RC structures (Priestley *et al.* 1996, Wilson 2002) and the two natural circular frequencies adopted in the above calculation are 5.67 Hz and 29.52 Hz which are the first two fundamental frequencies obtained from the eigenvalue analysis (see Section 7.3.6.1). Thus the values of α and β can be calculated from Equation (7.3) to be 2.98 and 0.00045, respectively. Due to the characteristics of Rayleigh damping, the damping ratio will be less than 0.05 for frequencies between 5.67 Hz and 29.52 Hz.

7.3.5 Analysis model

The LUSAS Multi-crack model and time stepping dynamic analysis are used to obtain the response of the bridge pier under artificial time-histories. Several techniques including Fourier analysis, normalised cumulative spectrum analysis, energy dissipation, and damage index analysis have been selected in order to obtain representative number of non-linear dynamic analysis and to quantify damage in the pier for different artificial time-histories.

7.3.5.1 Eigenvalue analysis

Eigenvalue analysis is also used because it can provide the natural frequencies of the linear system before degradation. The eigenvalue calculation is available in the program LUSAS so it can be used straight away to calculate the natural frequencies. The natural frequencies obtained from this analysis can be used to compare with the one obtained from the time stepping non-linear dynamic analysis for the steady state vibration. In this work, the eigenvalues and eigenvectors of the first two modes have been considered to be sufficient and have been evaluated. The following equation is used for the eigenvalue analysis:

$$[[K] - \omega_n^2[M]] = 0 \tag{7.7}$$

where K and M are the linear elastic stiffness and mass matrices and ω_n is the natural circular frequency of the nth mode. Due to the nature of the eigenvalue analysis, only the stiffness matrix at a particular incidence such as linear elastic material behaviour can be used. Even though eigenvalue analysis can also be performed for damaged stiffness matrix, LUSAS does not provide this opportunity at the moment. Also, the exact composition of the damaged stiffness matrix is path-dependent making it difficult to obtain the exact value of the natural frequencies of the damaged structure.

7.3.5.2 Fourier analysis

The Fourier analysis is also used because it can be used to transform the seismic excitation data and results from the time domain to frequency domain. In analysing a structure under dynamic loading, the frequency response of the structure is usually regarded to be very important because it tells us how much response at a particular frequency is present in the time domain. In this work, the results obtained from the time stepping dynamic analysis are transformed into the frequency domain using this analysis. The following equation is used for the Fourier analysis.

$$U(\omega) = \int_{-\infty}^{+\infty} a(t) e^{-i\omega t} dt \tag{7.8}$$

where $a(t)$ is the response, for instance, acceleration response, in the time domain and $U(\omega)$ is the Fourier spectrum in the frequency domain.

7.3.5.3 Cumulative spectrum analysis

The structural responses under different artificial earthquakes can sometimes be difficult to distinguish between them as the response values are very random in time or frequency domain. However, the total power of a response in time or frequency domain is very smooth because it cumulates the response amplitudes at a specific time or frequency. Therefore, the total power of a response (it is called "cumulative spectrum" in this study for reason to be explained later) is also used for comparison between the structural responses under different earthquakes. The cumulative spectrum P_i at a specific circular frequency ω_i is calculated as the total power of the "periodic" motion:

$$P_i = \sum_{i=1}^{n} \frac{A_i^2}{2} \tag{7.9}$$

In which A_i = the Fourier amplitude of the response at frequency ω_i

In accordance with the acceleration, velocity and displacement responses, we have the acceleration, velocity and displacement cumulative spectra, respectively. The cumulative spectrum for displacement is the same as its power spectrum but this is not true for velocity and acceleration. To clearly observe the comparison between cumulative spectra of different sets of

responses, resulting cumulative spectra are then normalised such that they all have unit ordinate at the highest frequency. The cumulative spectrum is normalised by dividing all cumulative spectral amplitudes by the final cumulative value, then the final cumulative value will have the value of unity and all other values will be a fraction of that. The normalised cumulative spectra will be used for comparison of different time history responses in this chapter.

7.3.5.4 Energy dissipation

The cumulative energy dissipation is represented by the area of the force-displacement hysteretic loop. The cumulative energy dissipation (E) in the structure at any time t can be determined as:

$$E = \int_0^t dE \tag{7.10}$$

In which, dE is the increment of energy dissipation.

As the time step used in the non-linear dynamic analysis is very small (e.g. Δt = 0.005 seconds), the segment connecting two successive points in the load-displacement loop is almost linear. Thus, a trapezoid rule numerical integration is used to evaluate the integral in Equation (7.10) to determine the cumulative energy dissipation E.

7.3.5.5 Damage index analysis

The Park-Ang model (1985) was selected for this study (see Section 7.2.2.3). According to this model, the seismic damage can be expressed as a linear combination of the damage caused by maximum inelastic deformation and cumulative dissipated energy through a damage index:

$$D = \frac{\delta_m}{\delta_u} + \frac{\beta}{Q_y \delta_u} \int_0^t dE \tag{7.11}$$

Where δ_m is the maximum displacement reached in the current cyclic loading; δ_u is the ultimate displacement under monotonic load; β is the structural parameter dependent on several structural

parameters; Q_y is the yield strength; $\int_0^t dE$ is the cumulative dissipated energy; and D is the damage index.

The maximum displacement δ_m and the cumulative dissipated energy $\int_0^t dE$ are dependent on the loading history and their values at any time or any cycle can be accurately obtained from the hysteretic behaviour. In particular, $\int_0^t dE$ is determined as shown in the previous section. The other three parameters, β, Q_y and δ_u, specify the structural capacity, not depends on the loading history.

In order to obtain an expression for the structural parameter β, Park and Ang (1985) used a significant amount of observed seismic damage from experimental data. On the basic of a trial-and-error procedure, they found that the value of β is a function of the shear span ratio, axial stress, and longitudinal steel ratio. The reported value of β ranged from -0.3 to 1.2 with an average of about 0.15 (Park *et al*. 1984, Park and Ang 1985). Since the cumulative damage is dependent on the β value, a small β value leads to a low damage index. Therefore, RC structures that possess high β value are subjected to high damage due to a high effect of the cumulative damage. Park *et al.* (1987) suggested a rather smaller β value of 0.05 for reinforced concrete structures while Williams *et al.* (1997) mentioned that a value of approximately 0.1 is appropriate for well-reinforced concrete structures. The value of β = 0.11 - 0.15 has been chosen as a mean value to represent typical reinforcement details (Usami and Kumar 1996, Stone and Taylor 1992, Ciampoli *et al.* 1989, Chai *et al.* 1995). In this study, the parameter β is assumed to be 0.05 as suggested by Park *et al.* (1987).

The values of Q_y and δ_u can be approximately found from the numerical load-displacement curve for monotonic loading. However, there appears to be no reliable method for determining ultimate displacement of reinforced concrete members δ_u, especially when shear displacement and bond

slippage may be dominant. Even highly sophisticated FE analysis cannot trace the displacement up to ultimate stage in every case because of uncertainties in dowel action, shear cracking, concrete crushing, bond deterioration, and computational difficulties (Park and Ang 1985). In this study, the bridge pier is modelled by using LUSAS Multi-crack model for concrete and is tested under static monotonic loading in order to determine the values of Q_y and δ_u. A complete load-displacement result, unfortunately, cannot be produced at this stage because the analysis failed to converge at the maximum linear elastic behaviour (see for example Figure 7.4). Various necessary steps including reducing the time step, increasing the number of iteration, and adjusting the control parameters were taken in order to solve the problem. The arc-length method was also used in some analyses. Unfortunately, these steps were not able to solve this problem. The reason may be due to the pier is too brittle (the steel ratio is small and the pier length is long in comparison with the pier width) and therefore it causes a sudden failure in the response. Therefore, the value of load at the maximum linear elastic behaviour, Q_y = 820 kN, from Figure 7.4, is taken for the damage study but there is no loss of generality for the objectives of this study, since Q_y is the structural capacity index and it is the same for the bridge pier under different earthquake time-histories. In addition, a value $\delta_u = 4.0\delta_y$, is assumed as referred to Shome *et al.* (1998), in which δ_y is the yield displacement and is taken as the displacement at maximum linear elastic point, δ_y = 10.50 mm from Figure 7.4. Thus, $\delta_u = 4.0\delta_y$ = 42 mm is used. A simple calculation using analytical solution (results not shown) confirms that the values of Q_y = 820 kN and δ_y = 10.50 mm at the maximum behaviour is accurate.

7.3.6 Results of analysis

7.3.6.1 Eigenvalue analysis

From the eigenvalue analysis, the natural frequencies of the first three modes (Clough and Penzien 1975) are 5.67 Hz, 29.52 Hz, and 42.23 Hz, respectively. Therefore, the fundamental period can be found to be approximately 0.18 s. This result can be compared with that obtained from the time stepping non-linear analysis and the Fourier analysis in later sections.

7.3.6.2 Time stepping analysis

In this study, a set of 20 artificial earthquake time-histories (Appendix 7A) generated with the characteristics shown in Table 7.2 are used to analyse the bridge pier. This representative number of ground motion time-histories has been suggested to use at the beginning for a non-linear dynamic analysis in some existing publications (Shome *et al.* 1998, Kurama and Farrow 2003). While this number is larger than and hence unrepresentative of current practice, it assures more accurate estimates, and thus firm general conclusions (Shome *et al.* 1998). Although this number is used, it will be checked again in terms of probability concepts in the section of damage analysis (Section 7.3.6.7).

The non-linear dynamic analysis employs the appropriate integration scheme in which the integration solution, time step, finite element mesh, numerical damping and viscous damping are selected as presented in Section 7.3.4.

The relative displacements at the top of the bridge pier were obtained from numerical analysis for 20 artificial time-histories (Appendix 7B), in which they are numbered from 1 to 20, respectively, in the same numerical order as the input artificial earthquakes. Here only the first five displacement responses are presented, as shown in Figure 7.5. It can be seen that under different time-histories, even though all of them were generated from the same EC8RS, the non-linear responses of the bridge pier are very different because each time history has its own earthquake characteristics, including magnitude for each frequency and the phase angle. Generally, the bridge pier initially oscillated from side to side but it eventually started tilting to one dominant side with its residual displacements (e.g. after 2.5 - 7.0 seconds of vibrating). However, some of them do not have a residual displacement at the end of vibration, i.e. earthquakes 3, 12, 19 and 20 (Appendix 7B), as the pier behaviour would mainly be elastic.

By analysing the free vibration motion in the relative displacements (Figure 7.5) at the end of the earthquake, it can be seen that the natural frequency is about 5.6 ~ 6.0 Hz. Therefore, the fundamental period can be calculated to be 0.17 ~ 0.18 seconds. With reference to Section

7.3.6.1, it can be seen that the results obtained from the eigenvalue analysis and the time stepping analysis agree with each other. It means that at the end of the analysis, the behaviour is almost elastic. This is because the unloading and reloading behaviour in the LUSAS Multi-crack model are linear elastic. However, it can generally be observed from the responses that the Multi-crack model is capable of capturing the key non-linear behaviours under earthquake time-histories, i.e. elongated periods and hysteretic behaviour in load-displacement (see also Chapter 5). Although in the model stiffness degradation is not included at a Gauss point level, it still includes plasticity behaviour so there is an overall stiffness degradation of the bridge pier and therefore it can capture the global stiffness degradation under earthquake loading.

In order to understand the vibratory responses for different time-histories in details, a study which focuses upon the relative displacement responses at the top of the pier is presented here. There is no loss of generality for this study to limit the investigation to the first three earthquakes in the vibration range of 0.0 to 5.0 seconds. The responses are shown in Figures 7.6(a) and 7.6(b), in which they are presented in pairs between earthquakes 1 and 2, and earthquakes 2 and 3, respectively. It can be seen from Figure 7.6(a) that under earthquake 1 and 2, the top pier starts to vibrate on the same one-side at around 2.4 seconds and 3.3 seconds, respectively, and does not come back to its initial position afterwards. It can also be seen that under earthquake 1, the pier vibrates in longer periods than that under earthquake 2. The period is calculated using the following method: in the first 5 seconds, there is 25 cycles of vibration for the first response, and 29 cycles for the second response. The reason for that is due to the pier has more global stiffness degradation under earthquake 1 than that under earthquake 2. It could be due to earthquake 1 has higher amplitudes than that of earthquake 2. As the residual displacement obtained at the pier top during earthquake 1 is larger than that of earthquake 2, this also shows that there is an increase in the accumulation of damage in the pier. Again, this is due to global stiffness degradation. These observations above also imply that the pier sustained more damage under earthquake 1 than under earthquake 2. Figure 7.6(c) shows the damage index, i.e. calculated from Equation (7.11), of the pier under all three earthquakes, and it clearly confirms the above conclusion. Only the result of damage index is presented here, more details about damage index analysis will be provided in the later sections.

The responses under earthquakes 2 and 3 are shown in Figure 7.6(b). It can be seen that under earthquakes 2 and 3, the pier vibrates almost at the same frequency and the number of cycles for the first and second responses are 28 and 29, respectively. However, the response under earthquake 2 results in residual displacements to one side after 3.3 seconds while that under earthquake 3 remains vibrating about zero displacements. In the first 3 seconds, the two responses have the same number of cycles, i.e. 17, but the response under earthquake 3 has higher relative displacement amplitude and thus higher plastic strain. Therefore, in the first 3 seconds, the pier under earthquake 3 has suffered more damage than under earthquake 2. In the next 2 seconds, the amplitude of relative displacement under earthquake 2 is much higher than that of earthquake 3. Thus the pier under earthquake 2 has sustained more damage then. As damage is cumulated within time, the pier under earthquake 2, thus, sustained that under earthquake 3, at end of the first 5 seconds. This conclusion can be confirmed in Figure 7.6(c) which compares the damage index for the pier under various earthquakes.

Discussions

The non-linear dynamic responses of the bridge pier under 20 artificial earthquakes have been obtained using the numerical time stepping analysis. The relative displacement responses under the first three earthquakes are compared in detail. It can be seen that the response of the bridge pier under different artificial earthquakes generated from the same EC8 RS, are quite different in terms of vibration periods, the number of vibration cycles, and magnitudes. It is because under different earthquakes, the bridge pier experiences different mechanical degradation for which the material consistency and structural properties undergo different changes. This is reflected in the difference in the vibratory response of the pier. That also means that, at same instance in time, the dissipated energy and damage of the pier are different under different earthquakes. It can be noted that there is a relationship between them, that the longer the structural period and/or the higher the amplitude of relative displacement, the higher the damage in the bridge pier. Similar observations were also reported by Beshara and Virdi (1991), Sucuoglu and Erberik (2004).

It can be concluded that the Multi-crack model and time stepping analysis is generally capable of modelling the non-linear dynamic response of the bridge pier under artificial earthquakes. The vibratory analysis based on the numerical results can be used as a useful tool to assess the responses under different artificial earthquakes. The observations obtained from vibratory analysis completely agree with those obtained from damage analysis that the longer the structural period and/or the higher the amplitude of relative displacement, the higher the damage in the bridge pier.

7.3.6.3 Fourier analysis

The responses in frequency domain are obtained by transforming the acceleration responses using a FORTRAN program. The program incorporated Fast Fourier Transforms subroutine from Press *et al*. (1992).

Twenty frequency spectra of the bridge pier obtained from the acceleration responses of the pier for the range of 0 and 100 Hz are shown in Appendix 7C. It can be seen from the Appendix 7C that the frequency spectra show the first spike in the range of 5.4 ~ 6.0 Hz. The second spike can be found in most of frequency spectra at around 25 ~ 30 Hz although in some other spectra, i.e. under earthquakes 3, 12, 19 and 20, this spike does not emerge clearly. These natural frequencies show very good agreement with those obtained from eigenvalue analysis (5.67 Hz and 29.52 Hz for the first and second modes, respectively). In order to see more clearly these spikes in the frequency space, an average spectrum of several frequency spectra are calculated so that the random elements in each individual spectrum is compensated by combining as many as possible individual spectra. Therefore, an average spectrum of 20 frequency spectra is plotted as shown in Figure 7.7. It can be seen from the figure that the first and second spikes emerge from the frequency spectrum with frequencies of 5.85 Hz and 28.42 Hz, respectively. These values are in good agreement with the natural frequencies obtained from eigenvalue analysis in 7.3.6.1. It can also be seen that the first mode dominates the behaviour of the bridge pier under artificial earthquakes but the second mode is slightly evident. In addition, it can also be seen that the third mode of vibration is not evident for the bridge pier as mentioned in Section 7.3.4.3.

Figures 7.8(a) - 7.8(f) show the comparisons between the average of 3, 5, 10, 12, 15 and 16 acceleration spectra with the total number analysed, i.e. 20 acceleration spectra (the average of all frequency spectra of 2 to 20 are calculated and examined but only the above averages are shown here, and this is the same for later studies). Generally, it can be seen that the more acceleration spectra used to perform the average, the closer is the average spectra to the average of 20. The average of 3 and 5 acceleration spectra are very coarse compared with that of 20 acceleration spectra (Figures 7.8(a) and 7.8(b)) while the average of 10 and more acceleration spectra seems to be close to that of 20 acceleration spectra (Figures 7.8(c) - 7.8(f)). In order to examine the difference in details, Table 7.4, as an example, shows the values of the spectral amplitude of the average of 3, 5, 10, 12, 15, 16 and 20 acceleration spectra at some particular frequencies. It can be seen from this table that, the convergent values of the average spectral amplitudes can be found when the number of acceleration spectra is about 10 to 12. Especially, the comparison shows very good convergence when the number of acceleration spectra is about 15 or 16.

7.3.6.4 Cumulative spectrum analysis

Figures 7.9(a) - 7.9(f), respectively, show the comparisons between the average of 3, 5, 10, 12, 15 and 16 normalised displacement cumulative spectra (NDCS) with the average of 20. The average of NDCS is the most important because it expresses the representative power of the displacement response contributed with frequencies. The maximum and minimum of NDCS are also plotted in the same figures to give extra information about the extremes and range of the values. However, they are not as important as the average one because they place too much emphasis on the extremes and neglect the bulk of the data which lies within the extremes. The average, maximum, and minimum of normalised cumulative spectra in terms of acceleration and velocity are also calculated but only the NDCS is shown here because they showed the same behaviour in convergent results.

For the comparison between pairs of different averages of NDCS and the average of 20 NDCS, it is clear that the averages of 3 and 5 NDCS are different from that of 20 NDCS (Figures 7.9(a)

and 7.9(b)). The same observations can be found for the maximum and minimum NDCS. Figures 7.9(c) - 7.9(f) illustrate that the average, maximum and minimum NDCS of 10, 12, 15 and 16 are close to the NDCS of 20. It can be said that the minimum number of earthquakes to be used for the convergent values of NDCS is again about 10 to 12. Especially, when the number of earthquakes used is about 15 or 16, a very good convergence can be found. This observation is similar to the one made in Fourier analysis in Section 7.3.6.3.

7.3.6.5 Energy Dissipation

The cumulative energies dissipated through the bridge pier subjected to 20 artificial time-histories are also obtained, and the energy dissipation histories are given in Appendix 7D. The amount of energy dissipated up to a certain time during the earthquake is determined by the cumulative area of the force-displacement hysteretic loop generated up to that time. The figures indicates that during the some first seconds of vibration, the behaviour of the bridge pier is linear elastic and therefore there is no energy dissipated through the pier except Rayleigh damping and numerical damping due to the Newmark time stepping scheme. After that, the dissipated energy gradually increases with time. The cumulatively dissipated energy rapidly increases after few seconds because of large relative displacement or plastic strain. The reason is due to the structural degradation in the bridge pier such as the global stiffness. The cumulative dissipated energy then reaches the maximum value at around 10 - 14 seconds where its steady state free vibration almost takes over. The steady state free vibration is the reason why the energy dissipation is constant at the end of the earthquake excitation. The zero further energy dissipation means that the free vibration, as expected for the Multi-crack model, is linear elastic.

The comparisons between the average, maximum, and minimum of 3, 5, 10, 12, 15, 16 and 20 energy dissipation histories (EDH) were investigated but not shown here. It was found that the conclusions about the number of EDH, which converged to those of 20 EDH, are similar to those of damage index histories as studied next. Also, the case of damage index histories is more general than because it contains the energy dissipation histories. For that reason, the comparisons

between the average, maximum, and minimum of 3, 5, 10, 12, 15, 16 and 20 damage index histories are presented here.

7.3.6.6 Damage index analysis

Figure 7.10 shows five typical damage index histories calculated from Equation (7.11) of the bridge pier when subjected to the first five artificial time-histories. The results of 20 damage index histories are calculated and shown in Appendix 7E. As the damage index history is a linear combination of the maximum displacement from the displacement history and the energy dissipation history, it shows the capacity of the bridge pier to undergo inelastic deformations and dissipate energy during an earthquake excitation.

Figures 7.11(a) - 7.11(f) respectively show the comparisons between the average, maximum, and minimum damage index histories (DIH) of 3, 5, 10, 12, 15, 16 and 20 earthquakes used. It can be seen from the figures that the results of 3 and 5 DIH are obviously not sufficient to be representative for 20 DIH because their values are quite different from those of 20 DIH, especially for the maximum and minimum ones (Figures 7.11(a) - 7.11(b)). It can also be seen from Figures 7.11(c) - 7.11(f) that the maximum and minimum DIH of 10, 12, 15, and 16 earthquakes are closer and smoother to that of 20, respectively. The average DIH of 10, 12, 15 and 16 are also smoother and closer to that of 20 though there is still a gap between them after 5.0 seconds. The convergence in the results in terms of average, maximum, and minimum values can be found when the number of earthquakes used is from 16 (Figure 7.11(f)). Again, this observation is similar to those observed in Fourier, cumulative spectrum and energy dissipation analyses.

It is important to note here that the conclusion about the number of time-histories suggested for use in non-linear analysis as observed in the above studies is quite reasonable. It is very useful that the whole progress of the structural responses in time and frequency domain is investigated. However, it is a little rough because the comparison is totally based on the visual observation and there is no particular criteria applied for checking the quantitative difference between the average

(or maximum or minimum) of different responses. Nevertheless, in the above studies, we assumed that the responses are grouped into sets in an order from 1 to 20 in consistent with the input artificial time-histories numbered from 1 to 20. It can be questioned that should the same suggested number of representative responses be obtained if the order of the responses is grouped in any arbitrary order?

The damage index technique shall be used further in detail to address directly the issue about the number of artificial time-histories to be used so that the results would be representative of the typical behaviour of a predefined earthquake event. Different orders of the responses of the bridge pier subjected to different number of artificial time-histories to perform the average of damage index are also included in the study.

7.3.6.7 Representative number of non-linear dynamic analysis

In the following part of this chapter, the averages of different responses of the bridge pier subjected to different number of artificial time-histories will be calculated and compared in a quantitative manner by using the criterion of damage index. It is noted that the most important parameter to be addressed is the damage in the bridge pier at the end of an earthquake excitation because it determines the seismic capacity remained in the pier. Therefore only the damage indices at the end of the artificial earthquakes are extracted for this study. The damage indices of different sets of earthquakes at any time during earthquake events can be easily obtained and inspected by the same procedure but it needs not necessarily be done as the Author reckons that the conclusions drawn would be similar.

Table 7.5 shows the damage indices in the bridge pier obtained at the end of the 20 artificial time-histories which were numbered from 1 to 20, and they are also shown in Figure 7.12. It can be seen from the figure that there are many different damage index values distributed around a value of about 0.70 - 0.80.

In the present study, the primary interest is in a "best estimate" of the damage indices of the bridge pier subjected to 20 artificial time-histories. For this purpose, we shall use the mean in Statistics for the damage index data (see Appendix 7F for reference on how to calculate the mean, μ). This best estimate should be unbiased with the minimum variance possible for the effort as measured by computation time. The minimum variance objective ensures the narrowest possible confidence band on the mean and therefore reduces the number of non-linear structural analyses required to achieve a desire level of accuracy. We also have an interest in estimating a measure of dispersion or standard deviation of the damage index data (see Appendix 7F for reference on how to calculate the dispersion, δ). Hence, the damage indices within the "± one-sigma confidence band" (or "± 1.00σ confidence band") as defined in Statistics and Probability will be expressed as $\mu \pm 1.00\ \sigma$ or $\mu \pm 1.00 \times \frac{\delta}{\sqrt{n}}$, in which n = 20 is the number of artificial time-histories. In addition, the "standard error of estimation", Δ, which is approximately the dispersion expressed as percentage and divided by $\sqrt{n}$ or 4.5, is also used as percentage of the mean. So, for example, if the sample data has n = 20, the mean μ = 0.71 and the dispersion δ = 0.25, the standard error of estimation Δ is calculated as $\frac{\delta}{\sqrt{n}} \times 100(\%) = \frac{0.25}{\sqrt{20}} \times 100(\%)$ = 5.68 (%). Thus the "± 1.00σ confidence band" on the mean is 0.71 ± 1.00 x 5.68 (%) or 0.65 to 0.77. In practical cases, an estimate of δ is needed, for example, a relevant design basis may call for an "84 percentile demand" or "84 percent confidence level" (Cornell *et al*. 2002, Shome *et al.* 1998).

In this study, we shall find the number of non-linear structural analyses required to allow their mean lying in 4 specified damage confidence bands from the mean of 20 analyses: (i) "68 percent confidence band", (ii) "84 percent confidence band", (iii) "90 percent confident band", and (iv) "95 percent confidence band", which, alternatively, we shall called the "± 1.00σ confidence band", "± 1.40σ confidence band", "± 1.64σ confidence band", and, "± 1.96σ confidence band", respectively. It should be noted that the mean and dispersion of the distribution obtained using 20 earthquakes are μ and δ respectively, and they are used as references to determine a particular confidence band or a corresponding number of earthquakes. As clearly shown in Figure 7.13(a),

when the "confidence band" is narrow, i.e. "± 1.00σ confidence band" or "68 percent confidence band", the range of the mean of damage indices is also narrow, i.e. within the area inside $\mu \pm 1.00 \times \frac{\delta}{\sqrt{n}}$ and under the normal distribution. Therefore, a large number of earthquakes are required so as their damage means are within the band $\mu \pm 1.00 \times \frac{\delta}{\sqrt{n}}$. In contrast, when the "confidence band" is larger, i.e. "± 1.96σ confidence band" or "95 percent confidence band", as shown in Figure 7.13(b), the range of the mean of damage indices is larger and therefore, a smaller number of earthquakes are required. It can be concluded that less number of earthquakes is needed for the higher confidence band on the mean of damage of 20 earthquakes. But it does not cause any conflicting meaning as a higher confidence band always leads to a large range of the mean of damage indices (see also Table 7.6 and later sections). In other words, the terminology "higher confidence band" used in this thesis totally does not mean higher confidence in the band and the values obtained. In order to avoid the misunderstanding we can use the terminology "wider confidence band" instead.

We have mentioned the dispersion measure of an observed damage indices which can show us a confidence band for the mean of the 20 earthquakes. However, the confidence bands we expect have to be based on the normal distribution. In order to check if the damage data exhibits the properties of a normal distribution, the normal probability plot and normal distribution (see Appendix 7G) are performed. The "Normal Probability Plot" in z-scores is shown in Appendix 7H. This graph shows that the points are indeed very close to a straight line and the correlation coefficient is very high (R^2 = 0.91). Also, Appendix 7H shows the normal distribution expressed in terms of Probability Mass Function (PMF) and Cumulative Distribution Function (CDF). This graph indicates that the distribution follows standard shape of normal distribution in Statistics (Benjamin and Cornell 1970). From the two figures in Appendix 7H, it is clear that the damage indices of the RC behaviour under the 20 earthquakes exhibit properties that are close to a normal distribution. Therefore the statistical techniques could be applied with high confidence. Particularly, the mean of 20 damage responses (μ) is the same as the mean of a population, or very large number, of responses. In addition, it is simple to check that in this study, the dispersion

of 20 damage responses (δ = 0.25) is approximate the dispersion of a population of responses (δ_0 = 0.248). Therefore, it confirms that a set of 20 artificial time-histories are large enough to be used as representative inputs for this study, as mentioned at the beginning.

In this study, we look at the mean (μ) and dispersion (δ) for sets of damage indices from 2 to 20 and try to find which sets that have the mean within one of four confidence bands of accuracy as mentioned above. There are many different orders of picking up a set of different damage responses from 20 possibilities. For example, a combination calculation shows that there are 3628800 orders to choose the order of a set of 10 damage responses. In the later parts in this chapter, a very large number of different orders will be selected in a random manner to see how different ordering can affect the results.

7.3.6.7.1 Some typical cases

We shall first look at some "typical orders" of arranging the damage indices:

1. Order-I: From top to bottom

1-2-3-4-5-6-7-8-9-10-11-12-13-14-15-16-17-18-19-20

2. Order-II: From bottom to top

20-19-18-17-16-15-14-13-12-11-10-9-8-7-6-5-4-3-2-1

3. Order-III: From middle to bottom

10-11-12-13-14-15-16-17-18-19-20-9-8-7-6-5-4-3-2-1

4. Order-IV: From middle to bottom

14-15-16-17-18-19-20-1-2-3-4-5-6-7-8-9-10-11-12-13

The mean of damage indices for different numbers of non-linear dynamic analyses in the four orders are illustrated in Figure 7.14. It is clear that when the number of analyses is small, the mean values are very random and different from each order; when the number of analyses used is large enough to the maximum of 20, the mean values are less random and convergent to lie in a narrow band. For example, when the number of analyses used is about 7, the mean damage values (from 4 different orders) seem to stably lying within a band of 0.67 and 0.80.

The values of damage index of the bridge pier subjected to artificial earthquakes of Order-I, Order-II, Order-III and Order-IV are shown in Tables 7.6(a), 7.6(b), 7.6(c) and 7.6(d), respectively. In each of these "orders", the mean (μ), the dispersion (δ) and the standard error of estimation, as percentage of the means (Δ) are calculated for sets of damage indices from 2 to 20 in that order. These values are also shown in Tables 7.6(a) - 7.6(d), respectively. It can be seen from the Tables that the standard error of estimation of the damage measures for sets of 20 damage indices is very small (5.68%), again suggesting that a set of 20 artificial time-histories are large enough to be used as inputs for this study.

For a given acceptable response confidence band width on the mean damage of 20 earthquakes, a necessary number of damage responses (or non-linear dynamic analyses) will be obtained to be lain in this band. For example, the "± one-sigma confidence band" on the mean of 20 damage responses is $0.71 \pm \left(25\%/\sqrt{20}\right)$ or 0.71 ± 5.68% or 0.65 to 0.77. If we look at Order-I, there is a set of 6 or more damage responses will satisfy this band. Similarly, the "± 1.40σ confidence band" is 0.63 to 0.79; the "± 1.64σ confidence band" is 0.62 to 0.80; and the "± 1.96σ confidence band" is 0.60 to 0.82. Based on these confidence bands in each Order, corresponding numbers of damage responses can easily be found. Table 7.7 shows the number of damage responses for 4 different confidence bands in each Order. With the meaning of "confidence band" used throughout this study, it confirms again that for the "wider confidence band" on the mean of damage of 20 earthquakes, less number of earthquakes is needed. It can be seen from Table 7.7 that for the same confidence band, the number of damage responses are different for every ordering. This is due to the different distribution of damage indices in each order. Clearly, the use of a large percentile confidence band has reduced the necessary number of damage responses to a smaller number. There may be a difference in the number of damage responses required for the "± 1.00σ confidence band", and the "± 1.96σ confidence band", for example it is 6 and 5 in Order-I; and 7 and 5 in Order-II. However, the numbers may be the same for different confidence bands as observed in Order-II and Order-IV as 4 and 6, respectively. Again, it is due to the ordering of damage indices in each consideration. From Table 7.7 it can be seen that if a relevant

design basis calls for an "84 percent confidence band", the necessary number of non-linear dynamic analyses required should be chosen to be at 3 to 7 dependent on a particular order.

By comparing the results of Order-I shown in Table 7.7 with the observations in Fourier, power spectrum, and energy dissipation analyses, it can be seen that the later predict a higher number of non-linear dynamic analyses in order to obtain a convergent response. For example, about 10 to 12 non-linear dynamic analyses will give close results while 16 analyses will provide more accurate representation. However, they are only based on visual observations and no quantitative criterion is applied to determine the level of convergence. Different from the others, damage analysis using statistical techniques predict the minimum number of non-linear dynamic analyses necessary in accordance with a confidence band or standard error of estimation. For instance, with an "84 percent confidence band", at least 3 non-linear dynamic analyses should be chosen; and with a "68 percent confidence band" (± one-sigma confidence band), at least 6 non-linear dynamic analyses should be chosen. It should be noted that Fourier, power spectrum, and energy dissipation analyses were conducted only for Order-I.

We also pay attention to the mean of the number of analyses within a particular confidence band for all 4 orders. In order to do that, for each confidence band, we first count the number of non-linear analyses for all 4 orders according to their appearance. Then the mean value is calculated to be 6 (from (6+7+4+6)/4 = 5.75 therefore 6), 5, 5, and 5 in accordance with the "± 1.00σ confidence band", "± 1.40σ confidence band", "± 1.64σ confidence band", and "± 1.96σ confidence band", respectively. (More details about calculating the mean number of analyses for all orders will be presented later in a general case of *N* orders).

7.3.6.7.2 General case

In the above investigation, we have presented the mean number of non-linear dynamic analyses required for 4 different orders. In this part, the mean number for a general case (*N* orderings, with *N* being very large) is required. For generality, we need to (1) find the necessary number of damage responses in a particular confidence band in each of *N* orders, and then (2) calculate the

mean of the number of damage responses for the particular confidence band for all *N* orders. In order to obtain the mean number quickly for any value of *N*, even a very large *N*, a small computer program is written for the calculations for *N* orderings generated using a random number. The FORTRAN code of this program is presented in Appendix 7I.

The mean of the number of damage responses (κ) for a particular confidence band for all *N* orders in the step (2) is calculated from the following:

$$\kappa = \frac{\sum_{i=1}^{n} r_i x_i}{N} \tag{7.12}$$

In which

x_i is the number of damage responses appeared within a confidence band for order *i*

r_i is the number of times x_i appears in a confidence band for order *i*

N is the total number of orders

For example, the "± 1.00σ confidence band" for the four orders shown in Table 7.7 has: $x_1 = 6$, $r_1 = 1$, $x_2 = 7$, $r_2 = 1$, $x_3 = 4$, $r_3 = 1$, and $x_4 = 6$, $r_4 = 1$. Thus the mean number of damage responses for the four Orders is: $\kappa = \frac{\sum_{i=1}^{n} r_i x_i}{N} = \frac{6\times1+7\times1+4\times1+6\times1}{4} = 5.75$ or chose the integer immediately larger i.e. 6. Similarly, the mean number of damage responses within the "± 1.40σ confidence band", "± 1.64σ confidence band", and "± 1.96σ confidence band" are 5, 5, and 4, respectively.

Table 7.8 shows the mean number, κ, of non-linear dynamic analyses for different values of *N*. It can be seen from this table that when *N* is large enough, i.e. $N > 100$, the mean numbers for different *N* appear to converge to the same values. Therefore, it can be concluded that the mean number, κ, is about 11, 8, 7, and 6 in accordance with the "± 1.00σ confidence band", "± 1.40σ confidence band", "± 1.64σ confidence band", and "± 1.96σ confidence band", respectively. This

mean number of damage response is adequate because it satisfactorily covers the number from each individual order (e.g. the number of damage response shown in Table 7.7).

Furthermore, the cumulative distribution of the number of damage responses (or earthquakes) is plotted against the number of different orders for the four confidence bands as illustrated in Figure 7.15. The figure shows that when the number of orders is small, the number of damage responses is therefore small, i.e. 3 or 4, and this observation is in good agreement with the one in the previous section (Section 7.3.6.7.1). It is also clear that with the same number of orders less non-linear dynamic analyses are required when passing from the "± 1.00σ confidence band", to the "± 1.96σ confidence band", respectively. It can be seen that for the "± 1.00σ confidence band", the number of 11 earthquake analyses appears in 6042 orders in a total of 10000, or 60.42% of the total orders. Similarly, the percentage of the appearance of the number of 8 earthquake analyses is 62.46% of the total orders for the "± 1.40σ confidence band"; the percentage of the appearance of the number of 7 earthquake analyses is 66.81% of the total orders for the "± 1.64σ confidence band"; and the percentage of the appearance of the number of 6 earthquake analyses is 71.88% of the total orders "± 1.96σ confidence band". This information from the figure is very useful because any number of earthquakes can be picked up with a particular confidence based on their appearance in the total number of orders used.

7.4 SUMMARY AND CONCLUSIONS

Brief literature reviews

This chapter has presented a literature review on the recommended number of earthquake time-histories and the seismic applications of finite element material models for the non-linear dynamic analysis of RC bridge piers. Also, several techniques suitable for analysing and quantifying the numerical responses under earthquake time-histories have been briefly reviewed. It was concluded that although some efforts have been made within these above areas, successful applications of FE material models and suitable analytical techniques to answer the question about the minimum number of time-histories required for the non-linear dynamic analysis are still

very limited. In particular, there is almost no firm suggestion about the number of artificially generated time-histories.

Numerical analysis

This chapter has then presented a detailed investigation on the numerical analysis of a RC bridge pier using a set of 20 artificial time-histories with the LUSAS Multi-crack model and time stepping analysis. In addition, further checking and understanding of the numerical results have been made by using eigenvalue analysis, Fourier analysis, cumulative spectrum, energy dissipation and damage index techniques. The conclusions obtained for these investigations can be summarised as follows:

(1) The non-linear dynamic response of the bridge pier under artificial earthquakes can be reasonably obtained by using the LUSAS Multi-crack model and time stepping analysis. This could be the first time that the model is successfully employed for seismic applications because the numerical analysis using this model was previously failed after a lot of efforts (Chuang 2001). The success in using the Multi-crack model for seismic applications could be due to the selection of the model's parameters and non-linear procedures as demonstrated in Chapters 4 and 5. It could also be due to the implementation of the earthquake into the analysis. There may be some drawbacks of the numerical results that the dissipated energy and unloading stiffness may have been overestimated because the chief flaw with the model, as mentioned in Chapter 5, is that unloading behaviour in tension is linear elastic which is unrealistic for concrete. However, the model has a plastic response so there is an overall stiffness degradation of the bridge pier. Therefore it is capable of capturing some of the key behaviours under earthquake time-histories, i.e. hysteretic behaviour.

(2) The numerical vibration analysis of the earthquake can be used as a useful tool to assess the responses under different artificial earthquakes. The observations obtained from vibratory analysis completely agree with those obtained from damage analysis.

(3) It can be concluded that the longer the structural period and/or the higher the value of amplitudes of relative displacement, the larger the damage in the bridge pier.

Minimum representative number of artificial time-histories

A crucial part of this chapter was devoted to the proposal for an appropriate minimum number of earthquake time-histories required for the non-linear dynamic analysis. Several techniques including Fourier analysis, cumulative power spectrum, dissipated energy and damage index were employed to analyse and quantify the structural responses for various sets of artificial time-histories. The maximum used was 20 artificial time-histories. An appropriate minimum number of artificial time-histories have then been obtained with respect to the convergence to a representative distribution response from different numbers of artificial time-histories.

Firstly, it was assumed that the 20 artificial time-histories are picked up in sets of a regular order which is numbered from 1 to 20. Several conclusions are presented as follows:

(1) By comparing the average of different numbers of acceleration spectra using Fourier analysis, it has been found that when the minimum required number of time-histories is about 10 to 12, the convergence of the average spectral amplitudes can be obtained. A very good convergence can be found when the number of time-histories is about 15 or 16.
(2) By comparing the average, maximum and minimum of different numbers of normalised cumulative spectra, it has also been found that when the number of time-histories is about 10 to 12, the convergent values of the average spectral amplitudes can be obtained. A very good convergence can be found when the number of time-histories is about 15 or 16.
(3) By comparing the average, maximum and minimum of different numbers of damage index histories, the convergent values of the average spectral amplitudes can be well obtained when the number of time-histories is from 16. However, the number of time-histories is about 10 to 12 can be also considered as the DIH is reasonably smoother and closer to each other.

(4) By comparing the average of different numbers of damage indices, the convergent values of the damage index to lie in a confidence band from the mean of 20 damage indices can be well obtained when the number of time-histories is about 6, 3, 3 and 3 for the "± 1.00σ confidence band", "± 1.40σ confidence band", "± 1.64σ confidence band", and "± 1.96σ confidence band", respectively.

It can be concluded that the representative minimum number of artificial time-histories required for the non-linear dynamic analysis is about 10 to 12 for a practical purpose, and about 16 for a good requirement, according to the Fourier, cumulative spectrum, energy dissipation and damage index techniques. However, it should be noted that except for the results from the damage analysis (and energy dissipation), all comparisons from the results of other techniques are totally based on the visual observation and there is no particular criteria applied for checking the quantitative difference between the averages (or maximum or minimum) of different response spectra. When the damage index is used, it is suggested that the representative minimum number of artificial time-histories required for the non-linear dynamic analysis is chosen based on a particular confidence band from the mean of 20 damage indices, i.e. 6 for the "± 1.00σ confidence band".

Secondly, for more general considerations, it was assumed that the 20 artificial time-histories can be picked up in sets of any possible order. It has been found that the mean number of non-linear dynamic analyses for different values of orders of earthquake N, i.e. $N > 10000$, is about 11, 8, 7, and 6 in accordance with the "± 1.00σ confidence band", "± 1.40σ confidence band", "± 1.64σ confidence band", and "± 1.96σ confidence band", respectively. If in practical design, a relevant design basis calls for the "± 1.40σ confidence band" or "84 percent confidence band", the minimum necessary number of non-linear dynamic analyses, therefore, shall be about 8.

Table 7.1 Summary of guidelines provided by seismic design codes for the use of time-histories in dynamic analysis (Bommer and Ruggeri 2002)

COUNTRY	**YEAR**	**DYNAMIC ANALYSIS**[1]	**RECORDS**[2]	**NUMBER**[3]
Albania	1989	Permitted	Real/Synthetic	Not specified
Algeria	1988	Permitted	Real/Synthetic	Not specified
Argentina	1983	Permitted	All	3 / 4[+]
Australia	1993	Permitted	Real/Synthetic	Not specified
Bulgaria	1987	Permitted	All	Not specified
China	1989	Compulsory	Real/Synthetic	Not specified
Colombia	1984	Permitted	Not specified	Not specified
Costa Rica	1986	Compulsory	All	3
Dominican Rep.	1979	Permitted	Not specified	4
Europe (EC8)	1994	Permitted	All	3 / 5[++]
Egypt	1988	Permitted	Not specified	Not specified
El Salvador	1989	Permitted	Not specified	Not specified
France	1990	Compulsory	All	3
Germany	1990	Permitted	Not specified	Not specified
Greece	1995	Permitted	All	5
Hungary	1978	Permitted	Not specified	Not specified
India	1984	Permitted	Not specified	Not specified
Indonesia	1983	Permitted	Not specified	4
Iran	1988	Compulsory	Real	2
Italy	1996	Compulsory	Real/Synthetic	4
Japan	1981	Permitted	Real/Synthetic	Not specified
Macedonia (FYR)	1995	Compulsory	Not specified	Not specified
Mexico	1995	Permitted	Real/Synthetic	4
New Zealand	1992	Compulsory	Real	3
Peru	1977	Permitted	All	3
Philippines	1992	Permitted	Not specified	Not specified
Portugal	1983	Compulsory	Artificial	<<several>>
Romania	1992	Permitted	All	Not specified
Spain	1994	Permitted	All	3
Turkey	1997	Permitted	Real/Artificial	3
USA (UBC)	1994	Permitted	Real/Synthetic	Not specified
USA (UBC)	1997	Permitted	Real/Synthetic	3
USA (IBC)	2000	Permitted	Real/Synthetic	3

Notes on Table 7.1:

[1] Indicates the requirements for full dynamic analysis (as opposed to spectral modal analysis) in each code: compulsory indicates that dynamic analysis is required for certain types of structure.
[2] The types of records specified: when codes refer to both <<real>> and <<artificial>> it is taken to mean any of three types in the paper (Bommer and Ruggeri 2002), when codes infer that motions must be based on seismological studies or representative of real motion, it is assumed that artificial records are excluded.
[3] The minimum number of records required to be used in analysis:
[+] Four for the highest importance category, three otherwise
[++] Three for real or synthetic records, five for artificial records

Table 7.2 Characteristics for generation of 20 artificial time-histories

Characteristics	**Input values**
Target response spectrum	EC8 velocity RS for $\xi = 0.05$ (prEN1998-1:2004)
Subsoil class	B
Duration	20 (s)
Peak Ground Acceleration (PGA)	0.35g (m/s^2)
Frequency range	0.25 - 33.33 (Hz)
Intensity envelope function	A compound intensity envelope function (Jennings *et al.* 1968)
Generated response spectrum for damping	$\xi = 0.05$
Iteration number	3

Table 7.3 Time step sizes according to the first five modes with reference to $\Delta t = (1/10 – 1/20)T_n$ and T_n/π

f_n (Hz)	5.67	29.52	42.23	71.10	116.10
$\Delta t = T_n/\pi$ (s)	0.057	0.011	0.004	0.0045	0.0029
$\Delta t = T_n/10$ (s)	0.018	0.0034	0.0024	0.0014	0.0009
$\Delta t = T_n/20$ (s)	0.009	0.0017	0.0012	0.0007	0.00045

Table 7.4 Spectral amplitudes of the average acceleration spectra at some frequencies

Frequency	Spectral amplitudes of the average of acceleration spectra						
(Hz)	**3**	**5**	**10**	**12**	**15**	**16**	**20**
1.71	0.01	0.01	0.02	0.03	0.03	0.03	0.03
3.03	0.08	0.06	0.07	0.07	0.07	0.07	0.07
5.47	0.32	0.30	0.40	0.41	0.40	0.40	0.43
5.76	0.64	0.59	0.49	0.51	0.49	0.49	0.49
6.01	0.68	0.55	0.49	0.49	0.46	0.47	0.48
6.30	0.53	0.46	0.43	0.44	0.42	0.41	0.41
6.54	0.25	0.23	0.32	0.32	0.31	0.30	0.33
7.13	0.31	0.31	0.27	0.26	0.24	0.26	0.26
8.50	0.08	0.12	0.14	0.14	0.13	0.13	0.13

Table 7.5 Damage indices in the bridge pier subjected to 20 artificial time histories

Earthquake number	Damage
1	0.89
2	0.84
3	0.31
4	0.71
5	0.51
6	0.82
7	1.07
8	0.75
9	0.94
10	0.56
11	0.85
12	0.28
13	0.99
14	0.90
15	0.74
16	1.01
17	0.69
18	0.79
19	0.30
20	0.28

Table 7.6(a) Damage index results of Order-I. Mean and dispersion of sets of nonlinear dynamic responses

Order-I	Damage	Ω*	μ	δ	Δ** (%)
1	0.89	1	0.89		
2	0.84	2	0.86	0.04	2.69
3	0.31	3	0.68	0.32	18.48
4	0.71	4	0.69	0.26	13.09
5	0.51	5	0.65	0.24	10.73
6	0.82	6	0.68	0.23	9.23
7	1.07	7	0.74	0.25	9.58
8	0.75	8	0.74	0.23	8.30
9	0.94	9	0.76	0.23	7.64
10	0.56	10	0.74	0.22	7.11
11	0.85	11	0.75	0.22	6.51
12	0.28	12	0.71	0.25	7.11
13	0.99	13	0.73	0.25	6.88
14	0.90	14	0.74	0.24	6.48
15	0.74	15	0.74	0.23	6.03
16	1.01	16	0.76	0.23	5.87
17	0.69	17	0.76	0.23	5.53
18	0.79	18	0.76	0.22	5.22
19	0.30	19	0.73	0.24	5.49
20	0.28	20	0.71	0.25	5.68

* Ω: Number of nonlinear dynamic responses

** Δ: Standard error of estimation

Table 7.6(b) Damage index results of Order-II. Mean and dispersion of sets of nonlinear dynamic responses

Order-II	Damage	Ω	μ	δ	Δ(%)
20	0.28	1	0.28		
19	0.30	2	0.29	0.02	1.10
18	0.79	3	0.46	0.29	16.72
17	0.69	4	0.52	0.26	13.12
16	1.01	5	0.61	0.32	14.11
15	0.74	6	0.64	0.29	11.71
14	0.90	7	0.67	0.28	10.59
13	0.99	8	0.71	0.28	9.98
12	0.28	9	0.66	0.30	10.02
11	0.85	10	0.68	0.29	9.14
10	0.56	11	0.67	0.28	8.34
9	0.94	12	0.69	0.27	7.93
8	0.75	13	0.70	0.26	7.31
7	1.07	14	0.72	0.27	7.27
6	0.82	15	0.73	0.26	6.80
5	0.51	16	0.72	0.26	6.51
4	0.71	17	0.72	0.25	6.11
3	0.31	18	0.69	0.26	6.19
2	0.84	19	0.70	0.26	5.90
1	0.89	20	0.71	0.25	5.68

Table 7.6(c) Damage index results of Order-III. Mean and dispersion of sets of nonlinear dynamic responses

Order-III	Damage	Ω	μ	δ	Δ(%)
10	0.56	1	0.56		
11	0.85	2	0.70	0.20	14.18
12	0.28	3	0.56	0.28	16.29
13	0.99	4	0.67	0.31	15.68
14	0.90	5	0.72	0.29	12.98
15	0.74	6	0.72	0.26	10.61
16	1.01	7	0.76	0.26	9.85
17	0.69	8	0.75	0.24	8.58
18	0.79	9	0.76	0.23	7.58
19	0.30	10	0.71	0.26	8.15
20	0.28	11	0.67	0.28	8.34
9	0.94	12	0.69	0.27	7.93
8	0.75	13	0.70	0.26	7.31
7	1.07	14	0.72	0.27	7.27
6	0.82	15	0.73	0.26	6.80
5	0.51	16	0.72	0.26	6.51
4	0.71	17	0.72	0.25	6.11
3	0.31	18	0.69	0.26	6.19
2	0.84	19	0.70	0.26	5.90
1	0.89	20	0.71	0.25	5.68

Table 7.6(d) Damage index results of Order-IV. Mean and dispersion of sets of nonlinear dynamic responses

Order-IV	Damage	Ω	μ	δ	Δ(%)
10	0.90	1	0.90		
11	0.74	2	0.82	0.11	7.80
12	1.01	3	0.88	0.13	7.65
13	0.69	4	0.83	0.15	7.28
14	0.79	5	0.83	0.13	5.70
15	0.30	6	0.74	0.24	9.86
16	0.28	7	0.67	0.28	10.59
17	0.89	8	0.70	0.27	9.56
18	0.84	9	0.72	0.26	8.57
19	0.31	10	0.68	0.27	8.66
20	0.71	11	0.68	0.26	7.84
9	0.51	12	0.66	0.25	7.29
8	0.82	13	0.68	0.25	6.82
7	1.07	14	0.70	0.26	6.91
6	0.75	15	0.71	0.25	6.44
5	0.94	16	0.72	0.25	6.19
4	0.56	17	0.71	0.24	5.89
3	0.85	18	0.72	0.24	5.61
2	0.28	19	0.70	0.25	5.78
1	0.99	20	0.71	0.25	5.68

Table 7.7 Number of damage responses in four Orders

Order	Number of damage responses			
	"±1.00σ CB*"	"±1.40σ CB"	"±1.64σ CB"	"±1.96σ CB"
Order-I	6	3	3	3
Order-II	7	6	6	5
Order-III	4	4	4	4
Order-IV	6	6	6	6

* CB: Confidence band

Table 7.8 Mean number of damage responses for *N* orders

N	Number of damage responses (κ)			
	"±1.00σ CB"	"±1.40σ CB"	"±1.64σ CB"	"±1.96σ CB"
4	9	6	6	5
20	10	7	6	6
50	11	8	7	5
100	11	8	6	5
1000	11	8	7	6
2000	11	8	7	6
10000	11	8	7	6

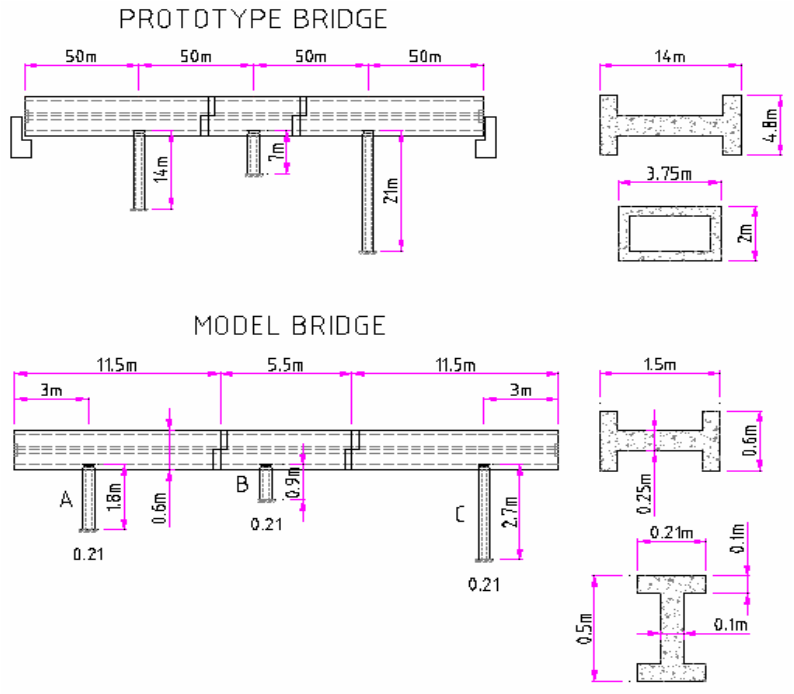

Figure 7.1 Prototype and experimental model bridge

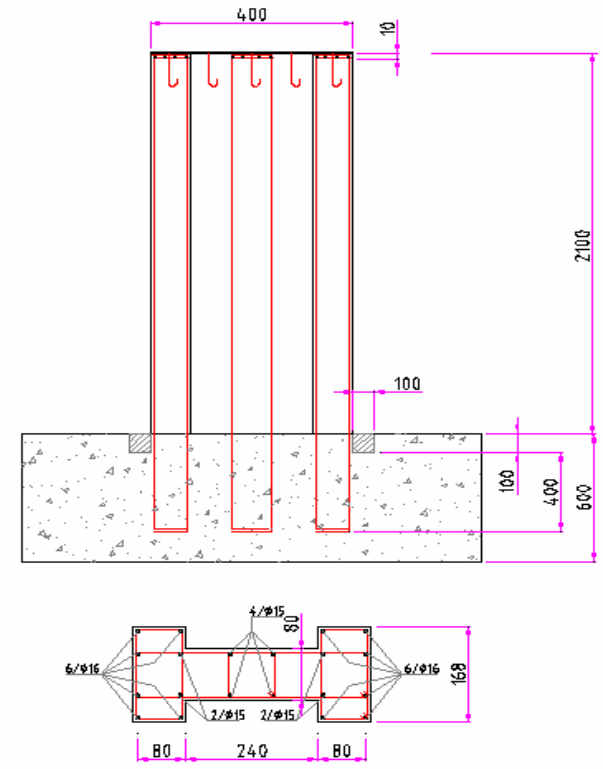

Figure 7.2 The full-scaled prototype bridge model (Geometry dimensions are in cm and not in scale)

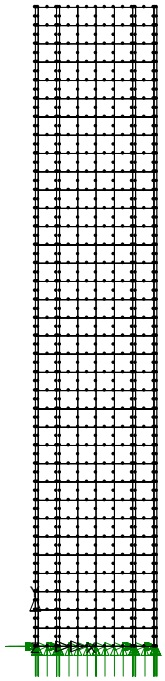

Figure 7.3 Finite element mesh. MESH I

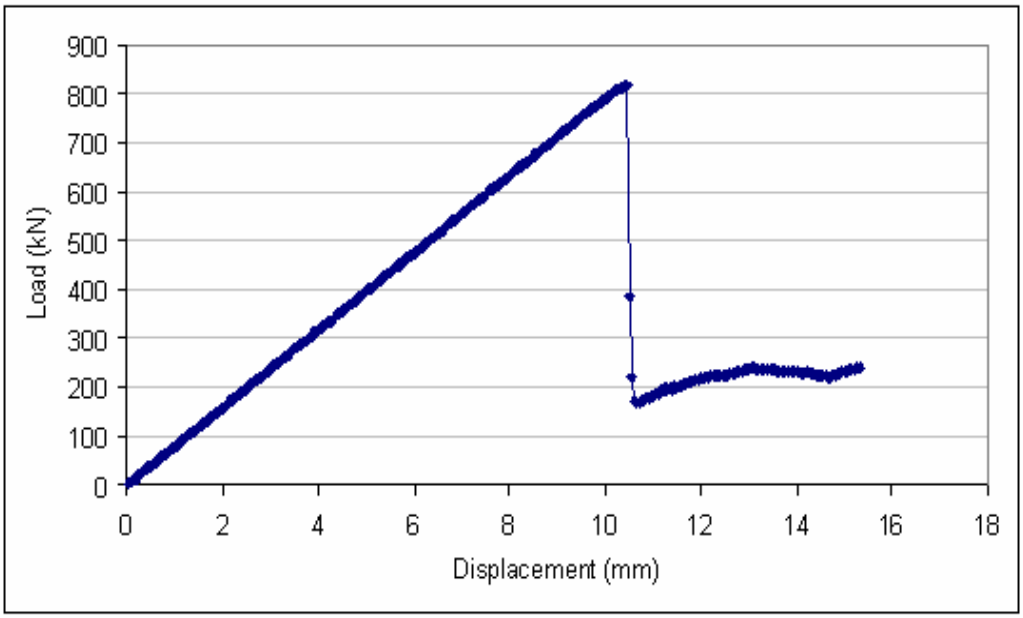

Figure 7.4 Load-displacement curve of the pier under statically monotonic loading

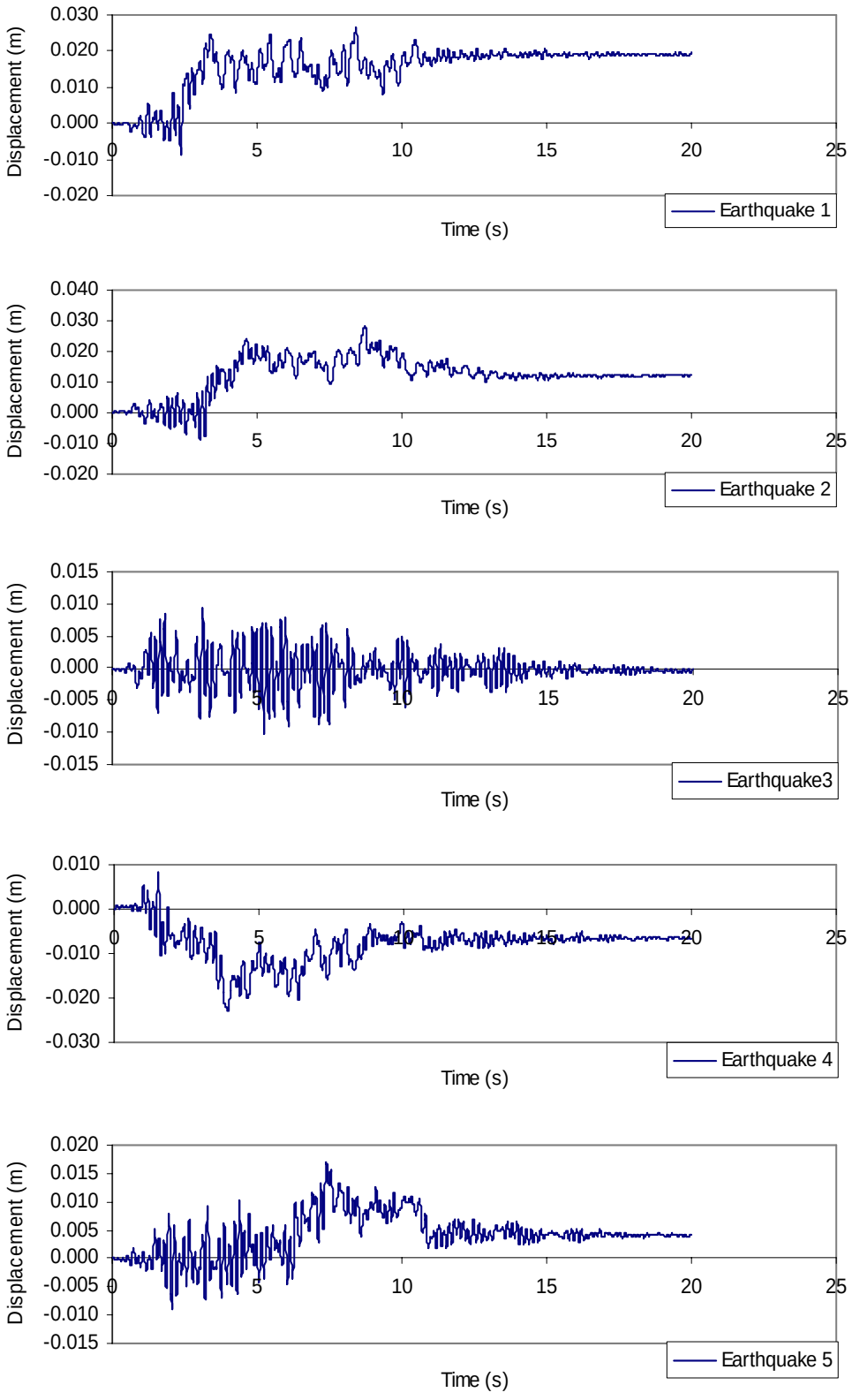

Figure 7.5 Five relative displacements obtained from non-linear dynamic analysis

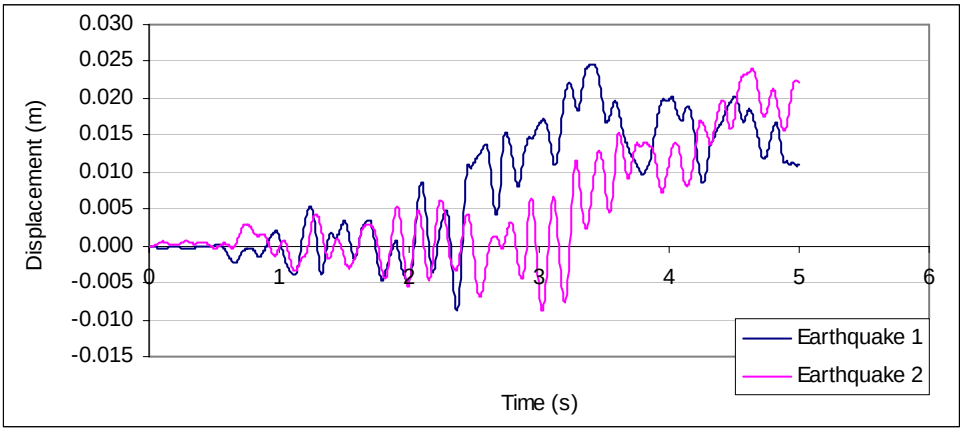

Figure 7.6(a) Relative displacements under Earthquakes 1 and 2 in range of 0-5 seconds

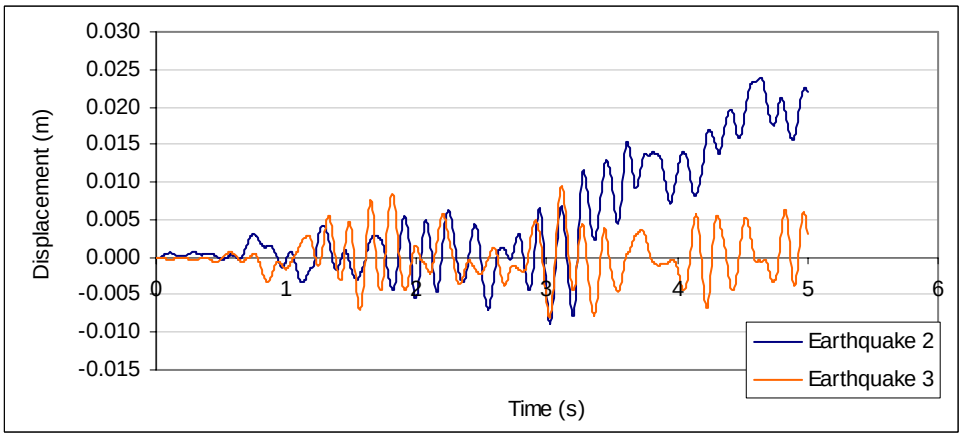

Figure 7.6(b) Relative displacements under Earthquakes 2 and 3 in range of 0-5 seconds

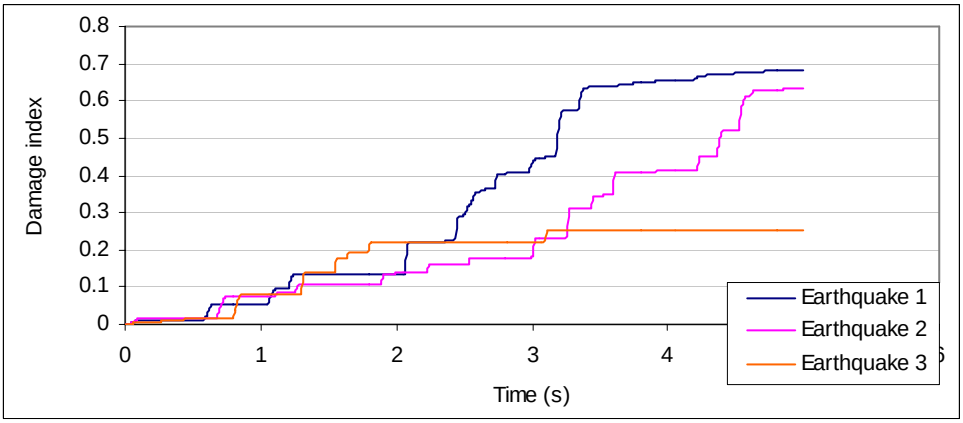

Figure 7.6(c) Damage index for the pier under Earthquakes 1, 2 and 3 in range of 0-5 seconds

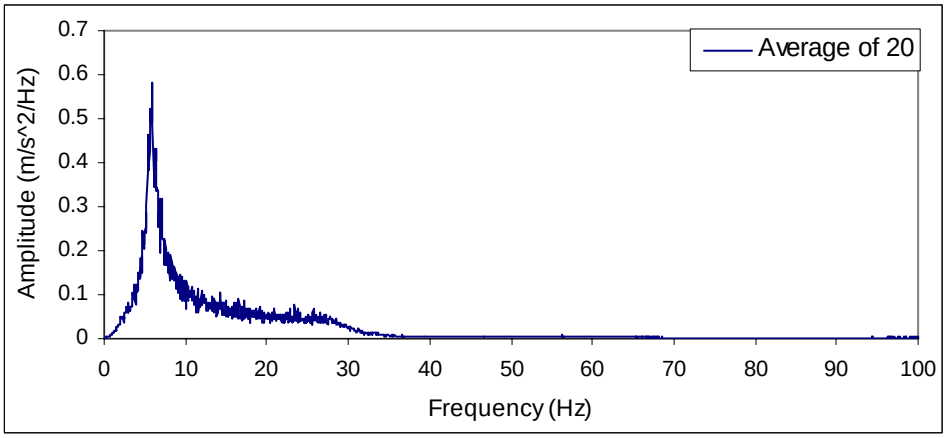

Figure 7.7 Average of 20 frequency spectra

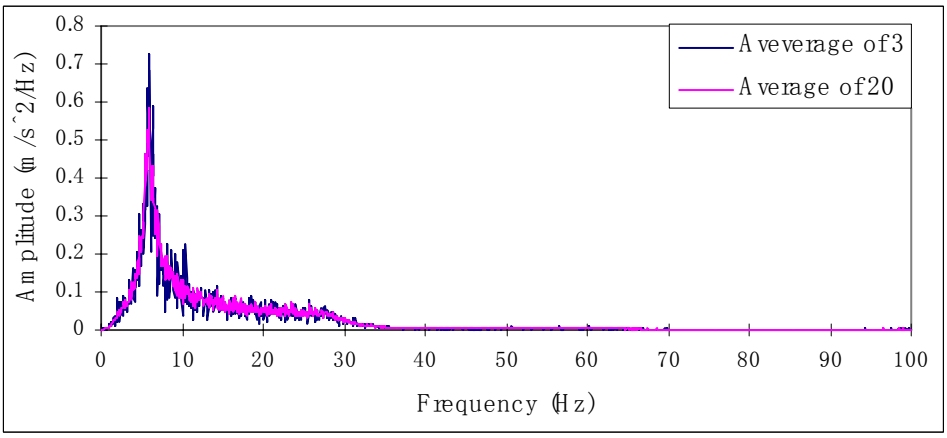

Figure 7.8(a) Comparison of the average of 3 and 20 frequency spectra

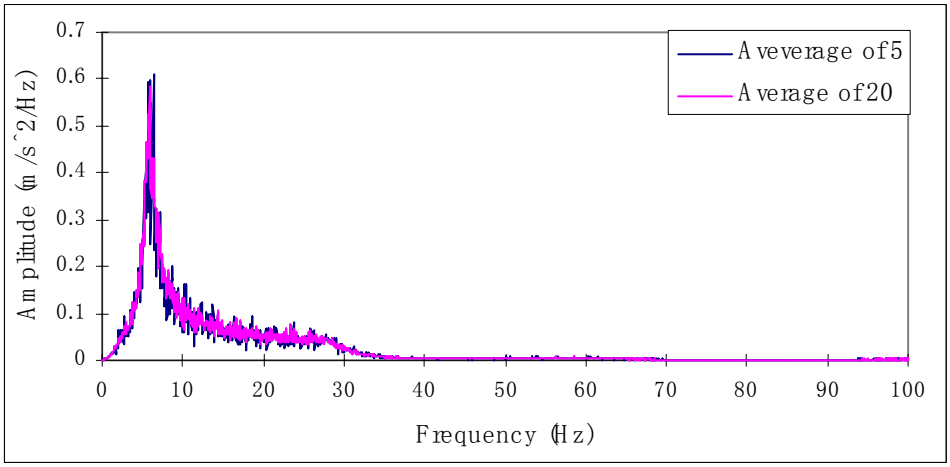

Figure 7.8(b) Comparison of the average of 5 and 20 frequency spectra

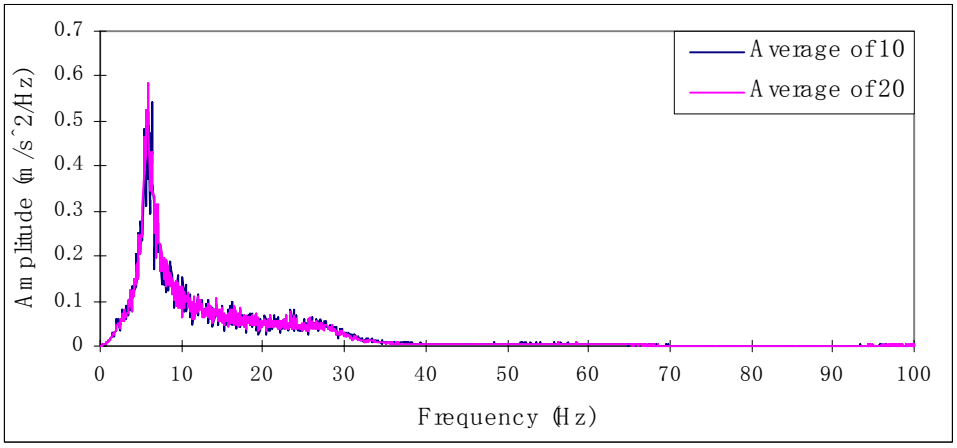

Figure 7.8(c) Comparison of the average of 10 and 20 frequency spectra

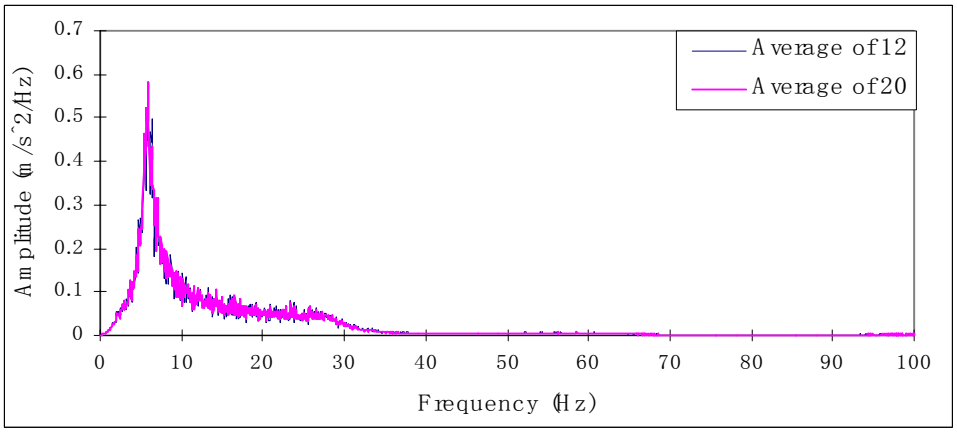

Figure 7.8(d) Comparison of the average of 12 and 20 frequency spectra

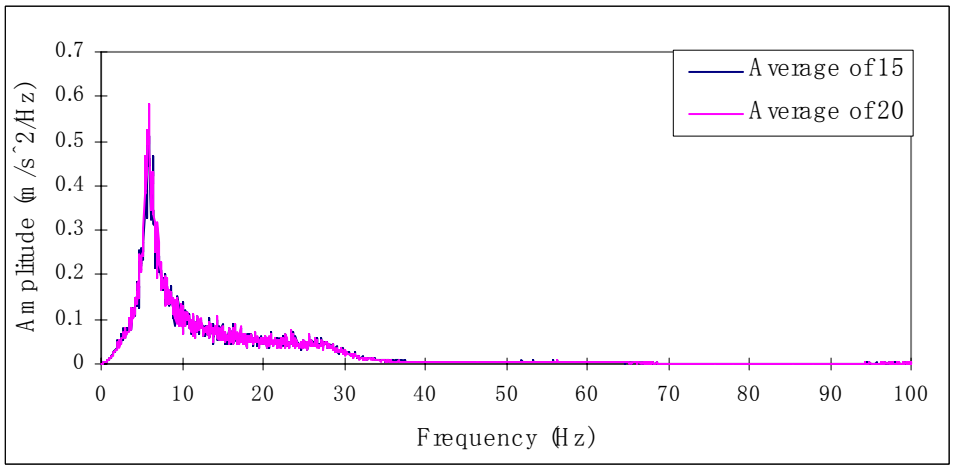

Figure 7.8(e) Comparison of the average of 15 and 20 frequency spectra

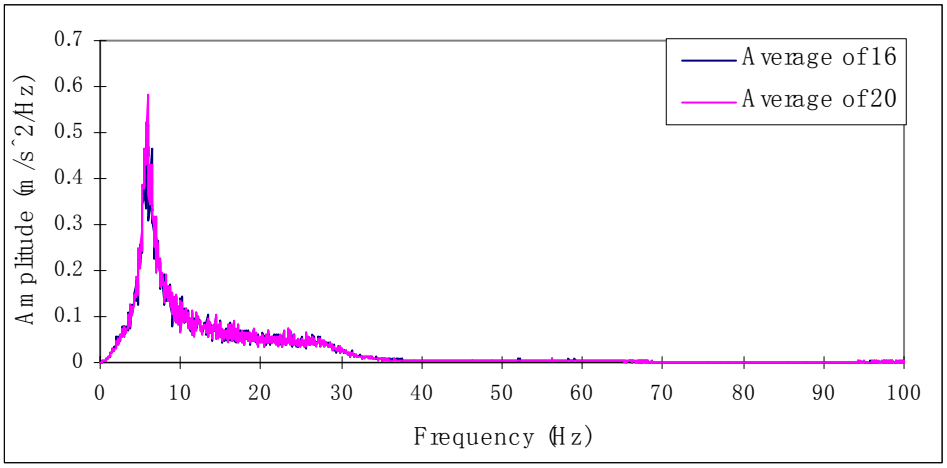

Figure 7.8(f) Comparison of the average of 16 and 20 frequency spectra

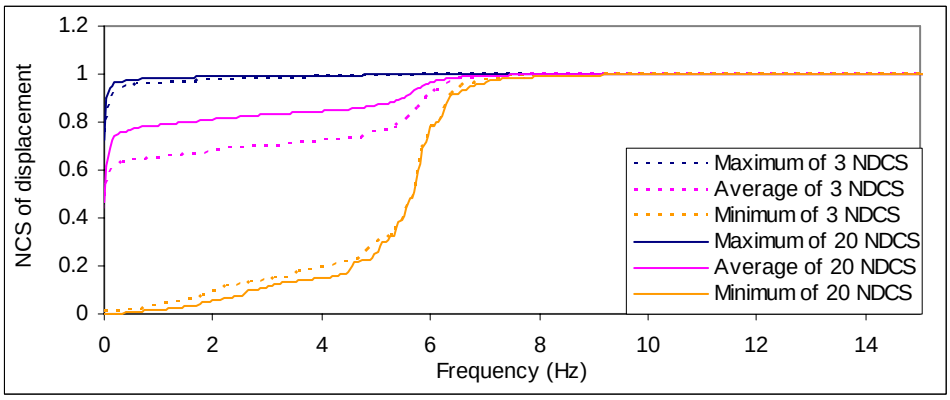

Figure 7.9(a) Comparison of the average of 3 and 20 normalized displacement power spectra

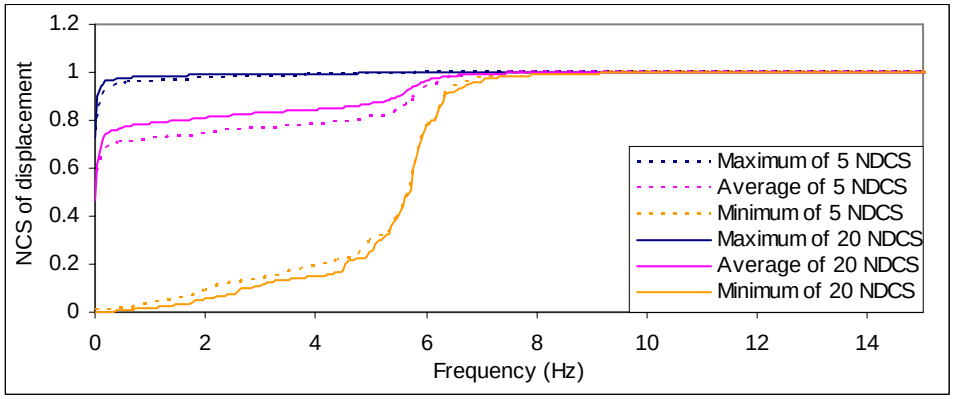

Figure 7.9(b) Comparison of the average of 5 and 20 normalized displacement power spectra

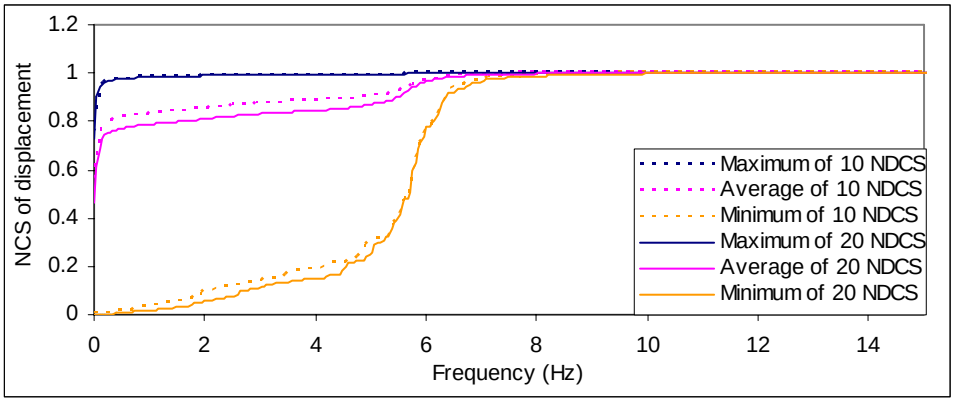

Figure 7.9(c) Comparison of the average of 10 and 20 normalized displacement power spectra

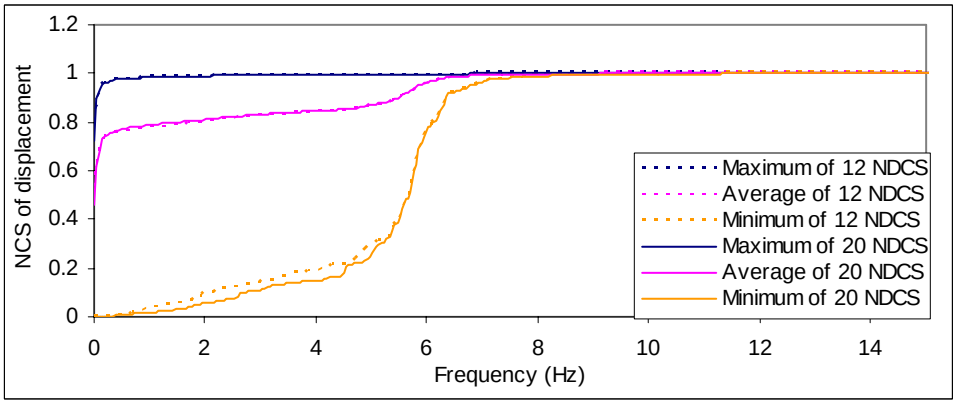

Figure 7.9(d) Comparison of the average of 12 and 20 normalized displacement power spectra

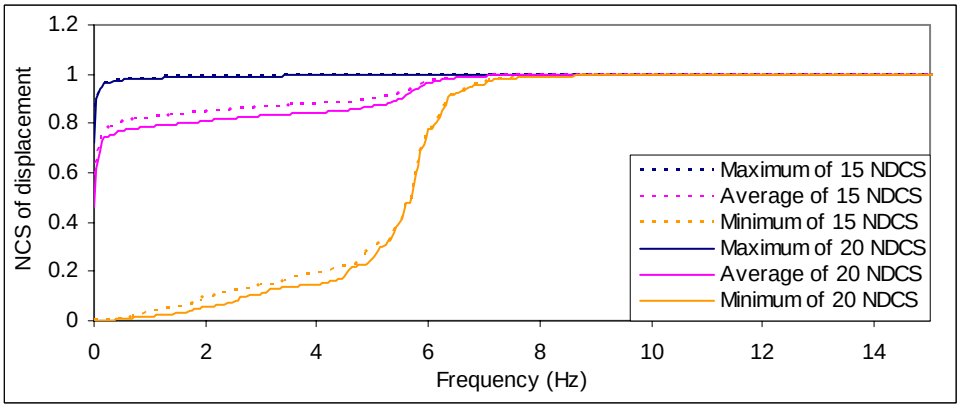

Figure 7.9(e) Comparison of the average of 15 and 20 normalized displacement power spectra

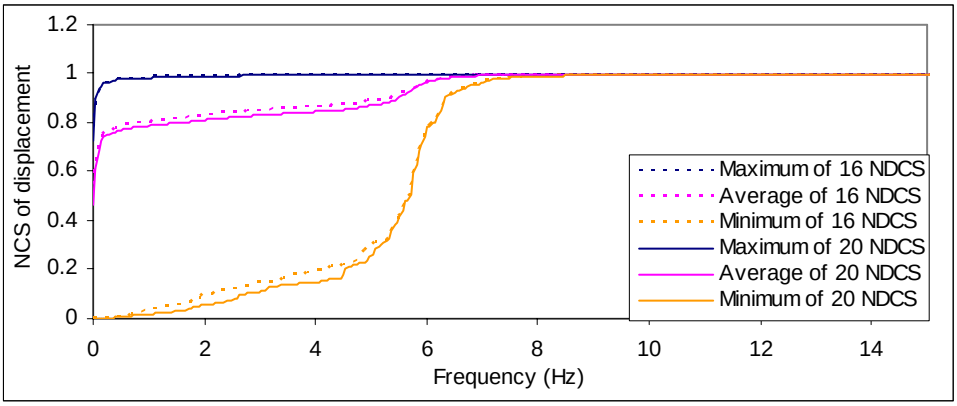

Figure 7.9(f) Comparison of the average of 16 and 20 normalized displacement power spectra

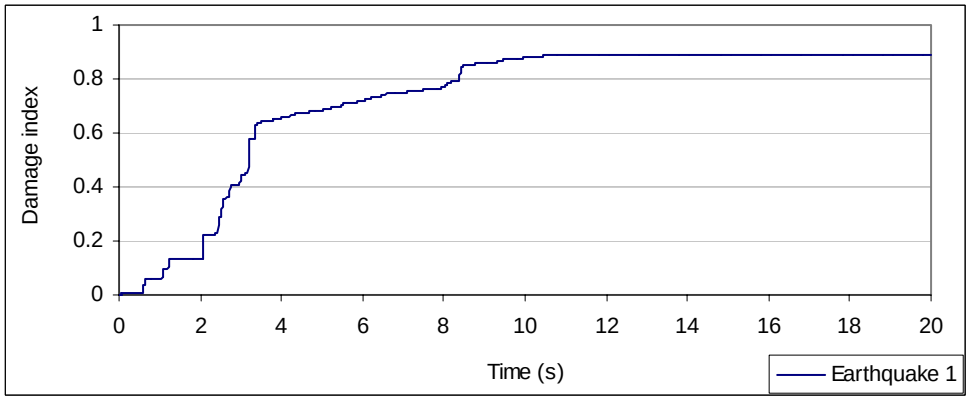

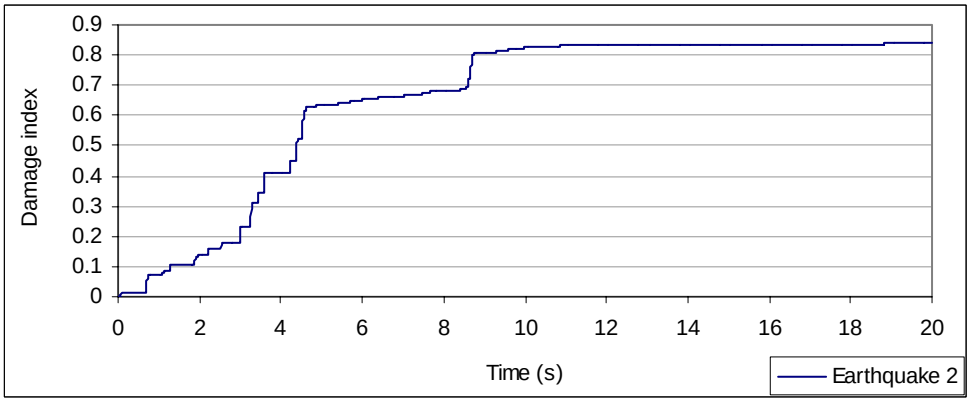

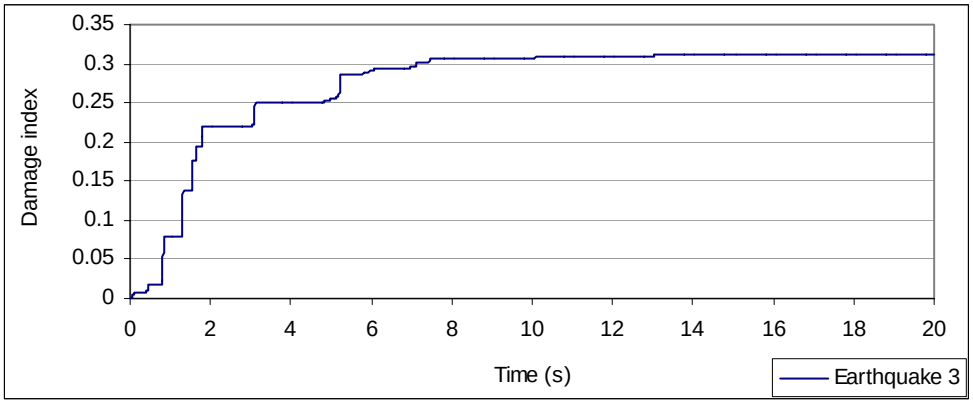

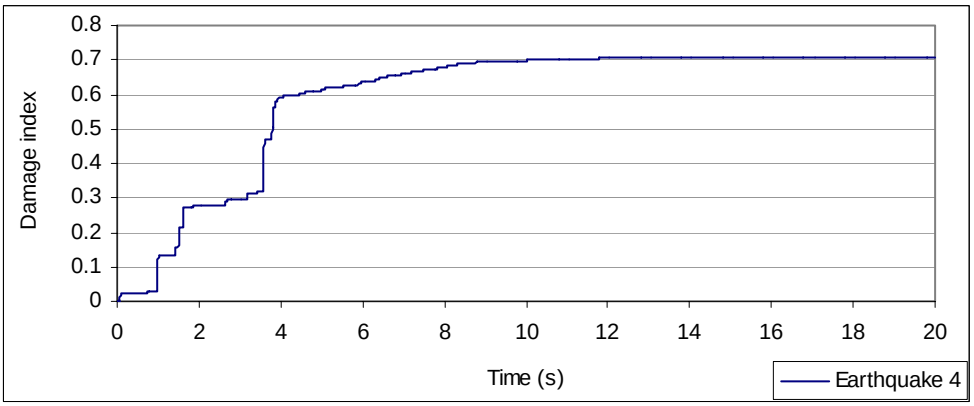

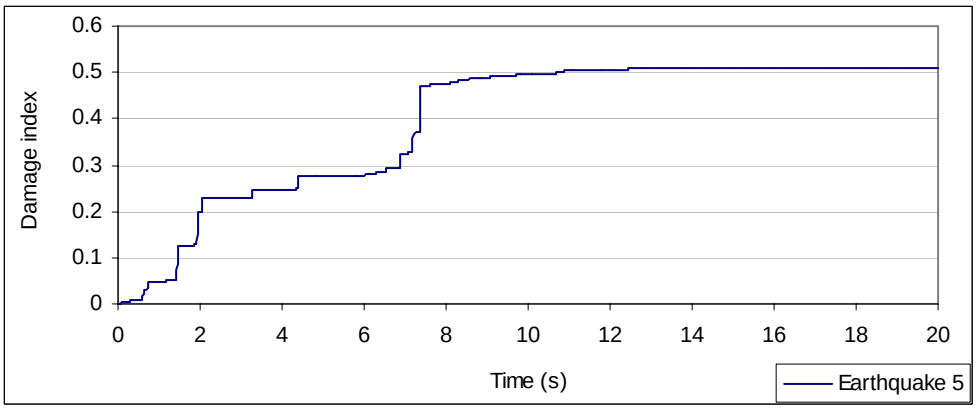

Figure 7.10 Damage index histories of the bridge pier under the first 5 earthquakes

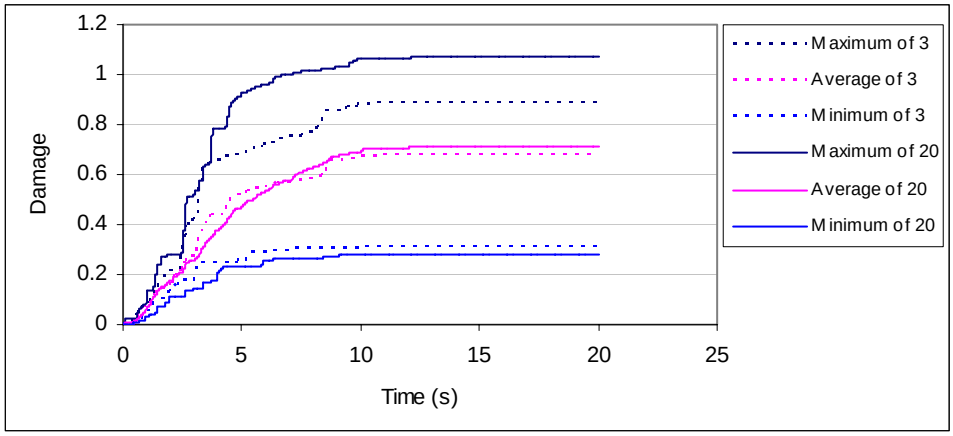

Figure 7.11(a) Comparison of the average, maximum and minimum of 3 and 20 DIH

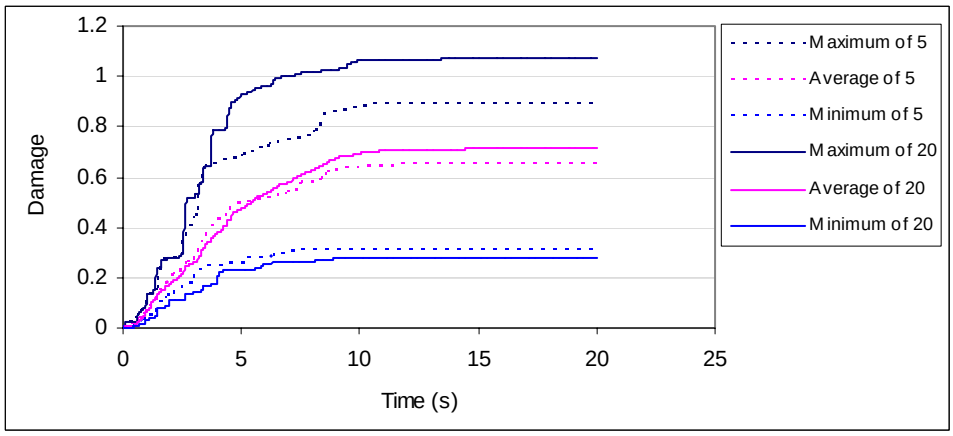

Figure 7.11(b) Comparison of the average, maximum and minimum of 5 and 20 DIH

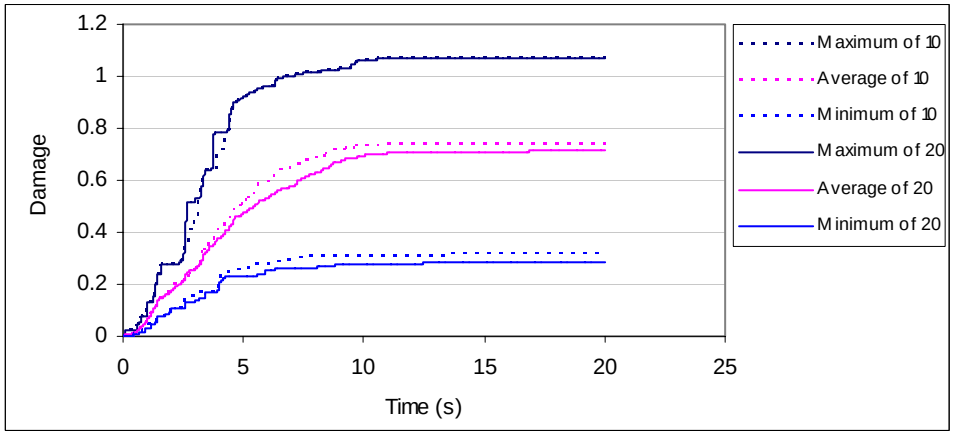

Figure 7.11(c) Comparison of the average, maximum and minimum of 10 and 20 DIH

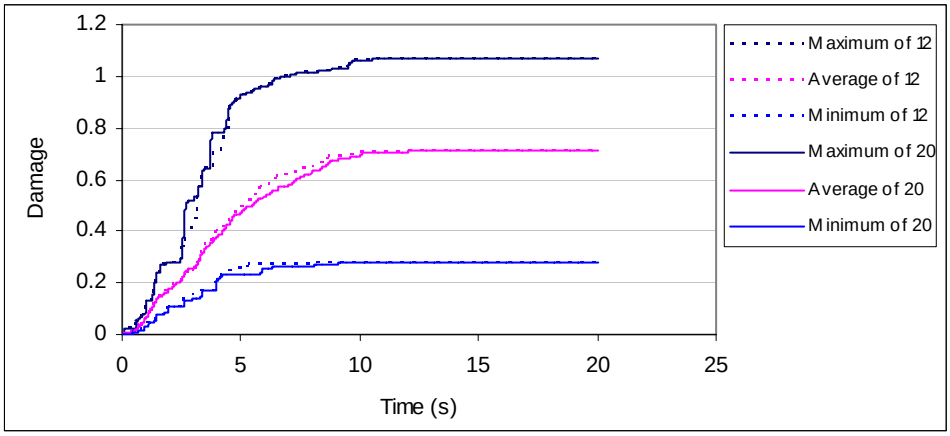

Figure 7.11(d) Comparison of the average, maximum and minimum of 12 and 20 DIH

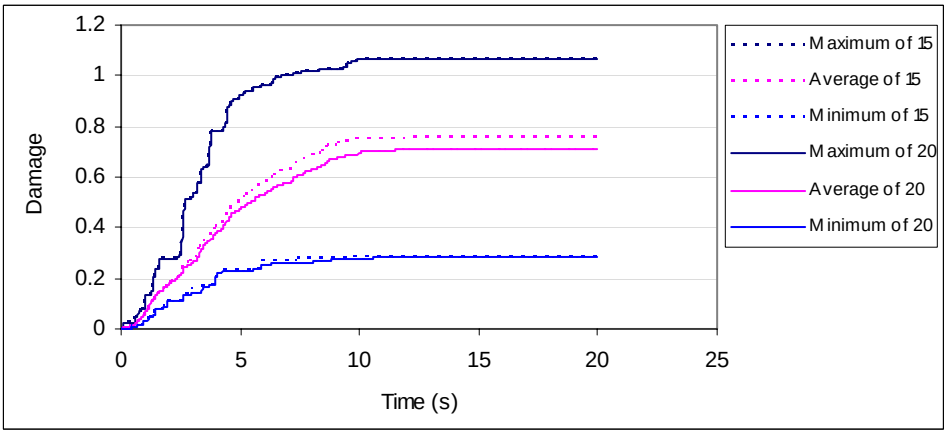

Figure 7.11(e) Comparison of the average, maximum and minimum of 15 and 20 DIH

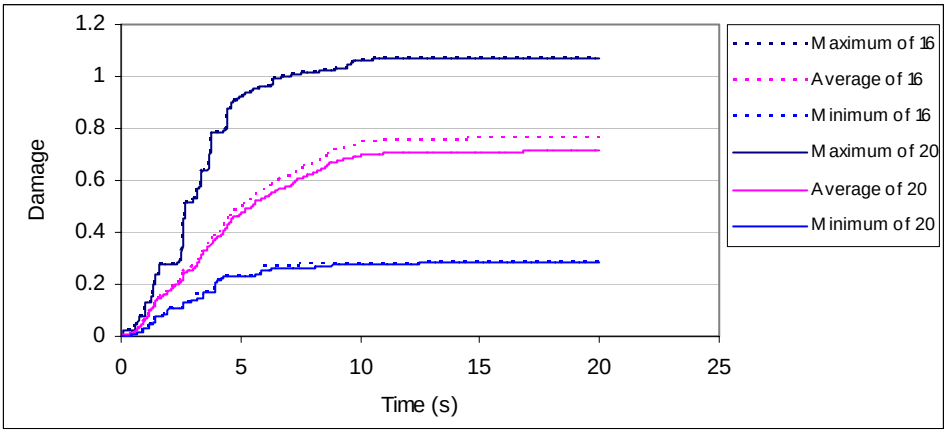

Figure 7.11(f) Comparison of the average, maximum and minimum of 16 and 20 DIH

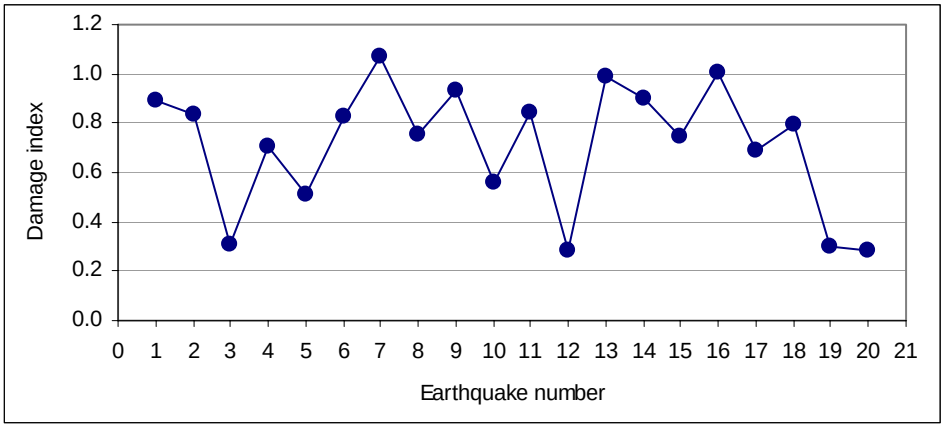

Figure 7.12 Damage index of the bridge pier subjected to 20 artificial earthquakes

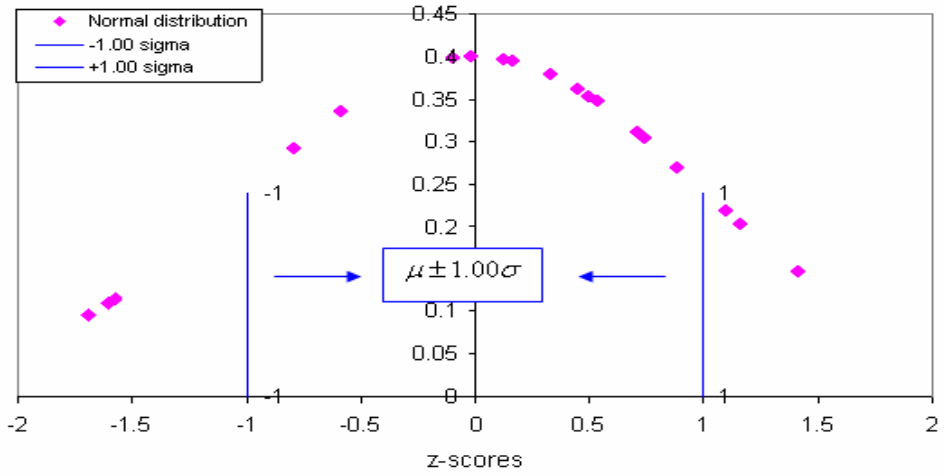

Figure 7.13(a) Normal distribution and the range of "± 1.00σ confidence band"

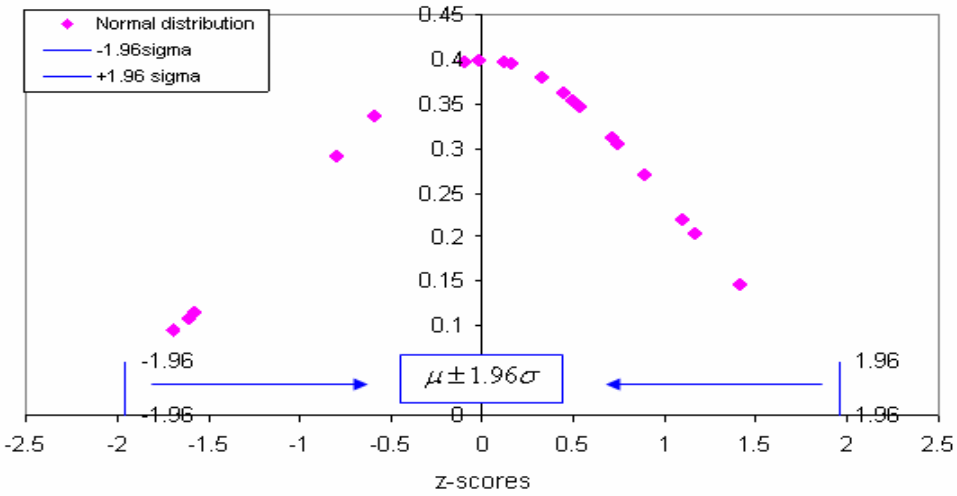

Figure 7.13(b) Normal distribution and the range of "± 1.96σ confidence band"

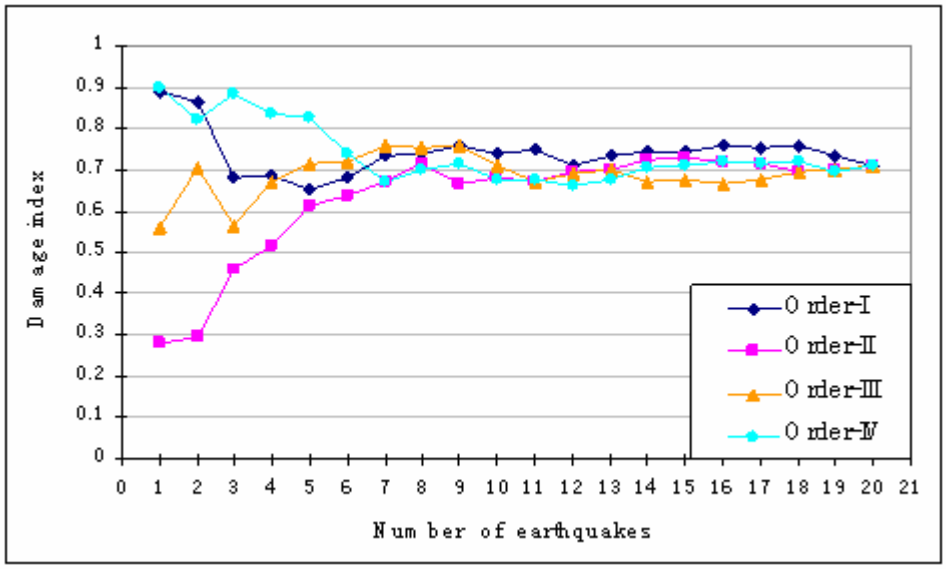

Figure 7.14 Damage indices for four orders of input earthquake time histories

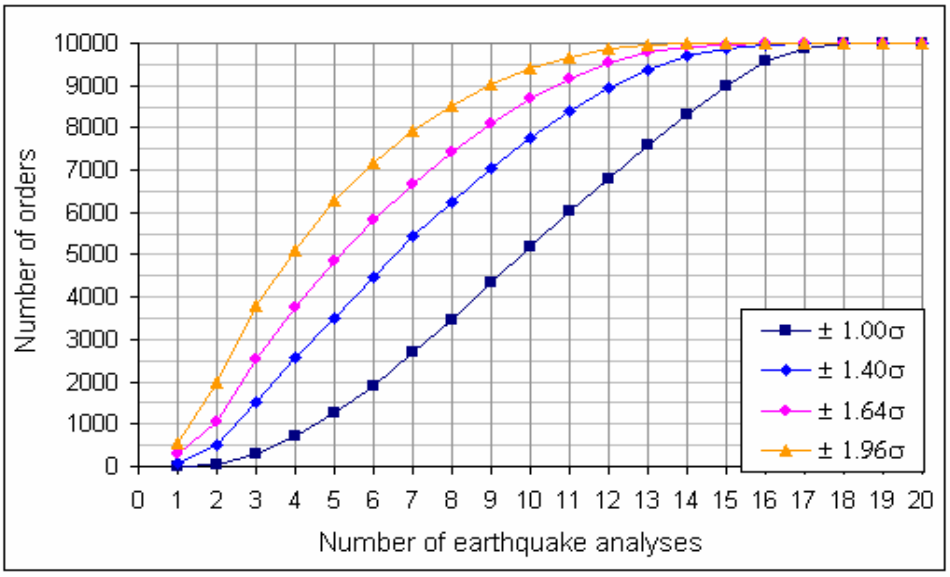

Figure 7.15 Distribution of number of earthquakes analyses in 10000 different orders

CHAPTER 8

PARAMETRIC STUDY AND VALIDATION OF THE MINIMUM REPRESENTATIVE NUMBER OF ARTIFICIAL TIME-HISTORIES REQUIRED FOR NON-LINEAR DYNAMIC ANALYSIS

8.1 INTRODUCTION

In this chapter, the influence of some of the principal parameters of the numerical integration such as time step, element mesh, numerical damping and viscous damping on the accuracy of integration are studied. It is then followed by a parametric study of the influence of a number of parameters of earthquake and structural characteristics such as peak ground accelerations, soil conditions, earthquake durations, random seed numbers, viscous damping ratios, the presence of axial load, pier heights, tensile strength, Young's modulus of concrete and the amount of steel reinforcement to the damage response of the bridge pier. In each parametric study, a set of twenty artificial time-histories, which were generated fitting to the EC8RS, are employed to study the structural response and damage. As different numbers of non-linear dynamic analyses from the same set of time-histories are used throughout this parametric study, the minimum representative number of time-histories to be used, which was suggested in Chapter 7, will be validated.

8.2 ACCURACY ANALYSIS

8.2.1 Numerical results

The integration accuracy of a non-linear dynamic analysis depends on a number of numerical parameters of which the most important are the time step, element mesh, numerical damping and viscous damping. The decision as to which integration operator to use in a practical analysis is governed by the cost of the solution, which in turn is determined by the selection of these above parameters. In this study, the influence of the time step, element mesh, numerical damping and

viscous damping to the integration accuracy is studied. It is assumed that there is no loss in generality for this study to observe the influence of all these parameters to the response under the same artificial time-history. Therefore only earthquake 1 is presented. The LUSAS Multi-crack model is used.

Table 8.1 shows a set of analyses in which each analysis is different from the others by changing the value of one of the parameters. The analysis names are explained as follows:

- ANALYSIS-1 is the analysis using all the parameters suggested and used in Chapter 7.
- ANALYSIS-2 with a finer mesh MESH II, which is a 16x70 mesh with 1120 elements, as shown in Figure 8.1, is used to study the influence of the element mesh to the integration accuracy.
- ANALYSIS-3 with a smaller time step (0.002 s) is used to study the influence of the time step size to the integration accuracy.
- ANALYSIS-4 with a larger damping ratio (10%) is used to study the influence of damping ratio to the integration accuracy.
- ANALYSIS-5 with an even larger damping ratio (20%) is used to study the influence of the damping ratio to the integration accuracy.
- ANALYSIS-6 using a set of Newmark's parameters with larger numerical damping is used to study the influence of the numerical damping on the integration accuracy with a time step of 0.005 s.
- ANALYSIS-7 using a set of Newmark's parameters with larger numerical damping is used to study the influence of the numerical damping on the integration accuracy with a time step of 0.002 s.

As mentioned in the previous chapter, in order to predict the non-linear dynamic response of the structure accurately, some of the higher frequency modes should be captured by using a suitable numerical integration. Theoretically, when the parameters including the time step, element mesh, numerical damping and viscous damping are made smaller, the presence of the higher frequency contents (modes) in the response would be more evident. Therefore, the influence of the time step, element mesh, numerical damping and viscous damping to the integration accuracy is

studied in terms of the presence of the high frequency contents in non-linear dynamic response. In this study, we are only interested in the presence of medium high frequency content in the acceleration response as it is representative for all the dynamic response in terms of the frequency content.

Figure 8.2 shows the normalised cumulative acceleration spectra for ANALYSIS-1 and ANALYSIS-2. It can be seen that though the two responses are similar, there is a little bit more high frequency content in the result of ANALYSIS-2. This observation agrees with practical considerations about using small element mesh in literature, i.e. Bathe (1982).

Figure 8.3 shows the normalised cumulative acceleration spectra for ANALYSIS-1 and ANALYSIS-3. It can be seen that again there is a little more high frequency content in the result of ANALYSIS-3. The reason is because smaller time step size cause less errors in the numerical integration especially for the higher frequency modes and therefore it can capture higher frequency content in the dynamic response.

Figure 8.4 shows the normalised cumulative acceleration spectra for ANALYSIS-1, ANALYSIS-4, and ANALYSIS-5. Again it can be seen that the one with higher frequency content in the result is ANALYSIS-1, then ANALYSIS-4 and finally, ANALYSIS-5. The reason is, for the Rayleigh damping parameters chosen, due to a larger damping ratio used is more effective in damping the more high frequency modes out of the solution. Therefore the structure with less damping has higher frequency content (modes) in its dynamic response.

Figure 8.5 shows the normalised cumulative acceleration spectra for ANALYSIS-1 and ANALYSIS-6 in which a time step size of 0.005 s is used. It can be seen that there is a slightly more high frequency content in the result of ANALYSIS-1. It is because Newmark's parameters α and β with larger numerical damping used has similar effects to the dynamic response as using a larger damping ratio.

Figure 8.6 shows the normalised cumulative acceleration spectra for ANALYSIS-3 and ANALYSIS-7 in which a time step size of 0.002 s is used. It can be seen that there is a slightly more high frequency content in the result of ANALYSIS-3. Similar to the comparison shown in Figure 8.5, the reason is because Newmark's parameters α and β with larger numerical damping has similar effects to the dynamic response as using larger damping ratio but it has more effect than the reduction in numerical damping because of the smaller time step used.

8.2.2 Conclusions

It can be observed from the above analyses that when the time step, element mesh, numerical damping and viscous damping are smaller, the presence of the higher frequency content in the response will be more evident, and therefore higher integration accuracy can be obtained.

This study aims to understand the influence of the numerical integration such as the time step, element mesh, numerical damping and viscous damping to the integration accuracy, not to seek the smallest values of these above parameters for later analyses. The reason is the parametric values chosen in Chapter 7 (or in ANALYSIS-1 in this study) are small enough to obtain reasonable results for practical purposes up to the second natural modes and significantly reduce the computational effort for large number of analyses required in the parametric study in this chapter. Therefore, for the parametric study in the following part of this chapter, all the non-linear dynamic analyses will employ the integration scheme with the time step, element mesh, numerical damping and viscous damping selected in Chapter 7, i.e. the same as ANALYSIS-1 in Table 8.1.

8.3 PARAMETRIC STUDY

A parametric study is performed in order to investigate the effect of several parameters of earthquake and structural characteristics as well as the LUSAS Multi-crack model's parameters to the structural behaviour and damage of the bridge pier. The parameters selected for the parametric study were:

a. viscous damping ratio for Rayleigh damping
b. soil conditions as given in Eurocode 8 (prEN 1998-1:2004)
c. the amount of steel reinforcement
d. tensile strength of the concrete material
e. Young's modulus of the concrete material
f. earthquake peak ground acceleration amplitudes
g. pier heights
h. the presence of axial load
i. seeds of random number of earthquake generation
j. and durations of the earthquake

As different numbers of artificial earthquake time-histories are used throughout this parametric study, by using the damage analysis and probabilistic approach as studied in the previous chapter, the appropriate minimum number of time-histories suggested will be validated in this section.

In this parametric study, only the results of the damage index are presented and it is sufficient to fulfil the aim of this study. Just in some cases where necessary, the relative accelerations, velocities and displacements are also given to offer additional information.

A great computational effort was required to carry out all the above analyses. Each parametric study includes 2 to 3 cases in which the value of a parameter is changed. In each case there are 20 runs in accordance with 20 input artificial earthquake time-histories. There were about 25 cases of analysis or approximately 500 analyses in total, not accounting for the analyses which failed and several runs performed in order to select the correct mesh and time step. A single run on average took nearly 6 hours and so it is estimated that all 500 analyses required approximately 2400 hours or 3 consecutive months and a half on a Pentium IV 1Ghz – PC running Windows 2000 and Visual Fortran. This estimation does not take into account the time required for data processing or anything else.

8.3.1 Viscous damping ratio for Rayleigh damping

The influence of the value of the viscous damping ratio (ξ = 0.05, 0.10 and 0.20) for Rayleigh damping on the relative displacement and the damage of the bridge pier subjected to 20 artificial time-histories are obtained but only the results of the first 5 are shown in Figures 8.7, and 8.8, respectively. The set of twenty artificial time-histories generated in Chapter 7 (or ANALYSIS-1 in this chapter) are used for this study and all other relative studies.

Figure 8.7 shows that the amplitude of the relative displacement is decreasing with increasing damping ratio. This can be expected naturally from the dynamic equilibrium equations (Equation 7.1). It is also observed from the figure that, when ξ = 0.05, the pier almost vibrates around the permanent displacements (except for the responses under earthquake 3) and the amplitude of the relative displacement is high; when the damping ratio ξ = 0.10 and 0.20, the pier remains mostly elastic behaviour and rests at zero displacements at the end of vibration. Therefore it can conclude that the higher damping ratio reduces the damage in the structure as less energy is available for inelastic damage. In the case of ξ = 0.10 and 0.20, increasing damping ratio reduce the amplitude of the relative displacement but not very much. Additionally, it was counted that for the first 15 seconds of vibration, there is about 64 cycles for the case of ξ = 0.05, and about 76 cycles for the cases of ξ = 0.10 and 0.20. Therefore, it can be concluded that when ξ = 0.05, the pier vibrates with longer structural period than when it vibrates across the zero displacements, i.e. with ξ = 0.10 and 0.20, implying that more damage has resulted in the case of less damping. This effect has masked the normal effect of period elongation due to higher damping.

Figure 8.8 shows a comparison of the damage indices of the non-linear dynamic analysis for ξ = 0.05, 0.10 and 0.20. It can be seen that the damage in the bridge pier decreases with increasing damping ratio. The reason for it is that the longer the structural period and/or the higher the value of amplitudes of relative displacement for lower value of damping, the higher the damage in the bridge pier (see Section 7.3.6).

From the results of the damage indices for ξ = 0.05, 0.10 and 0.20, the mean value for the number of damage responses required for non-linear dynamic analysis can be found by a procedure similar to the one presented in Section 7.3.6.7.2. Table 8.2 shows the mean number of non-linear dynamic analyses for a large number of orders of damage response (the number of orders is N = 10000). The mean number is presented in accordance with the four confidence bands used. It can be seen from the table that the mean numbers of non-linear dynamic analyses for different damping ratios converged to the almost same value. If a relevant design basis usually calls for a "84 percent confidence band" or "± 1.40σ confidence band", the minimum representative number of non-linear dynamic analyses shall be about 8 for various damping ratios. These observations concur with the minimum representative number suggested in the main study in Chapter 7.

In addition, the cumulative distribution of the number of analyses (or earthquakes) in different orders of input earthquakes for the four confidence bands is given in Figures 8.9 and 8.10, for ξ = 0.10 and 0.20, respectively. The distribution of the number of analyses for ξ = 0.05 can be referred to Figure 7.15 in Chapter 7. These figures show that the distributions of the number of analyses for different ratios of viscous damping are very similar when the number of analyses is large enough, i.e. about 6. Especially, at the mean number of analyses (11, 8, 7, and 6 in accordance with the "± 1.00σ confidence band", "± 1.40σ confidence band", "± 1.64σ confidence band", and the "± 1.96σ confidence band", respectively), their orders are completely the same for different ratios of viscous damping. When the number of analyses is small, i.e. less than 4, increasing damping ratio seems to increase the number of orders for the same confidence band. It can be explained that increasing damping ratio in the bridge pier it will reduces the non-linearity in the structural response and hence, the dispersion and error of estimation in their response or damage will also reduced. Therefore the probability of appearance of the number of analyses for higher damping is increased accordingly. In another word, the number of orders in which the number of analyses for the case of higher damping will be more than that of less damping cases. This observation agrees well with the explanation given in Section 7.3.6.7.

If the practicing engineer wants a high level of confidence in the number of earthquake used, e.g. they can select 16, 13, 11 and 9 from Figure 8.10. For these values, 95% (9500 out of 10000) of the ordering would give the correct convergence value. The value 11, 7, 6 and 4 are chosen as an average value.

8.3.2 Soil condition according to Eurocode 8

In this study, the twenty artificial time-histories, which were generated from three subsoil classes B, C, and D from prEN version of EC8 (Eurocode 8, 2003), are applied to the bridge pier to account for the influence of local ground conditions on the damage of the bridge pier.

Figure 8.11 shows a comparison of the damage indices of the non-linear dynamic analysis under 20 time-histories generated from three subsoil classes B, C, and D. From the figure, it generally shows that the damage indices in the bridge pier are different for subsoil classes B, C, and D, but the damage indices for subsoil classes B and C are closer to each other. It is because the EC8RS for the subsoil classes B and C are very close (Eurocode 8, 2003) and hence it is expected that the artificial time-histories generated from them are also similar to each other, thus their responses. In particular, Table 8.3 shows a comparison of the mean and dispersion of damage indices in the bridge pier under sets of 20 earthquakes for subsoil classes B, C and D. It can be seen that when the subsoil class is increasingly softened, i.e. from B to D, the mean damage in the bridge pier is slightly reduced but the dispersion increases.

It is known that softer soil can generally induce more damage in long-period structures. However, there is no evidence that a softer subsoil class would induce more damage in the bridge pier, i.e. damage under increasingly soft soil classes of B, C, and D, but the different damage responses under different earthquakes of different subsoil classes. The reason could be due the randomness of either the magnitudes of the spectral responses in short-period range (where the fundamental period of the bridge pier is) or different orders of input earthquakes for different subsoil classes.

The distribution of the number of analyses in different orders of input earthquakes for the four confidence bands is also calculated but the results and observations are similar to those mentioned above (see Sections 7.3.6.7.2 and 8.3.1 or Figures 7.15, 8.9, and 8.10). The same results and conclusions about the distribution of the number of analyses are also found for all other parametric studies in this chapter. Therefore, they will not be repeated again from this point onwards.

Table 8.4 shows the mean number of non-linear dynamic analyses for a large number of orders of damage response (the number of orders is N = 10000). The mean number is presented in accordance with the four confidence bands mentioned before. It can be seen from the table that the mean numbers of non-linear dynamic analyses for the subsoil classes B, C and D converged to similar values, i.e. 11, 8, 7, and 6 for the four confidence bands. These observations again concur with the conclusion suggested in the main study in Chapter 7.

8.3.3 Amount of steel reinforcement

The influence of the amount of steel reinforcement in the bridge pier (A_s, 2 x A_s, and 4 x A_s, in which A_s is the original steel area) on the damage of the bridge pier is investigated. Theoretically, it is expected that damage in the bridge pier should decrease with increasing the amount of steel reinforcement. The reason is because increasing the amount of steel reinforcement will make the bridge pier stiffer therefore the displacement is smaller for the same external force (actually slightly increased, due to the mass of the additional steel). Eventually, damage in the bridge pier will decrease. On the other hand, with less plastic dissipation in the case of increasing the amount of steel reinforcement, less potential energy is stored therefore the kinetic energy is higher during the vibration stage. As a result, the amplitude of the relative displacement vibration decreases while those of the relative velocity and acceleration are higher at the later stage.

Figure 8.12 demonstrates the above expectation by showing that with increasing the amount of steel reinforcement, the relative acceleration and velocity have higher frequency content while the relative displacement has smaller amplitudes (the responses under Earthquake 1 are taken as

an example). In addition, the number of cycles is counted from the relative displacement responses for the cases of steel areas of A_s, 2 x A_s, and 4 x A_s for the duration of 20 s. They are 90, 100, and 104, respectively. Therefore, it clearly shows that the damage in the bridge pier is decreasing with increasing the amount of steel reinforcement. Furthermore, eigenvalue analyses are done for the bridge pier with different amounts of steel reinforcements and the results for the first 5 modes are shown in Table 8.5. It clearly demonstrates that the higher frequency is due to the higher natural frequency associated with a stiffer structure.

As the damage in the bridge pier can be related to the material strains, and that material strains can be related to maximum response displacements. Figure 8.12(c) shows that the maximum response displacements decrease with increasing amount of steel reinforcement. In addition, damage in the bridge pier can also be related to the dissipated energy during the earthquake event. Figure 8.13 shows that dissipated energy in the bridge pier is much less with increasing the amount of steel reinforcement. Therefore with more steel reinforcement, the response is mostly in the elastic range. As damage in the bridge pier is the combination of the maximum response displacement and dissipated energy, it can be concluded that damage is decreasing with increasing amount of steel reinforcement.

Alternatively, the damage index (Equation 7.11) can be used to evaluate damage in the bridge pier for different amounts of steel reinforcement. For different amounts of steel reinforcement, the three structural parameters, Q_y, δ_u, and β, are actually different. It is reasonable to assume that increasing the amount of steel reinforcement will increase the total bending moment resistance in the bridge pier and then the yield strength Q_y. Also, experimental evidence and detailed analytical results (Priestley 1993, Priestley *et al.* 1996, Priestley 2003a) indicate that if the strength increase is obtained merely by increasing the flexural reinforcement ratios while keeping member dimensions constant, then the displacement capacity or the ultimate displacement δ_u of the structure will actually decrease as the strength increases, as a result of reduced ultimate curvature capacity. Nevertheless, increasing the amount of steel reinforcement will slightly increase the value of β (Park *et al.* 1987, Williams *et al.* 1997, Usami and Kumar 1996). However, there appears to be no reliable method for determining the ultimate displacement (δ_u) of reinforced

concrete structures, especially when shear deformation and bond slippage may be dominant. Even highly sophisticated finite element analysis cannot trace the physical deformation behaviour up to ultimate stage because of uncertainties in the dowel action, shear cracking, bond deterioration, etc. Therefore, it is actually difficult, if not impossible to determine the exact value of ultimate displacement and the factor β in this study. In the light of these complex effects, for simplicity, it will be assumed that β, Q_y and δ_u are unchanged for different amounts of steel reinforcement and we will show that with this assumption the results is still in good agreement with the above observations made in the first part of this section in a qualitative manner.

Figure 8.14 demonstrates that damage in the bridge pier, with β, Q_y and δ_u assumed to be unchanged for different amounts of steel reinforcement, is decreasing with increasing amount of steel reinforcement. This observation is in well agreement with the observations made above. Therefore, the assumption of constant values of β, Q_y and δ_u could be adopted in later studies.

From Figure 8.14, it can be seen that under a few of the earthquakes, e.g. Earthquakes 3, 12, 19 and 20, damage in the pier for the cases of different amounts of steel reinforcement are not very different. It is because under these earthquakes the amplitude of the pier response is small and it remains mostly in elastic behaviour (e.g. see Earthquake 3 in Section 7.3.6.2). Therefore, damage in the pier in these cases is almost the same.

Table 8.6 shows the mean number of non-linear dynamic analyses for a large number of orders of damage response (the number of orders is N = 10000) for different amounts of steel reinforcement. It can be seen that it supports the same conclusion as suggested in the main study in Chapter 7.

8.3.4 Tensile strength of the concrete material

Increasing the value of tensile strength will increase the load capacity in the concrete and consequently increase the stiffness of the bridge pier. As explained in the previous section, for simplicity, the assumption of constant values of β, Q_y and δ_u is adopted in this study but it should

not affect the qualitative observation for the damage analysis. The influence of the tensile strength (f_t = 3.0 and 4.2 N/mm^2) on the damage of the bridge pier is shown in Figure 8.15.

It can be seen that when a higher value of tensile strength is used, the bridge pier can resist a higher earthquake load and, therefore, leads to a lower damage (see also the parametric study in Chapter 4).

Table 8.7 shows the mean number of non-linear dynamic analyses for a large number of orders of damage response (the number of orders is N = 10000) for different values of tensile strength. This also supports the same conclusion as suggested in the main study in Chapter 7.

8.3.5 Young's modulus of the concrete material

Increasing the value of Young's modulus of the concrete will increase the force in concrete thus consequently leading to an increase in the stiffness of the bridge pier. Again, for simplicity, values of β, Q_y and δ_u are assumed to be constant in this study. The influence of the Young's modulus (E = 30000 and 32000 N/mm^2) on the damage of the bridge pier is shown in Figure 8.16.

It shows that the damage of the bridge pier slightly decreases with increasing Young's modulus. This can be explained as a higher value of Young's modulus leads to a higher value of stress and, therefore, leads to a higher reaction force for the same displacement and it results in a lower damage in the bridge pier. Because the values of Young's moduli are just slightly different, in some cases the damage indices in the pier for those Young's modulus are also not much different.

Table 8.8 shows the mean number of non-linear dynamic analyses for a large number of orders of damage response (the number of orders is N = 10000) for different values of Young's modulus. It can be seen that these mean number of non-linear dynamic analyses are similar to which as suggested in the main study in Chapter 7.

8.3.6 Peak Ground Acceleration

The influence of the Peak Ground Acceleration (PGA) (PGA = 0.35g and 0.525g m/s^2) on the damage of the bridge pier is shown in Figure 8.17.

Figure 8.17 shows that the damage of the bridge pier dramatically increases with increasing the value of PGA. The reason is that a higher value of PGA leads to higher amplitudes of the earthquake and it causes more damage in the bridge pier. It is clear that a change in PGA can make a significant change in the damage of the structure.

Table 8.9 shows the mean number of non-linear dynamic analyses for a large number of orders of damage response (the number of orders is N = 10000) for different values of PGA. It is interesting to note from this table that, the results still supports the same conclusion on the mean number of non-linear dynamic analyses suggested in the main study in Chapter 7.

8.3.7 Pier height

Decreasing the value of the pier height will decrease the bending moment at its base and consequently increase the stiffness of the bridge pier. Therefore, this is generally similar to increasing the amount of steel reinforcement. The values of β, Q_y and δ_u would obviously change due to the change in pier height. However, these values are assumed to be constant and, as explained in the previous section, it can be assumed that it would not affect the qualitative observation for the damage analysis. The influence of the pier height (H = 14 m, 18 m, and 21 m) on the damage of the bridge pier is shown in Figure 8.18.

Figure 8.18 shows that the damage of the bridge pier increases with increase in the height of the bridge pier. The reason is due to the increase of the moment at base of the pier, and so damage. Also, increasing in height will decrease its natural frequencies, not because of reduction in local stiffness but the flexural stiffness of the whole beam. As the input earthquakes are the same, due to the frequency distribution of the earthquake energy, the pier with smaller natural frequencies

will therefore suffer more damage than those with high natural frequencies. For the 18 m and 14 m heights, the pier has small plastic strain and its behaviour remains almost elastic, and therefore the damages in these piers are not much different. It means that when the pier length is higher, it would have more damage and high dispersion in the non-linear dynamic response.

The mean (μ) and dispersion (δ) of the damage of the pier are calculated and shown in Table 8.10. It can be seen from the table that the dispersion δ of the damage measures for the heights of 18 m and 14 m is very small (0.084 and 0.016, respectively, or 1.8% and 0.4% of standard errors of estimation, respectively) suggesting that when the pier height is short, the structure would remain elastic for most of the input earthquakes and this reduces the scatter in the non-linear response. In this case, if the same standard error of estimation (Δ) is used, the representative number of non-linear dynamic analyses will therefore be reduced significantly. For example, for the mean with "± 1.00σ confidence band", the number of non-linear dynamic analyses is calculated as $n = \left(\frac{\delta}{\Delta}\right)^2$ will be reduced when the dispersion (δ) is reduced. On the other hand, if the same representative number of non-linear dynamic analyses (n) is used for different values of the pier height, (e.g. the number for the mean with "± 1.00σ confidence band" in Table 8.11) the response in shorter piers will be predicted more accurately than that of the higher ones because they have smaller dispersions or standard errors of estimation. This observation is similar to that of van de Lindt (2005). It should be noted here that when a parameter of the structure or earthquake loading, i.e. the pier height, changes its value, the mean (μ) and dispersion (δ) of the damage of the pier for the reference number of 20 change accordingly but the above overall observations are still remained. As this would be the same for other parameter changes, therefore these will not be mentioned again in the study of other parameters. In addition, it is important to note that in this parametric study, our research aim is to present the minimum representative number of non-linear dynamic analyses for the mean damage with a particular confidence band to the mean of 20 responses in which, depending on different values of a parameter of the structure or earthquake loading, the corresponding dispersions of the response may be different. It implies that when we present the same representative number of non-linear dynamic analyses for

different values of a parameter, their dispersion or standard error of estimation are not necessary to be the same.

Table 8.11 shows the mean number of non-linear dynamic analyses for a large number of orders of damage response (the number of orders is N = 10000) for different values of the pier height. It can be seen from the table that, despite the different dispersion, the results still supports the notion that the minimum necessary of the number of non-linear dynamic analyses shall be about 8 for the "84 percent confidence band". However, the minimum number of non-linear dynamic analysis is slightly reduced with reducing the pier height for higher confidence band as shown in Table 8.11. Although there is a slight difference in the minimum number of analyses required of the 14 m-high pier to the other two, the minimum number for the case of more "non-linearity" (e.g. 21m-high pier) is chosen as it is appropriate to the objective of this study. However, in general, the conclusion remains the same as the expected dispersion also reduces although less scatter is expected.

8.3.8 The presence of the axial load

Assuming the "P-delta" effect can be ignored, the presence of the constant axial load causes more compressive forces in concrete and this makes the pier stronger than the case without axial load as this reduces the tensile force in the concrete. Therefore, this is generally similar to increasing the amount of steel reinforcement. Again, for the sake of simplicity, the assumption of constant values of β, Q_y and δ_u is adopted in this study but it is envisaged that this would not significantly affect the qualitative observation for the damage analysis.

In the prototype bridge, the total weight of the deck distributed over the top of the pier is about 730.53 kN. In the current finite element modelling, this load is modelled as a constant axial load distributed at the top of the pier body to model the transferred load from the deck to the pier. The influence of this axial load on the damage of the bridge pier is shown in Figure 8.19 which also shows damage indices of the pier without axial load. It is clear that the presence of the constant axial load, in this case, slightly decreases the damage in the bridge pier. It is because the constant

axial load causes more compressive forces in concrete and this makes the pier stronger than the case without axial load by reducing the tensile force in the concrete. It should be noted that in the LUSAS Multi-crack model, the compressive behaviour of concrete is modelled without any crushing effects. In addition, the "P-delta" effect is ignored in this study as the displacement is assumed to be small. Therefore the pier suffers less damage than the case without axial load.

Table 8.12 shows the mean number of non-linear dynamic analyses for a large number of orders of damage response (the number of orders is N = 10000) for the cases with and without axial load. It can be seen from the table that the conclusion is the same as suggested in the main study in Chapter 7.

8.3.9 Seed of random number

The influence of the seed of random number (r), which is used for generating different phase angles for different artificial earthquake time-histories, (r = 1235, 1300, and 1500) on the damage of the bridge pier is shown in Figure 8.20.

Figure 8.20 shows different random seed numbers cause different damages in the bridge pier. This can be explained as different seeds of random number result in different arrays of phase angles generated from these seeds of random number, and consequently different earthquake motions are generated (see Chapter 3). Under these different earthquake motions, damages in the bridge pier are different. In details, Table 8.13 shows the mean and dispersion of damage indices for the three different values of random seed numbers which shows the dispersions for the three cases are similar which implies the seed number generator is sufficiently random.

Table 8.14 shows the mean number of non-linear dynamic analyses for a large number of orders of damage response (the number of orders is N = 10000) for different random seed numbers and it supports that one suggested in the main study in Chapter 7.

It should be noted for all the other parametric studies the same 20 earthquakes are used, but except this study, one on different subsoil classes (Section 8.3.2) and one on the duration of the earthquake in Sub-section 8.3.10. The order of damage response re-orders them but the same 20 earthquakes are compared. However, in this study, the earthquakes generated using different random number seeds are different from those used in the other parametric studies. Therefore it is very re-assuring that the same conclusion can be drawn thus implying the parametric study the Author has performed on the same 20 earthquakes generated using the random number seed of 1235 can be applied to other sets of different 20 earthquakes. This greatly improves the applicability and generality of this research.

8.3.10 Duration of the earthquake

In this study, the influence of the duration (s = 20 s and 30 s) on the damage of the bridge pier is investigated. For the duration of 20 s, 20 artificial time-histories generated in this chapter are used. For the duration of 30 s, 20 new artificial time-histories are generated with similar earthquake characteristics to those with the duration of 20 s, but with different levelling and total durations. The characteristics for earthquake generation with the duration of 30 s are shown in Table 8.15. The influence of the duration (s = 20 s and 30 s) on the damage of the bridge pier is shown in Figure 8.21.

Figure 8.21 shows that the damage of the bridge pier generally increases with increase in the duration of the input earthquakes. It is mainly due to increasing the levelling duration (the duration of highest amplitudes in the earthquake intensity function) it will generally increase the number of cycles of highest amplitudes. Therefore it will increase the energy input and consequently, dissipated energy and damage in the bridge pier will also increase. Table 8.16 clearly shows that the average damage in the bridge pier under earthquakes with duration of 30 s is higher than that under earthquakes with duration of 20 s. However, the dispersion with duration of 30 s is also higher than that with duration of 20 s. As explained in Section 7.3.6.7, for the same representative number of non-linear dynamic analyses with a particular confidence band to the mean of 20 damage respones as shown in Table 8.17, the response in the pier under the 20

second-duration earthquake will be predicted more accurately than that under the 30-duration one because it has smaller dispersion (or standard error of estimation), i.e. 0.25 compared with 0.36. On the other hand, if the same standard error of estimation (Δ) is used, the representative number of non-linear dynamic analyses for the 20-duration earthquake will be certainly less than that for the 30 second-duration one.

Table 8.17 shows the mean number of non-linear dynamic analyses for a large number of orders of damage response (the number of orders is N = 10000) for different durations. It can be seen from the table that the same conclusion suggested in the main study in Chapter 7 still applies. This conclusion is important because as stated in the last section, the earthquake actually used in this analysis is not the same 20 earthquakes as used in most of the other parametric studies. It is important to note that the same set of conclusions still applies.

8.4 SUMMARY AND CONCLUSIONS

In this chapter, the accuracy of integration is studied through the influence of some principal numerical parameters of the numerical integration such as time step, element mesh, numerical damping and viscous damping. It is followed by the section of parametric study, in which the influence of a number of parameters of earthquake and structural characteristics to the non-linear response and damage are investigated. Through this parametric study, the minimum representative number of artificially generated earthquake time-histories required for non-linear dynamic analysis, which was suggested in Chapter 7, was validated.

First of all, it can be observed from the numerical analyses that higher integration accuracy can be obtained when principal integration parameters such as the time step, element mesh, numerical damping and viscous damping are smaller. Through this investigation, it can also be concluded that when the parameters of numerical integration are changed, the behaviour of the LUSAS Multi-crack model and the FE analysis in the non-linear dynamic response changed accordingly and as expected.

Next, a detailed parametric study is performed in order to investigate the influence on the damage of the bridge pier of several physical parameters of earthquake and structural characteristics as well as the LUSAS Multi-crack model's parameters, which includes peak ground acceleration, duration, seed of the random number for earthquake generation, soil conditions, viscous damping ratio, time step, Young's modulus, tensile strength, pier height, the presence of axial load and the amount of steel reinforcement to the structural behaviour. For some parameters including pier height, axial load and the amount of steel reinforcement, and for simplicity, the assumption of constant values of β, Q_y and δ_u is adopted in the damage index but it should not greatly affect the qualitative observation for the damage analysis. The conclusions are presented as follows:

(1) The time step size of 0.005 s is adopted in this study because it is small enough to give reasonable results for practical purposes up to the second natural modes and significantly reduce the computational effort for a lot of analyses required in this chapter. Smaller time steps, i.e. 0.002 and 0.001s, were also investigated. The difference between some responses using time step of 0.005 s and 0.002 s and 0.001 s is due to the high frequency content captured in the responses using time step of 0.002 s and 0.001 s, or it could be due to the amount of damping produced by Rayleigh's parameters used which is too small and not increasing with frequency fast enough.
(2) The comparison of the responses from different damping ratios, ξ = 0.05, 0.10 and 0.20, confirmed that the use of damping significantly reduces the peak amplitude and reduces the permanent displacements and the vibration about it. It can be concluded that damage in the bridge pier decreases with increasing damping ratio.
(3) The comparison of the damage of the bridge pier for subsoil classes B, C, and D shows that it is not for sure that under softer subsoil classes, the bridge pier will have more damage than those of stiffer ones. It may be because the bridge pier has high natural frequencies. If the bridge pier has low natural frequency, it would have more damage under softer soils than those of stiffer ones. The difference in orders of input earthquakes may be another cause.
(4) It is concluded that damage in the bridge pier decreases with increasing the amount of steel reinforcement because of the stiffer effect and the reduction in concrete stress.

(5) Increasing the value of tensile strength will increase the load capacity in the concrete and consequently increase the stiffness of the bridge pier and therefore, leads to a lower damage with the assumption that the same values of β, Q_y and δ_u can be adopted in the damage index calculation.

(6) Increasing Young's modulus of concrete material will decrease the damage of the bridge pier as the beam becomes stiffness and this reduces the displacement, i.e. the strain, thus the stress in the concrete with the assumption that the same values of β, Q_y and δ_u can be adopted in the damage index calculation.

(7) It is concluded that the damage of the bridge pier dramatically increases with increasing the value of PGA as the magnitude and energy input of the earthquake decreases accordingly. It is also clear that a change in PGA can cause a significant change in the damage of the structure.

(8) Increasing the height of the bridge pier will increase the damage of the bridge pier. When the pier height increases, the pier natural periods increase and the moment generated at the fixed end also increases. As the input earthquakes have low frequency contents (see Chapter 3), the pier with its longer structural periods will suffer more damage. The damage and statistics analyses also show that there is more scatter in the response for longer piers with the assumption that the same values of β, Q_y and δ_u can be adopted in the damage index calculation.

(9) It can be concluded that the presence of the constant compressive axial load, in this case, slightly decreases the damage in the bridge pier as the concrete suffers from less tensile stress as a result of initial compressive stress produced by the axial load. These results were obtained while ignoring the crushing effect in compressive concrete and the "P-delta" effects and with the assumption that the same values of β, Q_y and δ_u can be adopted in the damage index calculation.

(10) Different seeds of random number cause different damages in the bridge pier. However, the damage statistics analysis demonstrates that the dispersion of damage for the cases of r = 1235, 1300 and 1500 are not too different and therefore either one of these values can be used in the generation of artificial earthquake time-histories. This conclusion is important because the earthquake actually used in this analysis is not the same 20 earthquakes as used in most of

the other parametric studies. It is important to note that the same set of conclusions still applies.

(11) It can be concluded the damage of the bridge pier increases with increasing the duration of the input earthquakes. It is because increasing the duration it will generally increase the number of cycles and energy input to the pier. Therefore it will increase the damage in the bridge pier. This observation is very significant as it strengthens current issues about the influence of earthquake duration on the structural damage (Hancock and Bommer 2005). This conclusion is important as in the last one because the earthquake actually used in this analysis is not the same 20 earthquakes as used in most of the other parametric studies. It is important to note that the same set of conclusions still applies.

The structural damage and responses obtained through the parametric study of several physical parameters of earthquake and structural characteristics such as peak ground accelerations, soil conditions, earthquake durations, seeds of random numbers, viscous damping ratios, the presence of axial load, pier heights, tensile strength, Young's modulus of concrete and the amount of steel reinforcement in the pier show that the LUSAS Multi-crack is capable of capturing most of key behaviours of RC piers under earthquake time-histories. The behaviour is reasonably accurate though the dissipated energy and unloading stiffness may have been overestimated because the unloading behaviour in tension is modelled as linear elastic in the model (see Chapters 2 and 5).

Through the study of each parameter, the minimum mean number of non-linear dynamic analyses for a random number in ordering of input earthquake time-histories for a particular confidence band from the mean of 20 responses is calculated. It demonstrated that the representative number of time-histories required for non-linear dynamic analyses are similar to the ones suggested in the main study in Chapter 7. In particular, it is concluded that the representative number required for non-linear dynamic analysis is about 11, 8, 7, and 6 in accordance with the "$\pm$ 1.00σ confidence band", "$\pm$ 1.40σ confidence band", "$\pm$ 1.64σ confidence band", and "$\pm$ 1.96σ confidence band", respectively, from the mean of 20 damage responses (for a large number of different orders of earthquakes, i.e. N = 10000). If in practical design, a relevant design basis calls for an "84 percent confidence band" (or "$\pm$ 1.40σ confidence band"), the minimum representative number required

for non-linear dynamic analyses is approximately 8. Obviously, further studies with different concrete material model would still be needed, however, in particular for the LUSAS Multi-crack model, this value can be used with some confidence as it is virtually unchanged over a large number of parametric studies. Although the actual results with different concrete material models would be different, the minimum representative number of earthquake time-histories required for a particular confidence requirement should remain relatively stable. This is because it is a characteristic of the statistical distribution of the earthquake time-histories generated and this characteristic remains similar after going through the transfer function as supplied by the behaviour of the concrete and the numerical system. With the plastic dissipation, the transfer function should produce more or less the same statistical distribution in the output as the input earthquake. However, one would expect more dispersion in the results would happen if failure occurs in some the analysis or chaotic behaviour and complexity start to set in when the non-linearity is increased.

Table 8.1 Analyses with different parameters for numerical integration

Name	Earthquake No.	Mesh	Time step (s)	Damping ratio	Newmark parameters	
					α	β
ANALYSIS-1	1	MESH I	0.005	0.05	0.3025	0.60
ANALYSIS-2	1	MESH II	0.005	0.05	0.3025	0.60
ANALYSIS-3	1	MESH I	0.002	0.05	0.3025	0.60
ANALYSIS-4	1	MESH I	0.005	0.10	0.3025	0.60
ANALYSIS-5	1	MESH I	0.005	0.20	0.3025	0.60
ANALYSIS-6	1	MESH I	0.005	0.05	0.36	0.70
ANALYSIS-7	1	MESH I	0.002	0.05	0.36	0.70

Table 8.2 Mean number of damage responses for different damping ratios

ξ	Minimum number of damage responses			
	"±1.00σ CB"	"±1.40σ CB"	"±1.64σ CB"	"±1.96σ CB"
0.05	11	8	7	6
0.10	11	8	6	5
0.20	11	8	6	5

Table 8.3 Mean and dispersion of damage indices for different subsoil classes

Subsoil class	Mean (μ)	Dispersion (δ)
B	0.71	0.25
C	0.67	0.27
D	0.62	0.50

Table 8.4 Mean number of damage responses for subsoil classes B, C, and D

Subsoil Class	Minimum number of damage responses			
	"±1.00σ CB"	"±1.40σ CB"	"±1.64σ CB"	"±1.96σ CB"
B	11	8	7	6
C	11	8	7	6
D	11	8	7	6

Table 8.5 Natural frequencies of the bridge pier for different cases of steel areas

Steel area (mm^2)	Natural frequency (Hz)				
	f_1	f_2	f_3	f_4	f_5
As	5.67	29.52	42.23	71.10	116.10
2 x As	5.88	30.57	43.61	71.17	116.17
4 x As	5.90	30.65	43.71	71.30	116.30

Table 8.6 Mean number of damage responses for different steel areas

Steel area (mm^2)	Minimum number of damage responses			
	"±1.00σ CB"	"±1.40σ CB"	"±1.64σ CB"	"±1.96σ CB"
A_s	11	8	7	6
2 x A_s	11	8	7	6
4 x A_s	11	8	7	6

Table 8.7 Mean number of damage responses for different tensile strengths

Tensile strength f_t (N/mm^2)	Minimum number of damage responses			
	"±1.00σ CB"	"±1.40σ CB"	"±1.64σ CB"	"±1.96σ CB"
3.0	11	8	7	6
4.2	11	8	7	6

Table 8.8 Mean number of damage responses for different values of Young's modulus

Young's modulus E (N/mm^2)	Minimum number of damage responses			
	"±1.00σ CB"	"±1.40σ CB"	"±1.64σ CB"	"±1.96σ CB"
32000	11	8	7	6
30000	11	8	7	5

Table 8.9 Mean number of damage responses for different values of Peak Ground Acceleration (PGA)

PGA (m/s^2)	Minimum number of damage responses			
	"±1.00σ CB"	"±1.40σ CB"	"±1.64σ CB"	"±1.96σ CB"
0.35g	11	8	7	6
0.525g	11	8	7	6

Table 8.10 Mean and dispersion of damage indices for different heights

H (m)	Mean (μ)	Dispersion (δ)
21	0.71	0.25
18	0.21	0.084
14	0.06	0.016

Table 8.11 Mean number of damage responses for different values of pier height (H)

H (m)	Minimum number of damage responses			
	"±1.00σ CB"	"±1.40σ CB"	"±1.64σ CB"	"±1.96σ CB"
21	11	8	7	6
18	11	8	6	5
14	11	8	5	4

Table 8.12 Mean number of damage responses with and without axial load P

Axial load P 730.525 kN	Minimum number of damage responses			
	"±1.00σ CB"	"±1.40σ CB"	"±1.64σ CB"	"±1.96σ CB"
Without P	11	8	7	6
With P	11	8	7	6

Table 8.13 Mean and dispersion of damage indices for different random seed numbers

r	Mean (μ)	Dispersion (δ)
1235	0.71	0.25
1300	0.98	0.25
1500	0.76	0.25

Table 8.14 Mean number of damage responses for different random seed number (*r*)

r	Minimum number of damage responses			
	"±1.00σ CB"	"±1.40σ CB"	"±1.64σ CB"	"±1.96σ CB"
1235	11	8	7	6
1300	11	8	7	6
1500	11	8	7	6

Table 8.15 Parameters for earthquake generation of duration of 30 s

Characteristics	**Input values**
Target response spectrum	EC8 velocity RS for $\xi = 0.05$ (Ground Type 1 - EC8 prEN1998-1:2004)*
Subsoil class	B
Duration	30 (s)
Levelling duration	6 (s)
Peak Ground Acceleration (PGA)	0.35g (m/s^2)
Frequency range	0.25 - 33.33 (Hz)
Intensity envelope function	A compound intensity envelope function (Jennings *et al*. 1968)
Generated response spectrum for damping	$\xi = 0.05$

* EC8 velocity RS is obtained from the original acceleration RS in EC8

Table 8.16 Mean and dispersion of damage indices for different durations (*s*)

Duration *s* (s)	Mean (μ)	Dispersion (δ)
20	0.71	0.25
30	1.11	0.36

Table 8.17 Mean number of damage responses for different durations (*s*)

Duration *s* (s)	Minimum number of damage responses			
	"±1.00σ CB"	"±1.40σ CB"	"±1.64σ CB"	"±1.96σ CB"
20	11	8	7	6
30	11	8	7	6

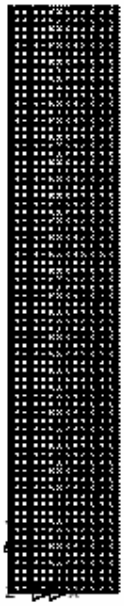

Figure 8.1 Finite element mesh, MESH II

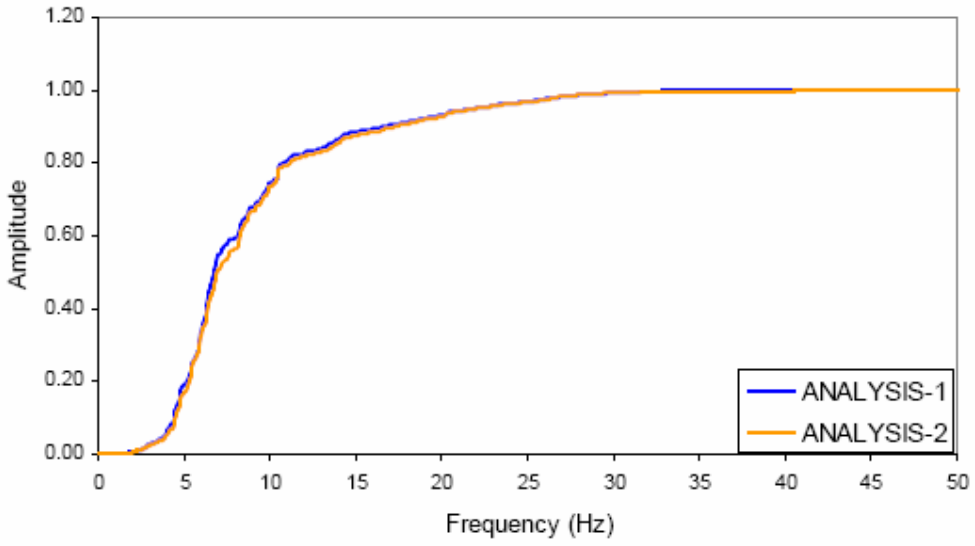

Figure 8.2 Normalised cumulative acceleration spectra for ANALYSIS-1 and ANALYSIS-2

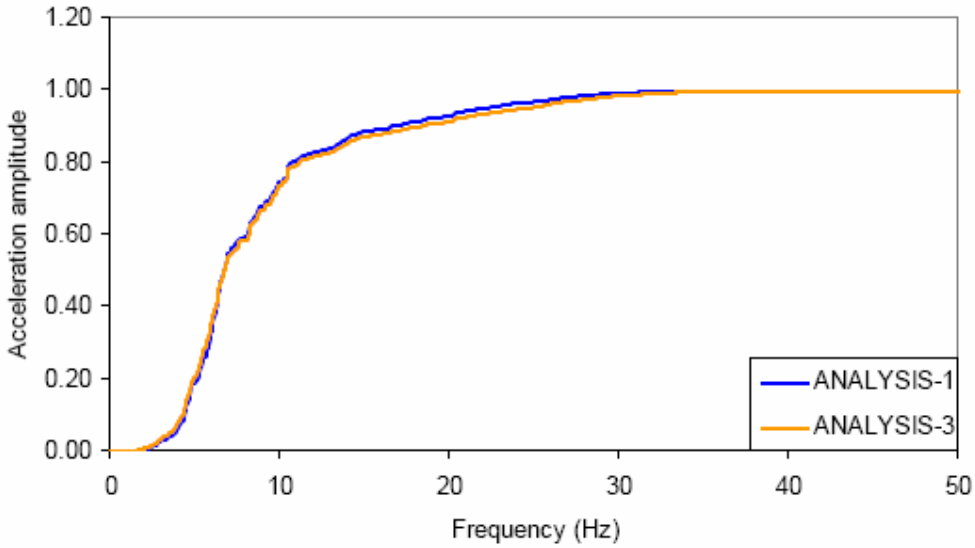

Figure 8.3 Normalised cumulative acceleration spectra for ANALYSIS-1 and ANALYSIS-3

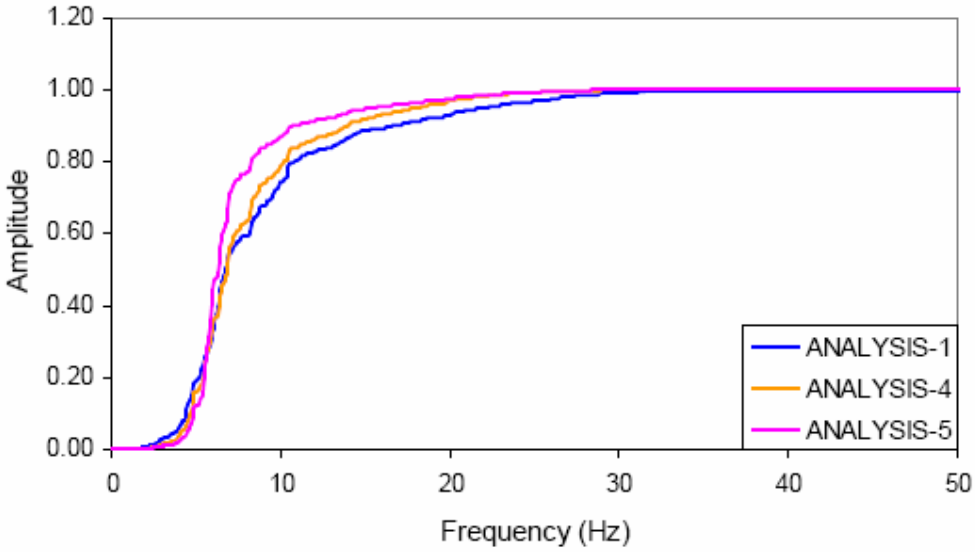

Figure 8.4 Normalised cumulative acceleration spectra for ANALYSIS-1, ANALYSIS-4, and ANALYSIS-5

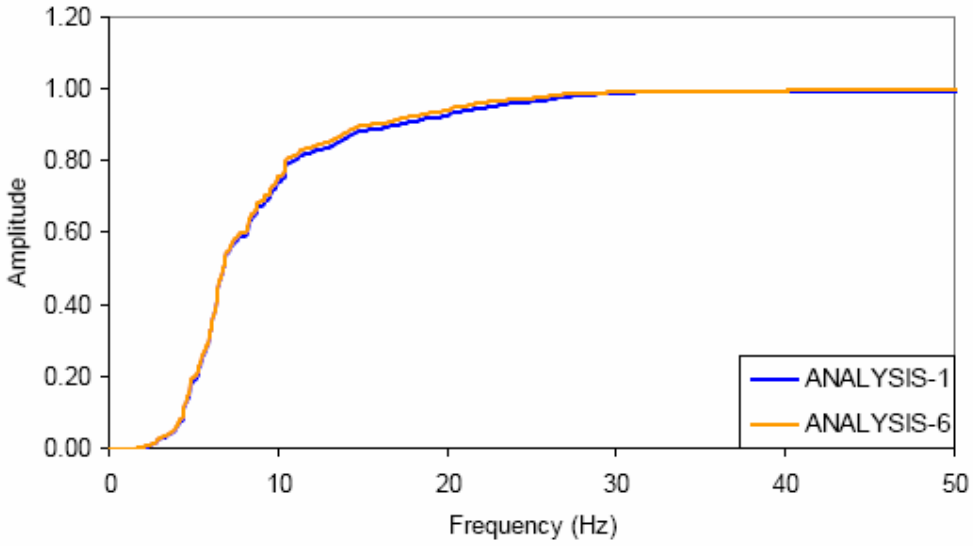

Figure 8.5 Normalised cumulative acceleration spectra for ANALYSIS-1 and ANALYSIS-6

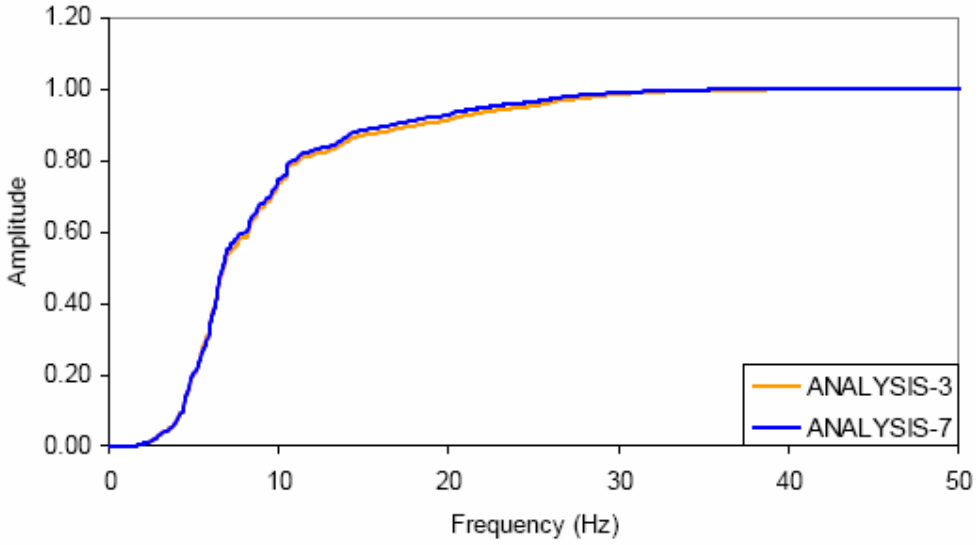

Figure 8.6 Normalised cumulative acceleration spectra for ANALYSIS-3 and ANALYSIS-7

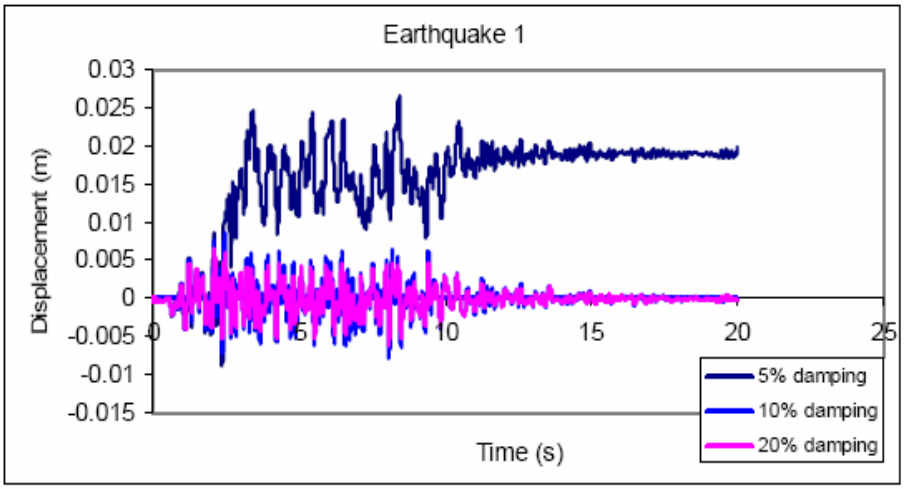
Earthquake 1
Displacement (m)
0.03
0.025
0.02
0.015
0.01
0.005
0
-0.005
-0.01
-0.015
0
5
10
15
20
25
Time (s)
5% damping
10% damping
20% damping

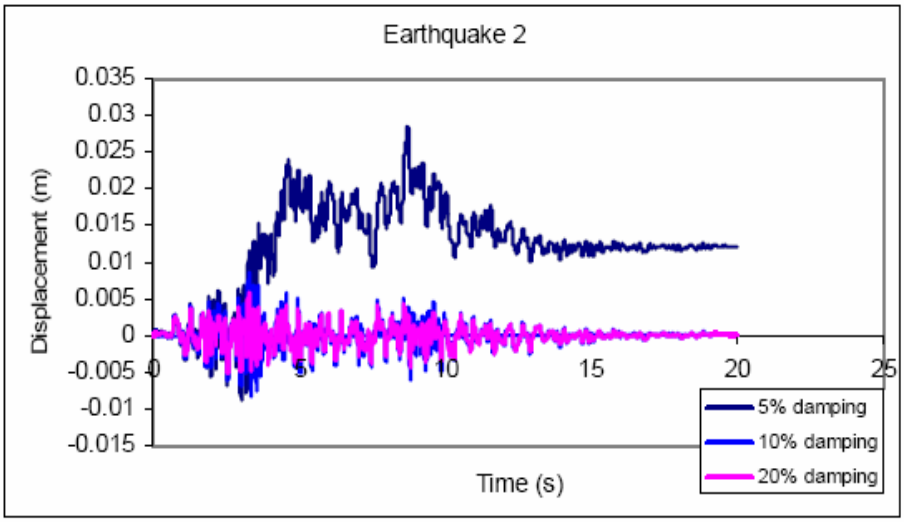
Earthquake 2
Displacement (m)
0.035
0.03
0.025
0.02
0.015
0.01
0.005
0
-0.005
-0.01
-0.015
0
5
10
15
20
25
Time (s)
5% damping
10% damping
20% damping

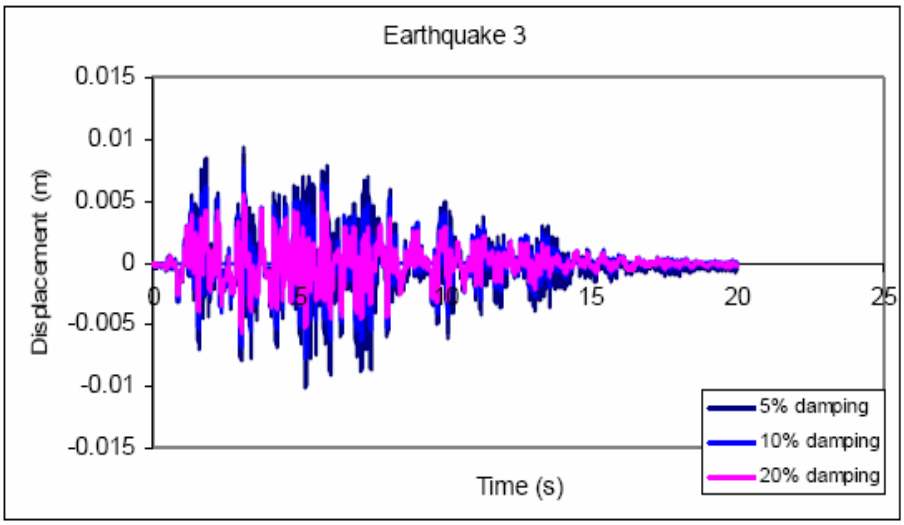
Earthquake 3
Displacement (m)
0.015
0.01
0.005
0
-0.005
-0.01
-0.015
0
5
10
15
20
25
Time (s)
5% damping
10% damping
20% damping

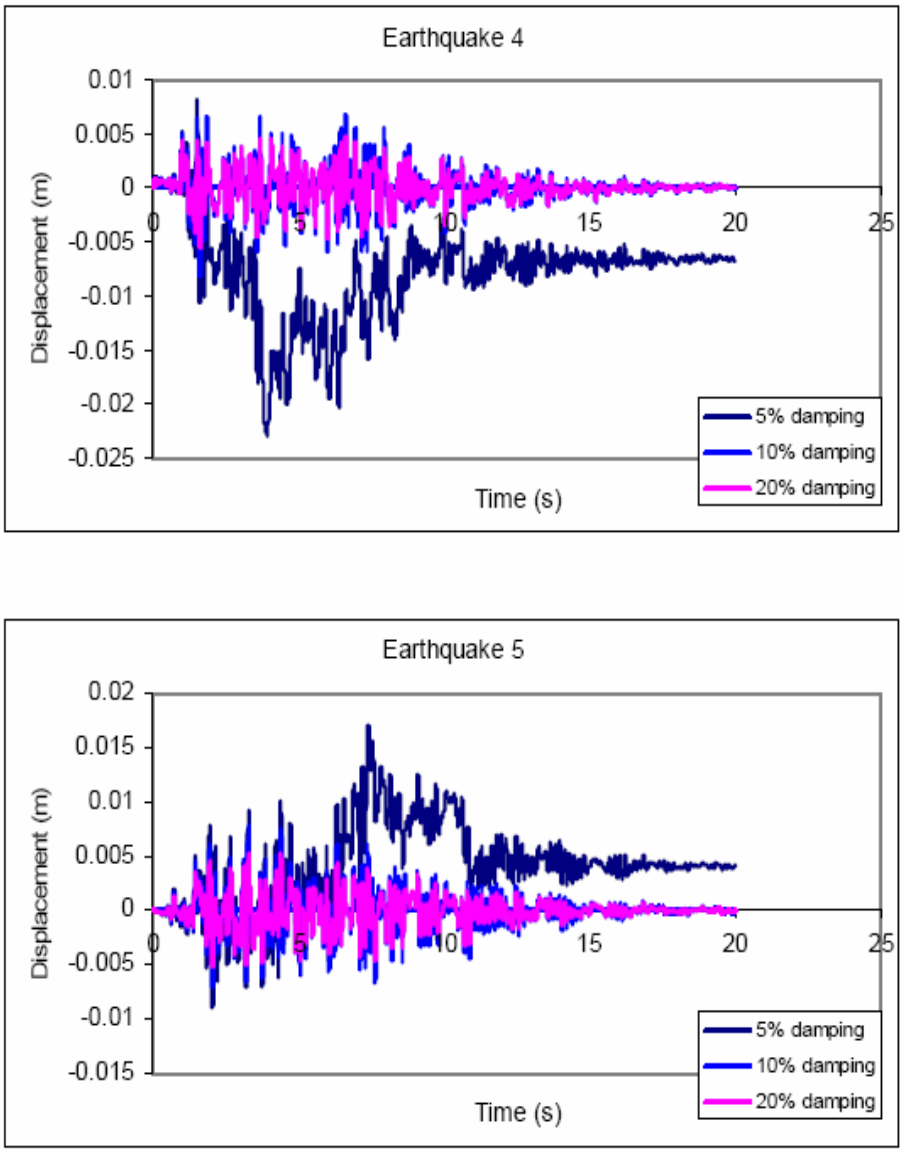

Figure 8.7 Relative displacements with various damping ratios (ξ = 0.05, 0.10, and 0.20)

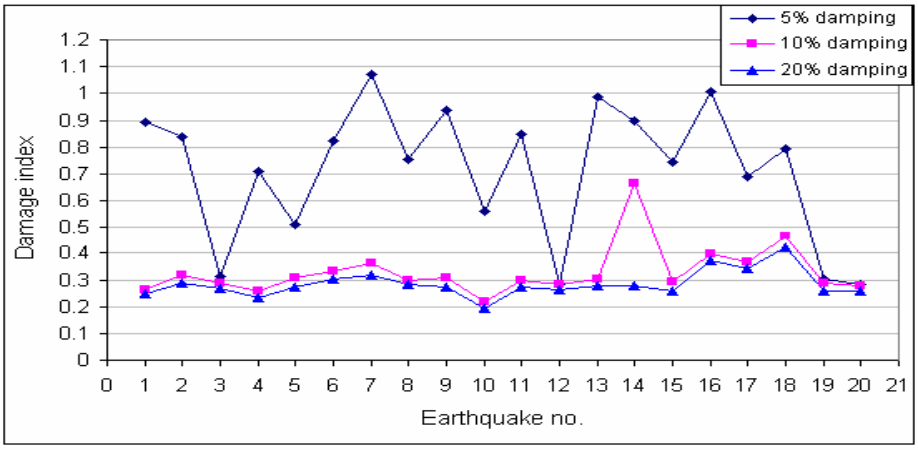

Figure 8.8 Damage index with various damping ratios (ξ = 0.05, 0.10, and 0.20)

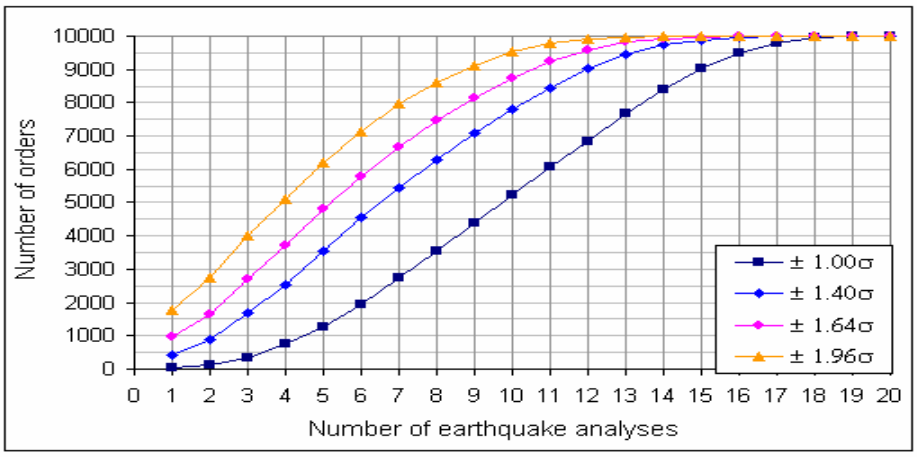

Figure 8.9 Cumulative distribution of number of earthquake analyses in 10000 different orders of 20 input earthquakes (ξ = 0.10)

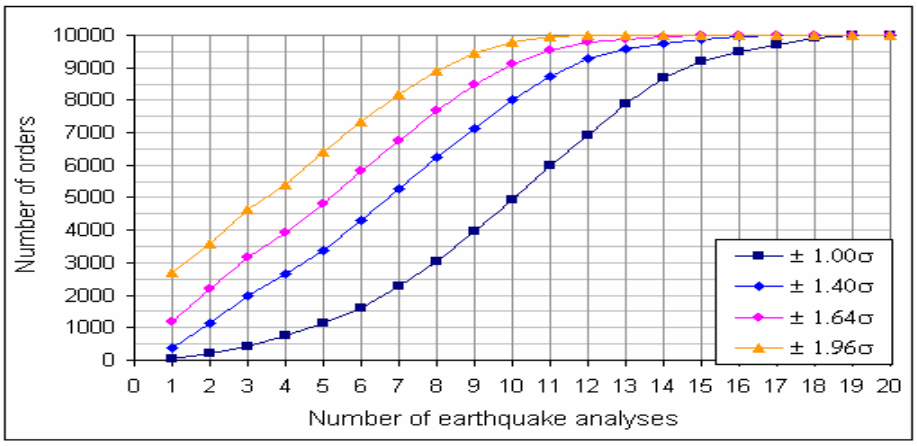

Figure 8.10 Cumulative distribution of number of earthquake analyses in 10000 different orders of 20 input earthquakes (ξ = 0.20)

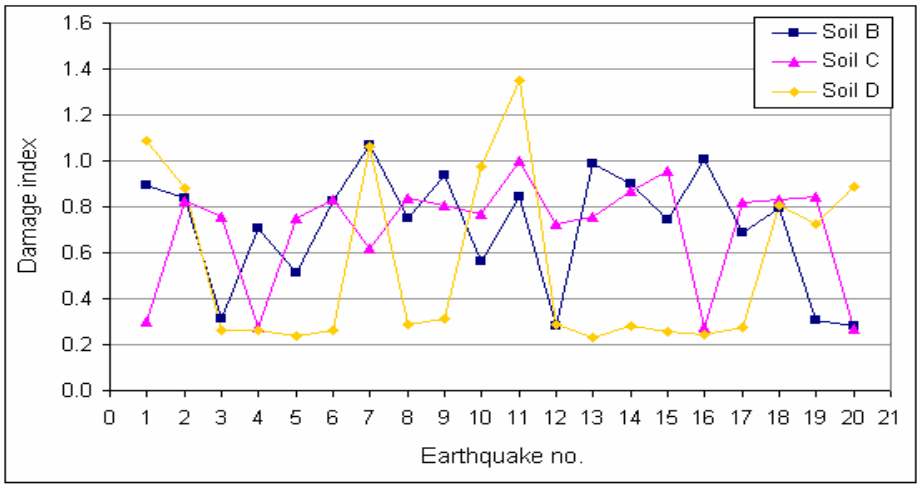

Figure 8.11 Damage index with various soil conditions (Subsoil classes B, C, and D from Eurocode 8, prEN 1998:1-2004)

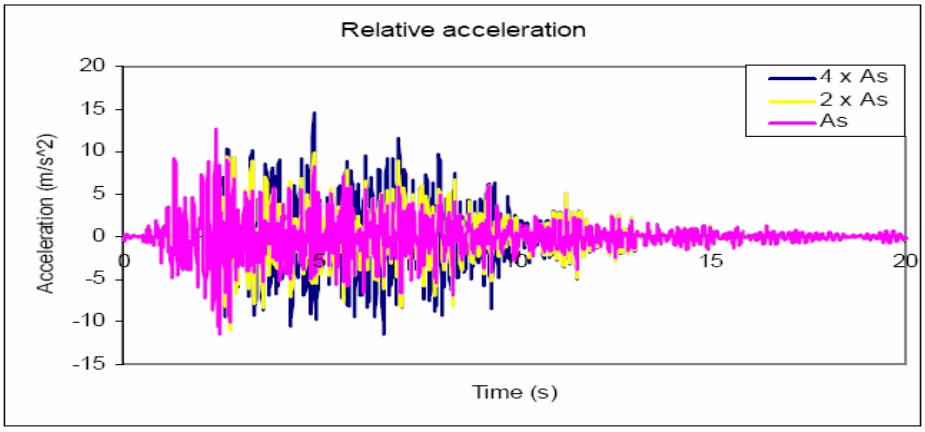

Figure 8.12(a) Relative acceleration for different amounts of steel under Earthquake 1

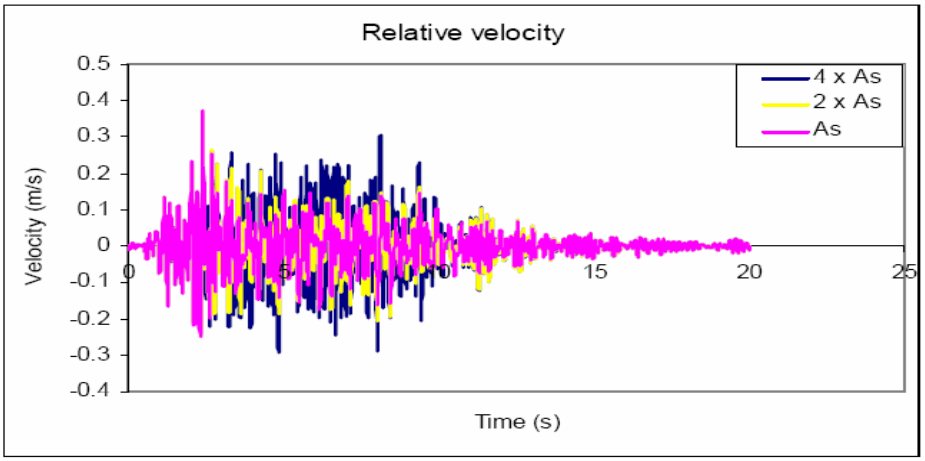

Figure 8.12(b) Relative velocity for different amounts of steel under Earthquake 1

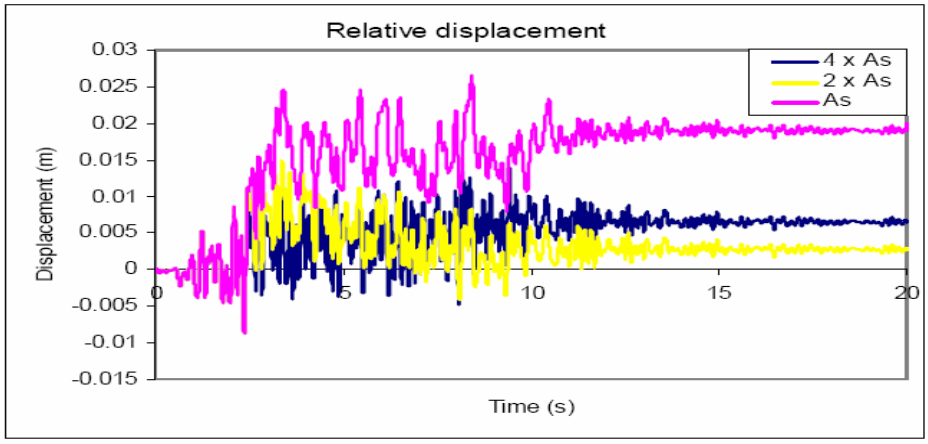

Figure 8.12(c) Relative displacement for different amounts of steel under Earthquake 1

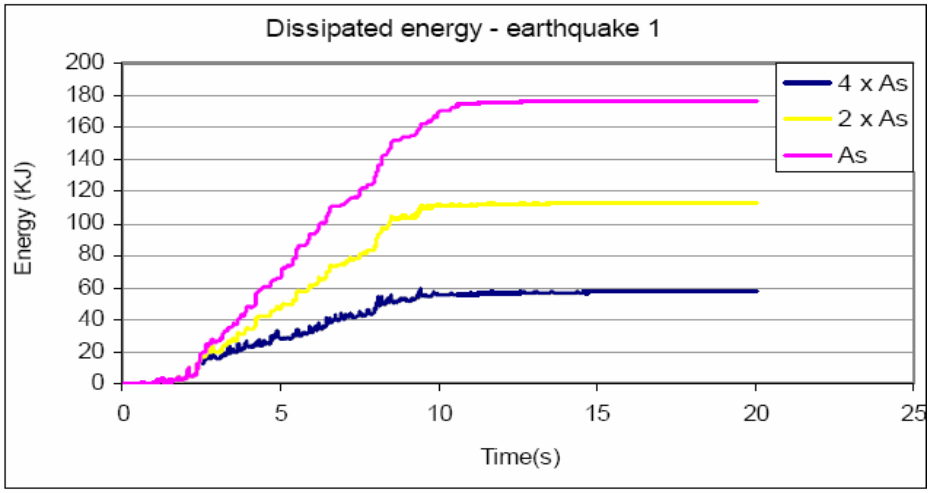

Figure 8.13 Dissipated energy for different amounts of steel under Earthquake 1

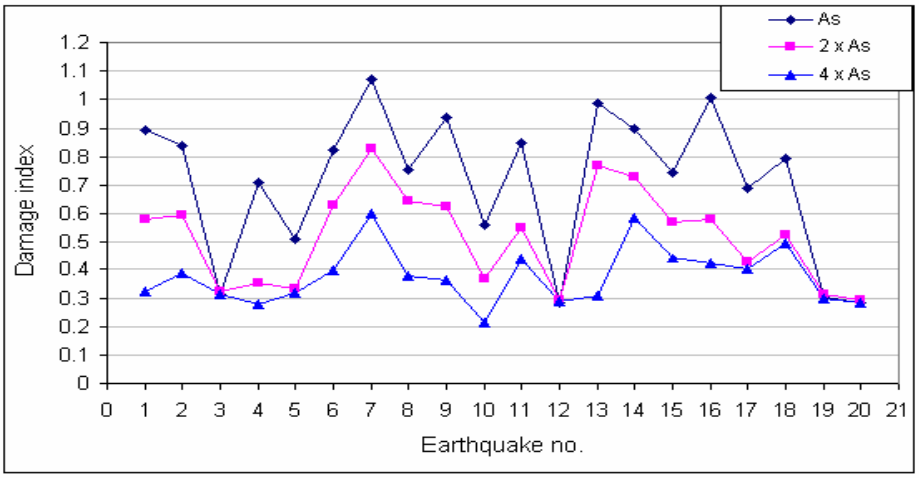

Figure 8.14 Damage index with various steel areas (A_s, 2 x A_s, and 4 x A_s)

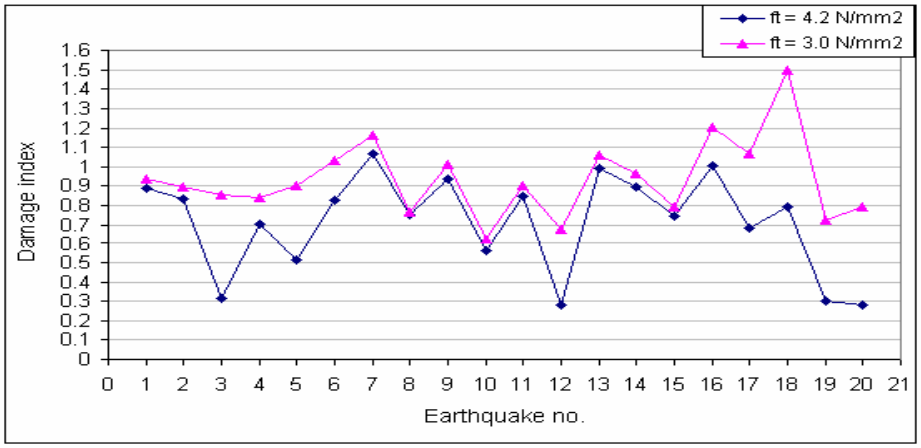

Figure 8.15 Damage index with various tensile strengths (f_t = 3.0 and 4.2 N/mm^2)

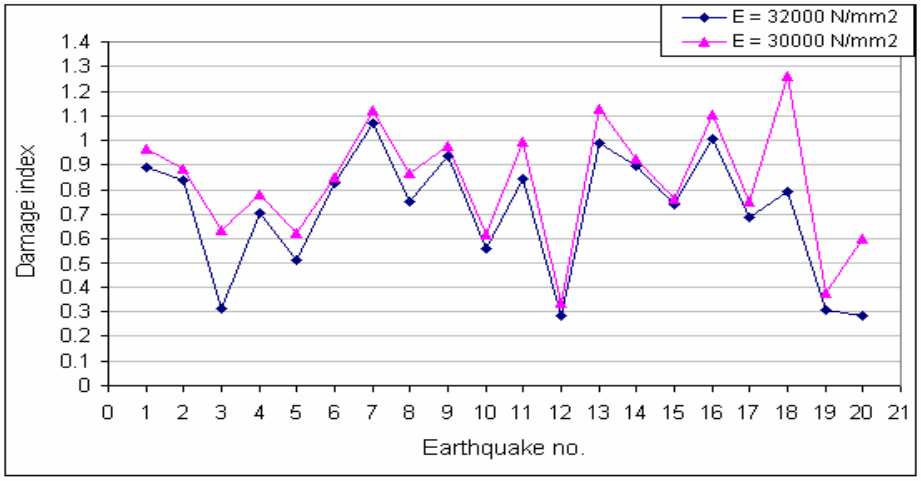

Figure 8.16 Damage index with various Young's modulus (E = 30000 and 32000 N/mm^2)

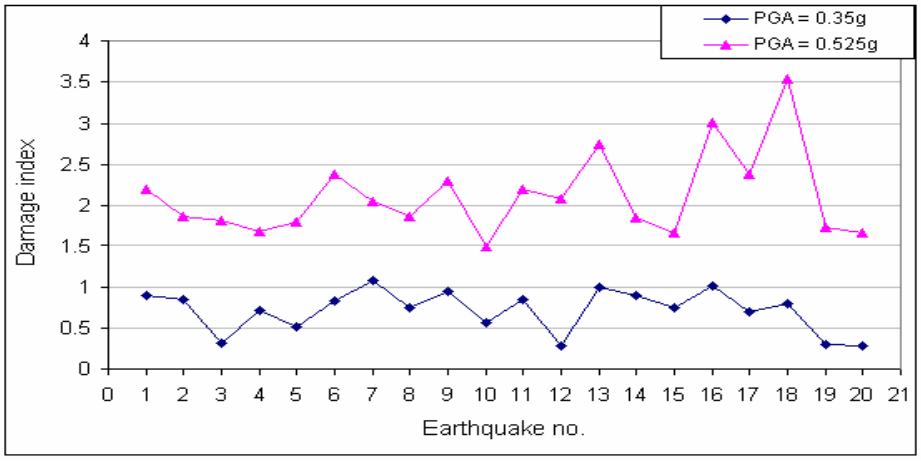

Figure 8.17 Damage index with various Peak Ground Acceleration (PGA = 0.35g and 0.525g in which g = 9.81 m/s^2)

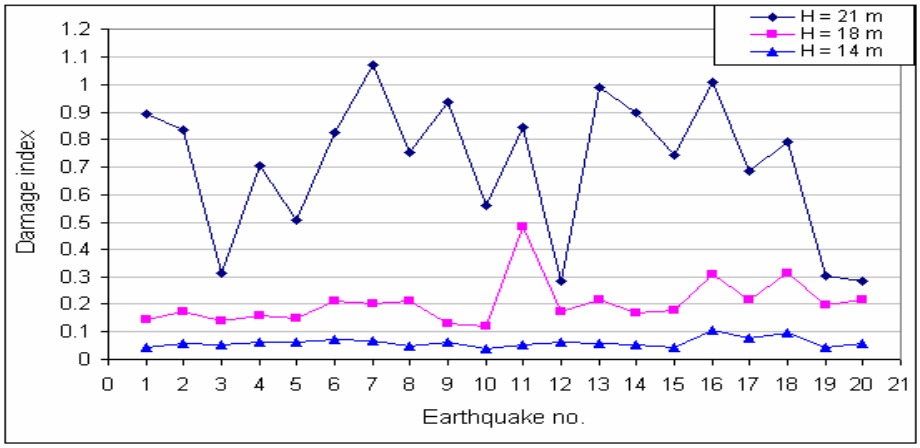

Figure 8.18 Damage index with different heights (H = 14 m, 18 m, and 21 m)

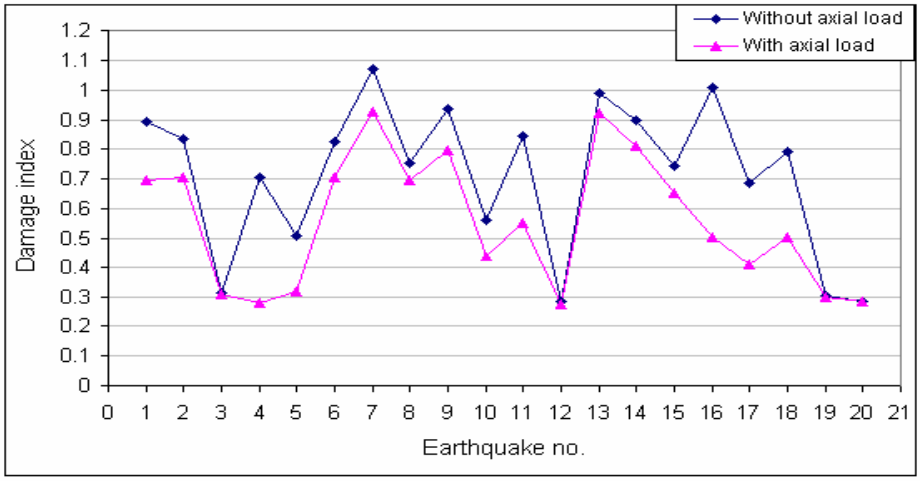

Figure 8.19 Damage index with and without axial load at the top of the pier

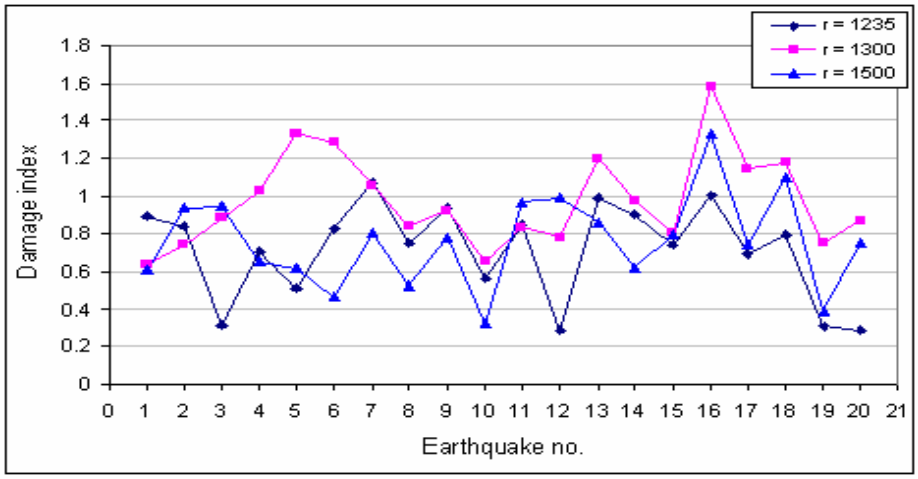

Figure 8.20 Damage index with different random seed number (r = 1235, 1300, and 1500)

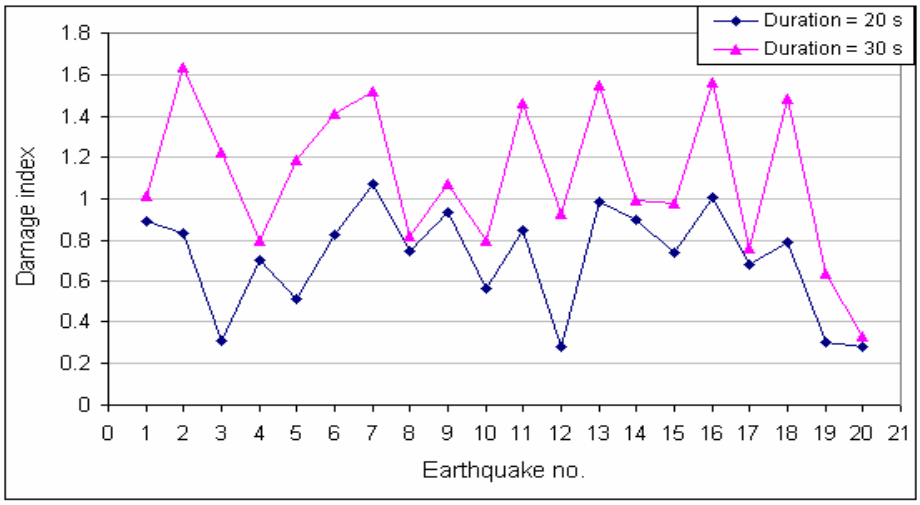

Figure 8.21 Damage index with different durations (s = 20 s and 30 s)

CHAPTER 9

CONCLUSIONS AND FURTHER WORKS

9.1 CONCLUSIONS

The primary aims of the work presented in this thesis are the numerical generation of artificial earthquake time-histories, the numerical modelling of concrete and reinforced concrete structures under monotonic, cyclic loading and artificially generated earthquake time-histories, and the minimum representative number of earthquakes required for non-linear dynamic analysis. The main objectives of this research are

(i) to generate and select suitable sets of artificial earthquake time-histories for non-linear dynamic analysis,

(ii) to examine the smeared crack models for concrete materials in finite element modelling of concrete and reinforced concrete structures under monotonic and cyclic loadings,

(iii) to propose an analytical solution for non-linear flexural behaviour of concrete and RC beams,

(iv) to evaluate the response of RC bridge piers under artificial earthquake time-histories and in particular, represent a minimum necessary number of time-histories required for a non-linear dynamic analysis, and

(v) to study the influence of several parameters of the material model, earthquake and structural characteristics to the structural response and damage

The main contributions of this research are:

(a) The insights obtained from the in-depth study of artificially generated earthquake time-histories compatible with an EC8 response spectrum using the program SIMQKE (Gasparini and Vanmarcke 1976) in order to understand effects from all the major parameters concerned so as to select the most suitable sets of artificial time-histories for a dynamic analysis (see Section 9.1.1)

(b) The validation of the Multi-crack model (Jefferson 1999) and Craft model (Jefferson 2003a, 2003b) against experimental results for un-notched concrete beams under monotonic loading. The modification of the fracture energy used in the Multi-crack model is implemented to deal with 2-D problems (see Section 9.1.2)

(c) The validation of the Multi-crack model and Craft model against experimental results for different reinforced concrete beams and columns under monotonic loading and cyclic loadings (see Section 9.1.3)

(d) The development and assessment of a simply analytical model for predicting non-linear flexural behaviour of un-notched concrete and RC beams in order to provide further understandings the softening-related problems (see Section 9.1.4)

(e) The non-linear dynamic response of RC bridge columns under artificially generated time-histories and the influence of several parameters of the material model, earthquake and structural characteristics to the structural response and damage (see Section 9.1.5)

(f) The minimum representative number of artificial time-histories required for non-linear dynamic analysis, and the validation of the number suggested (see Section 9.1.6)

The following sub-sections present the main goals as well as contributions of the research in this thesis and its weaknesses are discussed. In these sub-sections, the concluding remarks are collected from Chapters 3 to 8, where they have already been presented in detail at the end of each chapter.

9.1.1 Numerical generation of artificial time-histories fitting to an EC8 response spectrum

It is required in this study to generate appropriate sets of artificial time-histories fitting to an EC8 response spectrum to be used for non-linear dynamic analysis. This is to overcome the limitations and paucity of strong recorded time-histories in many seismic regions, which are not always available for seismic design. A well-known program for earthquake generation, namely SIMQKE (Gasparini and Vanmarcke 1976) has been adopted for this purpose. Program accuracy tests have been carried out first to assess the artificial time-histories in comparison with the EC8 requirements. To obtain suitable sets of artificial time-histories, it is essential to understand the

underlying theory of the program and effects from both the program parameters and properties of earthquake time-histories. For that reason, a parametric study of understanding the generated power spectral density function $G(\omega)$, the iteration technique of generation has been investigated. In addition, properties of generated time-histories including soil conditions, frequency ranges and earthquake durations are also studied. Based on these investigations, sets of appropriate artificial time-histories can be generated for use in a dynamic analysis. Here are some important conclusions:

1. In the program validation part, the computed velocity RS corresponding to the artificial time-histories follow relatively well the target EC8RS (from both ENV and prEN versions of EC8), especially in high frequencies. In some cases, the difference between the computed RS and the EC8RS in moderate or low frequencies can be tolerated by using iteration techniques, i.e. the number of smoothing cycles. Because the program SIMQKE is concerned with the matching of the computed RS and the target RS in a particularly popular range of frequency, i.e. from 0.04 Hz to 25 Hz, it is difficult to find a good agreement between computed and target response spectra in low frequency domain and very high frequency domain, i.e. less points define the computed response spectrum (Section 3.5). Nonetheless, when twenty artificial time-histories are generated, the averaged RS is smoother and better matched with the target EC8RS than that of five artificial time-histories. It shows that the more numbers of artificial time-histories are generated, the closer the averaged values to the target response spectrum (Section 3.4).
2. In the parametric study of program parameters, the generated $G(\omega)$ reasonably presents a typical spectral density function of a real earthquake in the case of damping $\xi \geq 0.05$ (Section 3.5.1). In order to ensure the generated $G(\omega)$ on a typical form of real earthquakes and to leave the structures enough time to perform steady-state response, duration $s \geq 20$ seconds should be considered for earthquake generation (Section 3.5.2). Iteration techniques, i.e. the number of smoothing cycles, could be used to match the computed RS with the target EC8RS in moderate and low frequency ranges. A number of

smoothing cycles from 1 to 4, especially 3 can be adopted in the generation (Section 3.5.3).

3. In the study of the properties of generated earthquake-like ground motions, it shows that local soil strongly affects the earthquake amplitude through its relative frequency and the duration of the earthquake (Section 3.5.4). The maximum frequency range of 0.2 Hz to a frequency of 33.33 Hz can be chosen for the generation of artificial earthquakes based on literature of earthquake engineering on the maximum frequency of real recorded earthquakes (Section 3.5.5).
4. The time interval in duration of an artificial earthquake should be small enough in order to accurately describe the wave form and frequency content of the earthquake motion as it may be important for non-linear dynamic analysis (Section 3.5.6).

In conclusion, suitably refined parameters such as $\xi \geq 0.05$, $s \geq 20$ seconds, maximum frequency range of 0.2 Hz to a maximum frequency ≤ 33.33 Hz, and iteration techniques, such as $n_c = 1$ to 4 cycles, should be used together to match the computed RS with the EC8RS in an allowable tolerance. Other parameters related to a specific seismic site such as soil conditions, peak ground acceleration, or the time interval used for generation of artificial time-histories will be studied in more details with a particular structure (see Chapters 7 and 8). It has been demonstrated that suitable sets of artificial time-histories are obtained in the manner that their corresponding response spectra are well matched with the target EC8RS, are in typical forms of real-strong earthquakes, and are satisfactory all the requirements from EC8. Thus, several sets of twenty artificial acceleration time-histories fitting to the 5% damping EC8 elastic response spectra can be generated for use in the FE non-linear dynamic analysis.

9.1.2 Validation of the Multi-crack and Craft models for un-notched concrete beams under monotonic loading

In order to apply the Multi-crack model (Jefferson 1999) and Craft model (Jefferson 2003a, 2003b) for numerical modelling work in this thesis, it is necessary to validate the models for many applications. In finite element modelling, there has been relatively little work dealing with

un-notched concrete beams because there is lack of good experimental data for un-notched beam tests, especially in aspects related to the determination of some of the material properties such as fracture energy. For that reason, the models have been examined against experimental data from un-notched three-point bending tests (Carpinteri 1989, Ozbolt and Bazant 1991). The key conclusions are:

1. The numerical result of Craft model shows a very good agreement with the experimental result in both pre- and post-peak regimes for un-notched concrete beams. For the Multi-crack model, however, the fracture energy is only referred to the characteristic length of 3-D problems in the program coding (Jefferson 2004). Therefore, a modification of the fracture energy is needed in order for it to be use for 2-D problems. The value of the fracture energy was estimated through reliable numerical result of Craft model and experiments.
2. Using the modification for fracture energy for the Multi-crack model it can guarantee the numerical results to converge to the same result and not mesh size dependency. Also, a model modification factor (α) was introduced to convert the input value of fracture energy of Craft model (or experiment) to the input value of fracture energy of Multi-crack model so that the result of the Multi-crack model can be well matched with those of Craft model and experiment. In particular, if in the crack zone, the second mesh size is double the first mesh size when the thickness is assumed to be the same, the model modification factor recommended for the two meshes (when fitting their results to those of Craft model) is $\alpha = \frac{1}{\sqrt[3]{2}} \cong 0.794$ (Sections 4.2.1 and 4.2.2).
3. The numerical results are stiffer than those of experiment after cracking in the un-notched concrete beams. In agreement with that, numerical cracks and stress distribution are spread out in a wider zone at the beginning of cracking progress as shown in pre-peak part in the load-deflection curve (Section 4.2.1.7). This widely spreading zone predicted by numerical analysis can explain the reason why the numerical results are stiffer than those of experiment after cracking in concrete. In fact, the experimental results would be softer than because concrete is localised in a narrow band and softened quicker than the

numerical study. Moreover, the pre-peak behaviour of an un-notched beam is much more affected by the heterogeneity of the material as widely seen in experiment (Petersson 1981), where the artificial flaw dominates the material imperfection. This is an aspect of the real behaviour which the smeared crack model cannot always capture. It can be concluded that, the numerical crack patterns and stress, strain distributions not only provide important pictures of the post-peak behaviour of un-notched concrete structures but also explain the difference between numerical and experimental responses.

9.1.3 Validation of the Multi-crack and Craft models for RC beams under monotonic loading and bridge pier under cyclic loading

First of all, the Multi-crack model and Craft model have been verified against well-known experimental RC beams (Bresler and Scordelis 1963 and Carpinteri 1989). Through this, it demonstrates that the models can predict the numerical mode of failure of RC beams subjected to flexural and shear loading. It is also to understand the application of the models for predicting the behaviour of RC beams owing to the amount of steel reinforcement included, especially the transition from brittle to ductile behaviour. These are problems that have not been studied much in numerical modelling. Furthermore, some features relating to non-linear strategy, numerical solution, FE mesh configuration, and load-step size are also investigated. This helps to achieve a better understanding of using the models for practical applications (see Chapter 5).

In addition, the capability of the two models to reproduce the most important features of a RC bridge pier under cyclic loading has been evaluated by comparison their results with available experimental data (Pinto 1996). It was found out that the Multi-crack model, in general, does not follow well the cyclic behaviour of RC bridge piers while still capture some key features such as plastic strains and coarse hysteretic behaviour. On the other hand, the result of Craft model was in good agreement with experimental results because the model takes into consideration most of mechanical behaviour of concrete under cyclic loading (see also Chapter 5).

Several sets of conclusions are presented as follows:

9.1.3.1 Reinforced concrete beams under monotonic loading

1. In the case of over-reinforced beams, the Multi-crack and Craft models are able to provide a good prediction not only of the failure load but also on the diagonal crack pattern and deformation behaviour. The crack patterns and the contour of maximum stresses obtained from the numerical model are in very good agreement with those of experiments. It is clear that the models give a complete picture of the response with peak and post-peak behaviour, mode of failure, and the stress distribution in the entire beam, which cannot easily achieved by other analytical or experimental methods (Section 5.2.2.4).
2. For the over-reinforced beams, distributed cracking model is appropriate for the modelling. As in well-reinforced concrete, reinforcement can stabilise the structural response during cracking and localised problems are not occurred in FE analysis. Therefore, not much care is required in the choice of the mesh configuration and the issue on fracture energy as when dealing with localised fracture for concrete.
3. The Multi-crack model predicts a slightly higher peak load compared with the experiment and Craft model. It is because this model does not include the non-linear behaviour and crushing failure of concrete in the compressive zone. The results predicted by Craft model, in contrast, is lower than that of Multi-crack model in cracking progress due to the model includes the non-linear behaviour and crushing effects in compressive concrete which can cause the loss of strength in the beam prematurely. The comparison between stress-strain curves at a Gauss point of the Multi-crack and Craft models demonstrates this conclusion.
4. In the case of under-reinforced beams, localised model becomes more appropriate for modelling the beams with small amount of steel reinforcement and thus, the input fracture energy and the mesh configuration should be obtained by the issues given in Chapter 4. The result of Craft model shows that the peak load and the post-peak responses were captured reasonably. As the non-linear behaviour and crushing of concrete in compressive zone is not included in the Multi-crack model, the numerical result overestimates the response (Section 5.2.3.4).

5. For under-reinforced beams and at the transition from brittle to ductile behaviour of RC beams, the numerical simulations are stiffer than the experimental results. In this case, it may be because it was assumed the same fracture energy is used in the models as for plain concrete cases. Therefore, regarding the analysis of under-reinforced concrete beams and the problem of transition, it is suggested that further investigations into the identification of parameters used for the model, i.e. the fracture energy or strains for the cracking model approach, are needed in order to simulate the structural behaviour more accurately.
6. Differences between the numerical results (of Multi-crack and Craft models) and the experimental results could be subject to some experimental errors (Section 5.2.2.4) and the assumption of perfect bond between concrete and steel reinforcement in the numerical modelling in the research.
7. Features of non-linear FE analysis including the load control, load-size step, convergence tolerance and iteration method have significant effects on the convergence progress as well as the numerical accuracy of the non-linear responses.

9.1.3.2 Reinforced concrete bridge pier under cyclic loading

1. The LUSAS Multi-crack model is, in general, not capable of capturing the cyclic behaviour of RC bridge piers. The chief flaw with the model is that unloading behaviour in concrete is linear elastic, which is unrealistic for concrete. However, it is still capable of reproducing some key features of cyclic behaviour such as plastic strains and a coarse hysteretic behaviour. Especially in this cyclic study, although the crushing effect is not included in the model, it does not affect the numerical results because experimental observations showed that there is no crushing failure in the pier (Pinto 1996). Nevertheless, the Multi-crack model should be used with care if used for analysis of structures under cyclic loading as the damping and unloading stiffness have been overestimated. In physical point of view, the model would be used reasonable in the structures which have high compressive strength and no crushing failure under cyclic loading (Section 5.3.5).

2. The result of Craft model is in good agreement with experimental results of the RC bridge pier under cyclic loading in terms of many key features of cyclic responses. They include the hysteretic behaviour, stiffness degradation, strength degradation and pinching effects. It is because the model takes into account most of non-linear effects of concrete and reinforced concrete under cyclic loading (see Chapter 2). However, as the peak load at each cycle and the stiffness are slightly too high in comparison with experiment, the consideration of bond slip between concrete and steel reinforcement may be necessary in order to obtain response close to reality (Section 5.3.5).
3. It is concluded that Craft model would be suggested to use for further analyses of RC bridge piers under cyclic and earthquake-like cyclic loading as it would capture the cyclic behaviour more accurately than the Multi-crack model. As this is the early stage of the implementation of Craft model in LUSAS for RC structures under cyclic loadings, a lot of difficulties had been faced relating to convergent problems and many problems were not completely solved (see Chapter 7). However, if the response or damage of RC bridge piers under different sets of artificial earthquake time-histories is studied in relative comparisons in terms of qualitative indices, the Multi-crack model should also be able to be used without leading to a wrong conclusion.

9.1.4 Analytical solution for non-linear flexural behaviour of concrete and RC beams

It is desirable in this study to build analytical model using beam theory and non-linear fracture mechanics, which can accommodate the strain-softening behaviour, for evaluating moment-curvature and load-deflection curves of concrete and RC beams under monotonic loading. In order to capture important features in non-linear flexural behaviour, and in particular, the deflection of the beam, the model employs a softening zone width in mid-section of the beam, of which the material exhibits a softening stress-strain relationship as proposed in the crack band model (Bazant and Oh 1983). While outside this softening area, the material unloads elastically. It was assumed that the displacement continuity conditions at the interface between the strain-softening and linear elastic unloading zones are preserved (Bazant and Zubelewics 1988) and that curvatures and moments at any cross-section inside the softening zone width are linearly

interpolated from those at the interface and mid-span cross-sections. The model also relates the width of the softening zone with the beam depth (Ulfkjaer *et al.* 1995) in order to partly include the structural size effect.

In depth, unlike previous models which proposed close-form solutions, the Author's analytical model uses the numerical approach to determine moment-curvature and load-displacement curves of concrete and RC beams. This helps to develop a general framework for evaluating flexural behaviour of both concrete beams and reinforced concrete beams. Nevertheless, the model has capability of capturing stress and strain distributions on cross-sections inside the softening zone. This is very consistent to compare with the FE solution using a smeared crack approach as in this thesis. Main conclusions are as follows:

1. In evaluating moments and curvatures, the model is compared well with an analytical model published in literature (Ulfkjaer *et al.* 1995).
2. The softening zone width (w_c) is an important parameter which can significantly affect the structural responses, i.e. deflections of the beam. When w_c is changed, the deflection is reasonably changed: if $w_c = 0$, the deflection is similar to the one calculated by the traditional beam theory; if $w_c = L$, where L is the beam length, the deflection is converged to the one obtained from the assumption that the whole beam is softened; and if w_c is small enough, only the material in that zone is softened and the material outside is elastically unloaded.
3. Through the parametric study of parameters of softening behaviour (e.g. softening zone width w_c, tensile strength f_t, fracture energy G_f, and type of strain-softening curve), it is encouraging that the models can theoretically predict non-linear flexural behaviour of concrete beams and provide further understandings of strain-softening behaviour. In addition, the analytical model shows that the relationship between the softening zone width w_c and the strain at end of softening curve ε_0 is possibly not unique with the given fracture energy. Therefore, if this is the case, an appropriate set of w_c and ε_0 from trial-and-error fitting the analytical results to the numerical and experimental results can be found instead of using an explicit expression for them.

4. In comparison with the experimental and numerical results for two concrete beams under three-point bending tests, it shows that the analytical model only gives good results in pre-peak regime for both linear and bilinear softening stress-strain relationships, and did not well capture in post-peak regime. It is clear that the use of the explicit expressions to determine the softening zone width w_c and strain at end of softening curve ε_0 is not a suitable way for this analytical model. However, good results can be found if using an appropriate set of w_c and ε_0 obtained from trial-and-error fitting procedure as mentioned previously. In this study, it is found that w_c is approximately equal 1 to 1.5 times the beam depth h; ε_0 is about 6 and 11 times the maximum elastic normal strain in the cases of linear softening and bilinear softening, respectively. This is a disadvantageous point of the analytical model as a suitable set of w_c and ε_0 have not been automatically found to give good predictions for post-peak behaviour. Therefore, it requires more studies to substantiate the analytical model, especially with the assumption on the continuity conditions (see the fifth assumption in Section 6.3.1).
5. The analytical model is able to provide a good prediction about the stress distributions in the softening zone width in comparison with the numerical results. It also shows a good agreement in the stress and strain distributions at the interface cross-sections between the strain-softening and linear elastic zones. Importantly, it shows the material in the interface and outside sections unloads elastically during the crack propagation in the softening zone. This is a very important point, which has rarely discussed in other analytical models in literature.
6. In the model, the strain distribution is linear in the softening zone width (Bernoulli-Navier hypothesis). In fact, the strain distribution is not linear but warped under loading due to the effects of shearing force (Timoshenko 1955). This is an existing problem that no analytical model has been able to overcome so far.
7. The analytical model has been extended to include RC beams while still using the linear stress-strain softening relationship for concrete. For over-reinforced beams, the analytical result is in very good agreement with experimental and numerical results because the assumption of “distributed” cracks for the whole beam is appropriate. For under-reinforced concrete beams, the load-deflection curves predicted by the analytical model

compare well with those of numerical models and experiment, especially in pre-yield regime. Also, the analytical model is capable of reproducing the transitional condition between brittle and ductile behaviours in RC beams. As it was assumed that there is perfect bond between steel reinforcement and concrete, and linear behaviour in compressive concrete, the analytical model usually predicts a stiffer behaviour than that of experiment and numerical models.

8. This study shows that the use of bilinear stress-strain softening gives a better result than the linear one.

9.1.5 Response of RC bridge pier and the minimum number of artificial earthquake time-histories required for non-linear dynamic analysis

Both the Multi-crack and Craft models have been employed for the analysis of a RC bridge pier subjected to a set of 20 artificial time-histories. However, the analysis using Craft model was not successful as it failed to converge at early steps though great efforts to correct this have been made. Therefore, only the responses obtained with the Multi-crack model and time stepping analysis have been presented in this study. In non-linear dynamic analysis, it is important to choose appropriate parameters for the time integration scheme used, in order to obtain an effective solution. This choice mainly depends on the parameters such as integration solution, time step, finite element mesh and damping. A set of suitable parameters which can give reasonable results for practical purposes up to the second natural modes of response and significantly reduce the computational effort for a large number of analyses required in this thesis have been chosen. In addition, the effects from a number of parameters of both earthquake and structural sides to the seismic response, especially in damage of a structure are addressed. In particular, some of them, which include the earthquake duration, soil conditions and structure height, are currently main concerns for seismic analysis. The conclusions of this study are that many of these concerns are fully or partly understood thanks to the application of artificially generated earthquake time-histories for earthquake loading and the FE modelling for the structure. Herein are some of the main conclusions:

9.1.5.1 Non-linear dynamic responses of the RC bridge pier

1. Several useful techniques such as vibration analysis, Fourier analysis, normalised cumulative spectrum, dissipated energy and damage index (Park and Ang 1985) can be used together to quantify the structural response of the RC bridge piers subjected to artificially generated earthquake time-histories (Section 7.3.6).
2. By theoretical assessments, it shows that the response of the bridge pier under artificial time-histories can be reasonably obtained by using the Multi-crack model. The structural responses obtained from vibratory analysis agree well with those obtained from damage analysis that the longer the structural period and/or the higher the value of amplitudes of relative displacement, the larger the damage in the bridge pier (Section 7.3.6).
3. Using the Multi-crack model, the numerical result contains some drawbacks. For example, the dissipated energy and unloading stiffness may have been overestimated because in the model unloading/reloading behaviour in tension is linear elastic which is unrealistic for concrete (see Chapter 5). However, as the model has a plastic response, it is still capable of reproducing an overall stiffness degradation of the bridge pier. Therefore it is capable of capturing some of the key behaviours under artificial earthquake time-histories, i.e. plastic strains and hysteretic behaviour.
4. It has been shown that when principal integration parameters of numerical integration (e.g. the time step, element mesh, numerical damping and viscous damping) are changed, the non-linear dynamic responses accordingly reflect the reasonable changes in the behaviour of the Multi-crack model and the FE analysis (see Chapters 7 and 8).
5. In addition, the response or damage of the same RC bridge pier are studied under different sets of artificial earthquake time-histories in terms of qualitative measures, i.e. damage index, and clearly, there is no significant loss of accuracy and generality to employ the Multi-crack model for this purpose.

9.1.5.2 Parameter identifications for FE non-linear dynamic analysis

1. In FE non-linear dynamic analysis, it is important to choose an appropriate time integration scheme which includes the integration solution, time step, finite element mesh and damping. In this study, these are chosen in order to gain reasonable results for practical purposes up to the second natural modes of response and significantly reduce the computational effort for a large number of analyses required. In this manner, the finite element mesh MESH I (see Chapters 7 and 8), time step size of 0.005 s, Newmark's parameters of α = 0.3025 and β = 0.6, and viscous damping ratio ξ = 0.05 have been suggested after a detailed investigation.
2. The difference between some responses using time step of 0.005 s and smaller time steps, i.e. 0.002 s and 0.001 s, is due to the high frequency content captured in the responses using time step of 0.002 s and 0.001 s. In addition, the increase in higher frequency content is also due to the amount of damping produced by Rayleigh's parameters, which may be too small and not increasing with frequency fast enough. Thus, it can be concluded that in order to numerically accurately obtain the higher modes of vibration, a very small time step and also a more appropriate frequency dependent damping should carefully be considered. This could make the analysis very time consuming and not suitable for practice.
3. When the time step, element mesh, numerical damping and viscous damping are smaller, higher integration accuracy can be obtained. However, it is not always realistic to choose very small values for these parameters so as to obtain higher integration accuracy. In fact, our studies on the time step show that in order to integrate accurately the response in even higher frequencies, this may require a very small time step (e.g. < 0.001 s). But the evidence of high-frequency vibration modes predicted by the FE modelling has not been justified for practical purposes and thus not really necessary (Section 7.3.4.3).

9.1.5.3 Parametric study of RC bridge piers under sets of 20 artificial time-histories

1. Damage in the bridge pier decreases with increasing viscous damping ratio (Section 8.3.1)

2. It is not for sure that under softer subsoil classes, the bridge pier should have more damage than those of stiffer ones. It depends on the natural frequencies of the structure. The difference in orders of input earthquake time-histories generated from different subsoil classes may be another cause (Section 8.3.2)
3. Damage in the bridge pier decreases with increasing the amount of steel reinforcement, with increasing the value of tensile strength of concrete or with increasing Young's modulus of concrete material under the assumption that the same values of β, Q_y and δ_u can be adopted in the damage index calculation (Sections 8.3.3, 8.3.4, and 8.3.5)
4. Damage of the bridge pier increases with increasing the value of Peak Ground Acceleration (Section 8.3.6)
5. Increasing the height of the bridge pier will increase the damage of the bridge pier under the assumption that the same values of β, Q_y and δ_u can be adopted in the damage index calculation. The damage statistics analysis also shows that there is more scatter in the response for longer piers (Section 8.3.7)
6. The presence of the constant compressive axial load slightly decreases the damage in the bridge pier with the assumptions that the "P-delta" effect is ignored and the same values of β, Q_y and δ_u can be adopted in the damage index calculation (Section 8.3.8)
7. Different seeds of random number cause different damages in the bridge pier. However, the damage statistics analysis demonstrates that the dispersion of damage for different cases of random seed number r (e.g. r = 1235, 1300 and 1500) are not much different and therefore either one of these values can be used in the generation of artificial earthquake time-histories (Section 8.3.9). Note that with a different random number seed, the generated earthquakes are completely different.
8. Damage of the bridge pier increases with increasing the duration of the input earthquakes. It is because increasing the duration it will generally increase the number of cycles and energy input to the pier (Section 8.3.10)

The conclusions made in the parametric study of soil conditions (point 2), peak ground acceleration (point 4), random seed number (point 7), and earthquake duration (point 8) are very important because the earthquakes actually used in these analyses are not the same 20

earthquakes as used in the other parametric studies. It is important to note that, from the results obtained, the same set of conclusions, i.e. damage indices and the number of time-histories required, still applies.

In addition, this parametric study also shows that the LUSAS Multi-crack is capable of capturing most of key behaviours of RC piers under artificial earthquake time-histories. The behaviour is reasonably accurate in terms of qualitative studies though the dissipated energy and unloading stiffness may have been overestimated.

9.1.6 The minimum representative number of artificial time-histories

The proposal for a minimum representative number of earthquake time-histories required for non-linear dynamic analysis is a crucial part of this study. For this purpose, several techniques consisting of Fourier analysis, cumulative response spectrum, energy dissipation, and damage index (Park and Ang 1985) have been utilised to quantify the structural responses for different sets of artificial time-histories in order to find a minimum representative number of responses or time-histories. In damage index analysis, the minimum number of non-linear dynamic analyses for a random number in ordering of input earthquake time-histories for a particular confidence band (from the mean of 20 analyses) has been calculated using probability theory. Furthermore, through the parametric study of several physical parameters of earthquake and structural characteristics such as peak ground accelerations, soil conditions, earthquake durations, seeds of random numbers, viscous damping ratios, the presence of axial load, pier heights, tensile strength, Young's modulus of concrete and the amount of steel reinforcement in the pier, the minimum representative number proposed has been validated. Herein are some concluding remarks:

1. In particular case, it was assumed that the 20 artificial time-histories are picked up in sets of a regular order which is numbered from 1 to 20. For this, by comparing the average of different numbers of structural response and damage using Fourier analysis, cumulative response spectrum, energy dissipation, and damage index, it has been found that the

convergent values of the average response can be obtained when the minimum required number of time-histories is about 10 to 12. A very good convergence can be found when the number of artificial earthquake time-histories used is about 15 or 16 (Section 7.3.6).

2. For general consideration, the concept of probability is used and it was assumed that the 20 artificial time-histories can be picked up in sets of any possible order. It has been found that the mean number of non-linear dynamic analyses for different values of *n* orders, i.e. $n > 10000$, is about 11, 8, 7, and 6 in accordance with the "$\pm 1.00\sigma$ confidence band", "$\pm 1.40\sigma$ confidence band", "$\pm 1.64\sigma$ confidence band", and "$\pm 1.96\sigma$ confidence band", respectively, from the mean of 20 damage responses. If a relevant design basis calls for the "$\pm 1.40\sigma$ confidence band" or "84 percent confidence band" (Cornell *et al*. 2002, Shome *et al*. 1998), the minimum necessary number of non-linear dynamic analyses, therefore, shall be about 8 (Section 7.3.6).
3. Alternatively, one can select any number of artificial earthquake time-histories with a particular confidence based on their appearance in the total number of orders used. For example, if the practicing engineer wants a high level of confidence in the number of earthquake used, e.g. they can select 16, 13, 11, and 9 earthquake time-histories for four confidence bands, respectively, with 95% (9500 out of 10000) of the ordering (Section 7.3.6) satisfying the required confidence band.
4. In each parametric study, the minimum mean number of non-linear dynamic analyses for a random number in ordering of input earthquake time-histories for a particular confidence band (from the mean of all responses) is calculated. It proves that the minimum representative number of time-histories required for non-linear dynamic analyses are similar to the ones suggested in the main study in Chapter 7. In particular, again, it is concluded that the number is about 11, 8, 7, and 6 for the four confidence bands concerned.
5. It is important to note that in the parametric study of soil conditions, peak ground accelerations, random seed numbers and earthquake durations, the artificial earthquakes actually used are not the same 20 earthquakes as used in the other parametric studies, but the same set of conclusions on the number of time-histories required are still relevant. In particular, the conclusion on different random seed numbers used is very important

because in this case the artificially generated earthquake time-histories are totally different.

9.2 FURTHER WORKS

Although great efforts have been made on the research subject, there still remains a great deal of work left to be done. They include:

1. As the application of Craft model for analysis of the RC bridge pier under artificial earthquake time-histories was not successful, i.e. being failed to converge at early steps though great efforts have been made. Further research is needed to validate Craft model against good experimental data and to successfully apply Craft model for further analyses of RC structures under cyclic and earthquake time-histories. As studied in Chapter 5, Craft model is more capable of capturing the cyclic behaviour of the RC bridge pier. It, therefore, should provide more accurate results for seismic analyses, i.e. hysteretic behaviour, than the LUSAS Multi-crack model; consequently, the energy dissipation and damage in the structure will be predicted more accurately and thus the minimum representative number of earthquake time-histories required for non-linear dynamic analysis will be more accurate in terms of quantitative measures. Alternatively, any other reliable concrete material models can also be applied for a comprehensive study of minimum representative number of earthquake time-histories as the approach presented in this study.
2. The bond slip between concrete and steel reinforcement is not included in the scope of the research. However, by comparing with experimental data, the numerical results obtained from analyses of RC beams under monotonic loading and RC bridge pier under cyclic loading have shown that the bond slip significantly affects the structural response. Therefore, the consideration of bond slip between concrete and steel reinforcement may be necessary in order to obtain response close to reality.
3. The analytical model can be refined to obtain more accurate deflections for the concrete beam in at least three ways. Firstly, more experimental work is needed to substantiate the

load-deflection response in post-peak regime. Secondly, there should obtain a more realistic relationship to calculate the curvature at any cross-section inside the softening width w_c, not being linearly interpolated from curvatures at the edge cross-sections and at mid-span cross-section. Last but not least importantly, it is believed that in reality, upon increasing the damage level, cracking tends to localise in a band of decreasing width not as constant as assumed in the current analytical model. Therefore, further work should attempt to formulate the decreasing softening zone width (w_c) and implement it into the analytical solution.

4. In generation of artificial earthquake time-histories, it is difficult to find the agreement between computed and target response spectra in low frequency domain and very high frequency domain because the program SIMQKE is interested in matching the computed RS and the target RS in a particularly popular range of frequency, i.e. from 0.04 Hz to 25 Hz. In addition, at frequencies below 0.4 Hz (or periods upper 2.5 s), the program generates less points of frequencies to define the computed response spectrum. Without enough number of points in the lower frequency region, i.e. below 0.4 Hz, the generated earthquake response spectrum is not reliable enough in that region. For these reasons, an improvement of the program for generating artificial earthquake time-histories at frequencies below 0.4 Hz is needed, especially when dealing with long-period structures.
5. The disadvantage of using artificially generated time-histories is that it can overestimate the input energy which may result in different estimates of the structural response (Naeim and Lew 1995). Therefore, if a set of real earthquakes with roughly the same magnitude is available for a particular seismic region, they can be used in non-linear dynamic analysis in stead of artificial time-histories. In this way, the minimum required number of earthquakes will be evaluated more accurately.
6. In this research, 2-D finite element modelling is studied. Alternatively, 3-D modelling can be applied for concrete and RC structures so as to understand more about the mechanical behaviour of concrete material such as triaxial confining stresses, and therefore to predict the non-linear response and the minimum representative number of earthquake time-histories required for non-linear dynamic analysis as close to reality as possible.

The work reported in this thesis aimed to establish the issues on generation of artificial earthquake time-histories fitting to an EC8 (ENV and prEN versions) elastic response spectrum; validation and use of ones of the most developed smeared crack models for concrete and RC structures under monotonic, cyclic and artificial earthquake time-histories; and the minimum representative number of earthquake time-histories required for non-linear dynamic analysis. The achievement on these subjects is very encouraging especially on the minimum representative number of artificial earthquake time-histories as this issue is a very important for the seismic analysis and design. This achievement is a result of an integrated approach of combining: (1) artificially generated earthquake time-histories, (2) state-of-the-art constitutive models for the materials in association with FE modelling for the structure, (3) relevant techniques to measure the structural response, and (4) a great number of parametric studies to sufficiently confirm the breadth of the conclusions made before. In addition, the further works reported above are very straightforward. Based on these recommendations, it may become possible to improve the current approach and provide more accurate results for numerical modelling of RC structures under artificially generated earthquake time-histories and, in particular, on the constitutive models and the minimum representative number of earthquake time-histories to be used in non-linear dynamic analysis and design of RC structures.

REFERENCES

Abrahamson, N. A., and Shedlock, K. M., (1997). Overview. Seismological Research Letters, Vol. 68, No. 1, 9-23.

Ambraseys, N. N., and Bommer, J. J., (1990). Database of European strong-motion records. European Earthquake Engineering, Vol. 5, No. 2, 18-37.

Ambraseys, N. N., Smit, P., Berardi, D., Cotton, F., and Berge, C., (2000). Dissemination of European strong-motion data. CD-ROM Collection, European Commission, Directorate-General XII, Environmental and Climate Programme, ENV4-CT97-0397, Brussels, Belgium.

Ang, A., (1974). Probability concepts in earthquake engineering. Applied Mechanics in Earthquake Engineering, ed. Iwan, W. D., AMD-Vol.8, America Society of Mechanical Engineers, New York, 225-259.

Ansari, F., (1987). Stress-strain response of microcracked concrete in direct tension. ACI Materials Journal, Vol. 84, No. 6, 481-490.

Ansari, F., and Li, Q., (1998). High strength concrete subjected to triaxial compression. ACI Materials Journal, Vol. 95, No. 6, 747-755.

Armero, F., and Oller, S., (2000). A general framework for continuum damage models. Part I - Infinitesimal plastic damage models in stress space. International Journal of Solids and Structures, Vol. 37, No. 48-50, 7409-7436.

Arrea, M., and Ingraffea, A. R., (1982). Mixed-mode crack propagation in mortar and concrete. Report 81-13, Department of Structure Engineering, Cornell University, Ithaca, New York.

Atkinson, G. M., and Boore, D. M., (1997). Stochastic point-source modelling of ground motion in the Cascadia region. Seismological Research Letters, Vol. 68, 74-85.

Atkinson, G. M., (1994). Empirical attenuation of ground motion spectral amplitudes in Southeastern Canada and Northeastern, United States. Bulletin of Seismological Society of America, Vol. 94, No. 3, 1079-1095.

Augusti, G., Baratta, A., and Casciati, F., (1984). Probabilistic methods in structural engineering. Chapman and Hall, London.

Bahn, B. Y., and Hsu, C. -T., T., (1998). Stress-strain behavior of concrete under cyclic loading. ACI Materials Journal, Vol. 95, No. 2, 178-193.

Banon, H., Biggs, J. M., and Irvine, H. M., (1981). Seismic damage in reinforced concrete frames. Journal of Structural Engineering, ASCE, Vol. 107, No. ST9, 1713-1729.

Barenberg, M. E., (1989). Inelastic response of a spectrum-compatible artificial accelerogram. Earthquake Spectra, Vol. 5, No. 3, 477-493.

Bathe, K. J., (1982). Finite element procedures in engineering analysis. Prentice-Hall, Inc., Englewood Cliffs, New Jersey.

Bazant, Z. P., (1983). Comment of orthotropic models for concrete and geomaterials. Journal of Engineering Mechanics, ASCE, Vol. 109, No. 3, 849-865.

Bazant, Z. P., (1984). Size effect in blunt fracture: concrete, rock, metal. Journal of Engineering Mechanics, ASCE, Vol. 110, No. 4, 518-535.

Bazant, Z. P., (1986). Fracture mechanics and strain-softening of concrete. Proceedings of U.S.-Japan Seminar on Finite Element Analysis of Reinforced Concrete Structures (Tokyo, May 1985), ASCE, New York, 121-150.

Bazant, Z. P., editor (1992). Fracture mechanics of concrete structures. Proceedings of the First International Conference on Fracture Mechanics of Concrete and Concrete Structures (FRAMCOS 1), Elsevier Applied Science, London, UK.

Bazant, Z. P., and Becq-Giraudon, E., (2002). Statistical prediction of fracture parameters of concrete and implications for choice of testing standard. Cement and Concrete Research, Vol. 32, No. 4, 529-556.

Bazant, Z. P., and Cedolin, L., (1979). Blunt crack band propagation in finite element analysis. Journal of Engineering Mechanics, ASCE, Vol. 105, No. EM2, 297-315.

Bazant, Z. P., and Cedolin, L., (1980). Fracture mechanics of reinforced concrete. Journal of the Engineering Mechanics, ASCE, Vol. 106, No. EM6, 1287-1306.

Bazant, Z. P., and Kazemi, M. T., (1991). Size effect on diagonal shear failure of beams without stirrups. ACI Structural Journal, Vol. 88, No. 3, 268-276.

Bazant, Z. P., and Kim S. S., (1979). Plastic-fracturing theory for concrete. Journal of Engineering Mechanics, ASCE, Vol. 105, No. 3, 407-428.

Bazant, Z. P., and Oh, B. H., (1983). Crack band theory for fracture of concrete. Materials and Structures (RILEM, Paris), Vol. 16, 155-177.

Bazant, Z. P., and Pfeiffer, P. A., (1986). Shear fracture test of concrete. Materiaux et Construction (RILEM), Vol. 19, 111-121.

Bazant, Z. P., and Tsubaki, T., (1980). Total strain theory and path dependence of concrete. Journal of the Engineering Mechanics, ASCE, Vol. 106, No. EM6, 1151-1173.

Bazant, Z. P., and Zubelewicz, A., (1988). Strain-softening bar and beam: Exact nonlocal solution. International Journal of Solids and Structures, Vol. 24, No. 7, 659-673.

Bedard, C., and Kotsovos, M. D., (1986). Fracture processes of concrete for NLFEA methods. Journal of Structural Engineering, ASCE, Vol. 112, No. 3, 573-587.

Benjamin, J. R., and Cornell, C. A., (1970). Probability, statistics, and decision for civil engineers. McGraw-Hill, New York, USA.

Beresnev, I. A., and Atkinson, G. M., (1998). FINSIM - A FORTRAN program for simulating stochastic acceleration time histories from finite faults. Seismological Research Letters, Vol. 69, No. 1, 27-32.

Beshara, F. B. A., and Virdi, K. S., (1991). Time integration procedure for finite element analysis of blast-resistant reinforced concrete structures. Computers and Structures, Vol. 40, No. 5, 1071-1336.

Bhatt, P., and Kader, M. A., (1998). Prediction of shear strength of reinforced concrete beams by non-linear finite element analysis. Computers and Structures, Vol. 68, No. 1-3, 139-155.

Blakey, F. A., and Beresford, F. D., (1962). Discussion of “Crack propagation and the fracture of concrete” by M. E. Kaplan. ACI Journal, Vol. 58, 919-923.

Bolander, J. E., and Le, B. D., (1999). Modeling crack development in reinforced concrete structures under service loading. Construction and Building Materials, Vol. 13, 23-31.

Bommer, J. J., (2005). Selection of earthquake time histories for analysis of structures. Newsletter, the Society for Earthquake and Civil Engineering Dynamics (SECED), UK, Vol. 18, No. 3, 6-9.

Bommer, J. J., and Acevedo, A. B., (2004). The use of real earthquake accelerograms as input to dynamic analysis. Journal of Earthquake Engineering, Vol. 8, (special issue No. 1), 43-91.

Bommer, J. J., and Ambraseys, N. N., (1992). An earthquake strong-motion databank and database. Proceedings of the 10th World Conference on Earthquake Engineering, Madrid, Spain, 207-210.

Bommer, J. J., and Martinez-Pereira, A., (1999). The effective duration of earthquake strong motion. Journal of Earthquake Engineering, Vol. 3, No. 2, 127-172.

Bommer, J. J., and Ruggeri, C., (2002). The specification of acceleration time-histories in seismic design codes. European Earthquake Engineering, Vol. 1, 3-17.

Boore, D. M., (2003). Simulation of ground motion using the stochastic method. Pure and Applied Geophysics, Vol. 160, 635-676.

Booth, E., (1999). SIMQKE1 - Generation of artificial time histories compatible with a specified target spectrum. URL: http://www.booth-seismic.co.uk/simqke.htm (last updated in 2006).

Bresler, B., and Bertero, V., (1968). Behavior of reinforced concrete under repeated load. Journal of Structural Engineering, ASCE, Vol. 94, 1576-1590.

Bresler, B., and Scordelis, A. C., (1963). Shear strength of reinforced concrete beams. ACI Journal, Vol. 60, No. 1, 51-72.

Bresler, B., and Wollack, E., (1952). Shear strength of concrete. Report, Department of Civil Engineering, University of California, Berkeley. Presented at Annual Convention, Structural Engineers Association of California, Riverside, CA, USA.

Brincker, R., and Dahl, H., (1989). On the ficticious crack model of concrete fracture. Magazine of Concrete Research, Vol. 41, No. 147, 79-86.

Burlion, N., Gatuingt, F., Pijaudier-Cabot, G., and Daudeville, L., (2000). Compaction and tensile damage in concrete: constitutive modelling and application to dynamics. Computational Methods in Applied Mechanics and Engineering, Vol. 183, 291-308.

Buyukozturk, O., and Shareef, S. S., (1985). Constitutive modeling of concrete in finite element analysis. Computers and Structures, Vol. 21, No. 3, 581-610.

Bycroft, G. N., (1960). White noise representation of earthquakes. Journal of the Engineering Mechanics, ASCE, Vol. 86, No. EM2, 1-16.

Carpinteri, A., (1989). Minimum reinforcement in reinforced concrete beams. RILEM TC 90-FMA, CODE WORK, Cardiff, 20-22 September 1989, UK.

Carol, I., and Bazant, Z. P., (1995). New developments in micro-plane and multicrack models for concrete. In Proceedings of FRAMCOS2, ed. Wittmann, F. H. Aedificatio, Germany, 841-856.

Carol, I., Jirásek, M., and Bazant, Z. P., (2001a). A thermodynamically consistent approach to micro-plane theory. Part I - Free energy and consistent microplane stresses International Journal of Solids and Structures, Vol. 38, No. 17, 2921-2931.

Carol, I., Rizzi, E., and Willam, K., (2001b). On the formulation of anisotropic elastic degradation. Part I - Theory based on a pseudo-logarithmic damage tensor rate. International Journal of Solids and Structures, Vol. 38, No. 4, 491-518.

Carol, I., Rizzi, E., and Willam, K., (2001c). On the formulation of anisotropic elastic degradation. II - Generalized pseudo-Rankine model for tensile damage. International Journal of Solids and Structures, Vol. 38, No. 4, 518-546.

Cedolin, L., Crutzen, Y. R. J., and Dei Poli, S., (1977). Triaxial stress-strain relationship for concrete. Journal of Engineering Mechanics, ASCE, Vol. 103, No. EM3, 423-439.

Cedolin, L., and Dei Poli, S., (1977). Finite element studies of shear critical R/C beams. Journal of the Engineering Mechanics, ASCE, Vol. 103, No. EM3, 395-410.

Cervera, M., Hinton, E., and Hassan, O., (1987). Nonlinear analysis of reinforced concrete plate and shell structures using 20-noded isoparametric brick elements. Computers and Structures, Vol. 25, No. 6, 845-869.

Cedolin, L., and Dei Poli, S., (1977). Finite element studies of shear-critical R/C beams. Journal of Energy Mechanics, ASCE, Vol. 103, No. 3, 395-410.

Chai, Y. H., and Fajfar, P., (2000). A procedure for estimating input energy spectra for seismic design**.** Journal of Earthquake Engineering**,** Vol. 4, No. 4, 539-561**.**

Chai, Y. H., Romstad, K. M., and Bird, S. M., (1995). Energy-based linear damage model for high-intensity seismic loading. Journal of Structural Engineering, Vol. 121, No. 5, 857-864.

Chen, W. F., (1982). Plasticity in reinforced concrete. McGraw-Hill Book Company.

Chen, W. F., and Han, D. J., (1988). Plasticity for structural engineers. Springer-Verlag, New York Inc.

Chen, A. C. T., and Chen, W. F., (1975). Constitutive relations for concrete. Journal of Engineering Mechanics, ASCE, Vol. 101, 465-481.

Chopra, A. K., (1995). Dynamics of structures: theory and applications to earthquake engineering. Prentice Hall, New Jersey.

Chuang, T. F., (2001). Numerical modelling of reinforced concrete structure under monotonic and earthquake-like dynamic loading. PhD thesis, University of Birmingham, UK.

Chuang, T., and Mai, Y. W., (1989). Flexural behaviour of strain-softening solids. International Journal of Solids and Structures, Vol. 25, No. 12, 1427-1443.

Chung, Y. S., Meyer, C., and Shinozuka, M., (1989). Modeling of concrete damage. ACI Structural Journal, Vol. 86, No. 3, 259-271.

Ciampoli, M., Giannini, R., Nuti, C., and Pinto, P. E., (1989). Seismic reliability of non-linear structures with stochastic parameters by directional simulation. Proceedings of the 5th International Conference on Structural Safety and Reliability (ICOSSAR 89), San Francisco, CA, Vol. 2, 1121-1128.

Clough, R. W., (1966). Effect of stiffness degradation on earthquake ductility requirements. Structural and Materials Research, Structure Engineering Laboratory, University of California, Berkeley, Report 66-16.

Clough, R. W., and Penzien, J., (1975). Dynamics of Structures. McGraw-Hill, New York and London.

Clough, R. W., and Johnson, S. B., (1966). Effects of stiffness degradation on earthquake ductility requirements. Proceedings of the 2nd Japan National Conference on Earthquake Engineering, Tokyo, 227-232.

Collins, K. R., Foutch, D. A., and Wen, Y. K., (1995). Investigation of alternative seismic design procedures for standard buildings. Civil Engineering Studies, Structural Research Series No. 600, University of Illinois, Urbana, 122-132.

Comi, C., and Perego U., (2001). Fracture energy based bi-dissipative damage model for concrete. International Journal of Solids and Structures, Vol. 38, No. 36-37, 6427-6454.

Cope, R. J., Rao, P. V., Clark, L. A., and Norris, P., (1980). Modelling of reinforced concrete behaviour for finite element analysis of bridge slabs. International Conference of Numerical Methods for Non-Linear Problems, 457-469 (Edited by C. Taylor *et al*.). Pineridge Press, Swansea.

Cornell, C. A., Jalayer, F., Hamburger, R. O., and Foutch, D. A., (2002). The probabilistic basis for the 2000 SAC/FEMA steel moment frame guidelines. Journal of Structural Engineering, ASCE, Vol. 128, No. 4, 526-533.

Cosenza, E., Manfredi, G., and Ramasco, R., (1993). The use of damage functionals in earthquake engineering: a comparison between different methods. Earthquake Engineering and Structural Dynamics, Vol. 22, 855-868.

Crandall, S. H., and Mark, W. D., (1963). Random vibration in mechanical systems. Academic Press, New York, USA.

Criesfield, M. A., (1982). Local instabilities in non-linear analysis of reinforced concrete beams and slabs. Proceedings of Institute of Civil Engineers, Part 2, Vol. 73, 135-145.

Crisfield, M. A., (1986). Snap-through and snap-back response in concrete structures and the dangers of under-integration. International Journal for Numerical Methods in Engineering, Vol. 22, 751-767.

Crisfield, M. A., (1996). Nonlinear analysis of solids and structures, Volume 1: Essentials, Willey & Sons, New York.

Crisfield, M. A., and Wills, J., (1989). The analysis of reinforced-concrete panels using different concrete models. Journal of Engineering Mechanics, ASCE, Vol. 15, No. 3, 578-597.

Crisfield, M. A., (1983). An arc-length method including line searches and accelerations. International Journal for Numerical Methods in Engineering, Vol. 19, 1269-1289.

Daschner, F., and Kupfer, H., (1982). Versuche zur Schubkraftübertragung in Russen von Normal-und Leichtbeton. Bauingenieur Vol. 57, 57-60.

Darwin, D., and Nmai, C. K., (1986). Energy dissipation in RC beam under cyclic load. Journal of Structural Engineering, ASCE, Vol. 112, No. 8, 1829-1846.

de Borst, R., and Nauta, P., (1985). Non-orthogonal cracks in a smeared finite element model. Engineering and Computations, Vol. 2, 35-46.

de Borst, R., (1987). Computation of post-bifurcation and post-filure behavior of strain-softening solids. Computers and Structures, Vol. 25, No. 2, 211-224.

de Borst, R., (2001). Some recent issues in computational failure mechanics. International Journal for Numerical Methods in Engineering. Vol. 52, 63-95.

de Borst, R., (2002). Fracture in quasi-brittle materials: a review of continuum damage-based approaches. Engineering Fracture Mechanics, Vol. 69, No. 2, 95-112.

de Borst, R., and Nauta, P., (1985). Non-orthogonal cracks in a smeared finite element model. Engineering and Computations, Vol. 2, 35-46.

Der Kiureghian, A., and Neuenhofer, A., (1992). Response spectrum method for multiple support seismic excitation. Earthquake Engineering and Structural Dynamics. Vol. 21, 713-740.

Der Kiureghian, A., (1979). On response of structures to stationary excitation. Report No. UCB/EERC-79/32, Earthquake Engineering Research Center, University of California, Berkeley, Carlifornia.

Devore, J. L., (2003). Probability and statistics for engineering and the sciences. The 6th Edition, Thomson Learning, Australia.

di Prisco, M., and Mazars, J., (1996). Crush-crack: a non-local damage model for concrete. Mechanics Cohesive Frictional Materials, Vol. 1, 321-347.

Dinesh Kumar, Khattri, K. N., Teotia, S. S., and Rai, S. S., (1998). Modelling of accelerograms of two Himalayan earthquakes using a novel semi-empirical method and estimation of accelerogram for a hypothetical great earthquake in Himalaya. Journal of Current Science, Indian Academy of Sciences.

DiPasquale, E., and Cakmak, A. S., (1988). Identification of the serviceability limit state and detection of seismic structural damage. Report NCEER-88-0022, National center for Earthquake Engineering Research, State University of New York at Buffalo, NY, USA.

Dougill, J. W., (1976). On stable progressively fracturing solids. Journal of Applied Mathematics and Physics (ZAMP), Vol. 27, 423-437.

Dougill, J. W., and Rida, M. A. M., (1980). Further consideration of progressively fracture solids. Journal of Engineering Mechanics, ASCE, Vol. 106, No. EM5, 1021-1038.

Edwards, A. D., and Yannopoulos, P. J., (1978). Local bond-stress-slip relationship under repeated loading. Magazine of Concrete Research**,** Vol. 30, No. 103, 62-72.

Ekh, M., and Runesson, K., (2000). Bifurcation results for plasticity coupled to damage with MCR-effect. International Journal of Solids and Structures, Vol. 37, No. 14, 1975-1996.

Elices, M., Guinea, G.V., Gomez, J., and Planas, J., (2002). The cohesive zone model: advantages, limitations and challenges. Engineering Fracture Mechanics, Vol. 69, No. 2, 137-163.

Elms, D., Paulay, T., and Ogawa, S., (1989). Code-implied structural safety for earthquake loading. Proceedings of the 5th International Conference on Structural Safety and Reliability (ICOSSAR 89), San Francisco, C.A., Vol. III, 2003-2010.

Erberik, A., and Sucuoglu, H., (2004). Seismic energy dissipation in deteriorating systems through low-cycle fatigue. Earthquake Engineering and Structural Dynamics, Vol. 33, No. 1, 49-67.

Este, G., and Willam, K., (1994). Fracture energy formulation for inelastic behaviour of plain concrete. Journal of Engineering Mechanics, ASCE, Vol. 120, No. 9, 183-2011.

Eurocode 8, 1994. Design provisions for earthquake resistance of structures. Part 1: General rules - Seismic actions and general requirements for structures. European prenorm ENV 1998-1: 1996, Brussels.

Eurocode 8, 1994. Design provisions for earthquake resistance of structures. Part 2: Bridges. European prenorm ENV 1998-2: 1996, Brussels.

Eurocode 8, 2003. Design of structures for earthquake resistance. European Standard, Final Draft, prEN 1998-1:2004, Brussels.

Fajfar, P., and Gaspersic, P., (1996). N2 method for the seismic damage analysis of RC buildings. Earthquake Engineering and Structural Dynamics, Vol. 25, No. 1, 31-46.

Freenstra, P. H., and de Borst, R., (1995). Constitutive model for reinforced concrete. Journal of Engineering Mechanics, ASCE, Vol. 121, No. 5, 587-595.

Foster, S. J., and Gilbert, R. I., (1996). Rotated crack finite element model for reinforced concrete structures. Computers and Structures, Vol. 58, No. 1, 43-50.

Garstka, B., Kratzig, W. B., and Stangenberg, F., (1994). Damage prediction in reinforced concrete structures under cyclic loading. Proceedings of the IASS-ASCE International Symposium, Atlanta, GA, USA, 280-289.

Gasparini, D. A., and Vanmarcke, E. H., (1976). Simulated earthquake motions compatible with prescribed response spectra. Evaluation of Seismic Safety of Buildings Report No. 2, Department of Civil Engineering, Massachusetts Institute of Technology, USA.

Ghaboussi, J., and Lin, C. -C. J., (1998). New method of generating spectrum compatible accelerograms using neural networks. Earthquake Engineering and Structural Dynamics, Vol. 27, No. 4, 377-396.

Ghobarah, A., Abou-elfath, H., and Biddah, A., (1999). Response-based damage assessment of structures. Earthquake Engineering and Structural Dynamics, Vol. 28, No.1, 79-104.

Gerstle, K. H., (1981a). Simple formulations of biaxial behaviour. ACI Journal, Vol. 78, No. 1, 62-68.

Gerstle, K. H., (1981b). Simple formulations of triaxial concrete behaviour. ACI Journal, Vol. 78, No. 5, 382-387.

Glucklick, J., (1962). Discussion of "Crack propagation and the fracture of concrete" by M. E. Kaplan. ACI Journal, Vol. 58, 919-923.

Gopalaratnam, V. S., and Shah, S. P., (1985). Softening response of plain concrete in direct tension. ACI Materials Journal, Vol. 82, No. 3, 310-323.

Gopalaratnam, V. S., and Ye, B. S., (1991). Numerical characterization of nonlinear process in concrete. Engineering Mechanics, Vol. 40, No. 6, 991-1006.

Gosain, N. K., Brown, R. H., and Jirsa, J. O., (1977). Shear requirements for load reversals on RC members. Journal of Structural Engineering, ASCE, Vol. 103, No. 7, 1461-1476.

Grassl, P., Lundgren K., and Gylltoft, K., (2002). Concrete in compression: a plasticity theory with a novel hardening law. International Journal of Solids and Structures, Vol. 39, 5205-5223.

Haddon, R. A. W., (1996). Use of empirical Green's function, spectral ratios, and kinematic source models for simulating strong ground motion. Bulletin of Seismological Society of America, Vol. 86, No. 3, 597-615.

Hadjian, A. H., (1972). Scaling of earthquake accelegrams - A simplified approach. Journal of the Structural Engineering, ASCE, Vol. 98, No. ST2, 547-551.

Hancock, J., and Bommer, J. J., (2005). The effective number of cycles of earthquake ground motion. Earthquake Engineering and Structural Dynamics, Vol. 34, No. 6, 637-664.

Hancock, J., and Bommer, J. J., (2004). The influence of phase and duration on earthquake damage in degrading structures. Proceedings of the 13th World Conference on Earthquake Engineering, paper No. 1990, Vancouver, B.C., Canada.

Han, D. J., and Chen, W. F., (1985). A non-uniform hardening plasticity model for concrete materials. Mechanics and Materials, Vol. 4, 283-302.

Han, D. J., and Chen, W. F., (1987). Constitutive modeling in analysis of concrete structures. Journal of Engineering Mechanics, ASCE, Vol. 113, No. 4, 577-593.

Hansen, N. R., Schreyer, H. L., (1994). A Thermodynamically consistent framework for theories of elastoplasticity coupled with damage. International Journal of Solids and Structures, Vol. 31, No. 3, 359-389.

Hasegawa, T., (1995). Enhanced micro-plane concrete model. In Proceedings of FRAMCOS2, ed. Wittmann, F. H. Aedificatio, Germany, 857-870.

Hesse, R., (1998). Normal probability plots. Decision Line News, Vol. 29, No. 1, 17-19.

Hillerborg, A., Modeer, M., and Pertersson, P. E., (1976). Analysis of crack formation and crack growth in concrete by means of fracture mechanics and finite element. Cement and Concrete Research, Vol. 6, 773-782.

Hilsdorf, H. K., and Brameshuber, W., (1991). Code type formation of fracture mechanics concepts for concrete. International Journal of Fracture, Vol. 5, No. 1, 61-72.

Hindi, R. A., and Sexsmith, R. G., (2001). A proposed damage model for RC bridge columns under cyclic loading. Earthquake Spectra, Vol. 17, No. 2, 261-290.

Hindi, R. A., and Sexsmith, R. G., (2004). Inelastic damage analysis of reinforced concrete bridge columns based on degraded monotonic energy. Journal of Bridge Engineering, ASCE, Vol. 9, No. 4, 326-332.

Hirao, K., Sawada, T., NariYuki, Y., and Sasada, S., (1987). The effect of frequency characteristics and duration of input earthquake on the energy response of structures. Structural Engineering and Earthquake Engineering, Proceedings of Japan Society of Civil Engineers, Vol. 4, No. 2, 165-174.

Hiroyuki Fujiwara, Shin Aoi, Takachi Kunugi, and Shigeki Adachi, (2004). Strong-motion observation networks of NIED : K-NET and KiK-NET. Cosmos Report.

Hofbeck, J. A., Ibrahim, I. O., and Mattock, A. H., (1969). Shear transfer in reinforced concrete. ACI Journal, Vol. 66, No. 2, 119-128.

Housner, G. W., and Jennings, P. C., (1964). Generation of artificial earthquakes. Journal of Engineering Mechanics, ASCE, Vol. 90, No. EM1, 113-150.

Housner, G. W., (1955). Properties of strong ground motion earthquakes. Bulletin of Seismological Society of America, Vol. 45, 187-218.

Hsieh, S. S., Ting, E. C., and Chen W. F., (1982). A plastic-fracture model for concrete. International Journal of Solids and Structures, Vol. 18, No. 3, 181-197.

Hudson, D. E., (1962). Some problems in the application of spectrum techniques to strong-motion earthquake analysis. Bulletin of the Seismological Society of America, Vol. 52, 417-430.

Imran, I., and Pantazopoulou, S. J., (1996). Experimental study of plain concrete under triaxial stress. ACI Materials Journal, Vol. 93, No. 6, 589-601.

Imran, I., and Pantazopoulou, S. J., (2001). Plasticity model for concrete under triaxial compression. Journal of Engineering Mechanics, ASCE, Vol. 127, No. 3, 281-290.

Ile, N., and Reynouard, J. M., (2000). Non-linear analysis of reinforced concrete shear wall under earthquake loading. Journal of Earthquake Engineering, Vol. 4, No. 2, 183-213.

Iwrin, G. R., (1962). Discussion of "Crack propagation and the fracture of concrete" by M. E. Kaplan. ACI Journal, Vol. 58, 919-923.

Iyengar, K. T. S. R., Prasad, P. K. R., Nagaraj, T. S., and Bharti, P., (1996). Parametric sensitivity of fracture behaviour of concrete. Nuclear Engineering and Design, Vol. 163, No. 3, 397-403.

Iyengar, K. T. S. R., and Raviraj, S., (2001). Analytical study of fracture in concrete beams using blunt crack model. Journal of Engineering Mechanics, ASCE, Vol. 127, No. 8, 828-834.

Iyengar, K. T. S. R., Raviraj, S., and Jayaram, T. N., (2002). Analysis of crack propagation in strain-softening beams. Engineering Fracture Mechanics, Vol. 69, No. 6, 761-778.

Iyengar, N. R., and Rao, P. N., (1979). Generation of spectrum compatible accelerograms. Earthquake Engineering and Structural Dynamics, Vol. 7, 253-263.

Jansen, D. C., and Shah, S. P., (1997). Effects of length on compressive strain softening of concrete. Journal of Engineering Mechanics, ASCE, Vol. 123, No. 1, 25-35.

Jefferson, A. D., (1989). Finite element analysis of composite structures. PhD Thesis, University of Wales, Cardiff, UK.

Jefferson, A. D., (2003a). Craft, a plastic-damage-contact model for concrete. Part I - Model theory and thermodynamics. International Journal of Solids and Structures, Vol. 40, No. 22, 5973-5999.

Jefferson, A. D., (2003b). Craft, a plastic-damage-contact model for concrete. Part II - Model implementation with implicit return-mapping algorithm and consistent tangent matrix. International Journal of Solids and Structures, Vol. 40, No. 22, 6001-6022.

Jefferson, A. D., (1999). A multi-crack model for the finite element analysis of concrete. Proceedings of BCA Concrete Conference, 275-286.

Jefferson, A. D., (2002a). Local plastic surfaces for cracking and crushing in concrete. Journal of Materials: Design and Application, Vol. 216(L), 257-266.

Jefferson, A. D., (2002b). Constitutive modeling of aggregate interlock in concrete. International Journal for Numerical and Analytical Methods in Geomechanics, Vol. 26, No. 5, 515-535.

Jefferson, A. D., (2004). Private communications containing the information about how the characteristic length of MC82 depends on elemental volume instead of elemental area for 2-D plane stress analysis.

Jenkins, J. M., (1961). General considerations in the analysis of spectra. Technometrics, Vol. 3, 133-166.

Jennings, P. C., Housner, G. W., and Tsai, N. C., (1968). Simulated earthquake motions. Earthquake Engineering Research Laboratory, California Institute of Technology, Pasadena, California.

Jeong, G. D., and Iwan, W. D., (1988). The effect of earthquake duration on the damage of structures. Earthquake Engineering and Structural Dynamics, Vol. 16, No. 8, 1201-1211.

Jirasek, M., and Bazant, Z. P., (2002). Inelastic analysis of structures. John Willey & Son, New York.

Johnson, W., and Melot, B. P., (1983). Engineering plasticity. Halsted Press, New York.

Kachanov, L. M., (1974). Fundamentals in the theory of plasticity. Mir, Moscow.

Kanai, K., (1957). Semi-empirical formula for the seismic characteristics of the ground. Bulletin of the Earthquake Research Insitute, University of Tokyo, Japan, Vol. 35, 309-325.

Kanai, K., (1961). An empirical formula for the spectrum of strong earthquake motions. Bulletin of the Earthquake Research Institute, University of Tokyo, Japan, Vol. 39, 85-95.

Kang, H. D., and Willam, K. J., (1999). Localization characteristics of triaxial concrete model. Journal of Engineering Mechanics, ASCE, Vol. 125, No. 8, 941-950.

Karihaloo, B. L., Abdalla, H. M., and Imjai, T., (2003). A simple method for determining the true specific fracture energy of concrete. Magazine of Concrete Research, Vol. 55, No. 5, 471-481.

Karihaloo, B. L., (1995). Fracture mechanics and structural concrete. Longman Scientific and Technical, England.

Kaplan, F. M., (1961). Crack propagation and the fracture of concrete. ACI Journal, Vol. 58, No. 11, 591-610.

Kaul, M. K., (1978). Spectrum-consistent time-history generation. Journal of Engineering Mechanics, ASCE, Vol. 104, No. EM4, 781-788.

Kawasumi, H., (1956). Notes on the theory of vibration analyzer. Bulletin of the Earthquake Research Institute, University of Tokyo, Japan, Vol. XXXIV, Part I.

Kim, T. -H., Lee, K. -M., Chung, Y. -S., and Shin, H. M., (2005). Seismic damage assessment of reinforced concrete bridge columns. Engineering Structures, Vol. 27, No. 4, 576-592.

Kimura, M., and Izumi, M., (1989). A method of artificial generation of earthquake ground motion. Earthquake engineering and structural dynamics. Vol. 18, 867-874.

King, A. C. Y., and Chen, C., (1977). Interactive artificial earthquake generation. Computers and Structures, Vol. 7, 503-506.

Klisinski, M., and Mroz, Z., (1988). Description of inelastic deformation and degradation of concrete. International Journal of Solids and Structures, Vol. 24, No. 4, 391-416.

Koksal, H. O., and Arslan, G., (2004). Damage analysis of RC beams without web reinforcement. Magazine of Concrete Research, Vol. 56, No. 4, 231-241.

Kong, F. K., and Evans, R. H., (1975). Reinforced and prestressed concrete. Thomas Nelson and Sons Ltd, UK.

Kolmar, H., and Mehlhorn, G., (1984). Comparison of shear stiffness formulation for cracked reinforced concrete elements. Computer aided analysis and design of concrete structure. Ed. Damjanic, F., Hinton, E., Owen, D.R.J., Bicanic, N. and Simovic, V. Proceedings of International Conference, Split, Yugoslavia, Pineridge, 133-147.

Kotsovos, M. D., and Newman, J. B., (1980). Mathematical description of deformable behaviour of concrete under generalized stress beyond ultimate strength. ACI Journal, Vol. 72, 340-346.

Krajcinovic, D., (1996). Damage Mechanics. Elsevier, Amsterdam.

Kratzig, W. B., Meyer, I. F., and Meskouris, K., (1989). Damage evolution in reinforced concrete members under cyclic loading. Proceedings of the 5th International Conference on Structural Safety and Reliability (ICOSSAR 89), San Francisco, C.A., Vol. II, 795-802.

Krenk, S., Jonsson, J., and Hansen, L. P., (1994). Fatigue analysis and testing of adhesive joints. Engineering Mechanics, Paper No. 23, Aalborg University, Denmark.

Kroplin, B., and Weihe, S., (1997). Aspects of fracture induced anisotropy. In Proceedings of the 5th International Conference on Computational Plasticity (COMPLAS5), Barcelona, 255-279.

Kumar, D., Khattri, K. N., Teotia, S. S., and Rai, S. S., (1999). Modelling of accelerograms of two Himalayan earthquakes using a novel semi-empirical method and estimation of accelerogram for a hypothetical great earthquake in Himalaya. Journal of Current Science, Indian Academy of Sciences, Vol. 76, No. 6, paper No. 819.

Kunnath, S. K., and Chai, Y. H., (2004). Cumulative damage-based inelastic cyclic demand spectrum. Earthquake Engineering and Structural Dynamics, Vol. 33, No. 4, 499-520.

Kunnath, S. K., and Gross, J. L., (1995). Inelastic response of the Cypress Viaduct to the Loma Prieta earthquake. Engineering Structures, Vol. 17, No. 7, 485-493.

Kunnath, S. K., Reinhorn, A. M., and Abel, J. F., (1991). Computational tool for evaluation of seismic performance of reinforced concrete buildings. Computers and Structures, Vol. 41, No. 1, 157-173.

Kurama, Y. C., and Farrow, K. T., (2003). Ground motion scaling methods for different site conditions and structure characteristics. Earthquake Engineering and Strutural Dynamics, Vol. 32, No. 15, 2425-2450.

Kupfer, H., Hilsdorf, H. K., and Rusch, H., (1969). Behavior of concrete under biaxial stresses. ACI Journal, Vol. 66, No. 8, 656-666.

Kupfer, H. B., and Gerstle, K. H., (1973). Behavior of concrete under biaxial stresses. Journal of Engineering Mechanics, ASCE, Vol. 99, No. EM4, 852-866.

Kwan, W. -P., and Billington, S. L., (2001). Simulation of structural concrete under cyclic load. Journal of Structural Engineering, ASCE, Vol. 127, No. 12, 1391-1401.

Kwan, W. -P., and Billington, S., L., (2003). Unbonded posttensioned concrete bridge piers. Part II - Seismic analyses. Journal of Bridge Engineering, ASCE, Vol. 8, No. 2, 102-111.

Laible, J. P., White, R. N., and Gergely, P., (1977). Experimental investigation of seismic shear transfer across cracks in concrete nuclear containment vessels. ACI Special Publication, Vol. 53, No. 9, 203-226.

Lee, S. C., and Han, S. W., (2002). Neural-network-based models for generating artificial earthquakes and response spectra. Computers and Structures, Vol. 80, No. 20-21, 1627-1638.

Lee, J., and Fenves, G. L., (1998a). A plastic-damage concrete model for earthquake analysis of dams. Earthquake Engineering and Structural Dynamics, Vol. 27, No. 9, 937-956.

Lee, J., and Fenves, G. L., (1998b). Plastic-damage model for cyclic loading of concrete Structures. Journal of Engineering Mechanics, ASCE, Vol. 124, No. 8, 892-900.

Lee, W. H. K., Shin, T. C., Kuo, K. W., Chan, K. C., and Wu, C. F., (2001). CWB free-field strong-motion data from the 21 September Chi-Chi, Taiwan, earthquake. Bulletin of Seismological Society of America, Vol. 91, No. 5, 1370-1376.

Lee, J. -H., Koo, G. -H., and Yoo, B., (2003). Excitation test response characteristics and simulations of a seismically isolated test structure. 17th International Conference on Structural Mechanics in Reactor Technology, Prague, Czech Republic, August 17-22.

Leibengood, L. D., Darwin, D., and Dodds, R. H., (1986). Parameters affecting FE analysis of concrete structures. Journal of Structural Engineering, ASCE, Vol. 112, No. 2, 326-341.

Lestuzzi, P., Schwab, P., Koller, M., and Lacave, C., (2004). How to choose earthquake recordings for non-linear seismic analysis of structures. Proceedings of the 13th World Conference on Earthquake Engineering, Vancouver, B.C., Canada, paper No. 1241.

Levy, S., and Wilkinson, J. P. D., (1976). Generation of artificial time histories, rich in all frequencies, from given response spectra. Nuclear Engineering Design, Vol. 38, 241-251.

Lin, C. -C. J., and Ghaboussi, J., (2001). Generating multiple spectrum compatible accelerograms using stochastic neural networks. Earthquake Engineering and Structural Dynamics, Vol. 30, No. 4, 1021-1042.

Lin, Y. K., and Yong, Y., (1987). Evolutionary Kanai-Tajimi earthquake models. Journal of Engineering Mechanics, ASCE, Vol. 113, No. 8, 1119-1137.

Liu, S. C., (1969). On intensity definitions of earthquakes. Journal of the Structural Engineering, ASCE, Vol. 95, No. ST5, 1037-1042.

Liu, S. C., and Jhaveri, D. P., (1969). Spectral and correlation analysis of ground motion accelerograms. Bulletin of the Seismological Society of America, Vol. 59, 1517-1534.

Loh, C., and Ho, R., (1990). Seismic damage assessment based on hysteretic rules. Earthquake Engineering and Structural Dynamics, Vol. 19, No. 5, 753-771.

Lowes, L. N., (1999). Finite element modeling of reinforced concrete beam-column connections. PhD Thesis, University of California, Berkeley.

Lubliner, J., Oliver, J., Oller, S., Oñate, E., (1989). A plastic-damage model for concrete. International Journal of Solids and Structures, Vol. 25, No. 3, 299-326.

LUSAS User Manual, (2001). FEA Ltd., London, England.

Ma, G., Hao, H., and Lu, Y., (2003). Modelling damage potential of high-frequency ground motions. Earthquake Engineering and Structural Dynamics, Vol. 32, No. 10, 1483-1503.

Malhotra, P. K., (2002). Cyclic-demand spectrum. Earthquake Engineering and Strutural Dynamics, Vol. 31, No. 7, 1441-1457.

Martha, L. F., Llorca, J., Ingraffea, A. R., and Ellices, M., (1990). Numerical simulation of the cracking of Fontana dam. Structural Engineering Report 81-7. School of Civil and Environmental Engineering, Cornell University, Ithaca, NY.

Mehta, P. K., and Monteiro, P. J. M., (1993). Concrete: structure, properties, and methods. Englewood Cliffs: Prentice-Hall, Inc., New York.

Mendelson, A., (1968). Plasticity: theory and application. Krieger Publishing Co., Florida.

Meschke, G., Lackner, R., and Mang, H. A., (1998). An anisotropic elastoplastic-damage model for plain concrete. International Journal for Numerical Methods in Engineering, Vol. 42, No. 4, 703-727.

Milford, R. V., and Schnobrich, W. C., (1985). The rotating crack model to the analysis of reinforced shells. Computers and Structures, Vol. 20, No. 1-3, 225-234.

Mills, L. L., and Zimmerman, R. M., (1970). Compressive strength of plain concrete under multiaxial loading conditions. ACI Journal, Vol. 67, No. 10, 802-807.

Mosalam, K. M., and Paulino, G. H., (1997). Evolutionary characteristic length method for smeared cracking finite element models. Finite elements in Analysis and Design, Vol. 27, No. 1, 99-108.

Murray, D. W., Chitnuyanondh, L., Rijub-Agha, K.Y., and Wong, C., (1979). Concrete plasticity theory for biaxial stress analysis. Journal of Engineering Mechanics, ASCE, Vol. 105, No. EM6, 989-1006.

Naeim, F. M., and Lew, M. M., (1995). On the use of design spectrum compatible time histories. Earthquake Spectra, Vol. 11, No. 1, 111-127.

Naeim, F., Alimoradi, A., and Pezeshk, S., (2004). Selection and scaling of ground motion time histories for structural design using genetic algorithms. Earthquake Spectra, Vol. 20, No. 2, 413-426.

Nayak, G. C., and Zienkiewicz, O. C., (1972). Elasto-plastic stress analysis. A generalization for various constitutive relations including strain softening. International Journal for Numerical Methods in Engineering, Vol. 5, 113-135.

Neville, A. M., (1959). Some aspects of strength of concrete. Civil Engineering, Vol. 54, Part 1, 1153-1156; Part 2, 1308-1311; Part 3, 1435-1439.

Newmark, N. M., (1959). A method of computation for structural dynamics. Journal of the Engineering Mechanics, ASCE, Vol. 85, No. EM3, 67-94.

Newmark, N. M., and Hall, W. J., (1982). Earthquake spectra and design. Engineering Monographs on Earthquake Criteria, Structural Design and Strong Motion Records, Vol. 3, Earthquake Engineering Research Institute, University of California, Berkeley, CA, USA.

Newmark, N. M., and Rosenblueth, E., (1971). Fundamentals of earthquake engineering. Prentice-Hall, New York.

Nechnech, W., (2000). Contribution a l'etude numerique du comportement du beton et des structures en beton arme soumises a des solicitations thermique et mecaniques couplees: une approche thermo-elsto-plastique endommageable. These de doctorat, L' institute national des sciences appliqués de Lyon, France.

Nilson, A. H., (1968). Nonlinear analysis of reinforced concrete by the finite element method. ACI Journal, Vol. 65, No. 9, 757-766.

Ngo, D., and Scordelis, A. C., (1967). Finite element analysis of reinforced concrete beams. ACI Journal, Vol. 64, No. 3, 152-163.

Nguyen, V. B., and Chan, A. H. C., (2003). Preliminary numerical analysis of bridge piers under randomly generated artificial earthquake-like ground motions. Proceedings (Extended Abstracts) of the 11th Annual ACME Conference, ed. Wheel, M. A., University of Strathclyde, Glasgow, UK, 141-144.

Ohtani, Y., and Chen, W. F., (1988). Multiple hardening plasticity for concrete materials. Journal of Engineering Mechanics, ASCE, Vol. 114, No. 11, 1890-1910

Oliver, J., (1989). A consistent characteristic length for smeared crack models. International Journal for Numerical Methods in Engineering, Vol. 28, 461-474.

Ortiz, M., (1985). A constitutive theory for the inelastic behavior of concrete. Mechanics of Materials, Vol. 4, 67-93.

Ottosen, N. S., (1979). Constitutive modeling for short time loading of concrete. Journal of Engineering Mechanics, ASCE, Vol. 105, No. EM1, 127-141.

Ottosen, N. S., (1977). A failure criterion for concrete. Journal of Engineering Mechanics, ASCE, Vol. 103, No. 4, 527-535.

Owen, D. R. J., Figueriras, J. A., Damjanic, F., (1983). Finite element analysis of reinforced and prestressed concrete structures including thermal loading. Computer Methods in Applied Mechanics and Engineering, Vol. 41, 323-366.

Owen, D. R. J., Peric, D., de Souza Neto, E. A., Yu, J., and Dutko, M., (1995). Advanced computational strategies for 3-D large scale metal forming simulations. In Proceedings of the 5th International Conference on Numerical Methods in Industrial Forming Processes (NUMIFORM'95) , Dawson, P. R., eds., Ithaca, New York, 18-21 June, 7-22.

Owen, D. R. J., and Hinton, E., (1980). Finite Element in Plasticity: theory and practice. Pineridge Press, Swansea.

Ozbolt, J., and Bazant, Z. P., (1991). Microplane model for cyclic triaxial behaviour of concrete. Journal of Engineering Mechanics, ASCE, Vol. 118, No. 8, 1365-1386.

Pal, O., (1998). Modelisation du comportment dynamique des ouvrages grace a des elements finis de haute precision. Thesis, L'universite Joseph Fourier - Grenoble I.

Palaniswamy, R., and Shah, S.P., (1974). Fracture and stress-strain relationship of concrete under triaxial compression. Journal of Structural Engineering, ASCE, Vol. 100, No. 5, 901-915.

Pam, H. J., Kwan, A. K. H., Ho, J. C. M., (2001). Post-peak behavior and flexural ductility of doubly reinforced normal- and high-strength concrete beams. Structural Engineering and Mechanics, Vol. 12, No. 5, 459-474.

Papageorgious, A. S., (2000). Ground motion prediction methodologies for Eastern North America. Research Progress and Accomplishments: 1999-2000, Multidisciplinary Center for Earthquake Engineering Research, University of Buffalo, 63-69.

Park, Y. J., Ang, A. H. S., Wen, Y. K., (1984). Stochastic Model For Seismic Damage Assessment. Engineering Mechanics in Civil Engineering, Proceedings of the 5th Engineering Mechanics Division Specialty Conference., Laramie, WY, USA.

Park, J. Y., and Ang, A. H. S., (1985). Mechanistic seismic damage model for reinforced concrete. Journal of Structural Engineering, ASCE, Vol. 111, No. 4, 722-739.

Park, Y. J., Ang, A. H. S., and Wen, A. K., (1987). Damage-limiting aseismic design of buildings. Earthquake Spectra, Vol. 3, No. 1, 1-26.

Park, W., Yen, W. P., Shen, J. J., and Liu, C. C., (2003). Shake-table test for cummulative seismic damage of reinforced concrete bridge column. Proceedings of the 4th Asia-Pacific Transportation Development Conference, Oakland, C.A., USA.

Paul, A., Gupta, S. C., and Pant, C. C., (2003). CODA Q estimates for Kumaun Himalaya. Proceedings of Indian Academiy Sciences (Earthquake Planet Sciences), Vol. 112, No. 4, 569-576.

Paulay, T., and Loeber, P. J., (1974). Shear transfer by aggregate interlock. ACI Special Publication SP 42-1 Detroit, Mich, 1-15.

Petersson, P. E., (1981). Crack growth and development of fracture zones in plain concrete and similar materials. Report TVBM-1006, Division of Building Materials, Lund Institute of Technology, Lund, Sweden.

Petrangeli, M., and Ozbolt, J., (1996). Smeared crack approaches - Material modeling. Journal of Engineering Mechanics, ASCE, Vol. 122, No. 6, 545-554.

Pfaffinger, D. D., (1983). Calculation of power spectra from response spectra. Journal of Engineering Mechanics, ASCE, Vol. 109, No. 1, 357-372.

Phillips, D. V., and Zhang, B., (1990). Fracture energy and brittleness of plain concrete specimens under direct tension. Volume II, Proceedings of the 8th European Conference on Fracture (ECF8), Fracture Behaviour and Design of Materials and Structures, ed. Firrao, D., Turin, Italy, 646-652.

Pinto, A. V., and Pegon, P., (1991). Numerical representation of seismic input motion. Experimental and numerical methods in earthquake engineering, Donea & Jones (eds.), ECSC, EEC, EAEC, Brussels and Luxembourg.

Pinto, A. V., (1996). Pseudo-dynamic and shaking table tests on RC Bridges. PREC8 Report, LNEC Lisbon, Portugal.

Pinto, A. V., Molina, J., and Tsionis, G., (2003). Cyclic tests on large-scale models of existing bridge piers with rectangular hollow cross section. Earthquake Engineering and Structural Dynamics, Vol. 32, No. 13, 1995-2012.

Pires, F. J., and Da Costa, M. A., (1995). Quasi-static test of a short pier. ISMES Report, Ispra, Italy.

Planas, J., and Elices, M., (1991). Nonlinear fracture of cohesive materials. International Journal of Fracture, Vol. 51, No.3, 139-157.

Planas, J., and Elices, M., (1992). Asymptotic analysis of a cohesive crack. Part I - Theoretical background. International Journal of Fracture, Vol. 55, 153-177.

Prange, B., (1977). Parameters affecting damping properties. Proceedings of DMSR 77, Karlsruhe, 5-16 September 1977, Vol. 1, 61-78.

Press, W. H., Teukolsky, W. H., Vetterling, S. A., and Flannery, B. P., (1992). Numerical recipes: the art of scientific computing. Cambridge University Press, UK.

Prevost, J. H., and Hoeg, K., (1975). Soil mechanics and plasticity analysis of strain softening. Geotechnique, Vol. 23, 279-297.

Priestley, M. B., (1967). Power spectral analysis of non-stationary random process. Journal of Sound and Vibration, Vol. 6, No. 1, 86-97.

Priestley, M. J. N., (1993). Myths and fallacies in earthquake engineering - Conflicts between design and reality. Bulletin of the Newzealand National Society for Earthquake Engineering, Vol. 26, No. 3, 329-341.

Priestley, M. J. N., (2003a). Myths and fallacies in earthquake engineering, revisted. The Mallet Milne Lecture, IUSS Press, Rose School, Italy.

Priestley, M. J. N., (2003b). Private communications on the advantages and disadvantages of the program SIMQKE.

Priestley, M. J. N., Seible, F., and Calvi, G. M., (1996). Seismic design and retrofit of bridges. John Wiley and Sons, New York.

Pritz, T., (2004). Frequency power law of material damping. Applied Acoustics, Vol. 65, No. 11, 1027-1036.

Ramtani, S., (1990). Contribution a la modelisation du comportment multiaxial du beton endommage avec description du caractere unilateral. These de Genie Civil, Universite de Paris 6, E.N.S. de Cachan, France.

Rashid, Y. R., (1968). Ultimate strength analysis of pre-stressed concrete vessels. Nuclear Engineering and Design, Vol. 7, No. 4, 334-344.

Ratanalert, S., and Wecharatma, M., (1989). Evaluation of existing fracture models in concrete. Fracture Mechanics Application to Concrete. SP-118, ACI, USA, 113-146.

Reinhardt, H., Cornelissen, H. A. W., and Hordjil, D. A., (1986). Tensile tests and failure analysis of concrete. Journal of Structural Engineering, ASCE, Vol. 112, No. 11, 2462-2477.

Rehm, G., and Eligehausen, R., (1979). Bond of ribbed bars under high cycle repeated loads. ACI Structural Journal, Vol. 76, No. 2, 297-309.

Rizzo, P. C., Shaw, D. E., and Jarecki, S. J., (1973). Develeopment of real/synthetic time histories to match smooth design spectra. Proceedings of the 2nd International Conference on Structural Mechanics in Reactor Technology, America Nuclear Society, Berlin, Germany.

Rosenblueth, E., (1964). Probabilistic design to resist earthquakes. Journal of Engineering Mechanics, ASCE, Vol. 90, No. EM5, 189-219.

Rosenblueth, E., and Bustamante, J. E., (1962). Distribution of structural response to earthquakes. Journal of Engineering Mechanics, ASCE, Vol. 88, 75-106.

Rots, J. G., (1988). Computational modeling of concrete structures. PhD Thesis, Technological University of Delft, the Netherlands.

Rots, J. G., and de Borst, R., (1987). Analysis of mixed-mode fracture in concrete. Journal of Engineering Mechanics, ASCE, Vol. 113, No. 11, 1739-1758.

Roufaiel, M. S. L., and Meyer, C., (1987). Analytical modeling of hysteretic behavior of R/C frames. Journal of Structural Engineering, ASCE, Vol. 113, No. 3, 429-444.

Row, L. W., (1996). An earthquake strong-motion data catalogue for personal computers SMCAT. User Manual (version 2.0), National Geophysical Data Center, Colorado, USA.

Rubin, S., (1961). Concepts in shock data analysis. Shock and Vibration Handbook, ed. Harris, C. M., and Crode, C. E., McGraw-Hill, New York.

Sabetta, F., and Pugliese, A., (1996). Estimation of response spectra and simulation of nonstationary earthquake ground motions. Bulletin of Seismological Society of America, Vol. 86, No. 2, 337-352.

Saiidi, M., (1982). Hysteresis models for reinforced concrete. Journal of Structural Engineering Divisions, ASCE, Vol. 108, No. 5, 1077-1087.

Salami, M. R., and Desai, D. S., (1990). Constitutive modeling including mutiaxial testing under low-confining pressure. ACI Materials Journal, Vol. 87, No. 3, 228-236.

Saragoni, G. R., and Hart, G. C., (1974). Simulation of artificial earthquakes. Earthquake Engineering and Structural Dynamics, Vol. 2, 249-267.

Satish, K., and Usami, T., (1994). A note on the evaluation of damage in steel structures under earthquake loading. Journal of Structural Engineering, Tokyo, Japan, Vol. 40A, 177-188.

Scanlan, R. H., and Sachs, K., (1974). Earthquake time histories and response spectra. Journal of Engineering Mechanics, ASCE, Vol. 100, No. EM4, 635-655.

Scotta, R., Vitaliani, R., Saetta, A., Onate, E., and Hanganu, A., (2001). A scalar damage model with a shear retention factor for the analysis of reinforced concrete structures: theory and validation. Computers and Structures, Vol. 79, No. 7, 737-755.

Sfer, D., Carol, I., Gettu, R., and Este, G., (2002). Study of the behaviour of concrete under triaxial compression. Journal of Engineering Mechanics, ASCE, Vol 128, No. 2, 156-163.

Shah, S. P., and Sankar, R., (1987). Internal cracking and strain-softening response of concrete under uniaxial compression. ACI Material Journal, Vol. 84, No. 3, 200-212.

Shome, N., Cornell, A. C., Bazzurro, P., and Carballo, J. E., (1998). Earthquakes, records, and nonlinear responses. Earthquake Spectra, Vol. 14, No. 3, 469-500.

Simo, J. C., and Ju, J. W., (1987). Relative displacement and stress based continuum damage models-I Formulation. International Journal of Solids and Structures, Vol. 23, No. 7, 821-840.

SIMQKE User Manual, 1976. NISEE Software Library, University of California, Berkeley, USA.

Sinha, B. P., Gerstle, K. H., and Tulin, L. G., (1964). Stress-strain relations for concrete under cyclic loading. ACI Journal, Vol. 61, No. 2, 195-210.

Sinha, S., and Roy, L., (2004). Fundamental tests of reinforced concrete columns subjected to seismic loading. Proceedings of the Institution of Civil Engineers, Structures and Buildings, Vol. 157, No. SB3, 185-199.

Sixsmith, E., and Roesset, J., (1970). Statistical properties of strong motion earthquakes. Report No. R70-7, Department of Civil Engineering, Massachusetts Institute of Technology, USA.

Spanos, P. D., and Mignolet, M. P., (1990). Simulation of stationary random processes: two-stage MA to ARMA approach. Journal of Engineering Mechanics., Vol. 116, No. 3, 620-641.

Sritharan, S., Priestley, M. J. N., Seible, F., (1996). Seismic response of column/cap beam tee connections with cap beam prestressing. University of California, San Diego, Structural Systems Research Project, Report No. SSRP-96/09.

Stankowski, T., and Gerstle, K. H., (1985). Simple formulation of concrete under multiaxial load histories. ACI Journal, Vol. 82, No. 2, 213-221.

Stephens, J. E., and Yao, J. T. P., (1987). Damage assessment using response measurements. Journal of Structural Engineering, Vol. 113, No. 4, 787-801.

Stone, W. C., and Cheok, G. S., (1989). Inelastic behaviour of full-scale bridge columns subjected to cyclic loading. NIST Building Science Series 166, U.S. Government Printing Office, Washing, D. C., USA.

Stone, W. C., and Taylor, A. W., (1992). A predictive model for hysteretic failure parameters. Proceedings of the 10th World Conference on Earthquake Engineering, Madrid, Spain, 2575-2580.

Sucuoglu, H., and Erberik, A., (2004). Energy-based hysteresis and damage models for deteriorating systems. Earthquake Engineering and Structural Dynamics, Vol. 33, No. 1, 69-88.

Suidan, M., and Schnobrich, W. C., (1973). Finite element analysis of reinforced concrete. Journal of Structural Engineering, ASCE, Vol. 99, No. 1, 2109-2122.

Tajimi, H., (1960). A statistical method of determining the maximum response of a building structure during an earthquake. Proceedings of the second World Conference on Earthquake Engineering. Tokyo and Kyoto, Japan.

Takeda, T., Sozen, M. A., and Nielsen, N. N., (1970). Reinforced concrete response to simulated earthquakes. Journal of Structural Engineering, ASCE, Vol. 96, No. 12, 2557-2573.

Timoshenko, S., (1955). Strength of materials. Part I - Elementary theory and problems. D. Van Nostrand Company, Inc, New Jersey.

Tsai, N. -C., (1972). Spectrum-compatible motions for design purposes. Journal of Engineering Mechanics, ASCE, Vol. 98, No. EM2, 345-356.

Ulfkjaer, J. P., Krenk, S., and Brincker, R., (1995). Analytical model for fictitious crack propagation in concrete beams. Journal of Engineering Mechanics, ASCE, Vol. 121, No. 1, 7-15.

Usami, T., and Kumar, S., (1996). Damage evaluation in steel box columns by pseudodynamic tests. Journal of Structural Engineering, ASCE, Vol. 122, No. 6, 635-642.

Usami, T., and Kumar, S., (1998). Inelastic seismic design verification method for steel bridge piers using a damage index based hysteretic model. Engineering Structures, Vol. 20, No. 4-6, 472-480.

van Mier, J. G. M., (1986). Fracture of concrete under complex stress. Heron Vol. 31, No. 3, Delft University of Technology, The Netherlands.

van Mier, J. G. M., and Nooru-Mohamed, M. B., (1990). Geometrial and structural aspects of concrete fracture. Engineering Fracture Mechanics, Vol. 35, No. 4/5, 617-628.

van de Lindt, J. W., (2005). Modelling earthquake risk based on approximate nonlinear reliability estimates. International of Modelling and Simulation, Vol. 25, No. 3, 1-24.

van de Lindt, J. W., and Goh, G., (2004). An earthquake duration effect on structural reliability. Journal of Structural Engineering, ASCE, Vol. 130, No. 5, 821-826.

Vanmarcke, E. H., (1976). Structural response to earthquakes. Chapter 8 of Seismic Risk and Engineering Decisions. Ed. Lomnitz, C., and Rosenblueth, E., Elsevier, New York.

Varpasuo, P., (2004). Private communications on generation of artificial earthquakes.

Varpasuo, P., and van Gelder, P., (2001). Generation of design ground motion time histories for the Lianyungang Nuclear Power Plant. ICOSSAR'01, Newport Beach, June 17-22.

Vecchio, F. J., and Shim, W., (2004). Experimental and analytical re-examination of classic concrete beam tests. Journal of Structural Engineering, Vol. 130, No. 3, 460-469.

Wald, D., (1997). Surfing the Internet for strong-motion data. Seismological Research Letters, Vol. 68, No. 5, 766-769.

Walraven, J. C., and Reinhardt, H. W., (1981). Theory and experiment of the mechanical behavior of cracks in plain and reinforced concrete subjected to shear loading. Heron Vol. 26, No. 1A, 1-68.

Wan, S., Loh, C. -H., and Peng, S. -Y., (2001). Experimental and theoretical study on softening and pinching effects of bridge column. Soil Dynamics and Earthquake Engineering, Vol. 21, No. 1, 75-81.

Warnitchai, P., and Panyakapo, P., (1999). Constant-damage design spectra. Journal of Earthquake Engineering, Vol. 3, No. 3, 329-347.

Weihe, S., Kroplin, B., and de Borst, R., (1998). Classification of smeared crack models based on material and structural properties. International Journal of Solids and Structures, Vol. 35, No. 12, 1289-1308.

Willam, K. J., and Warnke E. P., (1975). Constitutive model for the triaxial behavior of concrete. International association of bridge and structural engineers, Seminar on concrete structure subjected to triaxial stresses, paper III-1, Bergamo, Italy, May 1974, IABSE Proc. 19.

Williams, M. S., and Sexsmith, R. G., (1995). Seismic damage indices for concrete structures: a state-of-the-art review. Earthquake Spectra, Vol. 11, No. 2, 319-349.

Williams, M. S., Villemure, I., and Sexsmith, R. G., (1997). Evaluation of seismic damage indices for concrete elements loaded in combined shear and flexure. ACI Structural Journal, Vol. 94, No. 3, 315-322.

Wilson, E. L., (2002). Three dimensional static and dynamic analysis of structures. CSI Publication, Berkeley, California., USA.

Wittmann, F. H., (2002). Crack formation and fracture energy of normal and high strength concrete. Sadhana, Vol. 27, No. 4, 413-423.

Wong, H. L., and Trifunac, M. D., (1979). Generation of artificial strong motion accelerograms. Earthquake Engineering and Structural Dynamics, Vol. 7, 509-527.

Wood, W. L., (1990). Practical Time-stepping Schemes. Clarendon Press, Oxford University Press, UK.

Yankelevsky, D. Z., and Reinhardt, H. W., (1987). Response of plain concrete to cyclic tension. ACI Materials Journal, Vol. 84, No. 5, 365-373.

Yin, W. S., Su, E. C. M., Mansur, M. A., and Hsu, T. T. C., (1989). Biaxial tests of plain and fiber concrete. ACI Materials Journal, Vol. 86, No. 3, 236-243.

Zaman, M., Najjar, Y. M., Faruque, M. O., (1993). Modelling of stress-strain behaviour of plain concrete using a plasticity framework. Materials and Structures, Vol. 26, 129-135.

Zeng, Y., Anderson, J. G. and Yu, G., (1994). A composite source model for computing realistic synthetic strong ground motions. Geophysical Research Letters, Vol. 21, No. 8, 725-728.

Zhu, W. C., Teng, J. G., and Tang, C. A., (2002). Numerical simulation of strength envelope and fracture patterns of concrete under biaxial loading. Magazine of Concrete Research, Vol. 54, No. 6, 354-369.

Zienkiewicz, O. C., and Taylor, R. L., (1991). The finite element method. 4th edition. Vols. 1 and 2, Mc.Graw-Hill, London.

APPENDIX 2A

Stress invariants in the Haigh-Westergaard coordinates

Stress invariants can be expressed in terms of the Haigh-Westergaard coordinates ζ, ρ, and θ as: (for the tensorial notations, autosummation is assumed for the repeated indices)

$$\zeta = \frac{I_1}{\sqrt{3}};\ \text{where}\ I_1 = \delta_{ij}\sigma_{ij} = \sigma_{11} + \sigma_{22} + \sigma_{33} \tag{2A-1}$$

$$\rho = \sqrt{2J_2};\ \text{where}\ J_2 = \frac{1}{2}\sigma'_{ij}\sigma'_{ij};\ \text{and}\ \ \sigma'_{ij} = \sigma_{ij} - \frac{1}{3}\delta_{ij}\sigma_{kk} \tag{2A-2}$$

$$\cos 3\theta = \frac{3\sqrt{3}}{2}\frac{J_3}{J_2^{3/2}};\ \ \text{where}\ J_3 = \frac{1}{3}\sigma'_{ij}\sigma'_{jk}\sigma'_{ki} \tag{2A-3}$$

Where

I_1 is the first invariant of stress tensor

J_2 is the second invariant of deviatoric stress tensor

J_3 is the third invariant of deviatoric stress tensor

δ_{ij} is the Kroneker delta

σ_{ij} is the stress tensor

$\sigma_{11} = \sigma_1$, $\sigma_{22} = \sigma_2$, $\sigma_{33} = \sigma_3$ are the principal stresses

σ'_{ij} is the deviatoric stress tensor

APPENDIX 3A

Calculating velocity and displacement response spectra from an EC8 elastic response spectrum

The displacement response spectrum is determined from the velocity response spectrum as shown in the literature (Clough and Penzien 1975, Chopra 1995, Priestley *et al.* 1996)

$$S_d = \frac{S_v}{\omega} \tag{3A-1}$$

where S_v is the velocity response spectrum; S_d is the displacement response spectrum, and ω is the frequency in radians/second (rad/s).

The velocity response spectrum is derived from the acceleration response spectrum via the following the relationship

$$S_v = \frac{S_a}{\omega} \tag{3A-2}$$

Where S_a is the acceleration response spectrum.

APPENDIX 3B

EC8 elastic response spectra

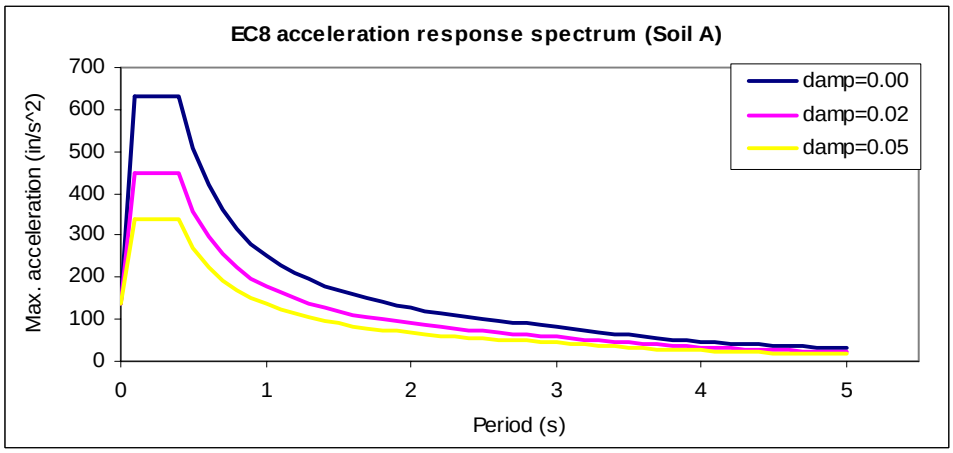

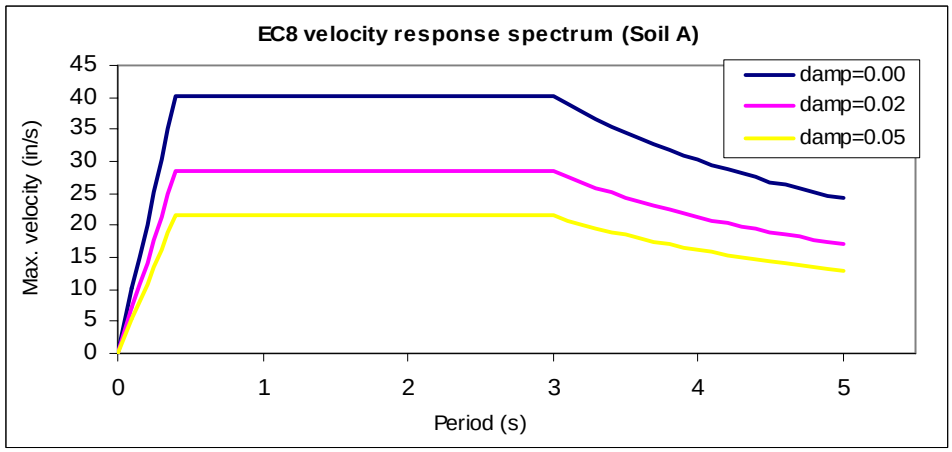

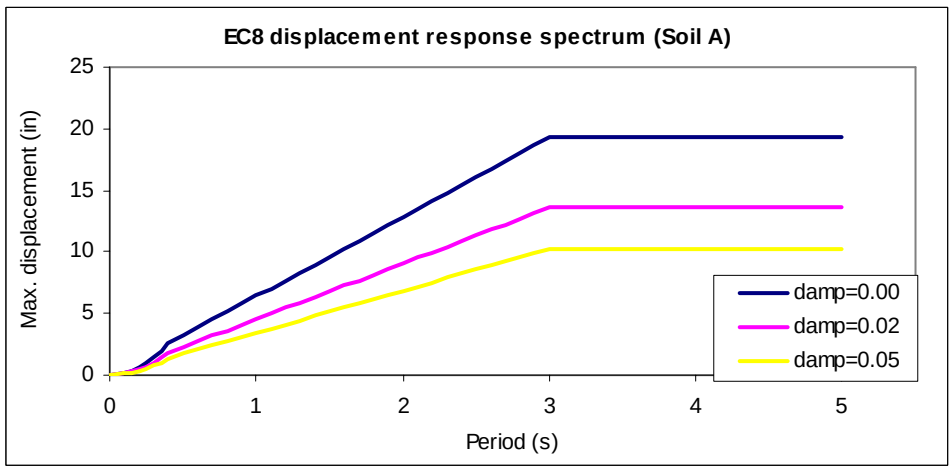

Figure 3B.1 Response spectra for the subsoil class A (Eurocode 8, ENV 1998-1:1996)

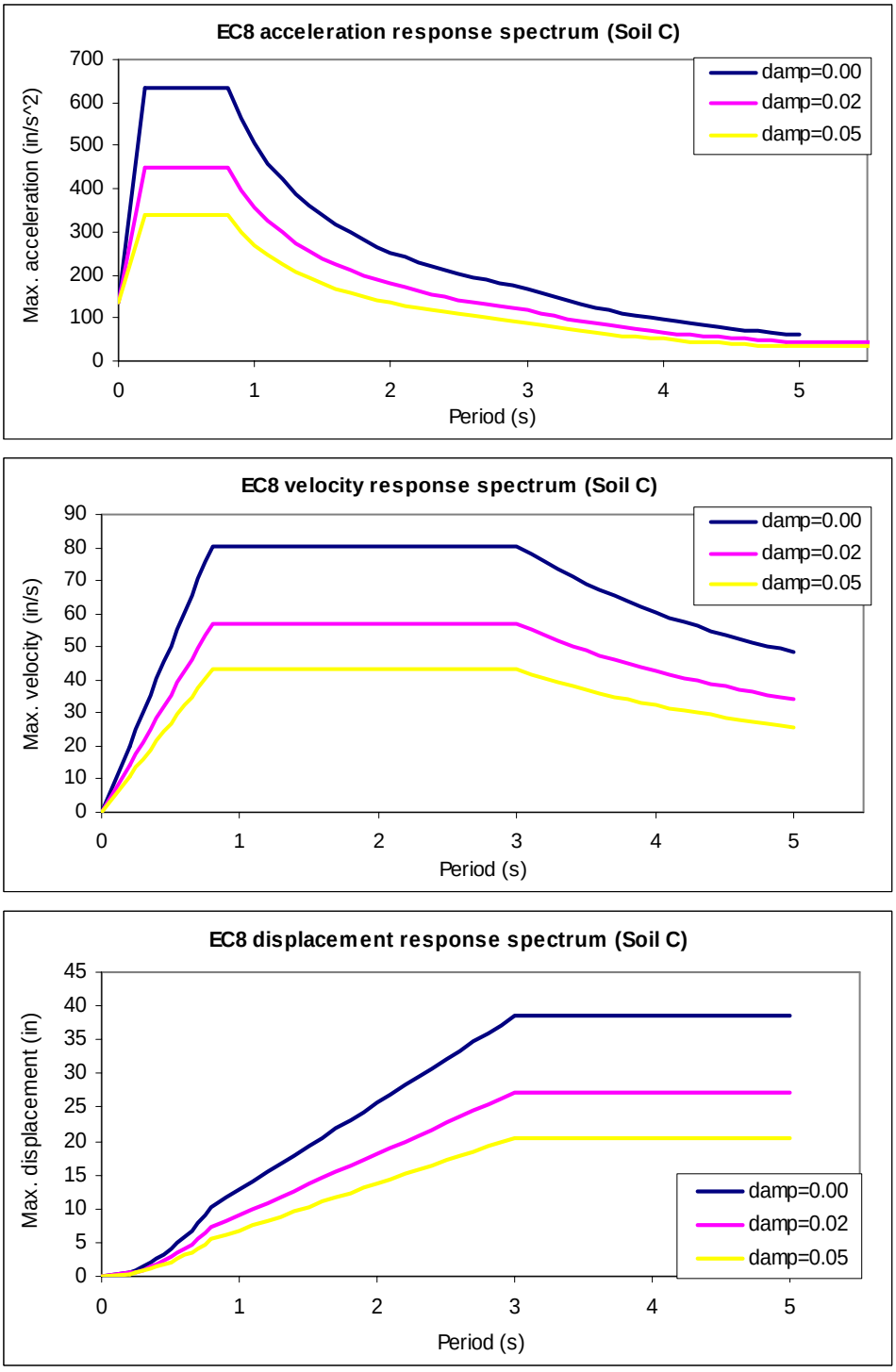

Figure 3B.2 Response spectra for the subsoil class C (Eurocode 8, ENV 1998-1:1996)

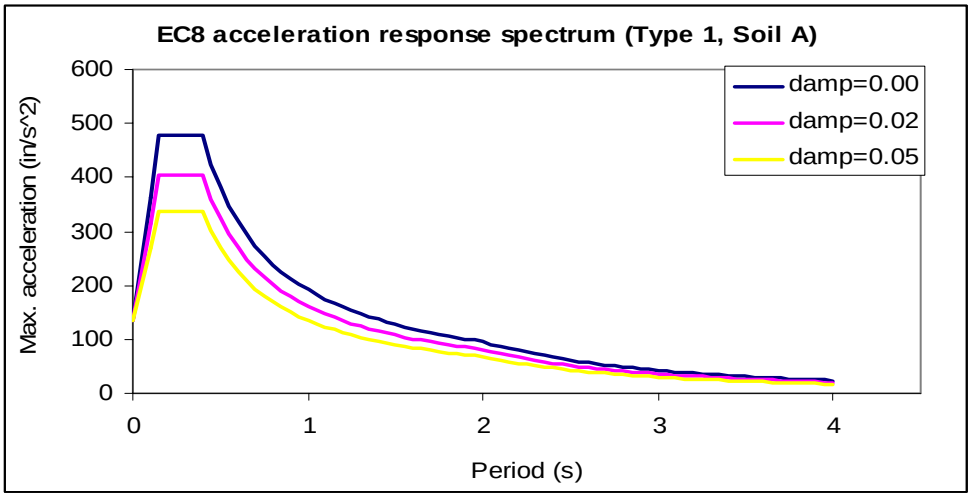

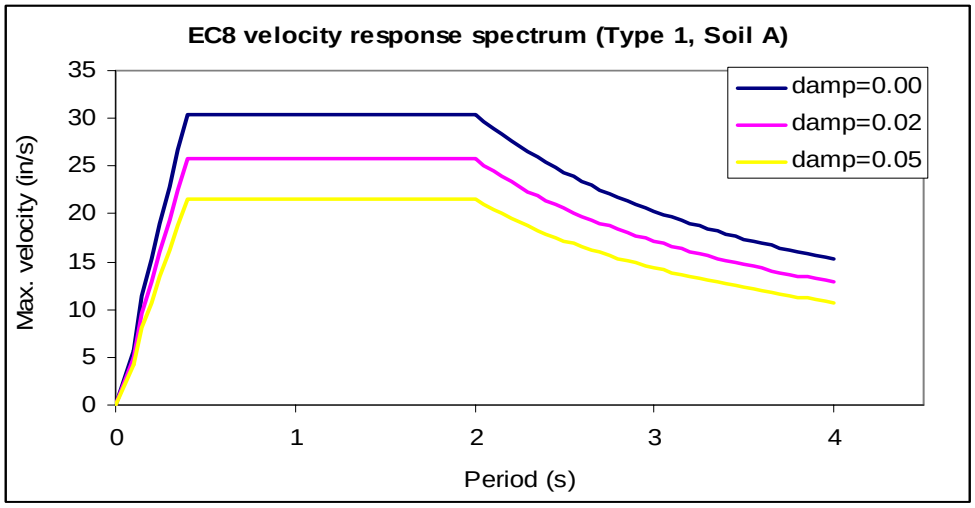

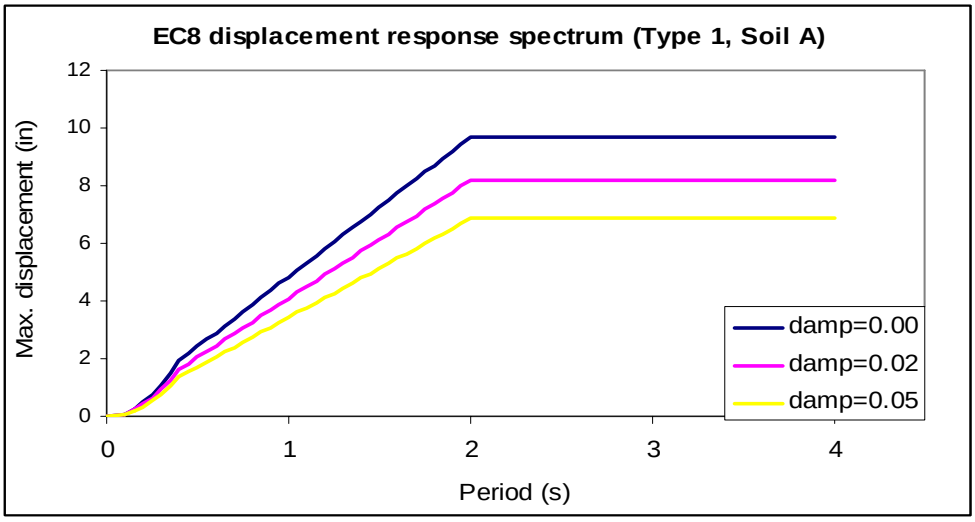

Figure 3B.3 Response spectra for the subsoil class A (prEN1998-1: 2004)

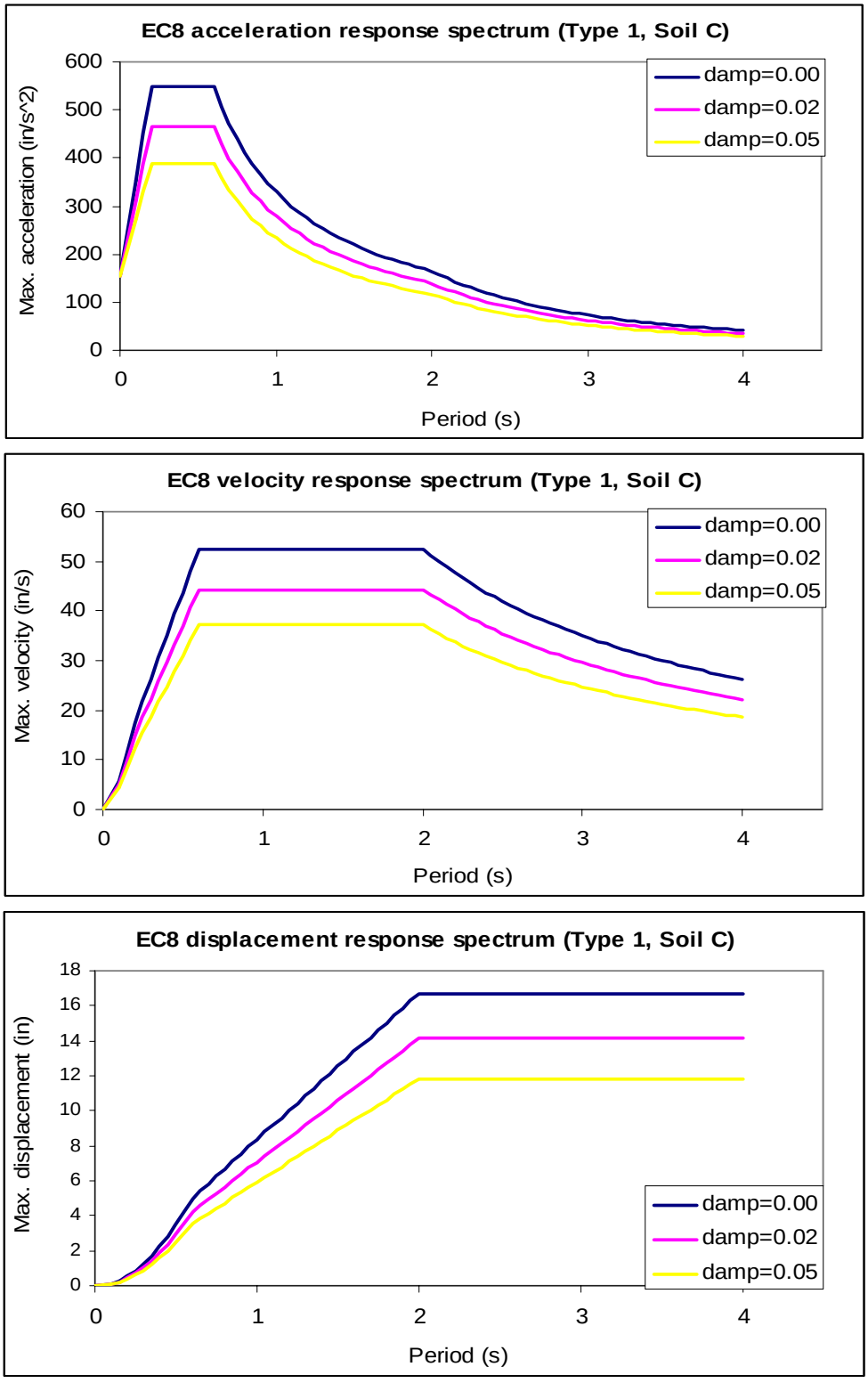

Figure 3B.4 Response spectra for the subsoil class C (prEN1998-1: 2004)

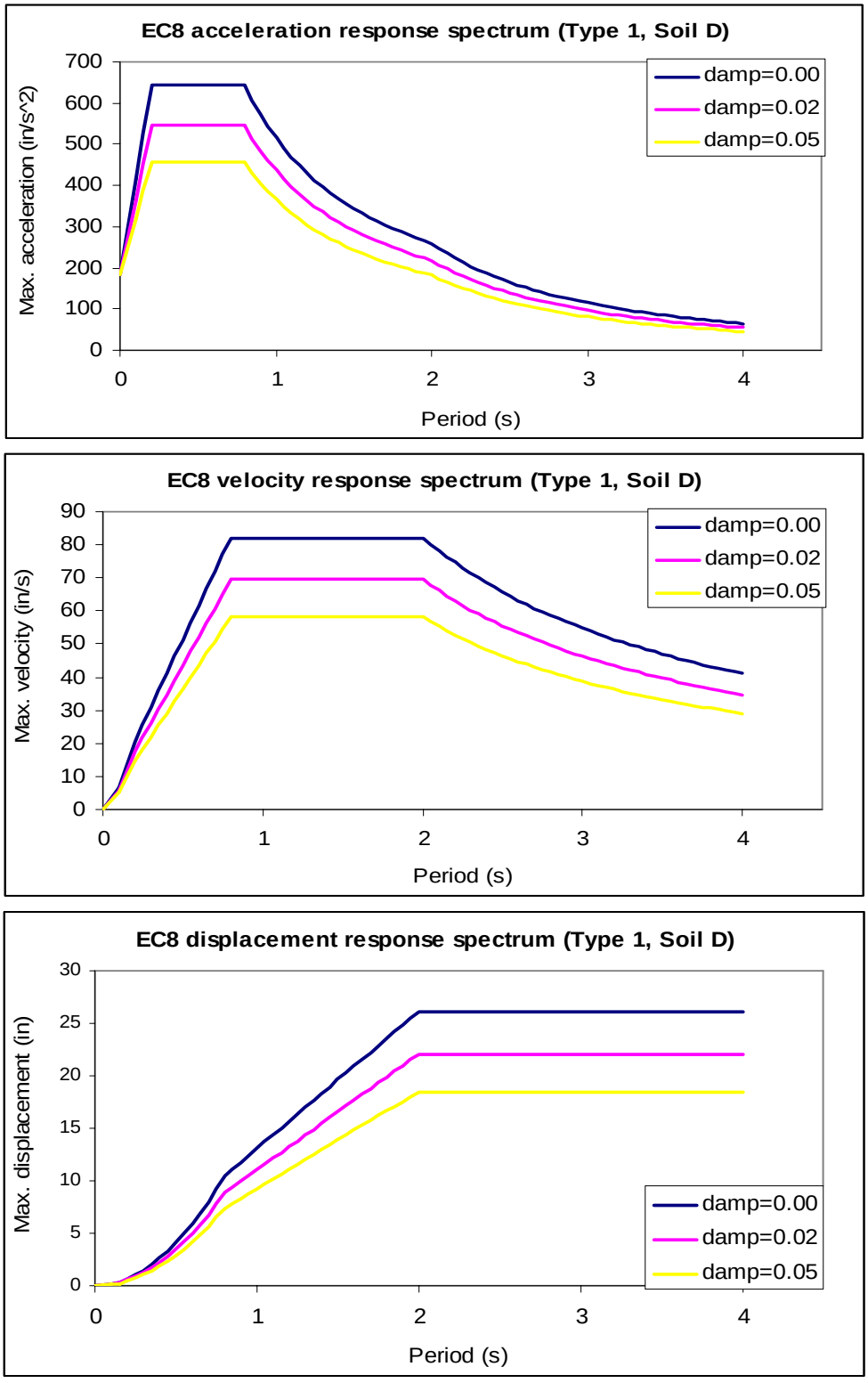

Figure 3B.5 Response spectra for the subsoil class D (prEN1998-1: 2004)

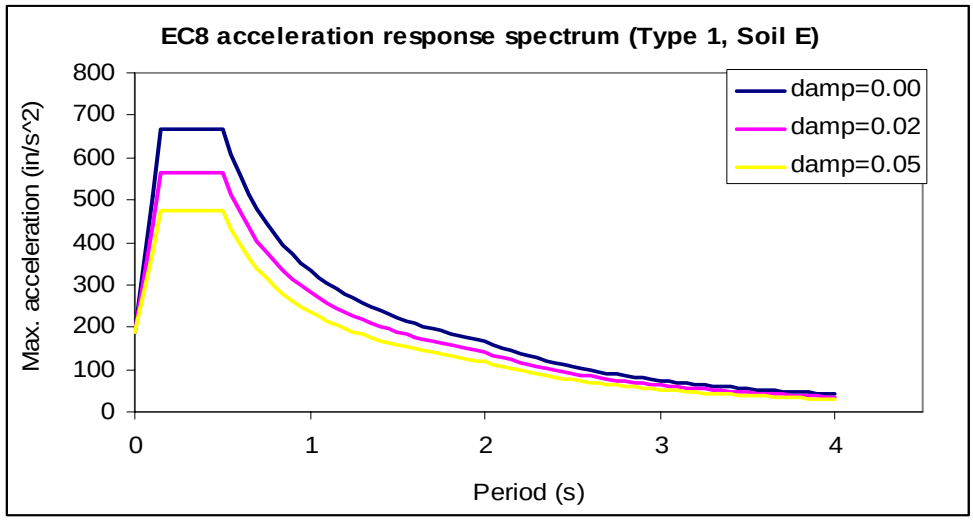

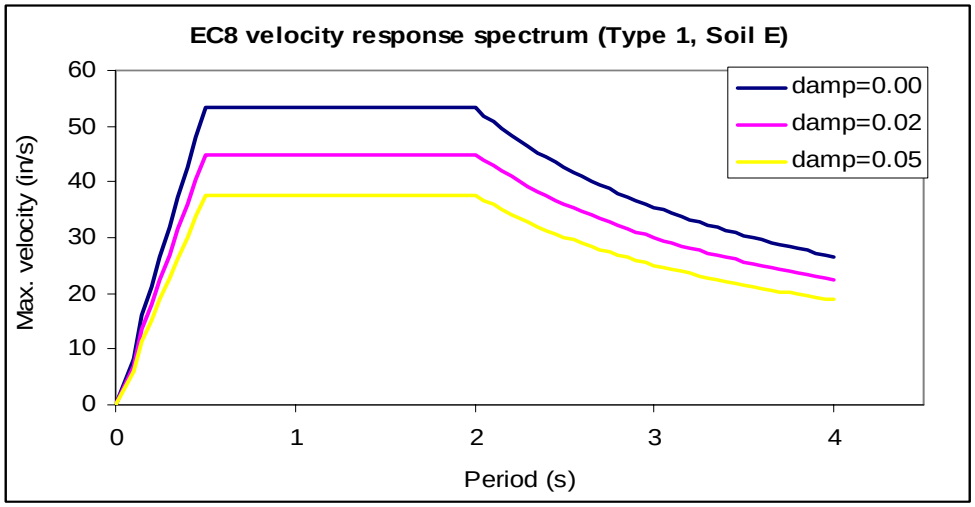

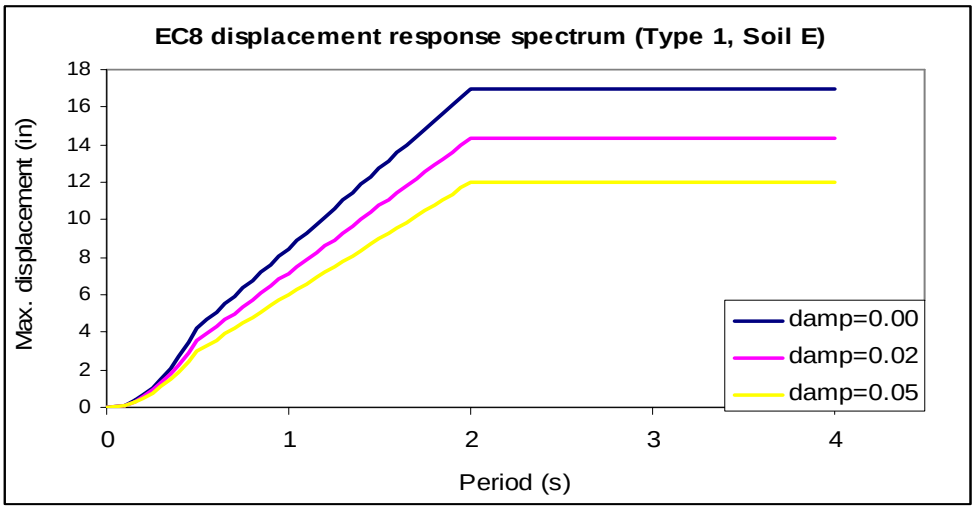

Figure 3B.6 Response spectra for the subsoil class E (prEN1998-1: 2004)

APPENDIX 6A

Main calculation steps of the moment-curvature and load-deflection curves for a linear softening rule

Here is the procedure used to calculate the analytical solution:

1. Calculate the compressive strain ε_{ci} of the extreme surface fibre using the condition that the resultant force acting on the cross-section is zero as it is assumed that an incremental value of the tensile strain at the extreme fibre of the beam is known and there is no external axial force acting on the cross-section. Detailed calculation is shown in Section 6A.1.

2. The curvature κ_i of the beam at this vertical section for the tensile strain ε_{ti} is calculated using $\kappa_i = \dfrac{\varepsilon_{ti} + \varepsilon_{ci}}{h}$ where *h* is the height of the beam section.

3. Calculate the total moment in a section M_i for the tensile strain ε_{ti} by taking moment. Detailed calculation is given in Section 6A.2.

4. The deflections y_{2i} at the mid-span cross-section is determined using the following procedures:

4.1. For the linear elastic regime (Phase I), the deflections are determined by using one of well-known methods from beam bending theory, i.e. integration or moment-area or strain energy methods.

4.2. For the non-linear regime (Phase II and III), the deflections are determined by using the fifth assumption and the moment-area method as shown in the following steps:

i. Assign a segment of width w_c of the softening material in the mid-span of beam after the strain of outer-fibre in tension side reaches ε_{tp}.

ii. Calculate the curvatures and moments at edge cross-section, Section 1, ($\kappa_{1,i}$, $M_{1,i}$) between the cracked and linear elastic unloading zones and at the mid-span cross-section, Section 2, ($\kappa_{2,i}$, $M_{2,i}$). It is assumed that the material inside the width w_c is strain-softening and the material of

the rest of the beam (containing the material at two edge cross-sections) is linear elastically unloading. Curvatures and moments at any cross-section in the softening width w_c is assumed to be linearly interpolated from those at the edge cross-section and at mid-span cross-section.

iii. Calculate the deflections of beam (e.g. deflections at the mid-span cross-section y_{2i}) from the diagrams of curvature using moment-area method. Details of this step are given in Section 6A.3.

5. Determine the load at mid-span cross-section using the equation $P_i = \frac{4M_{2i}}{L}$, in which M_{2i} is the bending moment at the mid-span cross-section, and L is the span-length of the beam.

6. The moment-curvature and load-displacement curves can then be plotted.

The notations used are taken from Figure 4.1(a)

6A.1 Calculation of the compressive strain ε_{ci} at the extreme surface fibre

The equilibrium equation for force at stage i is given as:

$$F_{ci} = F_{ti} \qquad \text{(6A-1)}$$

where

$F_{ci} = \int_0^{h_{1i}} \sigma_c b dy$ (6A-2) and $F_{ti} = \int_0^{h_{2i}} \sigma_t b dy'$ (6A-3) are the compressive and tensile forces in the cross-section, respectively

y, y' = the distances from the neutral axis to a particular compressive or tensile fibres, respectively

b = the beam width

h_{1i} = the distance from the neutral axis to the compressive extreme surface fibre

h_{2i} = the distance from the neutral axis to the tensile extreme surface fibre

h = the beam depth

σ_c = stress at the compressive fibre, $\sigma_c = \varepsilon_c E_c$ where $0 \le \varepsilon_c \le \varepsilon_{ci}$

σ_t = stress at the tensile fibre,

For $0 \le \varepsilon_{ti} \le \varepsilon_{tp}$, $\sigma_t = \varepsilon_t E_c$ (Phase I)

For $\varepsilon_{tp} \le \varepsilon_{ti} \le \varepsilon_0$, $\sigma_t = f_t\left[1-\dfrac{\varepsilon_t - \varepsilon_{tp}}{\varepsilon_0 - \varepsilon_{tp}}\right]$ (Phase II)

For $\varepsilon_0 \le \varepsilon_{ti}$, $\sigma_{ti} = 0$ (Phase III)

in which

ε_{ci} = compressive strain at the extreme surface fibre at stage *i*

ε_{ti} = tensile strain at the extreme surface fibre at stage *i*

ε_c = compressive strain at an internal fibre, $0 \le \varepsilon_c \le \varepsilon_{ci}$

ε_t = tensile strain at an internal fibre, $0 \le \varepsilon_t \le \varepsilon_{ti}$

σ_c = compressive stress at an internal fibre, $0 \le \sigma_c \le \sigma_{ci}$

σ_t = tensile stress at an internal fibre

σ_{ci} = compressive stress at the extreme surface fibre at stage *i*

σ_{ti} = tensile stress at the extreme surface fibre at stage *i*

ε_{tp} = tensile strain at the maximum tensile strength

The stress and strain distributions in the cross-section are shown in Figure 6A.1.

Details of the calculation are shown as follows

1. Determination of the heights of compressive and tensile zones of the cross-section

Using similar triangles in the strain distribution (Figure 6A.1), h_{1i} and h_{2i} can be calculated using the following equations

$$\frac{h_{1i}}{\varepsilon_{ci}} = \frac{h_{2i}}{\varepsilon_{ti}} \qquad \text{(6A-4)}$$

In addition,

$$h_{1i} + h_{2i} = h \qquad \text{(6A-5)}$$

where *h* is the beam depth

Solving simultaneously Equations (6A-4) and (6A-5), the results are

$$h_{1i} = \frac{h\varepsilon_{ci}}{\varepsilon_{ti} + \varepsilon_{ci}}\ , \qquad h_{2i} = \frac{h\varepsilon_{ti}}{\varepsilon_{ti} + \varepsilon_{ci}} \tag{6A-6}$$

The distances x_{1i}, $x_{2,i}$ and the crack length *a* (Figure 6A.1) are calculated from similarity triangles in Figure 6A.1.

2. Calculating compressive force in concrete

We begin by identifying a thin element of compressive area located at distance *y* from the neutral axis (Figure 6A.1). The element has width *b* and height *dy*, and the force acting on this element is $\sigma_c.b.dy$ (σ_c is the compressive stress of this thin element in concrete). Integrating this force over the upper part of the beam, we obtain the resultant compressive force F_{ci} as given in (6A-2).

Relating the variables ε_c and y using similar triangles (Figure 6A.1)

$$\varepsilon_c = \frac{\varepsilon_{ci}}{h_{1i}} \cdot y\ , \qquad y = \frac{h_{1i}\varepsilon_c}{\varepsilon_{ci}}\text{, and} \qquad dy = \frac{h_{1i}d\varepsilon_c}{\varepsilon_{ci}} \tag{6A-7}$$

Therefore, the compressive force F_{ci} is

$$F_{ci} = \int_0^{\varepsilon_{ci}} \sigma_c b\left(\frac{h_{1i}d\varepsilon_c}{\varepsilon_{ci}}\right) = \frac{bh_{1i}}{\varepsilon_{ci}}\int_0^{\varepsilon_{ci}} \sigma_c d\varepsilon_c \tag{6A-8}$$

Note that $\sigma_c = \varepsilon_c E_c$ and $h_{1i} = \dfrac{h\varepsilon_{ci}}{\varepsilon_{ti} + \varepsilon_{ci}}$ so (6A-8) becomes

$$F_{ci} = \frac{bh_{1i}}{\varepsilon_{ci}}\int_0^{\varepsilon_{ci}} \sigma_c d\varepsilon_c = \frac{bhE_c}{\varepsilon_{ti} + \varepsilon_{ci}}\int_0^{\varepsilon_{ci}} \varepsilon_c d\varepsilon_c \tag{6A-9}$$

3. Calculating tensile force in concrete

The resultant tensile force F_{ti} in the lower part of the beam is found in a similar manner with the resultant compressive force. The element has width *b* and height *dy'*, and the force acting on this element is $\sigma_t.b.dy'$ (σ_t is the tensile stress of the thin element in concrete). Integrating this force over the lower part of the beam, we obtain the resultant tensile force F_{ti} as given in (6A-3).

Relating the variables ε_t and y' by using similar triangles (Figure 6A.1)

$$\varepsilon_t = \frac{\varepsilon_{ti}}{h_{2i}} \cdot y', \qquad y' = \frac{h_{2i}\varepsilon_t}{\varepsilon_{ti}}, \text{ and} \qquad dy' = \frac{h_{2i}d\varepsilon_t}{\varepsilon_{ti}} \tag{6A-10}$$

Similarly, the tensile force F_{ti} is

$$F_{ti} = \int_0^{\varepsilon_{ti}} \sigma_t b\left(\frac{h_{2i}d\varepsilon_t}{\varepsilon_{ti}}\right) = \frac{bh_{2i}}{\varepsilon_{ti}}\int_0^{\varepsilon_{ti}} \sigma_t d\varepsilon_t = \frac{bh}{(\varepsilon_{ti}+\varepsilon_{ci})}\int_0^{\varepsilon_{ti}} \sigma_t d\varepsilon_t \tag{6A-11}$$

In Phase I: $0 \le \varepsilon_{ti} \le \varepsilon_{tp}$, $\sigma_t = \varepsilon_t E_c$

$$F_{ti} = \frac{bE_c h}{\varepsilon_{ti}+\varepsilon_{ci}}\int_0^{\varepsilon_{ti}} \varepsilon_t d\varepsilon_t \tag{6A-12}$$

In Phase II: $\varepsilon_{tp} \le \varepsilon_{ti} \le \varepsilon_0$, $\sigma_t = \varepsilon_{tp}E_c\left[1-\frac{\varepsilon_t-\varepsilon_{tp}}{\varepsilon_0-\varepsilon_{tp}}\right]$

$$F_{ti} = \frac{bE_c h}{\varepsilon_{ti}+\varepsilon_{ci}}\left\{\int_0^{\varepsilon_{tp}} \varepsilon_t d\varepsilon_t + \int_{\varepsilon_{tp}}^{\varepsilon_{ti}} \varepsilon_{tp}\left[1-\frac{\varepsilon_t-\varepsilon_{tp}}{\varepsilon_0-\varepsilon_{tp}}\right]d\varepsilon_t\right\} \tag{6A-13}$$

In Phase III: $\varepsilon_0 \le \varepsilon_{ti}$, $\sigma_t = 0$

$$F_{ti} = 0 \tag{6A-14}$$

4. Substituting F_{ci} derived from (6A-9), and F_{ti} derived from (6A-12) for linear elastic material and from (6A-13) and (6A-14) for softening material, into the condition $F_{ci} = F_{ti}$

Noting that in this equation, only the compressive strain ε_{ci} is the unknown. Therefore, the compressive strain ε_{ci} of the extreme surface fibre can be calculated. In this thesis, ε_{ci} is evaluated numerically using bisection method.

6A.2 Calculation of the total moment M_i at the tensile strain ε_i

The total moment of a cross-section M_i can be expressed generally from the summation of the moments in the compressive and tensile zones

$$M_i = M_{ci} + M_{ti} \tag{6A-15}$$

in which M_{ci}, and M_{ti} are moments produced by the compressive stress and tensile stress of concrete, respectively. As resultant axial force is zero, therefore it does not matter where the moment is taken.

1. Moment M_{ci} produced by the compressive stress

$$M_{ci} = \int_0^{h_{1i}} \sigma_c b y dy \tag{6A-16}$$

Using equation (6A-7) for *y* and *dy*, we have

$$M_{ci} = \int_0^{\varepsilon_{ci}} \sigma_c b \left(\frac{h_{1i}\varepsilon_c}{\varepsilon_{ci}} \right) \left(\frac{h_{1i} d\varepsilon_c}{\varepsilon_{ci}} \right) = \frac{b h_{1i}^2}{\varepsilon_{ci}^2} \int_0^{\varepsilon_{ci}} \sigma_c \varepsilon_c d\varepsilon_c \tag{6A-17}$$

Substituting $h_{1i} = \dfrac{h\varepsilon_{ci}}{\varepsilon_{ti} + \varepsilon_{ci}}$ and $\sigma_c = \varepsilon_c E_c$ into (6A-17), we have

$$M_{ci} = \frac{b h^2 E_c}{(\varepsilon_{ti} + \varepsilon_{ci})^2} \int_0^{\varepsilon_{ci}} \varepsilon_c^2 d\varepsilon_c \tag{6A-18}$$

2. Moment M_{ti} produced by the tensile stress

$$M_{ti} = \int_0^{h_{2i}} \sigma_t b y' dy' \tag{6A-19}$$

Using equation (6A-10) for y' and dy', we have

$$M_{ti} = \int_0^{\varepsilon_{ti}} \sigma_t b \left(\frac{h_{2i}\varepsilon_t}{\varepsilon_{ti}} \right) \left(\frac{h_{2i} d\varepsilon_t}{\varepsilon_{ti}} \right) = \frac{b h_{2i}^2}{\varepsilon_{ti}^2} \int_0^{\varepsilon_{ti}} \sigma_t \varepsilon_t d\varepsilon_t \tag{6A-20}$$

Substituting $h_{2i} = \dfrac{h\varepsilon_{ti}}{\varepsilon_{ti} + \varepsilon_{ci}}$ into (6A-20), we have

$$M_{ti} = \frac{b h^2}{(\varepsilon_{ti} + \varepsilon_{ci})^2} \int_0^{\varepsilon_{ti}} \sigma_t \varepsilon_t d\varepsilon_t \tag{6A-21}$$

In Phase I: $0 \le \varepsilon_{ti} \le \varepsilon_{tp}$, $\sigma_t = \varepsilon_t E_c$

$$M_{ti} = \frac{bh^2 E_c}{(\varepsilon_{ti} + \varepsilon_{ci})^2} \int_0^{\varepsilon_{ti}} \varepsilon_t^2 d\varepsilon_t \tag{6A-22}$$

In Phase II: $\varepsilon_{tp} \le \varepsilon_{ti} \le \varepsilon_0$, $\sigma_t = \varepsilon_{tp} E_c \left[1 - \frac{\varepsilon_t - \varepsilon_{tp}}{\varepsilon_0 - \varepsilon_{tp}} \right]$

$$M_{ti} = \frac{bh^2 E_c}{(\varepsilon_{ti} + \varepsilon_{ci})^2} \left\{ \int_0^{\varepsilon_{tp}} \varepsilon_t^2 d\varepsilon_t + \int_{\varepsilon_{tp}}^{\varepsilon_{ti}} \varepsilon_{tp} \varepsilon_t \left[1 - \frac{\varepsilon_t - \varepsilon_{tp}}{\varepsilon_0 - \varepsilon_{tp}} \right] d\varepsilon_t \right\} \tag{6A-23}$$

In Phase III: $\varepsilon_0 \le \varepsilon_{ti}$, $\sigma_t = 0$

$$M_{ti} = \frac{bh^2 E_c}{(\varepsilon_{ti} + \varepsilon_{ci})} \left[\int_0^{\varepsilon_{tp}} \varepsilon_t^2 d\varepsilon_t + \int_{\varepsilon_{tp}}^{\varepsilon_0} \varepsilon_{tp} \varepsilon_t \left[1 - \frac{\varepsilon_t - \varepsilon_{tp}}{\varepsilon_0 - \varepsilon_{tp}} \right] d\varepsilon_t \right] \tag{6A-24}$$

3. Governing equation for the total moment M_i

The total moment M_i can be obtained from $M_i = M_{ci} + M_{ti}$, in which M_{ci} is derived from (6A-18), and M_{ti} is derived from (6A-21). As a result,

$$M_i = \frac{bh^2 E_c}{(\varepsilon_{ti} + \varepsilon_{ci})^2} \int_0^{\varepsilon_{ci}} \varepsilon_c^2 d\varepsilon_c + \frac{bh^2}{(\varepsilon_{ti} + \varepsilon_{ci})^2} \int_0^{\varepsilon_{ti}} \sigma_t \varepsilon_t d\varepsilon_t \tag{6A-25}$$

In this thesis, M_i is evaluated numerically. By repeating these calculations for a series of values of strain ε_{ti} at different stage *i* (*i* = 1 to *n*), the relationship between moment M_i and strain ε_{ti} (or curvature κ_i) can be obtained as a table of numerical values as shown in Figure 6A.2.

4. From (6A-25) the secant flexural rigidity $(EI)_i$ at stage *i* for the softening material can be calculated. The calculation is shown as follows

$$M_i = \frac{bh^2 E_c}{(\varepsilon_{ti} + \varepsilon_{ci})^2} \int_0^{\varepsilon_{ci}} \varepsilon_c^2 d\varepsilon_c + \frac{bh^2 E_c}{(\varepsilon_{ti} + \varepsilon_{ci})^2} \left\{ \int_0^{\varepsilon_{tp}} \varepsilon_t^2 d\varepsilon_t + \int_{\varepsilon_{tp}}^{\varepsilon_{ti}} \varepsilon_{tp} \varepsilon_t \left[1 - \frac{\varepsilon_t - \varepsilon_{tp}}{\varepsilon_0 - \varepsilon_{tp}} \right] d\varepsilon_t \right\}$$

$$= \frac{\varepsilon_{ti} + \varepsilon_{ci}}{h} \cdot \frac{bh^3 E_c}{(\varepsilon_{ti} + \varepsilon_{ci})^3} \left\{ \int_0^{\varepsilon_{ci}} \varepsilon_c^2 d\varepsilon_c + \int_0^{\varepsilon_{tp}} \varepsilon_t^2 d\varepsilon_t + \int_{\varepsilon_{tp}}^{\varepsilon_{ti}} \varepsilon_{tp} \varepsilon_t \left[1 - \frac{\varepsilon_t - \varepsilon_{tp}}{\varepsilon_0 - \varepsilon_{tp}} \right] d\varepsilon_t \right\} \tag{6A-26}$$

But $\kappa_i = \dfrac{\varepsilon_{ti} + \varepsilon_{ci}}{h}$ (6A-27), therefore

$$M_i = \kappa_i \cdot \frac{bh^3 E_c}{(\varepsilon_{ti} + \varepsilon_{ci})^3} \left\{ \int_0^{\varepsilon_{ci}} \varepsilon_c^2 d\varepsilon_c + \int_0^{\varepsilon_{tp}} \varepsilon_t^2 d\varepsilon_t + \int_{\varepsilon_{tp}}^{\varepsilon_{ti}} \varepsilon_{tp}\varepsilon_t \left[1 - \frac{\varepsilon_t - \varepsilon_{tp}}{\varepsilon_0 - \varepsilon_{tp}} \right] d\varepsilon_t \right\}$$

or

$$\frac{M_i}{\kappa_i} = \frac{bh^3 E_c}{(\varepsilon_{ti} + \varepsilon_{ci})^3} \left\{ \int_0^{\varepsilon_{tp}} \varepsilon_t^2 d\varepsilon_t + \int_{\varepsilon_{tp}}^{\varepsilon_{ti}} \varepsilon_{tp}\varepsilon_t \left[1 - \frac{\varepsilon_t - \varepsilon_{tp}}{\varepsilon_0 - \varepsilon_{tp}} \right] d\varepsilon_t \right\} \quad \text{(6A-28)}$$

We can express the secant rigidity of softening material $(EI)_i$ in a similar manner to the linear elastic rigidity $E_c I$

$$(EI)_i = \frac{bh^3 E_c}{(\varepsilon_{ti} + \varepsilon_{ci})^3} \left\{ \int_0^{\varepsilon_{ci}} \varepsilon_c^2 d\varepsilon_c + \int_0^{\varepsilon_{tp}} \varepsilon_t^2 d\varepsilon_t + \int_{\varepsilon_{tp}}^{\varepsilon_{ti}} \varepsilon_{tp}\varepsilon_t \left[1 - \frac{\varepsilon_t - \varepsilon_{tp}}{\varepsilon_0 - \varepsilon_{tp}} \right] d\varepsilon_t \right\} \quad \text{(6A-29)}$$

This secant rigidity can also be seen in Figure 6A.2. If we assume that at each stage *i*, the secant rigidity obtained from (6A-29) is constant for the whole beam, then the deflection of the beam at this stage can be can calculated using the traditional beam theory (see Sub-section special case within Section 6A.3).

6A.3 Calculation of the deflection of beam for post-peak behaviour using moment-area method and the graph of curvatures

In this section, the calculation of the deflection of the beam is presented. Although, the deflections, moments and curvatures at any cross-section of the beam can be obtained, herein presents only the calculations at the two most important positions: the edge cross-section, section 1, ($\kappa_{1,i}$, $M_{1,i}$) between the crack and linear elastic unloading zones and the mid-span cross-section, section 2, ($\kappa_{2,i}$, $M_{2,i}$). In which, the moment and curvature at the mid-span cross-section ($\kappa_{2,i}$, $M_{2,i}$) are calculated accordingly to equations (6A-25) and (6A-27), respectively.

In order to determine moments and curvatures for cross-sections 1 and 2 at a stage *i*, we follow the bending behaviour into 3 phases as mentioned above.

Phase I

In Figure 6A.3(a), $M_{1,i}$ is the moment at the cross-section 1 (at virtual edge of the softening zone); and $M_{2,i}$ is the moment at the mid-span cross-section. We have

$$\frac{M_{1,i}}{M_{2,i}} = \frac{L/2 - w_c/2}{L/2} = \frac{L - w_c}{L} \tag{6A-30}$$

or

$$M_{1,i} = \frac{L - w_c}{L} \cdot M_{2,i} \tag{6A-31}$$

As $\frac{M_{1,i}}{E_c I} = \kappa_{1,i}$ (6A-32), and $\frac{M_{2,i}}{E_c I} = \kappa_{2,i}$ (6A-33) so

$$\kappa_{1,i} = \frac{L - w_c}{L} \cdot \kappa_{2,i} \tag{6A-34}$$

where

$\kappa_{1,i}$ = the curvature at the cross-section 1

$\kappa_{2,i}$ = the curvature at the mid-span cross-section.

$E_c I$ = the linear elastic flexural rigidity.

$M_{2,i}$ and $\kappa_{2,i}$ = the linear bending moment and curvature at the cross-section 2.

These moment-curvature relations are computed incrementally from equilibrium equations for the extreme surface fibres following the ascending part of the linear stress-strain curve.

Phase II and III

In Figure 6A.3(b), $M_{2,i}$ is the bending moment at the cross-section 2, and is calculated from equation (6A-25) as described in Section 6A.2. Due to the continuing strain-softening, the moment $M_{2,i}$ and curvature $\kappa_{2,i}$ at the mid-span cross-section (Section 2) follows the curve as shown in Figure 6A.3(b). From the diagram, the moment $M_{1,i}$ at the cross-section 1 can be calculated as

$$M_{1,i} = \frac{L - w_c}{L} M_{2,i} \tag{6A-35}$$

It is assumed that the material is softening in the crack band width w_c only. Outside this zone, the material is linear elastic (see Section 4.3.1). Therefore, the curvature at the cross-section 1 can be calculated as follows

$$\kappa_{1,i} = \frac{M_{1,i}}{E_c I} = \frac{L - w_c}{L} \cdot \frac{M_{2,i}}{E_c I} \tag{6A-36}$$

The curvature at the mid-span cross-section $\kappa_{2,i}$ is calculated from the strain increments as follows

$$\kappa_{2,i} = \frac{\varepsilon_{ti} + \varepsilon_{ci}}{h} \tag{6A-37}$$

where ε_{ti} and ε_{ci} are the strain increments at extreme tensile and compressive fibres, respectively; and *h* is the beam depth.

The curvatures of any cross-section in the softening zone are calculated by assuming linear interpolation between the curvatures at cross-sections 1 and 2. The diagram of curvatures in Phase II and III is shown in Figure 6A.4 when the further loading is applied.

Determine the angle of slope θ_i and deflection y_i at a cross-section

Determine the angle of slope

We have

$$\frac{d^2y}{dx^2} = \kappa \tag{6A-38}$$

Integrating (6A-38) with respect to points x_1 and x_2 gives

$$\int_{x_1}^{x_2} \frac{d^2y}{dx^2} = \int_{x_1}^{x_2} \kappa dx \tag{6A-39}$$

which can be reduced to

$$\left[\frac{dy}{dx}\right]_{x_1}^{x_2} = \int_{x_1}^{x_2} \kappa dx \tag{6A-40}$$

This is

$$\left.\frac{dy}{dx}\right|_{x_2} - \left.\frac{dy}{dx}\right|_{x_1} = \theta_2 - \theta_1 = \int_{x_1}^{x_2} \kappa dx \tag{6A-41}$$

The integral in the right side of (6A-41) is represented by the area in the diagram of curvature as shown in Figure 6A.5 (or diagram of M / EI) between x_1 and x_2.

Appling the above formulae to calculate the deflections of the beam

From Figure 6A.5

$$\theta_{2,i} - \theta_{1,i} = Area2 = \frac{1}{2}(\kappa_{1,i} + \kappa_{2,i})\frac{w_c}{2} \tag{6A-42}$$

Boundary condition for simply supported beam under a mid-span load: at mid-span cross-section $\theta_{2,i} = 0$, so

$$\theta_{1,i} = -\frac{1}{4}(\kappa_{1,i} + \kappa_{2,i})w_c \tag{6A-43}$$

Determine the deflection

Deflection at cross-Section 1

We have

$$\frac{d^2y}{dx^2} = \kappa$$

Multiply both sides by x and integrate between x_0 and x_1

$$\int_{x_0}^{x_1} \frac{d^2y}{dx^2} x dx = \int_{x_0}^{x_1} \kappa x dx \tag{6A-44}$$

It can be given in the following form

$$\int_{x_0}^{x_1} x d\left(\frac{dy}{dx}\right) = \int_{x_0}^{x_1} \kappa x dx \tag{6A-45}$$

Integrating the left side by parts

$$\int_{x_0}^{x_1} x d\left(\frac{dy}{dx}\right) = \left[x\frac{dy}{dx}\right]_{x_0}^{x_1} - \int_{x_0}^{x_1} \frac{dy}{dx} dx = \left[\frac{dy}{dx}x - y\right]_{x_0}^{x_1} = \left[\left.\frac{dy}{dx}\right|_{x_1} x_1 - \left.\frac{dy}{dx}\right|_{x_0} x_0\right] - \left[y_1 - y_0\right] \tag{6A-46}$$

As a result, we have

$$\left[\theta_1 x_1 - \theta_0 x_0\right] - \left[y_1 - y_0\right] = \int_{x_0}^{x_1} \kappa x dx \tag{6A-47}$$

The integral in the right side is the first moment of the area in the diagram of curvature as shown in Figure 6A.5.

Therefore, equation (6A-47) can be written as

$$\left[\theta_{1,i} x_1 - \theta_{0,i} x_0\right] - \left[y_{1,i} - y_{0,i}\right] = Area1 \times x_{C1} \tag{6A-48}$$

In which x_{C1} is the coordinate of the centroid of *Area1*. Boundary condition for simply supported beam under a mid-span load: at the support $y_{0,i} = 0$ and $x_{0,i} = 0$, so

$$\left[\theta_{1,i} x_1 - \theta_{0,i}.0\right] - \left[y_{1,i} - 0\right] = Area1 \times x_{C1}$$

Or

$$y_{1,i} = \theta_{1,i} x_1 - Area1 \times x_{C1} \tag{6A-49}$$

where

$\theta_{1,i}$ is given from (6A-43)

$$x_1 = \frac{L}{2} - \frac{w_c}{2}$$

$Area1$ = the area in the diagram of curvature between x_0 and x_1

$$Area1 = \frac{1}{2} x_1 \kappa_{1,i} = \frac{1}{2}\left(\frac{L}{2} - \frac{w_c}{2}\right)\kappa_{1,i} = \frac{1}{4}(L - w_c)\kappa_{1,i} \tag{6A-50}$$

x_{C1} = the distance from the left support to the centroid of $Area1$

$$x_{C1} = \frac{2}{3} x_1 = \frac{2}{3}\left(\frac{L}{2} - \frac{w_c}{2}\right) = \frac{1}{3}(L - w_c) \tag{6A-51}$$

Substitute θ_1, x_1, $Area1$, and x_{C1} into (6A-49) we obtain the deflection at cross-section 1

$$y_{1,i} = -\frac{1}{8}(\kappa_{1,i} + \kappa_{2,i})(L - w_c) w_c - \frac{1}{12}(L - w_c)^2 \kappa_{1,i} \tag{6A-52}$$

Deflection at cross-section 2

Deflection at the cross-section 2 is determined in the same manner with the one shown in part a. for deflection at the cross-section 1.

Multiply both sides by x and integrate between x_1 and x_2

$$\int_{x_1}^{x_2} \frac{d^2 y}{dx^2} x dx = \int_{x_1}^{x_2} \kappa x dx \tag{6A-53}$$

As a result, we have

$$\left[\theta_2 x_2 - \theta_1 x_1\right] - \left[y_2 - y_1\right] = \int_{x_1}^{x_2} \kappa x dx \tag{6A-54}$$

The integral in the left side is the first moment of the area in the diagram of curvature as shown in Figure 6A.5. Therefore, equation (6A-54) can be written as

$$\left[\theta_{2,i}x_2 - \theta_{1,i}x_1\right] - \left[y_{2,i} - y_{1,i}\right] = Area \times x_C \tag{6A-55}$$

in which x_C is the distance from the left support to the centroid C of the area between x_1 and x_2

$$x_C = \frac{L}{2} - x_{C0} \tag{6A-56}$$

where x_{C0} is obtained as

$$x_{C0} = \frac{w_c(2\kappa_{1,i} + \kappa_{2,i})}{6(\kappa_{1,i} + \kappa_{2,i})} \tag{6A-57}$$

Thus

$$x_C = \frac{L}{2} - x_{C0} = \frac{L}{2} - \frac{w_c(2\kappa_{1,i} + \kappa_{2,i})}{6(\kappa_{1,i} + \kappa_{2,i})} \tag{6A-58}$$

$$Area = \frac{1}{2}(\kappa_{1,i} + \kappa_{2,i})\frac{w_c}{2} \tag{6A-59}$$

Equation (6A-59) becomes

$$\left[\theta_{2,i}x_2 - \theta_{1,i}x_1\right] - \left[y_{2,i} - y_{1,i}\right] = \frac{w_c}{4}(\kappa_{1,i} + \kappa_{2,i})\left[\frac{L}{2} - \frac{w_c(2\kappa_{1,i} + \kappa_{2,i})}{6(\kappa_{1,i} + \kappa_{2,i})}\right] \tag{6A-60}$$

Boundary condition for simply supported beam under a mid span load: at mid-span cross-section $\theta_{2,i} = 0$, so

$$\left[0.x_2 - \theta_{1,i}x_1\right] - \left[y_{2,i} - y_{1,i}\right] = \frac{w_c}{4}(\kappa_{1,i} + \kappa_{2,i})\left[\frac{L}{2} - \frac{w_c(2\kappa_{1,i} + \kappa_{2,i})}{6(\kappa_{1,i} + \kappa_{2,i})}\right]$$

As the result, we can obtain the deflection at mid-span cross-section

$$y_{2,i} = y_{1,i} - \theta_{1,i}x_1 - \frac{w_c}{4}(\kappa_{1,i} + \kappa_{2,i})\left[\frac{L}{2} - \frac{w_c(2\kappa_{1,i} + \kappa_{2,i})}{6(\kappa_{1,i} + \kappa_{2,i})}\right] \tag{6A-61}$$

Substituting $y_{1,i}$ from (6A-52) and $\theta_{1,i}$ from (6A-43) into (6A-61) we have

$$y_{2,i} = -\frac{1}{8}(\kappa_{1,i} + \kappa_{2,i})(L - w_c)w_c - \frac{1}{12}(L - w_c)^2\kappa_{1,i} - \left(-\frac{1}{4}(\kappa_{1,i} + \kappa_{2,i})w_c\right)\frac{1}{2}(L - w_c)$$
$$-\frac{w_c}{4}(\kappa_{1,i} + \kappa_{2,i})\left[\frac{L}{2} - \frac{w_c(2\kappa_{1,i} + \kappa_{2,i})}{6(\kappa_{1,i} + \kappa_{2,i})}\right]$$

$$y_{2,i} = -\frac{1}{12}(L - w_c)^2\kappa_{1,i} - \frac{w_c}{4}(\kappa_{1,i} + \kappa_{2,i})\left[\frac{L}{2} - \frac{w_c(2\kappa_{1,i} + \kappa_{2,i})}{6(\kappa_{1,i} + \kappa_{2,i})}\right] \quad \text{(6A-62)}$$

We always have $0 \le w_c \le L$

Equation (6A-62) is for calculating the deflection at the mid-section of the beam and generally applied for all phases of I, II, and III.

In Phase I, $w_c = 0$ and the curvature is obtained from (6A-33) or (6A-34). The deflection obtained in (6A-62) becomes similar to that of other traditional methods using beam theory.

In Phase II and III, the curvatures at cross-sections 1 and 2 are obtained from (6A-35) to (6A-37) as shown above.

Special case

If one assumes that $w_c = L$, or the softening material is spread out for the whole beam, the deflection $y_{2,i}$ determined in (6A-62) will be the same with the one determined from the following calculations:

If one assumes that at each value of strain ε_{ti}, the secant rigidity $(EI)_i$ can be applied to all the sections in beam, and that the load-deflection can be determined from the same formula used for linear elastic beam, the deflection at the mid-span cross-section y_{2i} is calculated as

$$y_{2i} = \frac{P_i L^3}{48(EI)_i} \quad \text{(6A-63)}$$

where

$(EI)_i$ = the secant rigidity obtained from equation (6A-29)

P_i = the applied load

$$P_i = \frac{4M_i}{L} \tag{6A-64}$$

Using this special case it should be noted that the secant rigidity $(EI)_i$ is applied for the whole beam. It means that in the post-peak behaviour, the strain-softening material is assumed to be "spread out" for the whole beam. This assumption may be applicable for ductile materials, i.e. steel, or a beam with small span-to-depth ratio. But it is unlikely applicable for concrete material as a localised yielding will clearly occur at the mid-span zone of the beam, not for the whole beam. It means that after reaching the maximum tensile stress, only material in a small zone at mid-span continues into strain-softening behaviour while the rest of beam unloads linear elastically. However, in the validation part for RC beams in Chapter 6, the deflection calculated as suggested in (6A-63) is also presented for comparison.

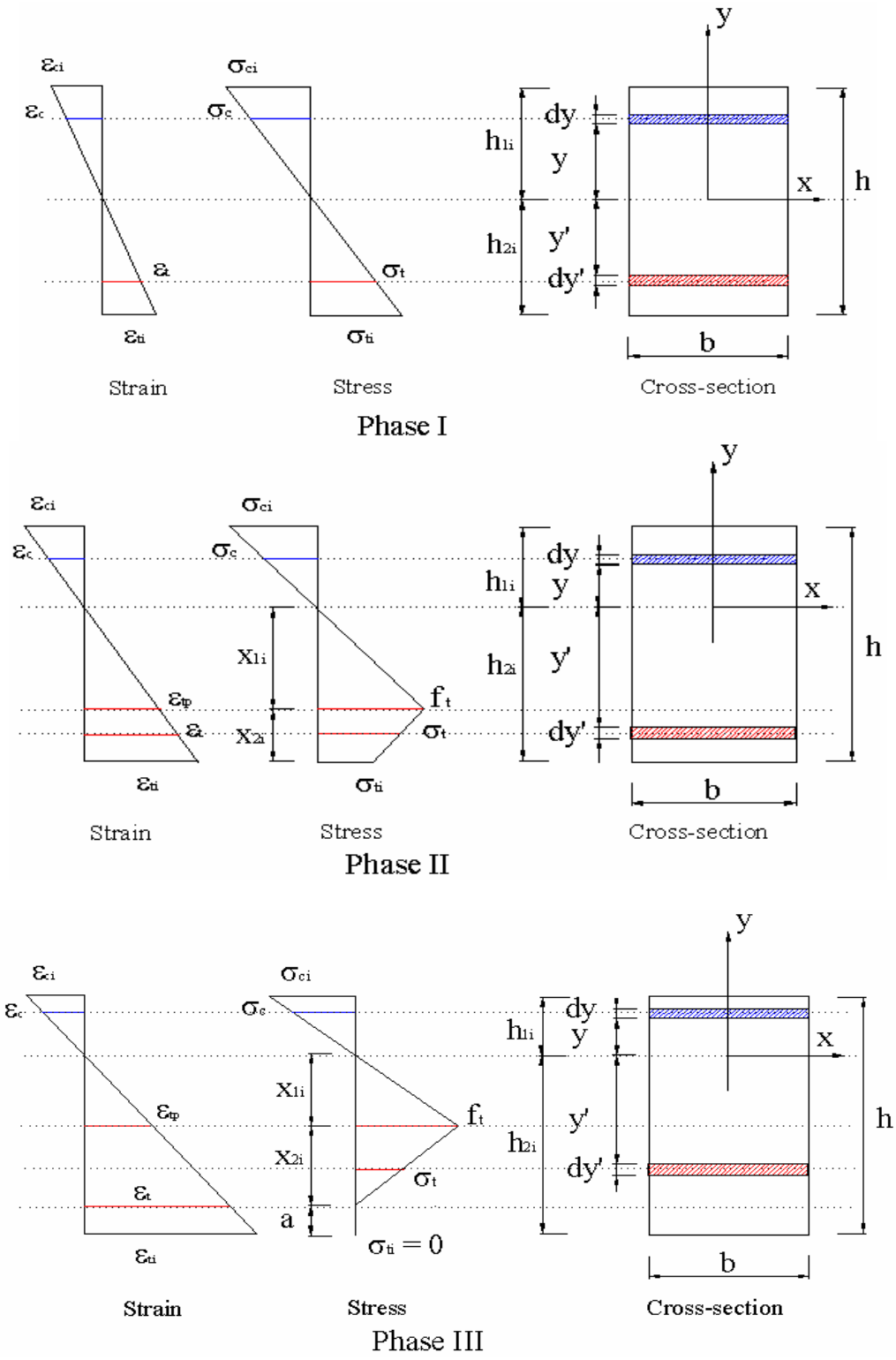

Figure 6A.1 Stress and strain distribution across the beam depth during 3 phases of loading

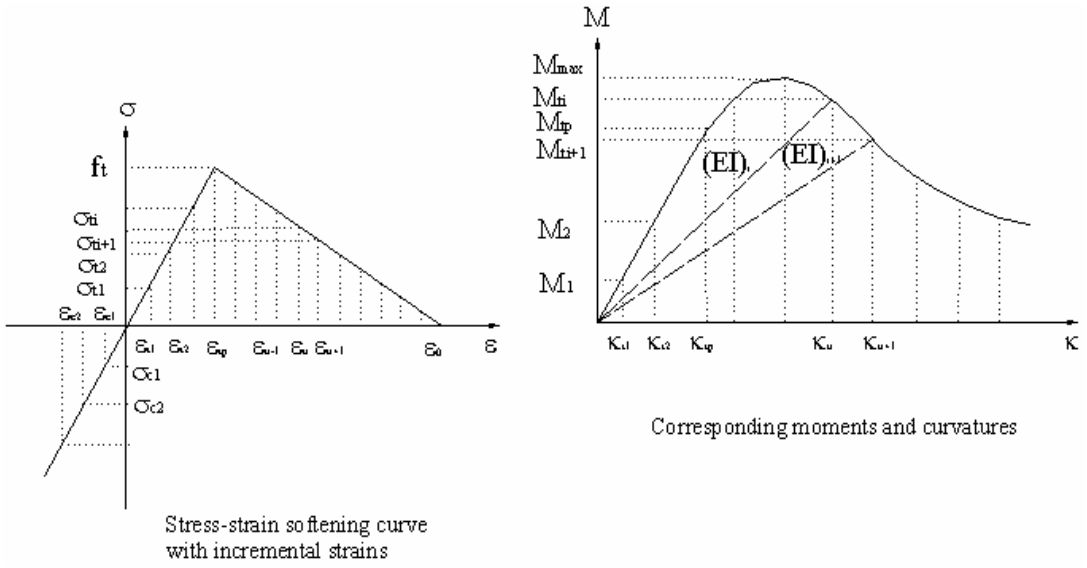

Figure 6A.2 Incremental strains and secant rigidity in the diagram of moment-curvature

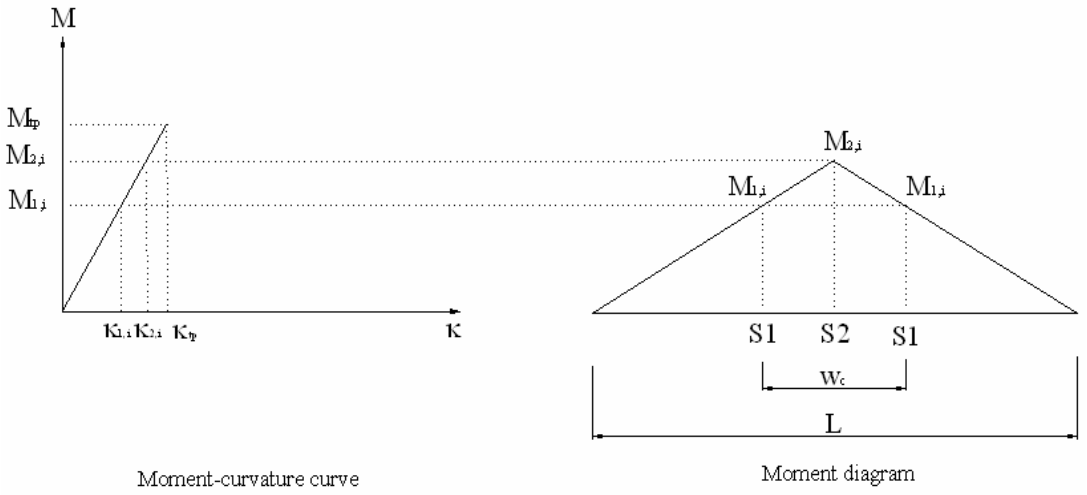

Phase I

(a)

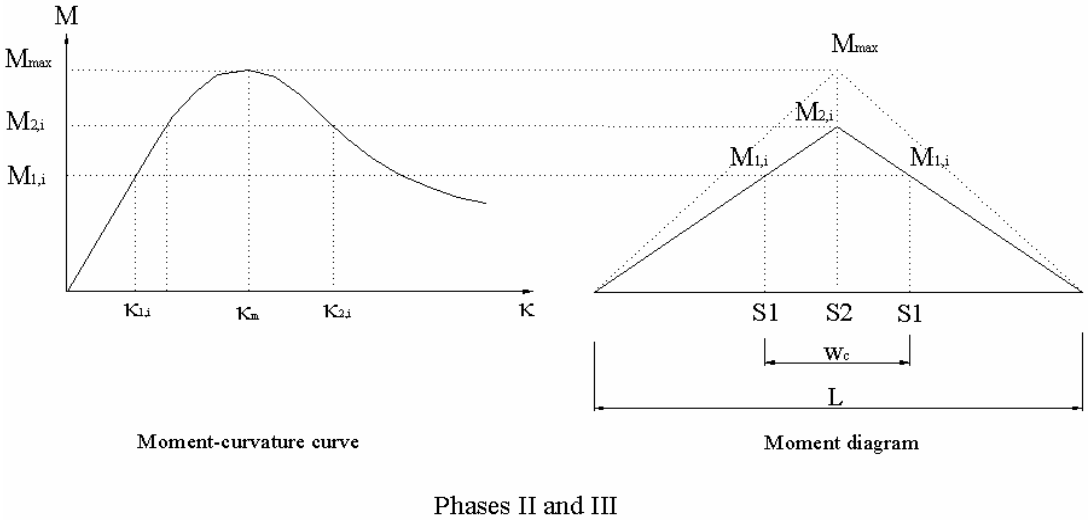

(b)

Figure 6A.3 Determination of moments and curvatures in cross-section 1 and 2 (S1 - Cross-section 1; S2 - Cross-section 2)

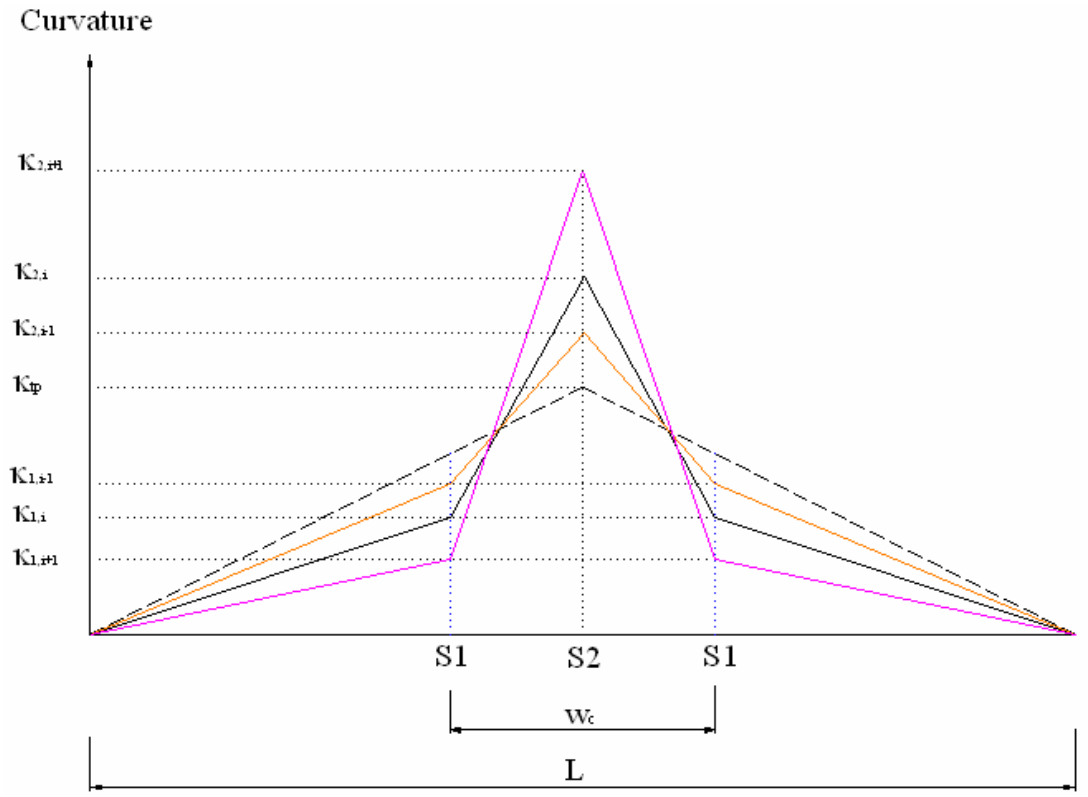

Figure 6A.4 Diagram of curvatures along the beam length in Phases II and III (not in scale)

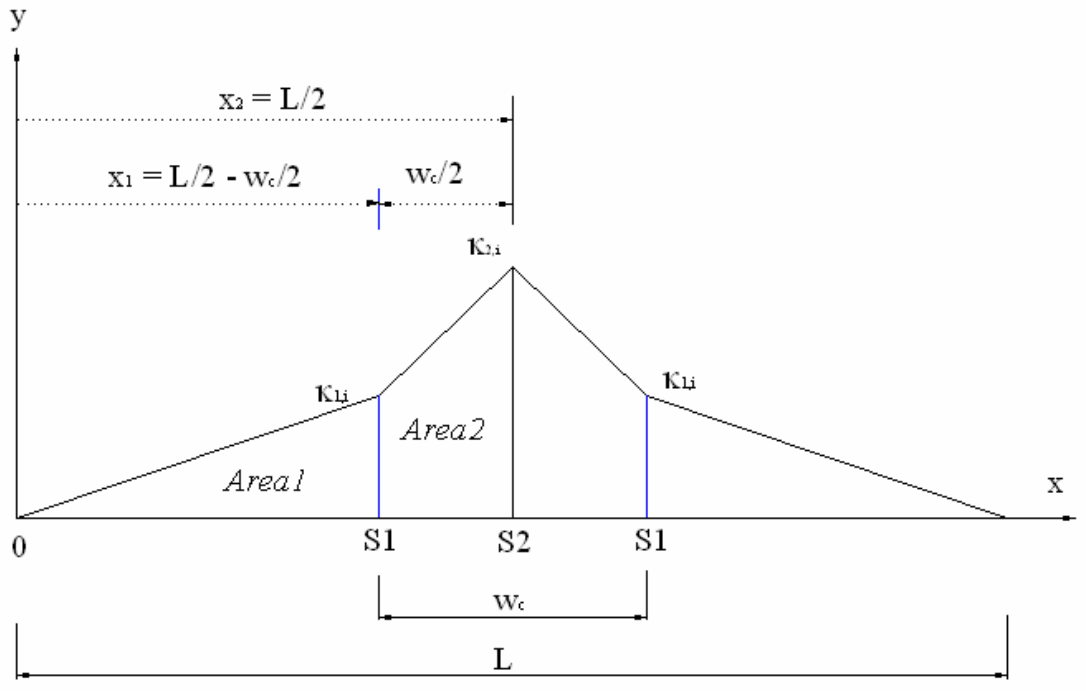

Figure 6A.5 Diagram of curvature for calculating the deflection of the beam (Moment-area method)

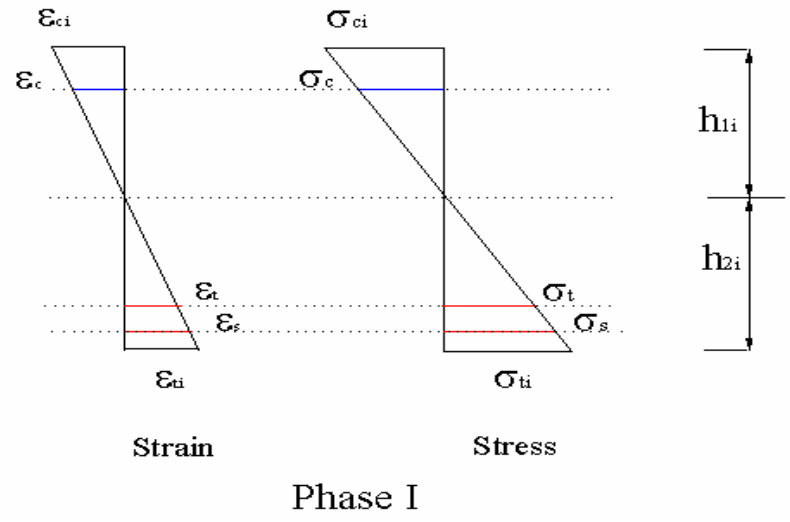

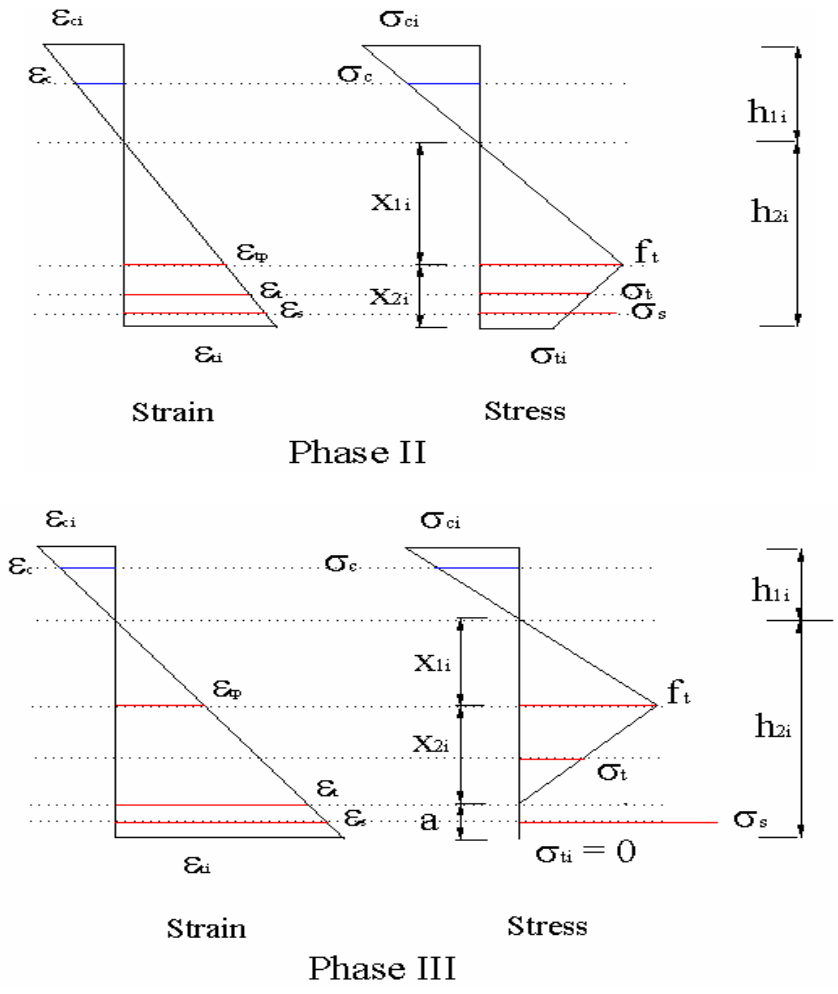

Figure 6A.6 Stress and strain distributions across the beam depth in RC beams

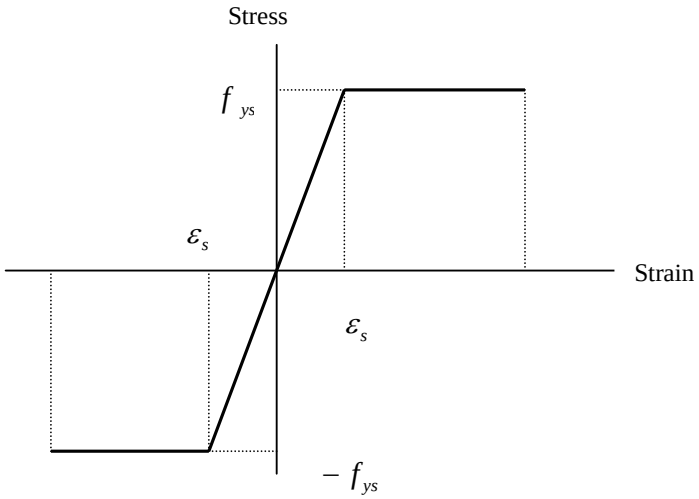

Figure 6A.7 Stress-strain curve for steel reinforcement with linear elastic-perfectly plastic

APPENDIX 7A

Twenty artificially generated earthquake time-histories

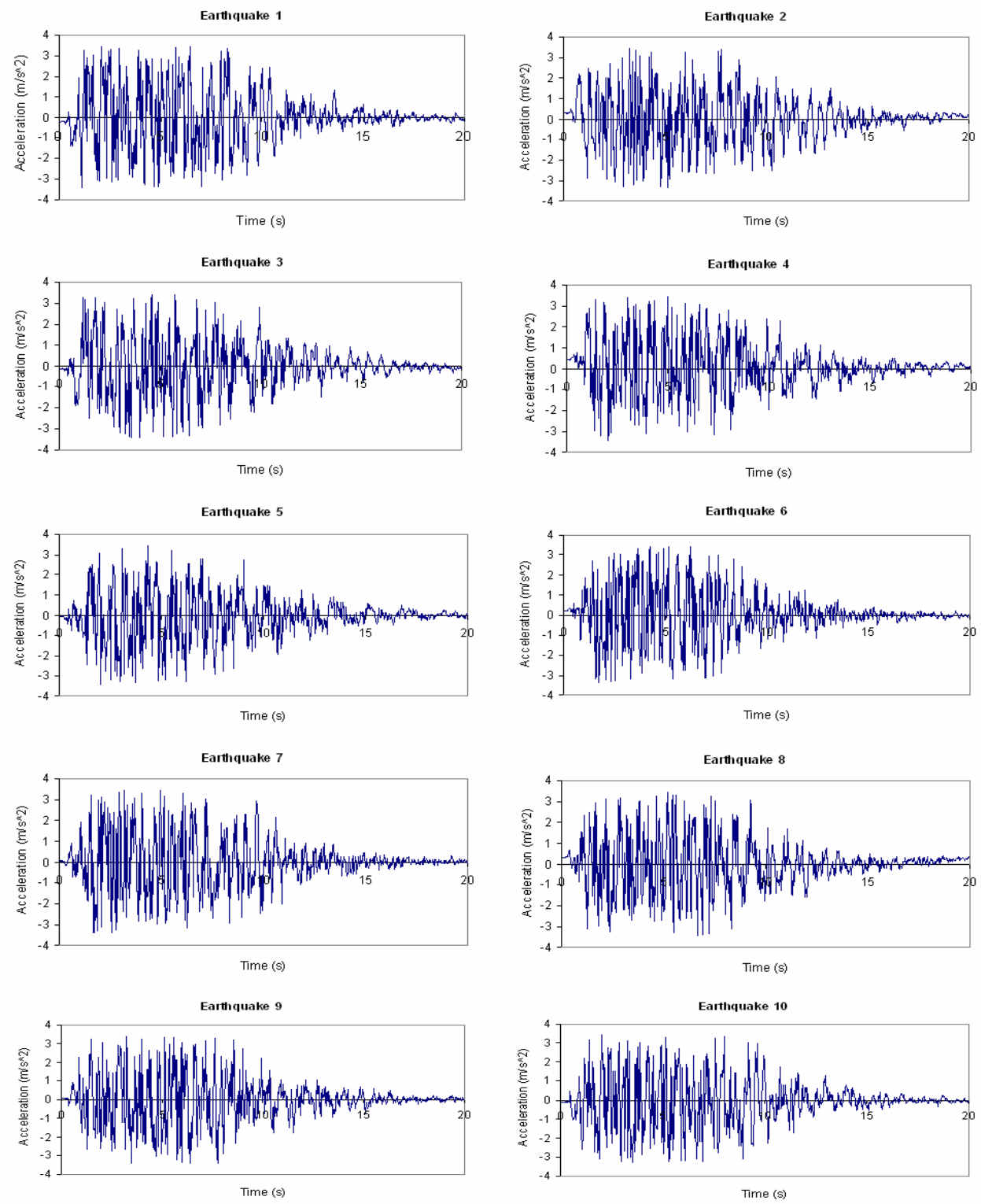

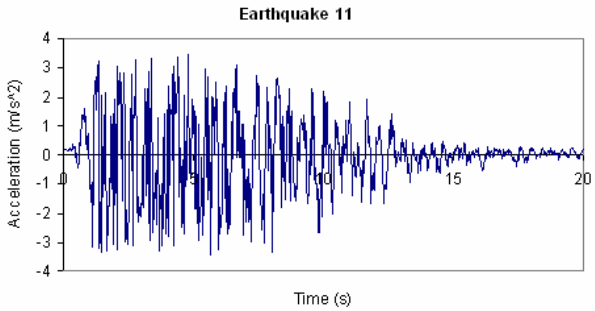
Earthquake 11
Acceleration (m/s^2)
Time (s)

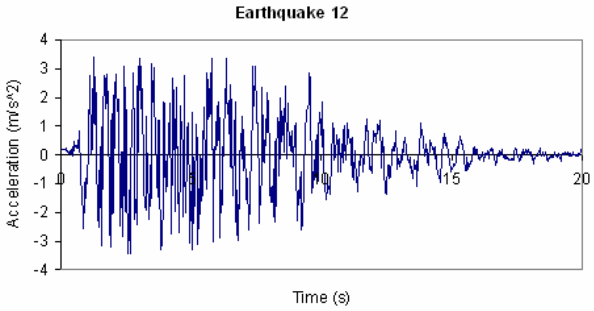
Earthquake 12
Acceleration (m/s^2)
Time (s)

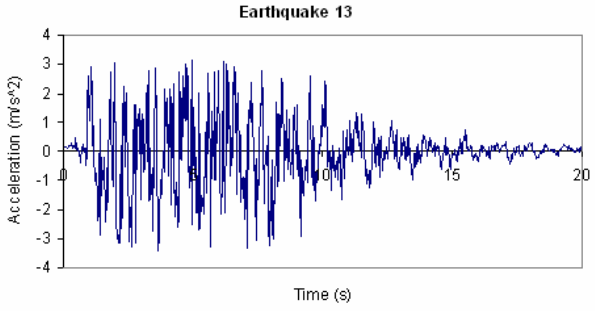
Earthquake 13
Acceleration (m/s^2)
Time (s)

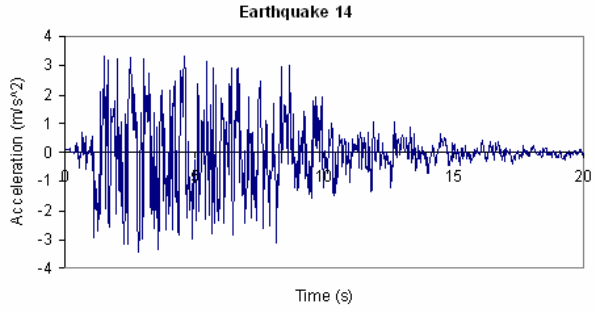
Earthquake 14
Acceleration (m/s^2)
Time (s)

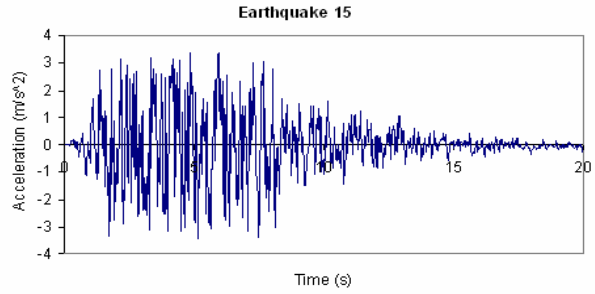
Earthquake 15
Acceleration (m/s^2)
Time (s)

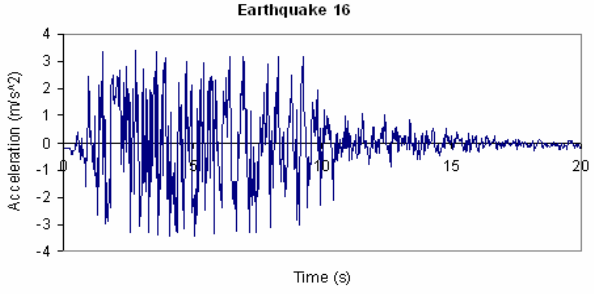
Earthquake 16
Acceleration (m/s^2)
Time (s)

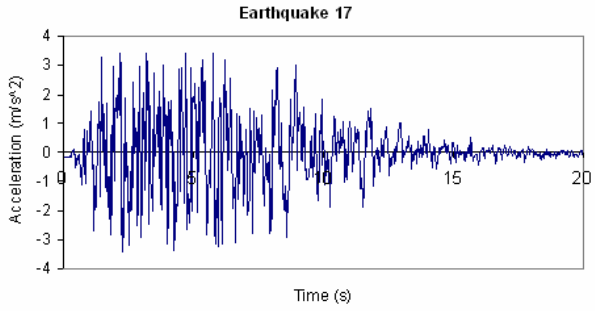
Earthquake 17
Acceleration (m/s^2)
Time (s)

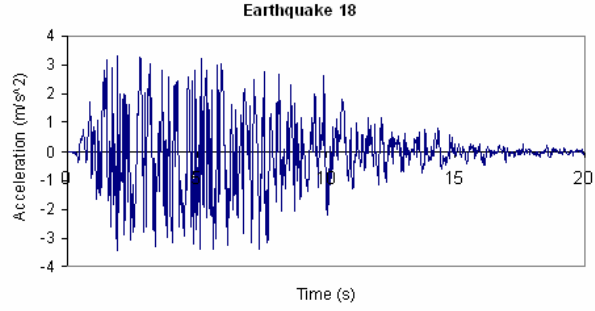
Earthquake 18
Acceleration (m/s^2)
Time (s)

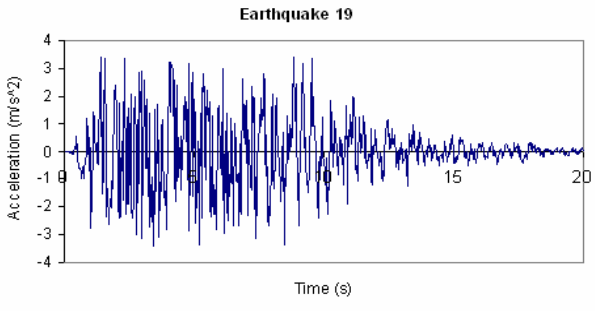
Earthquake 19
Acceleration (m/s^2)
Time (s)

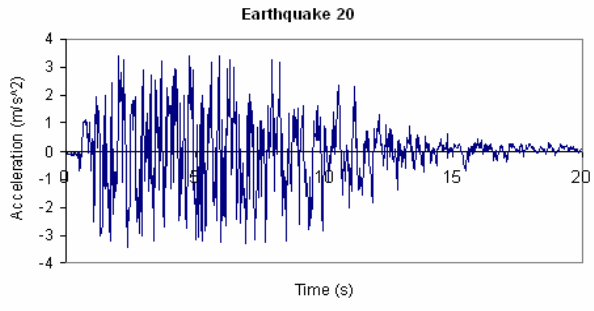
Earthquake 20
Acceleration (m/s^2)
Time (s)

APPENDIX 7B

Relative displacements under twenty artificial time-histories

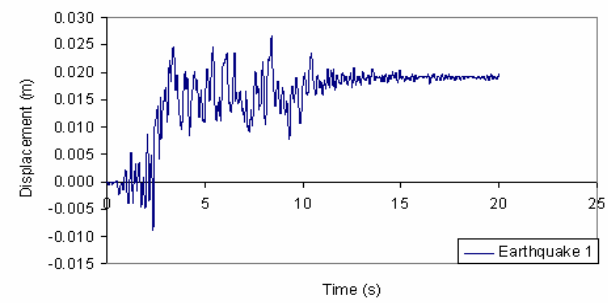

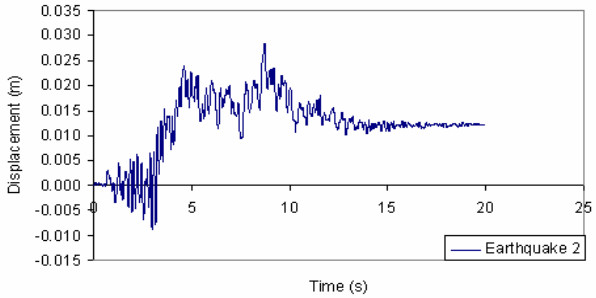

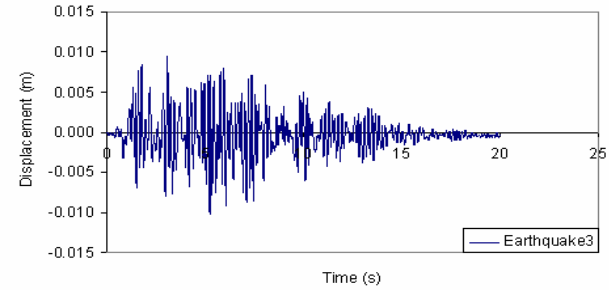

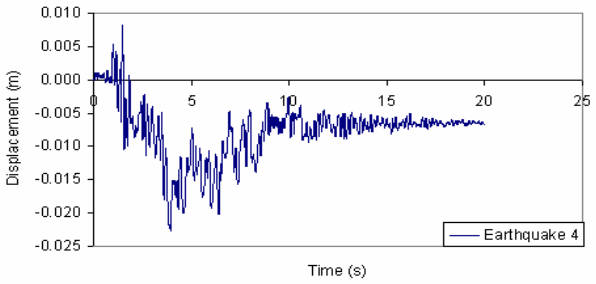

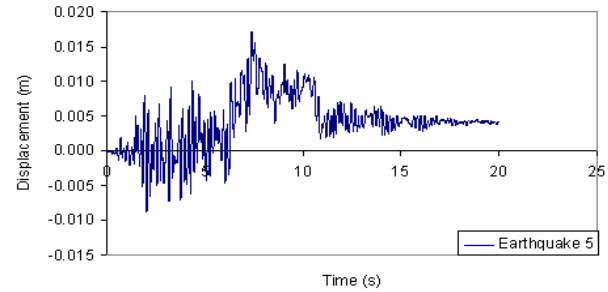

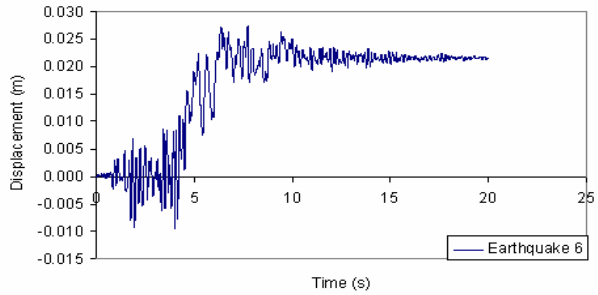

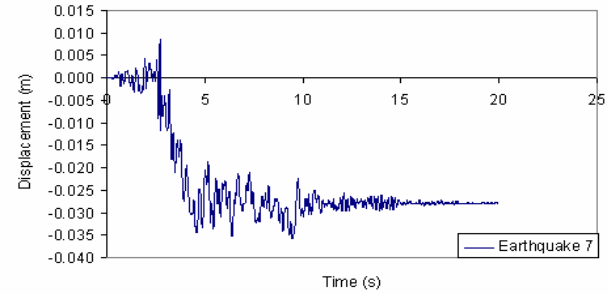

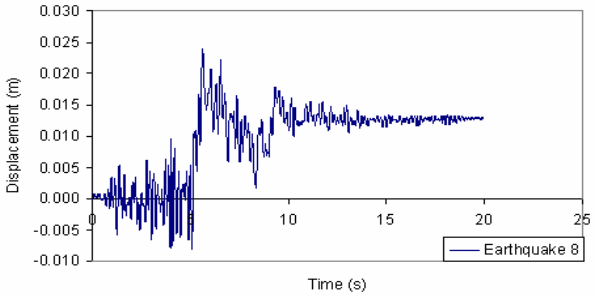

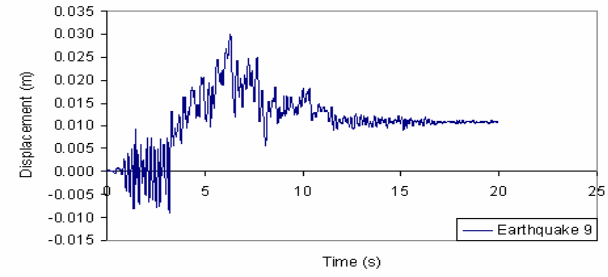

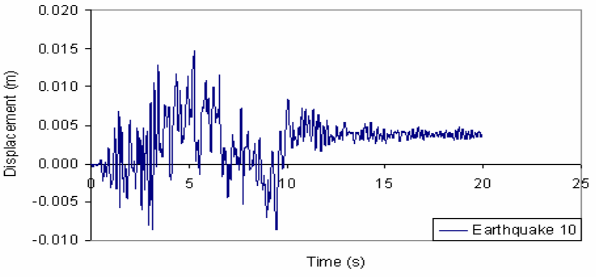

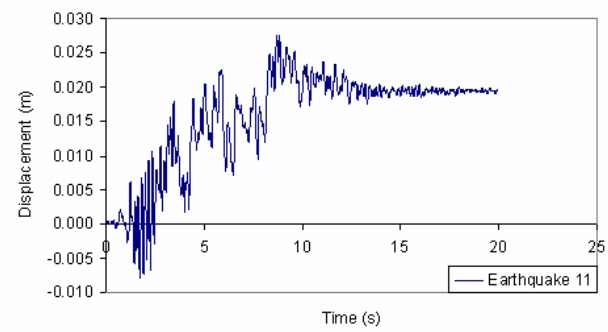
Displacement (m)
Time (s)
Earthquake 11

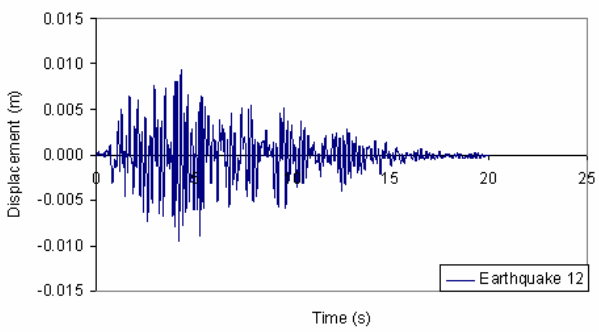
Displacement (m)
Time (s)
Earthquake 12

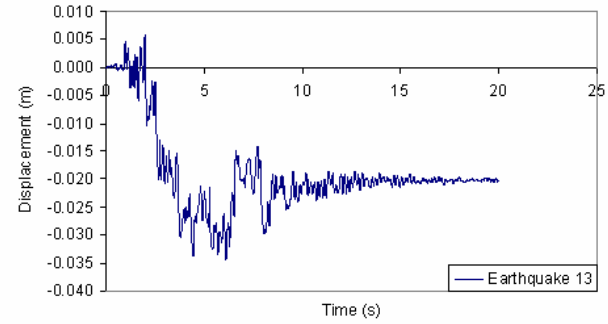
Displacement (m)
Time (s)
Earthquake 13

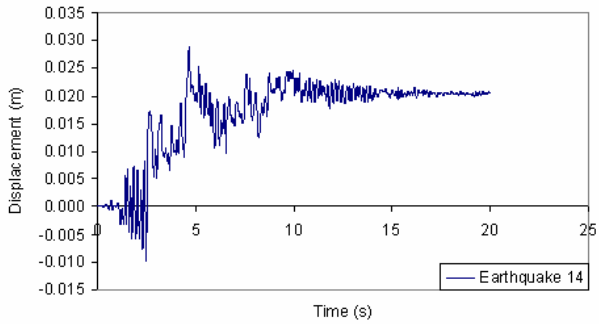
Displacement (m)
Time (s)
Earthquake 14

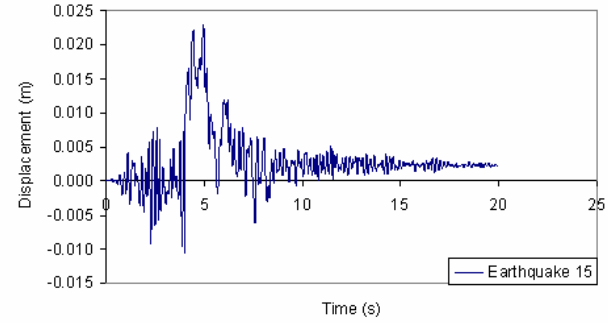
Displacement (m)
Time (s)
Earthquake 15

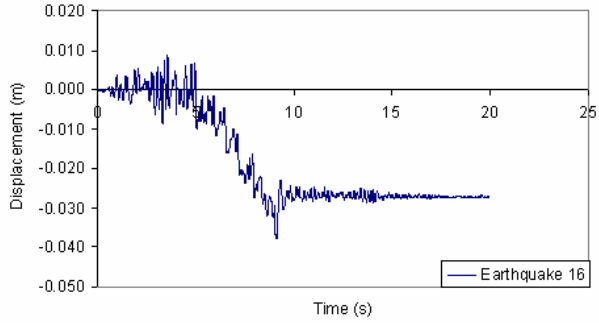
Displacement (m)
Time (s)
Earthquake 16

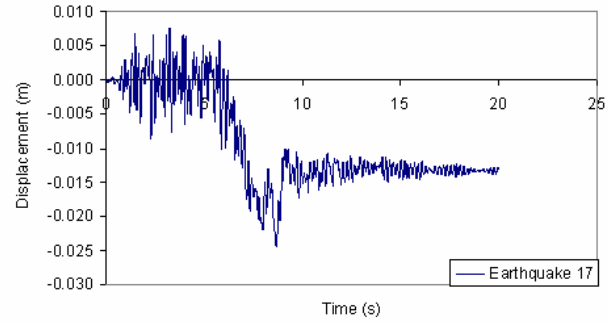
Displacement (m)
Time (s)
Earthquake 17

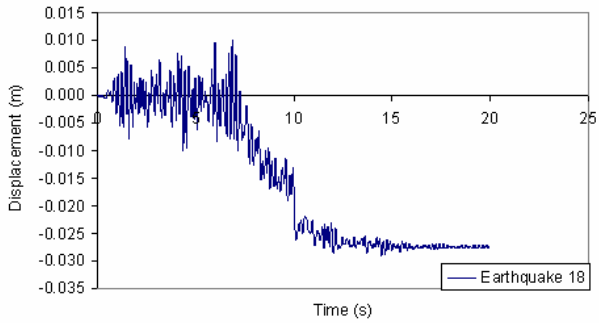
Displacement (m)
Time (s)
Earthquake 18

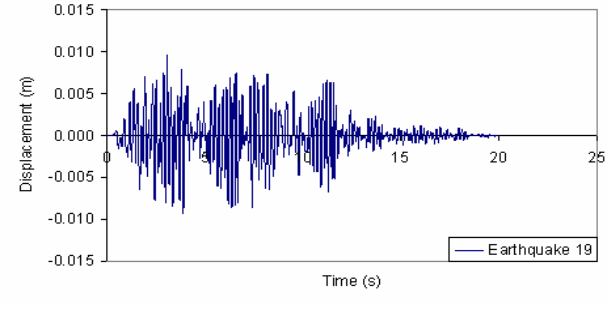
Displacement (m)
Time (s)
Earthquake 19

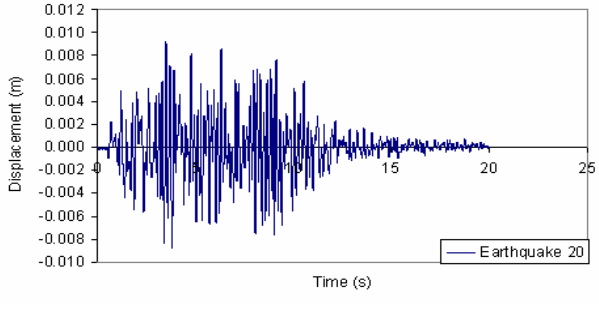
Displacement (m)
Time (s)
Earthquake 20

APPENDIX 7C

Fourier transforms of twenty acceleration responses

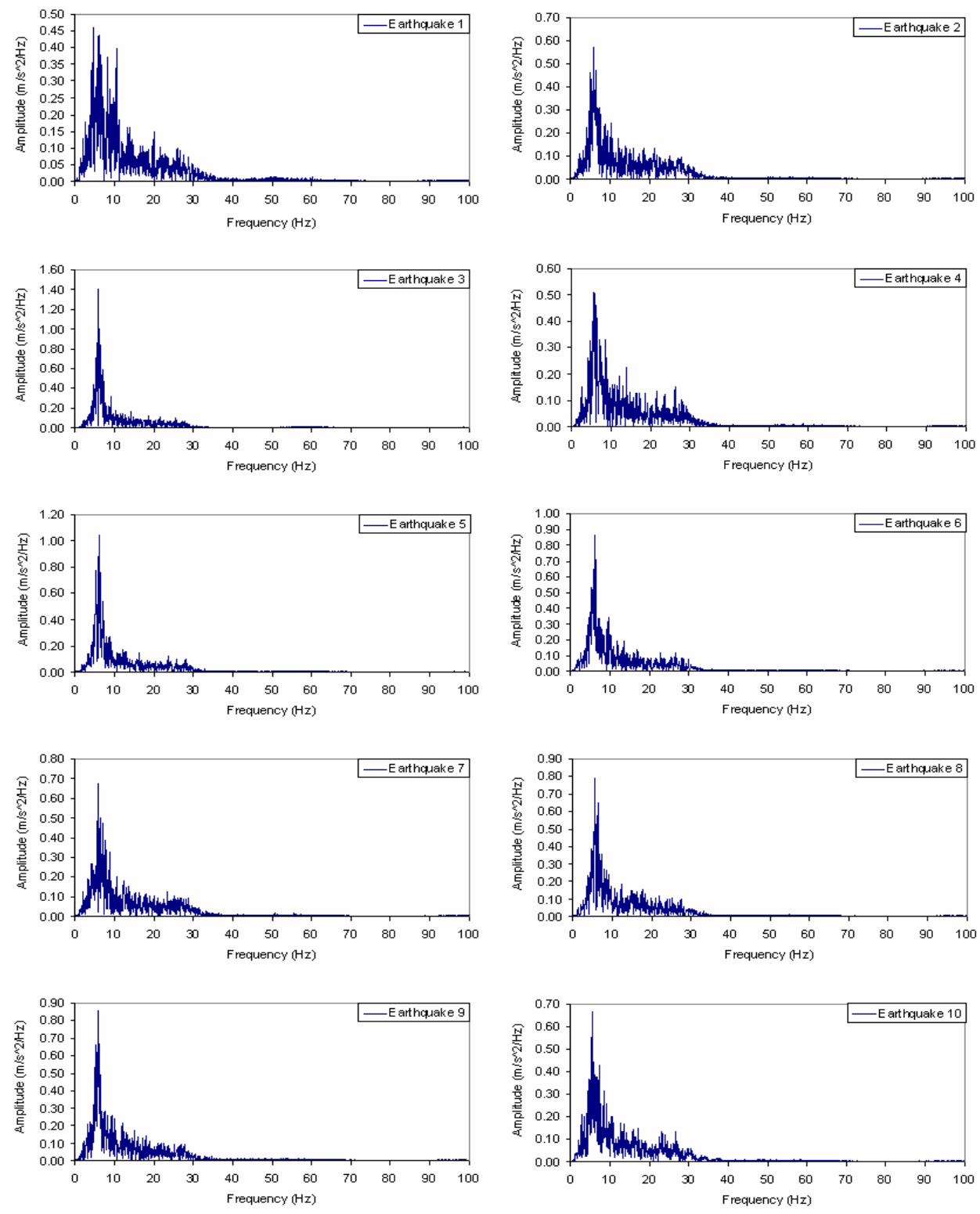

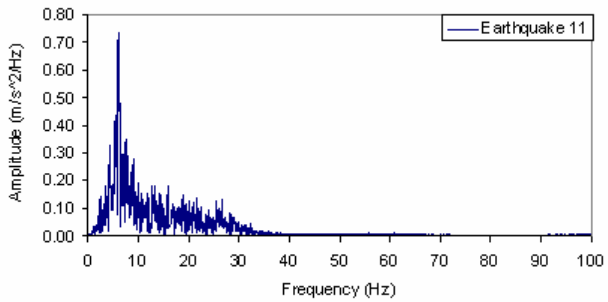
Earthquake 11
Amplitude (m/s^2/Hz)
Frequency (Hz)

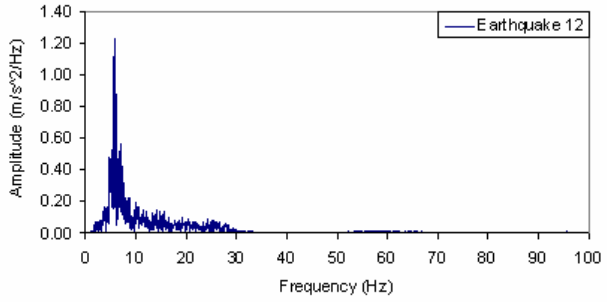
Earthquake 12
Amplitude (m/s^2/Hz)
Frequency (Hz)

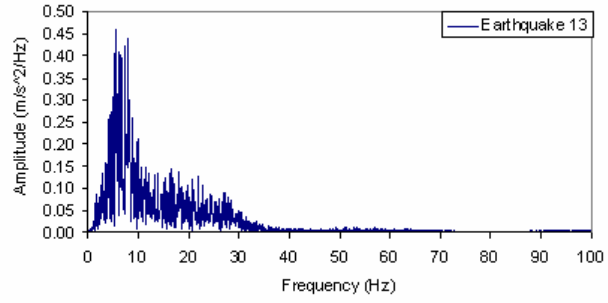
Earthquake 13
Amplitude (m/s^2/Hz)
Frequency (Hz)

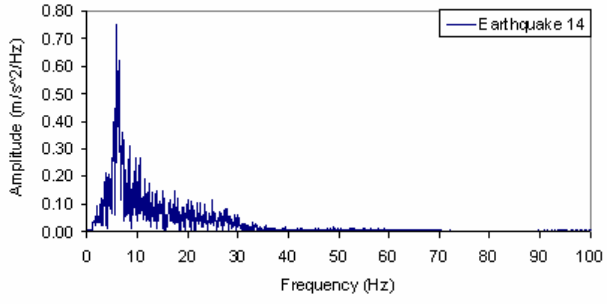
Earthquake 14
Amplitude (m/s^2/Hz)
Frequency (Hz)

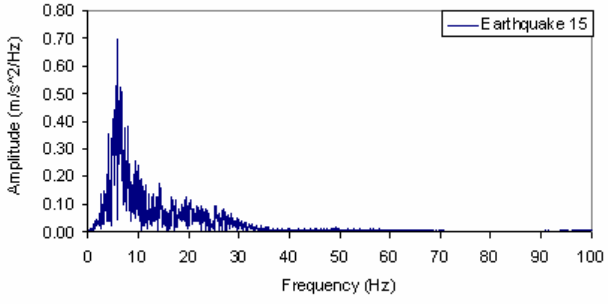
Earthquake 15
Amplitude (m/s^2/Hz)
Frequency (Hz)

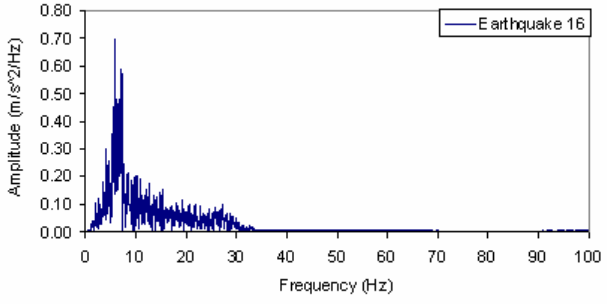
Earthquake 16
Amplitude (m/s^2/Hz)
Frequency (Hz)

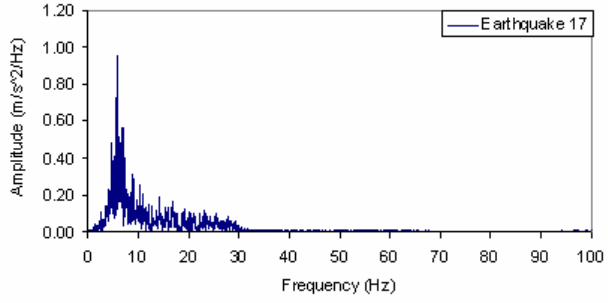
Earthquake 17
Amplitude (m/s^2/Hz)
Frequency (Hz)

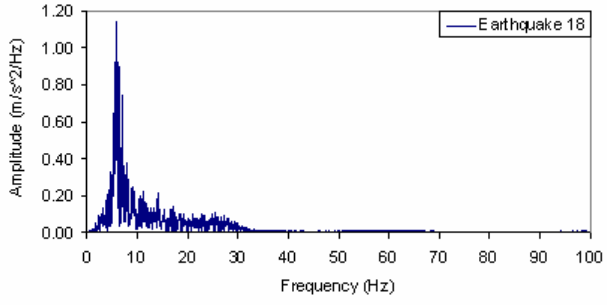
Earthquake 18
Amplitude (m/s^2/Hz)
Frequency (Hz)

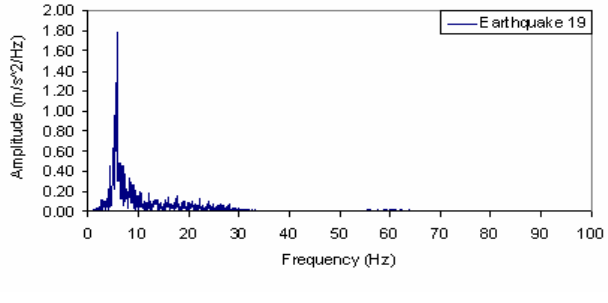
Earthquake 19
Amplitude (m/s^2/Hz)
Frequency (Hz)

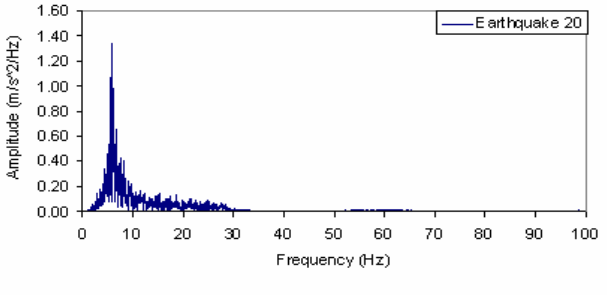
Earthquake 20
Amplitude (m/s^2/Hz)
Frequency (Hz)

APPENDIX 7D

Energy dissipation histories under twenty artificial time-histories

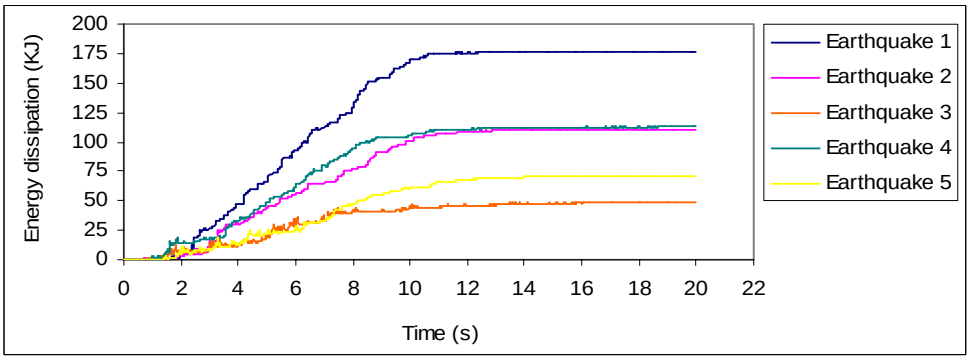

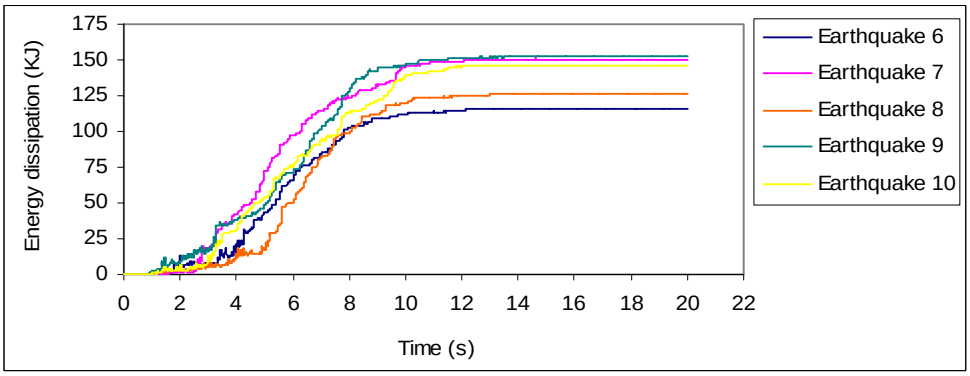

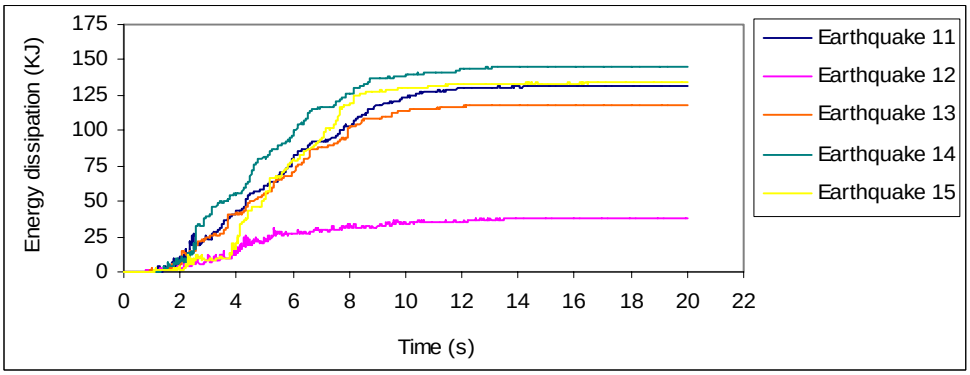

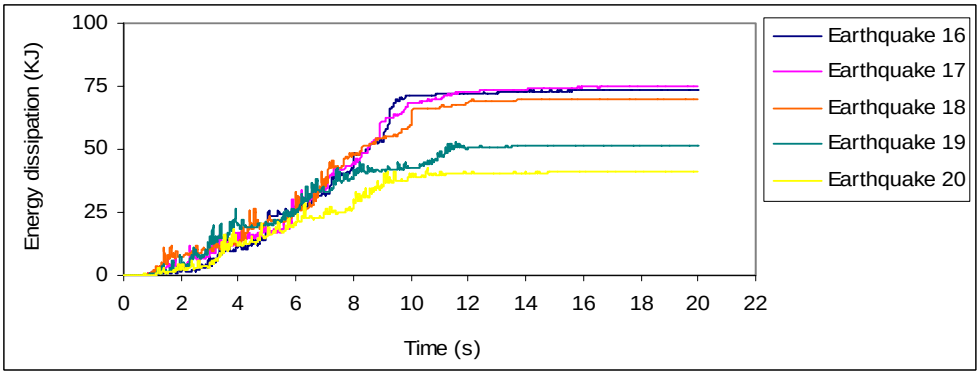

APPENDIX 7E

Damage index histories under twenty artificial time-histories

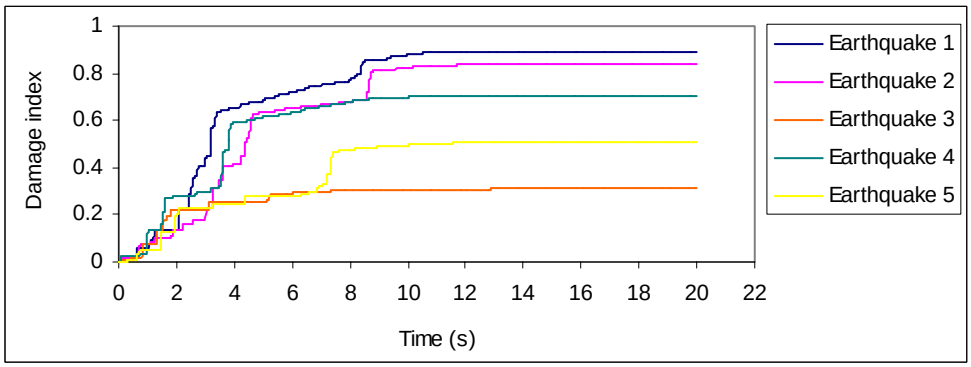

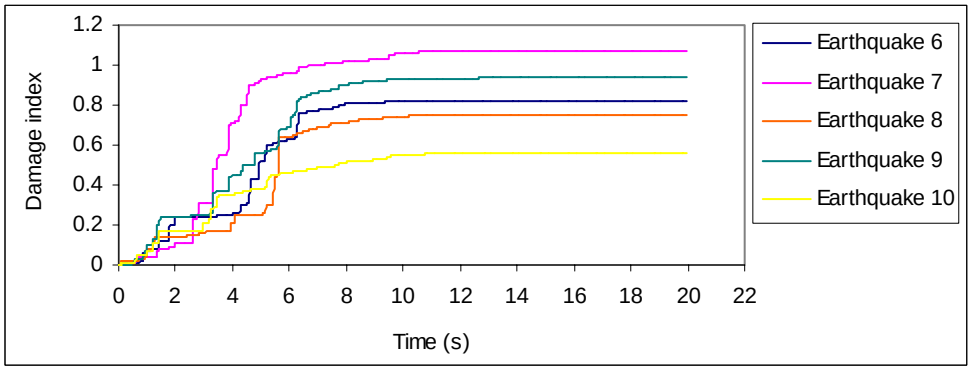

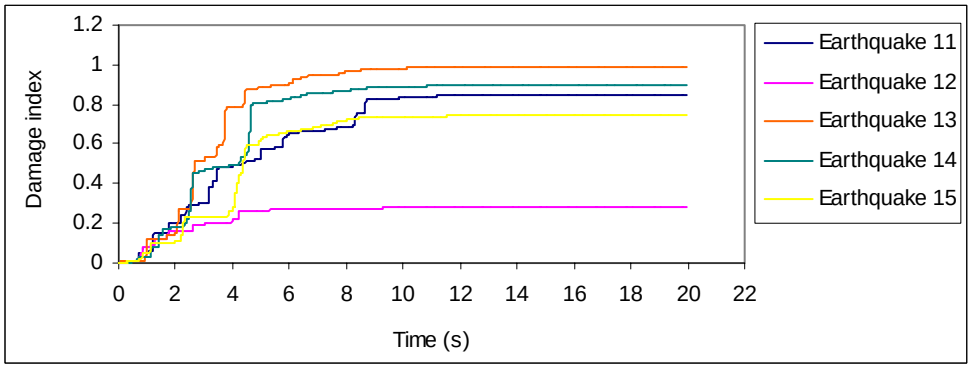

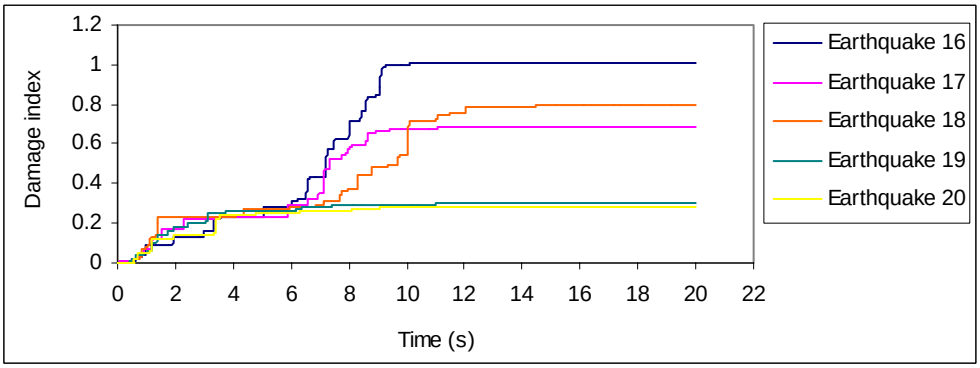

APPENDIX 7F

Definitions of two sample statistics: Mean and Dispersion (Benjamin and Cornell 1970)

Mean

In this chapter we refer the best estimate or "numerical average value" as the mean. Define the random variables x_1, x_2, …, x_n as the first, second, …, nth observations of the sample. Each x_i has the same distribution as the other random variables. The mean estimator is defined as the average value of the observed values, x_i, of the sample. This can be written as:

$$\mu = \frac{\sum_{i=1}^{n} x_i}{n} \tag{7F-1}$$

Where n is the number of observations.

The mean value μ may fluctuate rather violently for n small, but it gradually settles down to a steady value as n becomes large. This value is very helpful to find the steady response for nonlinear seismic analysis with a limited number of trials of artificial earthquakes.

Dispersion

In this study the dispersion measure δ is the standard deviation of the observed data. It is defined as follows:

$$\delta = \left[\frac{\sum_{i=1}^{n} (x_i - \mu)^2}{n-1} \right]^{\frac{1}{2}} \tag{7F-2}$$

The above estimator of dispersion is a measure of how widely values are biased from the mean value. Roughly speaking, the smaller the dispersion of the sample, the more clustered about the sample mean is the data and the less frequent are large variations from the mean value. Because

of the advantage described before of considering the natural data, the above dispersion measure is adopted in this study. The term “dispersion” or “bias” when referring to this parameter will be used loosely in this Chapter.

Standard error of estimation

The standard error of estimation Δ is approximately the sample dispersion expressed as percentage and divided by the square root of n observations as follows:

$$\Delta = \frac{\delta}{\sqrt{n}} \times 100(\%) \qquad \text{(7F-3)}$$

APPENDIX 7G

Normal probability plot and normal distribution

Normal probability plot

The dispersion measure of an observed sample as presented in Appendix 7F can show us a confidence level for the population mean based on the sample. However, the confidence levels we expect have to be based on the normal distribution. Therefore, it is important to identify whether or not the sample exhibits the properties of a normal distribution.

When the sample is very large (certainly more than 30 measurements, maybe a lot more), then the shape of the histogram will approach the shape of the distribution for the population, and it should be possible to identify an appropriate distribution. When a sample is small (e.g. 20 earthquake damage indices used in Chapter 7), it is difficult to judge the distribution of the population from a histogram of the sample because its histogram will not look exactly like any particular ideal distribution. There are a number of different ways to describe the normality of the sample, but we shall limit our attention in this thesis to a quick and effective visual graphing technique, namely "Normal Probability Plot" (Hesse 1998, Devore 2003).

The idea of the "Normal Probability Plot" is to rank the sample data and change the ranks into probabilities that would be converted to z-scores, and then the sample data and the z-scores are plotted to check the normality of the data. If the data is indeed approximately normally distributed, then the converted data points should lie in a straight line.

Normal distribution

A normal distribution for a variable x with a specified mean (μ) and dispersion (δ) is a statistic distribution with probability mass function which can be expressed as follows:

$$f(x,\mu,\delta) = \frac{1}{\sqrt{2\pi}\delta} e^{-\left[\frac{(x-\mu)^2}{2\delta^2}\right]} \qquad \text{(7G-1)}$$

A standard normal distribution is given from the general distribution in Equation (7G-1) by taking $\mu = 0$ and $\delta^2 = 1$ and by converting the variables to $z = \frac{x-\mu}{\delta}$. It can be expressed in terms of the cumulative distribution function:

$$f(z) = \frac{1}{\sqrt{2\pi}} e^{-\frac{z^2}{2}} \qquad \text{(7G-2)}$$

The normal distribution is a convenient model of quantitative phenomena and is the most widely used family of distributions in statistics and engineering applications. In this thesis, it is used to (1) to further check the normality of the sample data (e.g. damage indices of the RC bridge pier under different artificial earthquakes), and (2) represent the probability of the observations, i.e. damage indices, fall within the mean (μ) and "one-sigma confidence band" (σ). Thus the number of earthquake records may be chosen with that confidence band.

APPENDIX 7H

Normal probability plot and normal distribution of damage responses of twenty artificial time-histories

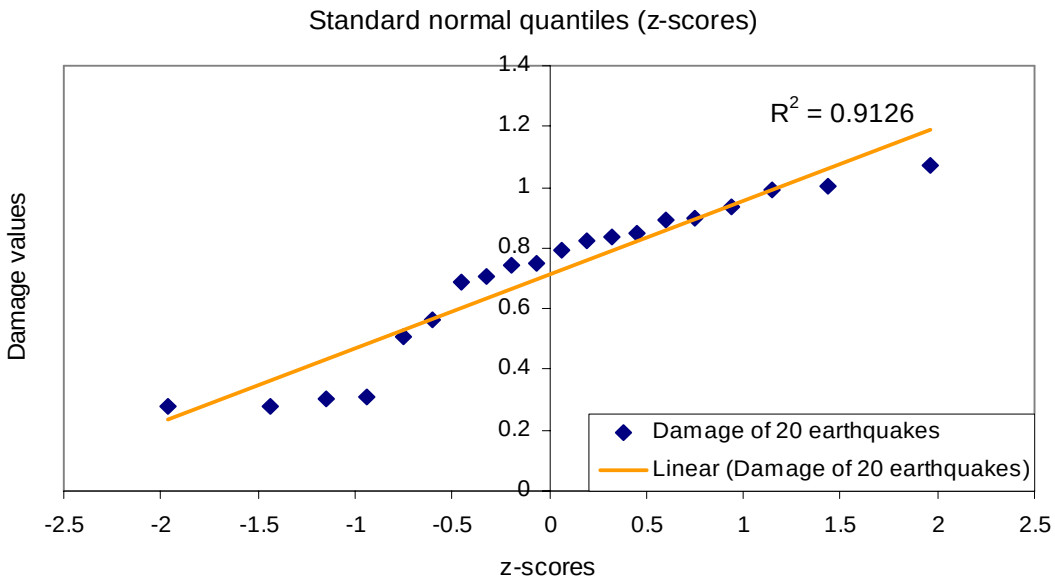

Figure 7H.1 Normal probability plot and its regression line

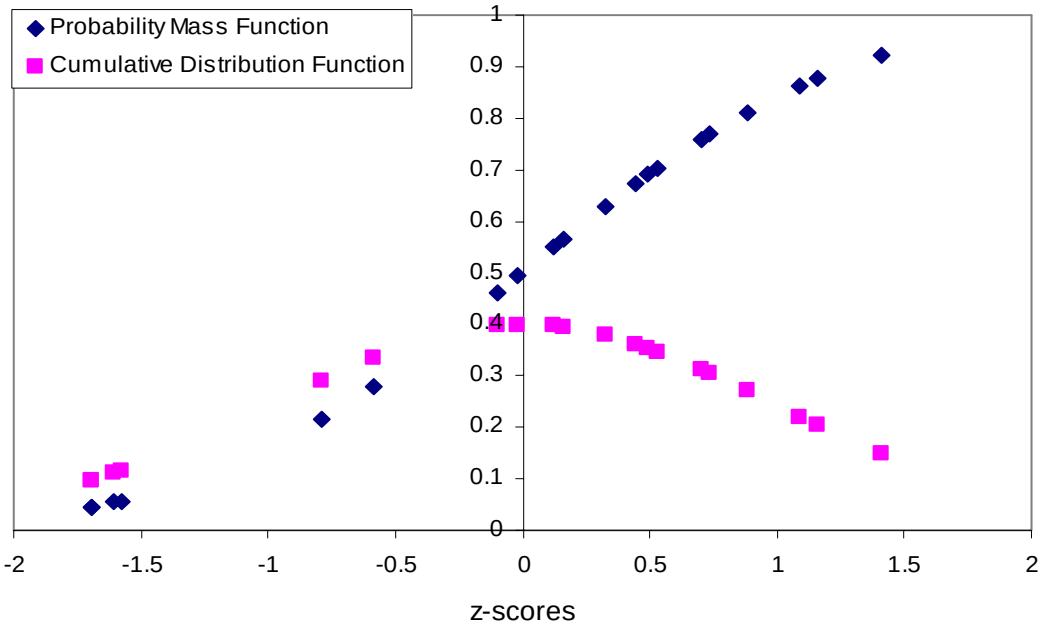

Figure 7H.2 Normal distribution including probability mass function and cumulative distribution function

APPENDIX 7I

FORTRAN 90 code for damage index analysis with any ordering numbers

```
      subroutine damage03(nn,io,nd,va,co,mm,nt,nprt)
      implicit none
      integer nn,io,nd(nn),i,ii,mm,nt(mm),nprt
      double precision va(nn),rm(nn),sd(nn),see(nn),co(mm),rl,ru
      do i=1,nn
         ii=nd(i)
         rm(i)=va(ii)
         sd(i)=va(ii)**2
         if (i.ne.1) then
            rm(i)=rm(i)+rm(i-1)
            sd(i)=sd(i)+sd(i-1)
         end if
      end do
      do i=1,nn
         sd(i)=sd(i)-rm(i)**2/dble(i)
         if (i.ne.1) sd(i)=sqrt(sd(i)/dble(i-1))
         if (nprt.gt.20) write(io,*)'sd:',i,sd(i)
      end do
      do i=1,nn
         see(i)=sd(i)/sqrt(dble(i))
         if (nprt.gt.20) write(io,*)'see:',i,see(i)
      end do
      do i=1,nn
         rm(i)=rm(i)/dble(i)
         if (nprt.gt.20) write(io,*)'mean:',i,rm(i)
      end do
      do ii=1,mm
         rl=rm(nn)-co(ii)*see(nn)
         ru=rm(nn)+co(ii)*see(nn)
         if (nprt.gt.10) write(io,*)'factor:',co(ii)
         if (nprt.gt.10) write(io,*)'range:',rl,ru
         do i=nn,1,-1
            if (rm(i).gt.ru.or.rm(i).lt.rl) exit
         end do
         nt(ii)=i+1
         if (nprt.gt.10) write(io,*)'number:',nt(ii)
      end do
      return
      end
collect c:\work\myprojects\nguyen\damage04\.\damage04.for
```

```
c23456
      program damage04
      implicit none
      integer nn,nseed(1),ntry,mm
      open (unit=15,file='damage04.txt',status='old')
      open (unit=16,file='damage04.out')
      read (15,*)nn,nseed,ntry
c.... make sure nseed is odd
      nseed=nseed+mod(nseed+1,2)
      write(16,*)nn,nseed,ntry
      call random_seed(put=nseed)
      read (15,*)mm
      write(16,*)mm
      call damage05(nn,15,16,ntry,mm)
      close(15)
      close(16)
      stop
      end
collect c:\work\myprojects\nguyen\damage04\.\damage05.for
      subroutine damage05(nn,in,io,ntry,mm)
      implicit none
      integer nn,in,io,nd(nn),mm,nprt,ntry,i,j,ncoun,i1,i2,kk
      parameter (nprt=0,ncoun=1000000)
      integer nt(mm),nres(nn,mm),nnd(nn,nn)
      double precision va(nn),co(mm),suma
      real a,b
      do i=1,mm
         read (in,*)co(i)
         write(io,*)co(i)
      end do
      write(io,*)
      do i=1,nn
         read (in,*)va(i)
         write(io,*)va(i)
      end do
      nres=0
      nnd=0
      do i=1,ntry
         do j=1,nn
            nd(j)=j
         end do
c.... randomise the order
         do j=1,ncoun
            call random_number(a)
            i1=max(0,min(int(nn*a)+1,nn))
            call random_number(b)
```

```
         i2=max(0,min(int(nn*b)+1,nn))
  if (i1.le.0.or.i1.gt.nn.or.i2.le.0.or.i2.gt.nn) print *,i1,i2,a,b
         kk=nd(i1)
         nd(i1)=nd(i2)
         nd(i2)=kk
      end do
      if (mod(i,10).eq.0) print 1,i,nd
1     format(i6,1h:,21i3)
      do j=1,nn
         nnd(nd(j),j)=nnd(nd(j),j)+1
      end do
      call damage03(nn,io,nd,va,co,mm,nt,nprt)
      do j=1,mm
         nres(nt(j),j)=nres(nt(j),j)+1
      end do
  end do
  write(io,2)0,(i,i=1,nn)
2     format(i6,1h:,10i6/7x,10i6)
  do j=1,mm
     write(io,*)'coefficient:',co(j)
     write(io,2)j,nres(:,j)
     suma=0.0d0
     do i=1,nn
        suma=suma+i*nres(i,j)
     end do
     write(io,*)'mean:',suma/dble(ntry)
  end do
  write(io,2)0,(i,i=1,nn)
  do i=1,nn
     write(io,2)i,nnd(i,:)
  end do
  return
  end
```